*Journal of Experimental and Theoretical Physics, Vol. 95, No. 2, 2002, pp. 181–193.*
*Translated from Zhurnal Éksperimental'noĭ i Teoreticheskoĭ Fiziki, Vol. 122, No. 2, 2002, pp. 211–226.*


**GRAVITATION, ASTROPHYSICS**

# Solar Neutrino Flux Measurements by the Soviet–American Gallium Experiment (SAGE) for Half the 22-Year Solar Cycle

**J. N. Abdurashitov[a], E. P. Veretenkin[a], V. M. Vermul[a], V. N. Gavrin[a,*], S. V. Girin[a], V. V. Gorbachev[a], P. P. Gurkina[a], G. T. Zatsepin[a], T. V. Ibragimova[a], A. V. Kalikhov[a], T. V. Knodel[a], I. N. Mirmov[a], N. G. Khairnasov[a], A. A. Shikhin[a], V. E. Yants[a], T. J. Bowles[b], W. A. Teasdale[b], J. S. Nico[c], J. F. Wilkerson[d], B. T. Cleveland[d], and S. R. Elliott[d]**
***SAGE Collaboration***

[a]*Institute for Nuclear Research, Russian Academy of Sciences, pr. Shestidesyatiletiya Oktyabrya 7a, Moscow, 117312 Russia*
[b]*Los Alamos National Laboratory, Los Alamos, New Mexico, 87545 USA*
[c]*National Institute of Standards and Technology, Gaithersburg, Maryland, 20899 USA*
[d]*University of Washington, Seattle, Washington, 98195 USA*
**e-mail: gavrin@adonis.iasnet.ru*
Received February 15, 2002

**Abstract**—We present measurements of the solar neutrino capture rate on metallic gallium in the Soviet–American gallium experiment (SAGE) over a period of slightly more than half the 22-year solar cycle. A combined analysis of 92 runs over the twelve-year period from January 1990 until December 2001 yields a capture rate of $70.8^{+5.3}_{-5.2}$ (stat)$^{+3.7}_{-3.2}$ (sys) SNU for solar neutrinos with energies above 0.233 MeV. This value is slightly more than half the rate predicted by the standard solar model, 130 SNU. We present the results of new runs since April 1998 and analyze all runs combined by years, months, and bimonthly periods beginning in 1990. A simple analysis of the SAGE results together with the results of other solar neutrino experiments gives an estimate of $(4.6 \pm 1.2) \times 10^{10}$ neutrinos cm$^{-2}$ s$^{-1}$ for the flux of the electron *pp* neutrinos that reach the Earth without changing their flavor. The flux of the *pp* neutrinos produced in thermonuclear reactions in the Sun is estimated to be $(7.6 \pm 2.0) \times 10^{10}$ neutrinos cm$^{-2}$ s$^{-1}$, in agreement with the value of $(5.95 \pm 0.06) \times 10^{10}$ neutrinos cm$^{-2}$ s$^{-1}$ predicted by the standard solar model. © *2002 MAIK "Nauka/Interperiodica".*

## 1. INTRODUCTION

The last several years in neutrino astrophysics are characterized by outstanding achievements in solar neutrino studies. This is primarily because the large SuperKamiokande (SK) water Cherenkov detector [1] and the Sudbury neutrino observatory (SNO) [2] were put into operation. These telescopes record high-energy solar neutrinos from $^8$B decay in real time and have high count rates.

The data obtained with these two giant new-generation neutrino telescopes make a crucially important complement to the available data from chlorine and gallium radiochemical experiments [3–5] and from the Kamiokande experiment [6]. Comparison of the SK data on elastic scattering of solar neutrinos by electrons with SNO data on charged currents indicates that, together with electron neutrinos, neutrinos of other flavors arrive at the Earth from the Sun. A combined analysis of the results from all these experiments provides compelling evidence that some of the electron neutrinos produced in thermonuclear reactions in the Sun change their flavor on their way to the Earth.

Investigating the details of the change in the flavor of solar neutrinos requires constructing neutrino telescopes of the next generation. These telescopes will record the low-energy part of the solar neutrino spectrum below 2 MeV, which contains the continuous spectra of *pp* neutrinos and neutrinos from the CNO cycle as well as monoenergetic lines from $^7$Be and *pep* neutrinos.

Despite a number of promising ideas of detecting low-energy neutrinos in real time widely discussed today [7], only radiochemical gallium experiments are currently capable of observing and providing information on this part of the solar neutrino spectrum. The low threshold (233 keV) of the neutrino capture reaction $^{71}$Ga($\nu_e$, $e^-$)$^{71}$Ge [8] allows the principal component of the solar neutrino spectrum, *pp* neutrinos, to be measured. If exotic hypotheses are excluded, the flux of these neutrinos is determined by energy release in the Sun and does not depend on solar-model parameters. These parameters significantly affect the rates of subsequent reactions in the chain of thermonuclear fusion in the Sun.

The expected neutrino capture rate on $^{71}$Ga calculated using the standard solar model (SSM) is $128^{+9}_{-7}$ SNU[1] [9], with the contribution of *pp* neutrinos being

[1] SNU = 1 interaction per second in a target containing $10^{36}$ atoms of the isotope interacting with neutrinos.

dominant, 69.7 SNU. As follows from the same calculations, the contributions of neutrinos from $^7$Be and $^8$B decays are 34.2 and 12.1 SNU, respectively. The independently calculated value of 127.2 SNU [10] may suggest that the neutrino capture rate on gallium is insensitive to solar-model parameters.

From the SNO and SK measurements, we know the neutrino flux from $^8$B decay with a high accuracy and what part of it is produced by the electron neutrinos which reach the Earth. In the immediate future, the KamLAND experiment [11] is expected to significantly reduce the range of possible oscillation parameters for electron neutrinos. This experiment and the BOREXINO experiment [12] will give the $^7$Be neutrino flux with a high accuracy. By subtracting the $^7$Be and $^8$B components of the solar neutrino spectrum from the result of the gallium experiment, we will obtain a fundamental astrophysical parameter, the neutrino flux from the *pp* reaction (with a minor contribution of neutrinos from the *pep* reaction and the CNO cycle). The latter can be determined by comparing the SK results with those of the chlorine experiment. At the end of this paper, we give a preliminary estimate of the *pp*-neutrino flux by using the currently available experimental data. Since only a gallium experiment can provide for these measurements in the foreseeable future, it is crucially important that both gallium experiments, SAGE [4] and GNO [13] (the successor to GALLEX), continue their measurements so asto improve the accuracy of their results.

Previously [4], we described the SAGE experiment in detail, including germanium extraction from the gallium target, the counting of single $^{71}$Ge atoms, and analysis of the data obtained. In [4], we presented the SAGE results for the period from January 1990 until December 1997. In this paper, we briefly describe basic principles of this experiment, perform a statistical analysis of the 1998–2001 data, and present the results of new analyses of some systematic uncertainties. In conclusion, we discuss the importance of the SAGE results for solar and neutrino physics.

## 2. AN OVERVIEW OF THE SAGE EXPERIMENT

### *2.1. The Laboratory of the Gallium–Germanium Neutrino Telescope*

SAGE measurements are carried out at the gallium–germanium neutrino telescope (GGNT) placed in a specially constructed deep underground laboratory at the Baksan Neutrino Observatory (Institute for Nuclear Research, Russian Academy of Sciences) in the Northern Caucasus, at the foot of Mount Elbrus [14]. The underground complex of the GGNT laboratory is located in a horizontal tunnel that runs into the Andyrchi Mountain, at a distance of 3.5 km from the entrance. The main room of the laboratory is an experimental hall 60 m long, 10 m wide, and 12 m high. The rocks above the laboratory produce a shield from cosmic-ray muons that is equivalent to 4700-m-thick water and attenuate the muon flux by a factor of $10^7$. The measured muon flux is $(3.03 \pm 0.10) \times 10^{-9}$ cm$^{-2}$ s$^{-1}$ [15]. To reduce the neutron and gamma-ray background from the surrounding rocks, the hall is clad with 600-mm-thick low-radioactivity concrete and with a 6-mm-thick steel sheet. The flux of neutrons with energy 1.0–11.0 MeV in the laboratory does not exceed $2.3 \times 10^{-7}$ cm$^{-2}$ s$^{-1}$ [16]. There are also rooms for research on analytical chemistry, for a $^{71}$Ge decay detection system, and for a low-background Ge semiconductor detector. Several rooms for auxiliary measurements are in the laboratory buildings located on the surface.

### *2.2. Procedures of the Experiment*

The gallium target of the telescope currently contains about 50 t of gallium in the form of a liquid metal in seven chemical reactors. A measurement of the solar neutrino capture rate (run) begins with the addition to the gallium target of a stable germanium carrier in the form of a Ga–Ge alloy with a known germanium content, in the amount of 350 μg, which is uniformly distributed between all reactors. The reactor contents are well mixed to uniformly distribute germanium in the bulk of gallium.

On completion of the exposure (four weeks), the germanium carrier together with $^{71}$Ge atoms from the solar neutrino capture reaction and from background reactions is extracted from the gallium by using the operations described in [4, 17]. The final stage of chemical extraction involves the synthesis of monogermane ($GeH_4$), which is placed in a proportional counter in a mixture with 70–90% of Xe. The total extraction efficiency, the ratio of the Ge mass in the monogermane to the initial mass of the Ge carrier, generally lies within the range of 80–90%. The systematic uncertainty in the extraction efficiency is 3.4%, mainly due to an uncertainty in the mass of the added and extracted carrier. About 0.1% of the gallium is dissolved during each extraction, passing into a muriatic solution in the form of chloride. The gallium-containing solutions are reprocessed to recover and purify gallium; subsequently, gallium must be returned to the target.

After its filling, the proportional counter is placed in the well of a NaI detector that is within a massive passive shield, where $^{71}$Ge decays are counted for about five months. $^{71}$Ge decays by electron capture with a half-life of 11.43 days. The low-energy Auger electrons from the *K* and *L* shells and the X-ray photons emitted when the electron shells are deexcited produce nearly point ionization in the counter gas. Therefore, the pulse from $^{71}$Ge decay taken from the counter has a rapidly rising leading edge. In contrast, the ionization tracks from most of the background events have an appreciable length, and, accordingly, the fronts of the pulses from such events rise more slowly. Thus, we select event candidates for $^{71}$Ge decay by the pulse energy in

the proportional counter, which must correspond to the energy of the *K* or *L* peak, and by the rise time of the pulse front. In addition, an event should not have coincidences with the pulse from the NaI detector, because no γ-ray photons are emitted during $^{71}$Ge decay.

The electronics for data acquisition was improved as the experiment developed. During the first two years, the amplitude-differentiated pulse (ADP) technique was used. This technique provided the selection of events in the *K* peak (10.4 keV) but could not be used to select events in the *L* peak (1.2 keV), which is more sensitive to instability of the electronics and in which the background is higher. In 1992, an eight-channel counting system was constructed. It consists of a 1-GHz digital oscilloscope that was used to record the pulse shape from the counters. The pulse amplitude and front rise time ($T_N$) can be determined by fitting the recorded pulse shape [18]. All results for the *L* peak and most of the results for the *K* peak were obtained from such an analysis of the pulse shape.

After their filling, the counters are regularly calibrated with a $^{55}$Fe source (5.9 keV) through a window in the counter iron cathode. Additional calibrations with a $^{109}$Cd source, whose emission produces the characteristic radiation of the iron cathode (6.4 keV) along the entire counter length, allow one to make a correction in the $^{71}$Ge peak positions due to the buildups of polymers on the anode wire during prolonged operation of the counter. In addition, the characteristic radiation from a $^{109}$Cd–Se source (1.4 and 11.2 keV) is used to check the energy scale within the measurement range for linearity.

The pulse energy can be determined by integrating the pulse shape for 800 ns after the pulse begins. The positions of the $^{71}$Ge peaks corrected for counter polymerization and the widths of the energy windows corresponding to these peaks, which are taken to be twice the peak width at half maximum, are calculated from the $^{55}$Fe calibration. Increasing the width of the energy windows causes no appreciable increase in the counting efficiency of $^{71}$Ge decays but significantly degrades the signal-to-noise ratio.

If the peak position changes between two calibrations, then the window for energy selection is linearly shifted in time between the two calibrations. The change in amplification between calibrations typically does not exceed a few percent, which gives an uncertainty in the counting efficiency of no more than 3.1%.

In order to determine the rise times of the pulse fronts during $^{71}$Ge decay, we carried out measurements in each counter channel using counters with $^{71}GeH_4$ added to the gas mixture. The rise times $T_N$ for all the events selected within the energy windows of the *K* and *L* peaks were arranged in increasing order. Subsequently an upper limit was set in such a way as to exclude 5% of events. The related small loss of counting efficiency is offset by a significant reduction in the number of background events. The derived ranges for $T_N$ in the *K* and *L* peaks are, respectively, 0.0 to 18.4 ns and 0.0 to 10.0 ns. The variations attributable to gas filling of the counters and to differences of the various counter channels are 1.2 ns, which introduces an uncertainty in the efficiency of about ±1%.

Table 1 gives the parameters of the 35 runs from 1998–2001 that are used for the solar neutrino measurements.

## 3. STATISTICAL ANALYSIS OF THE SOLAR DATA

After the counting of $^{71}$Ge decays in the proportional counter is finished, the selected (according to the criteria) $^{71}$Ge events are called a data set. A maximum of the likelihood function [19] is sought for the events from each data set. In constructing this function, we assume that an event is caused by an unknown constant (in time) background and by $^{71}$Ge decays whose number exponentially decreases with time. To minimize the possible effect of radon and its daughter elements that enter the passive shield during periodic counter calibrations and whose decays can imitate $^{71}$Ge decays, we exclude from our analysis 2.6 h after each closure of the passive shield. The radon that is brought into the gas volume of the counter itself during its filling (several atoms) is very dangerous for measurements of the number of $^{71}$Ge decays in the counters. Most of the radon decays within a counter produce slow pulses with energies above the energy range of the $^{71}$Ge decay detection system (called overflow pulses), but about 8% of the decays of radon and its daughter elements produce fast pulses that are indistinguishable from $^{71}$Ge pulses. The chain of radon decays leads to a long-lived isotope ($^{210}$Pb) after about 50 min, on average; excluding 15 min before each overflow pulse and 3 h after, we remove the overwhelming majority of events from the radon that decays within the counter.

The $^{71}$Ge production rate is determined by the position of the maximum of the likelihood function for each data set. We calculate the statistical error by integrating this function over all possible background count rates. In the derived likelihood function, which now depends on the $^{71}$Ge production rate alone, we find the minimum range of rate which contains 68% of the total area under the curve. This procedure is carried out separately for the events selected in the *L* and *K* peaks. The likelihood function for analysis of several runs (and for a combined analysis of the events selected in the *L* and *K* peaks in individual runs) is obtained by multiplying the likelihood functions for individual data sets with the additional requirement that the $^{71}$Ge production rate per unit gallium mass be constant and that the background count rates be different for each data set. In our analysis, we take into account the small change in the $^{71}$Ge

**Table 1.** The parameters of all runs since April 1998 used in our analysis to determine the solar neutrino flux

| Exposure date | Mean exposure date | Exposure time, days | Ga mass, t | Extraction efficiency | Counter name | Pressure, mm Hg | % $GeH_4$ | Working voltage, V | *K*-peak efficiency | *L*-peak efficiency | Polymerization coefficient |
|---|---|---|---|---|---|---|---|---|---|---|---|
| Apr. 98 | 1998.225 | 44.9 | 48.05 | 0.85 | A13 | 695 | 37.0 | 1480 | 0.243 | 0.219 | 1.01 |
| May 98 | 1998.347 | 30.0 | 51.17 | 0.91 | LY4 | 690 | 29.5 | 1366 | 0.238 | 0.245 | 1.00 |
| July 98 | 1998.477 | 45.6 | 51.06 | 0.90 | A12 | 680 | 32.0 | 1414 | 0.235 | 0.237 | 1.00 |
| Aug. 98 | 1998.611 | 45.7 | 50.93 | 0.89 | LA51 | 660 | 27.0 | 1356 | 0.234 | 0.244 | 1.04 |
| Oct. 98 | 1998.745 | 45.8 | 50.81 | 0.92 | A13 | 680 | 32.0 | 1404 | 0.244 | 0.212 | 1.00 |
| Nov. 98 | 1998.883 | 45.8 | 50.68 | 0.92 | LY4 | 680 | 26.5 | 1322 | 0.238 | 0.244 | 1.00 |
| Jan. 99 | 1999.014 | 44.7 | 50.54 | 0.92 | A12 | 700 | 30.0 | 1398 | 0.239 | 0.241 | 1.00 |
| Feb. 99 | 1999.130 | 38.7 | 50.43 | 0.89 | LA51 | 705 | 11.0 | 1194 | 0.248 | 0.234 | 1.05 |
| Apr. 99 | 1999.279 | 51.7 | 50.29 | 0.89 | A13 | 665 | 13.5 | 1206 | 0.253 | 0.231 | 1.05 |
| June 99 | 1999.417 | 46.7 | 50.17 | 0.87 | LY4 | 670 | 11.0 | 1140 | 0.246 | 0.239 | 1.00 |
| July 99 | 1999.551 | 45.7 | 50.06 | 0.90 | L116 | 635 | 12.5 | 1164 | 0.243 | 0.244 | 1.03 |
| Sept. 99 | 1999.685 | 45.7 | 49.91 | 0.91 | LA51 | 660 | 11.5 | 1172 | 0.242 | 0.238 | 1.05 |
| Oct. 99 | 1999.801 | 38.7 | 49.78 | 0.90 | A13 | 665 | 12.5 | 1186 | 0.254 | 0.202 | 1.01 |
| Jan. 00 | 2000.035 | 28.8 | 49.59 | 0.91 | LA51 | 700 | 13.5 | 1224 | 0.324 | 0.310 | 1.05 |
| Feb. 00 | 2000.127 | 30.7 | 49.48 | 0.83 | LY4 | 646 | 10.4 | 1130 | 0.320 | 0.316 | 1.01 |
| Mar. 00 | 2000.207 | 28.8 | 49.42 | 0.91 | A13 | 665 | 14.5 | 1206 | 0.332 | 0.329 | 1.10 |
| May 00 | 2000.359 | 30.7 | 49.24 | 0.92 | LA116 | 705 | 14.0 | 1244 | 0.329 | 0.315 | 1.03 |
| June 00 | 2000.451 | 33.7 | 49.18 | 0.84 | LA51 | 652 | 12.0 | 1160 | 0.317 | 0.314 | 1.03 |
| July 00 | 2000.541 | 32.0 | 49.12 | 0.92 | LY5 | 670 | 13.8 | 1182 | 0.321 | 0.316 | 1.01 |
| Aug. 00 | 2000.626 | 31.3 | 49.06 | 0.73 | A13 | 707 | 9.5 | 1176 | 0.343 | 0.321 | 1.08 |
| Sept. 00 | 2000.701 | 27.7 | 49.00 | 0.89 | A12 | 690 | 14.7 | 1224 | 0.324 | 0.312 | 1.00 |
| Oct. 00 | 2000.796 | 30.7 | 48.90 | 0.84 | LA116 | 734 | 9.4 | 1188 | 0.337 | 0.303 | 1.03 |
| Nov. 00 | 2000.876 | 28.7 | 48.84 | 0.93 | LA51 | 680 | 11.9 | 1196 | 0.345 | 0.330 | 1.03 |
| Dec. 00 | 2000.958 | 30.7 | 48.78 | 0.93 | LY4 | 697 | 12.0 | 1174 | 0.327 | 0.312 | 1.02 |
| Feb. 01 | 2001.122 | 29.8 | 41.11 | 0.87 | LA116 | 287 | 9.2 | 1144 | 0.330 | 0.314 | 1.04 |
| Mar. 01 | 2001.214 | 33.4 | 48.53 | 0.92 | LA51 | 635 | 13.5 | 1180 | 0.314 | 0.317 | 1.02 |
| Apr. 01 | 2001.290 | 22.7 | 48.43 | 0.90 | YCT1 | 695 | 13.1 | 1210 | 0.344 | 0.333 | 1.00 |
| May 01 | 2001.373 | 31.7 | 48.37 | 0.88 | YCT2 | 625 | 14.9 | 1178 | 0.332 | 0.342 | 1.00 |
| June 01 | 2001.469 | 31.7 | 48.27 | 0.92 | YCT3 | 678 | 12.2 | 1190 | 0.342 | 0.334 | 1.00 |
| July 01 | 2001.547 | 23.7 | 48.17 | 0.93 | LA116 | 690 | 12.7 | 1196 | 0.328 | 0.315 | 1.03 |
| Aug. 01 | 2001.624 | 28.7 | 48.11 | 0.59 | A12 | 768 | 7.2 | 1148 | 0.340 | 0.302 | 1.00 |
| Sept. 01 | 2001.701 | 27.7 | 48.06 | 0.90 | YCT1 | 665 | 15.0 | 1204 | 0.338 | 0.337 | 1.00 |
| Oct. 01 | 2001.793 | 30.7 | 47.96 | 0.88 | YCT2 | 758 | 12.2 | 1210 | 0.354 | 0.326 | 1.00 |
| Nov. 01 | 2001.887 | 34.8 | 47.91 | 0.92 | YCT3 | 685 | 14.2 | 1210 | 0.342 | 0.335 | 1.00 |
| Dec. 01 | 2001.955 | 22.8 | 47.86 | 0.86 | YCT4 | 685 | 11.4 | 1176 | 0.344 | 0.333 | 1.00 |

Note: The *K*- and *L*-peak efficiencies are defined as the ratio of the number of $^{71}$Ge decays recorded in the corresponding energy range to the total number of $^{71}$Ge decays. The efficiencies include the efficiencies of energy selection (0.98) and selection by the pulse-front rise time (0.95); they take into account the fact that the data acquisition system in 1996–1999 contained an error in the trigger logic (0.76). The polymerization coefficient is the correction coefficient of the energy scale determined from the peak ratio in $^{55}$Fe and $^{109}$Cd calibrations.

production rate due to the orbital eccentricity of the Earth which leads to a 3% annual change in distance from the Sun. The position of the maximum of the combined likelihood function sets the global $^{71}$Ge production rate. The 68% confidence interval is determined by the production rates at which the function decreases by a factor of 0.606 from its maximum value, all other variables being maximized. The results of our analysis

**Table 2.** Results of our analysis of the data from all runs since April 1998

| Extraction time | Number of $^{71}$Ge candidate events | Number of $^{71}$Ge decays | Result, SNU | 68% confidence interval, SNU | $Nw^2$ | Probability, % |
|---|---|---|---|---|---|---|
| Apr. 98 | 39 | 5.4 | 75 | 26–134 | 0.052 | 72 |
| May 98 | 23 | 3.4 | 44 | 10–88 | 0.051 | 68 |
| July 98 | 22 | 4.8 | 61 | 24–108 | 0.065 | 52 |
| Aug. 98 | 33 | 3.6 | 46 | 5–97 | 0.039 | 84 |
| Oct. 98 | 40 | 3.8 | 45 | 4–95 | 0.028 | 95 |
| Nov. 98 | 32 | 5.9 | 67 | 28–116 | 0.101 | 30 |
| Jan. 99 | 21 | 4.5 | 56 | 15–107 | 0.036 | 84 |
| Feb. 99 | 16 | 1.6 | 24 | 0–67 | 0.114 | 28 |
| Apr. 99 | 10 | 1.8 | 38 | 5–83 | 0.105 | 36 |
| June 99 | 14 | 12.9 | 172 | 123–232 | 0.048 | 80 |
| July 99 | 17 | 5.5 | 103 | 49–172 | 0.118 | 20 |
| Sept. 99 | 20 | 7.1 | 93 | 43–154 | 0.099 | 28 |
| Oct. 99 | 16 | 10.0 | 138 | 80–206 | 0.066 | 56 |
| Jan. 00 | 24 | 5.4 | 63 | 23–111 | 0.060 | 59 |
| Feb. 00 | 21 | 9.1 | 107 | 63–157 | 0.058 | 55 |
| Mar. 00 | 19 | 10.1 | 117 | 78–165 | 0.046 | 79 |
| May 00 | 15 | 0.0 | 0 | 0–32 | 0.143 | 40 |
| June 00 | 17 | 1.4 | 23 | 0–75 | 0.179 | 17 |
| July 00 | 29 | 6.4 | 69 | 33–111 | 0.088 | 34 |
| Aug. 00 | 14 | 5.2 | 74 | 39–117 | 0.086 | 33 |
| Sept. 00 | 30 | 9.2 | 111 | 64–166 | 0.093 | 24 |
| Oct. 00 | 14 | 3.0 | 37 | 8–75 | 0.020 | 99 |
| Nov. 00 | 25 | 2.9 | 32 | 0–73 | 0.208 | 9 |
| Dec. 00 | 27 | 7.6 | 81 | 43–127 | 0.062 | 68 |
| Feb. 01 | 21 | 6.3 | 79 | 43–125 | 0.088 | 34 |
| Mar. 01 | 18 | 3.8 | 44 | 14–80 | 0.120 | 24 |
| Apr. 01 | 17 | 6.7 | 76 | 43–117 | 0.074 | 45 |
| May 01 | 21 | 11.9 | 127 | 90–171 | 0.088 | 31 |
| June 01 | 20 | 9.4 | 93 | 57–135 | 0.025 | 96 |
| July 01 | 9 | 2.1 | 24 | 0–58 | 0.033 | 92 |
| Aug. 01 | 21 | 5.4 | 90 | 38–155 | 0.065 | 57 |
| Sept. 01 | 10 | 2.1 | 22 | 0–53 | 0.139 | 18 |
| Oct. 01 | 12 | 7.5 | 73 | 44–109 | 0.082 | 41 |
| Nov. 01 | 15 | 2.6 | 23 | 0–54 | 0.084 | 38 |
| Dec. 01 | 9 | 5.2 | 62 | 34–101 | 0.063 | 70 |
| Combined result | 711 | 191.8 | 67 | 60–74 | 0.080 | 42 |

Note: The test statistics of $Nw^2$ is described and interpreted in [20]. The probability that the sequence of measured events arose from the combination of $^{71}$Ge decay plus background events at a constant count rate was calculated by the Monte Carlo method and is given in the last column. The accuracy of the quoted probabilities is approximately 1.5% for individual runs and about 4% for the combined result.

of recent extractions are given in Table 2. The results of all SAGE runs are shown in Fig. 1.

After the publication of our paper [4], which contains the measurements made from January 1990 until December 1997, we found that we used an erroneous data acquisition program from June 1996 until December 1999. At the beginning of this period, a failed electronics module in the data acquisition system was replaced, which required modifying the system for

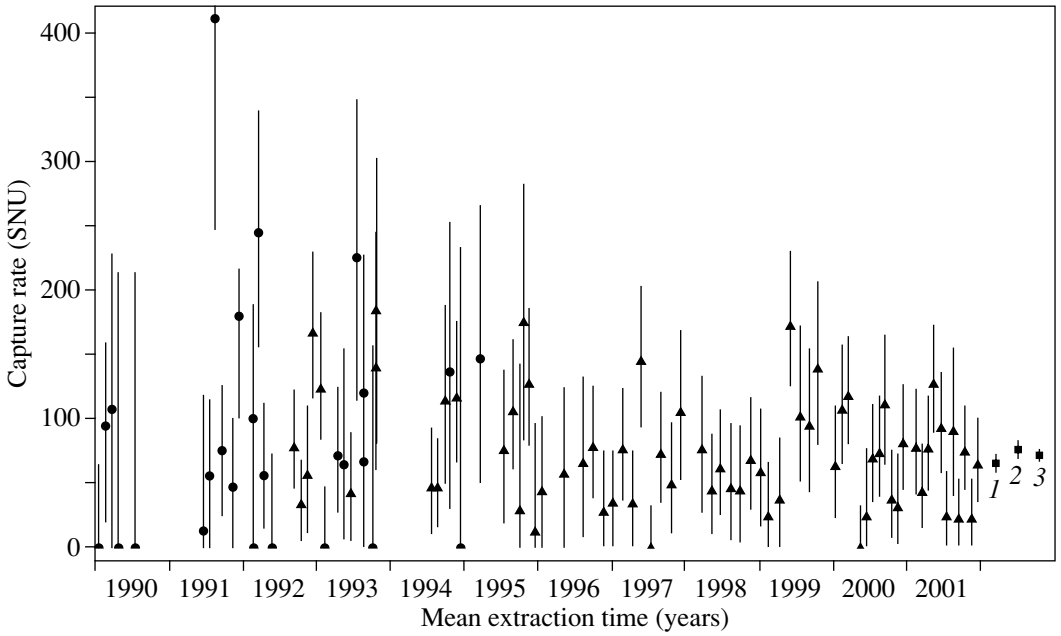


**Fig. 1.** The capture rate from all SAGE extractions versus time: the triangles are for the *L* and *K* peaks and the circles are for the *K* peak alone; the vertical bars near each point correspond to a statistical error of 68%. (*1*) The results of analysis for the *L* peak, *(2*) the results of analysis for the *K* peak, and (*3*) the combined result for the entire data set.

determining the coincidences of the pulses from events in the NaI detector and events in the proportional counters. The new system entailed a change in the data acquisition program and an error in the trigger logic was introduced. Because of this error, 23.9 ± 0.4 (stat) ± 0.5 (sys)% of triggers were lost. This error artificially underestimated the results of individual runs which were counting during this period, and affected the combined result. The corrected results are given in [21].

**Table 3.** Systematic effects and the related uncertainties in the measured neutrino capture rate (SNU). The extraction and counting efficiencies are based on a capture rate of 70.8 SNU

| | | |
|---|---|---|
| Extraction efficiency | Ge-carrier mass | ±1.5 |
| | Extracted Ge mass | ±1.8 |
| | Ge-carrier residue in reactor | ±0.6 |
| | Gallium mass | ±0.2 |
| Counting efficiency | Volume efficiency | ±1.3 |
| | Gain shifts | +2.3 |
| | Resolution | −0.4, +0.5 |
| | Rise time limits | ±0.7 |
| | Exposure time and time before counting begins | ±0.6 |
| Backgrounds | Neutrons | < −0.02 |
| | U and Th | < −0.7 |
| | Cosmic-ray muons | < −0.7 |
| | Internal radon | < −0.2 |
| | External radon | 0 |
| | Other Ge isotopes | < −0.7 |
| Total | | −3.2, +3.7 |

## 4. SYSTEMATIC EFFECTS

Table 3 presents the systematic effects that can affect the measured capture rate of solar neutrinos. These effects can be arbitrarily broken down into three main categories: uncertainties related to the extraction efficiency, the counting efficiency of $^{71}$Ge decays, and backgrounds. Some of these effects were considered above, and the remaining ones are briefly discussed in this section. The counter efficiency was determined in a series of measurements with different gas fillings; these fillings contained $^{71}$Ge, $^{37}$Ar, and $^{69}$Ge. The uncertainties in the measured counter efficiency are attributable to uncertainties in the volume efficiency, edge effects, and gas-mixture composition. A quadratic summation of these effects yields an uncertainty of ±1.8% in the counter efficiency.

The uncertainties also result from the systematic effects attributable to the background production sources of germanium isotopes in the gallium target and radon decays inside and near the counters. Limits on the $^{71}$Ge production rate by the (*n*, *p*) reaction on $^{71}$Ga were obtained from the measured fluxes of fast neutrons [16, 22] and cosmic-ray muons in the underground laboratory [15]. The limiting concentrations of U and Th in gallium, which can also give rise to germanium isotopes, were measured with a germanium semiconductor detector [23] and a mass spectrometer [24]. The total $^{71}$Ge production rate from all these processes does not exceed 1 SNU.

Radon is removed from the internal volume of the passive shield where the counters are located by evaporating liquid nitrogen. Special antiradon gas mixture purification procedures are used during the filling to reduce the possibility of radon penetration into the counter. The effect of the remaining radon on the measured $^{71}$Ge production rate was studied through special measurements with counters with the addition of some amount of radon to their gas mixture and when investigating the counter response to external γ-ray radiation [25, 26]. The upper limits on the systematic error due to radon decays inside and outside the counter obtained from these studies are 0.2 and 0.03 SNU, respectively.

The decays of $^{68}$Ge and $^{69}$Ge produced in the gallium target in background processes can imitate $^{71}$Ge events. The amount of $^{68}$Ge produced in cosmic-ray muon interactions can be estimated from the expected $^{71}$Ge production rate in muon interactions. It was found to be $0.012 \pm 0.006$ atom per day in 60 t of gallium [4, 27]. For the measured ratio of the $^{68}$Ge and $^{71}$Ge production cross sections in the reactions with gallium of muons with energy of 280 GeV equal to $2.1 \pm 0.05$ [28] in 50 t of gallium per day, $0.022 \pm 0.013$ $^{68}$Ge atoms are produced. For the $^{68}$Ge half-life of 271 days, these pulses are distributed almost uniformly in time during the counting, increasing only the mean background count rate. However, during the initial counting period, these pulses can cause an increase in the $^{71}$Ge count rate. Monte Carlo calculations show that for typical parameters of our measurements—an exposure time of 30 days, a gallium mass of 50 t, an extraction efficiency of 0.9, a counting efficiency ($L$ peak + $K$ peak) of 0.6, and a background count rate ($L$ peak + $K$ peak) of 0.175 event per day—a $^{68}$Ge production rate of 0.022 event per day gives a contribution of 0.0085 event per day to the $^{71}$Ge production rate, which is equivalent to 0.05 SNU.

The $^{69}$Ge isotope is produced in the gallium target through the interaction of α particles from internal radioactivity of the target and the neutrons emitted by the surrounding rocks and in the interactions of solar neutrinos with cosmic-ray muons. The $^{69}$Ge production rate in 60 t of gallium is 0.21 atoms per day [4] with an uncertainty of about 50%. Since most of the $^{69}$Ge decays are accompanied by γ-ray radiation recorded by the NaI detector with 90% efficiency and since the counter begins to count about 1.5 days after extraction, only 0.045 events from $^{69}$Ge are observed in one run; this is a factor of 100 fewer than the mean number of recorded $^{71}$Ge decays. Thus, the background effect from $^{69}$Ge is no more than 0.7 SNU.

The capabilities of the $^{71}$Ge decay detection system and the large number of measurements allowed us to search for events related to $^{68}$Ge and $^{69}$Ge decays in the solar runs [29]. The event selection techniques and efficiency were determined with allowance made for peculiarities of the decays of these isotopes. The inferred $^{68}$Ge production rate is $0.18^{+0.13}_{-0.12}$ atom in 60 t of gallium per day, which is approximately a factor of 7 higher than the expected value, although these values are in agreement within the error limits. Since the $^{68}$Ge production rate was derived from muon experiments with smaller errors, we use this value to determine the uncertainty. The possibility of directly measuring the production rate of germanium isotopes in cosmic-ray muon interactions for the underground conditions of the Baksan Neutrino Observatory (Institute for Nuclear Research, Russian Academy of Sciences) was explored in [29].

A similar search for $^{69}$Ge events shows that the $^{69}$Ge production rate in 60 t of gallium does not exceed 0.49 atom per day. This is in good agreement with the above value. The inferred constraint does not rule out the possibility that the production rate of this isotope during cosmic-ray muon interactions can be higher than its predicted value, which may be indicated by analysis of $^{68}$Ge events.

## 5. RESULTS

In this section, we present the measurements of the solar neutrino capture rate in gallium performed from January 1990 until December 2001. The capture rate determined by analyzing 92 runs and 158 individual data sets is $70.8^{+5.3}_{-5.2}$ SNU. Here, only the statistical uncertainties are given. We selected 1723 events within the designated boundaries of the $L$ and $K$ peaks of $^{71}$Ge, 406.4 of which were attributed to $^{71}$Ge by a time analysis (the total live counting time is 29.5 yr). The results of our analysis of the events selected separately in the $L$ and $K$ peaks are $64.8^{+8.5}_{-8.2}$ and $74.4^{+6.8}_{-6.6}$ SNU, respectively. Agreement between these two results serves as a check on the quality of the event selection criteria. The total systematic uncertainty is obtained by a quadratic summation of all the systematic contributions presented in Table 3. Thus, the SAGE result is $70.8^{+5.3+3.7}_{-5.2-3.2}$ SNU. For comparison, the latest GNO result (including GALLEX data) is $74.1^{+5.4+4.0}_{-5.4-4.2}$ SNU [13]. With the quadratic summation of statistical and systematic uncertainties, the SAGE result is $70.8^{+6.5}_{-6.1}$ SNU.

### *5.1. Checking the $^{71}$Ge Extraction Efficiency*

The technologies used in the experiment allow a few $^{71}$Ge atoms produced by neutrino interactions to be chemically extracted from the target containing $5 \times 10^{29}$ gallium atoms with a high, well-known efficiency. To measure this efficiency, about 350 μg of a stable germanium carrier is added to the gallium at the beginning of each exposure. In this case, given the carrier, there are $10^{11}$ gallium atoms per one germanium atom. We carried out a number of auxiliary measurements, which

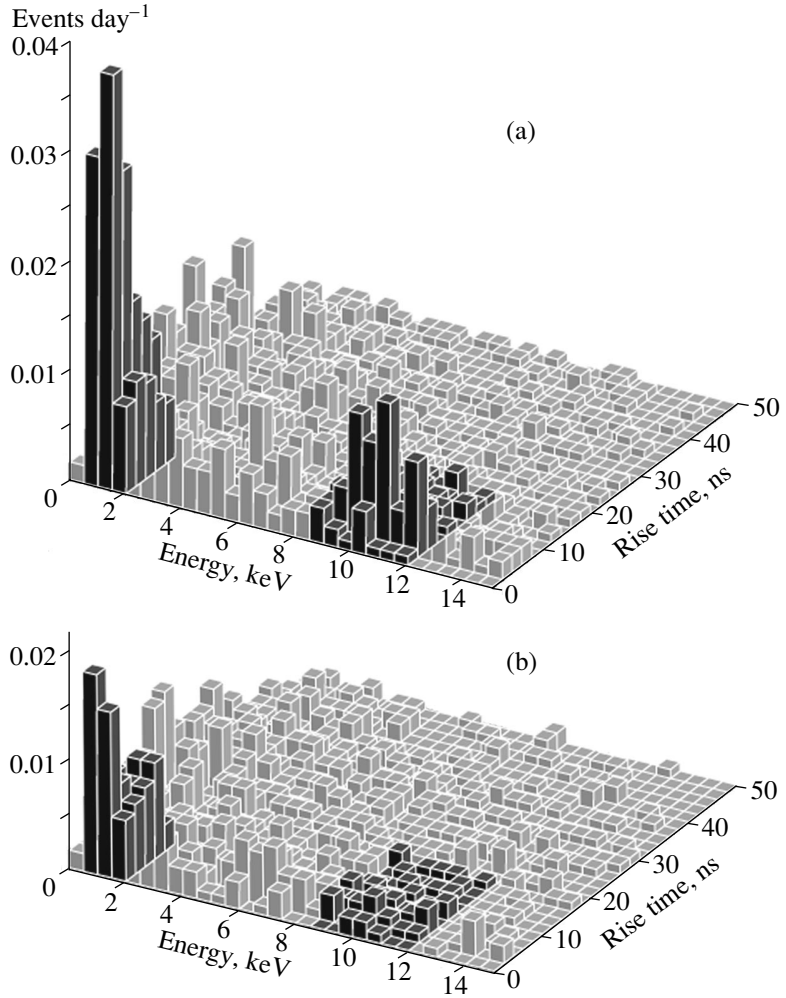


**Fig. 2.** The distribution of events in energy and in pulse rise time for all the runs in which these quantities were determined from the pulse shape. (a) The events recorded within the first 22.86 days of counting after extraction for all runs (except the May 1996 extraction). The total live counting time is 1169.9 days. The positions of the *L* and *K* peaks of $^{71}$Ge determined from calibrations are indicated in dark gray. (b) The same histogram for all the events that were recorded during an equal live time interval beginning 100 days after extraction.

confirmed the efficiency of our technology for extracting single $^{71}$Ge atoms from metallic gallium.

A germanium carrier with a known amount of $^{71}$Ge included in its composition was added to the reactor containing 7 t of gallium. We made three extractions and measured the number of atoms of extracted $^{71}$Ge in each of them. Our results [17] showed that the extraction efficiencies of a stable germanium carrier and $^{71}$Ge are the same.

The objective of the second experiment was to determine whether $^{71}$Ge, whose atoms can be produced in the reverse β-decay reaction in an excited or ionized state, forms chemical bonds that prevent its efficient extraction. We prepared and carried out several measurements to directly test this possibility, in which the β decay of radioactive gallium isotopes was observed in liquid metallic gallium. Our result [17] matches the expected value with 10% accuracy.

We checked the entire experiment (i.e., completely checked all experimental procedures, including the efficiency of chemical extraction, the counter efficiency, and the techniques of analysis) by using an artificial source of $^{51}$Cr neutrinos with an intensity of 19.1 PBq (517 kCi) [30, 31]. The result, expressed as the ratio of the measured $^{71}$Ge production rate to the expected rate, was $(0.95 \pm 0.12)$. This is evidence that the experimental efficiencies we use are correct and justifies the fundamental assumption of radiochemical experiments that the extraction efficiency of atoms produced in neutrino interactions does not differ from the carrier extraction efficiency.

### *5.2. Checking the Results of Analysis*

Figure 2 provides clear evidence that we actually observe $^{71}$Ge decay. This figure shows all events that survive the time cuts and that had no coincidences with pulses from the NaI detector. The expected posi-

tions of the *L* and *K* peaks of $^{71}$Ge are highlighted in dark gray. These peaks are clearly present in the upper histogram, but they are absent in the lower panel, because $^{71}$Ge has decayed by that time. Outside the peak regions, the numbers of events in Figs. 2a and 2b are approximately equal, because these events mostly have a background origin.

**5.2.1. The time sequence of events.** A major hypothesis of our analysis is that the time sequence of observed events for each run is a superposition of events from the decay of a fixed number of $^{71}$Ge atoms and background events that occur at a constant rate. The quantity $Nw^2$ [20] and the corresponding fitting probability gives a quantitative measure of how well the counting data fit this hypothesis. These quantities, which were calculated for each data set, are presented in Table 2. There are runs with a low fitting probability, but the number of such runs is no more than that expected for normal statistical variations.

The $Nw^2$ method can also be used to estimate the fitting quality of the combined time sequences for all events of the *L* and *K* peaks for any combination of runs. The test statistics for the combined data set from all runs is $Nw^2 = 0.053$; the corresponding fitting probability is $(72 \pm 4.5)\%$. The fitting quality is seen from Fig. 3, in which the mean count rate of events in the *L* and *K* peaks from all runs is plotted against the time elapsed after extraction. An additional quantitative confirmation that $^{71}$Ge is counted in the experiment can be obtained if the decay constant is allowed in the likelihood function to be a free parameter, as are the $^{71}$Ge production rate and all background count rates. The half-life determined in this way for all the selected events in the *L* and *K* peaks is $9.7^{+1.5}_{-1.3}$ days, in agreement with the measured value of 11.43 days [32].

**5.2.2. The $^{71}$Ge production rate.** Another hypothesis of our analysis is that the $^{71}$Ge production rate is constant with time. As we see from Fig. 1, there are no appreciable deviations of the rate from its mean value within large statistical uncertainties.

The constancy of the production rate can also be considered by using the distribution function of the production rate, $C(p)$, defined as the fractional number of data sets in which the production rate is less than $p$. Figure 4 shows this distribution for all experimental data sets. Also shown here for comparison is the distribution obtained by the Monte Carlo method by assuming that the true production rate is 70.8 SNU. The two curves are close to each other, and they can be compared by calculating the test statistics $Nw^2$ [20]. This calculation yields $Nw^2 = 0.337$, which corresponds to a probability of 11%.

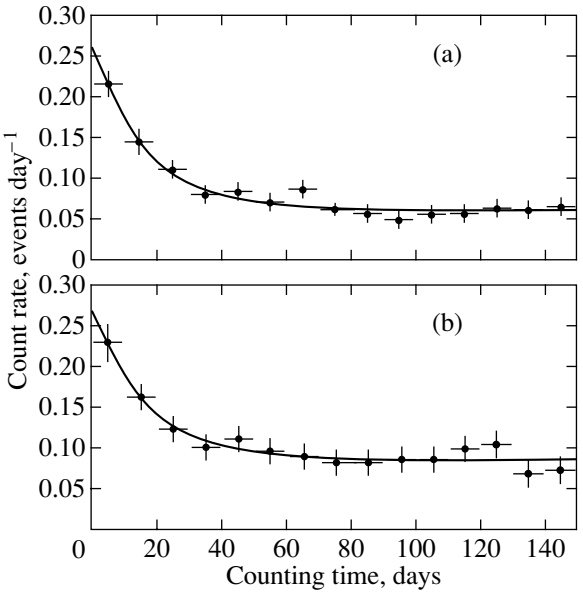


**Fig. 3.** The mean count rate of the events selected in the (a) *K* and (b) *L* peaks in all the runs since January 1990. The solid line represents the curve of $^{71}$Ge decay with a half-life of 11.4 days plus a constant background count rate of events. The errors indicated by vertical bars near each point are proportional to the square root of the number of events. The horizontal bars represent the ±5-day time intervals within which the mean count rate of events is taken.

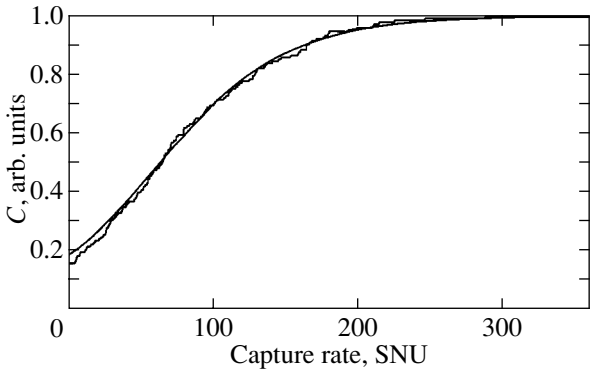


**Fig. 4.** Cumulative distribution functions for the neutrino capture rate measured in 158 SAGE data sets (histogram) and calculated by the Monte Carlo method (solid line). The capture rate in Monte Carlo calculations was taken to be 70.8 SNU.

### *5.3. Combining Data by Time*

If vacuum oscillations are responsible for the low measured capture rate of neutrinos by gallium compared to that predicted by the SSM, then one might expect seasonal variations in the capture rate [33, 34]. Other phenomena can also lead to temporal variations (see, e.g., [35, 36]). Table 4 presents the results of our analysis of the SAGE runs combined in different ways—by months, by pairs of months, and by years. In none of these combinations is there irrefutable evidence of temporal variations. The results of our analysis of the runs combined by years are shown in Fig. 5. We see

**Table 4.** Results of our analysis of the data from SAGE runs combined by years, by months, and by pairs of months

| Exposure period | Number of data sets | Number of $^{71}$Ge-candidate events | Number fit to $^{71}$Ge | Result, SNU | 68% confidence interval, SNU | $Nw^2$ | Probability, % |
|---|---|---|---|---|---|---|---|
| 1990 | 5 | 43 | 4.9 | 43 | 2–78 | 0.260 | 9 |
| 1991 | 6 | 59 | 25.5 | 112 | 82–145 | 0.120 | 17 |
| 1992 | 13 | 145 | 39.8 | 76 | 59–95 | 0.047 | 68 |
| 1993 | 15 | 97 | 33.2 | 84 | 62–105 | 0.199 | 6 |
| 1994 | 10 | 155 | 24.1 | 73 | 51–98 | 0.027 | 95 |
| 1995 | 13 | 210 | 37.7 | 102 | 77–129 | 0.041 | 82 |
| 1996 | 10 | 121 | 19.4 | 56 | 34–79 | 0.064 | 51 |
| 1997 | 16 | 183 | 35.7 | 62 | 48–78 | 0.057 | 62 |
| 1998 | 12 | 189 | 26.7 | 56 | 39–75 | 0.064 | 60 |
| 1999 | 14 | 114 | 40.8 | 87 | 66–110 | 0.068 | 33 |
| 2000 | 22 | 235 | 62.2 | 67 | 55–80 | 0.102 | 29 |
| 2001 | 22 | 173 | 64.4 | 65 | 55–76 | 0.050 | 70 |
| Jan. | 11 | 129 | 24.8 | 58 | 37–80 | 0.082 | 35 |
| Feb. | 12 | 101 | 25.5 | 60 | 44–77 | 0.045 | 74 |
| Mar. | 9 | 129 | 34.5 | 102 | 79–127 | 0.043 | 78 |
| Apr. | 9 | 80 | 16.9 | 54 | 37–73 | 0.072 | 39 |
| May | 12 | 114 | 34.7 | 75 | 59–94 | 0.051 | 62 |
| June | 11 | 101 | 33.6 | 79 | 58–102 | 0.175 | 5 |
| July | 15 | 176 | 26.6 | 52 | 37–69 | 0.091 | 35 |
| Aug. | 15 | 161 | 38.7 | 78 | 60–96 | 0.058 | 51 |
| Sept. | 20 | 220 | 48.5 | 68 | 54–84 | 0.035 | 91 |
| Oct. | 17 | 169 | 40.3 | 73 | 56–91 | 0.080 | 45 |
| Nov. | 15 | 197 | 37.6 | 59 | 44–75 | 0.033 | 90 |
| Dec. | 12 | 147 | 46.4 | 105 | 84–127 | 0.040 | 89 |
| Jan. + Feb. | 23 | 230 | 50.5 | 59 | 46–73 | 0.095 | 34 |
| Mar. + Apr. | 18 | 209 | 49.2 | 75 | 61–91 | 0.026 | >99 |
| May + June | 23 | 215 | 68.0 | 77 | 63–91 | 0.111 | 10 |
| July + Aug. | 30 | 337 | 65.4 | 65 | 53–78 | 0.075 | 50 |
| Sept. + Oct. | 37 | 389 | 88.7 | 71 | 60–82 | 0.041 | 85 |
| Nov. + Dec. | 27 | 344 | 84.3 | 78 | 66–91 | 0.040 | 85 |
| Feb. + Mar. | 21 | 230 | 58.8 | 77 | 63–91 | 0.037 | 84 |
| Apr. + May | 21 | 194 | 50.8 | 66 | 54–79 | 0.049 | 60 |
| June + July | 26 | 277 | 58.7 | 63 | 50–77 | 0.081 | 42 |
| Aug. + Sept. | 35 | 381 | 87.2 | 73 | 61–84 | 0.043 | 84 |
| Oct. + Nov. | 32 | 366 | 78.1 | 66 | 54–78 | 0.044 | 82 |
| Dec. + Jan. | 23 | 276 | 73.6 | 84 | 70–99 | 0.059 | 65 |
| Feb. + Nov. | 27 | 298 | 63.1 | 59 | 48–71 | 0.017 | 99 |
| Mar. + Oct. | 26 | 298 | 75.1 | 84 | 71–99 | 0.062 | 66 |
| Apr. + Sept. | 29 | 300 | 64.3 | 63 | 52–75 | 0.042 | 86 |
| May + Aug. | 27 | 275 | 73.3 | 77 | 64–89 | 0.045 | 75 |

Note: The runs are assigned to each time interval in accordance with the mean exposure time. The accuracy of estimating the probability is approximately 4%.

from this figure that the neutrino capture rate was constant during the entire data acquisition period. The test statistics under the assumption of a constant capture rate, 70.8 SNU, is $\chi^2 = 6.6$; for 11 degrees of freedom, this corresponds to a 83% probability.

## 6. THE *pp*-NEUTRINO FLUX

One of the prime objectives of the gallium experiment is to obtain the information required to determine the *pp*-neutrino flux that arrives at the Earth. In this section, we assess the state of this problem by using the currently available results of all solar neutrino experiments.

As follows from the SAGE, GALLEX, and GNO experiments, the mean capture rate of neutrinos in the gallium experiment is $72 \pm 5$ SNU. This rate is the sum of the rates from all components of the solar neutrino flux, which we designate as $[pp + {}^7\mathrm{Be} + \mathrm{CNO} + pep + {}^8\mathrm{B}|\mathrm{Ga}]_{\mathrm{exp}}$, where the subscript "exp" indicates that this is an experimentally measured quantity. Here, we ignore the *hep* neutrinos, because the contribution of this component is negligible, 0.05% of the total capture rate predicted by the SSM [9]. The only known component of the solar electron neutrino flux is $^8$B neutrinos, whose flux was measured by SNO: $[{}^8\mathrm{B}|\mathrm{CNO}]_{\mathrm{exp}} = (1.75 \pm 0.15) \times 10^6$ electron neutrinos cm$^{-2}$ s$^{-1}$ [2]. The measured SNO and SK spectra are similar in shape to the spectrum predicted by the SSM. The measured SNO flux of electron neutrinos and the capture cross section for $^8$B neutrinos from the SSM ($2.40^{+0.77}_{-0.36} \times 10^{-42}$ cm$^2$) can be used to determine the contribution of neutrinos from $^8$B to the capture rate measured in gallium experiments, because the cross section for neutrino capture by gallium increases sharply with energy. This yields

$$[{}^8\mathrm{B}\,|\,\mathrm{Ga}]_{\mathrm{exp}} = 4.2^{+1.4}_{-0.7}\ \mathrm{SNU}.$$

Subtracting this value from the total capture rate measured in gallium yields the contribution in a gallium experiment from *pp* neutrinos and intermediate-energy neutrinos

$$[pp + {}^7\mathrm{Be} + \mathrm{CNO} + pep|\mathrm{Ga}]_{\mathrm{exp}} = 67.8^{+5.1}_{-5.2}\ \mathrm{SNU}.$$

The measured neutrino capture rate in a chlorine experiment is

$$[{}^7\mathrm{Be} + {}^8\mathrm{B} + \mathrm{CNO} + pep|\mathrm{Cl}]_{\mathrm{exp}} = 2.56 \pm 0.23\ \mathrm{SNU}$$

[3]. We again ignored the contribution of *hep* neutrinos, because it accounts for a mere 0.5% of the total capture rate predicted by the SSM. Since neutrinos with energies above 5 MeV give a dominant contribution in a chlorine experiment, we can again use the measured SNO flux and the cross section calculated for the SSM,

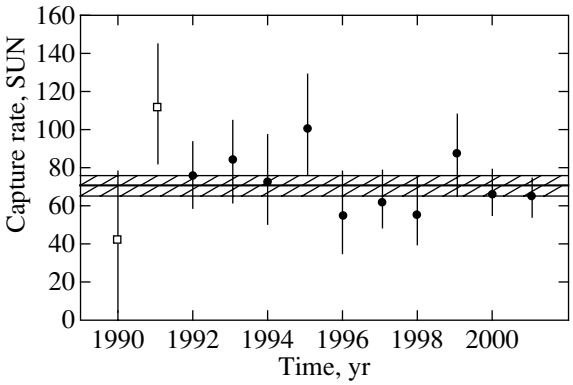


**Fig. 5.** Results of the measurements combined by years; open and filled symbols refer to *K* and *K* + *L* peaks, respectively; the hatched region corresponds to the SAGE result of $70.8^{+5.3}_{-5.2}$ SNU. The data shown have a statistical error of 68%.

$(1.14 \pm 0.04) \times 10^{-42}$ cm$^2$. Thus, the contribution of $^8$B neutrinos is

$$[{}^8\mathrm{B}\,|\,\mathrm{Cl}]_{\mathrm{exp}} = 2.0 \pm 0.2\ \mathrm{SNU}.$$

Subtracting this component yields the contribution of intermediate-energy neutrinos to the chlorine experiment

$$[{}^7\mathrm{Be} + \mathrm{CNO} + pep|\mathrm{Cl}]_{\mathrm{exp}} = 0.56 \pm 0.29\ \mathrm{SNU}.$$

The effect of neutrino oscillations is generally taken into account by introducing the so-called survival factor, the probability that neutrinos will preserve their flavor on their way to the Earth. For intermediate-energy neutrinos in the chlorine experiment, this factor can be determined from the ratio of the measured capture rate to that predicted by the SSM,

$$[{}^7\mathrm{Be} + \mathrm{CNO} + pep|\mathrm{Cl}]_{\mathrm{SSM}} = 1.79 \pm 0.23\ \mathrm{SNU}.$$

If we assume that the survival factor in the range of intermediate energies changes only slightly, then we may set it equal to

$$\frac{[{}^7\mathrm{Be} + \mathrm{CNO} + pep|\mathrm{Cl}]_{\mathrm{exp}}}{[{}^7\mathrm{Be} + \mathrm{CNO} + pep|\mathrm{Cl}]_{\mathrm{SSM}}} = 0.31 \pm 0.17.$$

Since neutrinos from $^7$Be in the range of intermediate energies mainly contribute to the result of the chlorine experiment and since their spectrum is a monoenergetic line, the error in this factor can be estimated by assuming that the relative contribution of the remaining components to the error is the same as their predicted contribution to the SSM, i.e., 36%. Thus, we increase the uncertainty in the survival factor: $0.17 + 0.31 \times 0.36 = 0.28$.

The relative contributions of intermediate-energy neutrinos in Ga to the capture rate are approximately

the same as those in Cl (e.g., from $^7$Be neutrinos, 75% in Ga and 64% in Cl). This gives grounds to apply the survival factor determined for Cl to a gallium experiment, i.e.,

$$[^7\mathrm{Be} + \mathrm{CNO} + pep|\mathrm{Ga}]_{\mathrm{exp}}$$
$$= (0.13 \pm 0.28)[^7\mathrm{Be} + \mathrm{CNO} + pep|\mathrm{Ga}]_{\mathrm{SSM}}$$
$$= 14.4 \pm 13.0\ \mathrm{SNU}.$$

Subtracting this contribution of intermediate-energy neutrinos from the capture rate in gallium obtained above yields the measured *pp*-neutrino capture rate in a gallium experiment,

$$[pp|\mathrm{Ga}]_{\mathrm{exp}} = [pp + {}^7\mathrm{Be} + \mathrm{CNO} + pep|\mathrm{Ga}]_{\mathrm{exp}}$$
$$- [{}^7\mathrm{Be} + \mathrm{CNO} + pep|\mathrm{Ga}]_{\mathrm{exp}} = 53.4 \pm 14.0\ \mathrm{SNU}.$$

Since the capture cross section for *pp* neutrinos interacting with Ga in the narrow energy range, 0.23–0.42 MeV, does not change appreciably, we divide the measured capture rate by the calculated electron-neutrino capture cross section $(11.7 \pm 0.3) \times 10^{-46}$ cm$^2$ for the SSM and obtain the measured *pp*-neutrino flux on Earth: $(4.6 \pm 1.2) \times 10^{10}$ electron neutrinos cm$^{-2}$ s$^{-1}$.

On the other hand, knowing the capture cross section and the survival factor, we can determine the *pp*-neutrino flux emitted in thermonuclear reactions in the Sun from the derived capture rate of neutrinos on gallium. If the neutrino oscillation parameters lie within the LMA range (the range of large mixing angles), which is now considered to be the preferred one, then the survival factor is 60% and the flux of the emitted *pp* neutrinos is $(7.6 \pm 2.0) \times 10^{10}$ cm$^{-2}$ s$^{-1}$. This is in agreement with the value predicted by the SSM, $(5.95 \pm 0.06) \times 10^{10}$ neutrinos cm$^{-2}$ s$^{-1}$ [37, 38]. A significant part of the measurement error in the *pp*-neutrino flux stems from the fact that the energy dependence of the survival factor is not well known.

In calculating these *pp*-neutrino fluxes, we made several assumptions; the errors that arise in this case cannot be determined in a simple way. Therefore, the errors given here may have been underestimated. As was pointed out in the Introduction, we will be able to significantly reduce this error when the range of possible mass and mixing angle parameters will be limited by the KamLAND experiment and when the flux of $^7$Be neutrinos will be directly measured, as expected in the BOREXINO experiment. In that case, the dominant error will be uncertainty in the measurements of the gallium experiment itself. Therefore, our efforts are now directed to reducing the statistical and systematic uncertainties in the SAGE experiment.

## 7. CONCLUSION

We have described the basic principles and techniques of the SAGE experiment and analyzed 92 extractions made over the twelve-year period from January 1990 until December 2001. The measured capture rate of solar neutrinos by gallium is $70.8^{+5.3}_{-5.2}$ SNU. Here, only the statistical uncertainties are given. Analysis of the well-known systematic effects showed that the total systematic uncertainty is smaller than the statistical error, being $^{+3.7}_{-3.2}$ SNU. Finally, we have examined the counting data and shown that there is good evidence that $^{71}$Ge is being counted, that the counting data fit the hypotheses of our analysis, and that the counting data are self-consistent.

The SAGE result of 70.8 SNU accounts for 55% of the value predicted by the SSM [9, 10]. A check of systematic effects and our additional measurements, in particular, the experiment with a $^{51}$Cr neutrino source [30, 31], suggest that the difference between our solar neutrino capture rate and the value predicted by the SSM ($6.0\sigma$, where $\sigma$ is the standard deviation) is strong evidence that the flux of solar neutrinos with energies below 2 MeV is much lower than the expected flux. This was also shown for the $^8$B-neutrino flux by the chlorine neutrino experiment and in the Kamiokande and CHO experiments. The SAGE result is even smaller than the minimum astrophysical capture rate of $79.5^{+2.3}_{-2.0}$ SNU [39].

The combined result of all solar neutrino experiments is discussed in several phenomenological papers [40–42]. Their main conclusion reduces to the following: the electron neutrinos produced in the Sun reach the Earth in a different flavor state, and Mikheev–Smirnov–Wolfenstein oscillations with the oscillation parameters in the LMA range are best suited as the mechanism of change in the flavor of solar neutrinos. A more accurate determination of the oscillation parameters requires additional data, particularly those obtained in experiments sensitive to low-energy neutrinos. To this end, the SAGE collaboration regularly performs solar neutrino extractions, every four weeks, from about 50 t of gallium, reducing the statistical error, and explores further possibilities for reducing the systematic uncertainties.

## ACKNOWLEDGMENTS

We thank J.N. Bahcall, M. Baldo-Ceolin, G.T. Garvey, W. Haxton, V.A. Kuzmin, V.V. Kuzminov, V.A. Matveev, L.B. Okun, R.G.H. Robertson, V.A. Rubakov, A.Yu. Smirnov, A.N. Tavkhelidze, and many members of GALLEX and GNO for their continued interest and for stimulating discussions. We greatly appreciate the work of our prior collaborators O.L. Anosov, O.V. Bychuk, M.L. Cherry, R. Davis, Jr., I.I. Knyshenko,

V.N. Kornoukhov, R.T. Kouzes, K. Lande, A.V. Ostrinsky, D.L. Wark, P.W. Wildenhain, and Yu.I. Zakharov.

This study was supported by the Russian Foundation for Basic Research (project nos. 96-02-18399, 99-02-16110b, and 00-15-96632), the Division of Nuclear Physics of the US Department of Energy (grant DEFG03-97ER4120), the International Science Foundation (grants M7F000 and M7F300), and the American Foundation for Civil Research and Development (grants RP2-159 and RP2-2253).

## REFERENCES

1. S. Fukuda, Y. Fukuda, M. Ishitsuka, *et al.*, hep-ex/0103032; Phys. Rev. Lett. **86**, 5651 (2001); hep-ex/0103033; Phys. Rev. Lett. **86**, 5656 (2001).
2. Q. R. Ahmad, R. C. Allen, T. C. Andersen, *et al.*, nucl-ex/0106015; Phys. Rev. Lett. **87**, 071301 (2001).
3. B. T. Cleveland, T. J. Daily, R. Davis, Jr., *et al.*, Astrophys. J. **496**, 505 (1998).
4. J. N. Abdurashitov, V. N. Gavrin, S. V. Girin, *et al.*, astro-ph/9907113; Phys. Rev. C **60**, 055801 (1999).
5. W. Hampel, J. Handt, G. Heusser, *et al.*, Phys. Lett. B **447**, 127 (1999).
6. Y. Fukuda, T. Hayakawa, K. Inoue, *et al.*, Phys. Rev. Lett. **77**, 1683 (1996).
7. www.sns.ias.edu/~jnb/Meetings/lownu/index.html; www.sk.icrr.u-tokyo.ac.jp/lownu/index.html.
8. V. A. Kuz'min, Zh. Éksp. Teor. Fiz. **49**, 1532 (1965) [Sov. Phys. JETP **22**, 1051 (1966)].
9. J. N. Bahcall, M. C. Gonzalez-Garcia, and C. Peña-Garay, hep-ph/0111150.
10. A. S. Brun, S. Turck-Chieze, and P. Morel, astro-ph/9806272; Astrophys. J. **506**, 913 (1998).
11. A. Piepke, Nucl. Phys. B (Proc. Suppl.) **91**, 99 (2001).
12. G. Alimonti, C. Arpesella, H. Back, *et al.*, hep-ex/0012030; Astropart. Phys. **16**, 205 (2002).
13. M. Altmann, M. Balata, P. Belli, *et al.*, hep-ex/0006034; Phys. Lett. B **490**, 16 (2000).
14. V. N. Gavrin, V. N. Kornoukhov, and G. T. Zatsepin, Preprint IYaI AN SSSR P-0690 (1991).
15. V. N. Gavrin, V. É. Gurentsov, V. N. Kornoukhov, *et al.*, Preprint IYaI AN SSSR P-0698 (1991).
16. J. N. Abdurashitov, V. N. Gavrin, A. V. Kalikhov, *et al.*, Nucl. Instrum. Methods Phys. Res. A (Proc. Suppl.) **476**, 322 (2002).
17. J. N. Abdurashitov, E. L. Faizov, V. N. Gavrin, *et al.*, Phys. Lett. B **328**, 234 (1994).
18. S. R. Elliott, Nucl. Instrum. Methods Phys. Res. A **290**, 158 (1990).
19. B. T. Cleveland, Nucl. Instrum. Methods Phys. Res. A **214**, 451 (1983).
20. B. T. Cleveland, Nucl. Instrum. Methods Phys. Res. A **416**, 405 (1998).
21. V. N. Gavrin, Nucl. Phys. B (Proc. Suppl.) **91**, 36 (2001).
22. V. N. Gavrin, V. N. Kornoukhov, and V. É. Yants, Preprint IYaI AN SSSR P-0703 (1991).
23. V. N. Gavrin, S. N. Dan'shin, A. V. Kopylov, *et al.*, Preprint IYaI AN SSSR P-0494 (1986).
24. Ch. Evans Associated Report (unpublished).
25. V. N. Gavrin, V. V. Gorbachev, and I. N. Mirmov, Yad. Fiz. **65**, 1 (2002) [Phys. At. Nucl. **65**, 843 (2002)].
26. E. P. Veretenkin, V. N. Gavrin, A. M. Grigor'ev, *et al.*, At. Énerg. **72**, 260 (1992).
27. V. N. Gavrin and Yu. I. Zakharov, Preprint IYaI AN SSSR P-0560 (1987).
28. M. Cribier, B. Pichard, J. Rich, *et al.*, Astropart. Phys. **6**, 129 (1997).
29. V. N. Gavrin, V. V. Gorbachev, T. V. Ibragimova, and B. T. Cleveland, Yad. Fiz. **65**, 1309 (2002).
30. J. N. Abdurashitov, V. N. Gavrin, S. V. Girin, *et al.*, Phys. Rev. Lett. **77**, 4708 (1996).
31. J. N. Abdurashitov, V. N. Gavrin, S. V. Girin, *et al.*, hep-ph/9803418; Phys. Rev. C **59**, 2246 (1999).
32. W. Hampel and L. Remsberg, Phys. Rev. C **31**, 666 (1985).
33. V. Berezinsky, G. Fiorentini, and M. Lissia, hep-ph/9904225; Astropart. Phys. **12**, 299 (2000).
34. G. L. Fogli, E. Lisi, D. Montanino, *et al.*, hep-ph/9910387; Phys. Rev. D **61**, 073009 (2000).
35. J. Pulido and E. Kh. Akhmedov, hep-ph/9907399; Astropart. Phys. **13**, 227 (2000).
36. P. A. Sturrock and J. D. Scargle, astro-ph/0011228; Astrophys. J. **550**, L101 (2001).
37. J. N. Bahcall, M. H. Pinsonneault, and S. Basu, astro-ph/0010346; Astrophys. J. **555**, 990 (2001).
38. J. N. Bahcall, hep-ph/0108148; Phys. Rev. C **65**, 025801 (2002).
39. J. N. Bahcall, hep-ph/9710491; Phys. Rev. C **56**, 3391 (1997).
40. J. N. Bahcall, M. C. Gonzalez-Garcia, and C. Peña-Garay, hep-ph/0106258; JHEP **0108**, 014 (2001).
41. P. I. Krastev and A. Yu. Smirnov, hep-ph/0108177; Phys. Rev. D **65**, 073022 (2002).
42. M. C. Gonzales-Garcia, M. Maltoni, and C. Peña-Garay, hep-ph/0108073.

*Translated by V. Astakhov*

*Journal of Experimental and Theoretical Physics, Vol. 95, No. 2, 2002, pp. 194–198.*
*Translated from Zhurnal Éksperimental'noĭ i Teoreticheskoĭ Fiziki, Vol. 122, No. 2, 2002, pp. 227–232.*


**GRAVITATION, ASTROPHYSICS**

# Nonlinear Electrodynamic Lag of Electromagnetic Signals in a Magnetic Dipole Field

**V. I. Denisov[a, *], I. V. Krivchenkov[a], and I. P. Denisova[b]**

[a]*Moscow State University, Vorob'evy gory, Moscow, 119899 Russia*
[b]*Tsiolkovsky Russian State Technological University, Moscow, 121552 Russia*
**e-mail: Denisov@srd.sinp.msu.ru*

Received February 20, 2002

**Abstract**—We investigate the propagation of electromagnetic waves in the magnetic dipole and gravitational fields of a neutron star, which follows the laws of nonlinear electrodynamics in a vacuum. Electromagnetic signals in these fields are shown to propagate along different rays and at different velocities, depending on their polarization. We found the law of motion for these signals along rays. We calculate the difference between the propagation times of electromagnetic signals with different polarizations from the same source to the detector. This difference is shown to reach a measurable value of 1 μs in some cases. *© 2002 MAIK "Nauka/Interperiodica".*

## 1. INTRODUCTION

According to quantum electrodynamics, the effective Lagrangian of a weak electromagnetic field in a vacuum is

$$L = -\frac{1}{8\pi}[\mathbf{B}^2 - \mathbf{E}^2] + \frac{\alpha}{360\pi^2 B_q^2} \times \{(\mathbf{B}^2 - \mathbf{E}^2)^2 + 7(\mathbf{B}\cdot\mathbf{E})^2\}, \quad (1)$$

where $\alpha = e^2/\hbar c \approx 1/137$ is the fine-structure constant and $B_q = m^2c^2/e\hbar \approx 4.41 \times 10^{13}$ G is the characteristic quantum-electrodynamic induction. Therefore, the electromagnetic-field equations in a vacuum take the form of nonlinear electrodynamic equations for continuous media:

$$\operatorname{curl}\mathbf{H} = \frac{1}{c}\frac{\partial \mathbf{D}}{\partial t}, \quad \operatorname{div}\mathbf{D} = 0,$$
$$\operatorname{curl}\mathbf{E} = -\frac{1}{c}\frac{\partial \mathbf{B}}{\partial t}, \quad \operatorname{div}\mathbf{B} = 0, \quad (2)$$

differing from these by the meaning of the vectors **D** and **H**:

$$\mathbf{D} = \mathbf{E} + \frac{\alpha}{45\pi B_q^2}\{2(\mathbf{E}^2 - \mathbf{B}^2)\cdot\mathbf{E} + 7(\mathbf{B}\cdot\mathbf{E})\mathbf{B}\},$$
$$\mathbf{H} = \mathbf{B} + \frac{\alpha}{45\pi B_q^2}\{2(\mathbf{E}^2 - \mathbf{B}^2)\cdot\mathbf{B} - 7(\mathbf{B}\cdot\mathbf{E})\mathbf{E}\}. \quad (3)$$

Since nonlinear electrodynamics in a vacuum had had no experimental confirmation for a long time, it was perceived by many physicists as an abstract theoretical model. Its current status has changed significantly. Experiments [1] on inelastic scattering of laser photons by gamma-ray photons confirmed that electrodynamics in a vacuum is actually a nonlinear theory. Therefore, its various experimentally testable predictions deserve serious attention.

In recent years, several experiments have been suggested to study such effects [2–7]. However, for the fields $B, E \sim 10^6$ G achievable in terrestrial laboratories, the nonlinear corrections to the Maxwell equations are so small that the effects produced by them in a vacuum are difficult to measure.

Therefore, several authors [8–10] explored the possibility of observing nonlinear electrodynamic effects in strong magnetic fields of neutron stars. Indeed, such neutron stars as pulsars have magnetic fields comparable in strength to the quantum-electrodynamic field $B_q$. The recently discovered magnetars possess even stronger fields, $B \sim 10^{15}$–$10^{16}$ G. Thus, the neighborhoods of neutron stars represent a unique natural laboratory for the manifestations of various nonlinear electrodynamic and gravitational effects.

Here, our goal is to investigate one effect of nonlinear electrodynamics in a vacuum that can reach a measurable magnitude in the magnetic fields of pulsars and magnetars. The basis for this effect is the birefringence of a vacuum in an external electromagnetic field and, as a result, the dependence of the propagation velocity of electromagnetic signals in this field on their polarization. Therefore, if two signals with two different polarizations are emitted at the same instant in time from one source and then pass through the field of a neutron star, then they will not reach the detector simultaneously. As a result, by measuring the time lag between the electromagnetic pulse with one normal polarization and the electromagnetic pulse with the other normal polarization, we can test in more detail various predictions of

nonlinear electrodynamics in a vacuum. Since the magnetospheres of pulsars and magnetars may contain matter that absorbs electromagnetic waves, below by electromagnetic waves we mean gamma-ray pulses to which the magnetosphere is definitely transparent.

## 2. THE RAY EQUATION IN A MAGNETIC DIPOLE FIELD

Let us consider a neutron star with a magnetic dipole field whose induction **B** can reach $B_q$. In this case, the electromagnetic-field equations of nonlinear electrodynamics in a vacuum have two small parameters. One is the relative value of the nonlinear terms in Eqs. (1) and (3), which can reach approximately $10^{-4}$ at $|\mathbf{B}| = B_q$. The other small parameter is $r_g/r$ for the Schwarzschild gravitational field of the star:

$$g_{00} = 1 - \frac{r_g}{r}, \quad g_{rr} = -\frac{r}{r - r_g},$$

$$g_{\theta\theta} = -r^2, \quad g_{\varphi\varphi} = -r^2\sin^2\theta.$$

Since the masses of typical neutron stars are close to the solar mass in order of magnitude and since their radii $R$ lie within the range 100 to 300 km, we assume that $r_g/R \sim 10^{-2}$. Therefore, to achieve the same accuracy, we must perform calculations by taking into account gravitation with an accuracy quadratic in $r_g/r$.

Let us rewrite the nonlinear electrodynamic equations (2) in a vacuum in general covariant form:

$$\frac{\partial F_{mn}}{\partial x^k} + \frac{\partial F_{nk}}{\partial x^m} + \frac{\partial F_{km}}{\partial x^n} = 0,$$

$$\frac{1}{\sqrt{-g}}\frac{\partial}{\partial x^n}\left\{\sqrt{-g}\left[\left(1 - \frac{\alpha}{18\pi B_q^2}J_2\right)F^{mn}\right.\right. \tag{4}$$

$$\left.\left. + \frac{7\alpha}{45\pi B_q^2}F^{ml}F_{lk}F^{kn}\right]\right\} = 0,$$

where $J_2 = F_{ik}F^{ki}$ is the electromagnetic-field invariant.

The solution to Eqs. (4) that describes the dipole magnetic field of the neutron star in the approximation concerned is

$$F_{31}^{(0)} = -\frac{|\mathbf{m}|}{r^2}\sin^2\theta, \quad F_{32}^{(0)} = \frac{2|\mathbf{m}|}{r}\sin\theta\cos\theta, \tag{5}$$

where **m** is the magnetic dipole moment of the star.

Let us consider an electromagnetic wave that propagates in the $\theta = \pi/2$ plane of the stellar magnetic equator. The eikonal equation for this wave that follows from the system of equations (4) and (5) depends on its polarization. In particular, for an electromagnetic wave polarized perpendicular to the $\theta = \pi/2$ plane, the eikonal $S_1$ satisfies the equation

$$\left(1 + \frac{r_g}{r} + \frac{r_g^2}{r^2}\right)\left(\frac{\partial S_1}{\partial x^0}\right)^2 - \left(1 - \frac{r_g}{r}\right)\left(\frac{\partial S_1}{\partial r}\right)^2 - \frac{1}{r^2}\left(\frac{\partial S_1}{\partial \varphi}\right)^2$$

$$+ \frac{7\alpha|\mathbf{m}|^2}{45\pi B_q^2 r^6}\left\{\left(\frac{\partial S_1}{\partial r}\right)^2 + \frac{1}{r^2}\left(\frac{\partial S_1}{\partial \varphi}\right)^2\right\} = 0, \tag{6}$$

while, for an electromagnetic wave polarized in the plane of the magnetic equator, the eikonal $S_2$ must satisfy the equation

$$\left(1 + \frac{r_g}{r} + \frac{r_g^2}{r^2}\right)\left(\frac{\partial S_2}{\partial x^0}\right)^2 - \left(1 - \frac{r_g}{r}\right)\left(\frac{\partial S_2}{\partial r}\right)^2 - \frac{1}{r^2}\left(\frac{\partial S_2}{\partial \varphi}\right)^2$$

$$+ \frac{4\alpha|\mathbf{m}|^2}{45\pi B_q^2 r^6}\left\{\left(\frac{\partial S_2}{\partial r}\right)^2 + \frac{1}{r^2}\left(\frac{\partial S_2}{\partial \varphi}\right)^2\right\} = 0. \tag{7}$$

Consider the first of these equations. Using the standard formalism, it is easy to derive the ray equation for an electromagnetic wave of the first type of polarization. If we denote the ray impact parameter by $b_1$, then we have in polar coordinates $r$ and $\varphi$

$$\varphi = \varphi_0 \mp b_1\int^r \frac{dr}{r^2\sqrt{F(r)}}\left[1 + \frac{r_g}{r} + \frac{r_g^2}{r^2}\right], \tag{8}$$

where

$$F(r) = 1 + \frac{2r_g}{r} + \frac{3r_g^2}{r^2} + \frac{7\alpha|\mathbf{m}|^2}{45\pi B_q^2 r^6} - \frac{b_1^2}{r^2}\left[1 + \frac{r_g}{r} + \frac{r_g^2}{r^2}\right].$$

However, it is inconvenient to use the ray equation in form (8) for our purposes. Therefore, we make use of the method by Darwin [11] and transform Eq. (8) to

$$r = \frac{b_1}{V_1 + W_1\sin\Psi_1(\varphi)}, \tag{9}$$

where

$$V_1 = \frac{r_g}{2b_1}, \quad W_1 = 1 + \frac{7\alpha|\mathbf{m}|^2}{90\pi B_q^2 b_1^6} + \frac{5r_g^2}{8b_1^2},$$

$$\Psi_1(\varphi) = \varphi + \varphi_1 + \frac{r_g}{2b_1}\cos(\varphi + \varphi_1)$$

$$- \frac{r_g^2}{32b_1^2}\{30(\varphi + \varphi_1) + \sin 2(\varphi + \varphi_1)\} - \frac{7\alpha|\mathbf{m}|^2}{2880\pi B_q^2 b_1^6} \tag{10}$$

$$\times\{60(\varphi + \varphi_1) + \sin 4(\varphi + \varphi_1) - 16\sin 2(\varphi + \varphi_1)\}.$$

By varying the angle $\varphi_1$ and the impact parameter $b_1$, we run the entire family of rays. In particular, if the

source of electromagnetic waves is at the point with $r = R_0$ and $\varphi = \pi$, then

$$\varphi_1 = -\xi_1 + \frac{r_g}{2b_1}\cos\xi_1 + \frac{3r_g^2}{32b_1^2}\{10(\pi - \xi_1) + \sin 2\xi_1\}$$
$$+ \frac{7\alpha|\mathbf{m}|^2}{2880\pi B_q^2 b_1^6}[60(\pi - \xi_1) - \sin 4\xi_1 + 16\sin 2\xi_1],$$

where, to save space, we designated

$$\xi_1 = \operatorname{ascsin}\left\{\frac{b_1}{R_0}\left[1 - \frac{7\alpha|\mathbf{m}|^2}{90\pi B_q^2 b_1^6} - \frac{5r_g^2}{8b_1^2}\right] - \frac{r_g}{2b_1}\right\}.$$

Using these expressions, we can easily determine the gravitational and nonlinear electrodynamic bending angle of a given ray:

$$\delta\varphi_1 = -\frac{2r_g}{b_1} - \frac{7\alpha|\mathbf{m}|^2}{48\pi B_q^2 b_1^6} - \frac{15\pi r_g^2}{16b_1^2}. \quad (11)$$

The minus sign in this expression indicates that the gravitational and magnetic fields of the neutron star in the plane of its magnetic equator act on electromagnetic waves as a converging lens.

The ray equations for electromagnetic waves of the second type of polarization can be build in a similar way. If we denote the ray impact parameter in this case by $b$, then we have

$$r = \frac{b}{V + W\sin\Psi(\varphi)}, \quad (12)$$

where

$$V = \frac{r_g}{2b}, \quad W = 1 + \frac{2\alpha|\mathbf{m}|^2}{45\pi B_q^2 b^6} + \frac{5r_g^2}{8b^2},$$

$$\Psi(\varphi) = \varphi + \varphi_0 + \frac{r_g}{2b}\cos(\varphi + \varphi_0)$$
$$- \frac{r_g^2}{32b^2}\{30(\varphi + \varphi_0) + \sin 2(\varphi + \varphi_0)\} - \frac{\alpha|\mathbf{m}|^2}{720\pi B_q^2 b^6}$$
$$\times\{60(\varphi + \varphi_0) + \sin 4(\varphi + \varphi_0) - 16\sin 2(\varphi + \varphi_0)\}.$$

For the ray passing through the point with $r = R_0$ and $\varphi = \pi$, the angle $\varphi_0$ is

$$\varphi_0 = -\xi_0 + \frac{r_g}{2b}\cos\xi_0 + \frac{3r_g^2}{32b^2}\{10(\pi - \xi_0) + \sin 2\xi_0\}$$
$$+ \frac{\alpha|\mathbf{m}|^2}{720\pi B_q^2 b^6}[60(\pi - \xi_0) - \sin 4\xi_0 + 16\sin 2\xi_0],$$

where we designated

$$\xi_0 = \arcsin\left\{\frac{b}{R_0}\left[1 - \frac{2\alpha|\mathbf{m}|^2}{45\pi B_q^2 b^6} - \frac{5r_g^2}{8b^2}\right] - \frac{r_g}{2b}\right\}.$$

The bending angle of the electromagnetic ray with this polarization is smaller than the bending angle (11):

$$\delta\varphi = -\frac{2r_g}{b} - \frac{\alpha|\mathbf{m}|^2}{12B_q^2 b^6} - \frac{15\pi r_g^2}{16b^2}. \quad (13)$$

It should be noted that Eqs. (11) and (13) transform to the corresponding equations for nonlinear electrodynamic ray bending [9, 10] when $r_g \longrightarrow 0$, and to the equation for the gravitational bending of these rays, when $|m|^2 \longrightarrow 0$ [12].

## 3. THE LAW OF MOTION FOR ELECTROMAGNETIC SIGNALS ALONG RAYS IN A MAGNETIC DIPOLE FIELD

Using Eqs. (6) and (7), we can determine the law of motion for electromagnetic signals along rays. For electromagnetic waves of the first type of polarization, we have

$$t = t_0 \pm \frac{1}{c}\int^r \frac{dr}{\sqrt{F(r)}}\left[1 + \frac{2r_g}{r} + \frac{3r_g^2}{r^2} + \frac{7\alpha|\mathbf{m}|^2}{45\pi B_q^2 r^6}\right]. \quad (14)$$

Note that $t$ is the time measured by the clock of an observer located far from the neutron star.

Differentiating Eq. (14) with respect to $r$ and using relations (8)–(10), we derive the equation

$$\frac{dt}{d\Psi_1} = -\frac{r^2}{cb_1}\left\{1 + \frac{7\alpha|\mathbf{m}|^2}{90\pi B_q^2 b_1^6} + \frac{r_g^2}{2b_1^2}\right\} - \frac{3r_g r}{2cb_1}$$
$$- \frac{b_1}{c}\left\{\frac{15r_g^2}{8b_1^2} + \frac{7\alpha|\mathbf{m}|^2}{90\pi B_q^2 b_1^6}[1 + \sin^2\Psi_1 + 2\sin^4\Psi_1]\right\}.$$

Integrating this differential equation yields the law of motion $t = t(\varphi)$

$$t = t_1 + \frac{r}{c}\left[1 + \frac{r_g^2}{8b_1^2}\right]\cos\Psi_1(\varphi)$$
$$- \frac{r_g}{c}\ln\left|\frac{V_1\tan\left(\frac{\Psi_1(\varphi)}{2}\right) + W_1 - \sqrt{W_1^2 - V_1^2}}{V_1\tan\left(\frac{\Psi_1(\varphi)}{2}\right) + W_1 + \sqrt{W_1^2 - V_1^2}}\right| \quad (15)$$
$$- \frac{b_1}{c}\left\{\frac{15r_g^2}{8b_1^2}\Psi_1(\varphi) + \frac{7\alpha|\mathbf{m}|^2}{360\pi B_q^2 b_1^6}\right.$$

$$\times [9\Psi_1(\varphi) - (2\sin^2\Psi_1(\varphi) + 5)\sin\Psi_1(\varphi)\cos\Psi_1(\varphi)] \Bigg\},$$

where $t_1$ is the integration constant.

Assuming that the electromagnetic signal was emitted from the point with $r = R_0$ and $\varphi = \pi$ at time $t = 0$, we obtain

$$t_1 = \frac{R_0}{c}\left[1 + \frac{r_g^2}{8b_1^2}\right]\cos\xi_1$$

$$+ \frac{r_g}{c}\ln\left|\frac{V_1\cot(\xi_1/2) + W_1 - \sqrt{W_1^2 - V_1^2}}{V_1\cot(\xi_1/2) + W_1 + \sqrt{W_1^2 - V_1^2}}\right|$$

$$+ \frac{b_1}{c}\Bigg\{\frac{15r_g^2}{8b_1^2}(\pi - \xi_1) + \frac{7\alpha|\mathbf{m}|^2}{360\pi B_q^2 b_1^6}$$

$$\times [9(\pi - \xi_1) + (2\sin^2\xi_1 + 5)\sin\xi_1\cos\xi_1] \Bigg\}.$$

Similarly, the law of motion $T = T(\varphi)$ for an electromagnetic signal with the other polarization is

$$T = t_0 + \frac{r}{c}\left[1 + \frac{r_g^2}{8b^2}\right]\cos\Psi(\varphi)$$

$$- \frac{r_g}{c}\ln\left|\frac{V\tan\left(\frac{\Psi(\varphi)}{2}\right) + W - \sqrt{W^2 - V^2}}{V\tan\left(\frac{\Psi(\varphi)}{2}\right) + W + \sqrt{W^2 - V^2}}\right| \qquad (16)$$

$$- \frac{b}{c}\Bigg\{\frac{15r_g^2}{8b^2}\Psi(\varphi) + \frac{\alpha|\mathbf{m}|^2}{90\pi B_q^2 b^6}$$

$$\times [9\Psi(\varphi) - (2\sin^2\Psi(\varphi) + 5)\sin\Psi(\varphi)\cos\Psi(\varphi)] \Bigg\}.$$

The integration constant $t_0$ under the same initial conditions takes the form

$$t_0 = \frac{R_0}{c}\left[1 + \frac{r_g^2}{8b^2}\right]\cos\xi_0$$

$$+ \frac{r_g}{c}\ln\left|\frac{V_1\cot(\xi_0/2) + W - \sqrt{W^2 - V^2}}{V_1\cot(\xi_0/2) + W + \sqrt{W^2 - V^2}}\right|$$

$$+ \frac{b}{c}\Bigg\{\frac{15r_g^2}{8b^2}(\pi - \xi_0) + \frac{\alpha|\mathbf{m}|^2}{90\pi B_q^2 b^6}$$

$$\times [9(\pi - \xi_0) + (2\sin^2\xi_0 + 5)\sin\xi_0\cos\xi_0] \Bigg\}.$$

Equations (15) and (16) together with (9), (10), and (12) give the law of motion for electromagnetic signals of the two different polarizations along rays in the magnetic dipole and gravitational fields of a neutron star.

## 4. ANALYSIS OF THE NONLINEAR ELECTRODYNAMIC LAG OF ELECTROMAGNETIC SIGNALS

Consider a gamma-ray source at the point with $r = R_0$ and $\varphi = \pi$. Let us assume that two electromagnetic signals polarized in mutually perpendicular planes are emitted from this source at time $t = 0$. For these signals to pass through the same detector located on the other side of the neutron star at distance $R_1$, they must propagate along different rays with different impact parameters: $b_1 \neq b$. It follows from Eqs. (11) and (13) that, for $R_1 \gg b_1$ and $R_1 \gg b$, the impact parameters $b_1$ and $b$ must be related by the equation

$$\frac{2r_g}{b_1} + \frac{7\alpha|\mathbf{m}|^2}{12B_q^2 b_1^6} + \frac{15\pi r_g^2}{16b_1^2} = \frac{2r_g}{b} + \frac{\alpha|\mathbf{m}|^2}{3B_q^2 b^6} + \frac{15\pi r_g^2}{16b^2}.$$

Since the nonlinear electrodynamic terms in our case are proportional to the square of $r_g/b$, this equation has the following approximate solution:

$$b = b_1\left[1 - \frac{\alpha|\mathbf{m}|^2}{8r_g B_q^2 b_1^5}\right]. \qquad (17)$$

Thus, there are two reasons why the signals will not arrive at the point of their recording simultaneously. First, the dependences of the propagation velocities for normal waves on the external magnetic field are different. Second, the signals with different polarizations must propagate along different rays with different lengths.

If the gamma-ray source lies far from the neutron star ($R_0 \gg b_1$), then it follows from Eqs. (15)–(17) that the first factor mainly contributes to the lag. As a result, the leading term of the difference $\delta t = t - T$ at the recording point takes the form

$$\delta t = \frac{3\alpha B_0^2 b_1}{40 B_q^2}\frac{b_1}{c}, \qquad (18)$$

where $B_0$ is the magnetic field of the star at distance $b_1$ from its center.

However, the intensity of the recorded signals in this case will be strongly attenuated, because the gamma-ray source and detector are far from the neutron star. Therefore, it is more realistic to observe this effect when the gamma-ray source lies near the neutron star.

Let us assume that this source lies at the pericenter of the first ray, i.e., at the distance

$$R_0 = b_1\left[1 - \frac{r_g}{2b_1} - \frac{7\alpha m^2}{90\pi B_q^2 b_1^6} - \frac{3r_g^2}{8b_1^2}\right].$$

It then follows from Eqs. (15)–(17) that

$$\xi_1 = \frac{\pi}{2}, \quad \xi_0 = \frac{\pi}{2} - \sqrt{\frac{\alpha m^2}{4\pi B_q^2 b_1^5 r_g} + \frac{7\alpha m^2}{120\pi B_q^2 b_1^6}}.$$

Substituting these relations into Eqs. (15) and (16), we can easily verify that the difference between the dependences of the normal-wave velocities on the magnetic field mainly contributes to the difference $\delta t = t - T$ in this case as well. The leading term of the difference $\delta t$ in this case is a factor of 2 smaller than Eq. (18):

$$\delta t = \frac{3\alpha B_0^2}{80 B_q^2}\frac{b_1}{c}. \tag{19}$$

Analysis shows that the intensity of the recorded signals for this location of the source is attenuated only slightly by nonlinear electrodynamic and gravitational ray scattering.

It follows from Eq. (19) that when electromagnetic signals with an impact parameter $b_1 \sim 10^3$ km pass through the magnetar magnetic-field regions where $B \leq B_q$, the time lag $\delta t$ is about 1 μs in order of magnitude. Since modern electronics allows gamma-ray pulses to be recorded with such a resolution, the effect under consideration is quite measurable.

## CONCLUSION

Thus, at the current state of the art in the development of extra-atmospheric gamma-ray astronomy, it is feasible to measure the nonlinear electrodynamic lag of electromagnetic signals in strong magnetic fields of neutron stars. Although such measurements are technically difficult to carry out, the results obtained will allow one not only to elucidate the experimental status of this prediction of nonlinear electrodynamics in a vacuum but also to independently estimate the magnetic-field strength near various neutron stars.

## ACKNOWLEDGMENTS

This study was supported in part by the Russian Foundation for Basic Research (project no. 02-02-16598).

## REFERENCES

1. D. L. Burke, R. C. Feld, G. Horton-Smith, *et al.*, Phys. Rev. Lett. **79**, 1626 (1997).
2. N. B. Narozhnyĭ, Zh. Éksp. Teor. Fiz. **55**, 714 (1968) [Sov. Phys. JETP **28**, 371 (1968)].
3. E. B. Aleksandrov, A. A. Ansel'm, and A. N. Moskalev, Zh. Éksp. Teor. Fiz. **89**, 1181 (1985) [Sov. Phys. JETP **62**, 680 (1985)].
4. N. N. Rozanov, Zh. Éksp. Teor. Fiz. **103**, 1996 (1993) [JETP **76**, 991 (1993)].
5. V. I. Denisov, Phys. Rev. D **61**, 036004 (2000).
6. V. I. Denisov, J. Opt. A **2**, 372 (2000).
7. V. I. Denisov and I. P. Denisova, Opt. Spektrosk. **90**, 1022 (2001) [Opt. Spectrosc. **90**, 928 (2001)].
8. V. L. Ginzburg and V. N. Tsytovich, Zh. Éksp. Teor. Fiz. **74**, 1621 (1973) [Sov. Phys. JETP **47**, 845 (1973)].
9. D. V. Gal'tsov and N. S. Nikitina, Zh. Éksp. Teor. Fiz. **84**, 1217 (1983) [Sov. Phys. JETP **57**, 705 (1983)].
10. V. I. Denisov, I. P. Denisova, and S. I. Svertilov, Dokl. Akad. Nauk **380**, 754 (2001) [Dokl. Phys. **46**, 705 (2001)].
11. C. Darwin, Proc. R. Soc. London, Ser. A **263**, 39 (1961).
12. R. Epstein and I. I. Shapiro, Phys. Rev. D **22**, 2947 (1980).

*Translated by V. Astakhov*

*Journal of Experimental and Theoretical Physics, Vol. 95, No. 2, 2002, pp. 199–205.*
*Translated from Zhurnal Éksperimental'noĭ i Teoreticheskoĭ Fiziki, Vol. 122, No. 2, 2002, pp. 233–240.*


**NUCLEI, PARTICLES, AND THEIR INTERACTION**

# Second-Order Orientation Effects in Light Scattering by Polarized Atoms

**M. Ya. Agre**
*International Solomon University, Kiev, 01135 Ukraine*
*e-mail: markag@aport2000.ru*
Received February 18, 2002

**Abstract**—A compact expression is derived for the part of the cross section for light scattering by axisymmetrically polarized atomic systems proportional to the third-rank state multipole. The effect of the second-order orientation determined by this state multipole on the polarization and angular distribution of the scattered light is studied. The polarization of the incident light can be arbitrary and is specified by the Stokes parameters. A number of orientation effects in the scattering process are shown to be induced precisely by the second-order orientation. In particular, when nonpolarized light is scattered by an oriented atom, the scattering intensity in the perpendicular direction depends on the second-order orientation alone. The second-order orientation also preserves circular dichroism in the linear polarization of the forward- and back-scattered light. © *2002 MAIK "Nauka/Interperiodica".*

## 1. INTRODUCTION

Under free-orientation conditions, the magnetic sublevels of an atom are populated uniformly. The breakdown of the uniform population of states with different moment projections (atomic polarization) significantly affects the interaction of an atom with electromagnetic radiation. An atom is polarized during light absorption, collisions, and other processes. A special optical pumping method was developed for polarization (see [1, 2]), and some photoprocesses (light emission and absorption, photoeffect) on polarized atoms have been studied extensively (see [3] and references therein and [4, 5]).

Recall that a polarized atom is in a mixed quantum-mechanical state. The expansion of its density matrix in irreducible parts called state multipoles [3] allows various types of polarization to be distinguished. The state multipole $\rho_{KQ}$, $K = 0, 1, 2, \ldots, 2j$ ($j$ is the quantum number of the total moment of the polarized atom), $Q = -K, -K + 1, \ldots, K$, is an irreducible tensor of rank $K$. In the absence of polarization, only the scalar $\rho_{00}$ is nonzero. If at least one of the odd-rank state multipoles is nonzero, then the atom is called oriented. If at least one of the even-rank state multipoles is nonzero, then the atom is called aligned. While following this terminology [3],[1] to be more specific, we differentiate the orientation and alignment of various orders. The first-order orientation implies that the vector $\rho_{1Q}$ proportional to the mean moment of the polarized atom is nonzero, the second-order orientation implies that the tensor $\rho_{3Q}$ is nonzero, etc.

A general theory of light scattering by a polarized atom was developed in [6]. Thus, we showed that the differential and total cross sections for dipole scattering could contain the state multipoles up to the fourth and second ranks inclusive, respectively. In the expression for the scattering cross section, we separated out the dependence on geometric parameters. However, we wrote the cross section in a cumbersome form that contained the irreducible tensors composed of the polarization vectors for the incident and scattered photons [see Eq. (4) below]. For this representation of the cross section, the various experimentally observable effects proved to be difficult to analyze. Subsequently, we managed to represent the cross section for light scattering by atoms oriented in the first order [7, 8] and axisymmetrically aligned in the first order [9] in a simpler form by expressing it in terms of the scalar and vector products of vectors. In this case, the so-called dissipative-induced effects stood out. These effects must be observed if the scattering takes place against the background of open light-energy dissipation channels. A dissipative system is characterized by a $T$-odd dissipative parameter $\Gamma$ (which changes sign after time reversal), and additional combinations of vectors appear in the expression for the light scattering cross section.

The effect of the second-order orientation on light scattering has not yet been analyzed in detail, because the corresponding part of the cross section (4) has a more complex structure. Meanwhile, when an atom with a moment $j \geq 3/2$ is polarized, the state multipole $\rho_{3Q}$ can be nonzero and the second-order orientation contributes to the scattering.

In this paper, we managed to represent the part of the cross section for light scattering by axisymmetri-

[1] In the first edition of Blum's book [3], the system was called oriented if the orientation vector $\rho_{1Q}$ was nonzero and aligned if the alignment tensor $\rho_{2Q}$ was nonzero.

cally polarized atoms related to the second-order orientation in a compact, invariant form. We analyze the effect of the second-order orientation on the polarization and angular distribution of the scattered light. The polarization of the incident light may be arbitrary and is generally specified by the Stokes parameters. In obtaining the main results, we used the identities that express the pseudoscalars composed of seven vectors according to the rule for constructing irreducible tensors in terms of the scalar and triple scalar products of vectors. The method for deriving these identities, which may be of interest in their own right, is briefly considered in the Appendix.

## 2. THE CONTRIBUTION OF THE SECOND-ORDER ORIENTATION TO THE CROSS SECTION FOR LIGHT SCATTERING

For an axisymmetric polarization with the symmetry axis specified by a unit vector **n**, the density matrix of an atom is diagonal in projections of the moment $m$ onto the direction **n** and only the components $\rho_{K0} = \rho_K^n$ of all state multipoles [3] are nonzero in a coordinate system with the $z$ axis directed along **n**. These components can be expressed in terms of the diagonal elements of the density matrix $w_m$ (the populations of atomic magnetic sublevels) as follows:

$$\rho_K^n = \sum_m (-1)^{j-m}(2K+1)^{1/2}\begin{pmatrix} j & j & K \\ m & -m & 0 \end{pmatrix} w_m. \quad (1)$$

The first-order orientation $\rho_1^n$ is proportional to the mean moment projection onto the direction **n**

$$\bar{m} = \sum_m m w_m;$$

the second-order orientation $\rho_3^n$ can be expressed, according to (1), in terms of $\bar{m}$ and $\overline{m^3}$:

$$\rho_3^n = \sqrt{7} \times \frac{5\overline{m^3} - \bar{m}[3j(j+1)-1]}{[(j-1)j(j+1)(j+2)(2j-1)(2j+1)(2j+3)]^{1/2}}.$$

Note that these quantities, as well as all $\rho_K^n$ with odd $K$, are $T$-odd pseudoscalars (the vector **n** after space inversion changes to –**n**).

We can establish what changes the second-order orientation effects make to the cross section for light scattering even from general symmetry considerations. Indeed, the state multipole $\rho_{1Q}$ is proportional to the spherical components of the vector **n**, while $\rho_{3Q}$ is proportional to an irreducible tensor of the third rank composed of **n**. Therefore, apart from the pseudoscalars that define the first-order orientation effects, the part of the cross section proportional to $\rho_3^n$ must contain pseudoscalars with three vectors **n**. Thus, for example, when nonpolarized light is scattered, the dependence of the angular distribution of the scattered light on the first-order orientation, being dissipative-induced, is retained because of the $T$-even pseudoscalar

$$\mathbf{n}\cdot(\mathbf{k}'\times\mathbf{k})(\mathbf{k}'\cdot\mathbf{k}) \quad (2)$$

[7, 8], where **k** and **k**' are the unit vectors that specify the propagation directions of the incident and scattered light, respectively. In this case, the second-order orientation effects are defined by the pseudoscalar (2) and the pseudoscalar

$$\mathbf{n}\cdot(\mathbf{k}'\times\mathbf{k})(\mathbf{k}'\cdot\mathbf{n})(\mathbf{k}\cdot\mathbf{n}). \quad (3)$$

Consequently, the scattering intensity of the nonpolarized light in the perpendicular direction can depend only on the second-order orientation.

To determine the part of the cross section related to the second-order orientation, we turn to a general expression for the differential cross section for light scattering by a polarized atom [6]:

$$\frac{d\sigma}{d\Omega'} = (4\pi)^{1/2}\omega\omega'^3\alpha^4 \sum_{K,k,k'} \rho_K^n(-1)^{j+j'+k+K} \times \begin{Bmatrix} k & k' & K \\ j & j & j' \end{Bmatrix}(2K+1)^{-1/2}T_k T_{k'}^* \times \sum_Q Y_{KQ}^*(\mathbf{n})\{\{\mathbf{e}'^*\otimes\mathbf{e}\}_k\otimes\{\mathbf{e}'\otimes\mathbf{e}^*\}_{k'}\}_{KQ}. \quad (4)$$

Here, $\omega$ ($\omega'$) and **e** (**e**') are the frequency and unit polarization vector of the incident (scattered) photons, respectively; $\alpha$ is the fine-structure constant (the atomic system of units is used); $j'$ is the quantum number for the total moment of the atom in its final state; and $T_k$ ($k = 0, 1, 2$) are the reduced matrix elements of the irreducible parts of the scattering tensor, which were determined in [6, 8]. Formula (4) also includes the spherical function $Y_{KQ}(\mathbf{n})$ and the irreducible tensors composed of polarization vectors. Of the two irreducible tensors $A_{k_1q_1}$ and $B_{k_2q_2}$ of ranks $k_1$ and $k_2$, the irreducible tensor of rank $K$ is composed as follows:

$$\{A_{k_1}\otimes B_{k_2}\}_{KQ} = \sum_{q_1,q_2} C_{k_1q_1k_2q_2}^{KQ} A_{k_1q_1}B_{k_2q_2}, \quad (5)$$

where $C_{k_1q_1k_2q_2}^{KQ}$ is the Clebsch–Gordan coefficient. The vector is equivalent to the irreducible tensor of the first rank $a_{1q} = a_{(q)}$, where $a_{(q)}$ are the spherical components of this vector:

$$a_{(0)} = a_z, \quad a_{(\pm1)} = \mp\frac{1}{\sqrt{2}}(a_x \pm i a_y). \quad (6)$$

In this paper, we do not give standard expressions for the cross section for light scattering by a nonpolarized atom (see [10, Para. 60] and [6]) and for the additions to it attributable to the first-order orientation and alignment [8, 9] but focus our attention on the addition proportional to the second-order orientation $\rho_3^n$. The spherical function $Y_{3Q}(\mathbf{n})$ is proportional to the irreducible tensor of the third rank composed of vectors $\mathbf{n}$ [11]:

$$Y_{3Q}(\mathbf{n}) = \sqrt{\frac{35}{8\pi}}\{\{\mathbf{n}\otimes\mathbf{n}\}_2\otimes\mathbf{n}\}_{3Q}.$$

Therefore, the sum over $Q$ in Eq. (4) at $K = 3$ is the scalar product of two irreducible tensors of the third rank composed of the vector $\mathbf{n}$ and polarization vectors:

$$\sum_Q (-1)^Q Y_{3-Q}(\mathbf{n})\{\{\mathbf{e}'^*\otimes\mathbf{e}\}_k\otimes\{\mathbf{e}'\otimes\mathbf{e}^*\}_{k'}\}_{3Q} = \sqrt{\frac{35}{8\pi}} \times(\{\{\mathbf{n}\otimes\mathbf{n}\}_2\otimes\mathbf{n}\}_3, \{\{\mathbf{e}'^*\otimes\mathbf{e}\}_k\otimes\{\mathbf{e}'\otimes\mathbf{e}^*\}_{k'}\}_3). \quad (7)$$

Using the formulas derived in the Appendix, we can express pseudoscalars (7) for all possible sets of the numbers $k$ and $k'$ ($k = 1$, $k' = 2$; $k = 2$, $k' = 1$; and $k = k' = 2$) in terms of the scalar and vector products of the vectors appearing in them. After separating out all combinations of vectors, the expression for the part of cross section (4) concerned can be written as

$$\frac{d\sigma^{(\mathrm{sor})}}{d\Omega'} = \omega\omega'^3\alpha^4\rho_3^n\left\{\frac{1}{10}a_+\eta_2\mathbf{n}\cdot\mathbf{k} + \frac{1}{10}a_-\eta_2'\mathbf{n}\cdot\mathbf{k}' - \frac{1}{2}a_+\eta_2\mathbf{n}\cdot\mathbf{k}|\mathbf{n}\cdot\mathbf{e}'|^2 - \frac{1}{2}a_-\eta_2'\mathbf{n}\cdot\mathbf{k}'|\mathbf{n}\cdot\mathbf{e}|^2 + \frac{1}{5}a_+\eta_2\mathrm{Re}[(\mathbf{n}\cdot\mathbf{e}')(\mathbf{k}\cdot\mathbf{e}'^*)] + \frac{1}{5}a_-\eta_2'\mathrm{Re}[(\mathbf{n}\cdot\mathbf{e})(\mathbf{k}'\cdot\mathbf{e}^*)] + b\eta_2\eta_2'\mathbf{n}\cdot(\mathbf{k}'\times\mathbf{k}) + b\mathbf{n}\cdot\mathrm{Re}[(\mathbf{e}'^*\times\mathbf{e})(\mathbf{e}'\cdot\mathbf{e}^*)] - 5b\mathbf{n}\cdot\mathrm{Re}[(\mathbf{e}'^*\times\mathbf{e})(\mathbf{e}'\cdot\mathbf{n})(\mathbf{e}^*\cdot\mathbf{n})]\right\}. \quad (8)$$

Here,

$$\eta_2 = i\mathbf{k}\cdot(\mathbf{e}\times\mathbf{e}^*)$$

has the meaning of the degree of circular polarization of the incident light; the parameter $\eta_2'$ is given by a similar expression,

$$\eta_2' = i\mathbf{k}'\cdot(\mathbf{e}'\times\mathbf{e}'^*).$$

The coefficients $a_\pm$ and $b$ can be expressed in terms of the 6$j$ symbols and the reduced matrix elements of the scattering tensor:

$$a_\pm = \sqrt{5}\left(R_{12}\pm\frac{1}{\sqrt{2}}R_{22}\right),$$
$$b = \frac{(-1)^{j+j'}}{\sqrt{5}}\begin{Bmatrix} j' & j & 2\\ 3 & 1 & j\end{Bmatrix}\mathrm{Im}(T_1T_2^*), \quad (9)$$
$$R_{kk'} = (-1)^{j+j'}\begin{Bmatrix} j' & j & k'\\ 3 & k & j\end{Bmatrix}\mathrm{Re}(T_kT_{k'}^*).$$

To determine the addition to the angular distribution of the scattered light attributable to the second-order orientation, Eq. (8) must be summed over two independent polarizations of the scattered photon. During the summation, the parameter $\eta_2'$ becomes zero, while the summation of the scalars containing the vector $\mathbf{e}'$ can be easily performed by using the identity [10, Para. 45]

$$\sum_\lambda(\mathbf{a}\cdot\mathbf{e}_\lambda')(\mathbf{b}\cdot\mathbf{e}_\lambda'^*) = (\mathbf{k}'\times\mathbf{a})\cdot(\mathbf{k}'\times\mathbf{b}). \quad (10)$$

As a result, we obtain the following expression for the orientation addition to the angular distribution of the scattered light:

$$\frac{d\sigma_s^{\mathrm{sor}}}{d\Omega'} = \omega\omega'^3\alpha^4\rho_3^n\left\{\frac{1}{2}a_+\eta_2\mathbf{n}\cdot\mathbf{k}(\mathbf{n}\cdot\mathbf{k}')^2 - \frac{1}{10}a_+\eta_2\mathbf{n}\cdot\mathbf{k} - \frac{1}{5}a_+\eta_2(\mathbf{n}\cdot\mathbf{k}')(\mathbf{k}\cdot\mathbf{k}') + b\mathbf{n}\cdot\mathrm{Re}[(\mathbf{e}^*\times\mathbf{k}')(\mathbf{e}\cdot\mathbf{k}')] - 5b\mathbf{n}\cdot\mathrm{Re}[(\mathbf{e}^*\times\mathbf{k}')(\mathbf{e}\cdot\mathbf{n})](\mathbf{k}'\cdot\mathbf{n})\right\}. \quad (11)$$

We showed above that the second-order orientation gives no contribution to the total cross section for light scattering [6]. Therefore, integrating Eq. (11) over all scattering directions must yield zero. The latter can be easily verified by using the following standard identity in the integration:

$$\int k_i'k_j'd\Omega' = \frac{4\pi}{3}\delta_{ij}.$$

## 3. THE SCATTERING OF PARTIALLY POLARIZED LIGHT

In the preceding section, we assumed the scattered light to be completely polarized, so its polarization could be specified by the vector $\mathbf{e}$. In the more general case of partial polarization, three polarization parameters, for example, the Stokes parameters $\eta_i$, $i = 1, 2, 3$,

should be specified [3, 12]: $\eta_2$ defines the degree of circular polarization, $\eta_3$ defines the degree of linear polarization along the $x$ and $y$ directions (the $z$ axis is assumed to be directed along the light-wave propagation), and $\eta_1$ defines the degree of linear polarization along the $p$ and $q$ axes rotated through an angle of 45° in the $xy$ plane in the positive direction relative to the $x$ and $y$ axes. The Stokes parameters satisfy the relation

$$\eta_1^2 + \eta_2^2 + \eta_3^2 \le 1,$$

with the equality sign corresponding to complete polarization. For nonpolarized light,

$$\eta_1 = \eta_2 = \eta_3 = 0.$$

As was shown in [8], the cross section for any photoprocess accompanied by the absorption or stimulated emission of a partially polarized photon can be expressed in terms of the Stokes parameters and three dichroisms of this process:

$$\frac{d\sigma}{d\Omega'} = \frac{d\sigma_0}{d\Omega'} + \frac{1}{2}\left[\eta_1\frac{d\sigma_{pq}}{d\Omega'} + \eta_2\frac{d\sigma_{+-}}{d\Omega'} + \eta_3\frac{d\sigma_{xy}}{d\Omega'}\right]. \quad (12)$$

Here, $d\sigma_0/d\Omega'$ is the cross section for the photoprocess involving a nonpolarized photon, $d\sigma_{+-}/d\Omega'$ is the difference between the cross sections for right- and left-hand circular polarizations specified by the vectors $\mathbf{e}_\pm$ (circular dischroism of the process), and $d\sigma_{xy}/d\Omega'$ is the difference between the cross sections for linear polarizations along the $x$ and $y$ axes (linear $xy$ dichroism). We denote the corresponding linear polarization vectors by $\mathbf{e}_x$ and $\mathbf{e}_y$. Finally, $d\sigma_{pq}/d\Omega'$ is the linear $pq$ dichroism of the process. Formula (12) allows expressions (8) and (11) to be easily transformed in such a way that they would be applicable to the scattering of partially polarized light.

Passing to nonpolarized light reduces to averaging Eqs. (8) and (11) over the two orthogonal polarization vectors $\mathbf{e}_\lambda$ with a statistical weight of 1/2. In this case, the terms containing $\eta_2$ vanish and the remaining terms containing the vector $\mathbf{e}$ can be easily averaged by using an identity similar to (10). The linear dichroism can be calculated by substituting the corresponding real linear polarization vectors in Eqs. (8) and (11). When the circular dichroism is calculated, the parameter $\eta_2$, which is equal to ±1 for right-hand (left-hand) circular polarization, is substituted by 2 in all terms of Eqs. (8) and (11). According to (12), these terms will formally enter into the final expressions without any changes, but $\eta_2$ will have the meaning of the degree of circular polarization of partially polarized light. When determining the contribution of the other $\mathbf{e}$-dependent terms, it is convenient to use the identity

$$(\mathbf{a}\cdot\mathbf{e}_\pm)(\mathbf{b}\cdot\mathbf{e}_\pm^*) = \frac{1}{2}[(\mathbf{k}\times\mathbf{a})\cdot(\mathbf{k}\times\mathbf{b}) \pm i\mathbf{k}\cdot(\mathbf{b}\times\mathbf{a})].$$

Below, we give the final expression for the addition to the cross section for the scattering of partially polarized light attributable to the second-order orientation:

$$\begin{aligned}\frac{d\sigma^{(\mathrm{sor})}}{d\Omega'} = \frac{1}{2}\omega\omega'^3\alpha^4\rho_3^n\Big\{&\frac{1}{2}a_-\eta_2'\mathbf{n}\cdot\mathbf{k}'(\mathbf{n}\cdot\mathbf{k})^2 \\ &- \frac{1}{10}a_-\eta_2'\mathbf{n}\cdot\mathbf{k}' - \frac{1}{5}a_-\eta_2'(\mathbf{k}'\cdot\mathbf{k})(\mathbf{n}\cdot\mathbf{k}) \\ &+ b\mathbf{n}\cdot\mathrm{Re}[(\mathbf{k}\times\mathbf{e}'^*)(\mathbf{k}\cdot\mathbf{e}')] \\ &- 5b\mathbf{n}\cdot\mathrm{Re}[(\mathbf{k}\times\mathbf{e}'^*)(\mathbf{e}'\cdot\mathbf{n})](\mathbf{k}\cdot\mathbf{n}) \\ &+ \eta_2 a_+\left[\frac{1}{5}\mathbf{n}\cdot\mathbf{k} - \mathbf{n}\cdot\mathbf{k}|\mathbf{n}\cdot\mathbf{e}'|^2 + \frac{2}{5}\mathrm{Re}[(\mathbf{n}\cdot\mathbf{e}')(\mathbf{k}\cdot\mathbf{e}'^*)]\right] \\ &+ \eta_1\Delta_{pq} + \eta_3\Delta_{xy}\Big\},\end{aligned} \quad (13)$$

where

$$\begin{aligned}\Delta_{\beta\gamma} = {}& \frac{1}{5}a_-\eta_2'\mathbf{n}\cdot[\mathbf{e}_\beta(\mathbf{k}'\cdot\mathbf{e}_\beta) - \mathbf{e}_\gamma(\mathbf{k}'\cdot\mathbf{e}_\gamma)] \\ &+ \frac{1}{2}a_-\eta_2'\mathbf{n}\cdot\mathbf{k}'[(\mathbf{n}\cdot\mathbf{e}_\gamma)^2 - (\mathbf{n}\cdot\mathbf{e}_\beta)^2] \\ &+ b\mathbf{n}\cdot\mathrm{Re}[(\mathbf{e}'^*\times\mathbf{e}_\beta)(\mathbf{e}'\cdot\mathbf{e}_\beta) - (\mathbf{e}'^*\times\mathbf{e}_\gamma)(\mathbf{e}'\cdot\mathbf{e}_\gamma)] \\ &- 5b\mathbf{n}\cdot\mathrm{Re}\{[(\mathbf{e}'^*\times\mathbf{e}_\beta)(\mathbf{e}_\beta\cdot\mathbf{n}) - (\mathbf{e}'^*\times\mathbf{e}_\gamma)(\mathbf{e}_\gamma\cdot\mathbf{n})]\mathbf{e}'\cdot\mathbf{n}\}.\end{aligned}$$

The orientation addition to the angular distribution can be written as

$$\begin{aligned}\frac{d\sigma_s^{(\mathrm{sor})}}{d\Omega'} = \frac{1}{2}\omega\omega'^3\alpha^4\rho_3^n\Big\{&b\mathbf{n}\cdot(\mathbf{k}'\times\mathbf{k})(\mathbf{k}'\cdot\mathbf{k}) \\ &- 5b\mathbf{n}\cdot(\mathbf{k}'\times\mathbf{k})(\mathbf{k}'\cdot\mathbf{n})(\mathbf{k}\cdot\mathbf{n}) \\ &+ \eta_2 a_+\left[\mathbf{n}\cdot\mathbf{k}(\mathbf{n}\cdot\mathbf{k}')^2 - \frac{1}{5}\mathbf{n}\cdot\mathbf{k} - \frac{2}{5}(\mathbf{n}\cdot\mathbf{k}')(\mathbf{k}'\cdot\mathbf{k})\right] \\ &+ \eta_1\delta_{pq} + \eta_3\delta_{xy}\Big\},\end{aligned} \quad (14)$$

where

$$\begin{aligned}\delta_{\beta\gamma} = {}& b\mathbf{n}\cdot[(\mathbf{e}_\beta\times\mathbf{k}')(\mathbf{e}_\beta\cdot\mathbf{k}') - (\mathbf{e}_\gamma\times\mathbf{k}')(\mathbf{e}_\gamma\cdot\mathbf{k}')] \\ &- 5b\mathbf{n}\cdot[(\mathbf{e}_\beta\times\mathbf{k}')(\mathbf{e}_\beta\cdot\mathbf{n}) - (\mathbf{e}_\gamma\times\mathbf{k}')(\mathbf{e}_\gamma\cdot\mathbf{n})](\mathbf{k}'\cdot\mathbf{n}).\end{aligned}$$

Formula (14) can also be derived by summing (13) over the two orthogonal polarizations of the scattered light.

## 4. THE EFFECTS OF ATOMIC ORIENTATION AND LIGHT-ENERGY DISSIPATION ON LIGHT SCATTERING

Before we discuss the observed effects during light scattering that are produced by the second-order orientation, we note that two types of terms appear in the scattering cross section when it is taken into account. The terms of the first type containing one vector **n** also enter into the part of the cross section related to the first-order orientation [8]. The terms of the second type containing three vectors **n** are completely new. Next, since $\rho_3^n$ is *T*-odd, all terms in curly brackets in (8), (11), (13), and (14) must be *T*-odd. It is easy to notice that, after time reversal, when each polarization vector changes to its complex conjugate and when the vectors **k** and **k**' reverse their directions, the pseudoscalars multiplied by the coefficient *b* remain unchanged. Therefore, the coefficient *b* defined in (9) must be *T*-odd. The physical nature of this *T*-oddness is the dissipation of light energy during light scattering. While referring the reader to [7, 8] for details, we note that the coefficient *b* proportional to the *T*-odd dissipative parameter $\Gamma$ is nonzero only for an open light-energy dissipation channel in the scattering process: the photoionization channel for above-threshold scattering and the radiative or collisional channel for resonance scattering. The photoionization probability and the resonance-level width (the resonance level must necessarily have a multiplet structure [7]) are the parameter $\Gamma$, which defines the light-energy dissipation rate, in the former and latter cases, respectively.

Note that the orientation-related effects can be separated from the effects related to the alignment of atoms, because the difference between the cross sections for the two opposite directions of vector **n** depends on the orientation alone. At the same time, when $\rho_1^n$ and $\rho_3^n$ are nonzero, the effects related to the first- and second-order orientations must be observed simultaneously.

The effect of the first-order orientation on light scattering was discussed in detail in [8]. All qualitatively new effects in light scattering related to the first-order orientation must also be observed for the second-order orientation. Therefore, we only briefly list the principal orientation effects and dwell below on the differences caused by the second-order orientation. Thus, a nonzero circular polarization of scattered light is induced through the orientation even at $\eta_2 = 0$. At the same time, the dependence on the degree of circular polarization of the incident light $\eta_2$ is retained in the angular distribution and linear polarization of the scattered light, which leads to circular dichroism. Interestingly, the alignment of an atom can produce such effects only for an open dissipative channel [9, 13]. Further, the dependences of the linear polarization and angular distribution of the scattered light on the orientations $\rho_1^n$ and $\rho_3^n$ at $\eta_2 = 0$ are induced by the dissipation of light energy; i.e., these dependences are retained only for above-threshold or resonance scattering.

Let us now consider some polarization properties of the scattered light related to the second-order orientation. Formula (13) allows these properties to be established. Thus, the circular polarization of the scattered light induced by the second-order orientation is proportional to the difference between expressions (13) for $\eta_2' = \pm 1$. The absence of a term proportional to $\eta_2\eta_2'$ in (13) implies that this circular polarization does not depend on the Stokes parameter $\eta_2$. By contrast, the circular polarization induced by the first-order orientation depends on $\eta_2$ for an open dissipative channel [8], which leads to circular dichroism. The circular dichroism in the linear polarization of the scattered light is preserved for the second-order orientation [see the terms containing the vector **e**' and proportional to the Stokes parameter $\eta_2$ in (13)]. In contrast to the first-order orientation, this effect does not disappear for forward or back scattering, when the linear polarization vector **e**' and the vector **k** are mutually perpendicular. It is also of interest to note that if the incident light is nonpolarized and if only linearly polarized light with the polarization vector perpendicular to **k** is recorded after scattering, then the scattering intensity retains the dependence on the second-order orientation [see the fifth term in (13)], whereas the dependence on the first-order orientation vanishes. When nonpolarized light is scattered, the same term ensures that the dependence of the linear polarization of the scattered light on the second-order orientation is retained for forward and back scattering.

The second-order orientation also produces several observable effects in the angular distribution of the scattered light. Thus, for example, for the scattering of nonpolarized light, when the contribution of the second-order orientation to the angular distribution is determined in (14) only by the first two terms of form (2) and (3), the dependence of the intensity of the light scattered in the perpendicular direction on the second-order orientation is retained, while its dependence on the first-order orientation vanishes. When the incident light is linearly polarized, the intensity of the scattering in the direction perpendicular to its polarization also depends on the second-order orientation alone [see (11)]. In addition, for forward and back scattering, the orientation dependence of the scattering intensity on the Stokes parameters $\eta_1$ and $\eta_3$ is retained precisely because of the second-order orientation [the second term that defines $\delta_{\beta\gamma}$ in (14) remains nonzero in this case].

Finally, recall that the second-order orientation does not show up in any way in the total cross section for light scattering.

In conclusion, we emphasize that formulas (8), (11), (13), and (14) derived here together with the results

from [8] completely describe the orientation effect on the scattering of light by a polarized atomic system. The first-order alignment effects were considered in [9, 13]. The second-order alignment effects, which are determined by the part of the cross section (4) proportional to $\rho_4^n$, should be studied separately.

## APPENDIX

When expressing pseudoscalars (7) in terms of the scalar and triple scalar products of the vectors appearing in them, we used the following two identities:

$$\begin{aligned}(\{\{\mathbf{n}\otimes\mathbf{n}\}_2\otimes\mathbf{n}\}_3, \{\{\mathbf{d}\otimes\mathbf{e}\}_1\otimes\{\mathbf{f}\otimes\mathbf{g}\}_2\}_3)\\ = \frac{i}{\sqrt{2}}\Big\{\mathbf{d}\cdot(\mathbf{e}\times\mathbf{n})(\mathbf{f}\cdot\mathbf{n})(\mathbf{g}\cdot\mathbf{n})\\ -\frac{1}{5}[\mathbf{d}\cdot(\mathbf{e}\times\mathbf{f})(\mathbf{g}\cdot\mathbf{n})+\mathbf{d}\cdot(\mathbf{e}\times\mathbf{g})(\mathbf{f}\cdot\mathbf{n})\\ +\mathbf{d}\cdot(\mathbf{e}\times\mathbf{n})(\mathbf{f}\cdot\mathbf{g})]\Big\},\end{aligned} \tag{A.1}$$

$$\begin{aligned}(\{\{\mathbf{n}\otimes\mathbf{n}\}_2\otimes\mathbf{n}\}_3, \{\{\mathbf{d}\otimes\mathbf{e}\}_2\otimes\{\mathbf{f}\otimes\mathbf{g}\}_2\}_3)\\ = \frac{i}{4}\Big\{\mathbf{n}\cdot(\mathbf{e}\times\mathbf{f})(\mathbf{d}\cdot\mathbf{n})(\mathbf{g}\cdot\mathbf{n})+\mathbf{n}\cdot(\mathbf{e}\times\mathbf{g})(\mathbf{d}\cdot\mathbf{n})(\mathbf{f}\cdot\mathbf{n})\\ +\mathbf{n}\cdot(\mathbf{d}\times\mathbf{f})(\mathbf{e}\cdot\mathbf{n})(\mathbf{g}\cdot\mathbf{n})+\mathbf{n}\cdot(\mathbf{d}\times\mathbf{g})(\mathbf{e}\cdot\mathbf{n})(\mathbf{f}\cdot\mathbf{n})\\ -\frac{1}{5}[\mathbf{n}\cdot(\mathbf{e}\times\mathbf{g})(\mathbf{d}\cdot\mathbf{f})+\mathbf{n}\cdot(\mathbf{e}\times\mathbf{f})(\mathbf{d}\cdot\mathbf{g})\\ +\mathbf{n}\cdot(\mathbf{d}\times\mathbf{g})(\mathbf{e}\cdot\mathbf{f})+\mathbf{n}\cdot(\mathbf{d}\times\mathbf{f})(\mathbf{e}\cdot\mathbf{g})]\Big\},\end{aligned} \tag{A.2}$$

where $\mathbf{n}$ is a unit real vector, so $\mathbf{n}\cdot\mathbf{n}=1$; and the irreducible tensors on the left-hand sides of (A.1) and (A.2) were constructed according to the rule (5). Yet another pseudoscalar of the form (7) can be determined by using identity (A.1), because it follows from the symmetry properties of the Clebsch–Gordan coefficients that

$$\begin{aligned}(\{\{\mathbf{n}\otimes\mathbf{n}\}_2\otimes\mathbf{n}\}_3, \{\{\mathbf{d}\otimes\mathbf{e}\}_2\otimes\{\mathbf{f}\otimes\mathbf{g}\}_1\}_3)\\ = (\{\{\mathbf{n}\otimes\mathbf{n}\}_2\otimes\mathbf{n}\}_3, \{\{\mathbf{f}\otimes\mathbf{g}\}_1\otimes\{\mathbf{d}\otimes\mathbf{e}\}_2\}_3).\end{aligned}$$

Below, we show how identities (A.1) and (A.2) and other identities of this kind can be derived.

First, note that irreducible tensors of the zero, first, and second ranks $K$ can be constructed from the components of the Cartesian tensor $A_{ik}$:

$$A_{KQ} = \sum_{q_1, q_2} C^{KQ}_{1q_1 1q_2} A_{(q_1 q_2)}, \tag{A.3}$$

where $A_{(q_1 q_2)}$ are the spherical tensor components, which are expressed in terms of the Cartesian components in each of the indices similarly to the spherical components of vector (6). In what follows, the Cartesian tensor components are denoted by the lowercase Roman letters $i$, $j$, $k$, $m$, and $n$. If $A_{ik}$ is a symmetric tensor with a zero trace constructed from two vectors,

$$A_{ik} = \frac{1}{2}(a_i b_k + a_k b_i) - \frac{1}{3}\mathbf{a}\cdot\mathbf{b}\delta_{ik}, \tag{A.4}$$

then only the irreducible tensor of the second rank

$$A_{2Q} = \{\mathbf{a}\otimes\mathbf{b}\}_{2Q}$$

is nonzero. If, alternatively, $B_{ik}$ is an antisymmetric tensor constructed from two vectors,

$$B_{ik} = \frac{1}{2}(d_i e_k - d_k e_i), \tag{A.5}$$

then only the irreducible tensor of the first rank

$$B_{1Q} = \{\mathbf{d}\otimes\mathbf{e}\}_{1Q}$$

is nonzero.

We also need the irreducible tensors composed of the antisymmetric pseudotensor of the third rank, $\varepsilon_{ijk}$ ($\varepsilon_{123}=1$). The irreducible components of this pseudotensor must be defined as

$$\varepsilon^k_{KQ} = \sum_{q_1, q_2, q_3, q} C^{KQ}_{1q_1 kq} C^{kq}_{1q_2 1q_3} \varepsilon_{(q_1 q_2 q_3)}. \tag{A.6}$$

Since the pseudotensor $\varepsilon_{ijk}$ does not change when rotating the coordinate system, only the irreducible tensor of the zero rank (pseudoscalar), $\varepsilon^1_{00}$, can be nonzero. By comparing the expression that defines this pseudoscalar with the pseudoscalar

$$\begin{aligned}\{\mathbf{a}\otimes\{\mathbf{b}\otimes\mathbf{c}\}_1\}_0 &= -\frac{i}{\sqrt{6}}\mathbf{a}\cdot(\mathbf{b}\times\mathbf{c})\\ &= -\frac{i}{\sqrt{6}}a_j\varepsilon_{jkm}b_k c_m\end{aligned}$$

(see formulas from [11]), we easily find that

$$\varepsilon^1_{00} = -\frac{i}{\sqrt{6}}\varepsilon^2_{jkm} = -i\sqrt{6}.$$

Let us introduce the following pseudoscalars in our analysis:

$$\begin{aligned}X_{J;k}\\ = (\{\{\mathbf{a}\otimes\mathbf{b}\}_2\otimes\mathbf{c}\}_J, \{\{\mathbf{d}\otimes\mathbf{e}\}_k\otimes\{\mathbf{f}\otimes\mathbf{g}\}_2\}_J),\end{aligned} \tag{A.7}$$

where $k=1, 2$ and $J=1, 2, 3$. The pseudoscalars $X_{1;k}$ are the scalar products of two irreducible tensors of the first rank (vectors) and can be easily expressed in terms of the scalar and triple scalar products of the vectors appearing in them using formulas from [11].

We are interested in $X_{3;k}$, because pseudoscalars of this type appear on the left-hand sides of identities (A.1) and (A.2). To determine them, let us consider the pseudoscalar

$$\begin{aligned} S_1 &= A_{ik}c_j\varepsilon_{inm}B_{kn}D_{mj} \\ &= \sum_{q_1,q_2,q_3,q_4,q_5} (-1)^{q_1+q_2+q_3+q_4+q_5} \\ &\times A_{(q_1q_2)}c_{(q_3)}\varepsilon_{(-q_1q_4q_5)}B_{(-q_2-q_4)}D_{(-q_5-q_3)} \end{aligned} \tag{A.8}$$

composed of Cartesian tensors. Reversing relations of type (A.3) and relation (A.6), the pseudoscalar $S_1$ can be expressed in terms of the sum of products of the irreducible components in all of the tensors appearing in (A.8) and five Clebsch–Gordan coefficients. The sum of the product of five Clebsch–Gordan coefficients over the moment projections is transformed by the graphical methods described in [14]; $S_1$ can then be written in terms of the pseudoscalars composed of irreducible tensors:

$$\begin{aligned} S_1 &= i\sqrt{6}\sum_{K,K_1,K_2,J} (-1)^{K_1+1} \\ &\times [(2K+1)(2K_1+1)(2K_2+1)]^{1/2} \\ &\times \begin{Bmatrix} 1 & 1 & 1 \\ 1 & K & K_1 \end{Bmatrix} \begin{Bmatrix} 1 & 1 & K_2 \\ J & K_1 & K \end{Bmatrix} \\ &\times (\{A_K \otimes \mathbf{c}\}_J, \{B_{K_1} \otimes D_{K_2}\}_J). \end{aligned} \tag{A.9}$$

The expression for the pseudoscalar

$$\begin{aligned} S_2 &= A_{ik}c_j\varepsilon_{ijn}B_{nm}D_{km} = i\sqrt{6}\sum_{K,K_1,K_2,J} (-1)^{K_1+K_2+1} \\ &\times [(2K+1)(2K_1+1)(2K_2+1)]^{1/2} \\ &\times \begin{Bmatrix} 1 & 1 & K_2 \\ J & K_1 & 1 \end{Bmatrix} \begin{Bmatrix} 1 & 1 & K \\ J & 1 & 1 \end{Bmatrix} \\ &\times (\{A_K \otimes \mathbf{c}\}_J, \{B_{K_1} \otimes D_{K_2}\}_J) \end{aligned} \tag{A.10}$$

can be derived in a similar way. If the symmetric tensors with a zero trace constructed according to the rule (A.4) from vectors **a** and **b**, **d** and **e**, and **f** and **g** are taken as the tensors $A_{ik}$, $B_{ik}$, and $D_{ik}$ in (A.8), respectively, then $S_1$ is expressed, according to (A.9), in terms of the pseudoscalars $X_{J;2}$ (A.7) with $J = 1, 2, 3$; $K = K_1 = K_2 = 2$. When substituting the antisymmetric tensor (A.5) for $B_{ik}$, $S_1$ is expressed in terms of $X_{J;1}$ with $J = 1, 2, 3$ with $K = K_2 = 2$ and $K_1 = 1$ on the right-hand side of (A.9). The scalars $S_2$ for these choices of tensors $A_{ik}$, $B_{ik}$, and $D_{ik}$ are expressed in terms of $X_{J;k}$ with $J = 1, 2$, because $J$ in the sum (A.10) satisfies the triangle condition $\Delta(1, 1, J)$, $\Delta(1, K, J)$, and $K = 2$.

Identity (A.10) allows $X_{2;k}$ to be expressed in terms of $S_2$ and $X_{1;k}$. The sought-for pseudoscalars $X_{3;k}$ can then be expressed in terms of $X_{2;k}$, $X_{1;k}$, and $S_1$ using (A.9). The pseudoscalars $S_1$ (A.8) and $S_2$ (A.10) can obviously be written in terms of the scalar and triple scalar products of the vectors constructed from them. As a result, $X_{3;k}$ (A.7) is expressed in terms of the scalar and triple scalar products of the vectors appearing in them. The formulas simplify in the case of $\mathbf{a} = \mathbf{b} = \mathbf{c} = \mathbf{n}$ and $\mathbf{n} \cdot \mathbf{n} = 1$ concerned, because some of the triple scalar products become zero and some of the scalar products become unity. We derived identities (A.1) and (A.2) by the method described here.

## REFERENCES


1. G. V. Skrotskiĭ and T. G. Izyumova, Usp. Fiz. Nauk **73**, 423 (1961) [Sov. Phys. Usp. **4**, 177 (1961)].
2. W. Happer, Rev. Mod. Phys. **44**, 169 (1972).
3. K. Blum, *Density Matrix Theory and Applications* (Plenum, New York, 1996, 2nd ed.).
4. H. Klar and H. Kleinpoppen, J. Phys. B **15**, 933 (1982).
5. N. A. Cherepkov and V. V. Kuznetsov, J. Phys. B **22**, L405 (1989).
6. M. Ya. Agre and L. P. Rapoport, Zh. Éksp. Teor. Fiz. **104**, 2975 (1993) [JETP **77**, 382 (1993)].
7. M. Ya. Agre and N. L. Manakov, J. Phys. B **29**, L7 (1996).
8. M. Ya. Agre, Zh. Éksp. Teor. Fiz. **120**, 562 (2001) [JETP **93**, 491 (2001)].
9. M. Ya. Agre, Zh. Éksp. Teor. Fiz. **110**, 2018 (1996) [JETP **83**, 1112 (1996)].
10. V. B. Berestetskii, E. M. Lifshitz, and L. P. Pitaevskii, *Course of Theoretical Physics*, Vol. 4: *Quantum Electrodynamics* (Nauka, Moscow, 1980; Pergamon, New York, 1982).
11. D. V. Varshalovich, A. N. Moskalev, and V. K. Khersonskii, *Quantum Theory of Angular Momentum* (Nauka, Leningrad, 1975; World Sci., Singapore, 1988).
12. L. D. Landau and E. M. Lifshitz, *Course of Theoretical Physics*, Vol. 2: *The Classical Theory of Fields* (Nauka, Moscow, 1973; Pergamon, Oxford, 1975), Para. 50.
13. M. Ya. Agre, Opt. Spektrosk. **92** (4), 550 (2002) [Opt. Spectrosc. **92**, 499 (2002)].
14. E. El Baz and B. Castel, *Graphical Methods of Spin Algebras in Atomic, Nuclear, and Particle Physics* (Dekker, New York, 1972; Mir, Moscow, 1974).


*Translated by V. Astakhov*

*Journal of Experimental and Theoretical Physics, Vol. 95, No. 2, 2002, pp. 206–209.*
*Translated from Zhurnal Éksperimental'noĭ i Teoreticheskoĭ Fiziki, Vol. 122, No. 2, 2002, pp. 241–244.*


**NUCLEI, PARTICLES, AND THEIR INTERACTION**

# On the Stability of Electromagnetic Field in Inverted Media

**V. A. Antonov[a] and B. P. Kondrat'ev[b, *]**

[a]*Pulkovo Observatory, Russian Academy of Sciences, Pulkovskoe shosse 65, St. Petersburg, 196140 Russia*
[b]*Udmurt State University, Krasnoarmeĭskaya ul. 71, Izhevsk, 426034 Russia*
**e-mail: kond@uni.udm.ru*

Received February 21, 2002

**Abstract**—The dispersion equation in the problem of electromagnetic field stability in an infinite inverted homogeneous medium is analyzed rigorously. The instability region for small quantum numbers $k$ is established. It is found that, in contrast to the prevailing opinion, a continuous transition is also possible between polariton waves and electromagnetic waves upon a gradual variation of $k$; in this case, the two types of waves cannot be separated. *© 2002 MAIK "Nauka/Interperiodica".*

## 1. INTRODUCTION

The instability of waves in inverted media has become the object of intense investigations. We are speaking of the situation described by V.V. Zheleznyakov, V.V. Kocharovskiĭ, and Vl.V, Kocharovskiĭ, [1, 2]. In spite of a detailed analysis of the equations for an electromagnetic field in a homogeneous infinite medium with inversion [1, 2], some aspects still remain unclear and will be investigated more thoroughly here.

It should be recalled that, in the semiclassical approximation, the rf electromagnetic field in a substance is described by the following equations:

$$\operatorname{curl}\mathbf{E} = -\frac{1}{c}\frac{\partial\mathbf{B}}{\partial t},\quad \operatorname{curl}\mathbf{B} = \frac{1}{c}\frac{\partial(\mathbf{E}+4\pi\mathbf{p})}{\partial t} + \frac{4\pi\sigma}{c}\mathbf{E}, \quad (1)$$

$$\frac{\partial^2\mathbf{p}}{\partial t^2} + \frac{2}{T_2}\frac{\partial\mathbf{p}}{\partial t} + \left(\omega_0^2 + \frac{1}{T_2^2}\right)\mathbf{p} = \frac{\omega_c^2}{4\pi}\mathbf{E}. \quad (2)$$

Here, we use the notation adopted in [1, 2]: **E** and **B** are the electric and magnetic field vectors, **p** is the polarization vector of the substance, $\omega_0$ is the frequency of transition between two levels, $1/T_2$ is the broadening of the corresponding spectral line, and $\omega_c$ is the plasma (cooperative) frequency of the substance in the given state.

Above all, we are interested in the case of inverted state, when $\omega_c^2 < 0$. Irrespective of the direction of polarization vector, we obtain from Eqs. (1) and (2)

$$1 + \frac{4\pi i\sigma}{\omega} - \frac{\omega_c^2}{(\omega + i/T_2)^2 - \omega_0^2} - \frac{k^2c^2}{\omega^2} = 0, \quad (3)$$

where $\omega$ is the frequency of the electromagnetic field and $k$ is the wave number. Equation (3) was derived in [1], but the analysis of this equation made in [1, 2] has some drawbacks.

First, the condition for the existence of the instability region on the scale of wave numbers,

$$\omega_c^2 < -\frac{8\pi\sigma}{T_2}, \quad (4)$$

was derived in [1] not quite rigorously, but to a certain approximation. In fact, it permits a quite exact derivation on the basis of Eq. (3). Second, the boundedness of the instability region for large as well as small values of $k$ was noted in [1, 2], but the second of these statements may be incorrect in the nonresonance case. Third, two types of waves (polariton and electromagnetic waves) are indicated in [1, 2] as two different entities on the basis of their physical differences. In actual practice, a continuous transition between them is sometimes possible upon a gradual change in $k$; consequently, a wave cannot be unambiguously attributed to a certain type of waves. In this paper, we fill these gaps.

## 2. CRITERION FOR THE EXISTENCE OF THE INSTABILITY ZONE

For $k \longrightarrow \infty$ and invariability of the remaining parameters, the difference between the two types of waves is manifested with maximum clarity. We can easily obtain the corresponding asymptotic form for all four roots of Eq. (3):

$$\omega_{1,2} = \pm kc - 2\pi i\sigma + O\left(\frac{1}{k}\right),$$
$$\omega_{3,4} = \pm\omega_0 - \frac{i}{T_2} + O\left(\frac{1}{k^2}\right). \quad (5)$$

The solutions (5) obviously satisfy the stability criterion $\mathrm{Im}\,\omega < 0$. We will gradually decrease the value of $k$. The instant of transition from stability to instability and back is characterized by a purely real-valued quan-

tity ω. Then the separation of the real and imaginary components in Eq. (3) leads to two equations

$$1 - \frac{k^2c^2}{\omega^2} - \frac{\omega_c^2(\omega^2 - 1/T_2^2 - \omega_0^2)}{(\omega^2 - 1/T_2^2 - \omega_0^2)^2 + 4\omega^2/T_2^2} = 0, \quad (6)$$

$$\frac{4\pi\sigma}{\omega} + \frac{2\omega\omega_c^2/T_2}{(\omega^2 - 1/T_2^2 - \omega_0^2)^2 + 4\omega^2/T_2^2} = 0. \quad (7)$$

It is convenient to eliminate, first, the cumbersome denominator of fractions in Eqs. (6) and (7), which gives the values of the roots:

$$\omega^2 = \frac{2\pi\sigma T_2(\omega_0^2 + 1/T_2^2) + k^2c^2}{1 + 2\pi\sigma T_2}. \quad (8)$$

The form of Eq. (3) rules out the possibility of $\omega = 0$ and $\omega = \infty$ at the very outset. The substitution of Eq. (8) into any of equations (6) or (7) allows us to obtain the required relation between the parameters at the critical point in the form of the quadratic equations for the auxiliary quantity $K = k^2c^2$:

$$K^2 + \left[-2\left(\omega_0^2 + \frac{1}{T_2^2}\right) + (1 + 2\pi\sigma T_2)\left(\frac{\omega_c^2}{2\pi\sigma T_2} + \frac{4}{T_2^2}\right)\right]K + \left(\omega_0^2 + \frac{1}{T_2^2}\right)^2 + 2\pi\sigma T_2(1 + 2\pi\sigma T_2) \times \left(\omega_0^2 + \frac{1}{T_2^2}\right)\left(\frac{\omega_c^2}{2\pi\sigma T_2} + \frac{4}{T_2^2}\right) = 0. \quad (9)$$

In some cases, the instability region does not exist at all. This is the case for a negative value of discriminant Δ of Eq. (9) or for the presence of two real-valued but negative roots for $K$. To be more precise, $\Delta < 0$ for

$$-\frac{4}{T_2^2} < \frac{\omega_c^2}{2\pi\sigma T_2} < 4\omega_0^2, \quad (10)$$

and both roots for $K$ are negative only if the coefficient of the first power of $K$ in Eq. (9) has positive sign, i.e.,

$$\frac{\omega_c^2}{2\pi\sigma T_2} > -\frac{4}{T_2^2} + \frac{2(\omega_0^2 + 1/T_2^2)}{1 + 2\pi\sigma T_2}. \quad (11)$$

After the deduction of regions (10) and (11), we are left with the range of $\omega_c^2$, namely, the region specified by inequality (4), in which a transition from instability to stability for any real $K$ takes place. Thus, criterion (4) is confirmed by rigorous calculations.

## 3. BOUNDEDNESS OF THE INSTABILITY REGION FOR SMALL WAVE NUMBERS

Under condition (4), the free term in Eq. (9) is positive if

$$\frac{\omega_c^2}{2\pi\sigma T_2} + \frac{4}{T_2^2} > -\frac{\omega_0^2 + 1/T_2^2}{2\pi\sigma T_2(1 + 2\pi\sigma T_2)}. \quad (12)$$

If this condition is satisfied, the instability region has a finite left boundary on the $K$ scale; otherwise, the instability region extends to infinitely small values of $K$ since one of the roots becomes negative for $k^2c^2$.

These relations can be conveniently illustrated for the particular case of resonance considered in detail in [1, 2]. In this case, a small correction

$$h = kc - \omega_0$$

is introduced, and the quantities σ, $|\omega_c|$, and $T_2^{-1}$ are also regarded as small. In this case, the roots ω from one of the pairs are also close to $kc$, and we can set

$$\omega = kc + \delta.$$

The relation between the small correction δ and the renormalized wave number $h$ is given (after disregarding quantities with a higher order of smallness) by the following simplified equation:

$$2\delta + 4\pi i\sigma - \frac{\omega_c^2}{2(\delta + i/T_2 + h)} = 0, \quad (13)$$

which is given in [1, 2] in a somewhat different form. In fact, it is a quadratic equation (the other two roots of Eq. (3) for ω are symmetric to those obtained by us and are close to $-kc$). The problem of the critical point of the stability–instability condition is solved as before: assuming that δ is purely real, we separate the real and imaginary components in Eq. (13). Under the same condition (4), both critical values for $h$ are always real-valued:

$$h_{cr} = \pm(1 + 2\pi\sigma T_2)\sqrt{\frac{1}{2\pi\sigma T_2}\left|\omega_c^2 + \frac{8\pi\sigma}{T_2}\right|}. \quad (14)$$

A simple analysis of this expression as a function of σ with respect to its extrema for the same values of the remaining parameters shows that the maximum and the minimum are attained at the levels

$$\sigma = \frac{2 + \mu \pm \sqrt{(2 + \mu)(\mu - 14)}}{16\pi T_2}, \quad (15)$$

where

$$\mu = -\omega_c^2 T_2^2.$$

Consequently, we can make the following refininement to Fig. 3 in [1]: the curve describing the dependence of σ on $h$ has the form of an inverted suspended drop only for $\mu > 14$; otherwise, we obtain a simple "hat" (in [1], only the condition $\mu > 4$ is used explicitly).

## 4. MAXIMUM INCREMENT

If we separate the real and imaginary components in the small correction $\delta$,

$$\delta = \delta_1 + i\delta_2,$$

the quantity $\delta_2$ will characterize the increment (if we choose solutions with $\delta_2 > 0$). The maximum of $\delta_2$ with respect to $h$ can be obtained from the following considerations. We consider, along with Eq. (13), the complex conjugate relation

$$2\delta^* - 4\pi i\sigma - \frac{\omega_c^2}{2(\delta^* - i/T_2 + h)} = 0, \qquad \delta^* = \delta_1 - i\delta_2. \tag{16}$$

We denote the left-hand sides of Eqs. (13) and (16) by $Q(\delta_1, \delta_2, h)$ and $Q^*(\delta_1, \delta_2, h)$ and vary $h$ as well as $\delta_1$ and $\delta_2$. Then we can write

$$\frac{\partial Q}{\partial \delta_1}d\delta_1 + \frac{\partial Q}{\partial \delta_2}d\delta_2 + \frac{\partial Q}{\partial h}dh = \frac{\partial Q^*}{\partial \delta_1}d\delta_1 + \frac{\delta Q^*}{\partial \delta_2}d\delta_2 + \frac{\partial Q^*}{\partial h}dh = 0. \tag{17}$$

For a value of $h$ corresponding to the maximum increment, we must have $d\delta_2 = 0$, so that the solvability condition for system (17) has the form

$$\begin{vmatrix} \frac{\partial Q}{\partial \delta_1} & \frac{\partial Q}{\partial h} \\ \frac{\partial Q^*}{\partial \delta_1} & \frac{\partial Q^*}{\partial h} \end{vmatrix} = 0. \tag{18}$$

According to the rule for differentiation of a complex function, we have

$$\frac{\partial Q}{\partial \delta_1} = \frac{\partial Q}{\partial \delta}, \quad \frac{\partial Q^*}{\partial \delta_1} = \frac{\partial Q^*}{\partial \delta^*}.$$

Evaluating determinant (18) and carrying out elementary cancellation, we obtain $h = 0$. In this case, the roots of Eq. (13) are purely imaginary, $\delta = iy$, and for a growing wave we have

$$y = \frac{-(2\pi\sigma + 1/T_2) + \sqrt{(2\pi\sigma - 1/T_2)^2 - \omega_c^2}}{2}. \tag{19}$$

Thus, the only maximum of $\mathrm{Im}\,\delta$ with respect to $h$ is attained at the middle of the instability interval. At the same time, function (19) is monotonic with respect to $\sigma$. It decreases from the maximum value

$$y_m = \frac{1}{2}\left(-\frac{1}{T_2} + \sqrt{\frac{1}{T_2^2} - \omega_c^2}\right) \tag{20}$$

for $\sigma = 0$ to zero for the known critical value $\omega_c^2 = -8\pi\sigma/T_2$.

## 5. SEPARATION OF TWO TYPES OF WAVES

As before, we confine our analysis to the region close to resonance. The solution of Eq. (13) is given by

$$\sigma = -\pi i\sigma - \frac{i}{2T_2} - \frac{h}{2} \pm \frac{\sqrt{R}}{2}, \tag{21}$$

where

$$R = h^2 + \frac{2ih}{T_2}(1 - 2\pi\sigma T_2) + \omega_c^2 - \left(2\pi\sigma - \frac{1}{T_2}\right)^2. \tag{22}$$

It is worth noting that $\mathrm{Im}R$ generally differs from zero and passes through zero only for $h = 0$ except in the special case mentioned in [1, 2], when $2\pi\sigma T_2 = 1$. This means that $\sqrt{R}$ as a complex-valued quantity remains within a quadrant upon a change in $h$ both for $h > 0$ (otherwise $R$ would be real-valued) and for $h < 0$ (but the quadrant will be different). At the point $h = 0$, we have $R^2 < 0$ and, hence, $\sqrt{R}$ passes through the imaginary axis at this moment.

Let us now consider large values of $h > 0$, assuming, for the time being, that $2\pi\sigma T_2 > 1$. From Eq. (22), we asymptotically obtain (see [3])

$$\sqrt{R} = \pm\left[h + \frac{i}{T_2}(1 - 2\pi\sigma T_2) + O\left(\frac{1}{h}\right)\right]. \tag{23}$$

For the "upper" solution (corresponding to the larger value of $\mathrm{Re}\,\delta$), we chose the plus sign. Thus, $\mathrm{Im}\sqrt{R} < 0$ and $\sqrt{R}$ are in the fourth quadrant. At point $h = 0$, a transition to the third quadrant takes place, while, for $h < 0$ and large $|h|$, the position of $\sqrt{R}$ in the third quadrant indicates, according to the same formula (23), that we have also chosen the plus sign. Thus, the choice of the sign for $\sqrt{R}$ is matched on the left and right of scale $h$. The same is also true for $2\pi\sigma T_2 < 1$ with the only difference that the values of $\sqrt{R}$ in the intermediate region pass through the upper (first and second) quadrants.

The quantity $X$ from formula (2.5) in [1] in the case of resonance has the following form in our notation:

$$X = -\frac{\omega_c^2}{8\pi kc(\delta + i/T_2 + h)} = -\frac{\delta + 2\pi i\sigma}{2kc}. \tag{24}$$

This quantity tends to a finite value if we take the upper sign in formula (23) and to infinity if we take the lower sign. According to the terminology used in [1, 2], the latter case corresponds to a polariton wave and, accordingly, the former case corresponds to an electromagnetic wave. However, taking the above arguments into consideration, we can verify that the solution with the

larger value of $\mathrm{Im}\delta$ in the intermediate region corresponds to a polariton wave for $2\pi\sigma T_2 > 1$ and to an electromagnetic wave for $2\pi\sigma T_2 < 1$. This conclusion can be found in [1], but it is drawn on the basis of energy considerations, while our arguments are purely algebraic. The physical interpretation also changes in our approach. In the intermediate region ($|h| < h_{cr}$ from Eq. (14)), unstable solutions form a continuous set. The interpretation of a wave as an electromagnetic or a polariton wave must be treated as subjective. This difference becomes objective only for $h \longrightarrow \infty$ far away from the instability region.

## 6. CONCLUSIONS

A number of results obtained semi-intuitively in [1, 2] are confirmed by rigorous calculations. Above all, this concerns the criterion for the emergence of the instability region (4) on the scale of $k$. A qualitative separation of the cases when $2\pi\sigma T_2 > 1$ and $2\pi\sigma T_2 < 1$ is also confirmed, albeit not for the corresponding waves directly, but only for their continuous extension to the nonresonance region. In the instability region, however, the waist shown graphically in [1] and separating the two types of waves is not observed necessarily.

In actual practice, a continuous transition may sometimes occur between polariton and electromagnetic waves upon a gradual change in $k$, and hence a wave cannot be assigned unambiguously to a certain type. The instability may also be manifested away from the resonance, but its region may or may not be bounded for small values of $k$.

## REFERENCES

1. V. V. Zheleznyakov, V. V. Kocharovskiĭ, and Vl. V. Kocharovskiĭ, Zh. Éksp. Teor. Fiz. **87**, 1565 (1984) [Sov. Phys. JETP **60**, 897 (1984)].
2. V. V. Zheleznyakov, V. V. Kocharovskiĭ, and Vl. V. Kocharovskiĭ, Usp. Fiz. Nauk **159**, 193 (1989) [Sov. Phys. Usp. **32**, 835 (1989)].
3. G. A. Korn and T. M. Korn, *Mathematical Handbook for Scientists and Engineers* (McGraw-Hill, New York, 1968; Nauka, Moscow, 1987), Chap. I.4.

*Translated by N. Wadhwa*

*Journal of Experimental and Theoretical Physics, Vol. 95, No. 2, 2002, pp. 210–220.*
*Translated from Zhurnal Éksperimental'noĭ i Teoreticheskoĭ Fiziki, Vol. 122, No. 2, 2002, pp. 245–257.*


**NUCLEI, PARTICLES, AND THEIR INTERACTION**

# Visualization of the Wave Function of a Quantum Particle in the Momentum Space by the Field-Emission Microscopy Technique

**S. K. Sekatskii* and V. S. Letokhov**

*Institute of Spectroscopy, Russian Academy of Sciences, Troitsk, Moscow oblast, 142190 Russia*

**e-mail: sekats@isan.troitsk.ru*

Received February 27, 2002

**Abstract**—An interpretation of the field-emission images of molecules, impurity ions, and nanostructures placed on the tip of a field-emission microscope is given. It is shown that often such images represent nothing else but the visualization of the wave function of the emitted quantum particle in the momentum space. The results of many earlier experiments are reinterpreted with regard to the results obtained in the present work. *© 2002 MAIK "Nauka/Interperiodica".*

## 1. INTRODUCTION

The field-emission microscopy of metal and semiconductor tips has been successfully applied to the study of various problems of surface physics, to the analysis of electrophysical properties of metals and alloys, etc. (see, for example, the monographs [1–3]). It is believed that the basic principles of the process are firmly established and the theory is well developed. In particular, an assertion is widely recognized that the spatial resolution of the method is limited to several nanometers, so that, in contrast to the field-ion microscopy technique, individual quantum particles cannot be directly observed.

This assertion is based on the following fact. The analysis of the motion of emitted particles in the radial electric field of a field-emission microscope shows that a particle of mass $m$ and charge $e$ possessing an initial transverse (radial) momentum of $p_\perp = \sqrt{2mE_\perp}$ hits a point on the detector displaced from its stereographic projection [1–3] by the quantity $H$ given by

$$H = 2L\sqrt{\frac{E_\perp}{eU}}. \quad (1)$$

Here, $U$ is the emitter potential and $L$ is the distance from the field-emission tip to the detector. In practical field-emission microscopy, one usually assumes that every point of the tip can serve as a source of emission. Then, the statistical distribution of the transverse momentum of electron gas in metals and alloys determines, according to (1), the diameter of the image of each point on the screen $\delta$ and, hence, the spatial resolution of the method. The analysis carried out by Gomer *et al.* with regard to the Fermi distribution of electrons in metal [3] yields the following result:

$$\langle E_\perp \rangle = \frac{2}{9}\frac{\hbar e}{\sqrt{2m}kr}\frac{U}{\sqrt{W}}. \quad (2)$$

Here, $W$ is the work function of electrons from metal (a barrier height) and $k \approx 5$ is the coefficient of proportionality between the electric field $F$ on the tip, its potential $U$, and the radius of curvature $r$, $F = U/kr$. The substitution of (2) into (1) shows that the resolution of a field-emission microscope does not depend on the potential of the tip and is proportional to $(r/W^{1/2})^{1/2}$; in the typical case ($r$ = 100 nm and $W$ = 4 eV), it amounts to about 2 nm, which is substantially greater than the interatomic distance. The spatial resolution cannot be increased drastically by decreasing the radius of curvature of the tip because the momentum dispersion is determined by the Heisenberg uncertainty principle: an electron source localized within a region of diameter $\delta$ necessarily has a transverse momentum on the order of $p_\perp \approx \hbar/\delta$. Thus, the observable dimension $A$ of the structure can be expressed as

$$A^2 = \frac{2L^2\hbar^2}{m\delta^2 eU} + \frac{L^2\delta^2}{(\gamma r)^2}, \quad (3)$$

where $\gamma$ is a numerical coefficient equal to 1.5–2, which is attributed to the difference between the geometry of the actual microscope and an ideal spherical condenser. The minimization of (3) yields the following well-known expression for the fundamental limit of resolution:

$$\delta = \left(\frac{2\hbar^2\gamma^2 r^2}{meU}\right)^{1/4}.$$

For $r$ = 10 nm, we have $\delta \approx 1$ nm, which also cannot guarantee a single-atom spatial resolution [1–4].

However, it is known that, if a single particle is placed on a field-emission tip and this particle has energy levels admitting resonance tunneling of electrons from the emitter, then the local value of the emission current increases by several orders of magnitude, and a bright spot appears on the detector screen (see the survey papers [5, 6]). Hence, the method of field-emission microscopy enables one to observe a single quantum particle; this was demonstrated for molecules [7] and atoms [8] and, later on, also for clusters [9] and impurity atoms in the dielectric coatings of field-emission tips [10]. In this case, the particles on the detector are represented by a wide structureless spot; therefore, it is more justified to describe such a situation merely as detecting an individual atomic particle rather than obtaining its image.

A different situation occurs when the field-emission processes from a quantum particle can be described as the ionization of precisely this particle, and a metal tip only serves as a source of emitted electrons and provides a radial imaging electric field. (Note that it is this situation that occurs in the recently developed method of laser photoelectron projection microscopy [11, 12].) In this case, one should interpret formula (1) as the transformation of the transverse momentum distribution of a quantum particle into its spatial image. Projection field-emission images of quantum particles on the tip of a microscope allow one to measure this momentum distribution experimentally and, hence, to observe the wave function of a quantum particle.

In this paper, we analyze the process of obtaining field-emission images of isolated quantum particles and nanostructures located on a field-emission tip. On the basis of the results obtained, we give another interpretation of the results of some earlier works in which the authors observed structuralized field-emission images of adsorbed molecules.

## 2. FIELD-EMISSION IMAGES OF ISOLATED QUANTUM PARTICLES: THEORY

### *2.1. Momentum Distribution*

Consider an isolated quantum particle (an atom, a molecule, or a nanostructure) located on the tip of a field-emission microscope. The state of such a particle differs from the state of an appropriate free quantum particle. Nevertheless, even when located on a metal surface, it often preserves its inherent energy levels and can be considered as a "quasi-free" particle. This is especially true when the field-emission tip is coated with a dielectric layer on which a particle under investigation is situated.

The field ionization of such a particle should be considered as the tunneling of an external electron from a quantum system characterized by a well-defined momentum distribution. Podolsky and Poling [13] were first to demonstrate that, for a hydrogen atom, this distribution can be obtained as the Fourier transform of a wave function $\psi(\mathbf{r})$ expressed in the coordinate space. We will consider a cylindrical coordinate system $z$, $\rho$, $\varphi$ with the $z$ axis coinciding with the symmetry axis of the field-emission cathode and a particle situated at the origin. The wave function of the ionized particle can nearly always be factorized as $\psi(\mathbf{r}) = g(\rho, z)f(\varphi)$, so that the corresponding momentum distribution $P(p_z, p_\rho, \Phi)$, i.e., the Fourier integral

$$P = \frac{1}{h^{3/2}}\int e^{-(i/\hbar)\mathbf{p}\cdot\mathbf{r}}\psi(r)dr,$$

can be obtained from the explicit expression for the scalar product $\mathbf{p}\cdot\mathbf{r}$ in cylindrical coordinates:

$$P(p_z, p_\rho, \Phi) = h^{-3/2}\int_{-\infty}^{\infty}\exp\left(-\frac{i}{\hbar}p_z z\right)dz \times \int_0^\infty 2\pi\rho g(\rho, z)d\rho \int_0^{2\pi}\exp\left(-\frac{i}{\hbar}p_\rho\rho\cos(\Phi-\varphi)\right)f(\varphi)d\varphi. \quad (4)$$

The distribution in $\varphi$ for free atoms is given by the function $f(\varphi) = \exp(im\varphi)$, where $m$ is an integer. Often, instead of the "formal" symmetry law $\exp(im\varphi)$, the state of quantum particles adsorbed on the surface can be characterized by a function of the type $\cos(\nu\varphi)$, which describes the real angular symmetry with integer or half-integer $\nu$. For integer $\nu = m$, the integral with respect to $\varphi$ is expressed in terms of the Bessel function of order $m$ by relations of the form

$$\int_\beta^{\beta+2\pi}\exp[i(m\alpha - z\sin\alpha)]d\alpha = 2\pi J_m(z)$$

[14]. This allows us to reduce (4) to

$$P(p_z, p_\rho, \Phi) = h^{-3/2}\exp(im\Phi)\int_{-\infty}^{\infty}\exp\left(-\frac{i}{\hbar}p_z z\right)dz \times \int_0^\infty 4\pi^2\rho g(\rho, z)J_m\left(\frac{p_\rho\rho}{\hbar}\right)d\rho. \quad (5)$$

In the case of a real angular symmetry, the function $\exp(im\Phi)$ in (5) is replaced by the function $\cos(m\Phi)$. Hence, we can draw the following conclusion: The $m$-fold angular symmetry of the spatial wave function is transferred to the wave function in the momentum space. According to (1), in the case of real symmetry, this gives rise to the angular symmetry in the field-emission images.

To analyze the case of arbitrary, including half-integer, $\nu$, the Fourier-transform (4) is expressed in terms of

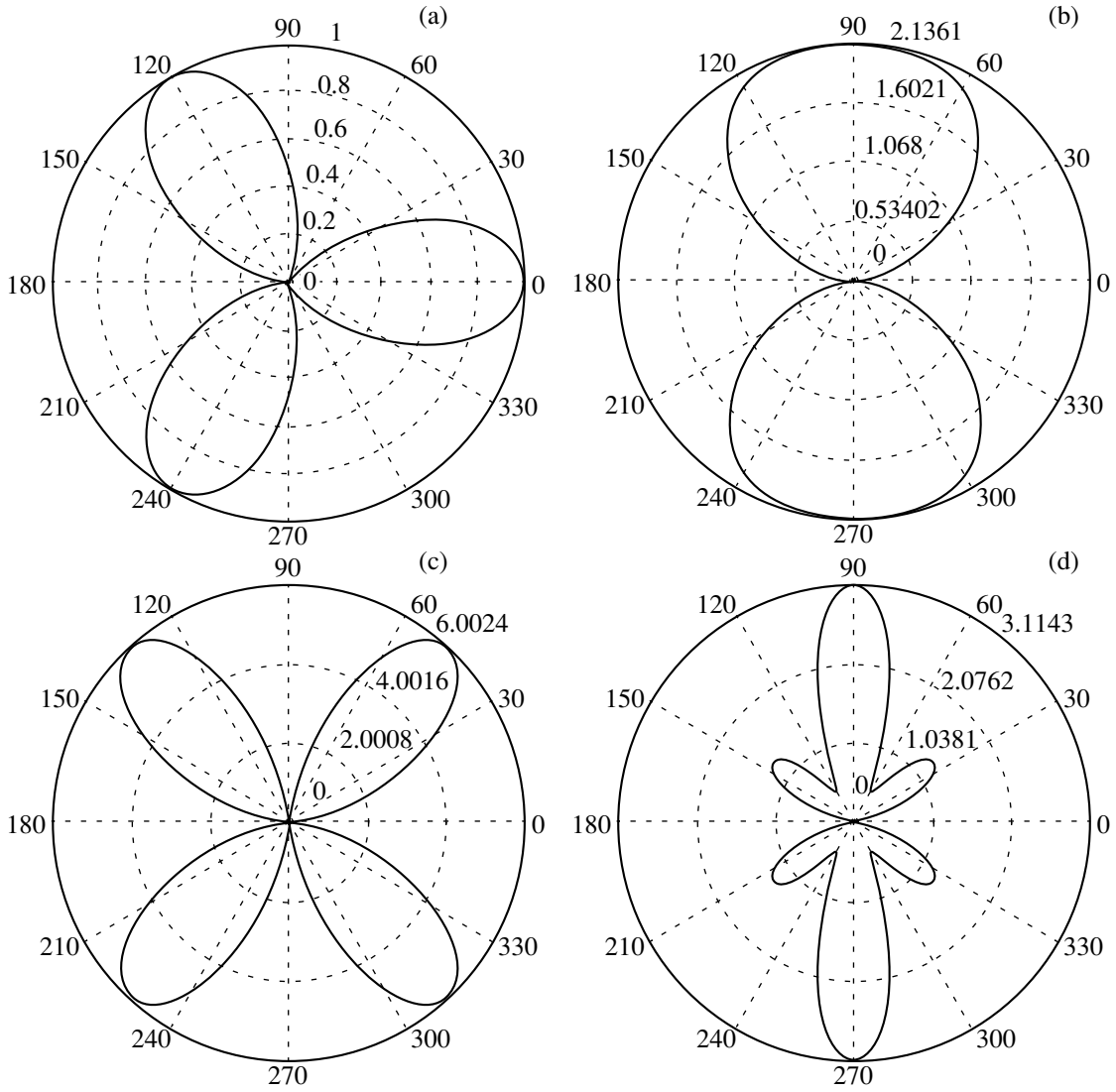


**Fig. 1.** (a) Square of the spatial wave function possessing a threefold angular symmetry and the corresponding probabilities of the angular momentum distribution for (b) $a = 1.1$, (c) 3.2, and (d) = 6.8.

the Anger and Weber functions $J_\nu(z)$ and $E_\nu(z)$, defined as

$$J_\nu(z) = \frac{1}{\pi}\int_0^\pi \cos(\nu\varphi - z\sin\varphi)\,d\varphi,$$

$$E_\nu(z) = \frac{1}{\pi}\int_0^\pi \sin(\nu\varphi - z\sin\varphi)\,d\varphi,$$

which coincide with the Bessel functions for integer $\nu$ and are closely related to the Struve functions [14]. However, these functions are not widely used and are poorly tabulated; the application of these functions has no advantages over the direct numerical integration of appropriate expressions.

Such integration shows that, to obtain half-integer $\nu$, one does not transfer the angular symmetry of the spatial wave function to the angular symmetry of the momentum wave function (which is evident from the structure of the corresponding integral). In Fig. 1, this result is illustrated by the results of calculating the wave function $w(\Phi)w^*(\Phi)$, where

$$w(\Phi) = \int_0^{2\pi} \exp[-ia\cos(\Phi - \varphi)]\cos\frac{3\varphi}{2}\,d\varphi,$$

for three arbitrarily chosen different values of the parameter $a \equiv p_\rho\rho/\hbar$. This function corresponds to the nonnormalized probability of the angular momentum distribution for the spatial electron density distribution

$$\psi^2(\rho, \varphi) = \cos^2\frac{3\varphi}{2}\delta(\rho_0),$$

which possesses a threefold angular symmetry (cf. (4) and (8)). One can see that there is nothing similar to the threefold angular symmetry in the momentum space: different angular distributions that often exhibit two- or fourfold symmetry are observed for different radial momenta $p_\rho = \hbar a/\rho_0$. This situation accounts for the fact that the field-emission image of an adsorbed molecule having a threefold spatial symmetry never exhibits a three-leaf structure resembling the molecule itself ([3]; see also Subsection 3.1 and the references cited there).

Consider the case of integer $m$ in greater detail. For the further analysis, we have to specify the wave function $g(\rho, z)$. We assume that it can be factorized (at least approximately) as the product $g(\rho, z) = u(\rho)b(z)$. Then, the momentum distribution is also factorized as a product of the normal momentum distribution of emitted electrons $a(p_z)$ (an ordinary Fourier-transform of $b(z)$) and the radial momentum distribution

$$q(p_\rho) = \int_0^\infty \rho J_m\left(\frac{p_\rho \rho}{\hbar}\right)u(\rho)d\rho, \qquad (6)$$

where, just as everywhere below, we omit the normalizing factors. Examples of calculating integral (6) are known for many functions $u(\rho)$ that can be used as model examples as applied to the problem under consideration. For example, for the function $u(\rho) = \rho^n\exp(-\gamma\rho)$, by which one can approximate wave functions in many cases, integral (6) is expressed in terms of elementary functions ([14, Example 2.12.8.4]):

$$q(p_\rho) = (-1)^{n+1}\left(\frac{p_\rho}{\hbar}\right)^{-m}\frac{\partial^{n+1}}{\partial\gamma^{n+1}}\frac{\left(\sqrt{\gamma^2 + (p_\rho/\hbar)^2} - \gamma\right)^m}{\sqrt{\gamma^2 + (p_\rho/\hbar)^2}}, \qquad (7)$$

where $m$ may even be noninteger. If the function $u(\rho)$ can be approximated by the delta function $\delta(\rho_0)$, then, obviously,

$$q(p_\rho) = \rho_0 J_m\left(\frac{p_\rho \rho_0}{\hbar}\right). \qquad (8)$$

The consideration of these and other examples shows that one can make another assertion virtually for all appropriate wave functions of an ionized particle: The angular symmetry of a spatial wave function leads to the radial momentum distribution that attains its maximum at a certain nonzero value of $p_\rho$.

In this case, formula (1) shows that the density of the field-emission current vanishes for $H = 0$, which implies that ring-shaped structures appear in the field-emission images.

### *2.2. The Narrowing of the Momentum Distribution under Tunneling*

Another important factor for analyzing the formation of field-emission images of isolated quantum particles situated on a field-emission tip is the narrowing of the radial momentum distribution (and the corresponding narrowing of the spatial emission pattern) as a result of tunneling. The tunneling is essentially three-dimensional. An emitted electron moves in a radial three-dimensional (quasi)-Coulomb field of an impurity particle in a homogeneous (quasi)-one-dimensional external electric field. One can assume that this field acts only in one direction since the characteristic length at which it varies (on the order of the curvature radius $r$ of the tip) is much greater than the barrier width. Such character of tunneling substantially narrows down the transverse momentum distribution, because the greater $p_\perp$, the greater the effective path passed by the particle in the classically forbidden region below the barrier, and the greater the effective width of the barrier [15–20].

This fact was first pointed out by Kapur and Peierls in their classical work [15], where they introduced the concept of imaginary quasiclassical trajectory of a particle passing below the barrier and showed that, in the WKB approximation, the tunneling probability can be obtained by integrating the particle momentum along this trajectory, by analogy with the well-known one-dimensional case. Thus, the trajectory of a particle with energy $E_0$ in a field with potential $U(r)$ can always be expressed by equation

$$\frac{m}{2}\left(\frac{dr}{dt}\right)^2 = |U(r) - E_0|, \qquad (9)$$

while the permeability of the barrier $P = \text{const}\exp(-D)$ can be expressed as an integral along this trajectory, parameterized by its length $s$:

$$D = \frac{2}{\hbar}\int\sqrt{2m|U(r) - E_0|}\,ds. \qquad (10)$$

Analytic expressions for the wave function of a tunneling electron were obtained in the case when its attractive interaction can be characterized by a Fermi potential (pseudopotential) of zero radius

$$-V\delta(r)\frac{\partial}{\partial r},$$

i.e., for the Schrödinger equation (in atomic units)

$$\left(E + \frac{1}{2}\nabla^2 - Fz\right)\psi(r) = V\delta(r)\frac{\partial\psi}{\partial r}$$

[16–18]. In the absence of an electric field, this equation describes the only bound state with energy of $E_0 = -0.5V^2$. The relevant solutions in the presence of an electric field satisfactorily describe the tunneling from spherically symmetric states of adsorbed particles; recently, we have used them for describing the pro-

cesses of field-induced ionization of bivalent samarium impurity ions (in the quantum ground state $^7F_0$) on the surface of Si/$CaF_2$ tips ([19, 20]; see also Subsection 3.2). In particular, from appropriate analytic expressions, one can obtain the evolution of the transverse momentum distribution $\chi(z, p_\perp)$ of emitted particles during tunneling (see [18], where it was shown that the same expressions are obtained by the quasiclassical analysis of this problem):

$$|\chi(z, p_\perp)|^2 = |\chi(0, p_\perp)|^2 \exp\left(-\frac{\kappa p_\perp^2}{mF}\right). \quad (11)$$

Here, $\kappa = \sqrt{2mI}/\hbar$, where $I$ is the barrier height that coincides with $-E_0$ in the present case. Thus, the mean kinetic energy associated with the transverse momentum is equal to

$$\langle E_\perp \rangle = \frac{F}{4\kappa}, \quad (12)$$

whence, according to (2), one can find the size of the field-emission image of such quantum particles. In turn, this size can be interpreted as the measurement of the tunneling time of an electron [20].

However, in the present paper, we primarily focus on the field-induced ionization of particles that are not in spherically symmetric states. We do not know any analytic solutions to appropriate problems. It seems that the most adequate approach here is a two-stage analysis: first, we determine (in momentum space) the wave function of the emitted particle in the absence of an external electric field and then analyze its variation during tunneling. Then, applying formula (1), we can simulate the field-emission image observed for any quantum particle situated on the tip. Note that, if the narrowing of the transverse momentum distribution during tunneling can be neglected, then the intensity of the field-emission image on the screen (the density of the emission current) as a function of distance $H$ from its center (see (1)) is proportional to

$$P^2(\Phi) q^2\left(\frac{H\sqrt{2meU}}{2L}\right).$$

Applying the concept of quasiclassical trajectory in the classically forbidden region under the barrier, we can calculate the permeability of the barrier for arbitrary initial values of the tunneling electron momentum. In this paper, we only present the final result of such calculations for the permeability $D$ of a triangular barrier of height $I$ and width $l = I/F$. For an electron with the initial velocity with components $v_\parallel^{(0)}$ and $v_\perp^{(0)}$ and the respective initial energies $E_\parallel^{(0)}$ and $E_\perp^{(0)}$, the permeability of such a barrier is equal to

$$D = \frac{2\sqrt{2mF}}{3\hbar}\{\sqrt{l-c}[(l+c-2b)E(\varphi, k^2) + (b-c)F(\varphi, k^2)] - \sqrt{lbc}\}. \quad (13)$$

Here,

$$b = -\frac{E_\parallel^{(0)}}{F}, \quad c = \frac{E_\parallel^{(0)} + E_\perp^{(0)}}{F},$$

$$\varphi = \arcsin\sqrt{\frac{l}{l-b}}, \quad k^2 = \frac{l-b}{l-c},$$

and $E(\varphi, k^2)$ and $F(\varphi, k^2)$ are incomplete elliptic integrals of the first and second kind [14]. Formula (13) is considerably simplified and reduced to complete elliptic integrals when $E_\parallel^{(0)} = 0$. If, moreover, $E_\perp^{(0)}$ is also zero, then (13) is reduced to the well-known expression for the permeability of a one-dimensional triangular barrier

$$D_0 \approx \frac{4}{3\hbar}\sqrt{2mI}l.$$

In the general case, the procedure of simulating field-emission images described above admits numerical analysis (see Subsection 3.2), although this is rather laborious. Qualitatively, we can note the following. Relatively simple results are obtained when one can neglect the initial longitudinal momentum of the emitted electron. The narrowing of the transverse momentum distribution during tunneling proves to be independent of the initial state of the electron and is sufficiently large under typical conditions. We also note that this result coincides with the result of an analytically solvable model that uses the contact Fermi pseudopotential (formulas (11) and (12)), which provides additional grounds for the applicability of the model used here.

For nonzero values of the initial longitudinal momentum of the emitted electron, the narrowing of the transverse momentum distribution strongly depends on the initial state of the transverse momentum. If $E_\perp$ is substantially less than the initial value $E_\parallel^{(0)}$, then the narrowing of the transverse momentum distribution due to tunneling can often be neglected in the first approximation. Such a situation often occurs when obtaining field-emission images of sufficiently "flat" molecules adsorbed on the surface of a metal field-emission tip (see Subsection 3.1).

## 3. FIELD-EMISSION IMAGES OF ISOLATED QUANTUM PARTICLES: A FEW SPECIFIC EXAMPLES

In this section, we consider three examples of obtaining field-emission images of isolated particles situated on the tip of a field-emission microscope: molecules, doping rare earth ions, and nanostructures (carbon nanotubes).

### *3.1. Molecules*

The first images of isolated organic molecules adsorbed on the tip of a field-emission microscope were obtained as early as the 1950s (see [7, 21–24] and other works). For some of these images, in particular, for copper phthalocyanine, pc-Cu, the spatial structure of the image corresponded to that expected from the stoichiometry of molecules (see Fig. 2): under different conditions, one observed quartet and doublet structures (four- and two-blade clover leaves) that usually reversibly turned one into another. Since the spatial size of a molecule is equal to 1 nm, i.e., is smaller than the limiting resolution of the field-emission microscope, the attempts to interpret these results as a manifestation of superhigh spatial resolution met very serious difficulties. Therefore, there were attempts to associate the images observed with much larger multimolecular structures ("polymerization") or with decomposition products of the initial molecules spread over the emitter [21], rather than with the molecules themselves. This is joined by the hypothesis put forward by Komar and Komar [25]: one observes the distribution (formed due to the waveguide effect on the adsorbed molecules) of the density of electrons tunneling from a metal tip, rather than the molecules themselves. A similar hypothesis about the importance of the diffraction of emitted electrons by an adsorbed molecule was also made by Gomer [26]. Gomer and Speer also suggested a quite general hypothesis that it is important to take into account the momentum distribution of emitted electrons when analyzing the field-emission images of molecules [3, 27]; however, this hypothesis was not further developed and was subsequently neglected.

The hypothesis that accounts for the superhigh spatial resolution by the existence of microprotrusions and other defects on a field-emission tip in the vicinity of adsorbed molecules [28, 24] has been recognized as the most probable. However, it neither explains the whole array of observed data. For example, it remains unclear why one never observed a spatial structure in the field-emission images of many other molecules of comparable size [22, 3]. The frequently observed dependence of the size of a molecule image on the emitter voltage also remains unexplained. The difficulties associated with the interpretation of the data obtained had been the main reason why the studies of adsorbed molecules by the field-emission microscopy method were soon virtually stopped, although similar publications still appear from time to time [29].

Below, we show that the observed field-emission images of molecules are quite satisfactorily interpreted as the visualization of their wave functions in momentum space. In particular, to analyze the images of a pc-Cu molecule adsorbed on a metal surface, we can use the available results of quantum-chemical calculations of the electron density (molecular orbitals) of adsorbed molecules [30]. In view of the moderate spatial resolution of the field-emission microscopy of the phthalocyanine molecules, it suffices to approximate this electron density by a very simple (nonnormalized) function of the type

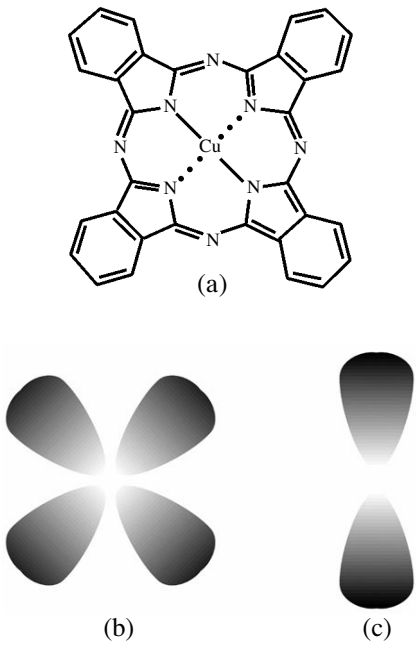


**Fig. 2.** (a) The stoichiometric formula of a copper phthalocyanine molecule and typical (b) quartet (four-blade clover leaf), and (c) doublet (two-blade clover leaf) field-emission images of this molecule.

$$\psi = \exp\left[-\frac{(\rho-\rho_0)^2}{\Delta\rho^2}\right]\cos(2\varphi),$$

where $\rho_0 = 0.9$ nm and $\Delta\rho = 0.22$ nm. Applying the formalism exposed in Section 2, we can express the wave function of a molecule in the momentum space (to be more precise, the nonnormalized radial and angular parts of this wave function) as

$$P(p_\rho, \varphi) = \cos(2\varphi) \times \int_0^\infty \rho \exp\left(-\frac{(\rho-\rho_0)^2}{\Delta\rho^2}\right) J_2\left(\frac{p_\rho \rho}{\hbar}\right) d\rho. \quad (14)$$

The integral in this formula can easily be calculated numerically. The results of calculations are presented in Fig. 3. One can see that the radial momentum distribution attains its maximum for $p_\rho^2/2m = 0.4$ eV and has the first zero at $p_\rho^2/2m = 1.2$ eV.

It follows from the same paper [30] that the size of the pc-Cu molecule in the direction perpendicular to the surface, $\delta z$, is much less than in the transverse direction: $\delta z \approx 0.5$ nm. This means that a typical magnitude of the longitudinal momentum $p_z$ of an emitted electron

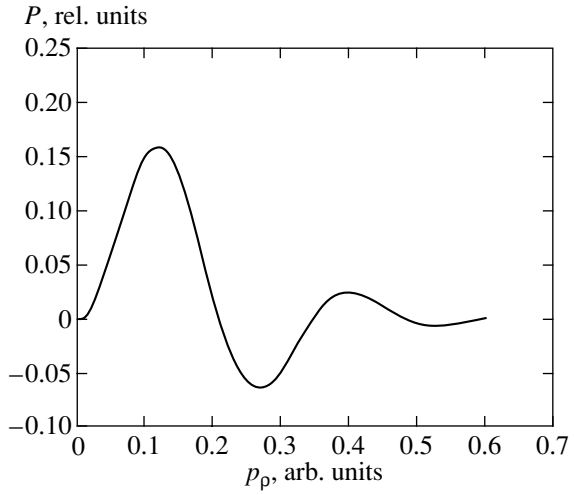


**Fig. 3.** The radial part of the momentum wave function of a copper phthalocyanine molecule adsorbed on a metal surface, calculated using the data of quantum-chemical calculations of the electron density (molecular orbitals) for these molecules.

is large enough, $p_z \approx \hbar/\delta z$, i.e., $E_\parallel^{(0)} = p_\rho^2/2m \approx 1.5$ eV. The analysis above shows that, for such large values of the longitudinal momentum, the narrowing of the transverse momentum distribution of emitted electrons during tunneling does not play a decisive role; therefore, we can neglect it in the first approximation when simulating the field-emission images of pc-Cu molecules.

The simulation shows that the copper phthalocyanine molecules adsorbed on a field-emission tip are represented as a quartet structure so as if they have a diameter of

$$d = \frac{4r}{\gamma}\sqrt{\frac{1.2\ \text{eV}}{eU}};$$

for $r = 100$ nm, $U = 4$ kV, and $\gamma = 1.5$, this yields $d = 4.7$ nm. These values are estimated on the basis of the results of Melmed and Mueller [21] and are in good agreement with the experimental results obtained there.

The images of pc-Cu molecules in the form of doublet structures, just like the doublet field-emission images of a flavanthrene and certain other molecules [21–24], can be understood within the concept described: for a different orientation of adsorbed molecules ("lying sideways"), the electron density of a molecule must be described by a function with a twofold angular symmetry of the type

$$\psi = \exp\left(-\frac{(\rho-\rho_0)^2}{\Delta\rho^2}\right)\cos\varphi.$$

We have no information on the quantum-chemical simulation of molecules adsorbed with such an orientation; therefore, we cannot obtain high-quality results on the simulation of their field-emission images. The doublet character of the images qualitatively follows merely from the form of this wave function. If we additionally assume that the parameters $\rho_0$ and $\Delta\rho$ are close to those describing a molecule with a different orientation, we can draw the following conclusion. The radial momentum distribution is given by integral (14) with the only difference that the Bessel function $J_2(p_\rho\rho/\hbar)$ is replaced by the function $J_1(p_\rho\rho/\hbar)$. A decrease in the index of the function considerably narrows down the momentum distribution (cf. (8)): both the maximum and the first zero of the distribution are shifted toward lesser values of the initial kinetic energy of the transverse motion of the emitted electron (for example, in our case, by 0.14 and 0.67 eV, respectively). Hence, the visible size of the field-emission image of such a molecule is considerably smaller than for the molecule whose symmetry axis is perpendicular to the cathode. This result is well supported in practice: the doublet images of molecules always have smaller size (and lower intensity) as compared with the quartet images [21].

Our model also makes clear why the field-emission images of many molecules with spatial dimensions comparable with that of a pc-Cu molecule do not have any structure and have a very small visible dimension [22]. If the electron density distribution of an adsorbed molecule has no angular anisotropy, the maximum of the transverse momentum distribution of emitted electrons is attained at very small (most frequently, at zero) values of the momentum, which corresponds to small-size structureless images. It also becomes clear why one could never succeed in observing field-emission images of molecules with a threefold angular symmetry (see Subsection 2.1); it is this circumstance that was regarded as the main obstacle preventing one from giving a detailed explanation of obtaining such images. For example, Gomer pointed out in his classical monograph [3, p.152] that "the absence of threefold patterns for molecules with that symmetry is extraordinarily hard to account for on any basis, except that of polymerization." We can see that this is not the case since the interpretation of field-emission images of molecules as the visualization of their wave functions in the momentum space quite successfully explains this phenomenon.

Another result that follows from our analysis is the fact that the visible size of a field-emission image of an adsorbed molecule is independent of the radius of curvature of the cathode. This result follows immediately from formula (1), which does not contain $r$. It is the difficulties associated with the "apparent" independence of the image sizes of the radius of curvature of the cathode that were the main factors in favor of the interpretations based on local microprotrusions existing near adsorbed molecules [28, 24]. Finally, formula (1) also implies that the visible size should decrease, although rather slowly, as the tip potential increases.

### *3.2. Impurity Ions*

In recent years, there has been considerable interest in the study of the field emission from the tips coated with thin (from several to 100–500 nanometers) dielectric layers rather than from pure metal or semiconductor tips. In particular, it was demonstrated that diamond coatings can substantially improve the emissive properties of isolated tips and arrays of tips due to the negative electron affinity of diamond [31]. A similar effect can also be achieved with the use of nondiamond dielectric coatings with negative or nearly zero electron affinity, such as lithium or calcium fluoride [32]. Silicon nanotips coated with calcium fluoride layers, $Si/CaF_2$, seem to be especially promising due to the well-developed manufacturing technique of arrays of silicon tips; the well-known excellent coincidence of the lattice parameters, which guarantees a perfect interface [33, 34]; and an abnormally large work function of electrons from $CaF_2$ [35]. These factors have stimulated our interest in the investigation of $Si/CaF_2$ structures [10, 32, 34]. In particular, we also investigated $Si/CaF_2$ structures in which calcium fluoride coating contains rare earth ions.

In addition, these structures are of great interest in relation to the problem of obtaining field-emission images of isolated quantum particles. Rare earth impurity ions in a fluoride matrix are characterized by very low (1.6–3.8 eV) ionization potentials, which is attributed to the very large Madelung constant in such crystals [36, 37]. This fact, combined with the presence of low-lying energy levels of these ions, enables one to observe their field-emission images. An example of such an image for bivalent samarium impurity ions is shown in Fig. 4. The two concentric circles correspond to the visualization of $Sm^{2+}$ ions in the states $^7F_0$ (central circle) and $^7F_1$ (exterior circle). The details of the experiment and the procedure of deriving the tunneling time from the observed width of the central circle were described by us with the use of the Fermi pseudopotential model ([19, 20]; see also Subsection 2.2). In the present paper, we concentrate on the interpretation of the observed shape of field-emission images (first of all, the exterior circle) as the visualization of the momentum wave function of doping ions.

The state of a samarium ion in the matrix can be described within the electrostatic model [36] as the state of a free ion SmIII with an ionization potential of $I_{fr}$ = 23.4 eV placed in a large electrostatic potential (corrected Madelung energy) of $E_M$ = 21.67 eV. Thus, the ionization potential $I$ of the ion in the matrix is strongly reduced as compared with the ionization potential of a free ion (the value $I$ = 1.7 eV was obtained experimentally [36, 37]), whereas the wave function of the valence electron of the impurity ion coincides with the corresponding wave function of a free ion. Hence,

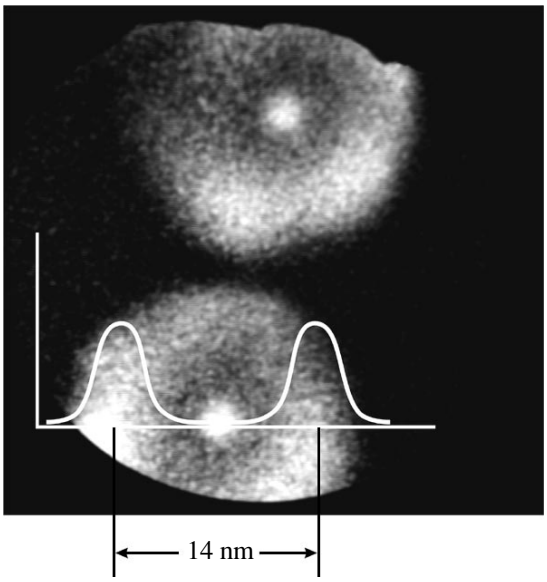


**Fig. 4.** The field-emission image of a $Si/CaF_2:Sm^{2+}$ tip. The radius of curvature is $r$ = 70 nm, the thickness of the calcium fluoride coating is 50 nm, and the concentration of samarium impurity ions is 0.02 mol %. The tip potential is $U$ = 1.9 kV, and the distance from the tip to the detector is $L$ = 10 cm. The figure shows two different samarium impurity ions each of which is represented by two concentric circles. The simulated field-emission image of the $^7F_1$ level of the samarium ion (exterior circle) is represented in the same scale.

we deal with large values of $E_\perp$, $E_\parallel^{(0)} \gg I$ during tunneling and, as follows from the analysis of formula (13), with the strong narrowing of the transverse momentum distribution during tunneling.

The angular part of the wave function of the valence electron of a samarium impurity ion in the state $^7F_1$ is determined by the function $\exp(i\varphi)$, while the determination of the radial part represents a separate problem. The complexity of this problem is associated with the fact that electrons with a total orbital momentum of $L$ = 3 and spin $S$ = 3 are added up so that they produce a total momentum of $J$ = 1. In the present paper, we restrict ourselves to a simple model where we take the delta function $\delta r_0$ in spherical coordinates as the radial wave function. Here, $r_0$ must be equal to the well-known value of the ion radius of a SmIII ion, $r_0$ = 1.18 Å [36], or can be chosen so that it correctly describes the experimental ionization potential $I_{fr} = 3e^2/2r_0$, i.e., $r_{01}$ = 1.03 Å. An interest in such an approach is associated with the fact that it allows one to obtain the momentum distribution in an analytic form and, therefore, provides a good illustration for the procedure of simulating field-emission images.

Omitting, as before, the normalization coefficients, we write the momentum wave function in cylindrical coordinates as (see (5))

$$P(p_z, p_\rho) = \int_{-\infty}^{+\infty} \exp\left(-\frac{ip_z z}{\hbar}\right) dz$$
$$\times \int_0^{+\infty} \rho\delta(r_0^2 - z^2) J_1\left(\frac{p_\rho \rho}{\hbar}\right) d\rho \qquad (15)$$
$$= 2\int_0^{r_0} \sqrt{r_0^2 - z^2}\, J_1\left(\frac{p_\rho \sqrt{r_0^2 - z^2}}{\hbar}\right) \cos\left(\frac{p_z z}{\hbar}\right) dz.$$

(The angular part of the wave function is described by the formally symmetric function $\exp(i\Phi)$.) By the change of variables $r_0^2 - z^2 = \rho^2$, we reduce (15) to the expression

$$P(p_z, p_\rho) =$$
$$\times 2\int_0^{r_0} \frac{\rho^2}{\sqrt{r_0^2 - \rho^2}} J_1\left(\frac{p_\rho \rho}{\hbar}\right) \cos\left(\frac{p_z \sqrt{r_0^2 - \rho^2}}{\hbar}\right) d\rho, \qquad (16)$$

which represents the tabulated integral no. 2.12.21.5 from [14]:

$$\int_0^a \frac{x^2}{\sqrt{a^2 - x^2}} \cos(b\sqrt{a^2 - x^2}) J_1(cx) dx$$
$$= \sqrt{\frac{\pi}{2}} a^{3/2} c (b^2 + c^2)^{-3/4} J_{3/2}(a\sqrt{b^2 + c^2}). \qquad (17)$$

Substituting appropriate values into (17) and omitting again all the numerical coefficients, we arrive at the following nonnormalized wave function in the momentum space:

$$P(p_z, p_\rho) = p_\rho p_r^{-1} j_1\left(\frac{r_0 p_r}{\hbar}\right). \qquad (18)$$

Here,

$$j_1(z) = \frac{\sin z}{z} - \frac{\cos z}{z}$$

is the Bessel function of half-integer order, and we introduced the obvious notation $p_r^2 = p_z^2 + p_\rho^2$ (the radial momentum in spherical coordinates).

Expression (18), which cannot be factorized as a product of radial and normal momentum distributions, can be used for simulating field-emission images of impurity ions precisely according to the following procedure (see Subsection 2.2).

1. The fraction $dN_1$ of electrons possessing a momentum with components $p_z$ and $p_\rho$ is given by

$$dN_1 = P^2(p_z, p_\rho) p_\rho dp_\rho dp_z.$$

Each such electron is assigned a tunneling probability proportional to $\xi = p_z \exp(-D(p_z, p_\rho))$, where $D$ is determined from (13). Hence, the number $dN_2$ of emitted electrons that contribute to the field-emission image and possess the momentum components $p_z$ and $p_\rho$ is $dN_2 = \xi dN_1$.

2. This quantity is integrated with respect to $p_z$ from zero to infinity (actually, the integration can be truncated at $E_\parallel^{(0)} \approx 1.5 I_{fr}$). The result obtained, INT = $\int dN_2 dp_z$, is proportional to the total number of electrons possessing the radial momentum $p_\rho$ and contributing to the field-emission image. The relative brightness of the field-emission image (the current density) at a distance of $H$ from its center is $\mathrm{INT}(p_\rho)/p_\rho$, where $p_\rho$ is determined from formula (1).

The results of calculations for our experimental data ($F = 0.854$ V/nm, $l = 2.0$ nm, and the other data are given in the figure captions) are represented in Fig. 4. In a way conventional for the field-emission microscopy, the distance $H$ is reduced to the object size on the field-emission cathode by dividing by the magnification factor $M$ (in our case, $M = 9.5 \times 10^5$). One can see that, although we used a rather rough approximation to the real momentum distribution, the experimental results are in surprisingly good agreement with the model proposed. Note that the observed radius of the exterior circle in the field-emission image corresponds to the kinetic energy of transverse motion of 1.9 eV, which is greater than the tunneling barrier height $I = 1.7$ eV. This fact seems very surprising and could not be adequately explained before, until we developed a model for interpreting field-emission images as the visualization of the momentum wave function in the present paper [19, 20].

Note that, because the radius of a samarium ion is very small (of the order of 1 Å), there are no interpretations of the observed field-emission images other than that as the visualization of the momentum wave function. Therefore, we consider the experimental results presented in this section as the most convincing proof of the validity of the model developed.

### *3.3. Nanostructures*

In recent years, a large number of publications have been devoted to the study of the field emission from nanotubes and other similar structures. The majority of these papers deal with the field emission from multitip cathodes, so that only current is a measurable parameter, not the field-emission images of nanostructures. Nevertheless, many authors presented the field-emission images of nanotubes [38–41]. The images of the so-called multiwalled nanotubes [38, 39] with a typical diameter of 5–10 nm can be well interpreted on the basis of the standard theory of field-emission microscopy. However, the interpretation of the field-emission

images of single-walled nanotubes with an inner diameter of $2\rho_0 = 0.8$–$1$ nm [40, 41] faces the same problems of abnormally high apparent spatial resolution that were discussed as applied to molecules and impurity atoms.

Here, we want to draw one's attention to the fact that the field-emission images of single-walled nanotubes should also be interpreted as the visualization of the electron wave function in momentum space. It follows from numerous theoretical models that deal with the electron energy levels in a single-walled nanotube that the charge density of the valence electrons possesses a real angular symmetry along a cylindrical surface (see, for example, [42], where the authors demonstrated this symmetry). This symmetry follows from the fact that the nanotube surface is formed from compact hexagons of carbon atoms, and the valence electron is largely localized inside these hexagons. As applied to our problem of simulating field-emission images, the molecular orbital of a valence electron in an open single-walled nanotube can be expressed as (cf. [42])

$$\psi = \delta(\rho_0)\cos(3\varphi). \qquad (19)$$

(A similar angular symmetry also exists in closed single-walled nanotubes [43].) Hence, according to (8), we have a radial momentum distribution $J_3(p_\rho\rho_0/\hbar)$, which corresponds to the maximum kinetic energy of transverse motion equal to 3.3 eV. Based on (1), we can expect, as a field-emission image, a structure with a diameter of $d = 9.4$ mm (for $U = 1.5$ kV and $L = 5$ cm) that is well resolved on the screen and possesses a sixfold angular symmetry (i.e., bright emission spots located at the vertices of a regular hexagon).

Similar field-emission images were frequently obtained indeed in [40, 41]. Moreover, one usually also observed a central spot. In our opinion, this is naturally accounted for by the fact that the angular modulation depth of electron density is not 100%, as required by (19), but is less. As in the case of samarium impurity ions considered above (Subsection 3.2), this results in a bimodal transverse momentum distribution and an appropriate structure of the field-emission image, which consists of a central spot and a concentric ring-shaped structure (in this case, possessing an additional sixfold angular symmetry).

The experimental data, including those obtained in [40, 41], are insufficient for a more detailed interpretation within the present model. Therefore, here we do not analyze the problem of narrowing down the transverse momentum distribution as a result of tunneling: although the electron work function from nanotubes (4–5 eV) is greater than the typical kinetic energy of transverse motion, in general, this phenomenon can be quite appreciable.

## 4. CONCLUSION

Thus, in this paper, we demonstrated that the field-emission images of many isolated molecules adsorbed on a field-emission tip, as well as the images of impurity ions and nanostructures, can be interpreted as the visualization of appropriate wave functions of these quantum particles in momentum space. The first application of such an approach can be the determination of the tunneling time of electrons from the characteristics of the measured wave function [20].

There is an analogy between electron emission from individual quantum particles situated on the emitter and emission from supersharp single-atom field-emission tips (see, for example, [44, 45]) in which a tunneling current is provided by a single or several atoms on the tip. In both cases, the emission current is characterized by a very sharp angular distribution and a high degree of coherence, which is of great interest for electron holography and electron microscopy of superhigh spatial resolution. Here, the application of adsorbed quantum particles allows one to dispense with single-atom tips, which are difficult to obtain and troublesome; ordinary field-emission tips can be used repeatedly.

## ACKNOWLEDGMENTS

One of the authors (S. Sekatskii) is grateful to Alan Melmed for useful discussions. We acknowledge a considerable contribution made by V.N. Konopsky, E.I. Givargizov, V.V. Zhirnov, N.S. Sokolov, and J. Alvarez to the fabrication of $Si/CaF_2:Sm^{2+}$ tips and carrying out experiments on them. We are also grateful to the Japanese company Hamatsu Photonics for kindly giving us an opportunity to carry out research on their experimental equipment.

This work was supported by the Russian Foundation for Basic Research, the US Department of Defense, and the Swiss Foundation for Fundamental Research (SCOPES grant).

## REFERENCES

1. T. T. Tsong, *Atom-Probe Field Ion Microscopy* (Cambridge Univ. Press, New York, 1990).
2. A. L. Suvorov, *Structure and Properties of Surface Atomic Layers of Metals* (Énergoatomizdat, Moscow, 1990).
3. R. Gomer, *Field Emission and Field Ionization* (American Inst. of Physics, New York, 1993).
4. I. Brodie, Surf. Sci. **70**, 186 (1978).
5. J. W. Gadzuk and E. W. Plummer, Rev. Mod. Phys. **45**, 487 (1973).
6. J. W. Gadzuk, Phys. Rev. B **47**, 12832 (1993).
7. E. W. Mueller, Z. Naturforsch. A **5**, 473 (1950).
8. H. E. Clark and R. D. Young, Surf. Sci. **12**, 385 (1968).
9. M. E. Lin, R. P. Anders, and R. Reifenberger, Phys. Rev. Lett. **67**, 477 (1991).

10. V. N. Konopsky, S. K. Sekatskii, and V. S. Letokhov, J. Phys. IV **6**, C5-125 (1996).
11. S. K. Sekatskii and V. S. Letokhov, Pis'ma Zh. Éksp. Teor. Fiz. **65**, 491 (1997) [JETP Lett. **65**, 465 (1997)].
12. S. K. Sekatskii, S. V. Chekalin, A. L. Ivanov, *et al.*, Zh. Éksp. Teor. Fiz. **115**, 1680 (1999) [JETP **88**, 921 (1999)].
13. B. Podolsky and L. Pauling, Phys. Rev. **34**, 109 (1929).
14. A. P. Prudnikov, Yu. A. Bryuchkov, and O. I. Marichev, *Integrals and Series* (Nauka, Moscow, 1983; Gordon and Breach, New York, 1986), Vols. 1, 2.
15. P. L. Kapur and R. Peierls, Proc. R. Soc. London, Ser. A **163**, 606 (1937).
16. Yu. N. Demkov and V. N. Ostrovskii, *Zero-Range Potentials and Their Applications in Atomic Physics* (Nauka, Moscow, 1985; Plenum, New York, 1988).
17. B. Gottlieb, M. Kleber, and J. Krause, Z. Phys. A **339**, 201 (1991).
18. C. Bracher, W. Becker, S. A. Gurvitz, *et al.*, Am. J. Phys. **66**, 38 (1998).
19. S. K. Sekatskii, Surf. Sci. **453**, L303 (2000).
20. S. K. Sekatskii and V. S. Letokhov, Phys. Rev. B **64**, 233311 (2001).
21. A. J. Melmed and E. W. Mueller, J. Chem. Phys. **29**, 1037 (1958).
22. R. Haefer, Acta Phys. Austriaca **8**, 105 (1953).
23. P. Wolf, Z. Angew. Phys. **6**, 529 (1954).
24. J. A. Becker and R. G. Brandes, J. Appl. Phys. **27**, 221 (1956).
25. A. P. Komar and A. A. Komar, Zh. Tekh. Fiz. **31**, 231 (1961) [Sov. Phys. Tech. Phys. **6**, 166 (1961)]; Zh. Tekh. Fiz. **32**, 867 (1962) [Sov. Phys. Tech. Phys. **7**, 634 (1963)].
26. R. Gomer, J. Chem. Phys. **19**, 1072 (1951).
27. R. Gomer and D. A. Speer, J. Chem. Phys. **21**, 73 (1953).
28. D. J. Rose, J. Appl. Phys. **27**, 215 (1956).
29. G. R. Condon and J. A. Panitz, J. Vac. Sci. Technol. B **18**, 1216 (2000).
30. P. Sautet and C. Joachim, Surf. Sci. **271**, 387 (1992).
31. C. Wang, A. Garcia, D. Ingram, *et al.*, Electron. Lett. **27**, 1459 (1991).
32. V. N. Konopsky, V. V. Zhirnov, N. S. Sokolov, *et al.*, J. Phys. IV **6**, C5–129 (1996).
33. F. Schowalter and L. J. Fathauer, J. Vac. Sci. Technol. A **4**, 1026 (1986).
34. S. K. Sekatskii, D. V. Serebryakov, V. S. Letokhov, *et al.*, Appl. Surf. Sci. **140**, 46 (1999).
35. B. Quiniou, W. Schwarz, Z. Wu, *et al.*, Appl. Phys. Lett. **60**, 183 (1992).
36. C. Pedrini, F. Rogemond, and D. S. McClure, J. Appl. Phys. **59**, 1196 (1986).
37. S. K. Sekatskii, V. S. Letokhov, and S. B. Mirov, Opt. Commun. **95**, 260 (1993).
38. Y. Saito, K. Hamaguchi, K. Hata, *et al.*, Nature (London) **389**, 554 (1997).
39. W. A. de Heer, J.-M. Bonard, T. Stoekli, *et al.*, Z. Phys. D **40**, 418 (1997).
40. K. A. Dean and B. R. Chalamala, J. Appl. Phys. **85**, 3832 (1999).
41. K. A. Dean, P. von Allmen, and B. R. Chalamala, J. Vac. Sci. Technol. B **17**, 1959 (1999).
42. G. Zhou, W. Duan, and B. Gu, Phys. Rev. Lett. **87**, 095504 (2001).
43. J. W. G. Wildoer, L. C. Venema, A. G. Rinzler, *et al.*, Nature (London) **391**, 59 (1998).
44. H.-W. Fink, Phys. Scr. **38**, 260 (1988).
45. V. T. Binh, J. Microsc. **152**, 355 (1988).

*Translated by I. Nikitin*

*Journal of Experimental and Theoretical Physics, Vol. 95, No. 2, 2002, pp. 221–225.*
*From Zhurnal Éksperimental'noĭ i Teoreticheskoĭ Fiziki, Vol. 122, No. 2, 2002, pp. 258–263.*


**PLASMA, GASES**

# Nonlinearity Effects in Wave Propagation in Multicomponent Bose–Einstein Condensates¶

**I. E. Mazets[a, *], E. V. Orlenko[b], and B. G. Matisov[b]**

[a]*Ioffe Physics and Technology Institute, Russian Academy of Sciences, Politekhnicheskaya ul. 26, St. Petersburg, 194021 Russia*

[b]*St. Petersburg State Technical University, Politekhnicheskaya ul. 29, St. Petersburg, 195251 Russia*

**e-mail: mazets@astro.ioffe.rssi.ru*

Received January 22, 2002

**Abstract**—We consider a spinor Bose–Einstein condensate in its polar ground state. We analyze magnetization waves of a finite amplitude and show that their nonlinear coupling to density waves dramatically changes the dependence of the frequency on the wave number. On the contrary, the density wave propagation is much less modified by nonlinearity effects. A similar phenomenon in a miscible two-component condensate is also studied. © *2002 MAIK "Nauka/Interperiodica".*

Recent advances in the experimental creation of multicomponent atomic Bose–Einstein condensates (BEC) [1–3] have given rise to the interest in physical properties of such systems. There are numerous works on the properties of degenerate Bose gas mixtures in magnetic traps related to both the ground state [4] and the collective excitations [5]. In [5], the early work [6] related to a homogeneous Bose gas mixture was generalized to the case of the external harmonic trap potential. Evidently, the number of branches of the dispersion law is equal to the number of different components in the mixed BEC. Because of a nonzero interaction between them, the normal mode oscillations imply a simultaneous mutually coherent motion of the components. In the present paper, however, we first consider a multicomponent BEC of another kind, namely, a spinor BEC. Such a degenerate quantum system can be created in an optical trap, where all the atoms are confined practically independently of $m_f$, their momentum projection to an arbitrary axis. This independence of the confinement from the spin orientation is a striking feature and a key advantage of optical traps, well justified experimentally [2, 3]. The spin orientation then becomes a new degree of freedom. The differences and similarities between a two-component BEC with fixed values of $m_f$ for both components and a spinor BEC in the context of our study are discussed at the end of this paper.

We note that, in all the cited works on collective excitations in multicomponent BECs and in the seminal works on spinor BEC dynamics [7], the oscillation amplitudes were assumed to be sufficiently small to provide linearization of the set of the coupled time-dependent Gross–Pitaevskii equations (GPE). A proper linear transformation then yields equations of the harmonic-oscillator type for the normal modes. But the GPE is essentially nonlinear, and the effects of a finite amplitude of oscillations therefore occur. There are some approaches to taking the nonlinearity into account. The first is to find particular solutions of the GPE in the form of solitons (see, e.g., recent work [8] and references therein). The second approach is to find the oscillating nonlinear solutions that in the case of an infinitesimally small oscillation amplitude coincide with the corresponding eigenfunctions of the linearized version of the GPE or of the equivalent set of quantum hydrodynamical equations. An elegant formalism has been developed for nonlinear oscillations of a scalar BEC in a harmonic trap in the Thomas–Fermi regime [9]. It has been found that nonlinear effects become important if the fraction of mass of the scalar BEC involved in the oscillatory motion is comparable to unity.

In the present paper, we investigate the validity of the approximation based on the linearization of the GPE by proceeding as follows. We consider plane waves in a spatially homogeneous multicomponent BEC. This can serve as a WKB approximation for excitations in a trapped BEC if the excitation wavelength is much smaller than the atomic cloud size. Moreover, this approach allows us to use, in the most direct and straightforward way, the standard technique of expanding a solution into a series in a small parameter, known as the standard perturbation theory in classical mechanics [10]. The analysis of plane waves in a translationally invariant BEC also provides a possibility of comparing the results with the rigorous analytic formulas in [6, 7].

The main result of our work is that certain modes in a multicomponent BEC exhibit a strongly nonlinear behavior: the anharmonicity effects become significant

¶This article was submitted by the authors in English.

even for a relatively small wave amplitude. This effect is absent for the scalar BEC.

We consider a spinor BEC composed of atoms with the spin $f = 1$ at zero temperature. In the mean-field approximation, the GPE governing the evolution of the complex order parameter (the macroscopic wave function) $\psi(\mathbf{r}, t)$ of the BEC is given by [7]

$$i\hbar\frac{\partial}{\partial t}\psi = -\frac{\hbar^2}{2M}\nabla^2\psi - \mu\psi + \hbar c_0(\tilde{\psi}^*\psi)\psi + \hbar c_2(\tilde{\psi}^*\hat{\mathbf{f}}\psi)\cdot(\hat{\mathbf{f}}\psi), \quad (1)$$

where $\hat{\mathbf{f}}$ is the single-atom angular momentum operator, a vector whose Cartesian components are $3 \times 3$ matrices, $M$ is the mass of the atom, and $\mu$ is the chemical potential. The coupling constants are defined as

$$\hbar c_0 = \frac{g_0 + 2g_2}{3}, \quad \hbar c_2 = \frac{g_2 - g_0}{3}, \quad g_F = \frac{4\pi\hbar^2 a_F}{M}$$

and $a_F$ is the $s$-wave scattering length for a pair of slow atoms with the total angular momentum $F$ equal to 0 or 2, respectively. Practically, the magnitudes of these two scattering lengths are close each to other, and hence, $|c_2/c_0| \ll 1$. The order parameter $\psi$ has three components corresponding to the momentum projections to the $z$ axis given by $m_f = 0, \pm 1$,

$$\psi = \begin{pmatrix} \zeta_1 \\ \zeta_0 \\ \zeta_{-1} \end{pmatrix}\sqrt{n},$$

where $n$ is the total equilibrium density of the BEC. We let $\tilde{\psi}$ denote the transposed vector. In other words, the ground state components of the vector $\zeta$ are normalized by the condition

$$\sum_{m_f=-1}^{1}\left|\zeta_{m_f}^{(\text{ground})}\right|^2 = 1. \quad (2)$$

We assume that the interaction of atoms in the BEC is repulsive, i.e., $c_0 > 0$. For definiteness, we also assume that $c_2 > 0$. It follows from the latter condition that the ground state of the system is the so-called polar state [7]. This implies that, in the mean-field picture, all the atoms have zero momentum projection on a certain axis. This state is degenerate with respect to the orientation of this axis. We let this axis be the $z$ axis; in equilibrium, with the time derivative of $\psi$ in Eq. (1) vanishing, we then have

$$\zeta_{\pm 1}^{(\text{ground})} = 0, \quad \zeta_0^{(\text{ground})} = 1.$$

The chemical potential of the BEC in the polar state is $\mu = c_0 n$.

Before writing Eq. (1) in the explicit form, we introduce the new unknown functions

$$\xi_\pm = \frac{\zeta_1 \pm \zeta_{-1}^*}{\sqrt{2}}, \quad \eta_p = \mathrm{Re}\zeta_0 - 1, \quad \eta_i = \mathrm{Im}\zeta_0.$$

Equation (1) can then be transformed to the set of equations

$$-\frac{\partial}{\partial t}\xi_- = -\frac{\hbar}{2M}\nabla^2\xi_+ + 2c_2 n\xi_+ + c_0 n(\xi_+^*\xi_+ + \xi_-^*\xi_- + 2\eta_p + \eta_p^2 + \eta_i^2)\xi_+ + c_2 n \times[(\xi_+\xi_-^* - \xi_+^*\xi_- + 2\eta_i + 2\eta_p\eta_i)\xi_- + 2(2\eta_p + \eta_p^2)\xi_+], \quad (3)$$

$$\frac{\partial}{\partial t}\xi_+ = -\frac{\hbar}{2M}\nabla^2\xi_- + c_0 n \times(\xi_+^*\xi_+ + \xi_-^*\xi_- + 3\eta_p + \eta_p^2 + \eta_i^2)\xi_- + c_2 n[(\xi_+\xi_-^* - \xi_+^*\xi_- + 2\eta_i + 2\eta_p\eta_i)\xi_+ + 2\eta_i^2\xi_-], \quad (4)$$

$$-\frac{\partial}{\partial t}\eta_i = -\frac{\hbar}{2M}\nabla^2\eta_p + 2c_0 n\eta_p + c_0 n[(\xi_+^*\xi_+ + \xi_-^*\xi_- + 3\eta_p + \eta_p^2 + \eta_i^2)\eta_p + \xi_+^*\xi_+ + \xi_-^*\xi_- + \eta_i^2] + c_2 n \times[2\xi_+^*\xi_+\eta_p + 2\xi_+^*\xi_+ + (\xi_+^*\xi_- + \xi_+\xi_-^*)\eta_i], \quad (5)$$

$$\frac{\partial}{\partial t}\eta_p = -\frac{\hbar}{2M}\nabla^2\eta_i + c_0 n(\xi_+^*\xi_+ + \xi_-^*\xi_- + 2\eta_p + \eta_p^2 + \eta_i^2)\eta_i + c_2 n[2\xi_-^*\xi_-\eta_i + (\xi_+^*\xi_- + \xi_+\xi_-^*)\eta_p + \xi_+^*\xi_- + \xi_+\xi_-^*]. \quad (6)$$

If we neglect all the nonlinear terms in Eqs. (3)–(6), we immediately obtain solutions in the form of plane monochromatic waves and the corresponding dispersion laws [7]. The first mode is the density wave; in the linear approximation, it corresponds to the periodic oscillations of the $m_f = 0$ component of the order parameter only (i.e., of $\eta_p$, $\eta_i$), while $\xi_+$ and $\xi_-$ remain zero. Density waves in a spinor BEC are the same as sound waves in a scalar BEC. The dependence of the frequency $\omega_{d0}$ of density waves on the wave number $k$ is of the Bogolyubov type,

$$\omega_{d0}^2(k) = \omega_r(k)[\omega_r(k) + 2c_0 n],$$

where

$$\omega_r(k) = \frac{\hbar k^2}{2M}$$

is the recoil frequency associated with the kinetic momentum $\hbar k$. Another branch of the excitation spectrum in a spinor BEC is related to magnetization waves. The left and right circularly polarized magnetization modes are degenerate: in the linear regime; their frequency is given by

$$\omega_{m0}^2(k) = \omega_r(k)[\omega_r(k) + 2c_2 n].$$

The quantum mechanical mean values of the atomic magnetic momentum operator are proportional to $\xi_+$ and $\xi_+^*$ for the left and right polarization, respectively.

We can now determine the effects of nonlinearity on the magnetization wave propagation using the perturbation theory of classical mechanics [10]. We expand our unknown functions into series as

$$\xi_+ = \sum_{j=0}^{\infty} \xi_+^{(j)},$$

where $\xi_+^{(j)}$ is proportional to the $j$th power of a certain small parameter $\varepsilon$ (in fact, the square of the magnetization amplitude can be naturally regarded as this parameter). Similar expansions hold for the remaining three functions. The zeroth order approximation can also be taken in the form of a plane wave,

$$\xi_+^{(0)} = A_+ \sin(\omega t - \mathbf{k}\cdot\mathbf{r}),$$

but with the frequency $\omega$ shifted with respect to the nonperturbed value $\omega_{m0}$. The validity of this method is restricted to the case where the resulting correction to the frequency is small,

$$\left|\frac{\omega - \omega_{m0}}{\omega_{m0}}\right| \ll 1.$$

We also take

$$\xi_-^{(0)} = \omega_r(k)^{-1}\omega A_+ \cos(\omega t - \mathbf{k}\cdot\mathbf{r}),$$

$$\eta_p^{(0)} = 0, \quad \eta_i^{(0)} = 0.$$

The difference between $\omega$ and $\omega_{m0}$ can also be represented as a series in $\varepsilon$, beginning with the term of the order $\varepsilon^1$.

To find the correction to the frequency of a magnetization wave, we make the following transformation of our set of GPEs. We add to and subtract from the right-hand side of Eq. (1) the term $\omega^2\xi_+/\omega_r(k)$. We then note that our zeroth order approximation satisfies the set of equations

$$-\frac{\partial \xi_-}{\partial t} = \frac{\omega^2 \xi_+}{\omega_r(k)}, \quad \frac{\partial \xi_+}{\partial t} = \omega_r(k)\xi_-$$

identically. The remaining terms must be regarded as a perturbation leading to the frequency shift in higher orders of the approximation. Equations (3)–(6) must be satisfied in every order in $\varepsilon$ separately, and therefore, all the terms of the order $\varepsilon^j$ on the right-hand side must be grouped and set equal to the $O(\varepsilon^j)$ part of the left-hand side of the equation. We restrict our analysis to the linear order in $\varepsilon$, where we obtain

$$\begin{aligned} -\frac{\partial}{\partial t}\xi_-^{(1)} &= \frac{\omega^2}{\omega_r(k)}\xi_+^{(1)} + \left\{\omega_r(k) + 2c_2 n - \frac{\omega^2}{\omega_r(k)}\right\}^{(1)} \\ &\times A_+ \sin(\omega t - \mathbf{k}\cdot\mathbf{r}) \\ &+ c_0 n\left[\sin^2(\omega t - \mathbf{k}\cdot\mathbf{r}) + \frac{\omega^2}{\omega_r^2(k)}\cos^2(\omega t - \mathbf{k}\cdot\mathbf{r})\right] \\ &\times A_+^3 \sin(\omega t - \mathbf{k}\cdot\mathbf{r}), \end{aligned} \tag{7}$$

$$\begin{aligned} \frac{\partial}{\partial t}\xi_+^{(1)} &= \omega_r(k)\xi_-^{(1)} + \frac{\omega}{\omega_r(k)}c_0 n \\ &\times \left[\sin^2(\omega t - \mathbf{k}\cdot\mathbf{r}) + \frac{\omega^2}{\omega_r^2(k)}\cos^2(\omega t - \mathbf{k}\cdot\mathbf{r})\right] \\ &\times A_+^2 \cos(\omega t - \mathbf{k}\cdot\mathbf{r}). \end{aligned} \tag{8}$$

Here, the symbol $\{\ldots\}^{(1)}$ means that only the linear contribution in $\varepsilon \sim A_+^2$ to the expression in curly brackets is retained. The amplitude $A_+$ is taken to be real without losing generality.

Equations (7) and (8) can be easily reduced to the differential equation

$$\begin{aligned} &\frac{\partial^2}{\partial t^2}\xi_+^{(1)} + \omega^2\xi_+^{(1)} + \left\{\omega_{m0}^2 - \omega^2 + \frac{c_0 n \omega_r(k)}{4}\right. \\ &\left.\times\left[3 + 4\frac{\omega^2}{\omega_r^2(k)} + 3\frac{\omega^4}{\omega_r^4(k)}\right]A_+^2\right\}^{(1)} \\ &\times A_+ \sin(\omega t - \mathbf{k}\cdot\mathbf{r}) + CA_+^3 \sin[3(\omega t - \mathbf{k}\cdot\mathbf{r})] = 0, \end{aligned} \tag{9}$$

where $C$ is a certain combination of various frequency parameters of the problem; its calculation is not needed for the determination of the lowest order correction to the wave frequency.

Equation (9) is inhomogeneous, and the presence of the resonant source term proportional to $\sin(\omega t - \mathbf{k}\cdot\mathbf{r})$ leads to the occurrence of oscillations in the solution for $\xi_+^{(1)}$ with the amplitude growing linearly in time. The essence of the method used here [10] is to avoid these nonphysical (secular) solutions proportional to $t\sin(\omega t - \mathbf{k}\cdot\mathbf{r})$ by setting the prefactor of the resonance term to zero. To the lowest order in the square of the

wave amplitude, the magnetization wave frequency is therefore given by

$$\omega^2 = \omega_{m0}^2 + \frac{c_0 n \omega_r(k)}{4}\left[3 + 4\frac{\omega_{m0}^2}{\omega_r^2(k)} + 3\frac{\omega_{m0}^4}{\omega_r^4(k)}\right]A_+^2. \quad (10)$$

In the two limiting cases (of the short and long wavelength), we obtain

$$\omega^2 = \omega_r^2(k) + \frac{5}{4}u_0^2 k^2 A_+^2, \quad \hbar k \gg M u_2, \quad (11)$$

and

$$\omega^2 = u_2^2 k^2 + 6u_0^2 k^2 \left(\frac{M u_2}{\hbar k}\right)^4 A_+^2, \quad \hbar k \ll M u_2. \quad (12)$$

Here,

$$u_F = \sqrt{\hbar c_F n / M}$$

are the propagation velocities of the density ($F = 0$) and magnetization ($F = 2$) waves of an infinitely small amplitude in the long-wavelength limit. We can therefore conclude that the nonlinearity effects are small until

$$A_+^2 \ll 1, \quad \hbar k \gg M u_0, \quad (13)$$

$$A_+^2 \ll \left(\frac{\hbar k}{M u_0}\right)^2, \quad M u_2 \lesssim \hbar k \lesssim M u_0, \quad (14)$$

$$A_+^2 \ll \frac{c_2}{c_0}\left(\frac{\hbar k}{M u_2}\right)^4, \quad \hbar k \ll M u_2. \quad (15)$$

Interestingly, the condition that the nonlinearity is small coincides with the trivial condition that $A_+^2$ is small compared to the sum of squares of the absolute values of all three components $\zeta_{m_f}^{(\mathrm{ground})}$ in the ground state, which is unity in accordance with Eq. (2) only in the short-wavelength limit of Eq. (13). In the other cases [Eqs. (14) and (15)], even a small but finite excitation amplitude can result in a significant modification of the wave propagation.

It is easy to show that, in the case of magnetization waves, there are no resonance terms on the right-hand sides of Eqs. (5) and (6) in the first order in $\varepsilon$, and these equations therefore do not contribute to the evaluation of the corresponding correction to the wave frequency.

Density waves can be analyzed similarly, and the lowest order correction results in the formula

$$\omega^2 = \omega_{d0}^2 + \frac{3}{4}c_0 n \omega_r(k) A_p^2, \quad (16)$$

where $A_p$ is the amplitude of the oscillations of $\eta_p$. For all momenta $k$, the correction is small provided that $A_p \ll 1$; i.e., nonlinear effects play a less significant role for waves of this type than for the magnetization waves. Equation (16) also applies to sound waves in a single-component (scalar) BEC.

Because $\omega_{m0}$ is independent of $c_0$ but the latter quantity appears on the right-hand side of Eq. (10), we conclude that the nonlinear coupling to density waves plays a key role in the modification of the magnetization wave frequency. On the contrary, Eq. (16) does not contain $c_2$, and a travelling density wave is therefore not coupled to magnetization modes.

We now briefly discuss the case of a mixture of two BECs, each of which has a fixed value of $m_f$, or, equivalently, of two scalar BECs. Here, we first must introduce the coupling constants

$$g_{j'j} = 2\pi\hbar a_{j'j}\frac{M_j + M_{j'}}{M_j M_{j'}},$$

where $M_j$ is the mass of an atom of the $j$th kind and $a_{j'j}$ is the $s$-wave scattering length for a pair of atoms of the $j$th and $j'$th kind, $j', j = 1, 2$. The dispersion laws for the two excitation branches were obtained in the analytic form in [6] (see also [5]). If all three relevant scattering lengths are positive, the criterion of stability of a homogeneous BEC mixture against phase separation is simply $g_{12} < \sqrt{g_{11} g_{22}}$. In this case, the eigenmode frequencies are positive for all values of the momentum $k$. For simplicity, we consider here the case of equal atomic masses, $M_1 = M_2 \equiv M$. The eigenfrequencies are then simply

$$\omega_\pm^2 = \omega_r(k)[\omega_r(k) + 2\Lambda_\pm],$$

where

$$\Lambda_\pm = [g_{11} n_1 + g_{22} n_2 \pm \sqrt{(g_{11} n_1 - g_{22} n_2)^2 + 4 g_{12}^2 n_1 n_2}]/2,$$

$n_1$, $n_2$ are the equilibrium number densities of the components, and $w_r(k)$ is defined above.

The order parameter perturbation for the $j$th component is given by

$$\delta\psi_j = \sqrt{n_1} A_j \times [\sin(\omega t - \mathbf{k}\cdot\mathbf{r}) + i\omega_r^{-1}(k)\omega\cos(\omega t - \mathbf{k}\cdot\mathbf{r})].$$

After some tedious but straightforward calculations, which are similar to those described above and are valid under the same condition of smallness of the frequency correction, we arrive at the following formula for the wave frequency shifted due to the nonlinearity effects:

$$\omega^2 = \omega_\pm^2 + \frac{\omega_r(k) g_\pm n_1}{2} \times \left[3 + 4\frac{\omega_\pm^2}{\omega_r^2(k)} + 3\frac{\omega_\pm^4}{\omega_r^4(k)}\right]B_\pm^2. \quad (17)$$

Here, the upper sign corresponds to the case where $B_+ \neq 0$ and $B_- = 0$, and the lower sign corresponds to the opposite case, $B_+ = 0$ and $B_- \neq 0$. The eigenmode amplitudes are defined as

$$B_+ = \cos\theta_g A_1 + \sqrt{\frac{n_2}{n_1}}\sin\theta_g A_2,$$
$$B_- = -\sin\theta_g A_1 + \sqrt{\frac{n_2}{n_1}}\cos\theta_g A_2. \quad (18)$$

By definition, we also set

$$g_+ = g_{11}\cos^4\theta_g + 2g_{12}\cos^2\theta_g\sin^2\theta_g + g_{22}\sin^4\theta_g, \quad (19)$$

$$g_- = g_{11}\sin^4\theta_g + g_{22}\cos^4\theta_g, \quad (20)$$

$$\tan\theta_g = \frac{g_{22}n_2 - g_{11}n_1 + \sqrt{(g_{22}n_2 - g_{11}n_1)^2 + 4g_{12}^2 n_1 n_2}}{2g_{12}\sqrt{n_1 n_2}}. \quad (21)$$

Equation (17) is similar to Eq. (10) and leads to a similar restriction on the wave amplitude. If the two BECs are composed of atoms accumulated on two different magnetic or hyperfine sublevels of the ground internal state, the difference between $g_{12}$ and $\sqrt{g_{11}g_{22}}$ is relatively small, and the lower frequency mode is extremely sensitive to the effects of nonlinearity in the long-wavelength limit. We note that both branches of the excitation spectrum of a two-component BEC in an external magnetic field are sensitive to nonlinear effects for small $k$, while the spinor BEC collective excitations exhibit a different behavior: the nonlinearity effects are much more important for magnetization waves than for density waves.

In summary, we must note that the nonlinearity effects in the wave propagation in a BEC studied here are related to the Beliaev damping [11] (cf. the closely related recent publication [12] on an efficient damping of the relative motion of two condensates in a trap by a nonlinear interaction). The Beliaev damping is also described by the cubic nonlinear term in the GPE. It is in fact the decay of a collective excitation quantum into two quanta of lower energies, provided that the energy and momentum are conserved. This process results in the occurrence of an imaginary part of the wave frequency (the damping constant). In the present paper, we have calculated the real small addend to the wave frequency. While the Beliaev damping becomes less important as $k$ approaches zero, nonlinear corrections to the magnetization mode in the spinor BEC and to each of the modes in the usual two-component BEC become more pronounced.

Finally, we present a numerical example. The ground state of a spinor BEC of sodium atoms with $f = 1$ is simply a polar (antiferfomagnetic) state [2]. We take $(a_0 + 2a_2)/3 \approx 5$ nm, $(a_2 - a_0)/3 \approx 0.08$ nm and set $n \approx 10^{14}$ cm$^{-3}$. We let the excitation wave number be about $3.5 \times 10^3$ cm$^{-1}$(the corresponding wavelength is several times smaller than the atomic cloud size in the experiment with a large number of atoms in a trap as in [2], and therefore, the WKB approximations is still satisfactory). As $A_+ \longrightarrow 0$, the linear theory [7] gives the magnetization wave frequency $\omega_{m0} \approx 300$ s$^{-1}$. But if $A_+ \approx 0.044$, in other words, only

$$[1 + \omega_r^{-2}(k)\omega^2]A_+^2/2 \approx 0.005$$

of the total mass of the BEC is involved in the motion, then the frequency rises by one-third of its primary value and becomes equal to 400 s$^{-1}$ in accordance with Eq. (10). Similarly, a strongly nonlinear behavior of low-lying magnetization modes of the spinor BEC in a finite-size optical trap can be expected because the trapped BEC spectrum must reveal the most important qualitative features present in the translationally invariant case, as has been shown for two-component BECs in magnetic traps [5].

This work is supported by the NWO (project NWO-047-009.010), the state program "Universities of Russia" (grant VR.01.01.040), and the Ministry of Education of Russia (grant E00-3-12).

## REFERENCES

1. C. J. Myatt, E. A. Burt, R. W. Ghirst, *et al.*, Phys. Rev. Lett. **78**, 586 (1997); D. S. Hall, M. R. Matthews, J. R. Ensher, *et al.*, Phys. Rev. Lett. **81**, 1539 (1998).
2. J. Stenger, S. Inouye, D. M. Stamper-Kurn, *et al.*, Nature **396**, 345 (1998).
3. M. D. Barrett, J. A. Sauer, and M. S. Chapman, Phys. Rev. Lett. **87**, 010404 (2001).
4. T.-L. Ho and V. B. Shenoy, Phys. Rev. Lett. **77**, 3276 (1996).
5. R. Graham and D. Walls, Phys. Rev. A **57**, 484 (1998); B. D. Esry and C. H. Greene, Phys. Rev. A **57**, 1265 (1998); D. Gordon and C. M. Savage, Phys. Rev. A **58**, 1440 (1998).
6. Yu. A. Nepomnyashchii, Zh. Éksp. Teor. Fiz. **70**, 1070 (1976) [Sov. Phys. JETP **43**, 559 (1976)].
7. T.-L. Ho, Phys. Rev. Lett. **81**, 742 (1998); T. Ohmi and K. Machida, J. Phys. Soc. Jpn. **67**, 1822 (1998).
8. Th. Busch and J. R. Anglin, Phys. Rev. Lett. **87**, 010401 (2001).
9. Y. Castin and R. Dum, Phys. Rev. Lett. **77**, 5315 (1996); Yu. Kagan, E. L. Surkov, and G. V. Shlyapnikov, Phys. Rev. A **54**, R1753 (1996).
10. A.-H. Nayfeh, *Perturbation Methods* (Wiley, New York, 1973; Mir, Moscow, 1976); L. D. Landau and E. M. Lifshitz, *Course of Theoretical Physics*, Vol. 1: *Mechanics* (Nauka, Moscow, 1982; Pergamon, New York, 1988).
11. S. T. Beliaev, Zh. Éksp. Teor. Fiz. **34**, 417 (1958) [Sov. Phys. JETP **7**, 289 (1958)].
12. A. Sinatra, P. O. Fedichev, Y. Castin, *et al.*, Phys. Rev. Lett. **82**, 251 (1999).

*Journal of Experimental and Theoretical Physics, Vol. 95, No. 2, 2002, pp. 226–241.*
*Translated from Zhurnal Éksperimental'noĭ i Teoreticheskoĭ Fiziki, Vol. 122, No. 2, 2002, pp. 264–281.*


**PLASMA, GASES**

# Particle Dynamics during Adiabatic Expansion of a Plasma Bunch

**V. F. Kovalev[a, *], V. Yu. Bychenkov[b], and V. T. Tikhonchuk[c]**

[a]*Institute of Mathematical Modeling, Russian Academy of Sciences, Miusskaya pl. 4a, Moscow, 125047 Russia*
[b]*Lebedev Physical Institute, Russian Academy of Sciences, Leninskii pr. 53, Moscow, 119991 Russia*
[c]*Institute of Fundamental Physics, Bordeaux University, B.P. 120, 33175, Gradignan cedex, France*
**e-mail: kovalev@imamod.ru*

Received February 7, 2002

**Abstract**—The renormalization-group approach is used to obtain an exact solution to the self-consistent Vlasov kinetic equations for plasma particles in the quasi-neutral approximation. This solution describes the one-dimensional adiabatic expansion of a plasma bunch into a vacuum for arbitrary initial particle velocity distributions. Ion acceleration is studied for two-temperature Maxwellian and super-Gaussian initial electron distributions, which predetermine distinctly different ion spectra. The solution found is used to describe the acceleration of ions of two types. The relative acceleration efficiency of light and heavy ions as a function of atomic weights and number densities is analyzed. The solutions obtained are of practical importance in describing ion acceleration during the interaction of an ultrashort laser pulse with nanoplasma, for example, cluster plasma or plasma produced when thin foils are irradiated by a laser. *© 2002 MAIK "Nauka/Interperiodica".*

## 1. INTRODUCTION

Although more than thirty years have elapsed since the first publications [1, 2] on the theory of plasma expansion into a vacuum, the physics of this process is still the subject of investigation. This is primarily because it is necessary not only to understand the physics of ion acceleration during the interaction of laser radiation with plasma but also to quantitatively describe the characteristics of accelerated particles. Ion acceleration is a key problem for various high-intensity laser applications, such as laser-driven thermonuclear fusion; fast-particle injectors, including fast ignitors; extremely hot cluster plasma; and radiation sources for medicine, materials science, and nuclear physics. Although ion acceleration in expanding hot laser plasma was described in detail [3, 4], recent experiments with nanoplasma bunches [5, 6] and thin foils [7] have revealed that ions can reach energies above the predicted level.

The largest number of works on plasma expansion into a vacuum is based on the model of a semibounded medium with isothermal electrons and cold ions [8–12], which implies the presence of a steady source of particles and admits isothermal plasma expansion. This model is definitely inadequate in studying the expansion of small plasma bunches, for example, clusters [13] or foils. This expansion is accompanied by adiabatic particle cooling and, as we show below, differs from the previously studied expansion of semibounded plasma into a vacuum by distinctly different patterns in the ion number and temperature distributions. It was studied by using a hydrodynamic phenomenological theory [14] and numerical simulations [15, 16]. An important step in its study was the paper by Dorozhkina and Semenov [17], who obtained an exact self-similar solution to the Vlasov equations for electrons and ions in the quasi-neutral approximation. However, the kinetic solution for the expansion of a plasma bunch into a vacuum found in [17] corresponds to the special case of a quadratic spatial dependence of the plasma electrostatic potential and, accordingly, of the initial conditions described by identical coordinate and velocity dependences of the electron and ion distribution functions. The latter condition significantly restricts the use of the analytic theory for interpreting experiments.

In this paper, which elaborates and details the ideas formulated in [18], we found a more general (than in [17]) class of solutions to the initial-value problem for the Vlasov equations in the quasi-neutral approximation for arbitrary initial particle, electron and ion, velocity distributions. This is achieved by using the renormalization-group approach [19, 20], in which the solution to the initial-value problem of the perturbation theory on short time scales, $t \longrightarrow 0$, is extended to the range of finite $t$ by means of renormalization-group symmetries. The solution of Dorozhkina and Semenov [17] is shown to be a special case of this solution. We apply the general renormalization-group approach to the problem of plane expansion. A generalization to the three-dimensional case involves no fundamental difficulties, although it requires cumbersome calculations. As the initial electron velocity distributions, we discuss three typical distributions: Maxwellian, two-temperature Maxwellian, and super-Gaussian, which are characteristic of certain modes of interaction between laser radiation and plasma. It is hoped that our results will

shed light on the nature of the experimentally detected high energy cutoff in the ion spectrum [5, 6], because this method allows one to analyze essentially nonequilibrium electron distribution functions similar to those that emerge under experimental conditions [5, 6], where accelerated electrons are generated during the interaction of laser radiation with plasma.

In addition, we solve the initial-value problem as applied to the expansion of a plasma bunch with two types of ions. Recently, in connection with experiments on the laser-plasma method of ion acceleration and nuclear processes on its basis [7, 21], a need has arisen to predict the energy of a given type of ions with allowance made for the fact that the laser-irradiated plasma may contain ions of a different type. In this case, allowance for the hydrogen impurity, which is always present because of the adsorption of water vapor on the laser-target surface, is of greatest urgency. Being the lightest component, protons are well captured by the field and accelerated most efficiently, thereby suppressing the acceleration of the heavier ions flying behind. Thus, for example, in the deuteron acceleration experiment [7] where no special measures were taken to remove water from the target surface, the deuteron energy was 2 MeV, whereas the protons that emerge due to surface contamination were accelerated to 9 MeV. Naturally, for this kind of problems, it is highly desirable to formulate surface-purity (hydrogen-concentration) requirements for the target ions to be efficiently accelerated. On the other hand, even when the surface is well cleaned [22] but the targets used contain various chemical elements, quantitative criteria for the acceleration of ions of various types of a given concentration are necessary. The analytic theory for the expansion of multicomponent plasma developed below is an important step in this direction.

## 2. BASIC EQUATIONS

In order to describe the dynamics of a plasma bunch inhomogeneous in coordinate $x$, let us consider the standard system of kinetic equations

$$\partial_t f^\alpha + v\partial_x f^\alpha + \frac{e_\alpha}{m_\alpha} E \partial_v f^\alpha = 0 \qquad (1)$$

for the distribution functions $f^\alpha$ of particles of type $\alpha$ (with charge $e_\alpha$ and mass $m_\alpha$) that depend on time $t$, coordinate $x$, and one velocity component $v$ along the plasma inhomogeneity. The quantity $E(t, x)$ is a self-consistent electric field determined by the plasma-flow quasi-neutrality condition. In this quasi-neutral approximation, the charge, $\rho$, and current, $j$, densities are assumed to be zero:

$$\rho \equiv \int dv \sum_\alpha e_\alpha f^\alpha = 0,$$
$$j \equiv \int dv v \sum_\alpha e_\alpha f^\alpha = 0. \qquad (2)$$

Accordingly, the self-consistent electric field $E$ can be expressed in terms of the moments of the distribution functions as follows:

$$E = \int dv v^2 \partial_x \sum_\alpha e_\alpha f^\alpha \left\{ \int dv \sum_\alpha \frac{e_\alpha^2}{m_\alpha} f^\alpha \right\}^{-1}. \qquad (3)$$

We seek a solution to the system of Eqs. (1) and (2) with the boundary conditions that correspond to the electron and ion distribution functions specified at the initial time $t = 0$,

$$f^\alpha\big|_{t=0} = f_0^\alpha(x, v). \qquad (4)$$

This formulation of the problem can model the expansion of a plasma bunch driven by a short laser pulse, with duration much shorter than the bunch evolution time scale. In this case, the interaction of laser radiation with plasma and its heating, in which electrons play a major role, are not specified and are modeled by specifying an arbitrary initial electron velocity distribution function.

## 3. SYMMETRY OF THE EQUATIONS AND RENORMALIZATION-GROUP SYMMETRY FOR THE SOLUTION OF THE INITIAL-VALUE PROBLEM

The standard method for analyzing Eqs. (1) is the method of characteristics (see, e.g., [1, 2]). The characteristic equations for (1) contain the electric field (3). The latter is expressed in terms of the integrals of the velocity distribution functions, which makes it difficult to analytically study these equations and forces us to resort to numerical methods. Therefore, below, we use a different analytic approach. To solve the initial-value problem (1), (2), (4), we use the possibility of extending this solution written in the small neighborhood, $t \longrightarrow 0$, as a series of the perturbation theory in powers of the variable $t$ to the range of much longer times, $t \neq 0$, by means of a special, renormalization-group, symmetry. For this extension, we use finite group transformations that relate the initial distribution functions (4) to the values of these functions at times $t \neq 0$. The sought-for renormalization-group symmetry is found as a subgroup of the group of point Lie transformations admitted by system (1) and (2) specified by the following set of infinitesimal operators:

$$X_0 = \partial_t, \quad X_1 = \partial_x,$$
$$X_2 = t\partial_t - v\partial_v, \quad X_3 = x\partial_x + v\partial_v,$$
$$X_4 = \sum_\alpha f^\alpha \partial_{f^\alpha}, \quad X_5 = t\partial_x + \partial_v, \qquad (5)$$
$$X_6 = t^2\partial_t + tx\partial_x + (x - vt)\partial_v,$$
$$X_\alpha = \frac{1}{Z_{\alpha+1}}\partial_{f^{\alpha+1}} - \frac{1}{Z_\alpha}\partial_{f^\alpha}$$

with the general element of the algebra represented by their linear combination

$$X = \sum_{j=0}^{6} c_j X_j + \sum_{\alpha} b_\alpha X_\alpha. \quad (6)$$

In the operators $X_\alpha$ in system (5), $Z_\alpha = e_\alpha/|e|$ is the charge number of the particles of type $\alpha$ and the index $\alpha + 1$ denotes the type of particles that follows $\alpha$. The operators $X_\alpha$ exist only in plasma with the number of particle types larger than or equal to two, and their number is less than the number of plasma components by one.

The dependence of the electric field $E(t, x)$ in the kinetic equations (1) on time $t$ is described by a function containing six constants $c_j$, which determine the contribution of the various operators (5) to the general element of the algebra (6),

$$E = E_0(I^E)\exp\left(\int dt \frac{c_3 - 2c_2 - 3c_6 t}{c_0 + c_2 t + c_6 t^2}\right),$$
$$I^E = x\exp\left(-\int dt \frac{c_3 + c_6 t}{c_0 + c_2 t + c_6 t^2}\right) \quad (7)$$
$$-\int dt \frac{c_1 + c_5 t}{c_0 + c_2 t + c_6 t^2}\exp\left(-\int dt \frac{c_3 + c_6 t}{c_0 + c_2 t + c_6 t^2}\right).$$

The dependence of the electric field on coordinate $x$ is given by the form of function $E_0$ and can be derived from the quasi-neutrality condition (2) at time $t = 0$.

The method for calculating the allowable symmetry group used here qualitatively differs from the method used in [23] in that the electric field $E$ is treated not as one of the dependent variables but as an unknown function of the variables $t$ and $x$, $E = E(t, x)$. This case of finding the symmetry logically follows from the simpler quasi-neutral model of plasma description, in contrast to the complete system of Vlasov–Maxwell equations used in [23]. It is easy to verify that the translation operators $X_0$ and $X_1$, the Galilean transformation operator $X_5$, and the quasi-neutrality operators $X_\alpha$ are contained in the symmetry group obtained previously [24] by a different method without assuming that $E$ is an arbitrary function of two variables to be determined.[1] The two dilation operators specified in [24] are obtained by combining the three dilation operators $X_2$, $X_3$, and $X_4$ from (5) and by adding the contributions responsible for the dilation transformation of the electric field $E$, charge density $\rho$, and electric current density $j$. The conformal group operator $X_6$ is new among the operators (5). Below, we make sure that this operator makes it possible to construct new exact solutions to the initial-value problem concerned.

[1] Since here, in contrast to [24], we chose a different normalization of the particle distribution functions, the quasi-neutrality operators $X_\alpha$ contain factors that do not depend on particle mass.

In order to obtain the sought-for renormalization-group symmetry, we should separate out a linear combination from the set of operators (6) that leaves the solution $f^\alpha = \mathcal{F}^\alpha(t, x, v) \equiv f_0^\alpha(x, v) + O(t)$ to the initial-value problem for $t \longrightarrow 0$ invariant. Checking the satisfaction of the renormalization-group invariance conditions leads to restrictions on the type of initial particle distribution functions. These restrictions have the form of a system of equations of the first order in the number of particle types in plasma:

$$c_4 f_0^\alpha + \frac{1}{Z_\alpha}(b_{\alpha-1}(1-\delta_{\alpha,0}) - b_\alpha(1-\delta_{\alpha,p})) + (c_0 v - c_1 - c_3 x)\partial_x f_0^\alpha - \left(-c_0\frac{e_\alpha}{m_\alpha}E + c_5 + (c_3 - c_2)v + c_6 x\right)\partial_v f_0^\alpha = 0, \quad (8)$$
$$\alpha = 0, 1, \ldots, p,$$

where the Kronecker symbol $\delta_{\alpha,\beta}$ separates out the type of particles with $\alpha = 0$ (e.g., for definiteness, electrons) and $\alpha = p$. The solutions to these equations define the initial particle distribution functions in terms of arbitrary functions of the first integrals of the characteristic equations adjoint with (8), and the electric field at the initial time, $E_0(x)$, is determined from relation (3) or, equivalently, from the first relation in (2). At $c_2 = 2c_3$, the expressions for these integrals have a comparatively simple form, which, at the same time, admits an analytic study for an arbitrary $E_0(x)$ (their number is equal to the number of particle types):

$$I^\alpha = \frac{1}{2}(c_0 v^2 - 2c_3 x v + c_6 x^2) + c_5 x - c_1 v + c_0\frac{e_\alpha}{m_\alpha}\Phi_0(x). \quad (9)$$

In this case, the solutions to Eqs. (8) are written in terms of the integrals $I^\alpha$ for an arbitrary dependence of the potential $\Phi_0$ for the electric field $E_0 = -\partial_x\Phi_0$ on coordinate $x$:

$$c_4 f_0^\alpha + \frac{1}{Z_\alpha}(b_{\alpha-1}(1-\delta_{\alpha,0}) - b_\alpha(1-\delta_{\alpha,p})) = c_4 F^\alpha(I^\alpha)\exp\left\{-\frac{c_4}{c_0}\int dx\left[\frac{2I^\alpha}{c_0} - \frac{2e_\alpha}{m_\alpha}\Phi_0(x) - \left(\frac{c_6}{c_0} - \frac{c_3^2}{c_0^2}\right)x^2 + \left(2\frac{c_3 c_1}{c_0^2} - \frac{2c_5}{c_0}\right)x + \frac{c_1^2}{c_0^2}\right]^{-1/2}\right\}. \quad (10)$$

Here, $F^\alpha$ are arbitrary functions of their arguments. Using the results (10) in relations (2) generally leads to integral equations for the potential $\Phi_0(x)$. A simpler case in which the problem of calculating the potential $\Phi_0(x)$ is significantly simplified and, at the same time,

it is still possible to construct a broad class of analytic solutions, is realized for the constants $c_4 = b_\alpha = 0$, when the sought-for renormalization-group symmetry operator takes the form

$$R = (c_0 + 2c_3t + c_6t^2)\partial_t + (c_1 + c_3x + c_5t + c_6tx)\partial_x + (c_5 - c_3v + c_6(x - vt))\partial_v. \quad (11)$$

In this case, the absence of contributions responsible for the transformation of the distribution functions $f^\alpha$ in the operator (11) implies that they are invariants of the corresponding renormalization-group transformation; i.e., the relationship

$$f^\alpha = F^\alpha(I^\alpha) \quad (12)$$

is also retained at $t \neq 0$. The dependence of the distribution functions $f^\alpha$ on time, coordinates, and velocities is established with allowance made for the form of the invariants for the renormalization-group symmetry operator that relate the variables $(x', v')$ at the initial time $t = 0$ with their values $(x, v)$ at $t \neq 0$:

$$x' = \frac{x\sqrt{c_0}}{\sqrt{c_0 + 2c_3t + c_6t^2}} - \sqrt{c_0}\int_0^t \frac{c_1 + c_5t}{(c_0 + 2c_3t + c_6t^2)^{3/2}},$$
$$\left(v' - \frac{c_1 + c_3x'}{c_0}\right)^2 = v^2 - \frac{c_6}{c_0}((x')^2 - (x - vt)^2) - 2\frac{c_5}{c_0}(x' - (x - vt)) - 2v\left(\frac{c_1}{c_0} + \frac{c_3}{c_0}(x - vt)\right) + \left(\frac{c_1 + c_3x'}{c_0}\right)^2. \quad (13)$$

These formulas essentially define the sought-for finite group (renormalization-group) transformations and allow the distribution functions at an arbitrary time, $t \neq 0$, to be expressed in terms of their initial values, which are functions of the variables with primes. Thus, identifying $x$ and $v$ in relations (9) and (12) with $x'$ and $v'$ and substituting the expressions from (13) into these relations yields an explicit dependence of the distribution functions $f^\alpha$ on time $t$, coordinate $x$, and velocity $v$. The time dependence of the potential $\Phi$ is obtained by integrating formula (7) over $x$ to give

$$\Phi = \Phi_0(I^E)(c_0 + 2c_3t + c_6t^2)^{-1}. \quad (14)$$

The physical meaning of the constants $c_j$ in (9), (13), and (14) is determined in each specific case by the form of distribution functions at the initial time. In particular, the choice of the constants $c_1 = c_3 = c_5 = 0$ corresponds to initial particle distributions symmetric in $x$ and $v$ in the absence of a mean velocity.

## 4. DYNAMICS OF THE PARTICLE DISTRIBUTIONS IN AN EXPANDING PLASMA BUNCH

To analyze the space-time behavior of the distribution functions, let us consider several examples of using the solution that is given by formulas (9) and (12)–(14) and that corresponds to different initial conditions (4). We dwell on four examples: the first three describe electron–ion plasma ($\alpha = \{e, i\}$, $m_\alpha = \{m_e, m_i\}$, $Z_\alpha = \{-1, Z\}$), and the last example corresponds to plasma with several types of ions ($\alpha = \{e, 1, 2, \ldots\}$, $m_\alpha = \{m_e, m_1, m_2, \ldots\}$, $Z_\alpha = \{-1, Z_1, Z_2, \ldots\}$).

**Example 1.** For a plasma bunch composed of electrons and one type of ions with Maxwellian initial distribution functions characterized by the densities $n_{e0}(x)$ and $n_{i0}(x)$ and temperatures $T_{e0}(x)$ and $T_{i0}(x)$, respectively, we have from relations (12)

$$f_0^\alpha = \frac{n_{\alpha 0}}{\sqrt{2\pi}v_{T\alpha}}\exp\left(-\frac{I^\alpha}{v_{T\alpha}^2}\right), \quad (15)$$

where the thermal particle velocities are defined in the standard way,

$$v_{T\alpha} = \sqrt{\frac{T_{\alpha 0}}{m_\alpha}}.$$

In this case, the following constants $c_j$ in the integrals $I^\alpha$ are chosen:

$$c_0 = 1, \quad c_1 = c_3 = c_5 = 0, \quad c_6 = \Omega^2. \quad (16)$$

As was pointed out above, zero constants $c_1$, $c_3$, and $c_5$ correspond to initial particle distributions symmetric in $x$ and $v$ in the absence of a mean velocity. Without loss of generality, the constant $c_0$ in (9) may be chosen arbitrarily (equal to unity). The physical meaning of the constant $c_6$, which has the dimensions of frequency squared, can be established if we introduce the initial plasma density inhomogeneity scale length. As will be seen from the subsequent analysis, $c_6$ is defined by the square of the ratio of the characteristic ion expansion velocity to this inhomogeneity scale length.

The case of initial conditions (15) corresponds to the problem of plasma-bunch expansion considered in [17, 25] and will be used below as a test. Using the initial functions (15) in the quasi-neutrality conditions (2), we obtain (for $Zn_{i0} = n_{e0}$) a quadratic dependence of the potential $\Phi_0$ on coordinate $x$ [25],

$$\Phi_0(x) = \frac{\Omega^2x^2}{2e}\frac{m_iT_{e0} - m_eT_{i0}}{T_{i0} + ZT_{e0}}. \quad (17)$$

Substituting (17) into (15) and using relations (13) and (14), we derive formulas that explicitly describe the

dynamics of variations $f^{e,i}$ in the plasma particle distribution functions at $t \neq 0$:

$$f^{\alpha} = \frac{n_{\alpha 0}}{\sqrt{2\pi}v_{T\alpha}}\exp\left[-\frac{1+\Omega^2 t^2}{v_{T\alpha}^2}\right.$$
$$\left.\times\left(\frac{(v-u)^2}{2}+\frac{v_{T\alpha}^2(1+Zm_e/m_i)}{v_{Te}^2-v_{Ti}^2}\frac{e\Phi}{m_e}\right)\right]. \quad (18)$$

Here, the local plasma flow velocity $u$ and the potential $\Phi$ are defined by the relations

$$u = \frac{xt\Omega^2}{1+\Omega^2 t^2},$$
$$\Phi = \frac{\Omega^2 x^2}{2e(1+\Omega^2 t^2)^2}\frac{m_i T_{e0}-m_e T_{i0}}{C_s^2(m_i+Zm_e)}, \quad (19)$$

where

$$C_s = \sqrt{\frac{T_{i0}+ZT_{e0}}{m_i+Zm_e}}$$

is the speed of sound calculated from the initial particle temperatures.

**Example 2.** This example matches the previous example in the initial ion distribution function but differs from it by the initial electron distribution function. Here, this function has the form of a two-temperature Maxwellian distribution with the densities and temperatures corresponding to cold ($c$) and hot ($h$) electrons:

$$f_0^e = \frac{n_{c0}}{\sqrt{2\pi}v_{Te}}\exp\left(-\frac{I^e}{v_{Te}^2}\right)+\frac{n_{h0}}{\sqrt{2\pi}v_{Th}}\exp\left(-\frac{I^e}{v_{Th}^2}\right),$$
$$f_0^0 = \frac{n_{i0}}{\sqrt{2\pi}v_{Ti}}\exp\left(-\frac{I^i}{v_{Ti}^2}\right). \quad (20)$$

This example can model the expansion of a plasma bunch (e.g., a cluster with a size larger than the Debye length) rapidly preheated by laser radiation to produce a group of hot electrons. Using (15) in the quasi-neutrality conditions (2) leads (for $Zn_{i0} = n_{c0} + n_{h0}$) to the dependence of the initial potential $\Phi_0$ on coordinate $x$ that is implicitly defined in terms of the characteristic velocity $U_0 = \Omega x$ from the equation

$$U_0^2 = 2C_s^2\left\{\mathscr{E}_0-\frac{T_{i0}}{T_{i0}+ZT_{e0}}\right.$$
$$\left.\times\ln\left\{1-\varrho+\rho\exp\left[\left(1-\frac{T_{e0}}{T_h}\right)\right]\mathscr{E}_0\right\}\right\}, \quad (21)$$

$$\mathscr{E}_0 = \frac{e\Phi_0}{T_{e0}}+\frac{U_0^2}{2v_{Te}^2}, \quad \varrho = \frac{n_{h0}}{Zn_{i0}}.$$

Substituting (21) into (20) and using (13) and (14), we derive formulas that describe the dynamics of variations in the plasma particle distribution functions $f^{e,i}$ at $t \neq 0$ in parametric form:

$$f^e = (1-\rho)\frac{Zn_{i0}}{\sqrt{2\pi}v_{Te}}\exp\left[-\frac{U^2}{2v_{Te}^2}\right.$$
$$\left.-\frac{(1+\Omega^2 t^2)}{v_{Te}^2}\left(\frac{(v-u)^2}{2}+\frac{e\Phi}{m_e}\right)\right]+\rho\frac{Zn_{i0}}{\sqrt{2\pi}v_{Th}}$$
$$\times\exp\left[-\frac{U^2}{2v_{Th}^2}-\frac{(1+\Omega^2 t^2)}{v_{Th}^2}\left(\frac{(v-u)^2}{2}+\frac{e\Phi}{m_e}\right)\right], \quad (22)$$

$$f^i = \frac{n_{i0}}{\sqrt{2\pi}v_{Ti}}\left\{1-\rho+\rho\exp\left[\left(1-\frac{T_{e0}}{T_h}\right)\mathscr{E}\right]\right\}$$
$$\times\exp\left[-\frac{U^2}{2v_{Te}^2}-(1+\Omega^2 t^2)\left(\frac{(v-u)^2}{2v_{Ti}^2}+\frac{e\Phi}{T_{e0}}\right)\right].$$

Here, the local plasma flow velocity $u(t, x)$ is defined by formula (19) as before. In this case, the dependence of the potential on coordinates and time is determined by the solution of an equation that formally matches Eq. (21) after the substitution $U_0 \longrightarrow U$ and $\mathscr{E}_0 \longrightarrow \mathscr{E}$, but it explicitly includes the time dependences of the potential $\Phi$ and characteristic velocity $U$,

$$U^2 = 2C_s^2\left\{\mathscr{E}-\frac{T_{i0}}{T_{i0}+ZT_{e0}}\right.$$
$$\left.\times\ln\left\{1-\varrho+\varrho\exp\left[\left(1-\frac{T_{e0}}{T_h}\right)\mathscr{E}\right]\right\}\right\}, \quad (23)$$

$$\mathscr{E} = \frac{e\Phi}{T_{e0}}(1+\Omega^2 t^2)+\frac{U^2}{2v_{Te}^2}, \quad U = \frac{\Omega x}{\sqrt{1+\Omega^2 t^2}}.$$

**Example 3.** This is another example of two-component plasma with ions whose initial velocity distribution function is Maxwellian (as in Example 1) but with electrons whose initial velocity distribution is super-Gaussian,

$$f_0^e = \mathscr{C}\frac{n_{e0}}{\sqrt{2\pi}v_{Te}}\exp\left(-\frac{2(I^e)^2}{v_{Te}^4}\right),$$
$$f_0^i = \frac{n_{i0}}{\sqrt{2\pi}v_{Ti}}\exp\left(-\frac{I^i}{v_{Ti}^2}\right). \quad (24)$$

Here, $\mathscr{C} = \sqrt{\pi}2^{5/4}/\Gamma(1/4)$, where $\Gamma(\xi)$ is the gamma function and $n_{e0} = Zn_{i0}$. This example can be related to

the expansion of a plasma bunch rapidly heated by a moderately intense laser field through backscattered bremsstrahlung absorption, when an electron distribution function with a flattening of the main body and a cutoff of the suprathermal tail can be established [26]: $\propto\exp(-v^m)$, $2 \le m \le 5$. The quantity $v_{\mathrm{Te}}$ in the expression for $f_0^e$ formally does not match the definition of the thermal velocity $\sqrt{T_{e0}/m_e}$, differing from it by a factor of the order of unity [26]. Since the difference between this quantity, which characterizes the thermal straggling of electrons, and $\sqrt{T_{e0}/m_e}$ is of no fundamental importance, we use the standard designation for it. Substituting (20) into the quasi-neutrality conditions (2) yields the coordinate dependence of the initial potential implicitly determined, as above, from the relation

$$U_0^2 = \frac{2}{m_i + Zm_e} \times [T_{i0}\mathscr{E}_0^2 + ZT_{e0}\mathscr{E}_0 - T_{i0}\ln(a\sqrt{\mathscr{E}_0}K_{1/4}(\mathscr{E}_0^2))], \quad (25)$$

$$a = \frac{2^{3/4}}{\Gamma(1/4)} \approx 0.46.$$

Substituting (25) into (24) and using relations (13) and (14), we obtain formulas that describe the dynamics of variations in the plasma particle distribution functions $f^{e,i}$ at $t \neq 0$ in parametric form:

$$f^e = \frac{\mathscr{E}n_{e0}}{\sqrt{2\pi}v_{Te}}\exp\left\{-2\left[\frac{U^2}{2v_{Te}^2} + \frac{(1+\Omega^2t^2)}{v_{Te}^2} \times \left(\frac{(v-u)^2}{2} + \frac{e\Phi}{m_e}\right)\right]^2\right\},$$

$$f^i = \frac{an_{i0}\sqrt{\mathscr{E}}}{\sqrt{2\pi}v_{Ti}}K_{1/4}(\mathscr{E}^2) \times \exp\left[-\mathscr{E}^2 - \frac{(v-u)^2}{2v_{Ti}^2}(1+\Omega^2t^2)\right]. \quad (26)$$

Here, $u$, $U$, and $\mathscr{E}$ are given by formulas (19) and (23), while the equation that reflects the relation between $U$ and $\mathscr{E}$ (i.e., specifies the dependence of the potential $\Phi$ on time and coordinates) formally matches Eq. (25) after the substitution $U_0 \longrightarrow U$ and $\mathscr{E}_0 \longrightarrow \mathscr{E}$:

$$U^2 = \frac{2}{m_i + Zm_e} \times [T_{i0}\mathscr{E}^2 + ZT_{e0}\mathscr{E} - T_{i0}\ln(a\sqrt{\mathscr{E}}K_{1/4}(\mathscr{E}^2))]. \quad (27)$$

**Example 4.** In this example, our results are applied to plasma that contains ions of several types with initial Maxwellian velocity distribution functions,

$$f_0^q = \frac{n_{q0}}{\sqrt{2\pi}v_{Tq}}\exp\left(-\frac{I^q}{v_{Tq}^2}\right), \quad (28)$$

where the index $q$ numbers the ion types, $q = 1, 2, \ldots$. The electrons at $t = 0$ are also assumed to be Maxwellian:

$$f_0^e = \frac{n_{e0}}{\sqrt{2\pi}v_{Te}}\exp\left(-\frac{I^e}{v_{Te}^2}\right), \quad n_{e0} = \sum_q Z_q n_{q0}. \quad (29)$$

Thus, this example is a generalization of example 1 to multicomponent plasma. Using this example, we can study, in particular, the role of a small number of impurity ions. Such a study was the subject of traditional research on plasma expansion into a vacuum [27]. It is of current interest in connection with modern experiments on the heating of solid targets composed of various materials by ultrashort laser pulses due to the constant presence of protons; the latter emerge, because the target surface is not perfectly clean and always contains a small amount of $H_2O$. Numerous experiments show efficient proton acceleration from non-hydrogen-containing targets unless precautions are taken to clean the surface (see, e.g., [28, 29]).

Using (28) and (29) in the quasi-neutrality conditions (2) leads to the dependence of the initial potential $\Phi_0$ on coordinate $x$ that is implicitly determined from the equations

$$\sum_q Z_q n_{q0}\left\{\exp\left[\left(1 + \frac{Z_q T_{e0}}{T_{q0}}\right)\mathscr{E}_0 - \frac{U_0^2}{2v_{Tq}^2}\left(1 + \frac{Z_q m_e}{m_q}\right)\right] - 1\right\} = 0. \quad (30)$$

Substituting (30) into (28) and (29) and using relations (13) and (14), we derive the following formulas that describe the dynamics of the plasma particle distribution functions $f^\alpha$ and potential $\Phi$ at $t \neq 0$ in parametric form:

$$f^e = \frac{n_{e0}}{\sqrt{2\pi}v_{Te}} \times \exp\left[-\frac{U^2}{2v_{Te}^2} - \frac{(1+\Omega^2t^2)}{v_{Te}^2}\left(\frac{(v-u)^2}{2} + \frac{e\Phi}{m_e}\right)\right],$$

$$f^q = \frac{n_{q0}}{\sqrt{2\pi}v_{Tq}} \times \exp\left[-\frac{U^2}{2v_{Tq}^2} - \frac{(1+\Omega^2t^2)}{v_{Tq}^2}\left(\frac{(v-u)^2}{2} - Z_q\frac{e\Phi}{m_q}\right)\right]. \quad (31)$$

Here, the local plasma flow velocity $u$, the characteristic velocity $U$, and the characteristic dimensionless energy $\mathscr{E}$ are given by formulas (19) and (23), while the equation that reflects the relation between $U$ and $\mathscr{E}$ (i.e., specifies the dependence of the potential $\Phi$ on time and coordinates) formally matches Eq. (30) after the substitution $U_0 \longrightarrow U$ and $\mathscr{E}_0 \longrightarrow \mathscr{E}$,

$$\sum_q Z_q n_{q0} \left\{ \exp\left[ \left(1 + \frac{Z_q T_{e0}}{T_{q0}}\right)\mathscr{E} - \frac{U^2}{2v_{Tq}^2}\left(1 + \frac{Z_q m_e}{m_q}\right)\right] - 1 \right\} = 0. \tag{32}$$

Thus, the above examples clearly show that the renormalization-group approach is an efficient tool for constructing analytic solutions to the self-consistent Vlasov kinetic equations for plasma particles. Below, we present quantitative characteristics of the plasma-bunch expansion into a vacuum as a function of the initial particle velocity distributions in accordance with examples 1–4.

## 5. INTEGRATED CHARACTERISTICS FOR THE PARTICLE DISTRIBUTION FUNCTIONS

When experimental data are analyzed, apart from formulas for the plasma particle distribution functions, the integrated characteristics defined by them are also of considerable interest. In this section, being concerned with the dynamics of ion acceleration during plasma-bunch expansion, we use the solutions obtained to study such practically important characteristics as the density of ions of type $q$, $n_q(t, x)$, and their spatially averaged (over coordinate $x$) distribution, $\langle f^q \rangle$, which characterizes the ion energy spectra. These characteristics are represented by using the standard definitions

$$n_q = \int_{-\infty}^{\infty} dv\, f^q, \quad \langle f^q \rangle = \int_{-\infty}^{\infty} dx\, f^q, \tag{33}$$

which clearly illustrate the dynamics of adiabatic plasma-bunch expansion.

For the above examples, the density of ions of type $q$ depends on coordinate and time as follows:

$$n_q = \frac{n_{q0}}{\sqrt{1 + \Omega^2 t^2}} N_q\left(\frac{x}{\sqrt{1 + \Omega^2 t^2}}\right), \tag{34}$$

where the specific form of the dimensionless ion density $N_q$ is established by integrating (33) over velocities using formulas (18), (22), (26), and (31). This integration allows $N_q$ to be represented as the following dependences on the characteristic velocity

$$U = \frac{\Omega x}{\sqrt{1 + \Omega^2 t^2}}:$$

*Example 1*

$$N_i(U) = \exp\left(-\frac{U^2}{2C_s^2}\right). \tag{35}$$

*Example 2*

$$N_i(U) = \exp(-\mathscr{E}) \times \left[1 - \rho + \rho \exp\left(\left(1 - \frac{T_{e0}}{T_h}\right)\mathscr{E}\right)\right]. \tag{36}$$

*Example 3*

$$N_i(U) = a\sqrt{\mathscr{E}} K_{1/4}(\mathscr{E}^2)\exp(-\mathscr{E}^2), \quad a = \frac{2^{3/4}}{\Gamma(1/4)} \approx 0.46. \tag{37}$$

*Example 4*

$$N_q(U) = \exp\left[\frac{Z_q T_{e0}}{T_{q0}}\mathscr{E} - \frac{U^2(1 + Z_q m_e/m_q)}{2v_{Tq}^2}\right]. \tag{38}$$

In examples 2, 3, and 4, the relation between $\mathscr{E}$ and $U$ is given by the corresponding Eqs. (23), (27), and (32).

For the second integrated characteristics, $\langle f^q \rangle$, apart from the results of numerical integration, we can obtain analytic asymptotic expressions in the limit of large $\Omega t \longrightarrow \infty$, when we use the saddle-point method to calculate the integrals that define $\langle f^q \rangle$. The major contributions to the asymptotic expressions for the ion energy spectra, $\langle f^q \rangle$, that emerge in this case are related to $N_q$ by simple relations,

$$\langle f^q \rangle = n_{q0}\Omega^{-1} N_q(v), \tag{39}$$

where the corresponding dependences $N_q(U = v)$ are given by formulas (35)–(38).

In Figs 1–3, the integrated characteristics $N_q$ under discussion for one- and two-component plasma ion compositions and for the dimensionless self-consistent electric potential $\Phi$ are plotted against the dimensionless coordinate $\chi^2 = U^2/v_{Tq}^2$. For electron–ion plasma, $U$ is normalized to the thermal velocity of the only plasma ion component; for a two-component ion composition, it is normalized, for definiteness, to the thermal velocity of the first, densest, ion component: $v_{Tq} \equiv v_{T1}$. The function $\phi$ naturally appears in our theory, because a factorization similar to that [see (34)] emerging for the partial densities takes place for the electric potential,

$$\Phi = -\frac{m_e}{e}\frac{v_{Te}^2}{1 + \Omega^2 t^2}\phi, \quad \phi = \frac{U^2}{2v_{Te}^2} - \mathscr{E}. \tag{40}$$

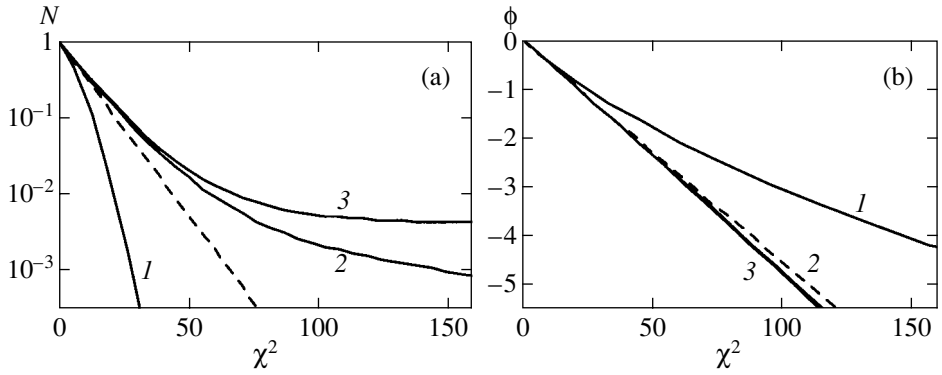


**Fig. 1.** The distributions of ion density $N$ (a) and potential $\phi$ (b) in plasma with one type of ions versus dimensionless coordinate $\chi$ for various initial electron distribution functions: *1* for a super-Gaussian distribution, *2* and *3* for a two-temperature distribution with $T_h/T_{e0} = 10$ (*2*), 100 (*3*) and the relative density $\rho = 0.1$. The dashed curve represents the initial Maxwellian electron distribution function.

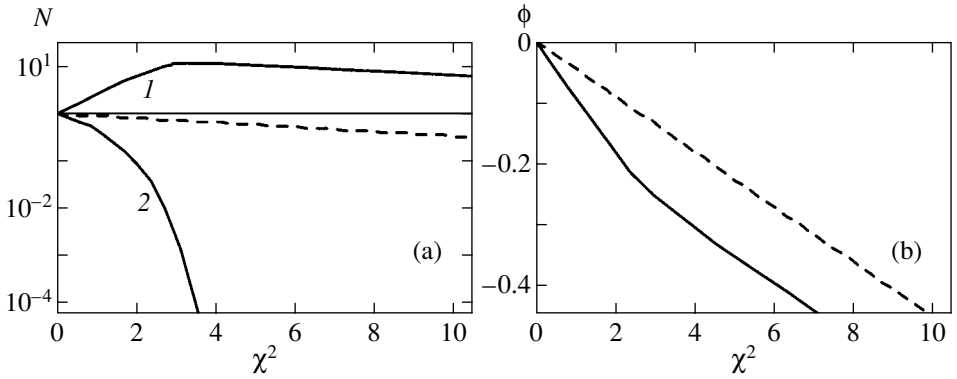


**Fig. 2.** The distributions of ion density $N_q$ (a) and potential $\phi$ (b) in plasma with two types of ions with the atomic and charge numbers $A_1 = 1$, $Z_1 = 1$ (H, curve *1*) and $A_2 = 12$, $Z_2 = 6$ (C, curve *2*). The initial electron and ion distribution functions are Maxwellian with the temperatures $T_{10}/T_{e0} = T_{20}/T_{e0} = 0.1$; $n_{10}/n_{20} = 2$. The dashed curve represents the hydrogen ion distribution function from example 1.

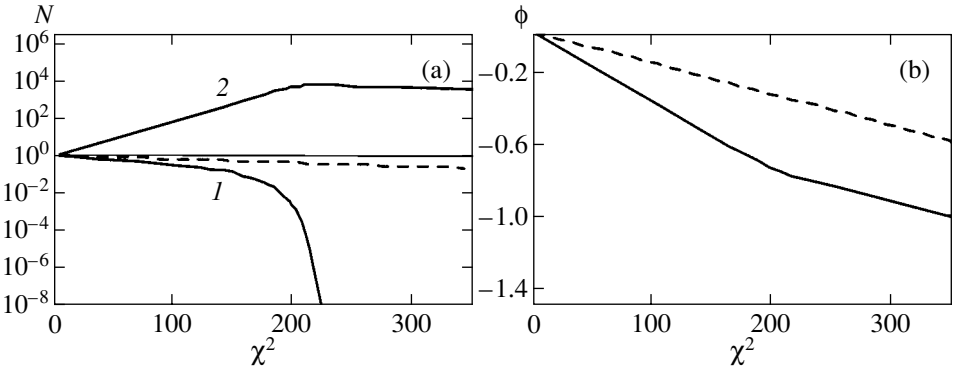


**Fig. 3.** Same as Fig. 2 for $A_1 = 27$, $Z_1 = 13$ (Al, curve *1*) and $A_2 = 1$, $Z_2 = 1$ (H, curve *2*); $n_{10}/n_{20} = 1300$.

Here, the dependence $\mathscr{E}(U)$ is determined by the solutions to the corresponding Eqs. (23), (27), and (32). In order to make the physical meaning of the dependences on dimensionless coordinate $\chi$ discussed below clearer, we recall that the frequency $\Omega$ is the ratio of the characteristic ion expansion velocity, $V$, to the initial ion density inhomogeneity scale length, $L_0$. On comparatively short time scales, $t \ll L_0/V$, the $\chi$ dependences of $N_q$ and $\phi$ actually describe the initial ion density and potential distributions as functions of the dimensionless coordi-

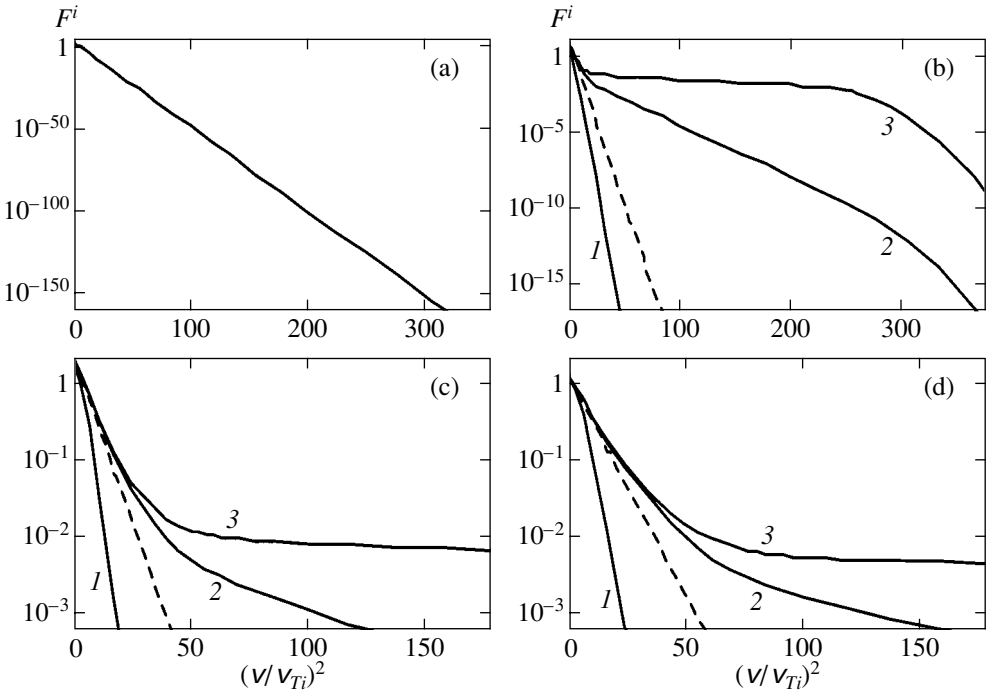


**Fig. 4.** The ion distribution $F^i(v)$ in plasma with one type of ions ($q \equiv i$) at the times $\Omega t = 0$ (a), 0.4 (b), 1 (c), and 2 (d) for various initial electron distributions: *1* for a super-Gaussian distribution, *2* and *3* for a two-temperature distribution with $T_h/T_{e0} = 10$ (*2*) and 100 (*3*) and the relative density $\rho = 0.1$. The dashed curve represents the initial Maxwellian electron distribution.

nate $(x/L_0)(V/v_{Tq})$. On long time scales, $t \gg L_0/V$, the dependence of $\chi$ on the initial density inhomogeneity scale $L_0$ disappears and $\chi$ takes the form of an ordinary self-similar variable, $\chi \longrightarrow (x/t)(1/v_{Tq})$. On the other hand, given relation (39), the $\chi$ dependence of $N_q$ on long time scales, $t \gg L_0/V$, may be considered as a dependence of the ion energy spectrum on the dimensionless velocity $v/v_{Tq}$.

Figure 1 shows the distributions of the dimensionless ion density and potential in two-component ($e$, $i$) plasma for various initial electron distribution functions but for the same (Maxwellian) initial ion distribution function. All curves were constructed for the following plasma parameters: $T_{e0}/T_{i0} = 10$, $m_i/m_e = 1836$, and $Z = 1$. Figures 2 and 3 correspond to the presence of two types of ions in plasma. In the former case (Fig. 2), the ions of the first and second types with a comparable initial density correspond to a completely ionized polyethylene film ($CH_2$); in the latter case (Fig. 3), the light ions of the second type (H) form an impurity with a low initial density compared to the heavier ions of the first type, which constitute the bulk of the plasma material, for which we chose aluminum.

Figures 4–6 show the ion energy spectra characterized by the functions $F^q(v, t) = (\Omega/n_{q0})\langle f^q\rangle$ for various times. The plasma parameters were chosen to be the same as in Figs. 1–3. We see that these curves actually take the form of the $N_q$ curves shown in Figs. 1–3 as the time $\Omega t$ increases, in accordance with asymptotic expression (39).

## 6. DISCUSSION OF THE RESULTS AND CONCLUSIONS

As in the classical papers on the theory of plasma expansion into a vacuum [1, 2, 27], the renormalization-group theory owes its progress in finding solutions of the Vlasov equations to the quasi-neutral-plasma approximation, when such a length dimension parameter as the Debye length is excluded. Whereas, in the theory [1, 2, 27] with a simplified electron kinetics, this approximation allowed plasma expansion to be described by using simple self-similar variables, in our renormalization-group approach, it is possible to pass to more complex symmetries that significantly expand the range of analytically solvable problems. A simple illustration is the problem of the expansion of a plasma sheet with initial Maxwellian electron and ion distributions [17]. The corresponding solution (example 1) is given by formulas (18) and (19), which, disregarding the contributions containing the small $m_e/m_i$ ratio, define the particle distribution functions

$$f^\alpha = \frac{n_\alpha(x,t)\sqrt{m_\alpha}}{\sqrt{2\pi T_\alpha(t)}}\exp\left[-\frac{m_\alpha(v-u)^2}{2T_\alpha(t)}\right],$$
$$u = \frac{xt\Omega^2}{1+\Omega^2 t^2}, \quad \Omega^2 = \frac{2C_s^2}{L_0^2}. \tag{41}$$

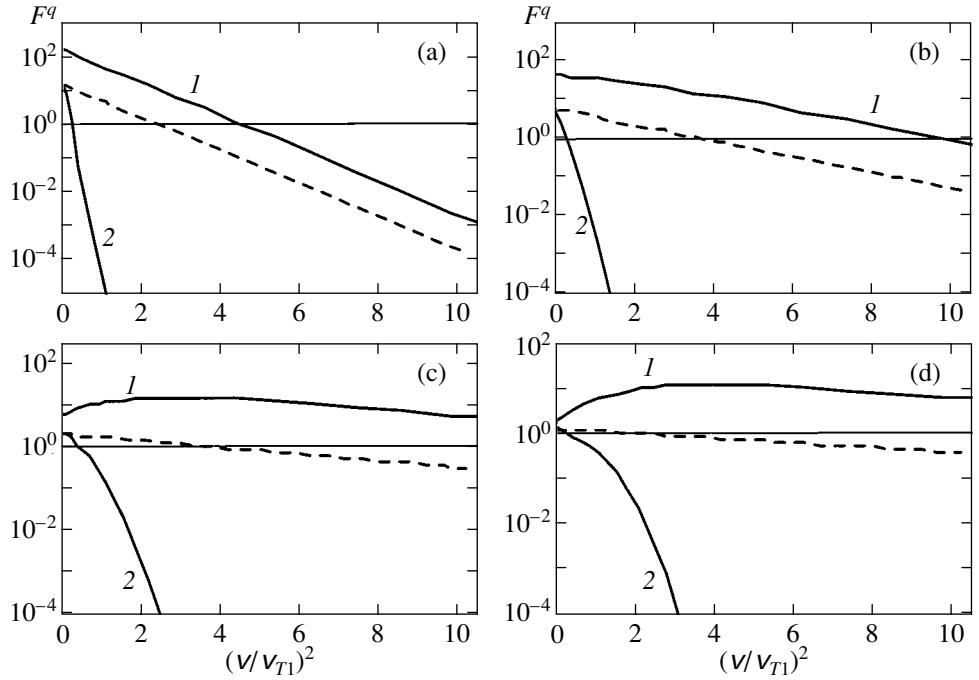


**Fig. 5.** The ion distribution functions $F^q(v)$ in plasma with two types of ions for the same $\Omega t$ as in Fig. 4. The plasma parameters correspond to Fig. 2. The dashed line represents the hydrogen ion distribution function from example 1.

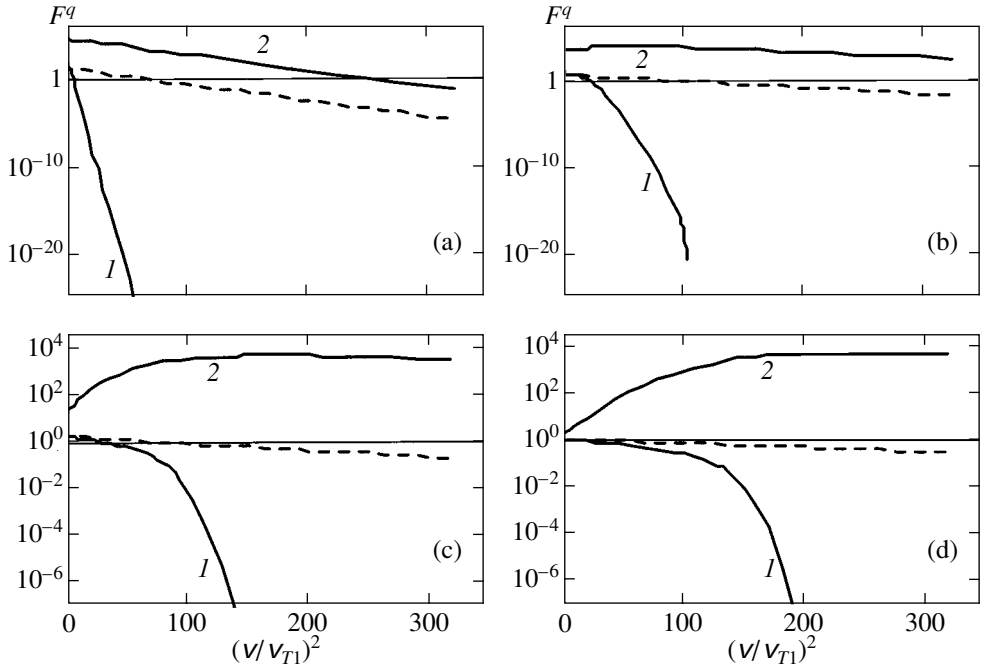


**Fig. 6.** Same as Fig. 5 for the plasma parameters of Fig. 3. The dashed curve represents the hydrogen ion distribution function from example 1.

Here, we explicitly present the effect of plasma cooling described by the time-dependent electron and ion temperatures

$$T_\alpha(t) = \frac{T_{\alpha 0}}{1 + \Omega^2 t^2}. \qquad (42)$$

In this case, according to (35), the electron and ion density distributions are given by

$$n_\alpha = \frac{n_{\alpha 0}}{\sqrt{1 + \Omega^2 t^2}} \exp\left[\frac{|e|\Phi(x, t)}{T_e(t)}\right], \qquad (43)$$

and the electric potential

$$\Phi = -\frac{m_i}{2e_i}\frac{\Omega^2 x^2}{(1+\Omega^2 t^2)^2}\frac{1}{(1+T_{i0}/ZT_{e0})} \quad (44)$$

that holds electrons and accelerates ions has a quadratic dependence on coordinate [17]. If we introduce the time-dependent plasma density inhomogeneity scale length

$$L(t) = L_0\sqrt{1+\frac{2C_s^2 t^2}{L_0^2}}, \quad (45)$$

then the variation of the electron and ion density distribution (43) with time can be represented as

$$n_\alpha = \frac{n_{\alpha 0}}{\sqrt{1+2C_s^2 t^2/L_0^2}}\exp\left(-\frac{x^2}{L^2(t)}\right). \quad (46)$$

In this case, for $t \gg L_0/\sqrt{2}\,C_s$, formulas (43) and (46) describe plasma expansion with a sonic speed $C_s \approx \sqrt{ZT_{e0}/m_i}$.

The fundamental difference between our approach and the approach described in [1, 2, 27], which are devoted to isothermal quasi-neutral plasma expansion, lies in relations (42). The cause of the plasma particle cooling is quite clear. Indeed, when a finite-size plasma bunch expands, the plasma particles acquire kinetic energy $n_\alpha m_\alpha u^2/2$ at the expense of thermal energy $n_\alpha T_\alpha$, which causes the temperature to decrease. For this reason, strictly speaking, the approximation of isothermal expansion is applicable only to massive targets, for example, to semi-bounded plasma with a limitless store of energy. Another difference lies in the distribution of electrons, which transfer their energy to ions through an electric field. In [1, 2, 27], the electrons were assumed to have an equilibrium distribution described by the Boltzmann formula, while the distribution (43) is a nonequilibrium one. It corresponds to the Boltzmann electron distribution only at the initial time, differing from the latter by a time-independent preexponential factor.

A common feature of our solutions for various initial particle distribution functions is nonisothermal plasma expansion. The form of these functions determines the specific dependence of the potential $\Phi$ on coordinate $x$, although qualitatively there is a common law of monotonic increase in $\Phi(x)$ in absolute value with $x$ for all of the above examples. As was pointed out above, the quasi-neutrality condition leads to the quadratic dependence $\Phi(x)$ discussed in [17, 25] for plasma composed of electrons and one type of ions when the velocity dependence of the distribution functions is the same in form for both types of particles (example 1). In general, the coordinate dependence of the potential is not quadratic for various electron and ion velocity distribution functions at $t = 0$ or for a multicomponent plasma ion composition.

As for the ion density distribution in a two-component plasma, it should be noted that the laws of decrease in density with increasing distance are different, depending on the initial electron distribution: the ion density in plasma depleted of suprathermal electrons (example 3) decreases most rapidly. The presence of even a small number of high-energy electrons (example 2) significantly slows down the decrease of $N(\chi^2)$ with increasing $\chi^2$. This is easy to notice by comparing the dependences of the ion distribution curves on the initial electron distribution function for examples 1 and 2. The differences between these curves show up at large coordinates $\chi^2$, i.e., for such $\mathscr{E} > \mathscr{E}_*$ that $\rho\exp(\mathscr{E}_*) \gg 1$. In this case, the relation between $\chi^2$ and $\mathscr{E}_*$ can be determined from (23) by taking into account only the last term under the logarithm associated with hot electrons. This linear relation between $\mathscr{E}_*$ and $\chi^2$ is valid for $\chi^2 \gtrsim \chi_{b1}^2$ and causes the ion density to decrease exponentially with increasing $\chi^2$. This exponential law is identical in form to (46),

$$N_i \approx \rho^{1/(1+T_{i0}/ZT_h)}\exp\left(-\frac{\chi^2}{2\chi_{d1}^2}\right),$$
$$\chi^2 = \frac{(\Omega x/v_{Ti})^2}{1+\Omega^2 t^2}, \quad (47)$$

but has a different characteristic scale of decrease $\chi_{d1}^2$, where

$$\chi_{d1}^2 \approx \frac{ZT_h}{T_{i0}}\frac{1+T_{i0}/ZT_h}{1+Zm_e/m_i},$$
$$\chi_{b1}^2 \approx 2\frac{T_{e0}}{T_h}\chi_{d1}^2\left[2+\left(1+\frac{T_{i0}/ZT_{e0}}{1+T_{i0}/ZT_h}\right)\ln\frac{Zn_{i0}}{n_{h0}}\right]. \quad (48)$$

For the parameters of Fig. 1, the domain of exponential decrease in $N_i$ of the form (47) begins at $\chi_{b1}^2 \approx 86$ for both curves. In this case, the characteristic scale of decrease (48) is $\chi_{d1}^2 \approx 10^2$ for curve *2* and $\chi_{d1}^2 \approx 10^3$ for curve *3*. For a low density of hot electrons, $n_{h0}/Zn_{i0} \ll 1$, the quantity $\Omega$ is determined, as above, from formula (41) using the initial ion density inhomogeneity scale and the speed of sound calculated from the temperature of most electrons. Consequently, the condition for the passage to a self-similar variable remains as previously, $t \gg L_0/\sqrt{2}\,C_s$. Formula (47) essentially describes a halo for $x > C_s t_{\gamma_h}$ that expands at the speed of sound determined by the temperature of the hot electron compo-

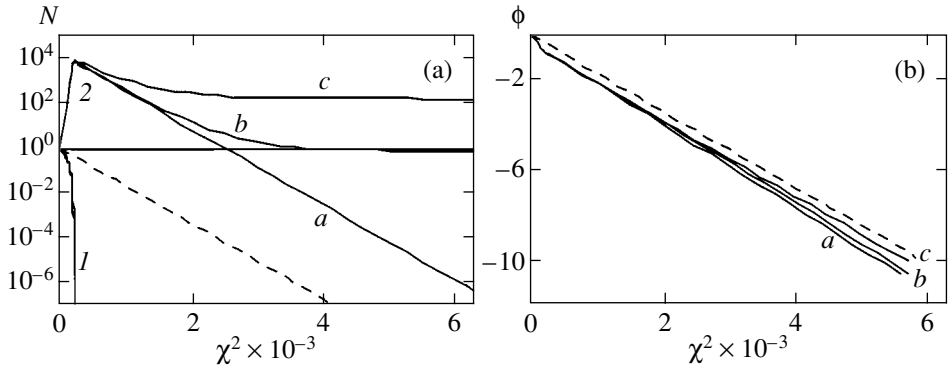


**Fig. 7.** The distribution of ion density $N_q$ (a) and potential $\phi$ (b) in plasma with two types of ions with the atomic numbers $A_1 = 27$, $A_2 = 1$ and charges $Z_1 = 13$, $Z_2 = 1$ versus dimensionless coordinate $\chi^2$. The initial ion distribution functions are Maxwellian with the temperatures $T_{10}/T_{e0} = T_{20}/T_{e0} = 0.1$ and $n_{10}/n_{20} = 1300$. The initial electron distribution function has the form of a two-temperature Maxwellian distribution with $T_h/T_{e0} = 100$ and various relative densities: $\rho = 0$ (curve *a*, the absence of hot electrons), $\rho = 0.01$ (curve *b*), and $\rho = 0.1$ (curve *c*). The curves of families *1* and *2* correspond to the plasma ions of the first and second types, respectively. The dashed curve represents the hydrogen ion distribution function from example 1.

nent, $C_{sh} \approx \sqrt{ZT_h/m_i} \gg C_s$. On the same time scales, formula (47) describes the Maxwellian ion spectrum

$$\langle f^i \rangle \propto \exp\left(-\frac{v^2}{2v_{Ti}^2\chi_{d1}^2}\right) \approx \exp\left(-\frac{v^2}{2C_{sh}^2}\right)$$

in the velocity range $v^2 > v_{Ti}^2\chi_{b1}^2 \approx C_s^2\gamma_h^2$, where

$$\gamma_h = \sqrt{2 + \ln\frac{Zn_{i0}}{n_{h0}}}$$

includes a weak logarithmic dependence on the plasma particle density.

Let us now discuss the patterns of variations in density $N_q$ during the expansion of plasma with several types of ions. As follows from the above formulas (31), (38) and Figs. 2, 3, 5, and 6, the presence of ions of several types significantly changes the dynamics of plasma-bunch expansion. The light ions ahead of the heavy ions are accelerated during the expansion most strongly. On long time scales, going far from the bunch center, they form a rarefied halo and its potential distribution. Here, Fig. 3 serves as the clearest illustration. We see that the presence of light low-density impurity ions changes the asymptotic behavior of the $\phi$ dependence for large coordinates $\chi^2$. The passage from the quadratic dependence $\phi \sim -C\chi^2$ to the shifted quadratic dependence $\phi \sim -A - B\chi^2$, where *A*, *B*, and *C* are constants (which exactly corresponds to the passage to the domain where the potential distribution is determined by impurity ions), takes place for the coordinate $\chi_*^2$ approximately determined from the relation

$$\chi_*^2 = 2\frac{T_{20}}{T_{10}}\left[\left(1 + \frac{Z_1m_e}{m_1}\right)\frac{(1 + T_{20}/Z_2T_{e0})Z_2}{(1 + T_{10}/Z_1T_{e0})Z_1}\right.$$
$$\left. - \left(1 + \frac{Z_2m_e}{m_2}\right)\frac{m_2}{m_1}\right]^{-1}\left\{\ln\frac{1}{\sigma} + \ln(1 + \sigma)\right.$$
$$\left. \times\left(1 - \frac{T_{10}Z_2}{T_{20}Z_1}\right)\left(1 + \frac{T_{10}}{Z_1T_{e0}}\right)^{-1}\right\}, \quad (49)$$
$$\sigma = \frac{Z_2n_{20}}{Z_1n_{10}} \ll 1.$$

For the parameters of example 4, this quantity is of the order of $\chi_*^2 \approx 248$, in good agreement with the numerical results presented in Fig. 3. At the point $\chi^2 \approx \chi_*^2$, the ratio of the local density of impurity ions to the density of major ions exceeds unity, $n_2/n_1 \approx (Z_1/Z_2) \gg 1$, and is equal to the ratio of the integrated distribution functions, $\langle f^2\rangle/\langle f^1\rangle = n_2/n_1$. Note, however, that the local density of impurity ions does not exceed the local ion density in a two-component plasma with ions of the same type as the impurity. This implies that the corresponding density $N_2$ multiplied by $\sigma/(1 + \sigma)$ (curve *2*) in Fig. 3 is lower than $N_i$ (dashed curve) shown for comparison at any $\chi^2$.

Thus, our results on particle acceleration in plasma with several types of ions are generally consistent with the general ideas [27] that light impurity ions are accelerated more efficiently against the background of the major heavy component. However, in contrast to [27], in which the approximation of a specified field was used to describe the motion of the light ion component, which breaks down for $\chi \gtrsim \chi_*$ (49), our theory allows one to consider also the domain where the impurity sig-

nificantly affects the form of the potential. In addition, the dependences given here are applicable to an arbitrary number of ion components with an arbitrary partial-density ratio.

Clearly, in this case, just as in plasma with one type of ions (example 2), the presence of hot electrons may lead to an even higher energy of the impurity ions. This physical situation can be easily modeled by using a combination of the initial conditions from examples 2 and 4. Such a modification of the initial conditions significantly changes the dynamics of impurity ions, as can be seen from Fig. 7 for the ion density and potential distributions similar to Fig. 3. Figure 7 was obtained by using formulas (38) in which, however, the function $\mathscr{E}_h$ given by the relation

$$\begin{aligned} &1 + \sigma - \rho + \rho\exp\left[\left(1 - \frac{T_{e0}}{T_h}\right)\mathscr{E}_h\right] \\ &= \exp\left[\left(1 + \frac{Z_1 T_{e0}}{T_{10}}\right)\mathscr{E}_h - \frac{U^2(1 + Z_1 m_e/m_1)}{2v_{T1}^2}\right] \\ &+ \sigma\exp\left[\left(1 + \frac{Z_2 T_{e0}}{T_{20}}\right)\mathscr{E}_h - \frac{U^2(1 + Z_2 m_e/m_2)}{2v_{T2}^2}\right], \\ &\rho = \frac{n_{h0}}{Z_1 n_{10} + Z_2 n_{20}} \end{aligned} \tag{50}$$

is substituted for $\mathscr{E}$. We see from Fig. 7 that the difference in curves *a*, *b*, and *c* for the density of impurity ions, $N_2(\chi)$, shows up for sufficiently large $\mathscr{E}_h$, such that $\rho\exp(\mathscr{E}_h) \gg 1$, i.e., for large $\chi$ (cf. similar relations for plasma with one type of ions). In this case, the relation between $\chi^2$ and $\mathscr{E}_h$ can be found from (50) by taking into account only the two contributions from impurity ions and hot electrons, which allows a lower limit on $\mathscr{E}_h$ to be written as the condition $\chi^2 \gtrsim \chi_{b2}^2 > \chi_{b1}^2$. For such coordinates $\chi^2$, the impurity ion density distribution corresponds to a Gaussian function similar to (47),

$$\begin{aligned} N_2 &\approx \left(\frac{\rho}{\sigma}\right)^{1/(1 + T_{20}/Z_2 T_h)}\exp\left(-\frac{\chi^2}{2\chi_{d2}^2}\right), \\ \chi^2 &= \frac{(\Omega x/v_{T1})^2}{1 + \Omega^2 t^2}, \end{aligned} \tag{51}$$

but with a different characteristic scale of variation in $\chi^2$ given by the relation

$$\begin{aligned} \chi_{d2}^2 &\approx \frac{Z_2 T_h}{T_{10}}\frac{m_1}{m_2}\frac{(1 + T_{20}/Z_2 T_h)}{(1 + Z_2 m_e/m_2)}, \\ \chi_{b2}^2 &\approx \frac{2T_{e0}}{T_h}\chi_{d2}^2\left(2 + \ln\frac{1}{\rho} + \frac{T_{20}/Z_2 T_{e0}}{1 + T_{20}/Z_2 T_h}\ln\frac{\sigma}{\rho}\right). \end{aligned} \tag{52}$$

For the parameters of Fig. 7, the domain of exponential decrease in $N_2$ of the form (51) begins at $\chi_{b2}^2 \approx 3.8 \times 10^3$ for curve *b* and at $\chi_{b2}^2 \approx 2.2 \times 10^3$ for curve *c*. In this case, the characteristic scale of decrease for both curves is $\chi_{d2}^2 \approx 27 \times 10^3$. As in the above example of ion expansion in electron–ion plasma in the presence of hot electrons, here, we may also say that there is a halo (51) formed not from ions of the major, heavy, component but from light impurity ions. At low densities of impurity ions, $(Z_2/Z_1)(n_{20}/n_{10}) \ll 1$, and hot electrons, $n_{h0}/Z_1 n_{10} \ll 1$, this halo for $t \gg L_0/\sqrt{2}C_s$ lies in the region $x > C_s^{imp} t\gamma_{imp}$ and the ion spectrum is Maxwellian,

$$\langle f^i \rangle \propto \exp\left(-\frac{v^2}{2(C_h^{imp})^2}\right),$$

in the velocity range $v^2 > (C_s^{imp})^2\gamma_{imp}^2$.

Here, we use the standard notation for the speed of sound,

$$C_s^{imp} \approx \sqrt{\frac{Z_2 T_{e0}}{m_2}}, \quad C_h^{imp} \approx \sqrt{\frac{Z_2 T_h}{m_2}},$$

determined by the mass of the impurity ions and by the temperature of the cold or, correspondingly, hot electrons, while the factor

$$\gamma_{imp} = \sqrt{2 + \ln\frac{Z_1 n_{10}}{h_{h0}} + \frac{T_{20}}{Z_2 T_{e0}}\ln\frac{Z_2 n_{20}}{n_{h0}}}$$

includes a weak logarithmic dependence on the plasma particle densities.

Presently, the most complete results on the spectra of laser-accelerated ions are obtained in experiments with thin films. Therefore, we discuss the possible applications of our theory to them. In experiments on the irradiation of thin films by short laser pulses, high-energy protons are commonly observed (see, e.g., [28]). Their energy spectrum is similar to a Maxwellian distribution that ends with a small plateau with a sharp cutoff at suprathermal energies. Despite the use of various substances as the target material, predominant proton acceleration is observed in experiments, which is always attributable to contamination of the target surface by water vapor. This corresponds to the acceleration of a minor impurity of light ions against the background of the major, heavier, ion component. According to the universally accepted view and to our calculations, hot electrons are responsible for proton acceleration; the bulk of the energy of a laser pulse is transferred to them as it is absorbed by the target. Their number is small compared to the cold electrons, but the energy contained in them generally exceeds the energy of the latter. Experimental data and numerical calcula-

tions suggest a root dependence of the hot-electron temperature on the laser energy flux density [30, 31]. Below, we follow the scaling for the hot-electron temperature proposed in [31]:

$$T_h \approx \sqrt{10^{-13} I\lambda^2}, \tag{53}$$

where the hot-electron temperature $T_h$ is in keV, the laser energy flux density $I$ is in W cm$^{-2}$, and the laser wavelength $\lambda$ is in μm.

Thus, experiments with short laser pulses suggest adiabatic plasma expansion, because the accelerated-ion spectrum is similar to a Maxwellian spectrum, $\propto \exp(-v^2)$, rather than to the spectrum $\propto \exp(-v)$ that corresponds to the theory of isothermal plasma expansion [1]. Formally, in both cases, the theory does not predict the existence of a finite maximum plasma expansion velocity, although this question is fundamental for explaining experimental observations. At the same time, it is clear that the breakdown of plasma quasi-neutrality and one-dimensionality of its expansion on long time scales are the factors that limit the maximum energy of the expanding ions.

In the classical case of two-component, electron–ion plasma (example 1), the quasi-neutrality breakdown condition arises when the density inhomogeneity scale length (45), $L(t) \approx \sqrt{2}\, C_s t$, becomes equal in order of magnitude to the electron Debye length

$$\lambda_D(t) = \sqrt{\frac{T_e(t)}{4\pi e^2 n_e(t, x)}}$$

calculated using (42) and (46). This condition determines the characteristic ion energy

$$\varepsilon^i(t) \approx 2ZT_{e0}\ln\left(\frac{C_s t}{\lambda_{D0}}\sqrt{\frac{C_s t}{L_0}}\right), \tag{54}$$

where $\lambda_{D0}$ is the electron Debye length specified by the electron temperature and maximum density at the initial time. Since the growth of the ion energy slows down sharply as one passes to three-dimensional plasma expansion, the condition $L(t) \sim D$ ($D$ is the scale size of a focal spot) can be used to estimate the ion acceleration time scale. Its substitution in the last formula yields

$$\varepsilon^i_{\max} \approx 2ZT_{e0}\ln\left(\frac{D}{\lambda_{D0}}\sqrt{\frac{D}{L_0}}\right), \tag{55}$$

where both ratios under the logarithm are large compared to unity. This estimate indicates that the Maxwellian spectrum is cut off at an energy that exceeds the electron temperature by several times.

Qualitatively, this reasoning is also valid for the acceleration of a light ion impurity (protons) with mass $m_2$ and charge $Z_2$ by hot electrons with a temperature $T_h \gg T_{e0}$ and density $n_{h0} \ll n_{e0}$, which has a direct bearing on the experiment. In this case, the analog of formula (54) takes the form

$$\varepsilon^{imp}(t) \approx 2Z_2 T_h \ln\left(\frac{C_h^{imp} t}{\lambda_{Dh}}\sqrt{\frac{C_s t}{L_0}}\right), \tag{56}$$

where the electron Debye length

$$\lambda_{Dh} = \sqrt{\frac{T_h}{4\pi e^2 n_{h0}}}$$

is determined by the hot-electron temperature and density, while the speed of sound is determined by the hot-electron temperature and the impurity-ion mass. This formula directly follows from comparison (in order of magnitude) of the second derivative of the electric potential with respect to the coordinate with the contribution that determines the impurity-proton charge density using (34), (50), (51), and (52). This estimate is valid for energies of the accelerated light ions higher than $\varepsilon^*$,

$$\varepsilon^* \approx 2T_{e0}\left(2 + \ln\frac{1}{\rho} + \frac{T_2}{Z_2 T_{e0}}\ln\frac{\sigma}{\rho}\right), \tag{57}$$

implying that the hot-electron temperature is much higher than the cold-electron temperature, $T_h \gg T_{e0}$.

Using the time for which the one-dimensionality of plasma expansion breaks down as an estimate of the proton acceleration time scale, we obtain the following formula, according to (56), which defines the boundary energy at which the Maxwellian proton spectrum is cut off:

$$\varepsilon^{imp}_{\max} \approx 2Z_2 T_h \ln\left[\frac{D}{\lambda_{Dh}}\sqrt{\frac{D}{L_0}}\left(\frac{Z_1 m_2 T_{e0}}{Z_2 m_1 T_h}\right)^{1/4}\right]. \tag{58}$$

The main results of [28] (see Fig. 3a) consist in the observation of a Maxwellian proton spectrum with a characteristic temperature of 230 keV, which transforms to a plateau-like spectrum at energy of about 1 MeV and is cut off at an energy of about 1.5 MeV. These results were obtained by irradiating a thin aluminum foil by a laser pulse with a wavelength of about 0.5 μm for an energy flux density of $2 \times 10^{18}$ W cm$^{-2}$ and a focal spot $D \approx 10$ μm. The target electron temperature did not exceed 1–2 keV. The high contrast of the laser radiation suggested a high initial density gradient with an inhomogeneity scale length that did not exceed the laser wavelength. According to the estimate (53), one might expect the generation of hot electrons with a temperature $T_h \approx 220$ keV that significantly exceeds the cold-electron temperature $T_{e0} \approx 1$–2 keV under experimental conditions [28], so condition (57) is satisfied with a large margin. The number of hot electrons was estimated in [28] to be of the order of $10^{20}$. In that case, according to our theory, we obtain from (34), (39),

and (51) for the accelerated-proton spectrum ($Z_2 = 1$, $m_2 = 1836m_e$)

$$\langle f^{imp}\rangle \propto N^{imp} \propto \exp\left(-\frac{\varepsilon}{T_{\text{eff}}}\right),$$

where

$$\varepsilon = \frac{m_2 v^2}{2}, \quad T_{\text{eff}} = \frac{Z_2 T_h + T_{20}}{1 + Z_2 m_e/m_2} \approx 220 \text{ keV},$$

in good agreement with experiment. The characteristic maximum ion energy, according to the estimate (58), is 1.5 MeV, which is also in agreement with experimental data.

Note also another possibility of the energy cutoff in the impurity-ion spectrum. For the halo expansion time scale, we have an estimate of $D/C_h^{imp}$ and the formation condition for this halo with a Maxwellian energy distribution is $1/\Omega \approx L_0/\sqrt{2}C_s$. For

$$\frac{D}{L_0} < \sqrt{\frac{T_h Z_2 m_1}{2T_{e0} Z_1 m_2}},$$

the ion energy spectrum has no time to reach the asymptotic distribution $\langle f^{imp}\rangle \propto N^{imp}(U = v)$ and can have a cutoff similar to that observed in the nonstationary spectra in Fig. 4.

## 7. CONCLUSION

In conclusion, note that we have obtained an exact solution to the kinetic equations for electrons and ions of various types in the quasi-neutral collisionless approximation by using the renormalization-group approach. This solution describes the one-dimensional nonisothermal expansion of a plasma bunch for arbitrary initial particle velocity distributions. The expansion is accompanied by the adiabatic cooling of plasma particles. The analytic solution that describes such an expansion is illustrated with examples in which two-temperature (hot and cold) Maxwellian and super-Gaussian initial electron distributions and Maxwellian initial ion velocity distributions characterized by various densities, temperatures, and velocities of particles of each type are considered. We deduced formulas for the distribution functions of particles of various types and derived expressions for such integrated characteristics as the local ion density and the ion energy distribution function. We indicated that these dependences (for an appropriate change of variables) asymptotically coincide on long time scales. Since the ion spectrum is determined by the initial electron distribution, its measurement can be used as the basis for diagnosing the electron distribution function that results from the interaction of an ultrashort laser pulse with nanoplasma, for example, cluster plasma or the plasma produced when thin foils are irradiated by a laser. For such plasma, the particle mean free path is generally large compared to the plasma bunch scale size and the collisionless-plasma approximation remains good.

The renormalization-group theory owes its success in finding exact solutions to the Vlasov equations with a self-consistent electric field to the quasi-neutral plasma approximation. This approximation requires that the Debye length be small compared to the spatial plasma inhomogeneity scale length. The latter cannot always hold for the high-energy, often relativistic, electrons produced through fast plasma heating by an intense laser pulse. A generalization of the renormalization-group theory to this case is undoubtedly an interesting problem that requires a special analysis.

## ACKNOWLEDGMENTS

This study was supported by the Russian Foundation for Basic Research (project nos. 00-15-96691, 00-02-16063, and 02-01-00185) and the INTAS grant no. 01-1B-233.

## REFERENCES

1. A. V. Gurevich, L. V. Pariĭskaya, and L. P. Pitaevskiĭ, Zh. Éksp. Teor. Fiz. **49**, 647 (1965) [Sov. Phys. JETP **22**, 449 (1966)].
2. A. V. Gurevich and L. P. Pitaevskiĭ, Zh. Éksp. Teor. Fiz. **56**, 1778 (1969) [Sov. Phys. JETP **29**, 954 (1969)].
3. S. J. Gitomer, R. D. Jones, F. Begay, *et al.*, Phys. Fluids **29**, 2679 (1986).
4. H. Haseroth *et al.*, Laser Part. Beams **14**, 393 (1996).
5. J. Zweiback, R. A. Smith, T. E. Cowan, *et al.*, Phys. Rev. Lett. **84**, 2634 (2000).
6. E. Springate, N. Hay, J. W. G. Tisch, *et al.*, Phys. Rev. A **61**, 063201 (2000).
7. K. Nemoto, A. Maksimchuk, S. Banerjee, *et al.*, Appl. Phys. Lett. **78**, 595 (2001).
8. L. M. Wickens, J. E. Allen, and P. T. Rumsby, Phys. Rev. Lett. **41**, 243 (1978).
9. B. Bezzerides, D. W. Forslund, and E. L. Lindman, Phys. Fluids **21**, 2179 (1978).
10. P. Mora and R. Pellat, Phys. Fluids **22**, 2300 (1979).
11. A. Gurevich, D. Anderson, and H. Wilhelmsson, Phys. Rev. Lett. **42**, 769 (1979).
12. A. V. Gurevich and A. P. Meshcherkin, Zh. Éksp. Teor. Fiz. **80**, 1810 (1981) [Sov. Phys. JETP **53**, 937 (1981)].
13. T. Ditmire, J. W. G. Tisoh, E. Springate, *et al.*, Nature **386**, 54 (1997).
14. Ch. Sack and H. Shamel, Phys. Rep. **156**, 311 (1987).
15. G. Manfredi, S. Mola, and M. R. Feix, Phys. Fluids B **5**, 388 (1993).
16. L. G. Garcia, J. Goedert, H. Figua, *et al.*, Phys. Plasmas **4**, 4240 (1997).
17. D. S. Dorozhkina and V. E. Semenov, Phys. Rev. Lett. **81**, 2691 (1998); Pis'ma Zh. Éksp. Teor. Fiz. **67**, 543 (1998) [JETP Lett. **67**, 573 (1998)].

18. V. F. Kovalev, V. Yu. Bychenkov, and V. T. Tikhonchuk, Pis'ma Zh. Éksp. Teor. Fiz. **74**, 12 (2001) [JETP Lett. **74**, 10 (2001)].
19. V. F. Kovalev, V. V. Pustovalov, and D. V. Shirkov, J. Math. Phys. **39**, 1170 (1998).
20. V. F. Kovalev and D. V. Shirkov, Phys. Rep. **352**, 219 (2001).
21. M. I. K. Santala, M. Zepf, F. N. Beg, *et al.*, Appl. Phys. Lett. **78**, 19 (2001).
22. M. Hegelich, G. Pretzler, S. Karsch, *et al.*, in *Abstracts of the II International Conference on Inertial Fusion Science and Applications, Kyoto, Japan (2001)*, p. 61.
23. V. F. Kovalev, S. V. Krivenko, and V. V. Pustovalov, Diff. Uravn. **29**, 1804 (1993); **29**, 1971 (1993); Pis'ma Zh. Éksp. Teor. Fiz. **55**, 256 (1992) [JETP Lett. **55**, 253 (1992)].
24. V. F. Kovalev, S. V. Krivenko, and V. V. Pustovalov, in *Proceedings of the International Workshop on Symmetry Methods in Physics in Memory of Professor Ya.A. Smorodinsky, Dubna, 1993*, Vol. 1, p. 253.
25. D. S. Dorozhkina and V. E. Semenov, Zh. Éksp. Teor. Fiz. **116**, 885 (1999) [JETP **89**, 468 (1999)].
26. A. B. Langdon, Phys. Rev. Lett. **44**, 575 (1980); J. P. Matte, M. Lamoureux, C. Moller, *et al.*, Plasma Phys. Controlled Fusion **30**, 1665 (1988).
27. A. V. Gurevich and L. P. Pitaevskiĭ, in *Reviews of Plasma Physics*, Ed. by M. A. Leontovich (Atomizdat, Moscow, 1980; Consultants Bureau, New York, 1986), Vol. 10.
28. A. Maksimchuk, S. Gu, K. Flippo, *et al.*, Phys. Rev. Lett. **84**, 4108 (2000).
29. K. Krushelnick, E. L. Clark, M. Zepf, *et al.*, Phys. Plasmas **7**, 2055 (2000).
30. Y. Sentoku, V. Yu. Bychenkov, K. Flippo, *et al.*, Appl. Phys. B **74**, 207 (2002).
31. A. G. Zhidkov, A. Sasaki, I. Fukumoto, *et al.*, Phys. Plasmas **8**, 3718 (2001).

*Translated by V. Astakhov*

*Journal of Experimental and Theoretical Physics, Vol. 95, No. 2, 2002, pp. 242–254.*
*Translated from Zhurnal Éksperimental'noĭ i Teoreticheskoĭ Fiziki, Vol. 122, No. 2, 2002, pp. 282–297.*


**PLASMA, GASES**

# Infrared Absorption in Dense Sodium Vapor

**A. G. Leonov[a, *], A. A. Rudenko[a], A. N. Starostin[b], M. D. Taran[b], D. I. Chekhov[a], and I. I. Yakunin[b]**

[a]*Moscow Institute of Physics and Technology (State University), Institutskiĭ proezd 9, Dolgoprudnyĭ, Moscow oblast, 141700 Russia*

[b]*Troitsk Institute for Innovation and Fusion Research (Russian State Scientific Center), Troitsk, Moscow oblast, 142190 Russia*

**e-mail: leonov@ape.relarn.ru*

Received February 27, 2002

**Abstract**—The absorption spectra of a dense resonance medium were experimentally studied for the example of thermally heated dense sodium vapor. Several mechanisms that might cause substantial absorption and enhanced intensity of emission in the IR spectral region, $\lambda > 0.9$ μm, were considered. For the first time, a detailed study of the structure of the absorption spectra of sodium vapor in the specified wavelength range was performed to determine the influence of the kind and pressure of the buffer gas. It was found that buffer gas characteristics had a substantial effect on the absorption coefficient of vapor. The presence of the molecular component (dimers and trimers) in sodium vapor could not explain the experimental dependences of absorption in the infrared region. Possible influence of microparticles formed in condensation of convective sodium vapor flows in heated cells on the optical properties of vapor was considered. Microparticles could contribute to the observed absorption, but were incapable of explaining the substantial intensity of vapor radiation reported earlier. Possible many-particle effects on the absorption in the far spectral line wing were discussed. For the first time, the method of molecular dynamics was used to show for the example of the distribution function of ionic microfields in a dense plasma that such effects were in principle capable of substantially raising the profile of the line and increasing absorption in the region of large detunings from the resonance compared with the simple quasi-static model in the nearest-neighbor approximation. © *2002 MAIK "Nauka/Interperiodica".*

## 1. INTRODUCTION

Studies of the mechanisms of formation of spectral lines of atoms and ions and the problems of resonance radiation transfer in dense gases and plasmas are a topical area primarily because of the necessity of correctly interpreting the emission and absorption spectra of dense plasma and gas objects including laser plasmas; plasmas of *Z*, *X*, etc., pinches; and plasmas of high-pressure gas-discharge lamps. The total intensity of dense medium radiation is to a substantial extent determined by the shape of the profiles of far spectral line wings at large detunings from the resonance $\Delta\omega \sim \omega_0$ ($\Delta\omega = \omega - \omega_0$, where $\omega$ is the current frequency and $\omega_0$ is the resonance transition frequency) [1–4]. One of the problems that arise in studying far line wings is the question of the origin of intense radiation and substantial absorption in the near-infrared spectral region, which is currently widely discussed. These effects have repeatedly been observed in mixtures of dense alkali metal vapors with buffer gases at atmospheric and higher pressures (outside the absorption bands of $Na_2$, $K_2$, etc., at wavelengths $\lambda > 0.9$ μm) by many authors including those of the present communication [3–12]. The theoretical model of the formation of the profile of far spectral line wings developed earlier [1–4] and based on the Boltzmann spectral distribution of resonance level population describes the experimental data on sodium vapor accurate to within an order of magnitude [3, 4], whereas the standard theory of radiation transfer [13, 14] gives values that differ by 4–5 orders of magnitude from the results of measurements at large detunings.

It has rigorously been shown in [1, 2, 4] that the spectral intensity of spontaneous emission $\varepsilon_\omega$ can be described in the two-level approximation by the equation

$$\varepsilon_\omega = \frac{1}{4\pi}\hbar\omega A_0\left(\frac{\omega}{\omega_0}\right)^3 \tilde{N}_2(\omega), \qquad (1)$$

where $A_0$ is the probability of spontaneous emission, and $\tilde{N}_2(\omega)$ is the effective spectral population of the upper level (see [1, 2, 4] for more detail),

$$\tilde{N}_2(\omega) = \tilde{N}_2 a(\omega)\exp[-\hbar(\omega-\omega_0)/kT]. \qquad (2)$$

Here, $T$ is the temperature, $k$ is the Boltzmann constant, $a(\omega)$ is the form factor of the line profile ($\int a(\omega)d\omega = 1$), and $\tilde{N}_2$ is the effective population of the upper level. At equilibrium, we have the Boltzmann spectral distribution ($g_1$ and $g_2$ are the statistical level weights, and $N_1$ is the total population of the lower level),

$$\tilde{N}_2(\omega) = \frac{g_2}{g_1}N_1 a(\omega)\exp\left(-\frac{\hbar\omega}{kT}\right) \qquad (3)$$

(in the absence of equilibrium, the $\tilde{N}_2$ effective population can be found from the kinetic equations given in [1, 2]). It follows from (3) that, strictly, the total population equal to the integral of $\tilde{N}_2(\omega)$ in frequency does not satisfy the Boltzmann equation even at equilibrium and coincides with the true population only for a very narrow line with $\hbar\Gamma \ll kT$ (where $\Gamma$ is the line width), whereas the $\tilde{N}_2$ effective population does satisfy the Boltzmann equation. Note that, earlier, equations similar to (1) and (2) but with an incorrect normalization of the line profile were obtained from simple physical considerations in [15, 16].

The intensity of the far wing of a wide line (see [2–4] for more detail) can substantially exceed the intensity calculated by the standard theory [13, 14] because of the presence of the exponential multiplier. The larger fraction of the energy emitted in the line can correspond to precisely its nonresonance "red wing" rather than the central near-resonance region (even the formation of an additional low-frequency maximum in the emission spectrum is then possible [3, 4]), which qualitatively explains the results obtained in [3, 4] in measuring intense thermal radiation of sodium vapor at wavelengths of 2–3 μm.

The theoretical model [4], which described radiation of sodium vapor at large detunings, was constructed on the assumption that the line profile was formed by buffer-gas-induced quasi-static broadening in the nearest-neighbor approximation. The validity of such a description in the region of large detunings is, however, not obvious. In addition, it was shown in several experimental works (e.g., see [17–20]) that, at wavelengths $\lambda$ larger than 0.64–0.70 μm (depending on the kind of the broadening gas), the intensity of the "red" quasi-static wing of sodium *D* lines began to exponentially decrease, which was in satisfactory agreement with the calculated interaction potentials between sodium atoms and atoms of various buffer gases such as argon and xenon. Taking this effect into account to a great extent balances the influence of the Boltzmann exponential factor in (1)–(3) and results (within the framework of the model [4]) in a substantial gap between the calculation results and the experimental intensities of sodium vapor radiation at $\lambda > 0.70$ μm. Note, however, that the theory of the formation of spectral line profiles at large detunings $\Delta\omega \sim \omega_0$ currently remains virtually undeveloped.

It follows that the problem of the nature of intense radiation and substantial absorption in the infrared spectral region in dense alkali metal vapors remains unsolved. An analysis of the available data and the results obtained by us earlier shows that, in addition to binary quasi-static broadening of sodium *D* lines by buffer gases, the observed special features of the infrared emission and absorption spectra of mixtures of dense alkali metal vapors with buffer gases can be caused by absorption and emission of the cluster components of the vapors including absorption and emission caused by infrared transitions in dimers, trimers, and more complex sodium polymers and also absorption and emission of microscopic liquid alkali metal droplets. Such droplets were repeatedly observed in experiments in the form of a fog, in particular, when heated cells of the "heat pipe" type were used to produce alkali metal vapors [7–10, 21, 22]. The influence of clusters and droplets on the optical properties of vapors in cells was not, however, studied earlier. Nor were inquiries made into the rules governing the formation of such microparticles, although their presence was *a priori* used to explain the observed characteristics of emission and absorption. Note that the problem is of interest in itself, because cells of this type are extensively used in experiments [23, 24].

Another possible reason for the observed effects can be many-particle broadening of the resonance level in combination with the Boltzmann character of the spectral distribution of resonance level populations (3). It may well be that such configurations of the emitting and several (possibly, many) perturbing atoms are then realized at which each perturbing atom only insignificantly shifts the energy levels of the emitting atom, whereas a set of perturbing atoms shifts these levels substantially, which results in intense emission at large detunings from the resonance. This problem also remains virtually unstudied, although some of its aspects have been touched upon in several works; e.g., see [25]. At the same time, such a mechanism can be essential at high sodium vapor and buffer gas pressures. It is pertinent to mention here that high buffer gas pressures, at which many-particle effects might be noticeable, were used in works [17–20] concerned with measuring far sodium resonance line wings. However, several points corresponding only to the onset of an exponential decrease were obtained in these works, while the behavior of the spectrum at larger detunings was not studied; note that, at detunings so substantial ($\lambda_0 \sim 0.59$ μm), the accuracy of measurements was fairly low. Moreover, it remains unclear whether or not the approximation of complete redistribution of absorbed and emitted photons over frequencies, which is explicitly present in absorption–fluorescence methods for measuring line profiles (used in many works including [17–20]), is valid. In any event, its applicability at large detunings is not obvious.

We have already discussed the possibility of effects caused by many-particle collisions and the presence of the cluster and microdroplet components in vapors [5, 26]. In this work, the experimental data on the absorption spectra of sodium vapor in a wide spectral range (0.35–1.10 μm) and the results of theoretically modeling both effects under consideration are described in more detail. Our goal was to analyze their influence on the infrared emission and absorption spectra of mixtures of dense alkali metal vapors and buffer gases.

## 2. EXPERIMENTAL UNIT

The absorption and thermal emission spectra of dense sodium vapor were studied on a unit whose main elements were specially designed cylindrical cells of the heat pipe type connected to a vacuum line and a line for introducing a buffer gas and a spectral diagnostics device for measuring the spectral intensity of emission and the spectral absorption coefficients of sodium vapor.

We used a cell similar to that described in [4]. The inside radius of the cell was $R_p = 10$ mm, and the distance between water-cooled flanges was $2L_1 = 150$ mm. Linked up to the flanges were pipes $L_2 = 7.5$ cm long with sapphire windows 2 mm thick attached vacuum-tight to their ends. The transmittance of the windows was varied from 0.3 μm up to wavelengths of the order of 5 μm and controlled by an infrared spectrophotometer. The vacuum system consisted of a fore and a diffusion pump and allowed the cell to be evacuated to $10^{-5}$ Torr or less. Prior to evacuation, the cell was loaded with sodium metal of VCh (high purity) grade. After evacuation, the cell was filled with an inert gas (helium or argon) to a 0.1–1.0 atm pressure and heated to the required temperature. The heater was nichrome wires placed into fused quartz tubes thermally insulated by a layer of asbestos and carbon cloth. The temperature of the external cell walls was measured by several chromel–alumel thermocouples accurate to 1 K. Temperature distribution along cells $T(z)$ in the heating zone approximately corresponded to a fourth-order parabolic curve with a maximum at the cell center [$T(z = 0) = T_c$]. The temperature at the water-cooled flanges $T(z = L_1) = T_0$ equaled the temperature of the water ($T_0 \approx 293$ K),

$$T(z) = \begin{cases} T_c - \dfrac{T_c - T_0}{L_1^4} z^4, & 0 \le |z| \le L_1, \\ T_0, & L_1 < |z| \le L_2. \end{cases} \qquad (4)$$

Density $N$ of sodium vapor in the cell was determined from the curve of saturated vapor pressure [27] at the temperature corresponding to the temperature of the cell walls. At temperatures up to 800 K, the density of vapors, integral along the cell axis, was also measured by the method of Rozhdestvenski hooks [28] with the use of a Michelson interferometer and a wideband dye laser. Both methods gave values coinciding to within 20% in the specified temperature range. This was evidence that the density of vapor was indeed determined by the saturated vapor pressure at the temperature of the cell walls, at least in the hot cell zone where $N$ was maximum.

The source of illumination for measuring the absorption coefficient in dense sodium vapor was collimated radiation from a SI-8-200 tungsten lamp. Measurements of the intensity of light after passage through sodium vapor in the near-axis part of the tube were performed as follows. Radiation at the exit from the cell was modulated by a mechanical chopper at a frequency of about 800 Hz. The modulated light beam was directed to the entrance slit of a monochromator (600 lines/mm grating and 16 Å/mm dispersion). The grating was rotated for tuning the instrument to the required wavelengths with the use of a step motor. Wavelength calibration of the spectrum was performed based on the spectrum of a neon lamp (the wavelengths of the spectrum of neon were taken from [29]). The spectral resolution of measurements was determined from the observed widths of neon spectral lines; it was about 15 $cm^{-1}$. The radiation detector, which was an FEU-84 photomultiplier (with a multialkali cathode for measurements at 0.30–0.76 μm) or an FEU-83 photomultiplier (with an oxygen–silver–cesium cathode for measurements at 0.76–1.10 μm), was placed in the focal plane of the spectrograph immediately behind the exit slit. The sensitivities of both photomultipliers were calibrated against the spectrum of a standard radiation source, which was a similar SI-8-200 tungsten lamp.

The signal from detectors was directed to a narrow-band amplifier (a V6-9 selective microvoltmeter) and, from its output, to a synchronous detector. DC voltage from the synchronous detector output was directed to an analog-to-digital converter whose output signal was processed on a computer.

The absorption by heated sodium vapor was determined as follows. In each experiment, we recorded the intensity $I_0$ of radiation that passed through the cell at room temperature, that is, in the absence of vapor, and the intensity of radiation that passed through the cell with sodium vapor at various temperatures, $I = I_r - I_v$, where $I_r$ is the recorded intensity of radiation and $I_v$ is the intensity of intrinsic emission of the vapor (note that the $I_v$ value was negligibly small compared with $I_r$ in all experiments). All the data obtained in this way were used to construct the dependences of the relative fractions of absorbed and scattered radiation intensities $K = (I_0 - I)/I_0$ on the parameters of the medium.

## 3. ABSORPTION SPECTRA OF DENSE SODIUM VAPOR

The absorption spectra of dense sodium vapor in the wavelength range 0.35–1.10 μm measured at various temperatures are shown in Fig. 1, and the temperature $T_c$ dependences of absorbed and scattered radiation intensities at 0.4 and 1.0 μm, in Fig. 2. Note that the $K$ values at 0.4 and 1.0 μm are close to each other at all temperatures except the lowest.

Figure 1 shows that the spectrum of vapor contains three well-defined absorption regions. One of these is centered at $\lambda = 0.59$ μm and corresponds to absorption at the $3S$–$3P$ atomic resonance transition of sodium; another centered at $\lambda = 0.49$ μm is largely caused by absorption at the well-known $X^2\Sigma_g^+$–$B^1\Pi_u$ molecular transition of the $Na_2$ sodium dimer [30] and by satellites

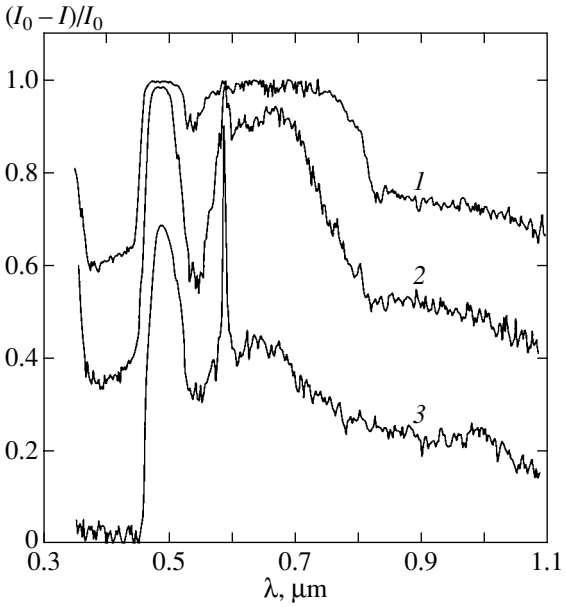


**Fig. 1.** Absorption spectra of sodium vapor at various cell center temperatures $T_c$ = 903 (*1*), 806 (*2*), and 709 K (*3*); buffer gas argon, buffer gas pressure 1 atm.

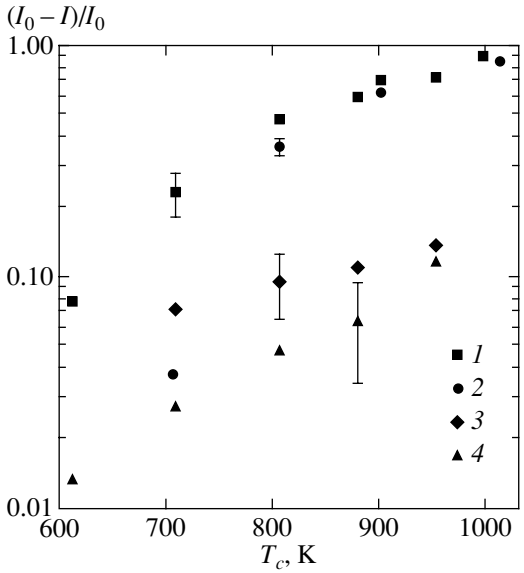


**Fig. 2.** Dependence of $K = (I_0 - I)/I_0$ on temperature in cell center $T_c$ for radiation wavelengths (*1, 3, 4*) 1.0 and (*2*) 0.4 μm; buffer gas (*1, 2, 4*) argon and (*3*) helium, buffer gas pressure (*1–3*) 1 and (*4*) 0.2 atm.

of absorption bands of the $X^1\Sigma_g^+ - 2^1\Sigma_u^+$ (0.452 μm) and $a^3\Sigma_u^+ - 2^3\Pi_g$ (0.437 μm) transitions [21, 31]. In addition, the spectrum contains a broad absorption band at 0.60–0.82 μm, which corresponds to the $A^1\Sigma_u^+ - X^1\Sigma_g^+$ transition of sodium dimers [30] (the long-wave edge of this band is especially sharp at $T > 800$ K, see Fig. 1). Apart from these bands, an increase in absorption is observed in the violet spectrum region ($\lambda < 0.38$ μm). This increase is related to satellites of absorption bands of the $X^1\Sigma_g^+ - 3^1\Sigma_u^+$ (0.38 μm) and $X^1\Sigma_g^+ - C^1\Pi_u$ (0.367 μm) transitions [21, 31] and to closeness of the 3*S*–4*P* atomic transition ($\lambda = 0.330$ μm).

In addition, we recorded noticeable absorption at 0.9–1.1 μm, where molecular sodium bands are absent, as follows from the theoretical calculations performed in [10, 21, 32, 33]. According to these calculations, wavelength 0.9 μm corresponds to the long-wave edge of the absorption and emission band of the $a^3\Sigma_u^+ - c^3\Sigma_g^+$ free-bound transition. It follows that, at larger wavelengths, the observed absorption cannot be related to absorption caused by molecular sodium transitions. Very close agreement between the calculation results and experiment was attained in the works cited above in the whole wavelength range 0.3–1.0 μm (we specially note [21], where absorption spectra were measured very thoroughly and compared in detail with theoretical calculation results). There is therefore no reason to assign absorption at $\lambda > 0.9$ μm to some nonidentified sodium dimer transitions. Nor can atomic absorption lines be observed in this region because of a vanishingly small thermal population of the resonance and higher levels in the absence of external excitation.

As mentioned in the Introduction, intense infrared emission and absorption were also observed in the spectra of purely thermal radiation of dense potassium [7, 10] and sodium [3, 4, 8, 10, 11] vapors in vapor jets and in heat-pipe-type tubes similar to that used in this work. These effects were explained in [7, 8, 10, 11] by possible absorption of alkali metal trimers and more complex polymers and by the presence of fog, that is, liquid metal droplets. These hypotheses were not, however, given experimental or theoretical substantiation. For instance, attempts made in [7, 8] to determine the activation energies of absorbing particles from the spectral data on the absorption coefficients in the infrared region and compare the results with the supposed activation energies of sodium and potassium trimers gave very contradictory results. What is more, intense emission in the near-infrared region has long since been observed in the well-known emission spectra of high-pressure sodium gas-discharge lamps [6, 34], which are extensively used in outdoor lighting devices. The fraction of infrared radiation energy loss called "mysterious" many years ago [6] can amount to 20–30% of the total power balance of sodium lamps. The phenomenon has not, however, received at least a qualitative explanation within the framework of some theoretical model as yet.

It should at the same time be noted that no noticeable absorption at 0.92–1.075 μm is observed in a uniformly heated cell in the absence of a buffer gas [21]. In our experiments, we for the first time obtained data on the dependence of emission attenuation in the wave-

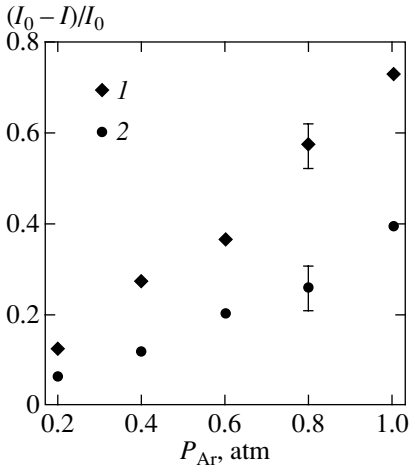


**Fig. 3.** The plot of $K = (I_0 - I)/I_0$ versus argon pressure $P_{Ar}$ for radiation at 1 μm; $T_c$ = 955 (*1*) and 808 K (*2*).

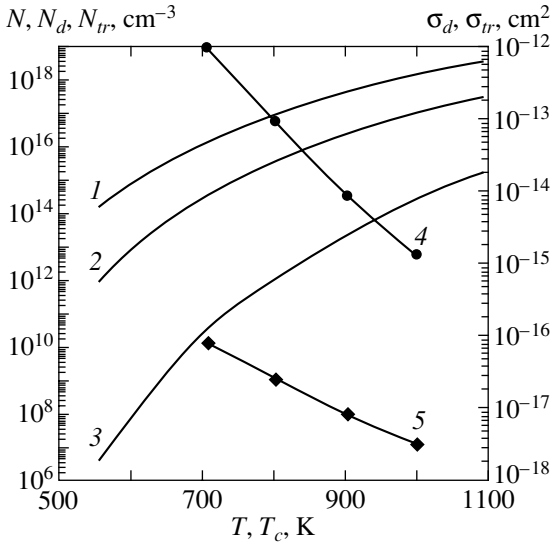


**Fig. 4.** Calculated temperature dependences of equilibrium densities of sodium (*1*) atoms, (*2*) dimers, and (*3*) trimers. Cell center temperature $T_c$ dependences of cross sections (*4*) $\sigma_{tr}$ and (*5*) $\sigma_d$ of possible absorption by trimers and dimers (estimated from the experimental data on the assumption that all absorption is caused by the corresponding component).

length region λ = 1 μm on the buffer gas pressure and type at various cell temperatures. These dependences are shown in Figs. 2 and 3. According to our results, the pressure and the type of the buffer gas fairly strongly influence the optical properties of the medium under study. Absorption increases as the buffer gas pressure grows, and is substantially stronger in the presence of argon than in the presence of helium. Note that we observed similar dependences in measuring the intensity of radiation for dense sodium vapor at 2–3 μm [3, 4]. In those experiments, the intensity of radiation was also approximately proportional to buffer gas pressure and increased severalfold when helium was replaced by argon.

## 4. ESTIMATION OF POSSIBLE INFLUENCE OF SODIUM TRIMERS ON ABSORPTION IN THE IR REGION

Substantial absorption in the λ > 0.9 μm infrared region is explained in several works [7–9] by the presence of alkali metal trimers. These molecules can be present in fairly large amounts in hot regions where the density of vapor is the highest. For this reason, we estimated the $\sigma_{tr}$ cross section of possible absorption of $Na_3$ trimers at various $T_c$ temperatures in the cell center on the assumption that all observed absorption was indeed caused by trimers. The estimates were obtained by the equation

$$\ln(I/I_0) = -2\int_0^{L_1+L_2} \sigma_{tr}(T(z))N_{tr}(T(z))dz, \qquad (5)$$

where $N_{tr}$ is the density of the trimeric component. Because of a very sharp dependence of $N_{tr}$ on temperature (and therefore on *z*), the integral in (5) is largely determined by the central region of the cell, and the details of vapor density distribution in cell peripheral regions are unimportant. It can then be assumed that $\sigma_{tr} \approx \sigma_{tr}(T_c)$, and the cross section value can be factored out of the integral. Estimates were made using the experimental $K = (I_0 - I)/I_0$ values and the results obtained in calculating the equilibrium concentration of the trimeric component. The $N_{tr}$ value was determined from the theoretical data on the fundamental trimer vibrational frequencies reported recently [35] ($\omega_1$ = 295.3 cm$^{-1}$, $\omega_2$ = 56.9 cm$^{-1}$, and $\omega_3$ = 102.9 cm$^{-1}$) and the dissociation energy calculated in [36–38] (approximately 3000 cm$^{-1}$). The moments of inertia of the molecule were calculated from the data on its geometric structure reported in [39]. Note that, according to [39], the $Na_3$ molecule has weak absorption bands in the near-infrared spectral region.

As mentioned, the long-wave absorption edge of $Na_2$ dimers lies at wavelengths below 900 nm according to many measurements and calculations. Accordingly, this vapor component cannot contribute to the observed absorption at wavelengths above 0.9 μm. Nevertheless, we performed similar calculations of the $\sigma_d$ cross section for possible absorption by the $Na_2$ dimeric component. The $N_d$ density of the dimeric component was calculated using the corresponding constants from [27].

The temperature dependences of the calculated molecular composition of sodium vapor and of the cross sections of absorption by sodium dimers and trimers are shown in Fig. 4. According to this figure, the equilibrium density of the trimeric component is 3–7 orders of magnitude lower than the atomic sodium

density. The plots given in Fig. 4 show that the estimated $\sigma_d$ and $\sigma_{tr}$ values for the dimeric and trimeric components strongly depend on temperature and change by two–three orders of magnitude when temperature changes by a factor of two. At the same time, actual absorption cross sections cannot depend on $T$ so strongly.

Because of the low density of trimers, the estimated $\sigma_{tr}$ value is in the range $10^{-12}$–$10^{-15}$ cm$^2$, which is more characteristic of narrow atomic lines than of comparatively broad molecular bands. In addition, according to the data reported in reviews [40, 41], the cross section of the sodium trimer does not exceed $4 \times 10^{-16}$ cm$^2$ even at the absorption maximum in the violet spectral region. It follows that the whole data set is evidence that the observed absorption cannot be caused by the $Na_2$ and $Na_3$ molecules, whose equilibrium density can only be fairly high in the central hot and comparatively uniform cell zone. As concerns the equilibrium concentrations of higher sodium polymers such as $Na_4$, their concentrations are much lower than those of trimers, and they cannot contribute to absorption either. In addition, as mentioned, the intensities of emission and absorption strongly depend on the type and pressure of the buffer gas, which is also at variance with the hypothesis of the influence of molecular components on the optical characteristics of vapor in the $\lambda > 0.9$ μm long-wave spectral region.

## 5. INFLUENCE ON ABSORPTION OF THE CLUSTER AND MICRODROPLET VAPOR COMPONENTS

As mentioned, absorption in the near-infrared spectral region (outside the spectral region of absorption of sodium dimers) can also be ascribed to heavy sodium clusters and to microscopic liquid sodium droplets formed in condensation in the cold zone of devices for creating dense alkali metal vapors. Note that there is no clear distinction in size between clusters and microdroplets (aerosols). For this reason, both will be called microparticles for simplicity.

The suggestion of the formation of microparticles in vapor jets [10] caused by condensation is quite reasonable because of sharp vapor medium expansion [41–43]. At the same time, in heat-pipe-type cells {used to produce dense stationary alkali metal vapors in [3, 4, 7–9, 11] at high buffer gas pressures $P_{buf}$ and fairly low vapor pressures $P_v$ ($P_v/P_{buf} < 0.2$–$0.1$)}, deviations from equilibrium are comparatively small, and the problem of the formation of microparticles under these conditions requires special consideration.

The degree to which condensate influences the optical characteristics of dense alkali metal vapors can be estimated based on measured spectral dependences of absorption. We used the model of a spherical drop of radius $R$ (nonsphericity effects at fairly high temperatures are negligibly small [43–45]). The experimental

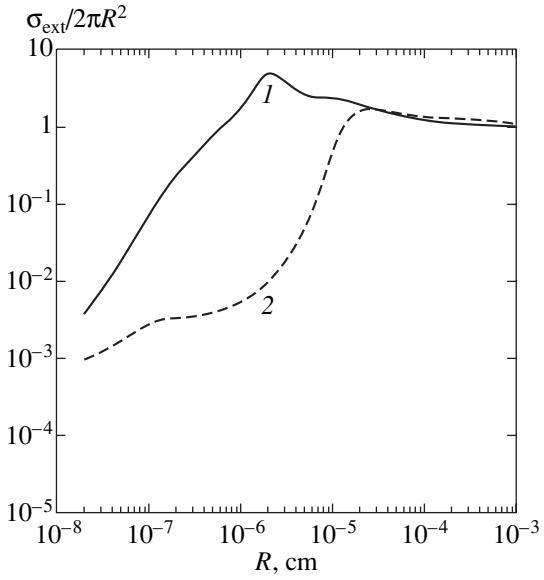


**Fig. 5.** Dependences of normalized extinction cross section on microparticle size $R$ for wavelengths (*1*) 0.4 and (*2*) 1.0 μm; $T = 1000$ K.

spectral dependences of the real and imaginary components of complex permittivity $\varepsilon_1$ and $\varepsilon_2$ obtained in [46] were used in calculations of the cross section of extinction $\sigma_{ext}$ for such a drop by the Mie theory [44, 47]. Note that the $\varepsilon_1(\lambda)$ dependence is well approximated by the plasma model within the framework of the Drude–Sommerfeld theory with corrections for the effective mass of the electron and ionic core polarizability [44, 46] in the wide wavelength range 0.3–2.0 μm. As concerns the $\varepsilon_2$ imaginary component, there are substantial discrepancies in the visible and near-ultraviolet regions, which are related to interband transitions. The data reported in [46] were obtained at room temperature; they were therefore recalculated using the ratio between the conductivities of sodium [27] at the given temperature and at $T = 293$ K. In addition, it was taken into account that, at a small particle size, an essential role in permittivity component values and, therefore, in absorption cross section is played by size effects, because the frequency of collisions $\nu$ at small $R$ is determined by collisions with microparticle boundaries, and $\nu$ is therefore a function of the microparticle size, $\nu = \nu(R)$ [44].

The calculation results for two wavelengths, 0.4 and 1.0 μm, at $T = 1000$ K are shown in Fig. 5. According to this figure, the cross sections of extinction differ severalfold at these two wavelengths for small-sized clusters, whereas the absorption coefficients measured at the specified temperature virtually coincide (see Fig. 2). The $\sigma_{ext}$ value calculated at $\lambda = 0.4$ μm exceeds the cross section at $\lambda = 1$ μm, whereas the experiment gives an inverse ratio (note that similar results are obtained in calculating $\sigma_{ext}$ at other temperatures). In

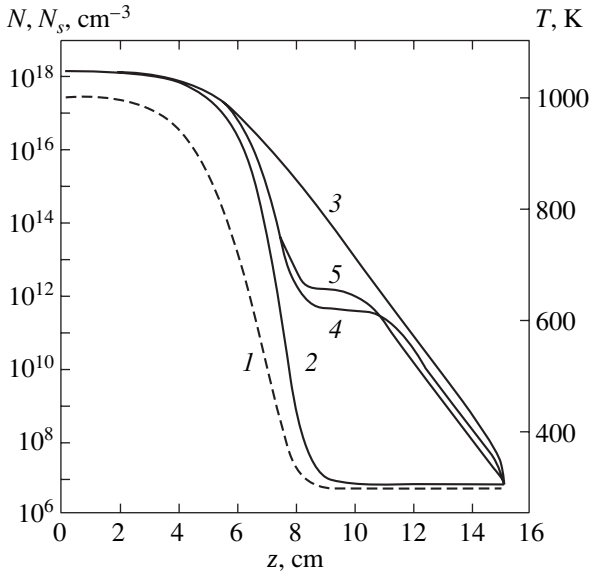


**Fig. 6.** Distributions along cell axis of (*1*) temperature, (*2*) saturated vapor density $N_s$, (*3*) vapor density $N$ in the absence of condensation, (*4*) vapor density in the presence of diffusion transfer, and (*5*) vapor density in the presence of convective transfer; $T_c$ = 1000 K, $P_{Ar}$ = 1 atm.

addition, small-sized sodium microparticles should have a resonance absorption peak in the ultraviolet region for the $\lambda \approx 0.4$ μm wavelength caused by the excitation of surface plasmons [39–44]. In experiments, we find no peak in this spectral region (see Fig. 1) that might be related to a plasmon absorption peak. It is, however, possible that this peak is obscured by the wings of the strong absorption bands of atomic sodium and sodium dimers (see above). It follows that small-sized clusters cannot be responsible for the observed absorption dependences.

For particles of size $R > 0.1$ μm (when multipole terms begin to play a substantial role in Mie expansions), the calculated extinction cross sections approach each other and become equal (at $R \gg \lambda$, $\sigma_{ext}$ tends to $2\pi R^2$ irrespective of the wavelength), which is, on the whole, in agreement with the experimental data. It follows that, to answer the question of a possible contribution of such particles, we must determine whether or not such microparticles can be formed in heat-pipe-type cells and estimate their concentration.

As the gradient of temperature and, accordingly, of saturated vapor pressure along the cell axis is substantial, an important role in establishing a stationary vapor density distribution must be played by the diffusion of sodium atoms in the buffer gas from the hot central cell zone to its cooled ends. In the peripheral cell regions, the density of vapor $N$ can substantially exceed the $N_s(T)$ saturated vapor density determined by the temperature at the given cell point. Under these conditions, homogeneous condensation can in principle cause the formation of fairly large microparticles. To inquire into the role played by condensation, we performed numerical calculations of heat conduction and diffusion processes in the cell for given measurement conditions. The boundary conditions were set in accordance with cylindrical symmetry of the problem and approximation (4) to the experimental temperature of cell walls; it was assumed that $N = N_s$ at cell walls. The calculated temperature and vapor density distributions along the cell axis in the absence of condensation and the corresponding distribution of the density of saturated sodium vapor calculated using the tables from [27] are plotted in Fig. 6 (curves *1–3*). These plots show that the degree of supersaturation $S = N/N_s$ in the cold region can be substantial ($S \sim 10^6$), which can cause intense condensation and formation of fairly large amounts of microdroplets of a substantial size.

Condensation was taken into account based on the classical theory of homogeneous condensation [48, 49]. According to this theory, condensation nuclei of a critical radius are largely formed in supersaturated vapor,

$$R_{cr} = \frac{2\sigma q}{kT \ln S}, \qquad (6)$$

where $q = m_{Na}/\rho_{Na}$ is the volume of the liquid sodium molecule, $m_{Na}$ is the mass of the sodium atom, $\rho_{Na}$ is the density of liquid sodium, and $\sigma$ is the surface tension coefficient of liquid sodium. Clusters or microdroplets of smaller sizes vaporize, and those of larger sizes grow. Note that the number of atoms in a particle is

$$n = (R/R_W)^3,$$

where

$$R_W = (3m_{Na}/4\pi\rho_{Na})^{1/3}$$

is the Wigner–Seitz radius [41]. Accordingly, the number of atoms in a microparticle of radius $R_{cr}$ is

$$n_{cr} = (R_{cr}/R_W)^3.$$

The rate of the formation of nuclei is determined in the classical theory by the equation [48, 49]

$$J_0 = \frac{1}{2}\alpha q N^2 v_T \sqrt{\frac{\sigma}{kT}} \exp\left(-\frac{4\pi\sigma R_{cr}^2}{3kT}\right), \qquad (7)$$

where $\alpha$ is the accommodation coefficient (the fraction of vapor molecules that stick to the drop surface in collisions; for pure alkali metals, $\alpha \approx 1$ [50]) and $v_T = (8kT/\pi m_{Na})^{1/2}$ is the thermal velocity of sodium atoms. Microparticles increase in size as time passes and gradually settle under gravity on the inside cell surface when their size reaches a maximum value, $R_{max}$ [$n_{max}$ then equals $(R_{max}/R_W)^3$].

Let such a microparticle be formed at time $t = 0$ and disappear (settle onto the bottom of the cell) at time $\tau$.

Clearly, the stationary concentration of microparticles $N_p$ will then be determined by the equation

$$N_p = J_0\tau.$$

The rate $Q$ of the disappearance of atoms in the cell volume as a result of condensation can then be determined as follows:

$$Q = \int_{n_{cr}}^{n_{max}} N_p W(n) F(n) dn, \quad (8)$$

where $n_{cr}$ is the number of atoms in a particle of the critical radius [$n_{cr} = (R_{cr}/R_W)^3$], $W(n)$ is the rate of particle growth, and $F(n)$ is the particle-size distribution function.

Growth of a microparticle under the conditions of a given experiment is largely determined by sticking of atoms to it from the vapor environment, whereas the role played by coagulation can easily be shown to be insignificant. The rate of growth through sticking $W(n)$ is substantially different for small-sized particles with $R \ll \lambda_f$ (free-molecular mode—$\lambda_f$ is the free path of sodium atoms in the buffer gas) and for large-sized particles with $R \gg \lambda_f$ (diffusion mode). In our calculations, we therefore used the interpolation formula given in [51],

$$W(n) = \frac{dn}{dt} = \frac{\alpha\pi n^{2/3} R_W^2 v_T}{1 + 3R_W n^{1/3}\alpha/(4\lambda_f/v_T)}(N - N_s). \quad (9)$$

This formula describes both limiting modes.

Condensation is accompanied by heat release, and, generally, the microparticle temperature $T_p$ increases compared with the temperature $T$ of the medium, which somewhat decreases the rate of its growth compared with that predicted by (9). In particular, as was shown in [52], this effect was, however, negligibly small under the conditions of our experiments, in which the buffer gas pressure was much higher than the sodium vapor pressure. In addition, note that the density of saturated vapor close to a microparticle depends on the curvature of its surface [51]. Curvature effects are, however, only substantial for the smallest particles; we will, therefore, ignore them.

Integrating (9) gives the explicit time dependence of $n$,

$$n = \left(-b^{-1} + \sqrt{b^{-2} + n_{cr}^{2/3} + 2b^{-1}n_{cr}^{1/3} + (8/9)\pi\lambda_f v_T R_W (N - N_s)t}\right)^3, \quad (10)$$

where $b = 3\alpha R_W/4\lambda_f$. The particle-size distribution function will be determined from the stationary kinetic equation

$$\frac{\partial}{\partial n}[W(n)F(n)] = 0, \quad \int_{n_{cr}}^{n_{max}} F(n)dn = 1. \quad (11)$$

It is easily found from (11) that

$$F(n) = C(n^{-2/3} + bn^{-1/3}),$$
$$C = \left[3(n_{max}^{1/3} - n_{cr}^{1/3}) + \frac{3}{2}b(n_{max}^{2/3} - n_{cr}^{2/3})\right]^{-1}. \quad (12)$$

Integrating (8) taking into account (9), (10), and (12) yields

$$Q = J_0(n_{max} - n_{cr}). \quad (13)$$

It follows that the problem reduces to finding the maximum size of microparticles, which is in turn determined by time $\tau$ of particle settling. Time $\tau$ will be found from the interpolation formula for a stationary settling rate under gravity (e.g., see [51]), which is valid for both free-molecular and diffusion modes,

$$v_{st} = \frac{dx}{dt} = \frac{C_c m_{Na} g}{6\pi\eta R_W} n^{2/3}, \quad (14)$$

where $x$ is the vertical coordinate ($0 < x < 2R_p$), $\eta = \eta(T)$ is the dynamic viscosity of the buffer gas (its value can be found in the tables from [27]), $g$ is the free fall acceleration, and $C_c$ is the so-called Cunningham correction [51],

$$C_c = 1 + \frac{\lambda_m}{R}\left[1.257 + 0.4\exp\left(-\frac{1.1R}{\lambda_m}\right)\right] \quad (15)$$

($\lambda_m$ is the free path of buffer gas molecules). Equation (14) can be used to obtain the equation for determining $\tau$,

$$2R_p = \int_0^\tau v_{st} dt. \quad (16)$$

We can then use (10) to calculate $n_{max} = n(\tau)$ and, accordingly, $Q$.

The results of numerically solving the equation for sodium vapor diffusion in the buffer gas taking into account the sink of sodium atoms caused by condensation are shown in Figs. 6 and 7. The distribution of vapor density along the cell axis that takes condensation into account is shown in Fig. 6 (curve *4*). It follows from this distribution that condensation substantially decreases vapor density in the cold cell zone and thereby considerably decreases supersaturation. The microparticle density $N_p$ distribution, the distribution of the maximum number of atoms in microparticles $n_{max}$, and the distribution of the density of sodium atoms condensed to microparticles $N_t$ along the cell axis are

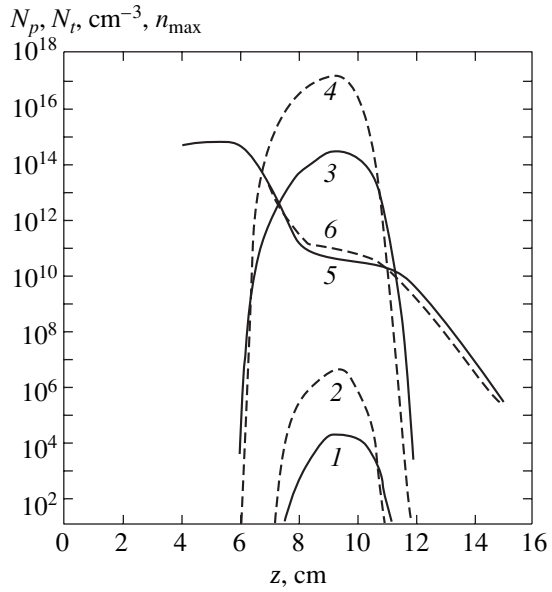


**Fig. 7.** Distributions along cell axis of (*1*, *2*) microparticle density $N_p$, (*3*, *4*) density $N_t$ of atoms present in microparticles, and (*5*, *6*) maximum number $n_{max}$ of atoms in microparticles for (*1*, *3*, *5*) diffusion and (*2*, *4*, *6*) convective transfer; $T_c$ = 1000 K, $P_{Ar}$ = 1 atm.

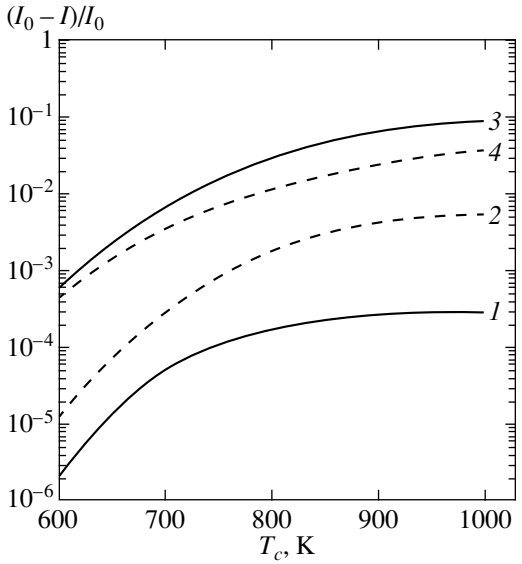


**Fig. 8.** Cell center temperature $T_c$ dependences of the calculated $K_p = (I_0 - I)/I_0$ value for radiation wavelength of 1 μm in (*1*, *2*) diffusion and (*3*, *4*) convective modes for (*1*, *3*) argon and (*2*, *4*) helium at 1 atm.

shown in Fig. 7 for $T_c$ = 1000 K and a 1 atm pressure of argon in the cell. Shown in Figs. 8 and 9 are the dependences of λ = 1μm radiation attenuation caused by microparticles and calculated at various temperatures and buffer gas pressures with the use of the calculated extinction cross section values discussed above (see Fig. 5):

$$K_p = \frac{I_0 - I}{I_0} = 1 - \exp\left( \int_{-(L_1 + L_2)}^{(L_1 + L_2)} N_p(z, r = 0) \times \int_{R_{cr}(z, r = 0)}^{R_{max}(z, r = 0)} F(n, z, r = 0)\sigma_{ext}(n, z, r = 0)\,dn\,dz \right). \quad (17)$$

These plots show that the calculated $K_p$ values are 2–3 orders of magnitude lower than those measured in the whole range of medium parameter variations. In addition, the experimental dependences of radiation absorption and scattering on buffer gas pressure and on the nature of the buffer gas are at variance with the calculation results.

Note that the question of the validity of describing condensation processes by (7) was raised in several works. In particular, Lothe and Pound [53] took into account all degrees of freedom of a nucleus to introduce a correction to (7), which increased the classical rate of nucleation $J_0$ by a factor of $10^{17}$. It was, however, shown in [54] that, in reality, the correction could vary in the range $10^{-2}$–$10^{6}$ {a similar conclusion was drawn in [55], where it was noted that the introduction of corrections changed the parameters of condensed microparticles by as little as 5% at $J = (10^{-2}–10^{2})J_0$}. In addition, it was shown in [56] that the size dependence of the surface tension coefficient could also have a strong effect on the rate of nucleation; at large supersaturations *S*, this effect considerably increased the $J_0$ value. We therefore modeled condensation with increasing rate of nucleation up to $J = 10^{10}J_0$. The calculations showed that even such an increase in $J_0$ did not very substantially influence the parameters of microparticles and absorption by vapor. The number of microparticles in the cell volume and the total number of atoms in them then increased severalfold, but their mean size simultaneously decreased severalfold. For instance, in argon at 1 atm and $T_c$ = 1000 K, the concentration of microparticles and the total number of atoms in them increased by as little as 4 and 1.5 times, respectively, and the maximum microparticle size decreased 1.6 times, whereas the $K_p$ value only increased 1.7 times (at $K_p \ll 1$ and at a large size of microparticles, $K_p \sim N_p\sigma_{ext} \sim 2\pi N_p R^2$). Such a situation arises because, at a limited diffusion flow rate, an increase in the rate of nucleation rapidly becomes limited by the exhaustion of atomic vapor in the condensation zone. This considerably decelerates growth of microparticles (whose rate is proportional to $N - N_s$), and microparticles settle down prior to attaining the previous size, because the time of settling is proportional to $(N - N_s)^{-1/2}$, as can easily be shown. It follows that, even when possible corrections to the rate of nucleation are included, purely diffusion flow cannot provide the concentration of microparticles and their size required to explain the experimental data.

Calculations of the temperature field in the cell, however, showed the existence of small temperature drops $\Delta T$ between the cell axis and cell walls (not larger than 15 K in the hot tube zone at 1000 K). For this reason, convective vapor transfer from near-wall layers to the axial zone and then from the hot to cold cell regions could occur. Such convective processes can hardly be modeled in detail. In a first approximation, they can, however, be described using the effective diffusion coefficient $D_{\text{eff}}$, which can be estimated on the assumption that convective and diffusion flows are equal,

$$D_{\text{eff}}\nabla N = v_{cz}N, \tag{18}$$

where $v_{\text{cz}}$ is the convective flow rate along the cell axis, which is assumed to be of the order of the vertical (radial) convective flow rate, $v_{\text{cz}} \sim v_{\text{cr}}$. The $v_{\text{cr}}$ value can in turn be estimated by the Boussinesq equation [57]

$$(v_{\text{cr}}\nabla)v_{\text{cr}} = \nu\Delta v_{\text{cr}} - \beta g\Delta T, \tag{19}$$

where $\nu$ is the kinematic viscosity of the medium, $\beta$ is the thermal expansion coefficient ($b = 1/T$ for gases), and $g$ is the free fall acceleration. Under the conditions of our experiment, the term caused by viscosity is small even at low buffer gas pressures. The rate of convection can then be estimated [on the assumption that $(v_{\text{cr}}\nabla)v_{\text{cr}} \sim v_{\text{cr}}^2/R_p$] as

$$v_{\text{cr}} \sim \sqrt{R_p g\frac{\Delta T}{T}}. \tag{20}$$

Hence, the $D_{\text{eff}}$ value is given by

$$D_{\text{eff}} \sim L_1\sqrt{R_p g\frac{\Delta T}{T}} \tag{21}$$

if it is assumed that the gradient of vapor density is established along the length of the hot cell zone and $\nabla N \sim N/L_1$. It follows that the $D_{\text{eff}}$ value does not depend on buffer gas pressure and the type of buffer gas. Note that, depending on temperature, $D_{\text{eff}}$ can be dozens and hundreds of times larger than the usual diffusion coefficient of a small admixture of sodium vapor in the buffer gas at atmospheric pressure.

We modeled diffusion and condensation processes with the use of (21) to estimate the influence of convection on the formation of microparticles. The $\Delta T$ value was set equal to 15 K over the whole cell length. Note that the temperature drop can be substantially lower if convective heat conduction is taken into account. The calculations results are given in Figs. 6–9. They show that absorption substantially increases in the presence of convection, although it does not reach experimental values. What is more, the calculated dependences of absorption on buffer gas pressure and the kind of buffer gas qualitatively reproduce the experimental dependences (cf. Figs. 2 and 8, 3 and 9), because although the effective diffusion coefficient is independent of buffer gas kind and pressure, these characteristics to a substantial extent determine the rate of settling. As with diffusive transfer, an increase in the nucleation rate by ten orders of magnitude compared with the classical nucleation rate under convective transfer conditions does not substantially influence the parameters of microparticles and absorption by vapor. Note that narrow condensation zones (see Figs. 6 and 7) situated at $z$ = 7–11 cm (where temperatures are already fairly low) formed in usual and convective diffusion virtually coincide.

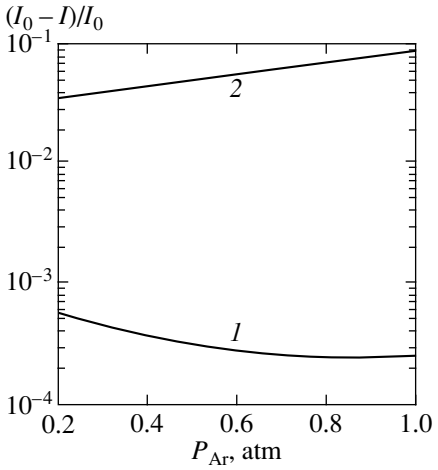


**Fig. 9.** Argon pressure $P_{\text{Ar}}$ dependences of the calculated $K_p = (I_0 - I)/I_0$ values for radiation wavelength of 1 μm in (*1*) diffusion and (*2*) convective modes; $T_c$ = 1000 K.

It follows that microparticles formed in the condensation of convective sodium vapor flows in cells can in principle (to within the approximations made in the calculations) contribute to the experimentally observed weakening of the intensity of transmitted radiation in the $\lambda > 0.9$ μm infrared spectra of sodium vapor. Nevertheless, considering that condensation occurs in the cold cell zone, the temperature of microparticles should be low. Even if we assume that microparticles radiate as a blackbody at the inside boundary of the condensation zone, the intensity of their radiation should be small. For instance, at $T_c$ = 1000 K and $P_{\text{buf}}$ = 1 atm, the inside condensation zone boundary corresponds to $z$ = 7 cm. Temperature $T$ in this region ($z$ = 7 cm, $r$ = 0) is about 510 K. The intensity of blackbody radiation at this temperature is about $2 \times 10^{-16}$ erg/(cm$^2$ sr). However, the intensity of sodium vapor emission recorded in experiments [3, 4] was many orders of magnitude higher [of the order of $10^{-11}$ erg/(cm$^2$ sr)]. Of the same order was also the intensity of radiation from a nonuniformly heated column of sodium vapor in the red wing of resonance *D* lines calculated in the approximation of their quasi-static broadening by the buffer gas taking into account the Boltzmann spectral distribution of population of resonance levels [4]. This leads us to conclude that, although condensation processes can in reality contribute to the observed absorption by sodium vapor,

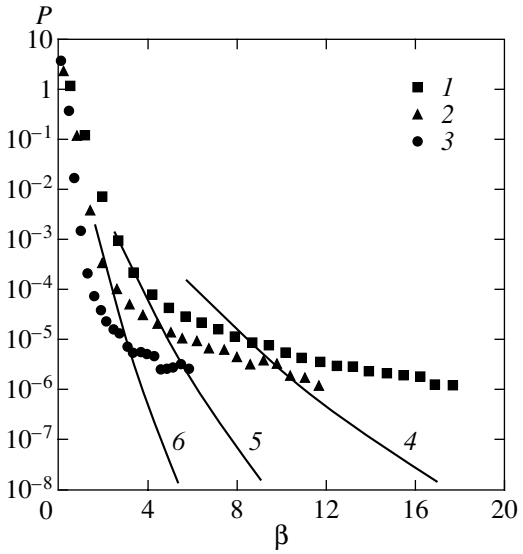


**Fig. 10.** Relative microfield β (β = $E/E_0$, $E_0 = Ze/R_e^2$) distributions calculated using (*1–3*) the method of molecular dynamics and (*4–6*) the nearest-neighbor asymptotic equation for various plasma parameters Γ = 18 (*1*, *4*), 36 (*2*, *5*), and 72 (*3*, *6*).

they are incapable of explaining the experimental intensity of sodium vapor radiation.

## 6. MODELING OF THE INFLUENCE OF MANY-PARTICLE EFFECTS ON THE SHAPE OF THE FAR SPECTRAL LINE WING

As mentioned above, an alternative mechanism that explains substantial emission and absorption at the far spectral line wing in a dense medium can be line broadening caused by many-particle interactions of atomic and molecular medium components. Such interactions can in principle substantially modify the profile of absorption and emission lines in comparison with the simple quasi-static model, which assumes the existence only of binary collisions in conformity with the nearest-neighbor approximation. Although every separate particle insignificantly perturbs the emitting atom, several such particles can effect a shift of the transition frequency sufficient for intense emission and absorption to be observed in the far line wing $\Delta\omega \sim \omega_0$. This problem, however, requires additional inquiries, because analytic methods for calculating the influence of many-particle interactions, which can manifest themselves at large medium densities, on the profile of spectral lines are currently lacking. What is more, this problem has not been solved even in the binary interaction approximation, when each particle perturbs the emitting atom independently from the others. Essentially the same problem arises in describing tails of the density of states of carriers in heavily doped semiconductors [58], when it is necessary to take into account interaction of impurities creating a fluctuating field that acts on electrons (holes).

For this reason, modeling many-particle effects requires the use of numerical methods (such as the method of molecular dynamics). Calculations of many-particle broadening at large detunings $\Delta\omega \sim \omega_0$ by the method of molecular dynamics in a neutral gas for the quasi-static broadening mechanism, when the intensity of a spectral line decreases fairly slowly [$a(\omega) \propto \Delta\omega^{-3/2}$], however, require computational capacity that is difficult to attain even at present. For this reason, modeling of many-particle effects for checking the validity of applying the nearest-neighbor approximation in the region of large detunings from the resonance was performed for another simpler example. Namely, we applied the method of molecular dynamics to numerically calculate the distribution function of ionic microfields $P(E)$ in a dense plasma at asymptotically large microfield values. The $a_{st}(\omega)$ line intensity caused by the Stark effect is known to be proportional to $P(E)$ in the quasi-stationary approximation and to $a_{st}(\omega) \propto \Delta\omega^{-5/2}$ in the nearest-neighbor asymptotics [59].

The calculations were performed for quasi-particles (ions) that moved in a cubic cell with periodic boundary conditions. Ensembles of 1500 particles were used. The time step of the integration was determined by the necessity of correctly describing rare strong rapidly proceeding collisions that formed the statistics of strong fields. The conservation of the total energy of the system was controlled in the integration. Test calculations showed close agreement with the results obtained by the Monte Carlo method for the distribution function of ionic microfields [60]. The calculations were performed for the isothermal ($T_e = T_i$) argon plasma ($Z$ = 17) with a density of 11.7 g/cm$^3$ at $N_e = 3 \times 10^{24}$ cm$^{-3}$ and $N_i = 1.76 \times 10^{23}$ cm$^{-3}$. The temperature was varied in such a way that the nonideality parameter

$$\Gamma = \frac{Z^2 e^2}{T R_e},$$

where $R_e$ is the mean distance between electrons, changed in the range 18–170. The modeling showed (see Fig. 10) that precisely many-particle collisions (collisions of three and more particles) were responsible for the formation of the far tail of the distribution function of microfields in a strongly nonideal plasma. In other words, the probability of observing configurations comprising two and more ions that create the given resultant field at the point of the occurrence of the emitter was much higher than the probability of finding a single perturbing ion creating the same field but at a closer approach to the emitter. The calculations showed that deviations from the nearest-neighbor asymptotic behavior occurred as Γ increased [59, 61] even at low relative microfield values $\beta = E/E_0 > \beta_{crit} \sim 1.5$ ($E_0$ is the

characteristic field equal to $Ze/R_e^2$) and had a sharply defined character. Note that $\beta_{crit} \sim 8$ at $\Gamma = 18$ and the microfield distribution function might exceed the asymptotic function by more than two orders of magnitude. To summarize, we for the first time showed that many-particle effects could have a very substantial influence on the formation of spectral line profiles. The nearest-neighbor approximation in the region of strong fields was quite applicable to a weakly nonideal plasma.

## 7. CONCLUSION

To summarize, our experimental data and the results of theoretical calculations performed in this work show that the presence of the cluster and microdroplet components in vapor cannot explain substantial absorption and thermal radiation observed in the near infrared spectral region at $\lambda > 0.9$ μm in mixtures of dense sodium vapor with various buffer gases (although condensate microparticles can make some contribution to the observed weakening of radiation that has passed through dense vapor). A possible reason for the observed effects can be many-particle broadening of the resonance level in combination with the Boltzmann character of the spectral population distribution for this level. The results of numerical molecular dynamics simulations performed for the example of the distribution of ionic microfields in a dense plasma show that many-particle effects can indeed cause a substantially slower line profile decline than that predicted by the nearest-neighbor approximation, which results in a substantial increase in absorption in a dense medium and, accordingly, in medium emission at large detunings. Applying molecular dynamics methods to the particular problem of resonance sodium line broadening by a buffer gas for describing the available experimental data should, however, be left for future work, for solving this problem requires perfecting computational methods and the use of much more powerful computers. It should, however, be noted that the result obtained for the distribution of microfields can be of importance for correctly interpreting the emission and absorption spectra of a hot dense laser spark plasma, plasmas of *Z* and *X* pinches, etc.

## ACKNOWLEDGMENTS

The authors are deeply indebted to B.M. Smirnov and A.S. Ivanov for useful discussions of the kinetics of sodium clusters and G.V. Simonova for providing the program for numerical computations of the cross sections of extinction of small spherical particles. This work was financially supported by the Russian Foundation for Basic Research (project nos. 00-15-96539-l and 02-02-16758-a).

## REFERENCES

1. Yu. K. Zemtsov and A. N. Starostin, Zh. Éksp. Teor. Fiz. **103**, 345 (1993) [JETP **76**, 186 (1993)].
2. Yu. K. Zemtsov, A. Yu. Sechin, and A. N. Starostin, Zh. Éksp. Teor. Fiz. **110**, 1654 (1996) [JETP **83**, 909 (1996)].
3. Yu. K. Zemtsov, A. Yu. Sechin, A. N. Starostin, *et al.*, Pis'ma Zh. Éksp. Teor. Fiz. **65**, 807 (1997) [JETP Lett. **65**, 839 (1997)].
4. Yu. K. Zemtsov, A. Yu. Sechin, A. N. Starostin, *et al.*, Zh. Éksp. Teor. Fiz. **114**, 135 (1998) [JETP **87**, 76 (1998)].
5. A. G. Leonov, A. A. Rudenko, A. N. Starostin, *et al.*, Pis'ma Zh. Tekh. Fiz. **26** (9), 52 (2000) [Tech. Phys. Lett. **26**, 382 (2000)].
6. D. O. Wharmby, IEE Proc., Part A: Phys. Sci., Meas. Instrum., Manage. Educ. **127**, 165 (1980).
7. N. D. Bhaskar, E. Zouboulis, T. McClelland, and W. Happer, Phys. Rev. Lett. **42**, 640 (1979).
8. A. Vasilakis, N. D. Bhaskar, and W. Happer, J. Chem. Phys. **73**, 1490 (1980).
9. E. Zouboulis, N. D. Bhaskar, A. Vasilakis, and W. Happer, J. Chem. Phys. **72**, 2356 (1980).
10. J. Huennekens, S. Schaefer, M. Ligare, and W. Happer, J. Chem. Phys. **80**, 4794 (1984).
11. M. Palle, S. Milosevic, D. Veza, and G. Pichler, Opt. Commun. **57**, 394 (1986).
12. M. Ligare and J. B. Edmonds, J. Chem. Phys. **95**, 3857 (1991).
13. L. M. Biberman, V. S. Vorob'ev, and I. T. Yakubov, *Kinetics of Nonequilibrium Low-Temperature Plasmas* (Nauka, Moscow, 1982; Consultants Bureau, New York, 1987).
14. L. A. Apresyan and Yu. A. Kravtsov, *Theory of Radiative Transport* (Nauka, Moscow, 1983).
15. A. Phelps, *Tunable Gas Laser Utilizing Ground State Dissociation*, JILA Report 110 (Univ. of Colorado, Boulder, Colorado, 1972).
16. G. York and A. Gallagher, *Power Gas Laser on Alkali Dimers A-X Band Radiation*, JILA Report 114 (Univ. of Colorado, Boulder, Colorado, 1974).
17. G. York, R. Scheps, and A. Gallagher, J. Chem. Phys. **63**, 1052 (1975).
18. W. P. West and A. Gallagher, Phys. Rev. A **17**, 1431 (1978).
19. M. J. Jongerius, J. Phys. B **20**, 3345 (1987).
20. K. J. Nieuwesteeg, T. Hollander, and C. Th. J. Alkemade, J. Phys. B **20**, 515 (1987).
21. J. Schlejen, C. J. Jalink, J. Korving, *et al.*, J. Phys. B **20**, 2691 (1987).
22. M. Shurgalin, W. H. Parkinson, K. Yoshino, *et al.*, Meas. Sci. Technol. **11**, 730 (2000).
23. C. R. Vidal and J. Cooper, J. Appl. Phys. **40**, 3370 (1969).
24. W. Demtroder, *Laser Spectroscopy: Basic Concepts and Instrumentation* (Springer-Verlag, New York, 1981; Nauka, Moscow, 1985).
25. D. A. Evensky and K. M. Sando, Phys. Rev. A **31**, 772 (1985).
26. A. N. Starostin, I. I. Yakunin, A. G. Leonov, *et al.*, in *Proceedings of the 15th International Conference on Spec-*

*tral Line Shapes (ICSLS), 2001*, Ed. by J. Seidel (American Inst. of Physics, Melville, 2001), Vol. 11, p. 16.

27. *Handbook of Physical Quantities* (Énergoatomizdat, Moscow, 1986).
28. A. N. Zaĭdel', G. V. Ostrovskaya, and Yu. I. Ostrovskiĭ, *Technology and Practice of Spectroscopy* (Nauka, Moscow, 1976).
29. *Tables of Spectral Lines* (Nauka, Moscow, 1977).
30. A. N. Klyucharev and M. L. Yanson, *Elementary Processes in Plasma of Alkali Metals* (Énergoatomizdat, Moscow, 1988).
31. J. Schlejen, J. Mooibroek, J. Korving, *et al.*, Chem. Phys. Lett. **128**, 489 (1986).
32. J. P. Woerdman and J. J. De Groot, Chem. Phys. Lett. **80**, 220 (1981).
33. H.-K. Chung, K. Kirby, and J. F. Babb, Phys. Rev. A **63**, 032516 (2001).
34. J. J. de Groot and J. A. J. M. van Vliet, *The High-Pressure Sodium Lamp* (Macmillan, Basingstoke, 1986), Series: Philips Technical Library.
35. B. Kendric, Phys. Rev. Lett. **79**, 2431 (1997).
36. R. L. Martin and E. R. Davidson, Mol. Phys. **35**, 1713 (1978).
37. J. L. Martins, R. Car, and J. Buttet, J. Chem. Phys. **78**, 5646 (1983).
38. T. C. Thompson, G. Izmiran, S. J. Lemon, *et al.*, J. Chem. Phys. **82**, 5597 (1985).
39. V. Bonavic-Koutecky, P. Fantucci, and J. Koutecky, Chem. Rev. **91**, 1035 (1991).
40. W. A. de Heer, Rev. Mod. Phys. **65**, 611 (1993).
41. B. M. Smirnov, Usp. Fiz. Nauk **167**, 1169 (1997) [Phys. Usp. **40**, 1117 (1997)].
42. Yu. I. Petrov, *Physics of Small Particles* (Nauka, Moscow, 1982).
43. B. M. Smirnov, Usp. Fiz. Nauk **170**, 495 (2000).
44. U. Kreibig and M. Vollmer, *Optical Properties of Metal Clusters* (Springer-Verlag, Berlin, 1995).
45. J. M. Pacheco and W.-D. Schone, Phys. Rev. Lett. **79**, 4986 (1997).
46. T. Inagaki, L. C. Emerson, E. T. Arakawa, and M. W. Williams, Phys. Rev. B **13**, 2305 (1976).
47. M. Born and E. Wolf, *Principles of Optics* (Pergamon, Oxford, 1969; Nauka, Moscow, 1970).
48. J. Frenkel, *Kinetic Theory of Liquids* (Akad. Nauk SSSR, Moscow, 1946; Clarendon, Oxford, 1946).
49. Ya. B. Zel'dovich, Zh. Éksp. Teor. Fiz. **12**, 525 (1942).
50. M. N. Ivanovskiĭ, V. P. Sorokin, and V. I. Subbotin, *Evaporation and Condensation of Metals* (Atomizdat, Moscow, 1976).
51. V. N. Piskunov, *Theoretical Kinetic Models of Aerosol Formation* (VNIIÉF, Sarov, 2000).
52. M. V. Brykin and K. G. Garnisov, Teplofiz. Vys. Temp. **32**, 267 (1994).
53. J. Lothe and G. M. Pound, J. Chem. Phys. **36**, 2080 (1962).
54. V. G. Shchukin and V. V. Marusin, Zh. Fiz. Khim. **55**, 1105 (1981).
55. V. G. Gorbunov, U. G. Pirumov, and Yu. A. Ryzhov, *Nonequilibrium Condensation in High-Speed Gas Flow* (Mashinostroenie, Moscow, 1984).
56. D. I. Zhukhovitskiĭ, Teplofiz. Vys. Temp. **32**, 261 (1994).
57. L. D. Landau and E. M. Lifshitz, *Course of Theoretical Physics*, Vol. 6: *Fluid Mechanics* (Nauka, Moscow, 1988; Pergamon, New York, 1987).
58. I. M. Lifshits, S. A. Gredeskul, and L. A. Pastur, *Introduction to the Theory of Disordered Systems* (Nauka, Moscow, 1982; Wiley, New York, 1988).
59. H. R. Griem, *Spectral Line Broadening by Plasmas* (Academic, New York, 1974; Mir, Moscow, 1978).
60. C. F. Hooper, Jr., Phys. Rev. **149**, 77 (1966).
61. E. Kh. Akhmedov, A. L. Godunov, Yu. K. Makhrov, *et al.*, Zh. Éksp. Teor. Fiz. **89**, 470 (1985) [Sov. Phys. JETP **62**, 266 (1985)].

*Translated by V. Sipachev*

*Journal of Experimental and Theoretical Physics, Vol. 95, No. 2, 2002, pp. 255–261.*
*From Zhurnal Éksperimental'noĭ i Teoreticheskoĭ Fiziki, Vol. 122, No. 2, 2002, pp. 298–305.*


**PLASMA, GASES**

# Glassy-Like States of Bulk Rare Gases¶

**R. S. Berry[a, *] and B. M. Smirnov[b, **]**

[a]*Department of Chemistry, University of Chicago, Chicago, IL 60637, USA*
[b]*Institute for High Temperatures, Moscow, 127412 Russia*
**e-mail: berry@uchicago.edu*
***e-mail: smirnov@orc.ru*
Received March 27, 2002

**Abstract**—Defining a glassy-like state of a system of bound atoms as a frozen, amorphous, thermodynamically unstable state, we consider a glassy-like state of a condensed rare gas as a configurationally excited state of bound atoms that tends to the thermodynamic equilibrium by diffusion of voids. The criterion for a critical cooling rate is the minimum cooling rate of the liquid state that leads to formation of a glassy-like state. Comparing this glassy-like state with that experimentally obtained by deposition of argon atoms on a cold target, we conclude that glassy-like states are characterized by short-range parameters. On the basis of cluster studies, peculiarities of the liquid aggregate states and glassy-like states are formulated. A glassy-like state of a cluster or a bulk system of bound atoms is a configurationally excited state below the freezing point; the liquid aggregate state exhibits configurational excitations but is characterized by thermal motion of atoms, consistent with the Lindemann criterion. © *2002 MAIK "Nauka/Interperiodica".*

## 1. INTRODUCTION

According to the standard definition [1–4], a glassy state is a frozen, thermodynamically nonequilibrium state of a condensed system that can be formed by sufficiently fast cooling of the system from a fluid state of thermodynamic equilibrium to low temperatures, to attain a persistent state that is not in equilibrium. Peculiarities of these states were first observed and studied for glasses, and we therefore call these states in other systems "glassy-like states." From this standpoint, we consider a bulk system of bound rare gas atoms, whose liquid state congeals and is not metastable as a fluid below the freezing point [5]; in other words, the liquid state of condensed rare gases can be transformed into a glassy-like state as a result of fast cooling from temperatures above the melting point to temperatures below the freezing point.

A glassy-like state of condensed rare gases can be prepared by two methods [4]. The first method involves a fast cooling of liquid rare gases; in the second, a glassy-like state can be prepared as a result of deposition of individual atoms on a target at a low temperature [4, 6]. Deposited atoms occupy initial positions in a random array, and because the temperature is low, the atoms cannot move from their initial positions enough to attain a distribution in thermodynamic equilibrium. This amorphous spatial distribution of atoms is a glassy-like state of the bulk system. A transition to the crystalline state is possible if the temperature is raised sufficiently high to allow annealing. Of course, parameters of this glassy-like state can differ from those of systems obtained by fast cooling of the liquid state. Below, we compare these states of bulk rare gases.

In comparing these forms of condensed rare gases, we account for the structures of the liquid and solid aggregate states that differ because of the presence of internal voids [7] in the second case. We define an individual void [8–10] as the result of the relaxation of individual vacancies. When a configurationally excited state of a system of bound atoms is formed from a compact solid state of this system by formation of some number of vacancies, these transform into voids when the system, with its vacancies, relaxes. We therefore characterize configurationally excited states of a bulk system of bound atoms by the concentration of voids and the parameters of an individual void at this concentration. We assume that the voids are the results of individual vacancies and that, if voids do become neighbors, their energies can be computed in the same manner as the energies of individual voids. This allows us to make a quantitative analysis of configurationally excited states, including glassy-like states. This analysis for condensed rare gases is the goal of this paper.

## 2. PROPERTIES AND FORMATION OF GLASSY-LIKE STATES OF RARE GASES

Characterizing configurationally excited states of condensed rare gases by only the number of voids inside it, we prepare our state as follows [8–10]. We take a bulk crystal of a rare gas consisting of $n + v$ atoms and remove $v$ atoms to the outside. This system is assumed to be sufficiently large such that almost all the removed atoms come from the inside of the system,

¶This article was submitted by the authors in English.

**Table 1.** Reduced parameters of the liquid aggregate states for condensed rare gases

| $v/n$ | $\varepsilon_v/D$ | $V_v\sqrt{2}/R_e^3$ | $n_c$ |
|---|---|---|---|
| 0.320 ± 0.001 | 3.3 ± 0.2 | 0.50 ± 0.06 | 10.2 ± 0.1 |

and surface effects are negligible. After relaxation, this system therefore contains $n$ atoms and $v$ internal voids, and according to the definition, an individual void results from the relaxation of an individual vacancy and its immediate environment. At temperatures significantly above 0 K, crystals in equilibrium have a low concentration of voids, but we here deal with quenched systems with much higher concentrations of voids. Under these conditions, the system is in a thermodynamically nonequilibrium state that would tend to equilibrium by migration of voids to the surface of the system. (A nonequilibrium state might also arise, in principle, from a concentration of voids below the equilibrium value.) But considering this system during short time intervals compared to the diffusion times of voids through the system, we can treat thermodynamic-like properties of states with any number of voids. In addition, we assume that the spatial distribution of voids is uniform throughout the system.

Although strictly the volume and shape of an individual void varies in time, we use average parameters of individual voids that depend only on the void concentration. In Table 1, void parameters are given for the liquid state of condensed rare gases near the triple point [11]. We assume that the interaction inside condensed rare gases is mostly determined by the interaction between nearest neighbors, and that the scaling law is valid for condensed and dense rare gases [11], which allows expressing various parameters of these systems through the atomic mass and two parameters of the pair interaction potential of atoms, the depth of the potential well $D$ and the equilibrium distance between atoms $R_e$, in the same manner. The accuracy of the data given in Table 1 gives the statistical error due to a difference in these parameters for different rare gases.

In Table 1, we give the relative number of voids, the ratio of the number of voids $v$ to the number of atoms $n$, the reduced mean energy $\varepsilon_v$ of the formation of an individual void, the average reduced volume $V_v$ of an individual void, and the average number of nearest neighbors for a test internal atom. All these parameters pertain to the liquid state of rare gases near the triple point [11], and we use them in what follows. We assume that parameters of a glassy-like state coincide with parameters of the liquid state if this glassy-like state is formed as a result of a fast cooling of the liquid state.

## 3. KINETICS OF HEATING AND COOLING PROCESSES INVOLVING GLASSY-LIKE STATES

We consider the evolution of the liquid state of rare gases subjected to fast cooling or transformation of an amorphous state into the crystal as a result of heating. We take the transition rate $1/\tau$ in the Arrhenius form

$$\frac{1}{\tau} = \frac{1}{\tau_0}\exp\left(-\frac{E_a}{T}\right), \tag{1}$$

where the temperature $T$ is expressed in energy units, i.e., as $k_BT$, and $E_a$ is the activation energy of the process.

Considering the cooling process and assuming the rate of the temperature variation $dT/dt$ to be constant, we express the typical time $\tau_c$ of the cooling process as

$$\frac{1}{\tau_c} = \frac{1}{\Delta T}\left|\frac{dT}{dt}\right| = \frac{E_a}{T^2}\left|\frac{dT}{dt}\right|, \tag{2}$$

where $\Delta T = T^2/E_a$ is the temperature range in which the transition rate varies weakly. This implies that the instantaneous liquid state structure is conserved at temperatures below the melting point if the cooling rate satisfies the relation

$$\left|\frac{dT}{dt}\right| > \frac{T_m^2}{E_a\tau_0}\exp\left(-\frac{E_a}{T}\right). \tag{3}$$

If this criterion is satisfied, subsequent cooling to temperatures below the melting point converts the system into a glassy-like state.

We now consider another scenario, in which a bulk system of bound atoms is prepared in an amorphous state at a low temperature and its heating leads to the transition into the ordered solid (crystalline) state. Considering the amorphous state to be a glassy-like one, we define the glass temperature $T_g$ by the relation

$$\tau(T_g) = \tau_c.$$

From Eqs. (1) and (2), we then have

$$T_g = \frac{E_a}{\ln\left(\dfrac{T_g^2}{E_a\tau_0(dT/dt)}\right)}. \tag{4}$$

Formula (4) relates the parameters of the processes that are responsible for the glassy transition.

We now take into account the nature of transitions involving the aggregate or glassy-like states of a bulk system of bound rare gas atoms as a result of the diffusion of voids in this system to its boundary or from it. The rate of transition between aggregate states of a bulk rare gas system or the rate of the glassy transition in this system is then expressed through the diffusion coefficient $D_v$ of voids that is related to the self-diffusion coefficient of atoms $D_a$ by

$$D_v = \frac{n}{v}D_a. \tag{5}$$

**Table 2.** Parameters of void diffusion in condensed rare gases

| | Ne | Ar | Kr | Xe | Average |
|---|---|---|---|---|---|
| $D$, K [11] | 42 | 143 | 200 | 278 | |
| $E_{sol}$, K | 480 ± 20 | 1900 ± 100 | 2500 ± 100 | 3700 ± 100 | |
| $E_{sol}/D$ | 11.4 ± 0.5 | 13.3 ± 0.7 | 12.5 ± 0.5 | 13.3 ± 0.4 | 12.6 ± 0.9 |
| $E_{liq}$, K [13, 14] | 113 | 352 | 405 | 607 | |
| $E_{liq}/D$ | 2.69 | 2.46 | 2.01 | 2.18 | 2.3 ± 0.3 |
| $\varepsilon_{liq}/D$ | 2.20 | 2.29 | 2.06 | 2.15 | 2.2 ± 0.1 |
| $D_0$, $10^{-2}$ cm$^2$/s | 2.7 | 3.7 | 1.5 | 2.2 | |
| $l^2\lvert(dT/dt)_{lim}\rvert$, $10^{-2}$ K cm$^2$/s | 0.014 | 0.11 | 0.15 | 0.22 | |

As an activation process, the diffusion of voids is characterized by an activation energy. We note that, for the solid state, the number of vacancies is

$$v \propto \exp(-\varepsilon_v/T),$$

where $\varepsilon_v$ is the energy of vacancy formation. Hence the activation energies for the self-diffusion coefficient of atoms $E_a$, for which the data in Table 2 are taken from [12], and the diffusion coefficients of voids and vacancies ($E_{sol}$) differ from those of the solid state by the energy $\varepsilon_v$ of formation of an individual vacancy ($E_{sol} = E_a + \varepsilon_v$). For the liquid state with $v \sim n$, the activation energies for these diffusion processes are identical. Table 2 contains the activation energies for self-diffusion of atoms in the solid ($E_{sol}$) and liquid ($E_{liq}$) states. For the liquid state, the diffusion coefficient of voids is given by

$$D_v = D_0 \exp\left(-\frac{E_{liq}}{T}\right). \quad (6)$$

The parameters of this formula given in Table 2 follow from measurements of the self-diffusion coefficients of atoms in liquid rare gases [13, 14] and Eq. (5). In Table 2, we in addition compare the energy of the formation of an individual void $\varepsilon_{liq}$ for the liquid aggregate state near the triple point [11] with the activation energy $E_{liq}$ of the diffusion process for voids in the liquid; we find that these values are identical with a suitable accuracy. We can therefore assume that the activation energy $E_a$ for diffusion of voids in Eq. (1) is equal to the energy of void formation $\varepsilon_v$.

For simplicity, we take a condensed rare gas in the form of a plane film located on a target. A typical diffusion time is given by

$$\tau = \frac{l^2}{D_v}. \quad (7)$$

In particular, Eqs. (3), (6), and (7) give the cooling rate for the formation of a glassy-like state of a film as a result of fast cooling,

$$\left|\frac{dT}{dt}\right| > \left|\left(\frac{dT}{dt}\right)_{lim}\right| = \frac{T_m^2}{E_{liq} l^2} D_0 \exp\left(-\frac{E_{liq}}{T_m}\right). \quad (8)$$

The threshold values of the parameter $l^2|dT/dt|$ given in Table 2 assure the formation of glassy-like states of rare gases as a result of cooling liquid rare gases.

## 4. HEATING PROCESS IN THE GLASS TRANSITION

Various parameters of the system can be used in order to distinguish the solid and glassy-like states; guided by the experiment [6], we use the saturated vapor pressure over the plane surface of the system for this purpose. According to the Clausius–Clapeyron law, the saturated vapor pressure is given by [15, 16]

$$p(v, T) = p_v \exp\left(-\frac{\varepsilon(v)}{T}\right), \quad (9)$$

where $\varepsilon(v)$ is the mean binding energy of a surface atom, which is the sublimation energy per atom for a bulk system with a given number of voids $v$ inside it. We assume that the saturated vapor pressures referred to any concentration of voids are identical at the triple point, as occurs for the solid and liquid states. For the preexponential coefficient in Eq. (9), this gives

$$p_v = p_0 \exp\left(\frac{\varepsilon(v) - \varepsilon_{sol}}{T_{tr}}\right), \quad (10)$$

where $\varepsilon_{sol}$ is the binding energy per atom for the solid state, $\varepsilon_{sol} = \varepsilon(0)$, $p_0$ is the preexponential factor in formula (9) for the solid state, and $T_{tr}$ is the triple point temperature. It follows from this formula that the preexponential factor in Eq. (9) drops as the density of voids increases. Evidently, Eq. (10) is correct for the liquid state.

It then follows that

$$\frac{p(v, T)}{p_{sol}(T)} = \exp\left[(\varepsilon_{sol} - \varepsilon(v))\left(\frac{1}{T} - \frac{1}{T_{tr}}\right)\right], \quad (11)$$

**Table 3**

| | $T_g$, K | $T_*$, K | $\varepsilon(\nu)$, K | $E_a$, K |
|---|---|---|---|---|
| Experiment [6] | 20 ± 1 | 24 ± 1 | 730 ± 90 | 330 ± 20 |
| Theory for liquid | 21 | 23 | 790 | 350 |

where $p_{\text{sol}}(T)$ is the saturated vapor pressure over the solid surface at a given temperature. In particular, for the metastable liquid state at a temperature $T$ below the triple point, Eq. (11) gives

$$\frac{p_{\text{liq}}(T)}{p_{\text{sol}}(T)} = \exp\left[\Delta H_{\text{fus}}\left(\frac{1}{T} - \frac{1}{T_{\text{tr}}}\right)\right], \tag{12}$$

where $\Delta H_{\text{fus}}$ is the specific fusion enthalpy.

Along with the temperature of the glassy transition given by Eq. (4), which characterizes the equality of the rate of heating and the process of void diffusion, we introduce the temperature $T_*$ from which the subsequent growth of the saturated vapor pressure can proceed. For heating of an amorphous state of a rare gas, this temperature is defined by the relation

$$p(\nu, T_g) = p_{\text{sol}}(T_*),$$

and in accordance with Eq. (11) we have

$$\varepsilon(\nu)\left(\frac{1}{T_g} - \frac{1}{T_{\text{tr}}}\right) = \varepsilon_{\text{sol}}\left(\frac{1}{T_*} - \frac{1}{T_{\text{tr}}}\right). \tag{13}$$

We now use these formulas to analyze the results of the experiment [6] in which amorphous argon was prepared by deposition of an argon stream on a copper substrate at a temperature of 10 K; the triple point of bulk argon is $T_{\text{tr}} = 83.7$ K. Amorphous argon is formed under these experimental conditions if the deposition rate is less than $3 \times 10^{-9}$ cm/s. We refer to this amorphous form of argon as a glassy state. Warming leads to an annealing transition to the crystal state [6, 4]. A typical film thickness in this experiment is 10 μm, exceeding the distance between nearest neighbors of bulk condensed argon by more than three orders of magnitude. This film can therefore be considered as bulk condensed argon. The heating rate $dT/dt \approx 2$ K/min leads to the glassy transition at $T_g = 20 \pm 1$ K and the saturated vapor pressure starts to grow from the temperature $T_* = 24 \pm 1$ K. In Table 3, the results of this experiment are compared with the above formulas, with the amorphous state assumed to be structurally analogous to the liquid state and the experimental data treated on the basis of Eqs. (4) and (13). This comparison shows that the amorphous state of argon obtained by deposition of atoms on a cold target is identical to the glassy-like state that we have described as a frozen liquid state at low temperatures.

## 5. PECULIARITIES OF LIQUID AGGREGATE STATES AND GLASSY-LIKE STATES

Assuming a kind of structure for condensed rare gases allowed us to formulate the concept of glassy-like states on the basis of elementary configurational excitations in this system. Because this understanding starts from the study of clusters, systems of a finite number of bound atoms, we consider the concepts of the glassy-like and liquid aggregate states for clusters simultaneously. On the one hand, taking a cluster to the limit of very many constituent particles makes it into a bulk system, allowing us to use and modify the cluster concepts for bulk systems. On the other hand, the cluster is a convenient vehicle for computer modeling, and the results for clusters give important information about the glassy and phase transitions for bulk systems. Next, considering clusters bound by pair interactions between atoms, we assume that these atoms can be treated as classical and examine excitations of two types, configurational excitations and phonons. Phonons of course result from vibrational motion of atoms, while a configuration excitation leads to a change of the atomic configuration. Both the true solid–liquid phase transition and the glassy transition result primarily from transitions involving configurationally excited states of the cluster. Computer modeling of clusters allows us to understand these phenomena in detail.

The potential energy surface of a typical cluster of more than very few particles bound by pair interactions between atoms has many local minima, determined by the configuration of atoms; this is possibly the principal characteristic of such systems [17–20]. Each local minimum corresponds to a specific configurational excitation of a cluster, and neighboring local minima are separated by saddle points of the potential energy surface. During its evolution at low temperatures, a cluster is therefore most often found at those local minima, and spends only a very small fraction of time in intermediate positions. We base our approach on the supposition that the cluster aggregate state is a group of configurationally excited states with very similar excitation energies. Within this definition, each cluster aggregate state is characterized by a certain energy and entropy that corresponds to the classical thermodynamic state in the limit of large cluster size. But the analysis of the cluster phase transitions on the basis of local minima of the potential energy does not include the Lindemann criterion [21, 22], which has proved itself very useful for real systems, and according to which the phase transition proceeds at the temperature at which the mean amplitude of atomic oscillations reaches a certain value. From the analysis of computer simulations of the phase transition in clusters, the compatibility of these two perspectives can be seen.

We consider a cluster consisting of 13 atoms bound by the Lennard-Jones interactions $LJ_{13}$. This cluster has icosahedral structure in its ground configurational state, as shown in Fig. 1. The lowest configurational excita-

tion of this cluster corresponds to the transfer of one atom from an icosahedron vertex to a surface face; the total number of such configurational excitations, and hence its statistical weight, is $g = 180$ (15 positions on the cluster surface times 12 vertex atoms). There are three positions of an excited atom on the cluster surface that correspond to different excitation energies; the parameters of these excitations are given in Fig. 2 [23]. Naturally, neighboring stable positions of a test atom are separated by barriers. The barrier character of the cluster potential surface can be understood in the simplest case where only the nearest neighbors interact. A test atom then has six bonds with nearest neighbors and three bonds if it transfers to the icosahedron surface; in this case, the excitation energy is $3D$, where $D$ is the depth of the Lennard–Jones well. But in the course of a transition between these states, at the lowest potential maximum along such a path (the saddle point), the test atom has bonds to only two atoms, and this transition is therefore characterized by the barrier height $1D$. The long-range contributions to the total interaction in the Lennard–Jones interaction coming from nonnearest neighbors smooth this picture such that the excitation energy and the barrier threshold slightly decrease in this case. We note that these data for atom excitations (Fig. 2) pertain to zero temperature and hence include no vibrational contributions to the energy.

We now analyze the phase transition that occurs when this cluster is heated. The important special property of any phase change in clusters is the coexistence of the phases (e.g., solid and liquid) within some nonzero temperature range [24–27], in contrast to bulk systems where any phase transition occurs at a specific temperature (both at a given pressure, of course). This follows from the cluster consisting of a relatively small, finite number of particles, and we now focus on the parameters of the liquid state of this cluster in the range of the phase transition [24–27]. We note that because the liquid state is analyzed on the basis of various correlations between cluster atoms, it can be reliably separated from the ordered solid state. In accordance with the previous computer simulations [24–27], the temperature range of the phase coexistence for $LJ_{13}$ is $(0.29–0.31)D$, the excitation energy of the liquid state is $\Delta\varepsilon \approx 2.5D$ on average, and the statistical weight of the liquid state with respect to the solid state of this cluster is approximately

$$g_{\mathrm{liq}} = \exp(\Delta\varepsilon/T_{\mathrm{eq}}) \approx 4 \times 10^3,$$

where $T_{\mathrm{eq}} = 0.30D$ is the classical melting point for this cluster, the (approximate) temperature at which the free energies of the solid and the liquid are equal. (The pressure is assumed to be zero.) We note that the model for the liquid state of this icosahedral cluster is based on one-atom configurational transitions. Comparing these data with the data at zero temperature, we find that only the statistical weight of the excited state varies significantly, whereas changes of other parameters of the cluster excited state are not very important.

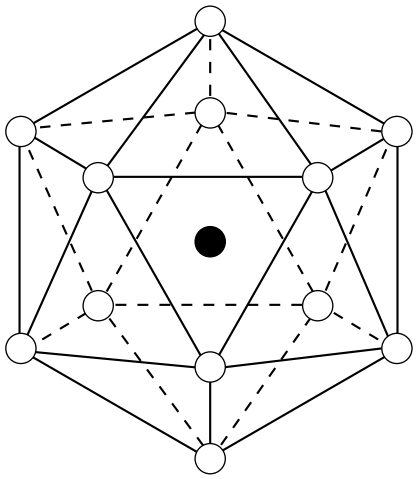

**Fig. 1.** The structure of the icosahedral cluster consisting of 13 atoms [30].

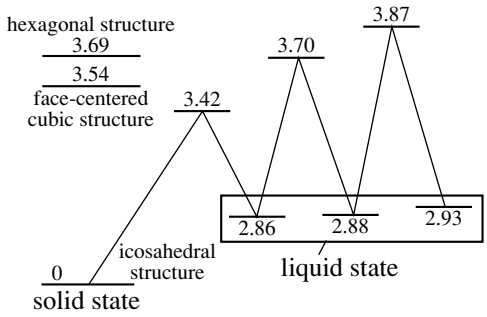


**Fig. 2.** The lowest excited states of the Lennard–Jones cluster of 13 atoms and the character of their formation through saddle points [23]. Values near levels indicate the excitation energies expressed in units of the binding energy $D$ per one bond. The energies of the close-packed structures are taken from [17]. The lowest excited cluster states may be linked to the cluster's liquid state in which the clusters spend most of the time if they begin with a sufficient excitation energy or temperature [24–27].

This implies that heating of the Lennard-Jones cluster of 13 atoms from zero temperature to the melting point changes the statistical weight of one-atom excitation from 180 to $4 \times 10^3$, and the entropy of this transition therefore changes from $\Delta S = 5.2$ to $\Delta S = 8.3$. The latter corresponds to the specific entropy change $\Delta s = \Delta S/13 = 0.64$. We note that the specific entropy change for bulk rare gases is $\Delta s = 1.68$ at the melting point.

From this consideration, it follows that, as a result of cluster heating, the statistical weight contributed by vibrations of individual atoms also increases with temperature, making the conditions still less stringent for the phase transition. This is why the Lindemann criterion is valid for the-phase transition, although the phenomenon results overwhelmingly from the configura-

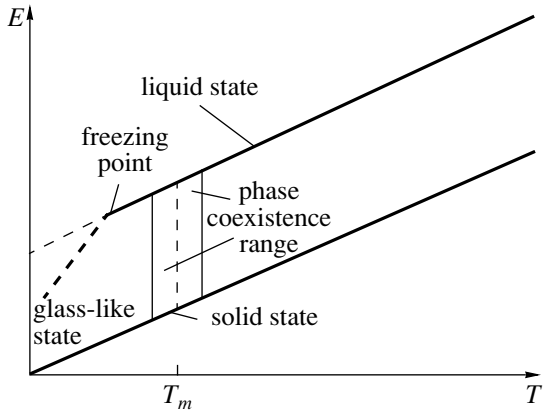


**Fig. 3.** The caloric curve for a cluster or bulk system with two aggregate states.

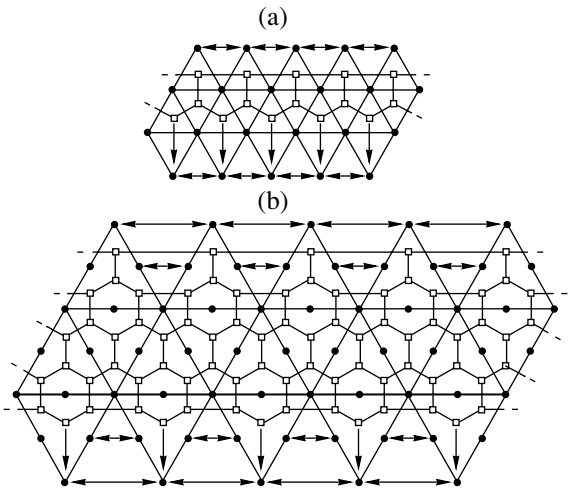


**Fig. 4.** The developed view of the surface of the icosahedral cluster with the completed layers consisting of 13 (a) and 55 (b) atoms. Solid circles are the surface cluster atoms, and the open squares are positions of an atom located on the cluster surface; transitions of this atom on the cluster surface are shown by solid lines, and the boundaries of the surface cluster triangles are denoted by fine solid lines. Arrows show transitions of a test atom into the ground state, and double arrows relate to the same atom of the three-dimensional structure; dotted lines connect identical positions for the three-dimensional cluster.

tional excitation of the system. We also note the example of a solid–solid phase transition in a large cluster [28, 29] in which the vibrational contribution to the thermodynamic parameters is quite small, although this contribution is significant in the case of the solid–liquid phase transition.

Returning to the problem under consideration, we conclude that the liquid and glassy-like cluster states have virtually identical structural nature, but are characterized by different statistical weights or entropies because the liquid state, corresponding to higher temperatures than glassy-like states, has significantly higher vibrational entropy (which reflects the mobilities and higher frequency motions of the atoms of the liquid). The caloric curve for a bulk rare gas system is schematically represented in Fig. 3. The liquid state is a thermodynamically stable or metastable aggregate state above the freezing point; in the course of a temperature decrease, it is transformed into a glassy state. For a cluster, this picture can be more complicated because a cluster can have several aggregate states, e.g., those based on different aggregate states of its shells (see, e.g., [31]). Considering a bulk system of bound atoms for which surface effects are not essential, we obtain only one kind of configurational excitations in the form of internal voids, and the caloric curve therefore takes a simple form.

In contrast to a bulk system, the transition of a cluster from a glassy-like state, or cluster relaxation, proceeds rapidly, because the elementary excitation does not become entangled inside the system, as it can in the case of the void diffusion inside a bulk. Nevertheless, this tendency occurs in clusters if their size increases. Figure 4 contains a developed view of clusters with the icosahedral structure consisting of 13 and 55 atoms; these clusters have completed shells of atoms in their ground configurational states. Elementary configurational excitations of these clusters correspond to transitions of one vertex atom (or several atoms) to the cluster surface, such that, in glassy-like states, a promoted atom drifts over the cluster surface, and the cluster relaxation corresponds to a transition of an atom to a free vertex position. Because all the positions of an excited atom on the cluster surface are almost identical, such an atom can have random displacements on the surface, similarly to a diffusion process. Thus, as a cluster increases in size, the character of the relaxation process for glassy-like states becomes identical to that of a bulk system.

From this analysis for the simplest bulk systems of bound atoms and clusters, it follows that the glassy and phase transitions have a common feature that consists in a change of configurational excitation in such transitions. The difference between these phenomena is such that thermal excitation of bound atoms influences the phase transition, e.g., as demonstrated by the Lindemann criterion. For glassy-like states of a system of bound atoms, the thermal motion of atoms is not very important.

## 6. CONCLUSIONS

On the basis of the above analysis, the glassy state concept can be carried over from complex (i.e., bulk macroscopic) systems to simple ones, specifically to atomic clusters. According to the definition [4], the glassy state is a thermodynamically unstable configurational state of bound atoms formed by fast cooling of a system for which extremely slow cooling leads to a transition, with an activation energy, between two truly stable aggregate states. For glasses [1–4], this transition

involves the change of positions of some constituent particles, and the system finally takes a crystalline structure as it undergoes an "infinitely" slow cooling. One more peculiarity of this transition is the difference in densities of the structures for the initial and final states. Together with restructuring of the particle positions, relaxation to the equilibrium therefore requires that voids must diffuse to the system boundary or into the system.

Focusing now on simple bulk systems of bound atoms, such as condensed rare gases, we find no need to invoke restructuring of chemical bonds in such systems, but transport of voids proceeds by analogy with glasses and has an activation character. The glassy-like state of such a system can be prepared by two methods, by fast cooling of the liquid aggregate state or by deposition of an atom flux on a substratum at low temperatures below the melting point with the formation of a random distribution of atoms.

In the case of clusters, the systems exhibiting a finite number of locally stable configurationally excited states formed by the transition of atoms from completed cluster shells to the surface conform to the model of a glassy state according to its definition. This corresponds to the formation of surface voids; the annihilation of voids results in a transition of atoms from the cluster surface to the outermost shell. This glassy-like state can also be considered from the standpoint of the concept of the cluster configurational excitation as a result of the transition to local minima of the potential energy surface of this cluster. Because neighboring local minima of the cluster configurational energy are separated by barriers [19, 20], transitions from the ground cluster shell to excited configurations have an activation character. Thus, the known excited structures of simple systems of bound atoms conform to the definition of the glassy state. Based on the nature of the glassy-like states of simple systems as a result of formation of voids, one can analyze these states in more detail.

## ACKNOWLEDGMENTS

R. S. B. wishes to acknowledge the support of the National Science Foundation.

## REFERENCES

1. W. Eitel, *The Physical Properties of Silicates* (University of Chicago Press, Chicago, 1954).
2. A. Bondi, *Physical Properties of Molecular Crystals, Liquids and Glasses* (Wiley, New York, 1968).
3. A. Feltz, *Amorphe und Glasartige Anorganische Festkörper* (Akademie-Verlag, Berlin, 1983).
4. I. Gutzow and J. Schmelzer, *The Vitreous State* (Springer-Verlag, Berlin, 1995).
5. R. S. Berry and B. M. Smirnov, Zh. Éksp. Teor. Fiz. **120**, 889 (2001) [JETP **93**, 777 (2001)].
6. A. Kouchi and T. Kuroda, Jpn. J. Appl. Phys. **29**, L807 (1990).
7. H. Reiss, H. L. Frisch, and J. L. Lebowitz, J. Chem. Phys. **31**, 369 (1959).
8. B. M. Smirnov, Inorg. Mater. **35**, 562 (1999).
9. B. M. Smirnov, in *Nucleation Theory and Applications*, Ed. by J. W. P. Schmelzer, G. Röpke, and V. B. Priezzhev (Joint Inst. for Nuclear Research, Dubna, 1999).
10. B. M. Smirnov, *Clusters and Small Particles in Gases and Plasmas* (Springer-Verlag, New York, 2000).
11. B. M. Smirnov, Usp. Fiz. Nauk **164**, 1165 (1994) [Phys. Usp. **37**, 1079 (1994)]; Usp. Fiz. Nauk **171**, 1291 (2001) [Phys. Usp. **44**, 1229 (2001)].
12. B. M. Smirnov, Usp. Fiz. Nauk **125** (2), 331 (1978) [Sov. Phys. Usp. **21**, 522 (1978)].
13. L. Bewilogua, L. Gladun, and B. Kubsch, J. Low Temp. Phys. **4**, 299 (1971).
14. J. Naghizadeth and S. A. Rice, J. Chem. Phys. **36**, 2710 (1962).
15. D. Ter Haar and H. Wergeland, *Elements of Thermodynamics* (Addison-Wesley, London, 1966).
16. L. D. Landau and E. M. Lifshitz, *Course of Theoretical Physics*, Vol. 5: *Statistical Physics* (Nauka, Moscow, 1995; Pergamon, Oxford, 1980), Part 1.
17. M. R. Hoare and P. Pal, Adv. Phys. **20**, 161 (1971).
18. R. S. Berry, Chem. Rev. **93**, 2379 (1993).
19. R. S. Berry, in *Theory of Atomic and Molecular Clusters*, Ed. by J. Jellinek (Springer-Verlag, Berlin, 1999), p. 1.
20. D. J. Wales, Adv. Chem. Phys. **115**, 1 (2000).
21. F. A. Lindemann, Z. Phys. **11**, 609 (1910).
22. Y. Zhou, M. Karplus, K. D. Ball, and R. S. Berry, J. Chem. Phys. **116**, 2323 (2002).
23. D. J. Wales and R. S. Berry, J. Chem. Phys. **92**, 4283 (1990).
24. G. Natanson, F. Amar, and R. S. Berry, J. Chem. Phys. **78**, 399 (1983).
25. J. Jellinek, T. L. Beck, and R. S. Berry, Chem. Phys. Lett. **107**, 227 (1984).
26. J. Jellinek, T. L. Beck, and R. S. Berry, J. Chem. Phys. **84**, 2783 (1986).
27. H. Davis, J. Jellinek, and R. S. Berry, J. Chem. Phys. **86**, 6456 (1987).
28. R. S. Berry and B. M. Smirnov, Zh. Éksp. Teor. Fiz. **117**, 562 (2000) [JETP **90**, 491 (2000)].
29. R. S. Berry and B. M. Smirnov, J. Chem. Phys. **113**, 728 (2000).
30. S. N. Khanna and P. Jena, Phys. Rev. Lett. **69**, 1664 (1992).
31. R. E. Kunz and R. S. Berry, Phys. Rev. E **49**, 1895 (1994).

*Journal of Experimental and Theoretical Physics, Vol. 95, No. 2, 2002, pp. 262–265.*
*From Zhurnal Éksperimental'noĭ i Teoreticheskoĭ Fiziki, Vol. 122, No. 2, 2002, pp. 306–309.*


**FLUIDS**

# Is the Critical Reynolds Number Universal?¶

**S. Novopashin* and A. Muriel**

*Institute of Thermophysics, Russian Academy of Sciences, Novosibirsk, 630090 Russia*
**e-mail: sanov@itp.nsc.ru*

Received December 26, 2001

**Abstract**—This paper is devoted to checking whether the critical Reynolds number is universal in identical conditions for the flow of different fluids. The laminar-turbulent transition in a circular pipe flow has been tested experimentally. The flows of inert gases (He, Ne, Ar, Kr, Xe), molecular gases ($N_2$, CO, $CO_2$, $SF_6$), and two similar liquids ($H_2O$, $D_2O$) have been tested. A considerable, up to 40%, difference in critical Reynolds numbers was observed. The possible reasons for nonuniversality of the critical Reynolds number are discussed.


## 1. INTRODUCTION

The mystery of turbulent flows has been intriguing researchers in mechanics, synergetics, hydrodynamics, plasma physics, geophysics, chemistry, and biology. In spite of more than two centuries of history, this problem is still unsolved. Numerous experiments since Reynolds's paper [1] show that the stationary flow of fluids is possible only if the Reynolds number is less than some critical value. It is confidently known that the Navier–Stokes equations govern laminar flows. The breakdown of the stationary flow is associated with the loss of stability with increasing Reynolds number. The analysis of stability of solutions sometimes allows predicting the critical Reynolds number. Most part of the research in the stability of laminar flows was devoted to incompressible flows. In this case, the analysis is considerably simplified because the only dimensionless parameter—the Reynolds number—determines the regime of the flow. Its value depends on the nature of the flow, but must be universal for different liquids in the same flow.

The Hagen–Poiseuille flow [2–4]—the flow in a long circular pipe—is stable with respect to infinitesimal disturbances [5, 6]. The transition to turbulence occurs as a result of finite perturbations or insufficiently smooth boundary conditions at the pipe entrance. Depending on the boundary conditions and external noise, the critical Reynolds number $R_c$ can vary in a wide range of magnitudes: from $2 \times 10^3$ to more than $10^5$. In the transition to the turbulent regime, the drag coefficient increases sharply, which makes it possible to monitor the critical Reynolds number reliably. This paper reports experimental results on the transition to turbulence in different gases and some liquids in the same pipe. The experiments are directed to check whether the critical Reynolds number is universal for the flows of different fluids.

## 2. EXPERIMENTAL

The experimental setup is shown in Fig. 1. The vessel *1* (with the volume 0.1 $m^3$) can be pumped up to a pressure of 0.1 Torr and then filled by any gas up to 1500 Torr. To study the transition in liquids, the basin *2* is installed inside. The air in the chamber can be compressed up to 750 Torr above the atmospheric pressure. Both gases and liquids can outflow into the atmosphere through the glass pipe *3* having an internal diameter of 1.3 mm and the length of 300 mm. The gas pressure inside the chamber varies the pressure drop on the pipe. It is measured by a membrane-type pressure gauge *4*. By varying the quality (roughness) of the pipe inlet, it was possible to change the critical Reynolds number in a wide range. The quality of the pipe inlet was chosen such that the critical Reynolds number was about 3500 for nitrogen. All noble gases (He, Ne, Ar, Kr, Xe), some molecular gases ($N_2$, CO, $CO_2$, $SF_6$), double distillate water, and 99.9% heavy water were used in experi-

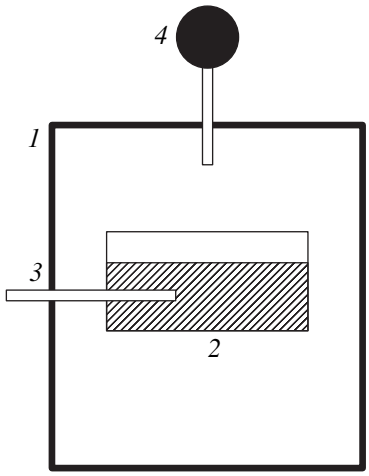


**Fig. 1.**

¶This article was submitted by the authors in English.

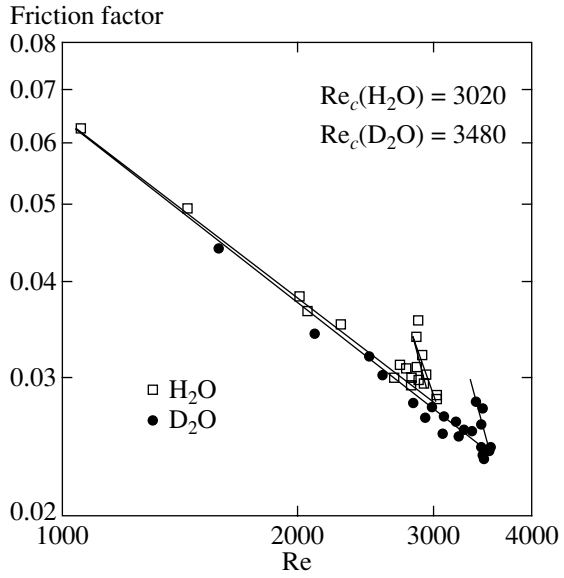


**Fig. 2.**

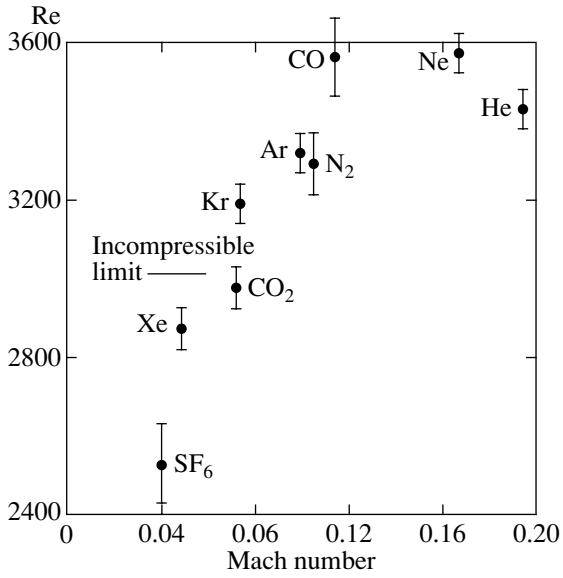


**Fig. 3.**

ments. The temperature of the liquids was controlled to an accuracy of 0.5 K. The flow rate was measured as a function of the pressure drop. For liquids, it was measured by collecting the liquid for a definite time period (normally, 1 min). The gas flow rate was measured by controlling the rate of pressure decrease. As an example, the data reduction for $H_2O$ and $D_2O$ is shown in Fig. 2. It is clearly seen that the dependence of the friction factor on Re is close to the theoretical one in the laminar flow, 64/Re. The transition to turbulence results in a sharp increase in the friction factor, which allows the critical Reynolds number to be determined with high accuracy.

## 3. RESULTS AND DISCUSSION

The data of all measurements are collected in Tables 1–3. The tables show that the critical Reynolds number varies in the range 2500–3570 ($SF_6$–Ne). The experiments were carried out under absolutely identical

**Table 1.** Noble gases

| Property/Gas | He | Ne | Ar | Kr | Xe |
|---|---|---|---|---|---|
| Molecular mass | 4.003 | 20.18 | 39.95 | 83.80 | 131.3 |
| Density, kg/m$^3$ (101325 Pa, 293 K) | 0.1785 | 0.900 | 1.784 | 3.73 | 5.897 |
| Dyn. visc., $10^6$ Pa s ($10^5$ Pa, 300 K) | 19.9 | 31.75 | 22.75 | 25.54 | 23.3 |
| Speed of sound, m/s (300 K) | 1012 | 454 | 334 | 222 | 177.4 |
| Critical Reynolds number | 3430 | 3570 | 3320 | 3190 | 2870 |
| Mach number | 0.20 | 0.17 | 0.10 | 0.074 | 0.048 |
| Second virial coefficient, cm$^3$/mol | 11.15 | 11.02 | –16.85 | –53 | –134.6 |

**Table 2.** Molecular gases

| Property/Gas | $N_2$ | CO* | $CO_2$ | $SF_6$ |
|---|---|---|---|---|
| Molecular mass | 28 | 28 | 44 | 146 |
| Density, kg/m$^3$ (101325 Pa, 293 K) | 1.25 | 1.25 | 1.977 | 6.5 |
| Dyn. visc., $10^6$ Pa s ($10^5$ Pa, 300 K) | 17.9 | 17.9 | 15.0 | 15.9 |
| Speed of sound, m/s (300 K) | 334 | 334 | 274 | 134.9 |
| Critical Reynolds number | 3290 | 3560 | 2970 | 2530 |
| Mach number | 0.105 | 0.114 | 0.072 | 0.04 |
| Second virial coefficient, cm$^3$/mol | –5.47 | –10.0 | –97.9 | –292 |

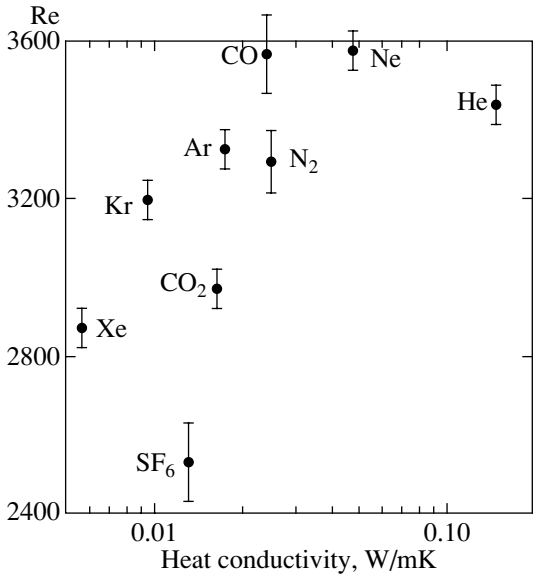


**Fig. 4.**

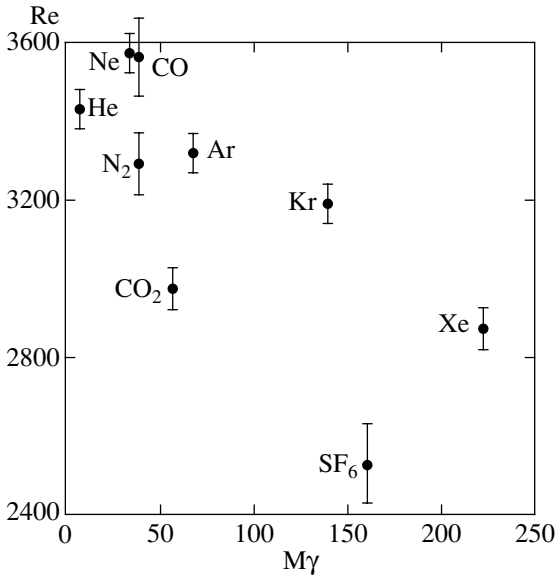


**Fig. 5.**

background conditions. The data obtained therefore demonstrate a nonuniversality of the critical Reynolds number, contrary to the conventional tenet.

For the Navier–Stokes equations, the Reynolds number is not the only parameter that can influence the flow stability. For compressible flows, the Mach number is the second important parameter. Figure 3 shows the dependence of the critical Reynolds number on the Mach number for gas flows at the transition point. We can see some correlation between the value of the critical Reynolds number and the Mach number. With the decrease in the Mach number, $R_c$ should reach the limit determined by incompressible flow. The data for water plotted by the horizontal solid line demonstrate that $R_c$ for water is far from the limit. This means that the Mach number cannot be the parameter that governs the difference in critical Reynolds numbers for gas flows.

The Navier–Stokes equations include three dissipative terms: normal viscosity, bulk viscosity, and heat conductivity. We first consider the role of bulk viscosity. Bulk viscosity is related to the relaxation of the molecular internal degrees of freedom; in particular, it is strictly equal to zero for inert gases. In [7, 8], the difference in the critical Reynolds numbers for $N_2$ and CO was explained by the difference in rotational relaxation. But additional experiments have shown [8] that the critical Reynolds numbers differ in a range that is sufficiently wide even for noble gases (see Table 1). This fact allows one to conclude that the relaxation of molecular internal degrees of freedom cannot be the only additional parameter that determines $R_c$.

**Table 3.** Liquids

| Property/Liquids | $H_2O$ | $D_2O$ |
|---|---|---|
| Molecular mass | 18 | 20 |
| Density, kg/m$^3$ (101325 Pa, 293 K) | 1000 | 1104 |
| Dyn. visc., Pa s (295 K) | 0.00096 | 0.0012 |
| Critical Reynolds number | 3020 | 3480 |

The difference in thermal conductivities could be important for gas flows because of its expansion and cooling during the flow. The plot of the critical Reynolds number against thermal conductivity is shown in Fig. 4. In spite of some correlation, we must admit that the dissipation due to thermal conductivity cannot be an important parameter.

The next factor that could play a role is the influence of the external noise. Although the experiments were carried out under the same external conditions, the role of the noise could be different for different substances. To characterize the noise, we suppose that the spectral components of the noise pressure $P_\omega$ are the same. The characteristic dimension of the pressure is $\rho C^2$, where $\rho$ is the density and $C$ is the speed of sound. The characteristic frequency $\omega$ is $C/D$, where $D$ is the characteristic size of the flow (e.g., the diameter of the pipe). Finally, to obtain a dimensionless parameter $P_\omega$, we must normalize this value to $(\rho C^2)/(C/D)$. $D$ is the same for all experiments, and $C$ is proportional to $\sqrt{\gamma T/\rho}$, where $\gamma$ is the adiabatic exponent, and $T$ is the temperature (it is the same for all gases). The reduction of the above formulas results in the parameter being normalized as $\gamma\rho$, or $\gamma M$, where $M$ is the molecular mass. This plot is shown in Fig. 5. It is clearly seen that the experimental points scatter out of any regular dependence. We therefore conclude that the difference in suscepti-

bilities cannot be the reason for the observed nonuniversality of the critical Reynolds number.

We also note the analysis in [9] based on weak nonideality of gases at normal conditions that allowed generalizing the experimental data for all tested gases as a function of the second virial coefficient. The flows of incompressible liquids are simpler in theory because the Reynolds number is the only parameter that should define the regime of the flow. Contrary to the conventional tenet, even in this case (see Table 3), the critical Reynolds numbers differ for water and heavy water. For liquids, the statistical approach similar to that for gases [9] is considerably more complex. The difficulty is in the exact calculation of the partition function and the individual phase volume even for simple liquids [10, 11].

## 4. CONCLUSION

The data obtained show that the critical Reynolds number is not universal and that the process of the laminar–turbulent transition is influenced by the individual molecular properties for both gas and liquid flows. Taking [12–14] and the present research into account, we conclude that a rigorous theory of turbulence should be based on a synthesis of hydrodynamic, statistical, and, possibly, quantum theories.

## REFERENCES

1. O. Reynolds, Philos. Trans. R. Soc. London **174**, 935 (1883).
2. G. Hagen, Pogg. Ann. **46**, 423 (1839).
3. J. Poiseuille, C. R. Hebd. Seances Acad. Sci. **11**, 961 (1840); **12**, 112 (1841).
4. L. Prandtl and O. Tietjens, *Hydro- und Aeromechanik* (Verlag von Julius Springer, Berlin, 1931).
5. J. A. Fox, M. Lessen, and W. V. Bhat, Phys. Fluids **11**, 1 (1968).
6. H. Salwen, F. W. Cotton, and C. E. Grosch, J. Fluid Mech. **92**, 273 (1980).
7. O. A. Nerushev and S. A. Novopashin, Phys. Lett. A **232**, 243 (1997).
8. O. A. Nerushev and S. A. Novopashin, Pis'ma Zh. Éksp. Teor. Fiz. **64**, 47 (1996) [JETP Lett. **64**, 47 (1996)].
9. S. A. Novopashin and A. Muriel, Pis'ma Zh. Éksp. Teor. Fiz. **68**, 557 (1998) [JETP Lett. **68**, 582 (1998)].
10. S. A. Novopashin and A. Muriel, Pis'ma Zh. Tekh. Fiz. **26** (6), 18 (2000) [Tech. Phys. Lett. **26**, 231 (2000)].
11. L. D. Landau and E. M. Lifshitz, *Course of Theoretical Physics*, Vol. 5: *Statistical Physics* (Nauka, Moscow, 1976; Pergamon, Oxford, 1980), Part 1.
12. H. N. V. Temperlley, J. S. Rowlinson, and G. S. Rushbrooke, *Physics of Simple Liquids* (North-Holland, Amsterdam, 1968).
13. A. Muriel, Physica D (Amsterdam) **124**, 225 (1998).
14. A. Groisman and V. Steinberg, Nature **405**, 53 (2000).
15. X. de Hemptinne, *Non-Equilibrium Statistical Thermodynamics* (World Sci., Singapore, 1992).

*Journal of Experimental and Theoretical Physics, Vol. 95, No. 2, 2002, pp. 266–274.*
*Translated from Zhurnal Éksperimental'noĭ i Teoreticheskoĭ Fiziki, Vol. 122, No. 2, 2002, pp. 310–319.*


**FLUIDS**

# Generation of Magnetic Field during Shearing Motion of a Conducting Viscous Medium

**S. V. Fedorov and A. V. Babkin**

*Bauman State Technical University, Vtoraya Baumanskaya ul. 5, Moscow, 107005 Russia*
*e-mail: pk@mx.bmstu.ru*

Received December 13, 2001

**Abstract**—Magnetic field generation in shear flows of an incompressible viscous conducting medium across the flux lines of the initial field created in them is considered in the framework of the plane 1D problem of magnetohydrodynamics. The conditions of free slip and "sticking" are stipulated at the boundary between the flows. The variations of the magnetic field and velocity of shear flow occurring in the moving medium correspond to an Alfven wave "spreading" during its propagation due to dissipative processes in the medium associated with its viscosity and electrical resistance. It is shown that a high-rate shear of metals under explosive or impact loading may lead to generation of megagauss magnetic fields. *© 2002 MAIK "Nauka/Interperiodica".*

## 1. INTRODUCTION

Rapid deformation of a conducting medium with a preliminarily created magnetic field, which is accompanied by the emergence of large strains with magnetic flux line "pulling," may amplify the field in the medium considerably. In accordance with the effect of magnetic field "freezing" in the substance [1], the field intensity in a poorly compressible conducting medium (in the case when the effect of its finite conductance and of the field diffusion associated with it is insignificant) must increase in direct proportion to the elongation of material fibers of the medium oriented initially along the magnetic flux lines.

In this paper, we consider the effect of magnetic field generation upon the elongation of its flux lines as a result of relative shearing motion of two flows of a conducting material, in which a magnetic field perpendicular to the direction of their subsequent relative motion has been created preliminarily. The conditions for such a generation are created, for example, when a high-speed striker penetrates a conducting obstacle with a transverse magnetic field preliminarily created in it at the contact boundary between the obstacle material and the lateral surface of the striker.

## 2. FORMULATION OF THE PROBLEM

Proceeding from the results obtained in [3], where the effect of magnetic field generation in the gap between rigid (undeformed) conducting half-spaces during their relative shearing motion was considered, as well the results from [2] dealing with the magnetic field generation in an incompressible viscous conducting medium deformed due to the shear motion of its boundary with a given velocity, we formulate the following problem.

Two half-spaces occupied by an incompressible viscous conducting medium are in contact and are moving at the initial instant along the contact plane with the relative velocity $2v_0$ (the velocity of motion of the entire medium in each half-space is the same). In the material of the half-spaces, there exists a uniform magnetic field with induction $B_0$ oriented along the normal to the plane of the contact. The half-spaces are filled with the same material.

While determining the mechanical interaction between the materials of the half-spaces at the contact boundary, we will consider two limiting cases: free slip (absence of surface friction and, hence, the mechanical shear stresses at the contact surfaces) and complete "sticking" (the absence of slip between the surfaces in contact, which means that the relative velocity of their motion is zero at all instants).

Without any loss of generality of the problem, we choose the frame of reference in which the materials of the half-spaces at the initial instant move in opposite directions with the same transverse velocity $v_0$ (Fig. 1). We direct the $x$ axis of coordinates along the normal to the contact surface, assuming this surface to be its origin and the $y$ axis, along the direction of relative motion. Obviously, in view of the symmetry in the chosen frame of reference, the velocity $v(x, t)$ of the transverse motion of the medium in the half-spaces is an odd function of coordinate $x$. The magnitude of this velocity will be affected by electromagnetic and viscous forces emerging in the medium under a shear strain [4] (we assume that no other force acts in the direction of the $y$ axis). The motion of the medium along the $x$ axis is ruled out since we assume that the action of electromagnetic forces in this direction is balanced by hydrodynamic pressure in the medium.

1063-7761/02/9502-0266$22.00 

The magnetic field $B(x, t)$ generated in the medium as a result of its shearing motion is oriented along the $y$ axis since it is an even function of coordinate $x$ in view of the symmetry of the problem. The magnetic induction vector component directed along the $x$ axis will not change under the formulated conditions, remaining equal to the induction $B_0$ of the field initially created in the medium.

The equations describing the motion of the medium and the magnetic field evolution in it for the given problem have the form [4]

$$\begin{aligned}\frac{\partial v}{\partial t} &= \frac{B_0}{\mu_0\rho}\frac{\partial B}{\partial x} + \nu\frac{\partial^2 v}{\partial x^2},\\ \frac{\partial B}{\partial t} &= B_0\frac{\partial v}{\partial x} + \nu_m\frac{\partial^2 B}{\partial x^2},\end{aligned} \tag{1}$$

where $\mu_0 = 4\pi \times 10^{-7}$ H/m is the magnetic constant, $\rho$ is the density of the medium, and $\nu$ and $\nu_m$ are the kinematic and magnetic viscosities, respectively ($\nu_m = 1/\mu_0\sigma$, $\sigma$ being the electrical conductivity of the medium).

Taking into account the symmetry of the flow relative to the plane of contact ($v(-x, t) = -v(x, t)$; $B(-x, t) = B(x, t)$), we can consider the system of equations (1) for the medium in the right half-space ($x > 0$). The form of electric and mechanical interactions of the materials in counterflows is determined by the boundary conditions for the sought functions at the contact surface ($x = 0$).

In the case of free slip, no mechanical shear stresses appear at contacting surfaces. In addition, surface electric currents are ruled out in the case of finite conductance of materials of the flows, and, hence, surface electromagnetic forces cannot appear. As a result, no viscous shear stresses $\tau$ will act in the material of the flows at the contact boundary ($\tau = \rho\nu(\partial v/\partial x) = 0$ for $x = 0$), which leads to the following condition of their mechanical interaction:

$$\left.\frac{\partial v}{\partial x}\right|_{x=0} = 0. \tag{2}$$

In this case, the velocity function $v(x, t)$ has a discontinuity at the boundary between the flows.

The boundary condition for the electric interaction in the case of free slip of the flows can be obtained, as in [3], on the basis of the law of electromagnetic induction and Ohm's law in differential form. The flow of material in a transverse magnetic field $B_0$ must induce at the boundary of the half-spaces an electric field of strength $v(0, t)B_0$ oriented along the normal to the coordinate plane $xy$. Connecting the electric field strength with the volume density $j = (\partial B/\partial x)/\mu_0$ of induced currents (taking into account their directions at the boundary of the right half-space) through Ohm's law, we

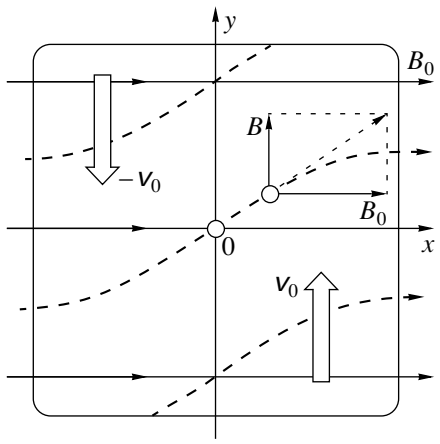


**Fig. 1.** Schematic diagram of magnetic field generation during shearing motion of a conducting medium.

arrive at the following condition of electric interaction of flows on the contact surface:

$$\left.\frac{1}{\mu_0}\frac{\partial B}{\partial x}\right|_{x=0} = -\sigma B_0 v(0, t). \tag{3}$$

In the case of complete sticking at the contact surface, the velocities of the boundaries of the left and right half-spaces must be identical and obviously equal to zero in view of symmetry (the flow velocity discontinuity at the contact boundary exists only at the initial instant $t = 0$). Thus, the mechanical interaction of flows in the absence of slip of contacting surfaces is determined by the boundary condition

$$v(0, t) = 0; \tag{4}$$

consequently, the condition of electric interaction (3) at the contact surface in the case of complete sticking has the form

$$\left.\frac{\partial B}{\partial x}\right|_{x=0} = 0. \tag{5}$$

Introducing the dimensionless time $\bar{t} = tc_A^2/\sqrt{\nu\nu_m}$ and coordinate $\bar{x} = xc_A/\sqrt{\nu\nu_m}$, where $c_A = B_0/\sqrt{\mu_0\rho}$ is the Alfven velocity [1], we can reduce the system of equations (1) to the form

$$\begin{aligned}\frac{\partial \bar{v}}{\partial \bar{t}} &= \frac{\partial \bar{B}}{\partial \bar{x}} + \gamma\frac{\partial^2 \bar{v}}{\partial \bar{x}^2},\\ \frac{\partial \bar{B}}{\partial \bar{t}} &= \frac{\partial \bar{v}}{\partial \bar{x}} + \frac{1}{\gamma}\frac{\partial^2 \bar{B}}{\partial \bar{x}^2},\end{aligned} \tag{6}$$

defining the dimensionless velocity $\bar{v}$ and the magnetic induction $\bar{B}$ of the field being generated as

$$\bar{v} = v/v_0, \quad \bar{B} = B/v_0\sqrt{\mu_0\rho}. \tag{7}$$

The dimensionless parameter $\gamma$ appearing in the system of equations (6) characterizes the ratio of the kinematic and magnetic viscosities of the medium:

$$\gamma = \sqrt{\nu/\nu_m}. \tag{8}$$

The initial conditions for the system of dimensionless equations (6) considered in the same spatial region as system (1) ($\bar{x} > 0$) have the form

$$\bar{v}(\bar{x}, 0) = 1, \quad \bar{B}(\bar{x}, 0) = 0.$$

The boundary conditions (2)–(5) assume the form

$$\left.\frac{\partial \bar{v}}{\partial \bar{x}}\right|_{\bar{x}=0} = 0, \quad \left.\frac{\partial \bar{B}}{\partial \bar{x}}\right|_{\bar{x}=0} = -\gamma \bar{v}(0, \bar{t}) \tag{9}$$

in the case of free slip of the flows and

$$\bar{v}(0, \bar{t}) = 0, \quad \left.\frac{\partial \bar{B}}{\partial \bar{x}}\right|_{\bar{x}=0} = 0 \tag{10}$$

when complete sticking of the materials of the flows takes place.

## 3. EVOLUTION OF MAGNETIC FIELD AND SHEAR VELOCITY AT THE CONTACT BOUNDARY

Solving the problem formulated above, we will first analyze the evolution of the sought functions $\bar{B}(\bar{x}, \bar{t})$ and $\bar{v}(\bar{x}, \bar{t})$ at the contact boundary of the flows ($\bar{x} = 0$). This analysis can be carried out completely in analytic form. The application of the Laplace integral transformation [5] for time to the system of equations (6) leads to a system of second-order ordinary linear differential equations with constant coefficients in the maps of functions of the magnetic induction,

$$B^*(\bar{x}, p) = \int_0^\infty \bar{B}(\bar{x}, \bar{t}) \exp(-p\bar{t}) d\bar{t},$$

and the velocity of particles of the medium,

$$v^*(\bar{x}, p) = \int_0^\infty \bar{v}(\bar{x}, \bar{t}) \exp(-p\bar{t}) d\bar{t},$$

namely,

$$\begin{aligned} \gamma \frac{d^2 v^*}{d\bar{x}^2} + \frac{dB^*}{d\bar{x}} - pv^* &= -1, \\ \frac{1}{\gamma}\frac{d^2 B^*}{d\bar{x}^2} + \frac{dv^*}{d\bar{x}} - pB^* &= 0. \end{aligned} \tag{11}$$

The characteristic equation for this system has the form

$$\lambda^4 - [1 + p(\gamma + 1/\gamma)]\lambda^2 + p^2 = 0. \tag{12}$$

From four roots of this biquadratic equation, the boundedness condition of the solution of system (11) for $\bar{x} \longrightarrow \infty$ is satisfied by the two negative roots,

$$\lambda_1 = -\frac{1}{\sqrt{2}} \times \sqrt{1 + p\left(\gamma + \frac{1}{\gamma}\right) - \sqrt{\left[1 + p\left(\gamma + \frac{1}{\gamma}\right)\right]^2 - 4p^2}},$$

$$\lambda_2 = -\frac{1}{\sqrt{2}} \times \sqrt{1 + p\left(\gamma + \frac{1}{\gamma}\right) + \sqrt{\left[1 + p\left(\gamma + \frac{1}{\gamma}\right)\right]^2 - 4p^2}}.$$

Taking into account this limitation imposed on the sign of characteristic values, we can write the general solution of system (11) for the maps of the required functions in the form

$$\begin{aligned} B^* &= A_1 \exp(\lambda_1 \bar{x}) + A_2 \exp(\lambda_2 \bar{x}), \\ v^* &= A_1 \frac{\lambda_1}{p - \gamma\lambda_1^2} \exp(\lambda_1 \bar{x}) \\ &+ A_2 \frac{\lambda_2}{p - \gamma\lambda_2^2} \exp(\lambda_2 \bar{x}) + \frac{1}{p}, \end{aligned} \tag{13}$$

where $A_1$ and $A_2$ are integration constants that have to be determined from the boundary conditions (9), (10) of the problem, written for the maps of the required functions.

Let us first consider the case of free slip of the flows. Using Eq. (9), we find the integration constants $A_1$ and $A_2$ from the system of equations

$$A_1 \frac{\lambda_1^2}{p - \gamma\lambda_1^2} + A_2 \frac{\lambda_2^2}{p - \gamma\lambda_2^2} = 0,$$

$$A_1\lambda_1 + A_2\lambda_2 = -\gamma\left(A_1 \frac{\lambda_1}{p - \gamma\lambda_1^2} + A_2 \frac{\lambda_2}{p - \gamma\lambda_2^2} + \frac{1}{p}\right).$$

Substituting the values of these constants into Eqs. (13), we obtain the following expressions for the maps of the sought functions on the contact surface:

$$B_s^* = B^*(0, p) = -\frac{\gamma(\lambda_1 + \lambda_2)}{\lambda_1\lambda_2(p + \gamma\lambda_1\lambda_2 + \gamma)},$$

$$v_s^* = v^*(0, p) = \frac{p + \gamma\lambda_1\lambda_2}{p(p + \gamma\lambda_1\lambda_2 + \gamma)}.$$

Since the roots of Eq. (12) satisfy the relations

$$\lambda_1^2\lambda_2^2 = p^2, \quad \lambda_1^2 + \lambda_2^2 = 1 + p(\gamma + 1/\gamma),$$

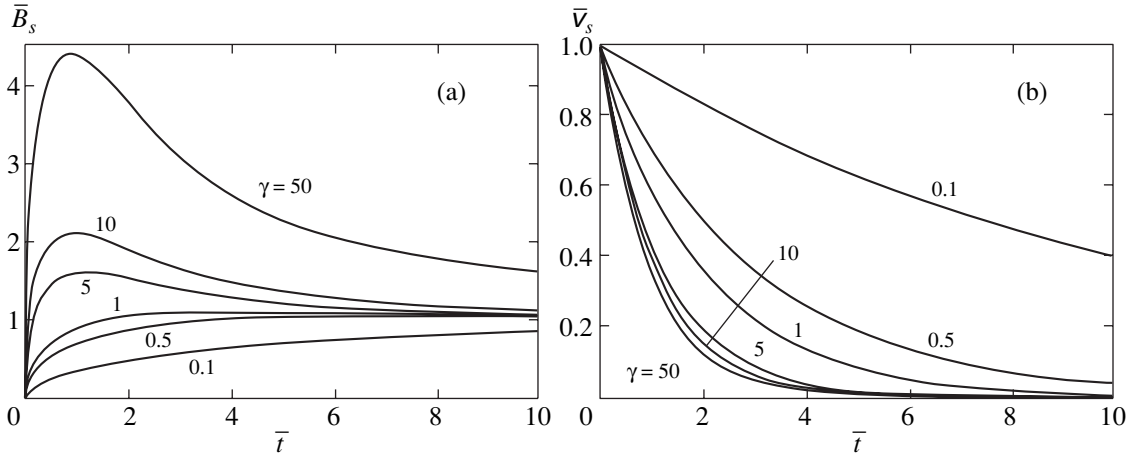


**Fig. 2.** Variation of (a) the magnetic induction of the longitudinal field and (b) the velocity at the slip boundary between flows for different values of parameter γ.

we assume in the latter relations that

$$\lambda_1\lambda_2 = p,$$
$$\lambda_1 + \lambda_2 = -\sqrt{(\lambda_1 + \lambda_2)^2} = -\sqrt{\lambda_1^2 + \lambda_2^2 + 2\lambda_1\lambda_2} \quad (14)$$
$$= -\sqrt{1 + p(\gamma + 1)^2/\gamma}$$

and write them in the final form

$$B_s^* = \frac{\sqrt{1 + p(\gamma + 1)^2/\gamma}}{p(1 + p(\gamma + 1)/\gamma)}, \quad v_s^* = \frac{1}{p + \gamma/(\gamma + 1)}.$$

The reversal of the maps written above [6] leads to the following laws of variation for magnetic induction of the generated field and the velocity of the material of the right half-space (see Fig. 1) on the contact surface in the case of free slip of the flows:

$$\bar{B}_s = \bar{B}(0, \bar{t}) = \operatorname{erf}\left(\frac{\sqrt{\gamma\bar{t}}}{\gamma + 1}\right)$$
$$+ 2\sqrt{\frac{\gamma}{\pi}}\exp\left(-\frac{\gamma\bar{t}}{(\gamma + 1)^2}\right)F\left(\frac{\gamma\sqrt{\bar{t}}}{\gamma + 1}\right), \quad (15)$$

$$\bar{v}_s = \bar{v}(0, \bar{t}) = \exp\left(-\frac{\gamma\bar{t}}{\gamma + 1}\right), \quad (16)$$

where

$$\operatorname{erf}(z) = \frac{2}{\sqrt{\pi}}\int_0^z \exp(-\xi^2)d\xi$$

is the error integral and

$$F(z) = \exp(-z^2)\int_0^z \exp(\xi^2)d\xi$$

is the Dawson integral [7].

Let us analyze the obtained results. Figure 2 illustrates the variation of the quantities $\bar{B}_s$ and $\bar{v}_s$ as functions of time for various values of parameter γ (8). In accordance with relation (16), the dimensionless velocity of the contact surface decreases monotonically from unity and tends exponentially to zero. The rate of deceleration of the boundary decreases with increasing parameter γ. The variation of the dimensionless magnetic induction (15) of the field generated at the contact boundary between the flows is more interesting. First, the field increases monotonically from zero value, exceeds unity, attains its peak value, and then decreases monotonically, tending to unity in the limit. Using the asymptotic expansion for the functions erf(*z*) and *F*(*z*) [7], we can easily establish that the asymptotic behavior of the field (15) for $\bar{t} \longrightarrow \infty$ can be described as

$$\bar{B}_s \approx 1 + O\left(\frac{\exp(-\gamma\bar{t}/(\gamma + 1)^2)}{\bar{t}\sqrt{\bar{t}}}\right).$$

Differentiating relation (15) with respect to time and equating the derivative to zero, we arrive at the equation

$$1 - \frac{2\gamma\sqrt{\bar{t}}}{\gamma + 1}F\left(\frac{\gamma(\bar{t})}{\gamma + 1}\right) = 0,$$

which allows us to determine the parameters of the extreme point. Taking into account the fact that the function *F*(*z*) satisfies the relation [7]

$$\frac{dF(z)}{dz} = 1 - 2zF(z),$$

we find that the solution of this equation leads to the following value of the dimensionless time $\bar{t}_m$ corre-

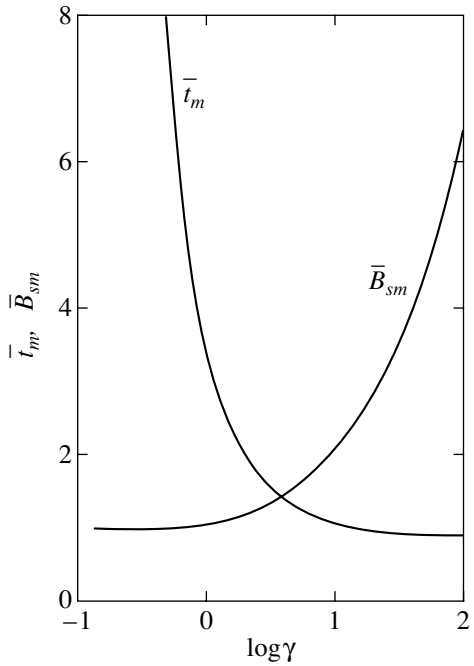


**Fig. 3.** Effect of the ratio of kinematic and magnetic viscosities of the medium on the maximum amplification of the longitudinal magnetic field at the slip boundary between the flows.

sponding to the attainment of the maximum magnetic induction:

$$\bar{t}_m = \frac{z_m^2(\gamma+1)^2}{\gamma^2}, \qquad (17)$$

where $z_m \approx 0.924$ is the value of the argument of the Dawson integral $F(z)$ for which it attains its peak value [7]. Substituting Eq. (17) into relation (15), we can determine the maximum amplification of the field $\bar{B}_{sm}$ at the slip boundaries of the flows:

$$\bar{B}_{sm} = \operatorname{erf}\left(\frac{z_m}{\sqrt{\gamma}}\right) + 2\sqrt{\frac{\gamma}{\pi}}F_m \exp\left(-\frac{z_m^2}{\gamma}\right), \qquad (18)$$

where $F_m = F(z_m) \approx 0.541$ is the maximum value of the Dawson integral.

It follows from relations (17) and (18) that the parameters of the point corresponding to the maximum field depend on the ratio of the kinematic and magnetic viscosities of the material of the flows, which is determined by parameter $\gamma$ (8). A decrease in this parameter leads to an increase in the time $\bar{t}_m$ at which the field attains its maximum value, accompanied by a simultaneous decrease in the maximum intensity of the generated field (Fig. 3).

Obviously, from a physical point of view, the variation of velocity and magnetic induction at the contact surface, which is established by formulas (15) and (16), is determined by the competition of electromagnetic and viscous forces acting on the material of the flows during their relative slip. The electromagnetic forces emerging as a result of interaction between the electric currents induced during such a slip and the transverse magnetic field $B_0$ decelerate the flows. On the contrary, viscous forces oppose this stagnation. The lower the magnetic viscosity of the medium (i.e., the higher its electrical conductivity), the higher the rate of the stagnation and hence the intensity of the field generated in this case. In the case of complete stagnation of the boundary between the flows, the magnetic field generation in this region ceases, and the field starts decreasing due to diffusion to the bulk of the flowing material and stabilizes, on account of the second relation from (7), at the level $B_s = v_0\sqrt{\mu_0\rho}$ corresponding to the field intensity in an Alfven wave [1].

Analyzing dependences (17) and (18) for very high and very low values of parameter $\gamma$, we can establish the following nature of variation of the maximum amplification of the field in the case of a considerable difference between the magnetic and kinematic viscosities:

$$\bar{t}_m \approx \frac{z_m^2}{\gamma^2}, \quad \bar{B}_{sm} \approx 1 + \frac{\gamma}{2}\sqrt{\frac{\gamma}{\pi}}\frac{\exp(-z_m^2/\gamma)}{z_m^3}$$

for $\gamma \longrightarrow 0$ ($\nu_m \gg \nu$) and

$$\bar{t}_m \approx z_m^2, \quad \bar{B}_{sm} \approx 2\sqrt{\frac{\gamma}{\pi}}F_m$$

for $\gamma \longrightarrow \infty$ ($\nu \gg \nu_m$).

These relations imply an unlimited increase in the field amplification for $\gamma \longrightarrow \infty$. For a fixed electrical conductivity of the medium (and, accordingly, magnetic viscosity), this is due to the fact that an increase in the kinematic viscosity of the medium (leading to an increase in parameter $\gamma$) hampers the shear deformation of the medium, as a result of which the latter becomes close to a rigid conductor. At the same time, the shearing motion of rigid conducting half-spaces leads to an unlimited increase in the field in the gap between [3].

The law of variation of the magnetic field generated at the contact boundary between rigid infinitely thick conductors sliding over each other can be established on the basis of relation (15). After the transition to dimensional variables, this relation is transformed to

$$B_s = B(0,t) = v_0\sqrt{\mu_0\rho}\left[\operatorname{erf}\left(\frac{c_A\sqrt{t}}{\sqrt{\nu}+\sqrt{\nu_m}}\right)\right.$$

$$\left. + \frac{2}{\sqrt{\pi}}\sqrt[4]{\frac{\nu}{\nu_m}}\exp\left(-\frac{c_A^2 t}{(\sqrt{\nu}+\sqrt{\nu_m})^2}\right)F\left(\frac{c_A\sqrt{t}\sqrt[4]{\nu/\nu_m}}{\sqrt{\nu}+\sqrt{\nu_m}}\right)\right].$$

Making $\nu$ tend to infinity, we can easily obtain the dependence

$$B_s = 2B_0 v_0 \sqrt{\frac{t}{\pi \nu_m}}.$$

The results obtained in [3] lead to the same law of increase in the magnetic field generated at the slip boundary between rigid conductors if the gap between the conducting half-spaces is assumed to be equal to zero.

Let us now consider the realization of the complete sticking condition for the materials of counterflows at the contact boundary. Using the boundary conditions (10) for determining the integration constants $A_1$ and $A_2$ in the general solution for the maps of the sought functions (13), we obtain the system of equations

$$A_1 \frac{\lambda_1}{p - \gamma\lambda_1^2} + A_2 \frac{\lambda_2}{p - \gamma\lambda_2^2} + \frac{1}{p} = 0,$$

$$A_1\lambda_1 + A_2\lambda_2 = 0.$$

Substituting the values of $A_1$ and $A_2$ into the first relation from (13), we arrive at the following expression for the map of the function of magnetic induction for the field generated at the contact surface ($\bar{x} = 0$):

$$B_s^* = -\frac{\lambda_1\lambda_2}{p^2(\lambda_1 + \lambda_2)}.$$

Taking into account relations (14), we can transform this map to

$$B_s^* = \frac{1}{p\sqrt{1 + p(\gamma + 1)^2/\gamma}};$$

after reversal [6], we arrive at the following law of magnetic field variation at the sticking surface:

$$\bar{B}_s = \operatorname{erf}\left(\frac{\sqrt{\gamma}\,\bar{t}}{\gamma + 1}\right). \qquad (19)$$

This relation shows that, in the case of "absolute sticking" of contacting surfaces of the flows, the solution obtained for the field is symmetric relative to the magnetic $\nu_m$ and kinematic $\nu$ viscosities (the form of the relation remains unchanged upon the replacement of $\gamma$ by $1/\gamma$). In accordance with this solution, the dimensionless induction of the generated field monotonically tends (as $\bar{t} \longrightarrow \infty$) to the limiting unit level with the asymptotic form

$$\bar{B}_s \approx 1 - O\left(\frac{\exp(-\gamma\bar{t}/(\gamma + 1)^2)}{\sqrt{\bar{t}}}\right).$$

Figure 4 illustrates the variation of the quantity $\bar{B}_s$ as a function of time for different values of parameter $\gamma$ (8).

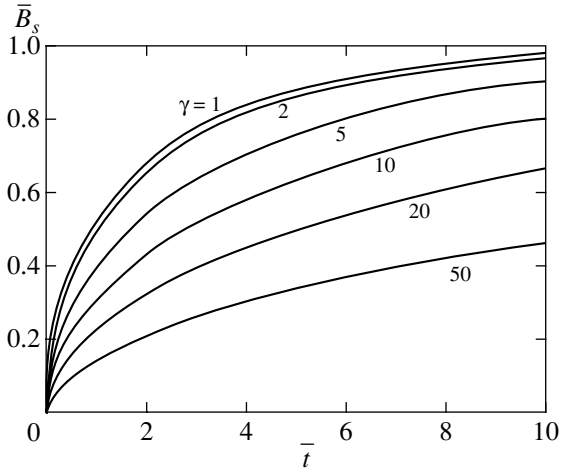


**Fig. 4.** Time variation of the magnetic induction of the longitudinal field at the sticking boundary of the flows.

It should be noted that, in the case of sticking of contacting surfaces, the symmetry relative to the change of $\gamma$ by $1/\gamma$ is also preserved for the law of magnetic field variation in the bulk of the moving medium. This follows from the expression for the map of the given law,

$$B^*(\bar{x}, p) = \frac{1}{\lambda_1^2 - \lambda_2^2}\left[\frac{\exp(\lambda_1\bar{x})}{\lambda_1} - \frac{\exp(\lambda_2\bar{x})}{\lambda_2}\right],$$

in which parameter $\gamma$ appears only through the roots $\lambda_1$ and $\lambda_2$ of the characteristic equation (12) that is invariant to the substitution of $1/\gamma$ for $\gamma$.

The absence of slip between the contacting surfaces of the flows in the case of their sticking must be ensured by the action of corresponding mechanical shear stresses $\tau_s$ at these surfaces. These stresses coincide with viscous shear stresses in the material of the flows at the contact boundary and can be calculated using the formula

$$\tau_s = \rho\nu \left.\frac{\partial v}{\partial x}\right|_{x = 0}.$$

Differentiating the second of maps (13) with respect to the dimensionless coordinate $\bar{x}$ and inverting it for $\bar{x} = 0$, we find that the dimensionless mechanical shear stresses $\bar{\tau}_s$ (divided by the dynamic pressure $\rho v_0^2/2$) ensuring the sticking of contacting surfaces vary according to the law

$$\bar{\tau}_s = \frac{\tau_s}{\rho v_0^2/2} = 2\frac{c_A}{v_0}\sqrt{\frac{\gamma}{\pi\bar{t}}}\exp\left(-\frac{\gamma\bar{t}}{(\gamma + 1)^2}\right).$$

In accordance with this relation, at the initial instant ($\bar{t} = 0$), when the velocity suffers discontinuity at the contact boundary of the flows, the contact shear stresses

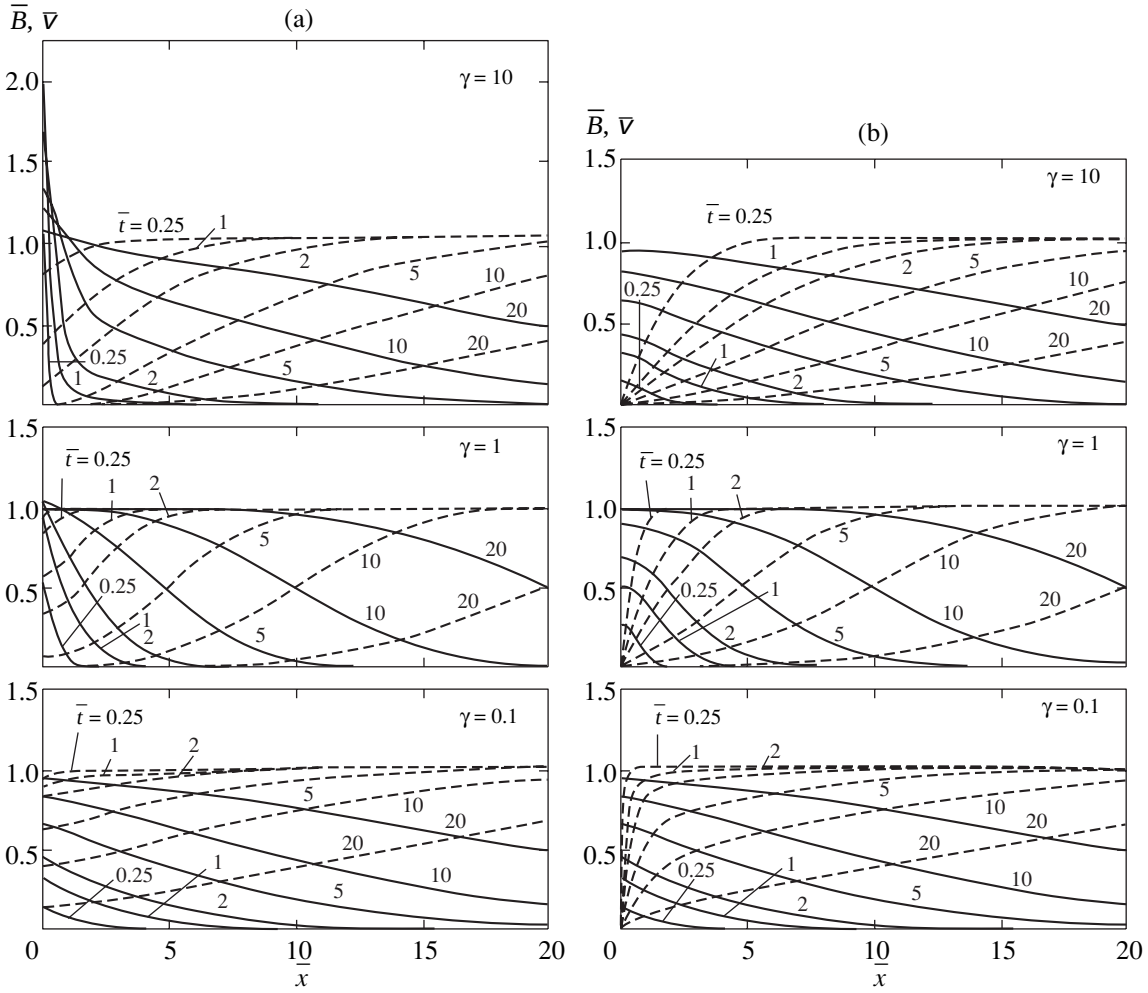


**Fig. 5.** Evolution of the longitudinal magnetic field $\bar{B}$ (solid curves) and the velocity $\bar{v}$ of shearing motion (dashed curves) during (a) free slip and (b) sticking of contact boundaries.

are found to be infinitely large. Subsequently, their values decrease monotonically, tending to zero.

## 4. PROPAGATION OF PERTURBATION REGION FROM THE CONTACT BOUNDARY TO THE BULK OF FLOWING MEDIUM

In order to determine the evolution of the functions $\bar{B}(\bar{x}, \bar{t})$ and $\bar{v}(\bar{x}, \bar{t})$ in the bulk of the moving medium, the system of equations (6) with the boundary conditions (9) and (10) was integrated numerically using the finiteness of the finite-difference methods [8]. The distributions of the induction of the generated magnetic field and the velocity of medium particles in the right half-space at different instants obtained as a result of numerical calculations (see Fig. 1) are presented in Fig. 5a (for free slip of flows) and in Fig. 5b (for "sticking" of contacting surfaces of the flows). It can be seen from Fig. 5 that the generation of the magnetic field and stagnation of the flow materials are wave processes: field and velocity perturbations emerging at the contact boundary gradually propagate to the bulk of the medium. The physical mechanism of the wave process corresponds to an Alfven wave [1] propagating in the medium with dissipation associated with its viscosity and electrical resistance.

The wave nature of the phenomenon is manifested in undistorted form for flows of perfectly conducting materials ($\nu_m = 0$) with zero viscosity ($\nu = 0$). In this case, the system of equations (1) can be reduced to wave equations for functions $B(x, t)$ and $v(x, t)$:

$$\frac{\partial^2 B}{\partial t^2} = c_A^2 \frac{\partial^2 B}{\partial x^2}, \quad \frac{\partial^2 v}{\partial t^2} = c_A^2 \frac{\partial^2 v}{\partial x^2}.$$

The solution of these equations for the right half-space (see Fig. 1) can be presented in the form of an Alfven wave running along the $x$ axis:

$$v = 0, \quad B = v_0 \sqrt{\mu_0 \rho} \quad \text{for} \quad x \le c_A t,$$
$$v = 1, \quad B = 0 \quad \text{for} \quad x > c_A t.$$

In this case, the sticking mode is realized for the flow contact surfaces (their slip is physically impossible for a perfect conductivity of the material since it leads to instantaneous unlimited amplification of the longitudinal field at the contact boundary and the emergence of infinitely large surface currents and, hence, unlimited surface electromagnetic forces tending to level out the velocities of the contacting surfaces).

The front of the Alfven wave is gradually blurred due to dissipative processes, the effect of the boundary conditions (free slip or sticking) being manifested only at a small distance from the contact boundary (approximately, for $\bar{x} \leq 5$; see Fig. 5). In the bulk of the medium, the magnetic induction of the longitudinal field and the velocity of material particles vary identically for both regimes at the boundary. It was mentioned above that, in the absence of slip between the contacting surfaces, the evolution of the field generated by the shear motion does not change upon the substitution of $1/\gamma$ for $\gamma$ (see the curves corresponding to $\gamma = 10$ and 0.1 in Fig. 5b). At a considerable distance from the contact surface, the law of variation of the longitudinal field in the case of free slip of the flows exhibits the same property (see Fig. 5a). As regards the evolution of the velocity of the flows, the rate of stagnation of their material at a large distance from the boundary (for a fixed time scale determined by the product of the kinematic and magnetic viscosities) increases with the parameter $\gamma$.

Irrespective of the conditions of mechanical interaction of contacting surfaces (free slip or sticking) and the intensity $B_0$ of the initial transverse field, the induction of the generated magnetic field attains the steady-state "Alfven" level $B = v_0\sqrt{\mu_0\rho}$ at all particles of the medium at the end of the transient process on account of the second relation from (7), while the motion of particles of the medium ceases. The intensity $B_0$ of the initial magnetic field (which was used for setting the time and space scales) determines the rate of generation of the longitudinal field at the particles of the medium, the dynamics of their stagnation, and the velocity of propagation of the perturbed region to the bulk of the medium. An increase in $B_0$ accelerates these processes.

It should be noted that, in the limiting cases of a medium with a finite electrical conductivity and zero viscosity ($\nu_m \neq 0$, $\nu = 0$) and of a perfectly conducting viscous medium ($\nu \neq 0$, $\nu_m = 0$), only the flow regime with sticking of contact boundaries remains possible from the physical point of view. Using relation (19), we can easily prove that the variation of the longitudinal field at the contact boundary between the flows occurs in accordance with relation $\bar{B}_s = \mathrm{erf}(\sqrt{\bar{t}})$ if the dimensionless time $\bar{t}$ is defined in this relation as $\bar{t} = tc_A^2/\nu_m$ for $\nu = 0$ and $\bar{t} = tc_A^2/\nu$ for $\nu_m = 0$.

## 5. ESTIMATION OF POSSIBLE AMPLIFICATION OF MAGNETIC FIELD DURING HIGH-RATE SHEAR DEFORMATION OF METALS

The mechanism of magnetic field generation at a high velocity of shearing motion of a conducting medium considered above may lead to a significant amplification of the initial field created in it. Let us consider some estimates. In the case of explosive or impact loading of a conducting medium (metal) with a level of developed pressures of $10^{10}$–$10^{11}$ Pa, velocities of the order of $10^3$ m/s are realized [9]. For such an intense loading, we can disregard the effect of strength properties of metals and use hydrodynamic models for describing their behavior. According to the results obtained in [10] and corresponding to high strain rates for metals, the kinematic viscosity of the medium may be estimated at 0.1–1 m$^2$/s. The magnetic viscosity for the electrical conductivity typical of such metals as copper and aluminum amounts to $10^{-2}$–$10^{-1}$ m$^2$/s. Taking into account these estimates, we obtain the value of parameter $\gamma$ (8) in the range 1–10. For such values of $\gamma$, the maximum amplification of the generated field (in the case of free slip of the flows) exceeds insignificantly the "Alfven" level $v_0\sqrt{\mu_0\rho}$ which sets the characteristic value of the induction of the field generated by the shear flow of a conducting medium. For $v_0 \sim 10^3$ m/s, this value for a metallic conductor is of the order of 100 T. The time of amplification of the field to the given level and the dynamics of variation of the thickness of the layer of the material in which the amplification takes place are determined by the induction $B_0$ of the field created initially in the medium. For values of $B_0$ of the order of 10 T, the characteristic time of generation (see Figs. 2 and 4) is estimated at a few dozen microseconds. The size of the region with enhanced field corresponding to this time (see Fig. 5) amounts to a few millimeters.

The conditions for generation of a strong magnetic field as a result of a high-rate shear deformation of a conducting medium, which are close to the one-dimensional model considered above, are created, for example, during the penetration of a plane cumulative jet into a metallic obstacle with a preliminarily created transverse magnetic field in it (Fig. 6). The plane cumulative jet (cumulative "knife") is formed during the explosion of a prolate cumulative charge [9]. The velocity of penetration of a cumulative knife into a metallic obstacle may be as high as several kilometers per second. The amplification of the field due to large shear strains must be observed in a layer of the obstacle material on the lateral surface of the cavern formed in the region of its contact with the cumulative knife. In this region, the particles of the obstacle are involved in motion across the magnetic flux lines by the knife material. Obviously, this model can also be employed for estimating the amplification of the field in the material subjected to shear strain at the surface of the cavern in the case of

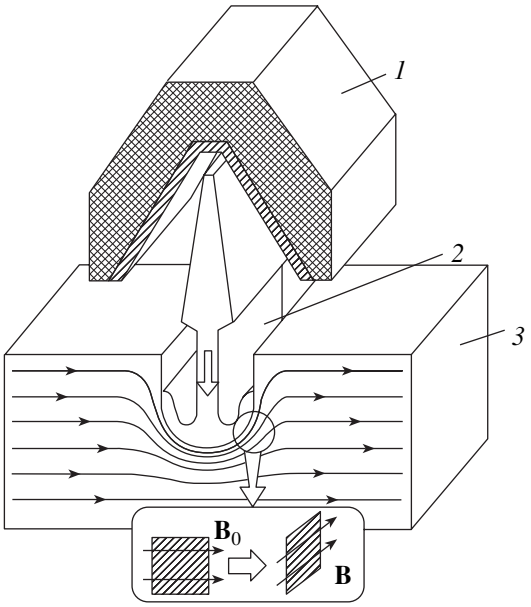


**Fig. 6.** Schematic diagram of amplification of the magnetic field at the surface of a cavern formed in a conducting obstacle during the penetration of a plane cumulative jet into it: prolate cumulative charge (*1*), cumulative "knife" (*2*), conducting obstacle with preliminarily created transverse magnetic field (*3*).

penetration of a high-speed axisymmetric striker in a "magnetized" conducting obstacle if the thickness of the generation layer remains smaller than the transverse size of the striker, so that the effect of non-one-dimensionality of the resulting magnetohydrodynamic flow can be neglected.

It is well known that the magnetic field strength at a level of 100 T, which can be attained in accordance with the above estimates in the case of high-rate shear strain of a conducting medium as a result of its explosive or shock loading, was exceeded long ago [11]. For example, in experiments on generation of ultrastrong magnetic fields using magnetocumulative generators and employing the principle of compression of the initial field by a conducting envelope collapsing under the action of pulsed loading, the field intensity within the envelope at the final stages of its compression may considerably exceed 100 T. In our opinion, the "deformation mechanism" of magnetic field generation in preliminarily "magnetized" rapidly deformed conductors may be interesting, above all, in connection with possible manifestations of strong accompanying mechanical, thermal, and electromagnetic effects [11, 12]. The electromagnetic forces emerging in a conducting material during "pumping" of a megagauss magnetic field and the pressure created by its Joule heating are comparable with the load applied to the materials during detonation of explosives and may strongly affect the deformation of the medium. For example, it is shown in [2] that the penetration of a high-speed striker into a conducting obstacle with a transverse magnetic field may lead to the collapse of the cavern formed by the striker due to the explosive scattering of its surface layers in which intense deformation of the material leads to strong enhancement of the field. Simultaneously, the premises for a decrease in the piercing action of the striker are created. Thus, the effect of magnetic field amplification in a conducting medium deformed at a high rate can be used for controlling the mechanisms of explosive and shock processes.

## REFERENCES

1. L. D. Landau and E. M. Lifshitz, *Course of Theoretical Physics*, Vol. 8: *Electrodynamics of Continuous Media* (Nauka, Moscow, 1982; Pergamon, New York, 1984).
2. S. V. Fedorov, Prikl. Mekh. Tekh. Fiz. **42** (3), 15 (2001).
3. E. I. Bichenkov, Prikl. Mekh. Tekh. Fiz. **41** (5), 32 (2000).
4. G. W. Sutton and A. Sherman, *Engineering Magnetohydrodynamics* (McGraw-Hill, New York, 1965; Mir, Moscow, 1968).
5. M. A. Lavrent'ev and B. V. Shabat, *Methods of the Theory of Functions of a Complex Variable* (Nauka, Moscow, 1987).
6. V. A. Ditkin and A. P. Prudnikov, *Reference Book on Operational Calculus* (Vysshaya Shkola, Moscow, 1965).
7. N. N. Lebedev, *Special Functions and Their Applications* (Fizmatgiz, Moscow, 1963; Prentice-Hall, Englewood Cliffs, 1965).
8. S. K. Godunov and V. S. Ryaben'kiĭ, *Difference Schemes* (Nauka, Moscow, 1977).
9. F. A. Baum, L. P. Orlenko, K. P. Stanyukovich, *et al.*, *Explosion Physics* (Nauka, Moscow, 1975).
10. N. I. Matyushkin and Yu. A. Trishin, Prikl. Mekh. Tekh. Fiz. **14** (3), 99 (1978).
11. E. I. Bichenkov and G. A. Shvetsov, Prikl. Mekh. Tekh. Fiz. **38** (4), 90 (1997).
12. S. V. Fedorov, A. V. Babkin, S. V. Ladov, *et al.*, Fiz. Goreniya Vzryva **36** (6), 126 (2000).

*Translated by N. Wadhwa*

*Journal of Experimental and Theoretical Physics, Vol. 95, No. 2, 2002, pp. 275–281.*
*Translated from Zhurnal Éksperimental'noĭ i Teoreticheskoĭ Fiziki, Vol. 122, No. 2, 2002, pp. 320–327.*


**FLUIDS**

# The Magneto-Optical Properties of an Ensemble of Ellipsoidal Dielectric Particles in a Magnetic Fluid

**A. F. Pshenichnikov* and P. A. Sosnin**

*Institute of Continuum Mechanics, Ural Division, Russian Academy of Sciences, Perm, 614013 Russia*
**e-mail: pshenichnikov@icmm.ru*

Received January 29, 2002

**Abstract**—The paper deals with an analytical investigation of magnetic birefringence in a dilute suspension of ellipsoidal dielectric particles in a magnetic fluid. The major axes of particles tend to line up along the field because of the difference in the "demagnetizing" coefficients along and across the ellipsoid axis, which brings about a multiple increase in the optical anisotropy of the system. Formulas are derived which describe the field dependence of magnetization of the system and of the difference between the refractive indices for ordinary and extraordinary rays. It is demonstrated that, given the bulk concentration of impurity particles of several percent, the magnetization of the system varies insignificantly, while the birefringence signal may increase by two orders of magnitude. *© 2002 MAIK "Nauka/Interperiodica".*

## 1. INTRODUCTION

In the absence of a magnetic field, magnetic fluids (liquid ferrocolloids), which represent stable colloid solutions of one-domain ferroparticles with a characteristic size of about 10 nm, are optically homogeneous. However, under the effect of an external field, they assume the properties of a uniaxial crystal with a very strong (compared with common liquids) optical anisotropy. So, in the case of magnetite colloids with a bulk concentration of particles of several percent, the Cotton–Mouton constant proves to be six–seven orders of magnitude higher than in liquid paramagnetics. It is the anomalously high value of this constant that is mainly responsible for increased interest of researchers in birefringence (BR) in magnetic fluids. It was subjected to a number of theoretical and experimental studies [1–12]. By now, the generally recognized viewpoint is that according to which the BR in magnetic fluids is caused by the anisometricity of particles, i.e., minor deviation of the shape of colloid particles from spherical [1]. The preferred orientation of the major axes of particles along the magnetic field leads to the emergence of a difference between the refractive indices of rays polarized along and across the field and makes the colloid solution optically anisotropic.

In spite of the anomalously high value of the Cotton–Mouton constant, the integral effect of BR in magnetic fluids turns out to be fairly weak, because the experiments in BR involve the use of either dilute solutions or thin (tenths and hundredths of a millimeter) layers of magnetic fluid. In view of this, it is of interest to investigate the problem of intensification of this effect. At first glance, it may appear that the problem is solved by a simple increase in the average size of colloid particles. Indeed, in weak fields, the difference between the refractive indices increases with the particle size as the cube of the particle volume [12]; therefore, even a doubling of the particle diameter may amplify the BR signal by two–three orders of magnitude. The problem, however, is that even a much smaller increase in the particle size brings about the formation of aggregates and the thermodynamic instability of colloid. The aggregation parameter $\lambda$ (i.e., the ratio of the energy of dipole–dipole interactions to the heat energy) increases rapidly with the particle size, and, at $\lambda > 3$, a colloid solution separates into weakly and strongly concentrated phases [13–17]. So-called drop aggregates are formed in the solution, i.e., droplets of condensed phase with the characteristic size of several micrometers, which are easily observable in a standard optical microscope [15, 18, 19]. The emergence of drop aggregates is analogous to the formation of fog in moist air. It disturbs the homogeneity of the solution on a mesoscopic level and causes a strong diffraction scattering of light. The average size of one-domain particles of about 10 nm, mentioned above, is optimal in the sense that it provides both for the thermodynamic stability of magnetic fluid and for a fairly high magnetic permeability. In this paper, we treat another method of raising the optical anisotropy of a colloid, that of introducing into the colloid fairly large (compared with one-domain) nonmagnetic ellipsoidal particles. The major axes of impurity particles tend to line up along the magnetic field because of the difference in the "demagnetizing" coefficients along and across the ellipsoid axis, which brings about an increase in the optical anisotropy of the system. Investigated below are the magnetic and optical properties of such a binary colloid solution.

In the general case, the properties of the system being investigated are defined by the interaction of one-domain particles with an external magnetic field, by the

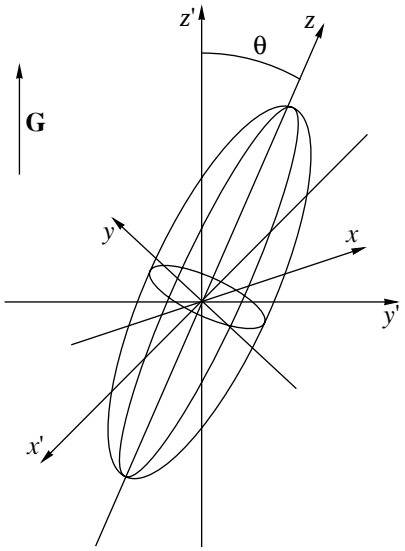


**Fig. 1.** An ellipsoidal particle in an external field. Coordinate systems.

number and shape of impurity particles, by interparticle interactions, and by the intensity of Brownian motion. The problem is solved in a "one-particle" approximation, within which the interactions between impurity particles are ignored. A magnetic fluid is treated as a continuum of a known magnetic susceptibility. In doing so, the dipole–dipole interactions of magnetic particles are included indirectly and to the extent to which they affect the magnetic susceptibility of the carrier (magnetic) fluid. Naturally, the impurity particles will also interact with one another; however, it is hoped that, given a rather low concentration of these particles, the interaction energy will be much lower than in the case of one-domain particles. According to the data of [20, 21], the one-particle approximation describes quite adequately the properties of magnetic fluids if the volume fraction of one-domain particles in a colloid solution does not exceed several percent. A similar restriction must be placed on the "binary" system treated here, but with respect to nonmagnetic impurity particles.

## 2. MAGNETIC PROPERTIES

Let nonmagnetic impurity particles shaped as prolate ellipsoids of revolution with semiaxes $b$, $b$, $a$ ($a > b$) be uniformly distributed in a homogeneous magnetic fluid. We will separate out one such particle and find the magnetic field within and in the neighborhood of the particle. We will place at the center of this particle the origin of a local system of coordinates $xyz$ so that the axis $z$ will be directed along the principal axis of symmetry of the particle (Fig. 1). The external magnetic field $\mathbf{G} = (G_x, G_y, G_z)$ is uniform. The solution of the magnetostatic problem for an ellipsoidal cavity in a uniform (with respect to susceptibility) magnetic is well known (see, for example, [22, 23]). Here, we will write only the results that are of importance for further treatment (in what follows, formulas (1)–(4)) and will relate them to the case of linear correlation between the induction $\mathbf{B}$ and the intensity $\mathbf{H}$. The Maxwell equations $\mathrm{curl}\mathbf{H} = 0$, $\mathrm{div}\mathbf{B} = 0$ lead to the boundary-value problem for magnetostatic potential $\Delta\phi = 0$ with standard boundary conditions, i.e., the continuity of the normal components of induction and the tangential components of intensity on the particle surface. In addition, the magnetostatic potential at long distances from the particle must coincide with the uniform field potential $\mathbf{G}$. The solution for the potential is conveniently written in the coordinates $\eta$, $\psi$, $\gamma$ of a prolate spheroid, related to Cartesian coordinates $x$, $y$, $z$ of the local system of coordinates by

$$x = c\sinh\eta\sin\psi\cos\gamma,$$
$$y = c\sinh\eta\sin\psi\sin\gamma,$$
$$z = \cosh\eta\cos\psi,$$

where $c^2 = a^2 - b^2$. This solution has the following form for regions inside and outside of the particle, respectively,

$$\begin{aligned}\phi_{\text{int}} &= -cP_1^1(\cosh\eta)P_1^1(\cos\psi)(H_1\cos\gamma + H_2\sin\gamma)\\ &\quad - cH_3P_1(\cosh\eta)P_1(\cos\psi),\\ \phi_{\text{out}} &= -cP_1^1(\cosh\eta)P_1^1(\cos\psi)\\ &\quad\times(G_x\cos\gamma + G_y\sin\gamma)\\ &\quad - cG_zP_1(\cosh\eta)P_1(\cos\psi)\\ &\quad + \frac{1}{c^2}Q_1^1(\cosh\eta)P_1^1(\cos\psi)(M_1\cos\gamma + M_2\sin\gamma)\\ &\quad + \frac{M_3}{c^2}Q_1(\cosh\eta)P_1(\cos\psi).\end{aligned} \tag{1}$$

Here, $P_l^m$ and $Q_l^m$ are Legendre functions of the first and second kind, respectively; the constants $H_1$, $H_2$, $H_3$, $M_1$, $M_2$, and $M_3$ are expressed in terms of the components of the external field $\mathbf{G}$,

$$\begin{aligned}H_1 &= \frac{2\mu G_x}{\mu_t}, \quad H_2 = \frac{2\mu G_y}{\mu_t}, \quad H_3 = \frac{2\mu G_z}{\mu_n},\\ M_1 &= \frac{3V(\mu-1)}{4\pi\mu_t}G_x, \quad M_2 = \frac{3V(\mu-1)}{4\pi\mu_t}G_y,\\ M_3 &= -\frac{3V(\mu-1)}{4\pi\mu_n}G_z,\end{aligned} \tag{2}$$

where $V = 4\pi ab^2/3$ is the particle volume,

$$\mu_t = \mu + 1 + \kappa(\mu - 1), \quad \mu_n = \mu - \kappa(\mu - 1), \tag{3}$$

$\mu$ is the magnetic permeability of the carrier liquid, and $\kappa$ is the demagnetizing factor along the major axis of an ellipsoidal particle with the eccentricity

$$e = \sqrt{1 - \frac{b^2}{a^2}}.$$

According to [22], the demagnetizing factor of a prolate ellipsoid of revolution is

$$\kappa = \frac{1 - e^2}{e^2}\left(\frac{1}{2e}\ln\frac{1+e}{1-e} - 1\right). \quad (4)$$

It follows from Eqs. (1) and (2) that the magnetic field within a particle is uniform, and the constants $H_1$, $H_2$, and $H_3$ are nothing but the components of this film in local coordinates. As to the field **H** induced by a nonmagnetic particle in the external medium in addition to **G**, it is equivalent to a field that would be produced by a uniformly magnetized ("diamagnetic") particle with the total magnetic moment of

$$\mathbf{m} = -\frac{V\mu(\mu-1)}{2\pi\mu_t}\left(G_x, G_y, \frac{\mu_t}{2\mu_n}G_z\right), \quad (5)$$

determined relative to the local coordinates. This expression enables one to estimate the energy $W$ of interaction between impurity particles and the respective dimensionless parameter defining the degree to which these interactions affect the properties of the system. It is apparent that the maximal effect is to be expected in magnetic fluids with a high permeability ($\mu \gg 1$). In this case,

$$\lambda = \frac{W}{kT} \approx \frac{\mu\rho V G^2}{4\pi^2 kT},$$

where $\rho = Vn$ is the volume fraction of impurity particles in a colloid solutions and $n$ is the particle number density. Under conditions typical of laboratory experiments, $\mu \le 10$, $\rho \approx 10^{-2}$, $G \le 10$ Oe, and $\lambda \le 10^{-2}$. Therefore, the interaction between impurity particles turns out to be insignificant, and the one-particle approximation employed by us is quite justified.

Expression (5) further helps to find the correction to the system magnetization, associated with the presence of impurity particles,

$$\Delta M = \langle m_\parallel \rangle n,$$

where $m_\parallel$ is the projection of the moment given by Eq. (5) on the external field direction. It is apparent that this addition is negative. In order to calculate this addition, we will introduce the spherical angles $\theta$ and $\varphi$ which define the direction of the particle major axis relative to a laboratory system of coordinates with the axis $z'$ directed along the field **G**. In this case, the matrix of transition from laboratory Cartesian to local coordinates related to the particle will have the form

$$\alpha = \begin{pmatrix} \cos\theta\cos\varphi & \cos\theta\sin\varphi & -\sin\theta \\ -\sin\varphi & \cos\varphi & 0 \\ \sin\theta\cos\varphi & \sin\theta\sin\varphi & \cos\theta \end{pmatrix}. \quad (6)$$

By virtue of orthogonality of transformation, the inverse matrix will coincide with the transposed one. The sought correction to magnetization will be

$$\Delta\mathbf{M} = \left(0, 0, -\frac{\rho\mu(\mu-1)(4\mu_n + \mu_t)}{12\pi\mu_n\mu_t} \times G\left(1 - \frac{2(2\mu_n - \mu_t)}{4\mu_n + \mu_t}S\right)\right), \quad (7)$$

where the scalar parameter of the order of

$$S = \frac{3\langle\cos^2\theta\rangle - 1}{2}$$

is the measure of ordering of the major axes of impurity particles. Note that expression (5) for the effective magnetic moment may also be derived from a variation of free energy associated with the introduction of an ellipsoidal particle into a magnetic fluid. The calculation procedure is similar to that employed in [22] for liquid dielectrics and spherical particles.

In the limit of weak fields, the distribution of the major axes of impurity particles is isotropic, and $\langle\cos^2\theta\rangle = 1/3$. From this, one can readily find the correction to the initial susceptibility of a magnetic fluid alloyed with ellipsoidal particles,

$$\Delta\chi = -\frac{\rho\mu(\mu-1)(4\mu_n + \mu_t)}{12\pi\mu_n\mu_t}. \quad (8)$$

In the case of spherical particles ($\kappa = 1/3$), formula (8) coincides with the known expression for the permittivity of a mixture [22]. For ellipsoidal particles, the correction $\Delta\chi$ to susceptibility increases in magnitude; however, its dependence on eccentricity turns out to be very weak and shows up only in concentrated magnetic fluids with a high permeability. In transition from spherical to needle-shaped particles ($\kappa \longrightarrow 0$), $\Delta\chi$ increases by approximately 10%. By and large, the relative decrease of the initial susceptibility of a system due to impurity particles is of the order of

$$\frac{4\pi\Delta\chi}{\mu - 1} \approx \frac{3\rho\mu}{2\mu + 1}$$

and, in the case of a low concentration of impurity particles, is small compared with unity. As was mentioned above, within the one-particle approximation, the volume fraction $\rho$ of impurity particles is taken to be a small quantity.

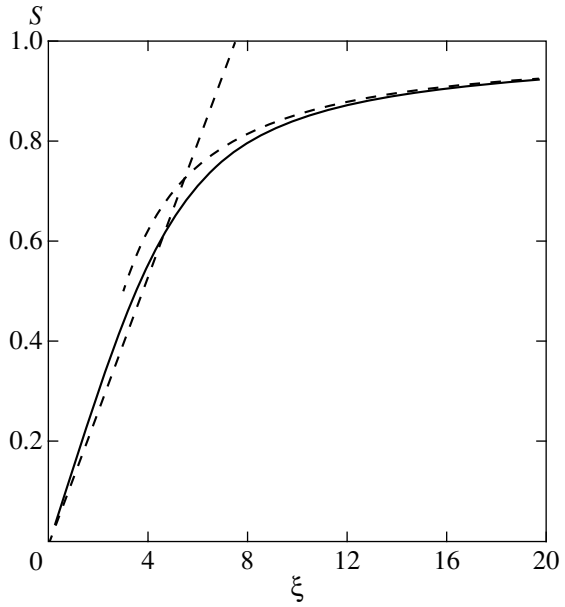


**Fig. 2.** The order parameter as a function of external field. The dashed curves correspond to the asymptotic expressions given by Eqs. (14) and (15) within weak and strong fields, respectively.

The calculation of the magnetization of a system that is valid for an arbitrary field calls for the computation of the potential energy of a particle. This may be done most simply by treating a virtual turn of the particle through a small angle $\delta\boldsymbol{\omega}$. The work performed by the field during such a turn must be compensated by a decrease in the potential energy $U$ of the particle,

$$\delta U = \mathbf{K}\delta\boldsymbol{\omega},$$

where $\mathbf{K}$ is the total mechanical moment acting on the particle. The mechanical moment is calculated in terms of the stress tensor $\sigma_{lk}$ in a magnetizing medium [22], which is written below on the assumption of linear correlation between the susceptibility of magnetic fluid and the magnetic phase concentration,

$$K_i = \oint e_{ijl} r_j \sigma_{lk} n_k ds, \quad \sigma_{ik} = -\frac{H^2}{8\pi}\delta_{ik} + \frac{\mu H_i H_k}{4\pi}. \quad (9)$$

Here, $e_{ijl}$ is the Levi-Civita antisymmetric pseudotensor, and $\mathbf{n}$ is the unit vector of external normal. The integration of local moments over the outer surface of an ellipsoidal particle with a major axis in the $xz$ plane results in the following expression for the components of the total torque:

$$K_x = 0,$$

$$K_y = -\frac{V}{8\pi}\frac{\mu(\mu-1)^2(1-3\kappa)}{\mu_n\mu_t}G^2\sin(2\theta), \quad (10)$$

$$K_z = 0.$$

We rotate the particle about the axis $y$ and integrate Eqs. (10) with respect to the polar angle to find the sought expression for the potential energy of impurity particle,

$$U = U_0 - \frac{V}{8\pi}\frac{\mu(\mu-1)^2(1-3\kappa)}{\mu_n\mu_t}G^2\cos^2\theta.$$

Here, $U_0$ is the part of the potential energy that is independent of the particle orientation relative to the external field. It is apparent that, for spherical particles, the orientation addition $\Delta U = U - U_0$ to energy is zero.

We will further introduce into treatment the equilibrium one-particle distribution function for the orientations of the major axes of impurity particles,

$$f(\cos\theta) = C\exp\left(-\frac{\Delta U}{kT}\right) = C\exp(\xi\cos^2\theta), \quad (11)$$

where $\xi$ is the ratio of the characteristic energy of interaction of an impurity particle with external field to the heat energy,

$$\xi = \frac{V\mu(\mu-1)^2(1-3\kappa)G^2}{8\pi\mu_n\mu_t kT}. \quad (12)$$

This parameter may be treated as an analog of the Langevin parameter for supermagnetic particles; however, unlike the latter parameter, the quantity $\xi$ increases with the field by a quadratic, rather than linear, law. The normalization constant $C$ and the order parameter $S(\xi)$ are expressed in terms of the Dawson integrals,

$$C^{-1} = \int_0^1 \exp(\xi x^2)dx,$$
$$S(\xi) = \frac{1}{2}\left(\frac{3}{C}\int_0^1 x^2\exp(\xi x^2)dx - 1\right). \quad (13)$$

Figure 2 gives the order parameter $S$ as a function of external field. In weak fields ($\xi \ll 1$), the distribution of the major axes of particles is close to isotropic, and the parameter $S$ increases with the field intensity by the quadratic law

$$S \approx \frac{2\xi}{15}. \quad (14)$$

One can see in the figure that formula (14) derived by expanding (13) into a power series in $\xi$ approximates well the dependence $S(\xi)$ up to $\xi \approx 1$. In strong fields ($\xi \gg 1$), the order parameter asymptotically approaches unity,

$$S \approx 1 - \frac{1.5}{\xi}. \quad (15)$$

One can readily see from Eqs. (7), (14), and (15) that the relative correction to the magnetization of the sys-

tem, associated with the introduction of impurity particles into a colloid, decreases as the field increases.

A significant orientation of ellipsoidal particles occurs in fields for which the orientation part of energy is comparable with the thermal part: $\xi \approx 1$. We will estimate the magnitude of these fields in application to ellipsoidal particles with the semiaxis ratio of 1/3 ($\kappa \approx 0.1$) and the volume of the order of $10^{-15}$ cm$^3$. The characteristic size of such ellipsoids is an order of magnitude higher than the characteristic size of one-domain magnetic particles; we believe that this provides reason enough for the foregoing continuum approximation of magnetic fluid. In view of the fact that the initial permeability of concentrated magnetic fluids $\mu \approx 10$ and the temperature is close to room temperature, we have $G \approx 10$ Oe. Such fields may be referred to as weak in the sense that they correspond to the linear segment of the magnetization curve for ferrocolloids [20]. This means that our assumption of the linear correlation between the field intensity and induction is well valid under real conditions.

An increase in the size of impurity particles results in an increased parameter $\xi$ and in a higher sensitivity of the system to the external field. However, this increase has an obvious limit associated with the formation of the Boltzmann distribution of particles over height and with the sedimentation stratification of the system in the gravitational field. In any case, in order to prevent a strong stratification of the system, the vertical dimension of a cell with colloid solution must be significantly less than the characteristic thickness $h^*$ of the "atmosphere" of impurity particles $h^* = kT/V\Delta\rho^* g$, where $\Delta\rho^*$ is the density difference between the magnetic fluid and the particle. With a fixed particle volume, a reduction of $\Delta\rho^*$ is the only way of suppressing the sedimentation effects. For a magnetic fluid based on liquid hydrocarbons and polymer impurity particles, a fairly small density difference may be selected ($\Delta\rho^* \approx 0.1$ g/cm$^3$). In this case, given the above-identified particle volume $V \approx 10^{-15}$ cm$^3$, we have $h^* \approx 4$ mm.

## 3. BIREFRINGENCE

We will follow Skibin *et al.* [1] and examine the propagation of a plane electromagnetic wave through an infinite volume of magnetic fluid in which nonmagnetic ellipsoidal particles are distributed uniformly. We take the carrier medium (magnetic fluid) and impurity particles to be nonconducting media. In the general case, magnetic fluids are characterized by a strong absorption of light; however, in the red and near infrared spectral regions (with the wavelength ranging from 0.6 to 1.2 μm), the absorption is very weak [24]. Below, we will keep this particular spectral region in mind: the effects associated with light absorption are ignored. In addition, for the above-identified frequency range, the magnetic permeability of the suspension of particles may, with good accuracy, be assumed to be unity. Because the linear dimensions of particles are small compared with the wavelength, one can assume that each one of these particles is in a uniform electric field. We will express the electric field intensity $\mathbf{E}^{(i)}$ and induction $\mathbf{D}^{(i)}$ within a particle in terms of the external field $\mathbf{E}$, using the known relations [22] and the constitutive equation $\mathbf{D}^{(i)} = \varepsilon_1 \mathbf{E}^{(i)}$,

$$\begin{aligned}
\varepsilon_0 E_x^{(i)} + 0.5(1-\kappa)(D_x^{(i)} - \varepsilon_1 E_x^{(i)}) &= \varepsilon_0 E_x, \\
\varepsilon_0 E_y^{(i)} + 0.5(1-\kappa)(D_y^{(i)} - \varepsilon_1 E_y^{(i)}) &= \varepsilon_0 E_y, \\
\varepsilon_0 E_z^{(i)} + \kappa(D_z^{(i)} - \varepsilon_1 E_z^{(i)}) &= \varepsilon_0 E_z.
\end{aligned} \tag{16}$$

Note that the electro- and magnetostatic problems are fully equivalent, and the coefficients of depolarization along and across the major axis of the ellipsoid coincide with the respective demagnetizing coefficients (see, for example, formula (4)). The method of calculating the permittivity of a suspension suggested by Landau and Lifshits [22] and used by Skibin *et al.* [1] for a magnetic fluid is valid in our case as well. The permittivity $\varepsilon$ of a dilute suspension is defined by the correlations between the fields of electric field induction $\mathbf{D}$ and intensity $\mathbf{E}$, averaged over a volume whose size is much larger than the size of impurity particle,

$$\langle D_k \rangle = \varepsilon_{kl} \langle E_l \rangle.$$

In the integral

$$\frac{1}{V}\int (D_k - \varepsilon_0 E_k) dV \equiv \langle D_k \rangle - \varepsilon_0 \langle E_k \rangle,$$

taken over a volume containing $N$ impurity particles, the integrand is other than zero only within the impurity particles (the surrounding medium is taken to be continuous). Therefore, the given integral must be proportional to the number of particles $N$ and (because the field within each particle is uniform) equal to

$$\langle D_k \rangle - \varepsilon_0 \langle E_k \rangle = \rho(\varepsilon_1 - \varepsilon_0)\langle E_k^{(i)} \rangle,$$

where $\langle \mathbf{E}^{(i)} \rangle$ is the mean field acting inside the impurity particles. We average the fields $E_k^{(i)}$ defined by relations (16) with the distribution function given by Eq. (11) to find the principal values of the permittivity tensor of the suspension,

$$\begin{aligned}
\varepsilon_\perp &= \varepsilon_0 \\
&\times \left\{ 1 + \frac{\rho\beta}{3}\left[ 1 + \frac{(\varepsilon_1 - \varepsilon_0)(3\kappa - 1)}{6\varepsilon_0 + (\varepsilon_1 - \varepsilon_0)(1 + 3\kappa)} S \right] \right\}, \\
\varepsilon_\parallel &= \varepsilon_0 \\
&\times \left\{ 1 + \frac{\rho\beta}{3}\left[ 1 - \frac{2(\varepsilon_1 - \varepsilon_0)(3\kappa - 1)}{6\varepsilon_0 + (\varepsilon_1 - \varepsilon_0)(1 + 3\kappa)} S \right] \right\}, \\
\beta &= \frac{(\varepsilon_1 - \varepsilon_0)[6\varepsilon_0 + (\varepsilon_1 - \varepsilon_0)(1 + 3\kappa)]}{3[\varepsilon_0 + \kappa(\varepsilon_1 - \varepsilon_0)][2\varepsilon_0 + (\varepsilon_1 - \varepsilon_0)(1 - \kappa)]}.
\end{aligned} \tag{17}$$

Here, $\varepsilon_\parallel$ and $\varepsilon_\perp$ denote the permittivity for a light wave polarized along and normal to the direction of the external magnetic field, respectively. Within the terms linear with respect to the concentration $\rho$ of the impurity particles, the difference between the respective refractive indices will be

$$\Delta n = n_\parallel - n_\perp = \frac{\rho S(\xi)}{2} \times \frac{(\varepsilon_1 - \varepsilon_0)^2 (1 - 3\kappa)\sqrt{\varepsilon_0}}{[\varepsilon_0 + \kappa(\varepsilon_1 - \varepsilon_0)][2\varepsilon_0 + (\varepsilon_1 - \varepsilon_0)(1 - \kappa)]}. \quad (18)$$

The general structure of formula (18) is close to that of formulas describing the birefringence in magnetic fluids [1, 7]. However, the difference is that, unlike one-domain magnetic particles, the impurity particles have no intrinsic magnetic moment. In magnetic fluids, the degree of ordering of the major axes of one-domain ellipsoidal particles is defined both by the external field and by the energy of magnetic anisotropy of a particle. The major axis of ellipsoid fluctuates relative to the magnetic moment if the energy of magnetic anisotropy is low or comparable with the heat energy. The induced "diamagnetic" moment of impurity particles is defined by the external field intensity, by the particle size and orientation, and by the properties of the surrounding medium, i.e., magnetic fluid. As a result of these differences, the field dependence of the signal in two cases being treated is described by different, though qualitatively similar, functions. In strong fields, a signal associated with impurity particles reaches saturation much faster than a signal associated with magnetic particles. In weak fields, the difference between refractive indices $\Delta n$ for a binary system increases with the field intensity by a quadratic law as in the case of magnetic fluids (see also formulas (12) and (14)); however, the characteristic magnitude of this difference is of a different order.

We will estimate the magnitude of $\Delta n$. One can see in formula (18) that this magnitude depends very strongly on the difference between permittivities $\Delta\varepsilon = \varepsilon_1 - \varepsilon_0$, i.e., on the choice of magnetic fluid and material of impurity particles. The permittivity $\varepsilon_0$ of magnetite-based magnetic fluids in the region of optical frequencies increases from 2.2 to 2.6 as the solid phase concentration increases [24]. The permittivity $\varepsilon_1$ of an impurity particle is defined by its material and varies from 2.2 for some polymers to 7.0 for mica and devitrified glass. For estimation, we take the values of $\Delta\varepsilon = 2$ and $G = 10$ Oe to derive $\Delta n \approx 3 \times 10^{-4}$ for a suspension with the volume fraction of particles $\rho = 0.01$. This value is two orders of magnitude higher than that which may be found from experiments in birefringence with typical magnetic fluids on the basis of magnetite and liquid hydrocarbons [12].

## 4. CONCLUSION

We have investigated the magneto-optical properties of a binary colloid solution, an ensemble of ellipsoidal dielectric particles suspended in a magnetic fluid. Unlike one-domain magnetic particles, the impurity particles have no intrinsic magnetic moment. Their induced "diamagnetic" moment is defined by the particle size, by the parameters of the surrounding medium (magnetic fluid), and by the internal field intensity. The external magnetic field has an orienting effect on the impurity particles because of the difference in the values of the longitudinal and transverse "demagnetizing" coefficients; it is this effect that brings about an increase in the optical anisotropy. The problem is solved in a one-particle approximation: the bulk concentration of impurity particles is low (of the order of $10^{-2}$); therefore, the effects associated with interparticle interactions are ignored. A magnetic fluid is treated as a continuum of a known magnetic susceptibility. The dipole–dipole interactions of magnetic particles are included indirectly and to the degree to which they affect the magnetic susceptibility of the carrier (magnetic) fluid. Within the assumptions made, formulas have been derived which describe the field dependence of magnetization of the system and of the difference of the refractive indices for ordinary and extraordinary rays. The main result of this study has been the demonstration of a multiple increase in the optical anisotropy of the system owing to impurity particles. Given the bulk concentration of impurity particles of several percent, the magnetization of the system varies insignificantly, while the birefringence signal in weak fields may increase by two orders of magnitude.

We are not aware of any attempts at synthesizing systems whose properties are similar to those of the binary colloid solution investigated by us. It is evidently a fairly serious problem associated with the choice of material of particles and with the technology of their preparation. In our opinion, impurity particles could be provided by rodlike antiferromagnetic goethite ($\alpha$-FeOOH) particles. Aqueous suspensions of such particles were recently investigated by Coey *et al.* [25] and Lemaire *et al.* [26]. In particular, Lemaire *et al.* [26] obtained a stable suspension of particles with an average length of 150 nm, width of 25 nm, and thickness of about 10 nm. In zero field, a transition to the nematic phase was observed in the suspension at $\rho = 0.085$. At lower concentrations, the suspension was optically isotropic. An induced anisotropy was observed in fields of the order of $10^2$ Oe and higher. Therefore, the range of concentrations and fields corresponding to an isotropic suspension of goethite particles agrees well with the range of validity of the formulas derived by us. As to the choice of stabilizer that would preclude the coagulation of particles in magnetic colloids, this stabilizer must apparently be the same for both one-domain and impurity particles. For liquid hydrocarbon-based

ferrocolloids, such a stabilizer is usually provided by oleic acid.

## ACKNOWLEDGMENTS

This study was supported by the Russian Foundation for Basic Research (project 01-02-17839) and by the Civil Research and Development Foundation for the CIS countries (CRDF, grant no. PE-009-0).

## REFERENCES

1. Yu. N. Skibin, V. V. Chekanov, and Yu. L. Raĭkher, Zh. Éksp. Teor. Fiz. **22**, 949 (1977) [Sov. Phys. JETP **45**, 496 (1977)].
2. C. F. Hayes and S. R. Hwang, J. Colloid Interface Sci. **60**, 443 (1977).
3. P. C. Sholten, IEEE Trans. Magn. **16**, 221 (1980).
4. S. Taketomi, Jpn. J. Appl. Phys. **22**, 1137 (1983).
5. J.-C. Bacri, R. Perzynski, D. Salin, and J. Servais, J. Phys. (Paris) **48**, 1385 (1987).
6. Yu. L. Raĭkher and Yu. N. Skibin, Dokl. Akad. Nauk SSSR **302**, 1088 (1988) [Sov. Phys. Dokl. **33**, 746 (1988)].
7. É. Ya. Blum, M. M. Maĭorov, and A. O. Tsebers, *Magnetic Liquids* (Zinatne, Riga, 1989).
8. S. Taketomi, N. Inaba, H. Takahashi, and Y. Miyajima, J. Phys. Soc. Jpn. **59**, 3077 (1990).
9. Y. L. Raikher and V. I. Stepanov, Europhys. Lett. **32**, 589 (1995).
10. E. Hasmonay, J. Depeyrot, M. H. Sousa, *et al.*, J. Magn. Magn. Mater. **201**, 195 (1999).
11. B. Payet, F. Donatini, and G. Noyel, J. Magn. Magn. Mater. **201**, 207 (1999).
12. V. M. Buzmakov and A. F. Pshenichnikov, Kolloidn. Zh. **63**, 305 (2001).
13. O. A. Tsebers, Magn. Gidrodin., No. 2, 42 (1982).
14. K. I. Morozov, Izv. Akad. Nauk SSSR, Ser. Fiz. **51**, 1073 (1987).
15. A. F. Pshenichnikov and I. Yu. Shurubor, Izv. Akad. Nauk SSSR, Ser. Fiz. **51**, 1081 (1987).
16. Yu. A. Buevich and A. O. Ivanov, Kolloidn. Zh. **53**, 1007 (1991).
17. A. F. Pshenichnikov and V. V. Mekhonoshin, Pis'ma Zh. Éksp. Teor. Fiz. **72**, 261 (2000) [JETP Lett. **72**, 182 (2000)].
18. E. E. Bibik and I. S. Lavrov, Kolloidn. Zh. **32**, 483 (1970).
19. E. A. Peterson and D. A. Krueger, J. Colloid Interface Sci. **62**, 24 (1977).
20. A. F. Pshenichnikov, J. Magn. Magn. Mater. **145**, 319 (1995).
21. A. F. Pshenichnikov and V. V. Mekhonoshin, J. Magn. Magn. Mater. **213**, 357 (2000).
22. L. D. Landau and E. M. Lifshitz, *Course of Theoretical Physics*, Vol. 8: *Electrodynamics of Continuous Media* (Nauka, Moscow, 1992; Pergamon, New York, 1984).
23. J. A. Stratton, *Electromagnetic Theory* (McGraw-Hill, New York, 1941; Gostekhizdat, Moscow, 1948).
24. Yu. N. Skibin, Doctoral Dissertation in Physics and Mathematics (Stavrop. Gos. Univ., Stavropol', 1996).
25. J. M. D. Coey, A. Barry, J.-M. Brotto, *et al.*, J. Phys.: Condens. Matter **7**, 759 (1995).
26. B. J. Lemaire, P. Davidson, J. Ferre, *et al.*, Phys. Rev. Lett. **88**, 125507 (2002).

*Translated by H. Bronstein*

*Journal of Experimental and Theoretical Physics, Vol. 95, No. 2, 2002, pp. 282–293.*
*Translated from Zhurnal Éksperimental'noĭ i Teoreticheskoĭ Fiziki, Vol. 122, No. 2, 2002, pp. 328–340.*


**FLUIDS**

# Clustering of the Low-Inertia Particle Number Density Field in Random Divergence-Free Hydrodynamic Flows

**V. I. Klyatskin[a, b, *] and T. Elperin[c]**

[a]*Oboukhov Institute of Atmospheric Physics, Russian Academy of Sciences, Pyzhevskii per. 3, Moscow, 109017 Russia*

[b]*Pacific Institute of Oceanology, Far East Division, Russian Academy of Sciences, ul. Baltiĭskaya 43, Vladivostok, 690041 Russia*

[c]*Pearlstone Center for Aeronautical Engineering Studies, Department of Mechanical Engineering, Ben-Gurion University of Negev, P.O. Box 653, Beer-Sheva 84105, Israel*

**e-mail: klyatskin@hotmail.com*

Received February 18, 2002

**Abstract**—We consider the diffusion of the low-inertia particle number density field in random divergence-free hydrodynamic flows. The principal feature of this diffusion is the divergence of the particle velocity field, which results in clustering of the particle number density field. This phenomenon is coherent, occurs with a unit probability, and must show up in almost all realizations of the process dynamics. We calculate the statistical parameters that characterize clustering in three-dimensional and two-dimensional random fluid flows and in a rapidly rotating two-dimensional random flow. In the former case, the vortex component of the random divergence-free flow generates a vortex component of the low-inertia particle velocity field, which generates a potential component of the velocity field through advection. By contrast, in the case of rapid rotation, a potential component of the velocity field is generated directly by the vortex component of the random divergence-free flow (linear problem). *© 2002 MAIK "Nauka/Interperiodica".*

## 1. INTRODUCTION

Since the classical paper of Stokes published in 1851 [1] (see also the classical book of Lamb [2]), the dynamics of inertial particles in hydrodynamic flows has attracted the attention of many researchers. This attention stems from its importance for various ecological problems in the Earth's atmosphere and oceans and from numerous technical applications (see, e.g., books [3, 4] and papers of the last decade [5–10], which contain extensive bibliography). Note that Maxey [7] was apparently the first to draw attention to the fact that, in contrast to inertialess passive particles, the velocity field of inertial particles in the divergence-free velocity field of a hydrodynamic flow is a divergence one. This circumstance was widely used in [11, 12] to analyze numerous applications in hydrodynamics, geophysics, and astrophysics.

## 2. DESCRIPTION OF THE FIELD OF PARTICLE NUMBER DENSITY

### *2.1. Basic Equations and Formulation of the Problem*

The diffusion of the number-density field, $n(\mathbf{r}, t)$, for particles moving in random hydrodynamic flows is described by the continuity equation

$$\left(\frac{\partial}{\partial t} + \frac{\partial}{\partial \mathbf{r}}\mathbf{V}(\mathbf{r}, t)\right)n(\mathbf{r}, t) = 0, \quad n(\mathbf{r}, 0) = n_0(\mathbf{r}). \quad (1)$$

Here, the velocity field $\mathbf{V}(\mathbf{r}, t)$ is described by the equation (see, e.g., [5–10])

$$\left(\frac{\partial}{\partial t} + \mathbf{V}(\mathbf{r}, t)\frac{\partial}{\partial \mathbf{r}}\right)\mathbf{V}(\mathbf{r}, t) = -\lambda[\mathbf{V}(\mathbf{r}, t) - \mathbf{u}(\mathbf{r}, t)], \quad (2)$$

which we consider as a phenomenological equation. The parameter $\tau = 1/\lambda$ is the standard Stokes time that depends on the particle size and molecular viscosity.

The total number of particles is conserved during the evolution, i.e.,

$$N_0 = \int n(\mathbf{r}, r)d\mathbf{r} = \int n_0(\mathbf{r})d\mathbf{r} = \text{const}.$$

The partial differential equations of the first order (1) and (2) (Eulerian description) are equivalent to the system of ordinary differential characteristic equations (Lagrangian description)

$$\begin{gathered}\frac{d}{dt}\mathbf{r}(t) = \mathbf{V}(\mathbf{r}(t), t), \quad \mathbf{r}(0) = \mathbf{r}_0,\\ \frac{d}{dt}\mathbf{V}(t) = -\lambda[\mathbf{V}(t) - \mathbf{u}(\mathbf{r}(t), t)],\\ \mathbf{V}(0) = \mathbf{V}_0(\mathbf{r}_0),\\ \frac{d}{dt}n(t) = -n(t)\frac{\partial \mathbf{V}(\mathbf{r}(t), t)}{\partial \mathbf{r}}, \quad n(0) = n_0(\mathbf{r}_0).\end{gathered} \quad (3)$$

1063-7761/02/9502-0282$22.00 

The solution to this system depends on the initial parameter $\mathbf{r}_0$ (this is denoted by a vertical bar):

$$\mathbf{r}(t) = \mathbf{r}(t|\mathbf{r}_0), \quad \mathbf{V}(t) = \mathbf{V}(t|\mathbf{r}_0), \quad n(t) = n(t|\mathbf{r}_0).$$

The Eulerian number-density field of inertial particles, $n(\mathbf{r}, t)$, is then described by

$$n(\mathbf{r}, t) = \int d\mathbf{r}_0 n_0(\mathbf{r}_0)\delta(\mathbf{r}(t|\mathbf{r}_0) - \mathbf{r}).$$

We assume that the variance of the random velocity field, $\sigma_{\mathbf{u}}^2 = \langle \mathbf{u}^2(\mathbf{r}^2, t)\rangle$, is sufficiently small and determines the principal small parameter of the problem. For a large $\lambda$ (low particle inertia), we can linearize Eq. (2) relative to the function

$$\mathbf{V}(\mathbf{r}, t) \approx \mathbf{u}(\mathbf{r}, t) \tag{4}$$

and pass to a simpler vector equation,

$$\left(\frac{\partial}{\partial t} + \mathbf{u}(\mathbf{r}, t)\frac{\partial}{\partial \mathbf{r}}\right)\mathbf{V}(\mathbf{r}, t)$$

$$= \left(-\mathbf{V}(\mathbf{r}, t)\frac{\partial}{\partial \mathbf{r}}\right)\mathbf{u}(\mathbf{r}, t) - \lambda[\mathbf{V}(\mathbf{r}, t) - \mathbf{u}(\mathbf{r}, t)],$$

which we write in coordinate representation as

$$\left(\frac{\partial}{\partial t} + \lambda\right)V_i(\mathbf{r}, t) = -u_k(\mathbf{r}, t)\frac{\partial V_i(\mathbf{r}, t)}{\partial r_k} - \frac{\partial u_i(\mathbf{r}, t)}{\partial r_k}V_k(\mathbf{r}, t) + \lambda u_i(\mathbf{r}, t). \tag{5}$$

The summation is always assumed to be performed over repetitive indices.

First, the question arises as to what equality (4) means statistically and what the conditions for its validity are. Below, we show that the validity of this equality in statistical problems essentially depends on the sequence of passages to the limit.

In order to describe the particle number-density field in Eulerian representation, we introduce an indicator function

$$\Phi(t, \mathbf{r}; n) = \delta(n(\mathbf{r}, t) - n), \tag{6}$$

concentrated on an $n(\mathbf{r}, t) = n = \text{const}$ surface in the three-dimensional case and on a contour in the two-dimensional case. The dynamics of this function is described by the Liouville equation

$$\left(\frac{\partial}{\partial t} + \mathbf{V}(\mathbf{r}, t)\frac{\partial}{\partial \mathbf{r}}\right)\Phi(t, \mathbf{r}; n) = \frac{\partial \mathbf{V}(\mathbf{r}, t)}{\partial \mathbf{r}}\frac{\partial}{\partial n}n\Phi(t, \mathbf{r}; n),$$
$$\Phi(0, \mathbf{r}; n) = \delta(n_0(\mathbf{r}) - n), \tag{7}$$

if $\mathbf{V}(\mathbf{r}, t)$ is a divergence velocity field, i.e., if $\partial \mathbf{V}(\mathbf{r}, t)/\partial \mathbf{r} \neq 0$.

The indicator function characterizes the geometric structure of the particle number-density field $n(\mathbf{r}, t)$ [13–15]. For example, in the two-dimensional case, such quantities as the total area of the region bounded by isolines where $n(\mathbf{r}, t) > n$,

$$S(t; n) = \int_n^\infty dn' \int d\mathbf{r}\Phi(t, \mathbf{r}; n'), \tag{8}$$

and the total number of particles contained in these regions,

$$N(t; n) = \int_n^\infty n' dn' \int d\mathbf{r}\Phi(t, \mathbf{r}; n'), \tag{9}$$

can be expressed in terms of function (6).

If the velocity field $\mathbf{V}(\mathbf{r}, t)$ is a random divergence field, then the field $n(\mathbf{r}, t)$ is clustered with a unit probability and the quantities $S(t; n) \longrightarrow 0$, $N(t; n) \longrightarrow N_0$. This is a coherent physical phenomenon, and it occurs in almost all realizations of the process. The coherent phenomena themselves do not depend on a particular model of the fluctuating parameters. However, the coherent values of the parameters that characterize a given phenomenon (e.g., the characteristic time and spatial scales of clusters) can significantly depend on the model. Note that the diffusion of a passive scalar in random flows was numerically simulated in [17–19].

### *2.2. A Statistical Analysis of Clustering*

Calculations can be easily performed for the model of a random Gaussian field $\mathbf{V}(\mathbf{r}, t)$ that is statistically uniform and isotropic in space and stationary in time with a zero mean and the correlation tensor

$$\langle V_i(\mathbf{r}, t)V_j(\mathbf{r}', t')\rangle = B_{ij}^{(\mathbf{V})}(\mathbf{r} - \mathbf{r}', t - t').$$

The one-point probability density for the solution of the dynamic equation (1) matches the indicator function averaged over an ensemble of realizations of the random field $\mathbf{V}(\mathbf{r}, t)$:

$$P(t, \mathbf{r}; n) = \langle \Phi(t, \mathbf{r}; n)\rangle.$$

In the approximation of a delta-correlated (in time) field $\mathbf{V}(\mathbf{r}, t)$, it is described by the equation [13–16]

$$\left(\frac{\partial}{\partial t} - D_0\frac{\partial^2}{\partial \mathbf{r}^2}\right)P(t, \mathbf{r}; n) = D^{(\mathbf{V})}\frac{\partial^2}{\partial n^2}n^2P(t, \mathbf{r}; n),$$
$$P(0, \mathbf{r}; n) = \delta(n_0(\mathbf{r}) - n), \tag{10}$$

where the diffusion coefficients

$$D_0 = \frac{1}{d}\int_0^\infty d\tau\langle \mathbf{V}(\mathbf{r}, t + \tau)\mathbf{V}(\mathbf{r}, t)\rangle = \frac{1}{d}\tau_{\mathbf{V}}\langle \mathbf{V}^2(\mathbf{r}, t)\rangle,$$

$$D^{(\mathbf{V})} = \int_0^\infty d\tau\left\langle \frac{\partial \mathbf{V}(\mathbf{r}, t + \tau)}{\partial \mathbf{r}}\frac{\partial \mathbf{V}(\mathbf{r}, t)}{\partial \mathbf{r}}\right\rangle = \tau_{\mathrm{div}\mathbf{V}}\left\langle \left(\frac{\partial \mathbf{V}(\mathbf{r}, t)}{\partial \mathbf{r}}\right)^2\right\rangle, \tag{11}$$

$d$ is the space dimension, and $\tau_{\mathbf{V}}$ and $\tau_{\mathrm{div}\mathbf{V}}$ are the time correlation lengths for the random fields $\mathbf{V}(\mathbf{r}, t)$ and $\partial\mathbf{V}(\mathbf{r}, t)/\partial\mathbf{r}$.

Knowing the solution to Eq. (10), we can calculate the time evolution of such functionals for the particle number-density field as the mean values of expressions (8) and (9). In particular, for $D^{(\mathbf{V})}t \gg 1$, the mean area where the particle number-density field exceeds a given $n$ decreases with time as

$$\langle S(t; n)\rangle = \frac{1}{\sqrt{\pi n D^{(\mathbf{V})}t}}\exp\left(-\frac{D^{(\mathbf{V})}t}{4}\right)\int\sqrt{n_0(\mathbf{r})}d\mathbf{r},$$

while the mean number of particles contained in this region,

$$\langle N(t; n)\rangle = N_0 - \sqrt{\frac{n}{nD^{(\mathbf{V})}t}} \times \exp\left(-\frac{D^{(\mathbf{V})}t}{4}\right)\int\sqrt{n_0(\mathbf{r})}d\mathbf{r},$$

monotonically tends to the total number of particles, $N_0 = \int n_0(\mathbf{r})d\mathbf{r}$. This implies that the inertial particles of a scalar tend to be collected in clusters with time, compact regions of enhanced particle number density $n(\mathbf{r}, t)$ in the random velocity field $\mathbf{V}(\mathbf{r}, t)$ surrounded by tenuous regions.

Thus, the problem reduces to estimating the diffusion coefficients (11) from the stochastic equations (2) and (5), i.e., to calculating the time correlation lengths $\tau_{\mathbf{V}}$ and $\tau_{\mathrm{div}\mathbf{V}}$ for the random fields $\mathbf{V}(\mathbf{r}, t)$ and $\partial\mathbf{V}(\mathbf{r}, t)/\partial\mathbf{r}$ and their spatial correlation scales and variances. This can be done for a certain statistical model of the random field $\mathbf{u}(\mathbf{r}, t)$.

Below, we calculate the statistical parameters of $\mathbf{V}(\mathbf{r}, t)$ in the first nonvanishing order of smallness in $\sigma_{\mathbf{u}}^2$. Note that the statistics of $\mathbf{V}(\mathbf{r}, t)$ described by the stochastic equations (2) and (5) are generally not Gaussian. However, it is easy to see that the highest cumulants of the field $\mathrm{div}\mathbf{V}(\mathbf{r}, t)$ are of a higher order of smallness than the second cumulant. Therefore, the approximation of a Gaussian field $\mathbf{V}(\mathbf{r}, t)$ can actually be used to derive Eq. (10).

We assume that $\mathbf{u}(\mathbf{r}, t)$ is a divergence-free velocity field, i.e.,

$$\mathrm{div}\mathbf{u}(\mathbf{r}, t) = \frac{\partial}{\partial\mathbf{r}}\mathbf{u}(\mathbf{r}, t) = 0,$$

is a Gaussian random field uniform and isotropic in space and stationary in time with a zero mean and the correlation tensor

$$B_{ij}(\mathbf{r}-\mathbf{r}', t-t') = \langle u_i(\mathbf{r}, t)u_j(\mathbf{r}', t')\rangle.$$

The time correlation length of $\mathbf{u}(\mathbf{r}, t)$ is given by the equality

$$\tau_0 B_{ii}(0, 0) = \int_0^\infty d\tau B_{ii}(0, \tau) = \int_0^\infty d\tau\langle\mathbf{u}(\mathbf{r}, t+\tau)\mathbf{u}(\mathbf{r}, t)\rangle.$$

For this model, we may introduce a spatial spectral function and a space-time spectral function of $\mathbf{u}(\mathbf{r}, t)$ using the integrals

$$B_{ij}(\mathbf{r}, t) = \int d\mathbf{k}E_{ij}(\mathbf{k}, t)e^{i\mathbf{k}\cdot\mathbf{r}},$$
$$B_{ij}(\mathbf{r}, t) = \int d\mathbf{k}\int_{-\infty}^{\infty} d\omega\Phi_{ij}(\mathbf{k}, \omega)e^{i\mathbf{k}\cdot\mathbf{r}+i\omega t}, \quad (12)$$

where

$$E_{ij}(\mathbf{k}, t) = E(k, t)\left(\delta_{ij} - \frac{k_i k_j}{\mathbf{k}^2}\right),$$
$$\Phi_{ij}(\mathbf{k}, \omega) = \Phi(k, \omega)\left(\delta_{ij} - \frac{k_i k_j}{k^2}\right). \quad (13)$$

Note that

$$B_{ij}(0, t) = \frac{d-1}{d}\int d\mathbf{k}E(k, t)\delta_{ij}; \quad (14)$$

for the tensor of the fourth order that is important for our subsequent analysis, we have

$$-\frac{\partial^2 B_{ij}(0, \tau)}{\partial r_k \partial r_l} = \frac{D(\tau)}{d(d+2)} \times [(d+1)\delta_{kl}\delta_{ij} - \delta_{ki}\delta_{lj} - \delta_{kj}\delta_{li}], \quad (15)$$

where the coefficient

$$D(\tau) = \int d\mathbf{k}\mathbf{k}^2 E(k, \tau) = -\frac{1}{d-1}\langle\mathbf{u}(\mathbf{r}, t+\tau)\Delta\mathbf{u}(\mathbf{r}, t)\rangle. \quad (16)$$

The quantity

$$D(0) = -\frac{1}{d-1}\langle\mathbf{u}(\mathbf{r}, t)\Delta\mathbf{u}(\mathbf{r}, t)\rangle$$

is related to the vortex structure of the random divergence-free field $\mathbf{u}(\mathbf{r}, t)$.

Thus, we will calculate the parameters (11) that characterize the clustering time evolution for the particle number density $n(\mathbf{r}, t)$.

## 3. RANDOM MULTIDIMENSIONAL FLOWS

Below, we study the statistical parameters of Eq. (5) in the Eulerian description in the diffusion approximation.

### 3.1. The Diffusion Approximation

The random field $\mathbf{u}(\mathbf{r}, t)$ correlates with the function $\mathbf{V}(\mathbf{r}, t)$, which is the functional of $\mathbf{u}(\mathbf{r}, t)$. The correlation splitting for a Gaussian field $\mathbf{u}(\mathbf{r}, t)$ is based on the Furutsu–Novikov formula

$$\langle u_k(\mathbf{r}, t)R[t; \mathbf{u}(\mathbf{r}, \tau)]\rangle = \int d\mathbf{r}' \int_0^t dt' B_{kl}(\mathbf{r}-\mathbf{r}', t-t') \times \left\langle \frac{\delta}{\delta u_l(\mathbf{r}', t')} R[t; \mathbf{u}(\mathbf{r}, \tau)] \right\rangle. \quad (17)$$

This formula is valid for a Gaussian random field $\mathbf{u}(\mathbf{r}, t)$ with a zero mean and an arbitrary functional $R[t; \mathbf{u}(\mathbf{r}, \tau)]$ $(0 \le \tau \le t)$ [20, 21] (see also [16]).

The equations for the corresponding means in the diffusion approximation can be written out exactly. The corresponding simplification of the problem is made at the level of a functional dependence of its solution on fluctuating parameters [22] (see also [14, 16, 23]).

For the variational derivatives in the diffusion approximation, we have the equation

$$\left(\frac{\partial}{\partial t} + \lambda\right)\frac{\delta V_i(\mathbf{r}, t)}{\delta u_l(\mathbf{r}', t')} = 0$$

with the initial condition at $t = t'$

$$\left.\frac{\delta V_i(\mathbf{r}, t)}{\delta u_l(\mathbf{r}', t')}\right|_{t=t'+0} = -\left[\delta(\mathbf{r}-\mathbf{r}')\frac{\partial V_i(\mathbf{r}, t')}{\partial r_l} + \delta_{il}\frac{\partial \delta(\mathbf{r}-\mathbf{r}')}{\partial r_k}V_k(\mathbf{r}, t')\right] + \delta(\mathbf{r}-\mathbf{r}')\lambda\delta_{il},$$

which follows from Eq. (5). The solution of this equation is

$$\frac{\delta V_i(\mathbf{r}, t)}{\delta u_l(\mathbf{r}', t')} = e^{-\lambda(t-t')}\left\{-\left[\delta(\mathbf{r}-\mathbf{r}')\frac{\partial V_i(\mathbf{r}, t')}{\partial r_l} + \frac{\partial \delta(\mathbf{r}-\mathbf{r}')}{\partial r_k}\delta_{il}V_k(\mathbf{r}, t')\right] + \delta(\mathbf{r}-\mathbf{r}')\lambda\delta_{il}\right\}.$$

The field $\mathbf{V}(\mathbf{r}, t)$ itself in the diffusion approximation has the structure

$$\mathbf{V}(\mathbf{r}, t') = e^{-\lambda(t-t')}\mathbf{V}(\mathbf{r}, t')$$

and, hence,

$$\mathbf{V}(\mathbf{r}, t') = e^{\lambda(t-t')}\mathbf{V}(\mathbf{r}, t).$$

Thus, for the variational derivative, we obtain the expression

$$\frac{\delta V_i(\mathbf{r}, t)}{\delta u_l(\mathbf{r}', t')} = -\left[\delta(\mathbf{r}-\mathbf{r}')\frac{\partial V_i(\mathbf{r}, t)}{\partial r_l} + \delta_{il}\frac{\partial \delta(\mathbf{r}-\mathbf{r}')}{\partial r_\mu}V_\mu(\mathbf{r}, t)\right] + \delta(\mathbf{r}-\mathbf{r}')\lambda e^{-\lambda(t-t')}\delta_{il}. \quad (18)$$

### 3.2. The Spatial Correlation Tensor of $\mathbf{V}(\mathbf{r}, t)$

The equation for the simultaneous spatial correlation tensor of the field $\mathbf{V}(\mathbf{r}, t)$ follows from Eq. (5):

$$\left(\frac{\partial}{\partial t} + 2\lambda\right)\langle V_i(\mathbf{r}, t)V_j(\mathbf{r}_1, t)\rangle = -\frac{\partial}{\partial r_k}\langle u_k(\mathbf{r}, t)V_i(\mathbf{r}, t)V_j(\mathbf{r}_1, t)\rangle - \frac{\partial}{\partial r_{1k}}\langle u_k(\mathbf{r}_1, t)V_i(\mathbf{r}, t)V_j(\mathbf{r}_1, t)\rangle - \left\langle \frac{\partial u_i(\mathbf{r}, t)}{\partial r_k}V_k(\mathbf{r}, t)V_j(\mathbf{r}_1, t)\right\rangle - \left\langle \frac{\partial u_j(\mathbf{r}_1, t)}{\partial r_{1k}}V_k(\mathbf{r}_1, t)V_i(\mathbf{r}_1, t)\right\rangle + \lambda[\langle u_i(\mathbf{r}, t)V_j(\mathbf{r}_1, t)\rangle + \langle u_j(\mathbf{r}_1, t)V_i(\mathbf{r}, t)\rangle].$$

Using the Furutsu–Novikov formula (17) and expression (18) for the variational derivative, we obtain an equation for the time-independent $(\mathbf{r}-\mathbf{r}_1 \longrightarrow \mathbf{r})$ stationary correlation tensor $F_{ij}(\mathbf{r}-\mathbf{r}_1) = \langle V_i(\mathbf{r}, t)V_j(\mathbf{r}_1, t)\rangle$:

$$2\lambda F_{ij}(\mathbf{r}) = 2\int_0^\infty d\tau[B_{\beta\gamma}(0, \tau) - B_{\beta\gamma}(\mathbf{r}, \tau)]\frac{\partial^2}{\partial r_\beta \partial r_\gamma}F_{ij}(\mathbf{r}) - \int_0^\infty d\tau\frac{\partial B_{\beta j}(\mathbf{r}, \tau)}{\partial r_\gamma}\frac{\partial}{\partial r_\beta}F_{i\gamma}(\mathbf{r}) - \int_0^\infty d\tau\frac{\partial B_{\beta i}(\mathbf{r}, \tau)}{\partial r_\gamma}\frac{\partial}{\partial r_\beta}F_{\gamma j}(\mathbf{r}) - \int_0^\infty d\tau\frac{\partial B_{i\gamma}(\mathbf{r}, \tau)}{\partial r_\beta}\frac{\partial}{\partial r_\gamma}F_{\beta j}(\mathbf{r}) - \int_0^\infty d\tau\frac{\partial B_{j\gamma}(\mathbf{r}, \tau)}{\partial r_\beta}\frac{\partial}{\partial r_\gamma}F_{i\beta}(\mathbf{r}) - 2\int_0^\infty d\tau\frac{\partial^2 B_{ij}(\mathbf{r}, \tau)}{\partial r_\beta \partial r_\gamma}F_{\beta\gamma}(\mathbf{r}) + 2\lambda^2\int_0^\infty d\tau e^{-\lambda\tau}B_{ij}(\mathbf{r}, \tau). \quad (19)$$

For a stationary correlation $\langle V_i(\mathbf{r}, t)V_j(\mathbf{r}_1, t)\rangle$ in the diffusion approximation, we obtain the following equation by setting $\mathbf{r} = 0$ in Eq. (19):

$$\lambda\langle V_i(\mathbf{r}, t)V_j(\mathbf{r}, t)\rangle = -\int_0^\infty d\tau\frac{\partial^2 B_{ij}(0, \tau)}{\partial r_\beta \partial r_\gamma} \times \langle V_\beta(\mathbf{r}, t)V_\gamma(\mathbf{r}, t)\rangle + \lambda^2\int_0^\infty d\tau e^{-\lambda\tau}B_{ij}(0, \tau). \quad (20)$$

Using formula (15), it can be rewritten as

$$\lambda\langle V_i(\mathbf{r}, t)V_j(\mathbf{r}, t)\rangle = \lambda^2\int_0^\infty d\tau e^{-\lambda\tau}B_{ij}(0, \tau) + \frac{D_1}{d(d+2)}$$
$$\times[(d+1)\langle\mathbf{V}^2(\mathbf{r}, t)\rangle\delta_{ij} - 2\langle V_i(\mathbf{r}, t)V_j(\mathbf{r}, t)\rangle],$$

where the coefficient

$$D_1 = \int_0^\infty d\tau D(\tau) = \int_0^\infty d\tau\int d\mathbf{k}\mathbf{k}^2E(k, \tau)$$
$$= -\frac{1}{d-1}\int_0^\infty d\tau\langle\mathbf{u}(\mathbf{r}, t+\tau)\Delta\mathbf{u}(\mathbf{r}, t)\rangle. \quad (21)$$

Consequently,

$$\left(\lambda - \frac{d-1}{d}D_1\right)\langle\mathbf{V}^2(\mathbf{r}, t)\rangle = \lambda^2\int_0^\infty d\tau e^{-\lambda\tau}B_{ii}(0, \tau) \quad (22)$$

if $\lambda > D_1(d-1)/d$.

Thus, we see that there is a critical value of $\lambda$: $\lambda_{cr} = D_1(d-1)/d$, and a stationary value exists only if $\lambda > \lambda_{cr}$.

If the inequality

$$\lambda \gg D_1 \sim \sigma_\mathbf{u}^2\tau_0/l_0^2, \quad (23)$$

where $l_0$ is the spatial scale of $\mathbf{u}(\mathbf{r}, t)$, holds, then we derive the expression

$$\langle\mathbf{V}^2(\mathbf{r}, t)\rangle = \lambda\int_0^\infty d\tau e^{-\lambda\tau}B_{ii}(0, \tau)$$
$$= \lambda(N-1)\int_0^\infty d\tau e^{-\lambda\tau}\int d\mathbf{k}E(k, \tau). \quad (24)$$

Below, we assume that inequality (23) holds always.

The variance of $\mathbf{V}(\mathbf{r}, t)$ can be estimated from equality (24). As a result, we obtain for $\lambda t \gg 1$

$$\sigma_\mathbf{V}^2 = \begin{cases}\sigma_\mathbf{u}^2, & \lambda\tau_0 \gg 1\\ \lambda\tau_0\sigma_\mathbf{u}^2, & \lambda\tau_0 \ll 1,\end{cases} \quad (25)$$

where $\tau_0$ is the time correlation length of $\mathbf{u}(\mathbf{r}, t)$. Thus, we see that the sequence of passages to the limit $\tau_0 \longrightarrow 0$ and $\lambda \longrightarrow \infty$ is not permutable.

### *3.3. The Correlation Tensor of the Spatial Derivatives of* $\mathbf{V}(\mathbf{r}, t)$

Let us now discuss such statistical parameters of the spatial derivatives of the field $\mathbf{V}(\mathbf{r}, t)$ as

$$\left\langle\frac{\partial V_i(\mathbf{r}, t)}{\partial r_k}\frac{\partial V_j(\mathbf{r}, t)}{\partial r_l}\right\rangle = -\left.\frac{\partial^2F_{ij}(\mathbf{r})}{\partial r_k\partial r_l}\right|_{\mathbf{r}=0}.$$

For these quantities, the equation

$$2\lambda\frac{\partial^2F_{ij}(0)}{\partial r_k\partial r_l} = 2\lambda^2\int_0^\infty d\tau e^{-\lambda\tau}\frac{\partial^2B_{ij}(0, \tau)}{\partial r_k\partial r_l}$$
$$-2\int_0^\infty d\tau\frac{\partial^2B_{\beta\gamma}(0, \tau)}{\partial r_k\partial r_l}\frac{\partial^2F_{ij}(0)}{\partial r_\beta\partial r_\gamma} - \int_0^\infty d\tau\frac{\partial^2B_{\beta j}(0, \tau)}{\partial r_\gamma\partial r_k}\frac{\partial^2F_{i\gamma}(0)}{\partial r_\beta\partial r_l}$$
$$-\int_0^\infty d\tau\frac{\partial^2B_{\beta j}(0, \tau)}{\partial r_\gamma\partial r_l}\frac{\partial^2F_{i\gamma}(0)}{\partial r_\beta\partial r_k} - \int_0^\infty d\tau\frac{\partial^2B_{\beta i}(0, \tau)}{\partial r_\gamma\partial r_k}\frac{\partial^2F_{\gamma j}(0)}{\partial r_\beta\partial r_l}$$
$$-\int_0^\infty d\tau\frac{\partial^2B_{\beta i}(0, \tau)}{\partial r_\gamma\partial r_l}\frac{\partial^2F_{\gamma j}(0)}{\partial r_\beta\partial r_k} - \int_0^\infty d\tau\frac{\partial^2B_{i\gamma}(0, \tau)}{\partial r_\beta\partial r_k}\frac{\partial^2F_{\beta j}(0)}{\partial r_\gamma\partial r_l} \quad (26)$$
$$-\int_0^\infty d\tau\frac{\partial^2B_{i\gamma}(0, \tau)}{\partial r_\beta\partial r_l}\frac{\partial^2F_{\beta j}(0)}{\partial r_\gamma\partial r_k} - \int_0^\infty d\tau\frac{\partial^2B_{j\gamma}(0, \tau)}{\partial r_\beta\partial r_k}\frac{\partial^2F_{i\beta}(0)}{\partial r_\gamma\partial r_l}$$
$$-\int_0^\infty d\tau\frac{\partial^2B_{j\gamma}(0, \tau)}{\partial r_\beta\partial r_l}\frac{\partial^2F_{i\beta}(0)}{\partial r_\gamma\partial r_k} - 2\int_0^\infty d\tau\frac{\partial^2B_{ij}(0, \tau)}{\partial r_\beta\partial r_\gamma}\frac{\partial^2F_{\beta\gamma}(0)}{\partial r_k\partial r_l}$$
$$-2\int_0^\infty d\tau\frac{\partial^4B_{ij}(0, \tau)}{\partial r_\beta\partial r_\gamma\partial r_k\partial r_l}F_{\beta\gamma}(0)$$

follows from Eq. (19). Note that the last term on the right-hand side of Eq. (26) is a source of order $\sigma_\mathbf{u}^4$ and may be discarded.

Setting $i = k$ and $j = l$ in Eq. (26), we derive the following steady-state equation using equality (15) for $\lambda \gg D_1$:

$$\lambda\left\langle\left(\frac{\partial\mathbf{V}(\mathbf{r}, t)}{\partial\mathbf{r}}\right)^2\right\rangle = \frac{4(d+1)D_1}{d(d+2)}\left\langle\frac{\partial V_i(\mathbf{r}, t)}{\partial r_k}\frac{\partial V_i(\mathbf{r}, t)}{\partial r_k}\right\rangle. \quad (27)$$

The quantity

$$\left\langle\frac{\partial V_i(\mathbf{r}, t)}{\partial r_k}\frac{\partial V_i(\mathbf{r}, t)}{\partial r_k}\right\rangle$$
$$= -\frac{\partial^2F_{ii}(0)}{\partial\mathbf{r}^2} = -\langle\mathbf{V}(\mathbf{r}, t)\Delta\mathbf{V}(\mathbf{r}, t)\rangle$$

is related to the vortex structure of the field $\mathbf{V}(\mathbf{r}, t)$, and Eq. (27) can be rewritten as

$$\left\langle\left(\frac{\partial\mathbf{V}(\mathbf{r}, t)}{\partial\mathbf{r}}\right)^2\right\rangle$$
$$= -\frac{4(d+1)D_1}{\lambda d(d+2)}\langle\mathbf{V}(\mathbf{r}, t)\Delta\mathbf{V}(\mathbf{r}, t)\rangle. \quad (28)$$

Now, let $i = j$ and $k = l$ in Eq. (26). Using formula (15) for $\lambda \gg D_1$, we obtain

$$\frac{\partial^2 F_{ii}(0)}{\partial \mathbf{r}^2} = \lambda \int_0^\infty d\tau e^{-\lambda\tau} \frac{\partial^2 B_{ii}(0, \tau)}{\partial \mathbf{r}^2},$$

i.e.,

$$\begin{aligned} \langle \mathbf{V}(\mathbf{r}, t)\Delta\mathbf{V}(\mathbf{r}, t)\rangle &= \lambda \int_0^\infty d\tau e^{-\lambda\tau} \frac{\partial^2 B_{ii}(0, \tau)}{\partial \mathbf{r}^2} \\ &= -(d-1)D_2(\lambda) = \lambda \int_0^\infty d\tau e^{-\lambda\tau} \langle \mathbf{u}(\mathbf{r}, t)\Delta\mathbf{u}(\mathbf{r}, t)\rangle, \end{aligned} \tag{29}$$

where the coefficient

$$\begin{aligned} D_2(\lambda) &= \int_0^\infty d\tau e^{-\lambda\tau} D(\tau) \\ &= \int_0^\infty d\tau e^{-\lambda\tau} \int d\mathbf{k} \mathbf{k}^2 E(k, \tau). \end{aligned} \tag{30}$$

Therefore, for the divergence of $\mathbf{V}(\mathbf{r}, t)$ under the condition $\lambda/D_1 \gg 1$, we derive the expression

$$\left\langle \left( \frac{\partial \mathbf{V}(\mathbf{r}, t)}{\partial \mathbf{r}} \right)^2 \right\rangle = \frac{4(d^2-1)}{\lambda d(d+2)} D_1 D_2(\lambda). \tag{31}$$

Note that the coefficient

$$D_1 = -\frac{\tau_0}{d-1} \langle \mathbf{u}(\mathbf{r}, t)\Delta\mathbf{u}(\mathbf{r}, t)\rangle$$

does not depend on $\lambda$. In contrast, the coefficient $D_2(\lambda)$ for $\lambda\tau_0 \gg 1$ is given by

$$D_2(\lambda) = -\frac{1}{\lambda(d-1)} \langle \mathbf{u}(\mathbf{r}, t)\Delta\mathbf{u}(\mathbf{r}, t)\rangle.$$

Thus, for the three-dimensional and two-dimensional cases, we obtain the equalities

$$\begin{aligned} \left\langle \left( \frac{\partial \mathbf{V}(\mathbf{r}, t)}{\partial \mathbf{r}} \right)^2 \right\rangle &= \frac{32}{15} D_1 D_2(\lambda), \\ \left\langle \left( \frac{\partial \mathbf{V}(\mathbf{r}, t)}{\partial \mathbf{r}} \right)^2 \right\rangle &= \frac{3}{2} D_1 D_2(\lambda), \end{aligned} \tag{32}$$

which in the limit of low particle inertia, $\lambda\tau_0 \gg 1$, transform to

$$\left\langle \left( \frac{\partial \mathbf{V}(\mathbf{r}, t)}{\partial \mathbf{r}} \right)^2 \right\rangle = \begin{cases} \frac{8}{15}\frac{\tau_0}{\lambda} \langle \mathbf{u}(\mathbf{r}, t)\Delta\mathbf{u}(\mathbf{r}, t)\rangle^2, \\ \frac{3}{2}\frac{\tau_0}{\lambda} \langle \mathbf{u}(\mathbf{r}, t)\Delta\mathbf{u}(\mathbf{r}, t)\rangle^2 \end{cases} \tag{33}$$

for the three-dimensional and two-dimensional cases, respectively.

Based on expression (29), we can estimate the spatial correlation scale $l_{cor}$ of $\mathbf{V}(\mathbf{r}, t)$. More specifically, using equality (25), we find that

$$l_{cor} \sim l_0 \tag{34}$$

regardless of the conditions $\lambda\tau_0 \ll 1$ or $\lambda\tau_0 \gg 1$.

### *3.4. The Time Correlation Tensor of* $\mathbf{V}(\mathbf{r}, t)$

For the time correlation function at $t > t_1$, we have the equation

$$\begin{aligned} \left( \frac{\partial}{\partial t} + \lambda \right) \langle V_i(\mathbf{r}, t) V_j(\mathbf{r}_1, t_1)\rangle &= \lambda \langle u_i(\mathbf{r}, t) V_j(\mathbf{r}_1, t_1)\rangle \\ &- \frac{\partial}{\partial r_k} \langle u_k(\mathbf{r}, t) V_i(\mathbf{r}, t) V_j(\mathbf{r}_1, t_1)\rangle \\ &- \left\langle \frac{\partial u_i(\mathbf{r}, t)}{\partial r_k} V_k(\mathbf{r}, t) V_j(\mathbf{r}_1, t_1) \right\rangle. \end{aligned}$$

Using the Furutsu–Novikov formula (17) and expressions (18) for the variational derivative, we obtain an equation in the steady-state regime with an initial condition for the function $\langle V_i(\mathbf{r}, t) V_j(\mathbf{r}_1, t_1)\rangle$:

$$\begin{aligned} &\left( \frac{\partial}{\partial t} + \lambda \right) \langle V_i(\mathbf{r}, t+\tau) V_j(\mathbf{r}_1, t)\rangle \\ &= \lambda e^{\lambda\tau} \int_\tau^\infty d\tau_1 B_{ii}(\mathbf{r} - \mathbf{r}_1, \tau_1) e^{-\lambda\tau_1}, \\ &\langle V_i(\mathbf{r}, t+\tau) V_j(\mathbf{r}_1, t)\rangle_{\tau=0} = \langle V_i(\mathbf{r}, t) V_j(\mathbf{r}_1, t)\rangle, \end{aligned} \tag{35}$$

where the stationary value of $\langle V_i(\mathbf{r}, t) V_j(\mathbf{r}_1, t)\rangle$, naturally, does not depend on time. The terms of order $\sigma_{\mathbf{u}}^4$ were discarded in Eq. (35). This can be done for a sufficiently large $\lambda$ (23).

Now, we can calculate the time correlation lengths in expressions (11). Integrating Eq. (35) over $\tau$ in the interval $(0, \infty)$, we derive the expression

$$\begin{aligned} \lambda \int_0^\infty d\tau \langle V_i(\mathbf{r}, t+\tau) V_j(\mathbf{r}_1, t)\rangle &= \langle V_i(\mathbf{r}, t) V_j(\mathbf{r}_1, t)\rangle \\ &+ \lambda \int_0^\infty d\tau B_{ij}(\mathbf{r} - \mathbf{r}_1, \tau)[1 - e^{-\lambda\tau}]. \end{aligned} \tag{36}$$

Setting $\mathbf{r} = \mathbf{r}_1$ and $i = j$ in equality (36), we obtain an expression for the time correlation length of $\mathbf{V}(\mathbf{r}, t)$:

$$\begin{aligned} &\lambda\tau_{\mathbf{V}} \langle \mathbf{V}^2(\mathbf{r}, t)\rangle \\ &= \langle \mathbf{V}^2(\mathbf{r}, t)\rangle + \lambda \int_0^\infty d\tau B_{ii}(0, \tau)[1 - e^{-\lambda\tau}], \end{aligned}$$

which, using equality (24), can be written as

$$\tau_{\mathbf{V}}\langle \mathbf{V}^2(\mathbf{r}, t)\rangle = \tau_0 B_{ii}(0, 0), \tag{37}$$

which does not depend on $\lambda$.

Now, differentiating expression (36) with respect to $r_i$ and $r_{1j}$ and setting $\mathbf{r} = \mathbf{r}_1$, we derive an expression for the time correlation length of $\partial\mathbf{V}(\mathbf{r}, t)/\partial\mathbf{r}$:

$$\tau_{\mathrm{div}\mathbf{V}} = \frac{1}{\lambda}. \tag{38}$$

It is valid for all sufficiently large values of $\lambda$ and, in particular, for $\lambda\tau_0 \gg 1$, when $\mathbf{V}(\mathbf{r}, t) \approx \mathbf{u}(\mathbf{r}, t)$ and, hence, $\tau_{\mathbf{V}} = \tau_0$.

Now, we can calculate the coefficients (11) in Eq. (10) for the probability density by using equalities (37), (38), and (31):

$$\begin{aligned} D_0 &= \frac{1}{d}\tau_{\mathbf{V}}\langle \mathbf{V}^2(\mathbf{r}, t)\rangle = \frac{1}{d}\tau_0 B_{ii}(0, 0) \\ &= \frac{d-1}{d}\tau_0\int d\mathbf{k}E(k, 0), \\ D^{(\mathbf{V})} &= \tau_{\mathrm{div}\mathbf{V}}\left\langle\left(\frac{\partial\mathbf{V}(\mathbf{r}, t)}{\partial\mathbf{r}}\right)^2\right\rangle \\ &= \frac{4}{\lambda}\frac{d^2-1}{d(d+2)}D_1 D_2(\lambda). \end{aligned} \tag{39}$$

In particular, in the three-dimensional case for $\lambda\tau_0 \gg 1$, we have

$$\begin{aligned} D_0 &= \frac{1}{3}\tau_{\mathbf{V}}\langle \mathbf{V}^2(\mathbf{r}, t)\rangle = \frac{1}{3}\tau_0 B_{ii}(0, 0) = \frac{2}{3}\tau_0\int d\mathbf{k}E(k, 0), \\ D^{(\mathbf{V})} &= \tau_{\mathrm{div}\mathbf{V}}\left\langle\left(\frac{\partial\mathbf{V}(\mathbf{r}, t)}{\partial\mathbf{r}}\right)^2\right\rangle \\ &= \frac{8}{15}\frac{\tau_0}{\lambda^2}\langle \mathbf{u}(\mathbf{r}, t)\Delta\mathbf{u}(\mathbf{r}, t)\rangle^2. \end{aligned} \tag{40}$$

In the two-dimensional case for $\lambda\tau_0 \gg 1$, we have

$$\begin{aligned} D_0 &= \frac{1}{2}\tau_{\mathbf{V}}\langle \mathbf{V}^2(\mathbf{r}, t)\rangle = \frac{1}{2}\tau_0 B_{ii}(0, 0) = \tau_0\int d\mathbf{k}E(k, 0), \\ D^{(\mathbf{V})} &= \tau_{\mathrm{div}\mathbf{V}}\left\langle\left(\frac{\partial\mathbf{V}(\mathbf{r}, t)}{\partial\mathbf{r}}\right)^2\right\rangle \\ &= \frac{3}{2}\frac{\tau_0}{\lambda^2}\langle \mathbf{u}(\mathbf{r}, t)\Delta\mathbf{u}(\mathbf{r}, t)\rangle^2. \end{aligned} \tag{41}$$

Thus, we see that the coefficient $D^{(\mathbf{V})} \propto \sigma_{\mathbf{u}}^4$. Initially, the vortex component of $\mathbf{u}(\mathbf{r}, t)$ generates a vortex component of $\mathbf{V}(\mathbf{r}, t)$ through the direct linear mechanism without involving advection. Subsequently, the vortex component of $\mathbf{V}(\mathbf{r}, t)$ generates a divergence component of $\mathbf{V}(\mathbf{r}, t)$ through advection.

### 3.5. The Validity Conditions

The validity conditions for our results are composed of several constraints:

(1) The validity conditions for the diffusion approximation for Eq. (5) are

$$\lambda > D_1\frac{d-1}{d} \quad \text{and} \quad D_1\tau_0 \ll 1, \quad D_2(\lambda)\tau_0 \ll 1,$$

and the quantities $D_1$ and $D_2$ are

$$D_1 \sim \frac{\sigma_{\mathbf{u}}^2\tau_0}{l_0^2}, \quad D_2(\lambda) \sim \begin{cases} \sigma_{\mathbf{u}}^2\tau_0/l_0^2, & \lambda\tau_0 \ll 1, \\ \sigma_{\mathbf{u}}^2\tau_0/\lambda l_0^2, & \lambda\tau_0 \gg 1, \end{cases}$$

where $l_0$ is the spatial correlation scale and $\tau_0$ is the time correlation length of $\mathbf{u}(\mathbf{r}, t)$. Thus, we obtain the condition

$$\frac{\sigma_{\mathbf{u}}^2\tau_0^2}{l_0^2} \ll 1. \tag{42}$$

(2) The validity condition for the approximation of a delta-correlated field $\mathbf{V}(\mathbf{r}, t)$ for Eq. (10) is $D^{(\mathbf{V})}/\lambda \ll 1$, i.e.,

$$\frac{D_1 D_2(\lambda)}{\lambda^2} \ll 1.$$

Thus, we obtain the conditions in the form

$$\begin{aligned} \sigma_{\mathbf{u}}^2\tau_0^2/l_0^2 &\ll \lambda\tau_0, \quad \lambda\tau_0 \ll 1, \\ \sigma_{\mathbf{u}}^2\tau_0^2/l_0^2 &\ll (\lambda\tau_0)^{3/2}, \quad \lambda\tau_0 \gg 1. \end{aligned} \tag{43}$$

(3) In all calculations, we used condition (23), which is valid when the condition

$$\frac{\sigma_{\mathbf{u}}^2\tau_0^2}{l_0^2} \ll \lambda\tau_0 \tag{44}$$

is satisfied.

Therefore, for low-inertia particles ($\lambda\tau_0 \gg 1$), the validity conditions for the approximations used above reduce to condition (42).

## 4. A RAPIDLY ROTATING TWO-DIMENSIONAL FLOW

Let us now discuss the two-dimensional equation with rotation,

$$\begin{aligned} &\left(\frac{\partial}{\partial t} + \mathbf{V}(\mathbf{r}, t)\frac{\partial}{\partial\mathbf{r}}\right)V_i(\mathbf{r}, t) \\ &= -\lambda[V_i(\mathbf{r}, t) - u_i(\mathbf{r}, t)] + 2\Omega\Gamma_{i\mu}V_\mu(\mathbf{r}, t), \end{aligned}$$

where the matrix

$$\Gamma = \begin{Vmatrix} 0 & 1 \\ -1 & 0 \end{Vmatrix}, \quad \Gamma^2 = -E,$$

and $E$ is a unit matrix. This equation can be written as

$$\left(\frac{\partial}{\partial t} + \mathbf{V}(\mathbf{r}, t)\frac{\partial}{\partial \mathbf{r}}\right)\mathbf{V}(\mathbf{r}, t) = -\Lambda[\mathbf{V}(\mathbf{r}, t) - \mathbf{U}(\mathbf{r}, t)], \quad (45)$$

where the matrix $\Lambda = \lambda E - 2\Omega\Gamma$ and the random velocity field has the structure

$$\mathbf{U}(\mathbf{r}, t) = \lambda\Lambda^{-1}\mathbf{u}(\mathbf{r}, t), \quad \Lambda^{-1} = \frac{\lambda E + 2\Omega\Gamma}{\lambda^2 + 4\Omega^2}. \quad (46)$$

When $\{\lambda \text{ or } \Omega\} \longrightarrow \infty$, we obtain the approximate expression

$$\mathbf{V}(\mathbf{r}, t) \approx \mathbf{U}(\mathbf{r}, t). \quad (47)$$

Note that a new vector $\mathbf{W}(\mathbf{r}, t) = \Gamma\mathbf{V}(\mathbf{r}, t)$ may be introduced and the quantity

$$\xi(\mathbf{r}, t) = \frac{\partial W_i(\mathbf{r}, t)}{\partial r_i} = \frac{\partial \mathbf{W}(\mathbf{r}, t)}{\partial \mathbf{r}} = \frac{\partial V_2(\mathbf{r}, t)}{\partial r_1} - \frac{\partial V_1(\mathbf{r}, t)}{\partial r_2}$$

then describes the vortex component of the velocity field $\mathbf{V}(\mathbf{r}, t)$.

Equation (45) differs from Eq. (2) in that the parameter $\Lambda$ is a tensor. In addition, $\mathbf{U}(\mathbf{r}, t)$ in Eq. (45) is a divergence field, and for the divergence-free field $\mathbf{u}(\mathbf{r}, t)$, the quantity

$$\mathrm{div}\mathbf{U}(\mathbf{r}, t) = \frac{\partial \mathbf{U}(\mathbf{r}, t)}{\partial \mathbf{r}} = \lambda\frac{\partial}{\partial r_k}\Lambda^{-1}_{k\mu}u_\mu(\mathbf{r}, t) = \frac{2\lambda\Omega}{\lambda^2 + 4\Omega^2}\Gamma_{k\mu}\frac{\partial u_\mu(\mathbf{r}, t)}{\partial r_k}$$

is related to the vortex component of $\mathbf{u}(\mathbf{r}, t)$.

As previously, we assume that the variance $\sigma_\mathbf{u}^2 = \langle \mathbf{u}^2(\mathbf{r}, t)\rangle$ is small and Eq. (45) can be linearized relative to the flow (47) for large$\{\lambda, \Omega\}$. As a result, we obtain the equation

$$\frac{\partial}{\partial t}\mathbf{V}(\mathbf{r}, t) + \left(\mathbf{U}(\mathbf{r}, t)\frac{\partial}{\partial \mathbf{r}}\right)\mathbf{V}(\mathbf{r}, t) + \left(\mathbf{V}(\mathbf{r}, t)\frac{\partial}{\partial \mathbf{r}}\right)\mathbf{U}(\mathbf{r}, t) = -\Lambda[\mathbf{V}(\mathbf{r}, t) - \mathbf{U}(\mathbf{r}, t)],$$

which in coordinate form is

$$\frac{\partial V_i(\mathbf{r}, t)}{\partial t} + \Lambda_{i\mu}V_\mu(\mathbf{r}, t) = -U_k(\mathbf{r}, t)\frac{\partial V_i(\mathbf{r}, t)}{\partial r_k} - \frac{\partial U_i(\mathbf{r}, t)}{\partial r_k}V_k(\mathbf{r}, t) + \Lambda_{i\mu}U_\mu(\mathbf{r}, t).$$

If $\{\lambda, \Omega\} \gg \sigma_\mathbf{u}^2\tau_0/l_{\mathrm{cor}}^2$, where, as previously, $l_{\mathrm{cor}}$ is the spatial correlation scale of $\mathbf{V}(\mathbf{r}, t)$, then we may discard the advective terms and pass to the simple linear equation

$$\frac{\partial V_i(\mathbf{r}, t)}{\partial t} + \Lambda_{i\mu}V_\mu(\mathbf{r}, t) = \lambda u_i(\mathbf{r}, t). \quad (48)$$

For the variational derivative at $t > t'$, we have the matrix equation

$$\frac{\partial}{\partial t}\frac{\delta V_i(\mathbf{r}, t)}{\delta u_l(\mathbf{r}', t')} + \Lambda_{i\mu}\frac{\delta V_\mu(\mathbf{r}, t)}{\delta u_l(\mathbf{r}', t')} = 0,$$

which in coordinate form is the system of equations

$$\left(\frac{\partial}{\partial t} + \lambda\right)\frac{\delta V_i(\mathbf{r}, t)}{\delta u_l(\mathbf{r}', t')} = 2\Omega\frac{\delta W_i(\mathbf{r}, t)}{\delta u_l(\mathbf{r}', t')},$$

$$\left(\frac{\partial}{\partial t} + \lambda\right)\frac{\delta W_i(\mathbf{r}, t)}{\delta u_l(\mathbf{r}', t')} = -2\Omega\frac{\delta V_i(\mathbf{r}, t)}{\delta u_l(\mathbf{r}', t')}$$

with the initial conditions at $t = t'$

$$\frac{\delta V_i(\mathbf{r}, t')}{\delta u_l(\mathbf{r}', t')} = \lambda\delta_{il}\delta(\mathbf{r} - \mathbf{r}'), \quad \frac{\delta W_i(\mathbf{r}, t')}{\delta u_l(\mathbf{r}', t')} = \lambda\Gamma_{il}\delta(\mathbf{r} - \mathbf{r}').$$

The solution to this system is

$$\frac{\delta}{\delta u_l(\mathbf{r}', l')}\begin{pmatrix} V_i(\mathbf{r}, t) \\ W_i(\mathbf{r}, t)\end{pmatrix} = \lambda e^{-\lambda(t-t')}\delta(\mathbf{r} - \mathbf{r}')A(t - t')\begin{pmatrix} \delta_{il} \\ \Gamma_{il}\end{pmatrix},$$

where the matrix

$$A(t) = \begin{pmatrix} \cos(2\Omega t) & \sin(2\Omega t) \\ -\sin(2\Omega t) & \cos(2\Omega t)\end{pmatrix}.$$

Thus, the final expression for the variational derivative is

$$\frac{\delta V_i(\mathbf{r}, t)}{\delta u_l(\mathbf{r}', t')} = \lambda\delta(\mathbf{r} - \mathbf{r}')e^{-\lambda(t-t')} \times \{\delta_{il}\cos[2\Omega(t - t')] + \Gamma_{il}\sin[2\Omega(t - t')]\}. \quad (49)$$

### *4.1. The Spatial Correlation Tensor of* $\mathbf{V}(\mathbf{r}, t)$

The equation

$$\frac{\partial}{\partial t}\langle V_i(\mathbf{r}, t)V_j(\mathbf{r}_1, t)\rangle + \Lambda_{i\mu}\langle V_\mu(\mathbf{r}, t)V_j(\mathbf{r}_1, t)\rangle + \Lambda_{j\mu}\langle V_i(\mathbf{r}, t)V_\mu(\mathbf{r}_1, t)\rangle = \lambda\langle u_i(\mathbf{r}, t)V_j(\mathbf{r}_1, t)\rangle + \lambda\langle u_j(\mathbf{r}_1, t)V_i(\mathbf{r}, t)\rangle \quad (50)$$

follows from Eq. (48) for the simultaneous spatial correlation tensor. Using the Furutsu–Novikov formula

(17) and expressions (49), we find that the stationary correlation tensor is described by the equation

$$\begin{aligned} &2\lambda\langle V_i(\mathbf{r}, t)V_j(\mathbf{r}_1, t)\rangle \\ &-2\Omega[\langle W_i(\mathbf{r}, t)V_j(\mathbf{r}_1, t)\rangle + \langle V_i(\mathbf{r}, t)W_j(\mathbf{r}_1, t)\rangle] \\ &= 2\lambda^2\int_0^\infty d\tau e^{-\lambda\tau}\cos(2\Omega\tau)B_{ij}(\mathbf{r}-\mathbf{r}_1, \tau) \\ &+\lambda^2\int_0^\infty d\tau e^{-\lambda\tau}\sin 2\Omega\tau \\ &\times[\Gamma_{j\mu}B_{i\mu}(\mathbf{r}-\mathbf{r}_1, \tau) + \Gamma_{i\mu}B_{j\mu}(\mathbf{r}-\mathbf{r}_1, \tau)]. \end{aligned} \tag{51}$$

Therefore, setting $\mathbf{r} = \mathbf{r}_1$ and $i = j$ in (51), we can obtain a stationary value for the variance $\langle \mathbf{V}^2(\mathbf{r}, t)\rangle$,

$$\langle \mathbf{V}^2(\mathbf{r}, t)\rangle = \lambda\int_0^\infty d\tau e^{-\lambda\tau}\cos(2\Omega\tau)B_{ii}(0, \tau), \tag{52}$$

because

$$B_{il}(0, \tau)\Gamma_{il} \equiv 0, \quad \Gamma_{i\mu}\langle V_i(\mathbf{r}, t)V_\mu(\mathbf{r}, t)\rangle \equiv 0.$$

Let us now discuss the statistical parameters of such spatial derivatives of $\mathbf{V}(\mathbf{r}, t)$ as $\langle(\partial V_i(\mathbf{r}, t)/\partial r_k)(\partial V_j(\mathbf{r}, t)/\partial r_l)\rangle$. For the two-dimensional velocity field $\mathbf{u}(\mathbf{r}, t)$, we derive the following expression using equality (15):

$$\begin{aligned} -\frac{\partial^2 B_{ij}(0, \tau)}{\partial r_k \partial r_l} &= \frac{1}{8}D(\tau) \\ &\times(3\delta_{kl}\delta_{ij} - \delta_{ki}\delta_{lj} - \delta_{kj}\delta_{li}), \end{aligned} \tag{53}$$

where $D(\tau) = \int d\mathbf{k}\mathbf{k}^2 E(k, \tau)$. Hence, from Eq. (51), we arrive at the equation

$$\begin{aligned} &2\lambda\left\langle\frac{\partial V_i(\mathbf{r}, t)}{\partial r_k}\frac{\partial V_j(\mathbf{r}, t)}{\partial r_l}\right\rangle - 2\Omega\left[\left\langle\frac{\partial W_i(\mathbf{r}, t)}{\partial r_k}\frac{\partial V_j(\mathbf{r}, t)}{\partial r_l}\right\rangle\right. \\ &\left.+\left\langle\frac{\partial V_i(\mathbf{r}, t)}{\partial r_k}\frac{\partial W_j(\mathbf{r}, t)}{\partial r_l}\right\rangle\right] \\ &= \frac{\lambda^2}{4}D_2(\lambda, \Omega)(3\delta_{kl}\delta_{ij} - \delta_{ki}\delta_{lj} - \delta_{kj}\delta_{li}) \\ &-\frac{\lambda^2}{8}D_3(\lambda, \Omega)(\delta_{ki}\Gamma_{jl} + \delta_{li}\Gamma_{jk} + \delta_{lj}\Gamma_{ik} + \delta_{kj}\Gamma_{il}), \end{aligned} \tag{54}$$

where the coefficients

$$\begin{aligned} D_2(\lambda, \Omega) &= \int_0^\infty d\tau e^{-\lambda\tau}\cos(2\Omega\tau)D(\tau), \\ D_3(\lambda, \Omega) &= \int_0^\infty d\tau e^{-\lambda\tau}\sin(2\Omega\tau)D(\tau). \end{aligned}$$

Setting $i = k$ and $j = l$ in Eq. (54), we obtain the steady-state equation

$$\lambda\langle d^2(\mathbf{r}, t)\rangle = 2\Omega\langle\xi(\mathbf{r}, t)d(\mathbf{r}, t)\rangle, \tag{55}$$

where

$$d(\mathbf{r}, t) = \frac{\partial \mathbf{V}(\mathbf{r}, t)}{\partial \mathbf{r}}, \quad \xi(\mathbf{r}, t) = \frac{\partial \mathbf{W}(\mathbf{r}, t)}{\partial \mathbf{r}}.$$

Setting now $i = j$ and $k = l$ in Eq. (54), we derive a steady-state expression for the vortex part of the velocity field $\mathbf{V}(\mathbf{r}, t)$:

$$-\langle \mathbf{V}(\mathbf{r}, t)\Delta\mathbf{V}(\mathbf{r}, t)\rangle = \lambda D_2(\lambda, \Omega). \tag{56}$$

Let us now write out the equation for the matrix $\left\langle\frac{\partial V_i(\mathbf{r}, t)}{\partial r_k}d(\mathbf{r}, t)\right\rangle$:

$$\begin{aligned} &\lambda\left\langle\frac{\partial V_i(\mathbf{r}, t)}{\partial r_k}d(\mathbf{r}, t)\right\rangle \\ &-\Omega\Gamma_{i\mu}\left\langle\frac{\partial V_\mu(\mathbf{r}, t)}{\partial r_k}d(\mathbf{r}, t)\right\rangle - \Omega\left\langle\xi(\mathbf{r}, t)\frac{\partial V_i(\mathbf{r}, t)}{\partial r_k}\right\rangle = 0. \end{aligned}$$

Multiplying it by $\Gamma_{ki}$ yields the equation

$$\lambda\langle\xi(\mathbf{r}, t)d(\mathbf{r}, t)\rangle = \Omega[\langle\xi^2(\mathbf{r}, t)\rangle - \langle d^2(\mathbf{r}, t)\rangle]. \tag{57}$$

Multiplying now Eq. (54) by $\Gamma_{ki}\Gamma_{lj}$ yields the third steady-state equation

$$\lambda\langle\xi^2(\mathbf{r}, t)\rangle + 2\Omega\langle d(\mathbf{r}, t)\xi(\mathbf{r}, t)\rangle = \lambda^2 D_2(\lambda, \Omega). \tag{58}$$

Thus, we derived the system of equations (55)–(58) whose solution is

$$\begin{aligned} \langle\xi^2(\mathbf{r}, t)\rangle &= \lambda\frac{\lambda^2 + 2\Omega^2}{\lambda^2 + 4\Omega^2}D_2(\lambda, \Omega), \\ \langle d^2(\mathbf{r}, t)\rangle &= \frac{2\lambda\Omega^2}{\lambda^2 + 4\Omega^2}D_2(\lambda, \Omega), \\ \langle\xi(\mathbf{r}, t)d(\mathbf{r}, t)\rangle &= \frac{\lambda^2\Omega}{\lambda^2 + 4\Omega^2}D_2(\lambda, \Omega). \end{aligned} \tag{59}$$

If $\lambda/\Omega \ll 1$ and $\Omega\tau_0 \gg 1$, then $D_2(\lambda, \Omega) \approx (\lambda/4\Omega^2)D(0)$ and we have

$$\begin{aligned} \langle\xi^2(\mathbf{r}, t)\rangle &= \langle d^2(\mathbf{r}, t)\rangle = \frac{\lambda^2}{8\Omega^2}D(0), \\ \langle\xi(\mathbf{r}, t)d(\mathbf{r}, t)\rangle &= \frac{\lambda^3}{16\Omega^3}D(0). \end{aligned} \tag{60}$$

If, alternatively, $\lambda/\Omega \gg 1$ but $\Omega\tau_0 \gg 1$, then $D_2(\lambda, \Omega) \approx D(0)/\lambda$ and, hence,

$$\langle \xi^2(\mathbf{r}, t)\rangle = D(0), \quad \langle d^2(\mathbf{r}, t)\rangle = \frac{2\Omega^2}{\lambda^2}D(0), \qquad \langle \xi(\mathbf{r}, t)d(\mathbf{r}, t)\rangle = \frac{\Omega}{\lambda}D(0). \tag{61}$$

Thus, the order of the solution to the problem is $\sigma_{\mathbf{u}}^2$ If, however, $\Omega \longrightarrow 0$, then, as we saw above, the order of the solution to the problem is $\sigma_{\mathbf{u}}^4$ and advective effects should be taken into account.

### *4.2. The Time Correlation Tensor of* $\mathbf{V}(\mathbf{r}, t)$

The equation for the space-time correlation tensor at $t > t_1$ is

$$\frac{\partial}{\partial t}\langle V_i(\mathbf{r}, t)V_j(\mathbf{r}_1, t_1)\rangle + \Lambda_{i\mu}\langle V_\mu(\mathbf{r}, t)V_j(\mathbf{r}_1, t_1)\rangle = \lambda\langle u_i(\mathbf{r}, t)V_j(\mathbf{r}_1, t_1)\rangle.$$

It can be written in the steady-state regime by using the Furutsu–Novikov formula (17) and equality (49) as

$$\begin{aligned}\frac{\partial}{\partial\tau}\langle V_i(\mathbf{r}, t+\tau)V_j(\mathbf{r}_1, t)\rangle &+ \lambda\langle V_i(\mathbf{r}, t+\tau)V_j(\mathbf{r}_1, t)\rangle \\ &- 2\Omega\Gamma_{i\mu}\langle V_\mu(\mathbf{r}, t+\tau)V_j(\mathbf{r}_1, t)\rangle \\ = \lambda^2 e^{\lambda\tau}\int_\tau^\infty d\tau_1 B_{ij}(\mathbf{r}-\mathbf{r}_1, \tau_1)e^{-\lambda\tau_1}\cos(2\Omega\tau) &+ \lambda^2 e^{\lambda\tau}\Gamma_{j\mu}\int_\tau^\infty d\tau_1 B_{i\mu}(\mathbf{r}-\mathbf{r}_1, \tau_1)e^{-\lambda\tau_1}\sin(2\Omega\tau)\end{aligned} \tag{62}$$

with the initial condition at $\tau = 0$

$$\langle V_i(\mathbf{r}, t+\tau)V_j(\mathbf{r}_1, t_1)\rangle_{\tau=0} = \langle V_i(\mathbf{r}, t)V_j(\mathbf{r}_1, t)\rangle.$$

We are concerned with the quantity

$$K_{ij}(\mathbf{r}-\mathbf{r}_1) = \int_0^\infty d\tau\langle V_i(\mathbf{r}, t+\tau)V_j(\mathbf{r}_1, t)\rangle \tag{63}$$

and quantities (11)

$$D_0 = \frac{1}{2}K_{ii}(0) = \frac{1}{2}\tau_{\mathbf{V}}\langle \mathbf{V}^2(\mathbf{r}, t)\rangle,$$

$$D^{(\mathbf{V})} = \left.\frac{\partial^2 K_{ij}(\mathbf{r}-\mathbf{r}_1)}{\partial r_i \partial r_{1j}}\right|_{\mathbf{r}=\mathbf{r}_1} = \tau_{\mathrm{div}\mathbf{V}}\left\langle\left(\frac{\partial \mathbf{V}(\mathbf{r}, t)}{\partial \mathbf{r}}\right)^2\right\rangle,$$

which define the diffusion coefficients in Eq. (10).

For quantity (63), we derive the following expression from Eq. (62):

$$\begin{aligned}\lambda K_{ij}(\mathbf{r}-\mathbf{r}_1) - 2\Omega\Gamma_{i\mu}(\mathbf{r}-\mathbf{r}_1) &= \langle V_i(\mathbf{r}, t)V_j(\mathbf{r}_1, t)\rangle \\ &+ \lambda\int_0^\infty d\tau B_{ij}(\mathbf{r}-\mathbf{r}_1, \tau)[1-e^{-\lambda\tau}]\cos(2\Omega\tau) \\ &+ \lambda\Gamma_{j\mu}\int_0^\infty d\tau B_{i\mu}(\mathbf{r}-\mathbf{r}_1, \tau)[1-e^{-\lambda\tau}]\sin(2\Omega\tau).\end{aligned} \tag{64}$$

Setting $i = j$ and $\mathbf{r}_1 = \mathbf{r}$ in (64), we obtain the equality

$$\lambda\tau_{\mathbf{V}}\langle \mathbf{V}^2(\mathbf{r}, t)\rangle = \langle \mathbf{V}^2(\mathbf{r}, t)\rangle + \lambda\int_0^\infty d\tau B_{ii}(0, \tau)[1-e^{-\lambda\tau}]\cos(2\Omega\tau),$$

where $\tau_{\mathbf{V}}$ is the time correlation length of $\mathbf{V}(\mathbf{r}, t)$. Given expression (52), the latter equality can be rewritten as

$$\begin{aligned}D_0 &= \frac{1}{2}\tau_{\mathbf{V}}\langle \mathbf{V}^2(\mathbf{r}, t)\rangle \\ &= \frac{1}{2}\int_0^\infty d\tau B_{ii}(0, \tau)\cos(2\Omega\tau) = \frac{\pi}{2}\int d\mathbf{k}\Phi(k, 2\Omega),\end{aligned} \tag{65}$$

where $\Phi(k, \omega)$ is the space-time spectral function (12), (13) of $\mathbf{u}(\mathbf{r}, t)$.

Let us act on Eq. (64) with the operator $\partial^2/\partial r_k \partial r_{1l}$ and set $\mathbf{r}_1 = \mathbf{r}$ and $j = l$. As a result, we obtain an equation for the matrix $\langle(\partial V_i(\mathbf{r}, t)/\partial r_k)d(\mathbf{r}, t)\rangle$ using expression (53) in the form

$$\begin{aligned}\lambda\int_0^\infty d\tau\left\langle\frac{\partial V_i(\mathbf{r}, t+\tau)}{\partial r_k}d(\mathbf{r}, t)\right\rangle \\ - 2\Omega\Gamma_{i\mu}\int_0^\infty d\tau\left\langle\frac{\partial V_\mu(\mathbf{r}, t+\tau)}{\partial r_k}d(\mathbf{r}, t)\right\rangle = \left\langle\frac{\partial V_i(\mathbf{r}, t)}{\partial r_k}d(\mathbf{r}, t)\right\rangle.\end{aligned} \tag{66}$$

Setting now $i = k$ in Eq. (66), we arrive at the steady-state equation

$$\begin{aligned}\lambda\int_0^\infty d\tau\langle d(\mathbf{r}, t+\tau)d(\mathbf{r}, t)\rangle \\ - 2\Omega\int_0^\infty d\tau\langle \xi(\mathbf{r}, t+\tau)d(\mathbf{r}, t)\rangle = \langle d^2(\mathbf{r}, t)\rangle.\end{aligned} \tag{67}$$

Multiplying (66) by $\Gamma_{ki}$ yields the equation

$$\lambda\int_0^\infty d\tau\langle\xi(\mathbf{r}, t+\tau)d(\mathbf{r}, t)\rangle + 2\Omega\int_0^\infty d\tau\langle(d(\mathbf{r}, t+\tau))d(\mathbf{r}, t)\rangle = \langle\xi(\mathbf{r}, t)d(\mathbf{r}, t)\rangle. \quad (68)$$

Thus, we derived the system of equations (67) and (68) whose solution can be written using expressions (59) as

$$D^{(\mathbf{V})} = \int_0^\infty d\tau\langle d(\mathbf{r}, t+\tau)d(\mathbf{r}, t)\rangle = \frac{\lambda\langle d^2(\mathbf{r}, t)\rangle + 2\Omega\langle\xi(\mathbf{r}, t)d(\mathbf{r}, t)\rangle}{\lambda^2 + 4\Omega^2} = \frac{4\lambda^2\Omega^2}{(\lambda^2+4\Omega^2)^2}\int_0^\infty d\tau e^{-\lambda\tau}\cos(2\Omega\tau)D(\tau).$$

If $\{\lambda, \Omega\}\tau_0 \gg 1$, then

$$D^{(\mathbf{V})} = \frac{4\lambda^3\Omega^2 D(0)}{(\lambda^2+4\Omega^2)^3} = \begin{cases} 4\Omega^2 D(0)/\lambda^3, & \lambda \gg \Omega, \\ \lambda^3 D(0)/16\Omega^4, & \lambda \ll \Omega, \end{cases} \quad (69)$$

where, as previously,

$$D(0) = \int d\mathbf{k}k^2 E(k, 0) = -\langle\mathbf{u}(\mathbf{r}, t)\Delta\mathbf{u}(\mathbf{r}, t)\rangle.$$

Thus, when the conditions $\{\lambda, \Omega\}\tau_0 \gg 1$ are satisfied, the generation of the divergence part of $\mathbf{V}(\mathbf{r}, t)$ in our problem is described by a linear equation without advective terms. If, in addition, $\lambda \gg \Omega$, then the following correction terms of order $\sigma_{\mathbf{u}}^4$ (41), which may be comparable to (69) in some cases, should be taken into account; i.e., in this case, we obtain

$$D^{(\mathbf{V})} = \frac{3}{2}\frac{\tau_0}{\lambda^2}\langle\mathbf{u}(\mathbf{r}, t)\Delta\mathbf{u}(\mathbf{r}, t)\rangle^2 - \frac{4\Omega^2}{\lambda^3}\langle\mathbf{u}(\mathbf{r}, t)\Delta\mathbf{u}(\mathbf{r}, t)\rangle = -\frac{4\Omega^2}{\lambda^3}\langle\mathbf{u}(\mathbf{r}, t)\Delta\mathbf{u}(\mathbf{r}, t)\rangle\left\{1 - \frac{3\lambda\tau_0}{2\Omega^2}\langle\mathbf{u}(\mathbf{r}, t)\Delta\mathbf{u}(\mathbf{r}, t)\rangle\right\}. \quad (70)$$

The spatial diffusion coefficient $D_0$ does not depend on $\lambda$ and is described by expression (65).

## 5. CONCLUSION

We have derived expressions for the diffusion coefficients that characterize the clustering of the low-inertial particle number density in hydrodynamic flows in various asymptotic regimes. We did not set the goal of studying these coefficients (and, hence, the clustering itself) for specific geophysical and astrophysical problems. These are completely independent problems that can be solved by using the derived expressions. The basic equation for us was the phenomenological nonlinear equation (2) in the Eulerian representation. Although the characteristic equations (3) in the Lagrangian representation are simple in form, the initial problem (2) is complex. This is clear at least from the fact that Eq. (2) is a quasi-linear partial differential equation and, in general, nonuniqueness of the solution to the problem, the existence of discontinuities in them, etc., are possible. In the asymptotic case of low particle inertia, the situation significantly simplifies and we pass to a linear problem in the Eulerian representation. However, even for this problem, it is difficult to specify the possible orders of smallness for the corresponding diffusion coefficients, because there are several dimensionless parameters. Thus, for example, for the problem with rotation, there are three time scales even in the formulation of the problem alone. In addition, two statistical scales emerge, the diffusion coefficients, which also have the dimensions of inverse time. Therefore, we have to perform a detailed analysis of the problem, which was done here.

## ACKNOWLEDGMENTS

This study was supported in part by the German–Israeli Project (DIP) of the Federal Ministry of Education and Research (BMBF) and the INTAS (grant no. 00-0309). One of us (V.I.K.) wishes to thank the Special Foundation for Young Scientists at the Faculty of Engineering of the Ben-Gurion University of Negev and the Russian Foundation for Basic Research (project nos. 00-15-98608, 01-05-64042, and 02-05-64375).

## REFERENCES

1. G. G. Stokes, Trans. Camb. Philos. Soc. **9**, 8 (1851).
2. H. Lamb, *Hydrodynamics* (Dover, New York, 1932; Gostekhizdat, Moscow, 1947).
3. M. Ungarish, *Hydrodynamics of Suspensions: Fundamentals of Centrifugal and Gravity Separation* (Springer-Verlag, New York, 1993).
4. *Sedimentation of Small Particles in a Viscous Fluid*, Ed. by E. M. Tory (Computational Mechanics Publications, Southampton, 1996), Advances in Fluid Mechanics, Vol. 7.
5. M. R. Maxey and J. J. Riley, Phys. Fluids **26**, 883 (1983).
6. M. R. Maxey and S. Corsin, J. Atmos. Sci. **43**, 1112 (1986).
7. M. R. Maxey, J. Fluid Mech. **174**, 441 (1987).
8. M. R. Maxey, Philos. Trans. R. Soc. London, Ser. A **333**, 289 (1990).
9. L. P. Wang and M. R. Maxey, J. Fluid Mech. **256**, 27 (1993).

10. M. R. Maxey, E. J. Chang, and L.-P. Wang, Exp. Therm. Fluid Sci. **12**, 417 (1996).
11. T. Elperin, N. Kleeorin, and I. Rogachevskii, Phys. Rev. E **53**, 3431 (1996); **58**, 3113 (1998); Phys. Rev. Lett. **76**, 224 (1996); **77**, 5373 (1996); **81**, 2898 (1998); Atmos. Res. **53**, 117 (2000).
12. E. Balkovsky, G. Falkovich, and A. Fouxon, Phys. Rev. Lett. **86**, 2790 (2001).
13. V. I. Klyatskin and A. I. Saichev, Zh. Éksp. Teor. Fiz. **111**, 1297 (1997) [JETP **84**, 716 (1997)].
14. V. I. Klyatskin and D. Gurarie, Usp. Fiz. Nauk **169**, 171 (1999).
15. V. I. Klyatskin, Izv. Akad. Nauk, Fiz. Atmos. Okeana **36**, 177 (2000).
16. V. I. Klyatskin, *Stochastic Equations as Point of View of Physicist (Basic Ideas, Exact Results, and Asymptotic Approximations)* (Fizmatlit, Moscow, 2001).
17. C. L. Zirbel and E. Çinlar, *Stochastic Models in Geosystems*, Ed. by S. A. Molchanov and W. A. Woyczynski (Springer-Verlag, New York, 1996), IMA Volumes in Mathematics and Its Applications, Vol. 85, p. 459.
18. K. V. Koshel' and O. V. Aleksandrova, Izv. Akad. Nauk, Fiz. Atmos. Okeana **35**, 638 (1999).
19. V. I. Klyatskin and K. V. Koshel', Usp. Fiz. Nauk **170**, 771 (2000).
20. K. Furutsu, J. Res. Natl. Bur. Stand., Sect. D **67**, 303 (1963).
21. E. A. Novikov, Zh. Éksp. Teor. Fiz. **47**, 1919 (1964) [Sov. Phys. JETP **20**, 1290 (1964)].
22. V. I. Klyatskin, *Mathematics of Random Media*, Ed. by W. Kohler and B. S. White (American Mathematical Society, Providence, 1991), Lectures in Applied Mathematics, Vol. 27, p. 447.
23. V. I. Klyatskin and I. G. Yakushkin, Zh. Éksp. Teor. Fiz. **118**, 849 (2000) [JETP **91**, 736 (2000)].

*Translated by V. Astakhov*

*Journal of Experimental and Theoretical Physics, Vol. 95, No. 2, 2002, pp. 294–299.*
*Translated from Zhurnal Éksperimental'noĭ i Teoreticheskoĭ Fiziki, Vol. 122, No. 2, 2002, pp. 341–346.*


**SOLIDS**
**Structure**

# Equilibrium Processes of Oxygen Diffusion between Bulk and (100) Surface of Tantalum

**N. R. Gall'*, E. V. Rut'kov, and A. Ya. Tontegode**

*Ioffe Physicotechnical Institute, Russian Academy of Sciences, St. Petersburg, 194021 Russia*

**e-mail: gall@ms.ioffe.rssi.ru*

Received December 24, 2001

**Abstract**—The diffusion exchange by oxygen atoms between bulk and (100) surface of tantalum at the earliest stages of oxygen adsorption was studied by high-temperature Auger electron spectroscopy (AES), whereby the spectra were recorded immediately in the course of heating the sample up to 2500 K. A difference of the potential barriers for the inward and outward diffusion of oxygen was determined, and an equilibrium character of these processes in the temperature interval from 1000 to 2000 K was demonstrated. Heating to higher temperatures results in the intense thermodesorption of oxygen. © *2002 MAIK "Nauka/Interperiodica".*

## 1. INTRODUCTION

The interaction of gases (especially of oxygen) with the surface of refractory metals (in particular, tantalum) has been extensively studied for a long time, beginning with the classical work of Langmuir [1]. Reliable data are now available on the solubility of oxygen, bulk diffusion characteristics, and the oxides formed [2–4], as well as on the laws of adsorption and desorption [5–10]. Many of these data can be found in handbooks (see, e.g., [11]). However, there are many questions which still remain unanswered. Elucidation of the laws of high-temperature oxygen adsorption and the diffusion exchange by oxygen atoms between bulk and surface of a metal are among currently important problems.

Previously, we have studied in detail the equilibrium diffusion of carbon atoms between (100) surface and bulk of several metals including W [12], Mo [13], and Ta [14]. Since oxygen, as well as carbon, belongs to interstitial impurities, the bulk diffusion of both proceeds in a similar manner [15]. However, the behavior of these atoms in the adsorbed state is significantly different. In particular, the surface oxygen does not penetrate into the bulk of tungsten and molybdenum [7], while it dissolves well in tantalum, which was selected as the substrate in this study. Our consideration will be restricted to the earliest stages of oxygen penetration into the bulk of tantalum, long before the formation of bulky oxides.

## 2. EXPERIMENTAL

The experiments were performed in an ultrahigh vacuum (UHV), high-resolution Auger spectrometer ($\Delta E/E < 0.1\%$) with a prism energy analyzer [16]. The Auger electron spectra were taken directly from strongly (up to 2200 K) heated samples, which was of principal significance for the study of equilibrium processes in the tantalum–oxygen system at medium and high temperatures. Sensitivity of the spectrometer with respect to characteristic impurities (C, O, …) was on the order of $10^{-2}$ monolayer. The analysis was performed using an Auger peak of oxygen observed at an electron energy of $E = 504$ eV and a triplet peak of tantalum at $E = 160$–$179$ eV.

The samples were prepared as thin tantalum ribbons with dimensions $1 \times 0.05 \times 40$ mm$^3$. The ribbons were thoroughly purified from various impurities, including oxygen. For this purpose, the samples were heated by passing alternating electric current, first, in an oxygen atmosphere at $P_{O_2} \approx 1 \times 10^{-3}$ Pa and $T = 1800$ K for about 60 min and, then, under UHV conditions ($P \approx 1 \times 10^{-8}$ Pa) at $T = 2700$ K for several minutes. After this pretreatment, the ribbon texture was represented for not less than 99.5% by the (100)Ta single crystal face. Examination in a scanning electron microscope showed that the average grain size on the sample surface amounts to approximately 10 μm. The surface of ribbon samples was homogeneous with respect to the electron work function, which amounted to $e\varphi = 4.1$ eV, being typical of the (100)Ta face [17]. The samples purified by annealing as described above exhibited only the Auger peaks characteristic of pure tantalum. Cooling of the samples, either at a slow or at a fast rate, did not lead to the segregation of any impurity at the surface. Subjected to a series of measurements, the ribbon samples were regenerated by high-temperature (~2400 K) annealing, after which the initial properties of the surface were fully restored. All the results reported below were well reproduced after regeneration of the used rib-

1063-7761/02/9502-0294$22.00 © 2002 MAIK "Nauka/Interperiodica"

bons and after changing samples. For the calibration purposes, a tungsten ribbon with the surface exposing (100) faces was mounted close to the tantalum sample and subjected to a cleaning and texturing processing as described in [12].

The temperature of ribbon samples was measured by a micropyrometer. Outside the pyrometry interval, the temperature was determined by linear extrapolation of the heating current versus temperature plot. The accuracy of temperature measurements in the pyrometry interval was ±20 K; the temperature homogeneity of the ribbons was better than ±10 K.

Oxygen was admitted, from a source employing thermal decomposition of cesium bichromate, directly into the working chamber up to a pressure of (1–5) × $10^{-6}$ Pa at $T$ = 300 K. Immediately after the formation of a submonolayer surface coverage, the working chamber was evacuated. Under the conditions when no bulky oxides were formed, all oxygen that diffused into the bulk of substrate occurred in the form of a solid solution at a concentration not exceeding 1–0.1 at. % [9, 18]. A contribution of this bulk oxygen to the Auger signal intensity was ignored, and it was assumed that the Auger peak intensity is entirely due to oxygen atoms adsorbed on the surface.

## 3. THE FORMATION OF A SURFACE TANTALUM OXIDE

As is known (see [5–10] and references therein), exposure of the (100)Ta face to an oxygen atmosphere at room temperature leads (as well as in the case of the (100)W surface [18]) to the dissociative adsorption of oxygen. The AES data indicate that the surface concentration of oxygen on the sample upon gas admission to the chamber at $T$ = 300 K rapidly increases to saturation. This result coincides with that reported in [7], where the same system was studied by the flash desorption technique.

In order to determine the absolute oxygen concentration on the (100)Ta surface, a surface oxide layer with an oxygen concentration of $N_O^W = 9 \times 10^{14}$ cm$^{-2}$ was grown by the well-known method [19] on the auxiliary tungsten ribbon surface. Then, by comparing intensities of the Auger peaks of oxygen on the (100) surfaces of tantalum ($I_O^{Ta}$) and tungsten ($I_O^W$) ribbons measured in the same experiment, we could calculate the absolute oxygen concentration on the (100)Ta surface by the formula

$$N_O^{Ta} = N_O^W \frac{I_O^{Ta}}{I_O^W}.$$

In these calculations, we ignored the secondary effects related to dissimilar properties of the two substrates, in particular, to a difference in the high-energy electron backscattering [20]. This approximation was justified by the fact that Ta and W, being neighbors in the periodic table, possess close densities and atomic concentrations.

Upon the adsorption of oxygen to saturation at room temperature, the working chamber was evacuated and the system was heated for a short time to 1000 K, after which the heating current was switched off. After this, the atomic oxygen concentration on the sample surface was $N_O^{Ta} = (7 \pm 1) \times 10^{14}$ cm$^{-2}$. This is higher than the value reported in [7], where the Ta/O system was studied by the flash desorption technique and the concentration of oxygen on the surface saturated at 300 K was about $4 \times 10^{14}$ cm$^{-2}$. It should be noted that this value was obtained using a complicated procedure requiring the knowledge of the exact electron-impact ionization cross sections of Ta atoms and TaO molecules, as well as of some other technical characteristics of the mass spectrometer employed. We believe that such a method provides only an estimate of the oxygen surface coverage on tantalum.

The maximum density of oxygen atoms on the (100) surface of tantalum, as well as that on (100)W, is somewhat smaller than the surface concentration of metal atoms $N^{Ta} = 9.3 \times 10^{14}$ cm$^{-2}$. This is probably related to the fact that the dissociative adsorption requires two adjacent vacant adsorption sites. For example, on the (100) face of a bcc metal, these are the surface wells with a coordination number of four. Upon saturation of the oxygen adsorption process, the surface still contains "single" wells surrounded by adsorbed oxygen species. According to the model adopted, these single wells are not suited for the adsorption of oxygen. Computer simulation of the oxygen adsorption, assuming random incidence of the molecules onto the substrate surface and the absence of surface migration, shows that 15–20% of the single centers (wells) remain free when the adsorption process ceases, in good agreement with experiment. For convenience, we took the surface oxygen concentration $N_O^{Ta} = 7 \times 10^{14}$ cm$^{-2}$ as corresponding to the unit coverage $\theta_O = 1$ and considered the corresponding adsorption state as an oxygen-deficient surface oxide of tantalum.

## 4. OXYGEN THERMODESORPTION FROM TANTALUM SURFACE

According to the mass spectrometric data reported in the literature, the thermal desorption of oxygen from the surface of tantalum is observed only at rather high temperatures [7]. During this process, oxygen is removed from the metal surface only as a result of desorption of TaO molecules [7], in contrast to tungsten, from which oxygen is desorbed in the form of isolated atoms [20]. Using the kinetic parameters of oxygen desorption [7], namely, the desorption activation energy $E_{des}$ = 5.6 eV and preexponential factor $\tau_0 = 2 \times 10^{-12}$ s

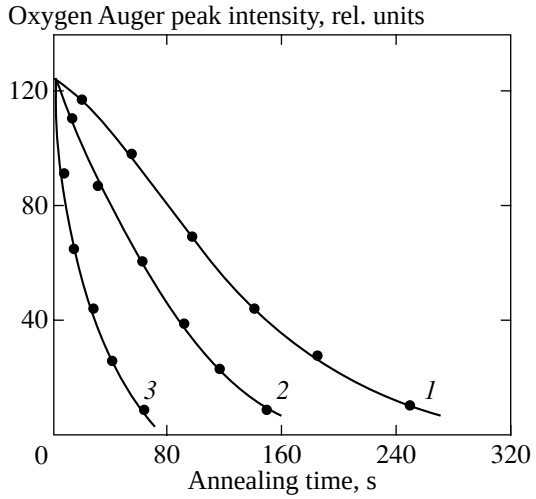


**Fig. 1.** Variation of the oxygen AES signal intensity on the (100)Ta surface with increasing time of annealing at various temperatures $T$ = 2250 (*1*), 2300 (*2*), and 2350 K (*3*). The initial surface concentration of oxygen is $N_O = 7 \times 10^{14}$ cm$^{-2}$. The Auger spectra were recorded upon rapid (below 1 s) cooling of a tantalum ribbon down to room temperature after switching off the heating current.

in the Arrhenius equation, it is possible to estimate the absolute values of the desorption flux.

The results of our AES measurements fully confirmed the above data. We measured the rate of decrease in the Auger peak of oxygen in the course of high-temperature annealing of the surface oxide formed on the (100)Ta face. The results of these experiments are presented in Fig. 1. For example, the complete removal of oxygen from the surface oxide at $T$ = 2350 K takes about 60 s.

In the other series of experiments, a surface oxide was created on an auxiliary tantalum ribbon with the properties completely identical to those of the working substrate. The auxiliary ribbon was placed at a distance of about 20 mm from the working ribbon, oriented parallel to this ribbon, and tilted so that the surfaces of the two ribbons would make an angle of 45°. Impurities desorbed from the auxiliary ribbon partly adsorbed on the working substrate and could be detected by AES. The desorption of oxygen and tantalum was monitored by AES using the surface of an auxiliary tungsten ribbon. The experimental conditions and procedures are described in more detail elsewhere [21].

It was found that the AES signal of desorbed oxygen is observed only upon heating the auxiliary ribbon above 2100 K. The AES signal of tantalum appears simultaneously and the two signals grow synchronously at all desorption temperatures studied. The coefficient of transfer from one ribbon to another, determined taking into account their mutual arrangement and assuming that the desorbed species are distributed by the cosine law, amounted to about 2.5% (the same value was obtained in [21]). Using this coefficient, we calculated absolute rates of the oxygen desorption from tantalum in the temperature interval from 2100 to 2400 K, which showed good agreement with the data reported in [7].

## 5. THERMAL STABILITY OF SURFACE OXIDE ON TANTALUM

Based on the above data, we concluded that adsorbed oxygen atoms do not leave the system at temperatures below 2100 K. The method of thermodesorption spectroscopy employed in [7, 22] is ineffective in the temperature range from 300 to 2200 K and provides information only about the amount of desorbed substance, rather than on the surface concentration. The conventional AES measurements, performed upon rapidly cooling the annealed sample down to room temperature, does not provide information about the high-temperature composition of the adsorbed layer (modified by fast diffusion processes). A true physical pattern of processes on the sample surface was revealed only by measuring the Auger spectra of oxygen immediately on the heated sample.

It was found that the AES signal of oxygen remains unchanged on heating the sample up to $T \approx 1000$ K. The intensity of the AES signal from the tantalum substrate also remained constant. Attenuated by a factor of 1.1 due to the layer of adsorbed oxygen, the substrate signal has proved to be not very informative in this study.

Heating above 1000 K led to a gradual decrease in intensity of the Auger peak of oxygen (Fig. 2, curve *1*). The results of measurements performed upon cooling give the same experimental points as those obtained in the course of direct heating, which indicates that the system behavior is completely reversible. No time delay was observed in variations of the Auger signal of oxygen at each particular temperature $T$ = const. This result implies that the oxygen coverage changes very rapidly in response to the temperature variations. This is possible only when a diffusion equilibrium takes place in the whole system: first, between the tantalum surface and bulk, whereby the flux of oxygen $\nu_{S1}$ leaving the surface is equal to the reverse flux $\nu_{1S}$ (Fig. 3) and, second, between any planes inside the metal, where the inward and outward fluxes of migrating oxygen atoms must be equal. Here, we ignore a possible difference between the first subsurface layer and the bulk layers [21], assuming the whole metal volume to be homogeneous.

The observed equilibrium is by no means surprising in view of a small activation energy for the bulk diffusion of oxygen in tantalum ($E_0$ = 1.2 eV [11]) and small thickness of the ribbons studied. Indeed, using the published data on the diffusion coefficient of oxygen in tantalum [11]

$$D = D_0 \exp\left(-\frac{E_0}{kT}\right) = 1.9 \times 10^{-2} \exp\left(-1.2\frac{eV}{kT}\right),$$

we can estimate the time required for an oxygen atom to travel, for example, from the middle to the surface of the ribbon at less than 1 s for $T = 1100$–$1200$ K and less than 0.1 s for $T > 1300$ K.

It should be noted that the equilibrium surface concentration of oxygen $N_S$ is much greater then the oxygen concentration $N_i$ in any interstitial plane, including that ($N_1$) in the first subsurface layer responsible for the escape of atoms from bulk to the surface (Fig 3). Indeed, for $T = 1600$ K, the surface coverage is $\theta = 0.5$ ($N_S = 3.5 \times 10^{14}$ cm$^{-2}$), while the density of oxygen atoms in the first subsurface layer can be estimated as

$$N_i = \frac{7 \times 10^{14} - 3.5 \times 10^{14}}{m/2} = 2.3 \times 10^9 \text{ cm}^{-2}.$$

Here, $m \approx 3 \times 10^5$ is the number of interatomic planes in the tantalum ribbon studied (we take into account that oxygen is adsorbed on both sides of the ribbon). A large difference between $N_S$ and $N_1$ is probably indicative of a significant difference in the magnitude of energy barriers for the oxygen dissolution ($E_{S1}$) and liberation ($E_{1S}$) in the O/(100)Ta system.

If part of the adsorbed oxygen is removed by desorption at $T > 2300$ K, the new equilibrium curves will be situated below the initial curve *1* in Fig. 2, while possessing qualitatively the same shape. At $T < 1000$ K, all oxygen present in the system will occur on the surface, which allows the total balance of oxygen atoms to be calculated as well.

## 6. A MODEL FOR CALCULATING THE BALANCE OF PARTICLES IN THE SYSTEM

The surface concentration of oxygen $N_S(T)$ at each particular temperature is experimentally determined by AES, while the concentration of oxygen atoms in any interstitial plane can be calculated by the formula

$$N_i = \frac{N_S(300 \text{ K}) - N_S(T > 1000 \text{ K})}{m/2},$$

taking into account that all oxygen at $T < 1000$ K occurs on the surface. The total amount of oxygen dissolved in the volume of a ribbon with a thickness of $h = 0.05$ mm (per cm$^2$) is

$$N_{\text{bulk}} = N_i m.$$

Let us analyze the equilibrium curves presented in Fig 2. Drawing a section along the $y$ axis and determining the ratio $N_{\text{bulk}}/N_S$ at each temperature $T = \text{const}$, we obtain an important result: the ratio $N_{\text{bulk}}/N_S$ is independent of the total amount of oxygen in the system ($N_{\text{bulk}} + N_S$), but strongly depends on the substrate temperature (Fig. 4). This result probably indicates that the values of barriers for the dissolution ($E_{S1}$) and liberation ($E_{1S}$) of oxygen are independent of the oxygen concentration on the surface and in the bulk of tantalum.

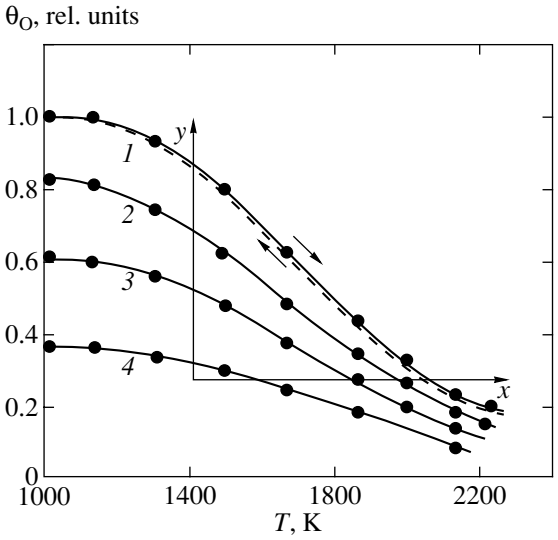


**Fig. 2.** Temperature dependence of the equilibrium adsorption coverage of oxygen on (100)Ta for the initial coverage of $\theta_O = 1.0$ (*1*), 0.82 (*2*), 0.61 (*3*), 0.38 (*4*); $\theta_O = 1$ corresponds to $N_O = 7 \times 10^{14}$ cm$^{-2}$.

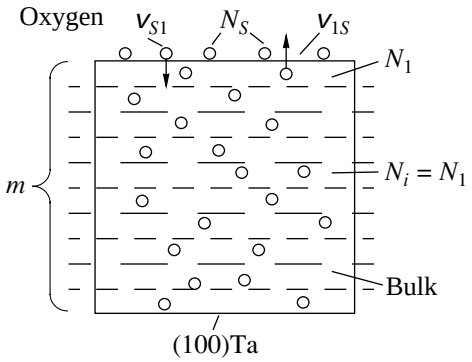


**Fig. 3.** Schematic diagram showing the cross section of a tantalum sample with dissolved and adsorbed oxygen atoms.

Indeed, the oxygen concentration in the bulk of the tantalum substrate in the temperature interval from 1000 to 2000 K is lower by 3–4 orders of magnitude than the limiting concentration $n_{\max}$ of dissolved oxygen in tantalum [9]. For example, $n_{\max} = 2.1$ at. % for $T = 1000$ K and $n_{\max} = 5.0$ at. % for $T = 1900$ K.

Let us process the data of Fig. 2 by drawing a section parallel to the $x$ axis. In equilibrium, the fluxes of dissolution ($\nu_{S1}$) and liberation ($\nu_{1S}$) are equal and can be described by the well-known expressions [10]

$$\begin{aligned} \nu_{S1} &= N_S C_S \left(1 - \frac{N_1}{N_{1\max}}\right) \exp\left(-\frac{E_{S1}}{kT}\right), \\ \nu_{1S} &= N_1 C_1 \left(1 - \frac{N_S}{N_{S\max}}\right) \exp\left(-\frac{E_{1S}}{kT}\right), \end{aligned} \quad (1)$$

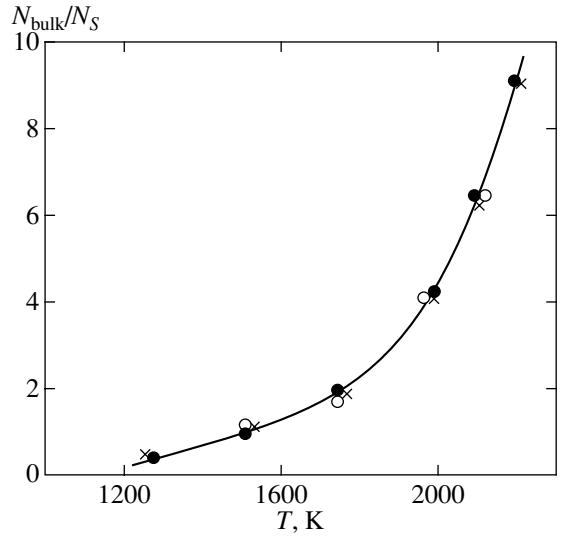


**Fig. 4.** Temperature variation of the ratio of oxygen concentrations in the bulk ($N_{bulk} = N_1 m$) and on the surface ($N_S$), representing a $y$ section of curves *1* (●), *2* (×), and *3* (○) in Fig. 2.

where $C_S$ and $C_1$ are the preexponential factors. In our experiments with small oxygen concentrations on the surface and in the bulk (far from the limiting values $N_{1max}$ and $N_{Smax}$), we can assume that $(1 - N_1/N_{1max}) \approx 1$ and $(1 - N_S/N_{Smax}) \approx 1$.

For $\nu_{S1} = \nu_{1S}$, Eqs. (1) can be transformed to

$$\frac{N_1}{N_S} = \frac{C_S}{C_1}\exp\left(-\frac{\Delta E}{kT}\right). \quad (2)$$

Determining the slopes of the straight lines $\ln N_1/N_S = f(1/kT)$ for each $N_S$ = cost, we obtained $\Delta E = E_{S1} - E_{1S} = 0.85 \pm 0.05$ eV. Then formula (2) yields $C_1/C_S = 178 \pm 20$.

Using the known values of $\Delta E$, $C_1/C_S$, and $N_1 = N_{bulk}/m$, relation (2) can be written in the following form:

$$\theta = \frac{1}{1 + \dfrac{C_S m}{2C_1}\exp\left(-\dfrac{0.85\ \text{eV}}{kT}\right)}. \quad (3)$$

The calculated temperature dependence $\theta = f(T)$ agrees very well with the experimental curve (see the dashed line in Fig. 2) in the whole temperature interval studied. This agreement is evidence in favor of validity of the proposed pattern of diffusion processes in the O/(100)Ta system and of the estimated energetic and kinetic parameters.

It is important to note that particular values of the surface oxygen concentrations $N_S = f(T)$ (but not the physical pattern or energetics of the involved processes) must significantly depend on the ribbon thickness $h$, because a change in the thickness alters the fraction of the total amount of oxygen dissolved in the substrate. Indeed, for a ribbon thickness of $h \sim 0.5$ mm (about ten times greater than the thickness of our samples) and the same experimental procedure, the equilibrium surface coverage at high temperatures will drop by almost one order of magnitude and the possibility of surface oxygen determination by AES will become problematic, although all values of the barriers will remain the same.

It is interesting to note that the equilibrium curves of variation of the surface concentration of impurity in the O/(100)Ta system are qualitatively the same as those in the systems C/(100)W [12, 23], C/(100)Mo [13], and C/(100)Ta [14]. However, the behavior of the curves in the "carbon" systems is much more complicated, which, probably, indicates that the energies of dissolution and liberation depend on the surface and bulk impurity concentrations.

## 7. CONCLUSION

The ability to "observe" the surface oxygen by AES immediately on a hot sample surface, with an allowance for the total particle balance in the system, permitted us to study in detail the equilibrium diffusion processes between the bulk and the (100) surface of tantalum involving oxygen at the earliest stages of adsorption. We have determined a difference $\Delta E$ of the energies of dissolution ($E_{S1}$) and liberation ($E_{1S}$) for oxygen in tantalum: $\Delta E = 0.85$ eV. An analytical expression was derived for the surface coverage of oxygen as a function of the temperature in the interval from 1000 to 2000 K. Probably, similar equilibrium curves can be observed for the surface of other refractory metals capable of dissolving oxygen.

## ACKNOWLEDGMENTS

This study was supported by the Ministry of Science and Technology of the Russian Federation within the framework of the Federal Program "Surface Atomic Structures" (project No. 4.6.99).

## REFERENCES

1. I. Lengmuir, Chem. Rev. **13**, 147 (1933).
2. J. K. Roberts, Proc. R. Soc. London, Ser. A **152**, 445 (1935).
3. J. L. Morrison and J. K. Roberts, Proc. R. Soc. London, Ser. A **173**, 13 (1939).
4. P. Kofstad, *High-Temperature Oxidation of Metals* (Wiley, New York, 1966; Mir, Moscow, 1969).
5. R. M. Barrer, *Diffusion in and through Solids* (Cambridge Univ. Press, Cambridge, 1941; Inostrannaya Literatura, Moscow, 1948).
6. U. R. Evans, *Corrosion and Oxidation of Metals: Scientific Principles and Practical Applications* (E. Arnold, London, 1960; Mashgiz, Moscow, 1962).

7. V. N. Ageev and N. I. Ionov, Fiz. Tverd. Tela (Leningrad) **13**, 1557 (1971) [Sov. Phys. Solid State **13**, 1305 (1971)].
8. M. W. Ruckman, S.-L. Qiu, and M. Strongin, Surf. Sci. **331–333**, 401 (1995).
9. K. Kukli, J. Aarik, A. Aidla, *et al.*, Appl. Surf. Sci. **112**, 236 (1997).
10. C. Chaneliere, J. L. Autran, R. A. B. Devine, and B. Balland, Mater. Sci. Eng., R **22**, 269 (1998).
11. G. V. Samsonov and I. M. Vinitskii, *Handbook of Refractory Compounds* (Metallurgiya, Moscow, 1976; Plenum, New York, 1980).
12. N. R. Gall', E. V. Rut'kov, and A. Ya. Tontegode, Izv. Akad. Nauk, Ser. Fiz. **62**, 1980 (1998).
13. N. R. Gall', E. V. Rut'kov, and A. Ya. Tontegode, Pis'ma Zh. Éksp. Teor. Fiz. **73**, 756 (2001) [JETP Lett. **73**, 671 (2001)].
14. N. R. Gall, E. V. Rut'kov, and A. Ya. Tontegode, Surf. Sci. **472**, 187 (2001).
15. H. J. Goldschmidt, *Interstitial Alloys* (Butterworths, London, 1967; Mir, Moscow, 1971), Vol. 2.
16. N. R. Gall, S. N. Mikhailov, E. V. Rut'kov, and A. Ya. Tontegode, Surf. Sci. **191**, 185 (1987).
17. V. S. Fomenko, *Emission Properties of Materials: a Handbook* (Naukova Dumka, Kiev, 1981).
18. E. Fromm and E. Gebhardt, *Gase und Kohlenstoff in Metallen* (Springer-Verlag, Berlin, 1976; Metallurgiya, Moscow, 1980).
19. N. P. Vas'co, Yu. G. Ptushinskii, and B. A. Chuikov, Surf. Sci. **14**, 448 (1970).
20. A. Joshi, L. E. Davis, and P. W. Palmberg, in *Methods of Surface Analysis*, Ed. by A. W. Czanderna (Elsevier, New York, 1975; Mir, Moscow, 1979).
21. N. R. Gall', E. V. Rut'kov, and A. Ya. Tontegode, Pis'ma Zh. Tekh. Fiz. **25** (14), 57 (1999) [Tech. Phys. Lett. **25**, 573 (1999)].
22. V. N. Ageev and N. I. Ionov, Zh. Tekh. Fiz. **38**, 1149 (1968) [Sov. Phys. Tech. Phys. **13**, 950 (1968)].
23. K. J. Rawlings, S. D. Foulias, and B. J. Hopkins, Surf. Sci. **109**, 513 (1981).

*Translated by P. Pozdeev*

*Journal of Experimental and Theoretical Physics, Vol. 95, No. 2, 2002, pp. 300–307.*
*Translated from Zhurnal Éksperimental'noĭ i Teoreticheskoĭ Fiziki, Vol. 122, No. 2, 2002, pp. 347–355.*


**SOLIDS**
**Structure**

# Transition from Antiferromagnetic to Ferromagnetic State of Systems $LaMnO_{3+\lambda}$ and $La_{1-x}Sr_x(Mn_{1-x/2}Nb_{x/2})O_3$

**I. O. Troyanchuk[a, *], O. S. Mantytskaya[a], A. N. Chobot[a], and H. Szymczak[b]**

[a]*Institute of Solid-State and Semiconductor Physics, Belarussian Academy of Sciences, Minsk, 220076 Belarus*
[b]*Institute of Physics, Polish Academy of Sciences, 02-668 Warsaw, Poland*
**e-mail: troyan@ifttp.bas-net.by*

Received January 28, 2002

**Abstract**—The crystal structure and magnetic and elastic properties of the system $LaMnO_{3+\lambda}$ are investigated for various concentrations of oxygen. Upon an increase in the oxygen concentration, the orbital-ordered phase is transformed into an orbital-disordered phase via a two-phase crystal-structure state in the interval $0.04 < \lambda < 0.06$. The transition is accompanied by a jumplike increase in the Curie temperature and spontaneous magnetization. An analysis of the magnetic properties in weak fields and of the temperature dependence of the Young modulus reveals the properties typical of the orbital-ordered antiferromagnetic phase up to $\lambda = 0.08$. It is proposed that the two-phase state is associated with the martensite type of the orbital order–disorder phase transformation. The system $La_{1-x}Sr_x(Mn_{1-x/2}Nb_{x/2})O_3$ in which all manganese ions are in the trivalent state exhibits a sequence of antiferromagnetic–ferromagnetic ($x > 0.2$) and ferromagnetic–spin glass ($x > 0.4$) transitions. In both systems, the orbital-disordered phases are ferromagnetic, indicating the crucial role of orbital ordering in the formation of magnetic properties. *© 2002 MAIK "Nauka/Interperiodica".*

## 1. INTRODUCTION

Lanthanum manganite is the ancestor in the class of manganites with perovskite structure that exhibit a variety of phase transformations. The relation between the magnetic state and electrical conductivity is of special interest [1, 2]. Considerable attention is paid at present to weakly doped compounds in which a transition from the antiferromagnetic state typical of the stoichiometric $LaMnO_3$ to the ferromagnetic state takes place. According to the theory of double exchange [3, 4], this transformation must occur through the formation of a noncollinear magnetic structure. However, the possibility of phase separation is indicated in a number of theoretical [5, 6] and experimental [7–9] studies. The role of orbital ordering in the formation of magnetic structure is of special importance [5, 10–12]. As a rule, the magnetic state of manganites changes as a result of substitution of alkali-earth bivalent ions for lanthanide ions. It has been established, however, that the properties of lanthanum manganite $La\,Mn^{3+}_{1-2\lambda}\,Mn^{4+}_{2\lambda}\,O_{3+\lambda}$ can be varied in a wide range by changing the oxygen concentration in the samples [13, 14]. Excess oxygen creates equal numbers of lanthanum and manganese vacancies since it was found that oxygen cannot be implanted in interstitial positions of the closely packed perovskite structure [15]. Consequently, the realistic formula looks like $La_{1-\varepsilon}Mn_{1-\varepsilon}O_3$, where $\varepsilon = \lambda/(3+\lambda)$. The emergence of $Mn^{4+}$ ions leads to a transition from the antiferromagnetic to the ferromagnetic state, which was described in the framework of the double exchange concept. However, the ferromagnetic phase in $LaMnO_{3+\lambda}$ is not metallic [16]. Consequently, charge carriers in this phase are localized as a rule. According to the model of double exchange, the ferromagnetic state is realized as a consequence of actual transitions of charge carriers between manganese ions with different valences [3, 4, 16, 17]. For this reason, we studied the system $La^{3+}_{1-x}Sr^{2+}_x(Mn^{3+}_{1-x/2}Nb^{5+}_{x/2})O_3$ in which the magnetic state changes not as a result of emergence of manganese ions with different valences, but through the substitution of pentavalent niobium ions for manganese ions. Our experiments revealed that the magnetic properties of $LaMnO_{3+\lambda}$ and $La_{1-x}Sr_x(Mn_{1-x/2}Nb_{x/2})O_3$ are qualitatively identical.

It should be noted that, in spite of a large number of publications devoted to lanthanum manganite, the magnetic properties of this material are studied insufficiently in the interval of oxygen concentrations corresponding to the ferromagnetic state. The elastic properties for various oxygen concentrations are also poorly studied. For this reason, the aim of this study is to generalize the available data describing the behavior of lanthanum manganite depending on the oxygen concentration and to carry out additional measurements required for constructing phase diagrams and for establishing the origin of phase transformations in $LaMnO_{3+\lambda}$.

## 2. EXPERIMENT

The compound $LaMnO_{3.08}$ was synthesized at $T$ = 1500°C in air with subsequent cooling to room temperature at a rate of 50°C/h. The oxygen content was deter-

mined using thermogravimetric analysis in the course of reduction of lanthanum manganite to $La_2O_3$ and MnO. Manganites with various oxygen concentrations were obtained by reduction of $LaMnO_{3.08}$ in evacuated quartz ampoules in the presence of metallic tantalum or by annealing in oxygen at $T$ = 900°C for 24 h. Solid solutions of $La_{1-x}Sr_x(Mn_{1-x/2}Nb_{x/2})O_3$ ($0 \le x \le 0.5$) were synthesized according to the conventional ceramic technology at $T$ = 1550°C for 2 h. To minimize the concentration of the tetravalent manganese, pellets were annealed after synthesis in an argon flow at $T$ = 900°C. The X-ray diffraction analysis was carried out on the diffractometer DRON-3 in the $K_\alpha$ radiation of Cr. Magnetic measurements were made on a commercial vibration magnetometer of the Foner type. Electrical conductivity was measured by the four-probe technique. The contacts were made of indium deposited by the ultrasonic method. Elastic properties were measured using the resonance method in the acoustic frequency range on samples having a length of 40–50 mm and a diameter of 5 mm.

## 3. RESULTS AND DISCUSSION

Compounds $LaMnO_{3+\lambda}$ crystallize in the concentration range $0 \le \lambda \le 0.07$ in the orthorhombic symmetry of the $GdFeO_3$ type (space group *Pbnm*). The stoichiometric perovskite $LaMnO_3$ exhibits the strongest distortion. The emergence of excess oxygen leads to a gradual decrease in structural distortions (up to compounds with $\lambda = 0.04$) and then to its abrupt decrease (for $0.05 \le \lambda \le 0.07$). In the interval $0.05 \le \lambda \le 0.07$, the *O*' orthorhombic symmetry (with $\sqrt{2} < a < b$) is transformed into the *O* orthorhombic symmetry ($a \approx c\sqrt{2} < b$). As in [15, 16], we did not observe superstructural reflections that could be interpreted in the model of ordering of vacancies of lanthanum or manganese. In our opinion, vacancies of cations are distributed over the lattice at random. It should be noted that, according to Goodenough [16], *O*' orthorhombic distortions in manganites are associated with orbital ordering. The compound with $\lambda = 0.05$ was successfully calculated in a model according to which it is a mixture of the *O*' and *O* phases (Fig. 1). The obtained result is in accord with the data obtained in [14]. The orthorhombic distortions were minimal for a compound with $\lambda = 0.07$. The rhombohedral symmetry (space group $R\bar{3}c$) was detected in samples with $\lambda \ge 0.08$, the compound with $\lambda = 0.08$ being calculated under the assumption that it is a mixture of the orthorhombic and rhombohedral phases.

All samples in the system $La_{1-x}Sr_x(Mn_{1-x/2}Nb_{x/2})O_3$ were single-phase perovskites in the concentration range $0 \le x \le 0.5$. The compounds with $x = 0$ and $x = 0.1$ possess the *O*' orthorhombic symmetry, while the compounds with $0.02 \le x \le 0.05$ exhibit *O* orthorhombic distortions. However, the magnitude of orthorhombic distortions is small, indicating unambiguously the

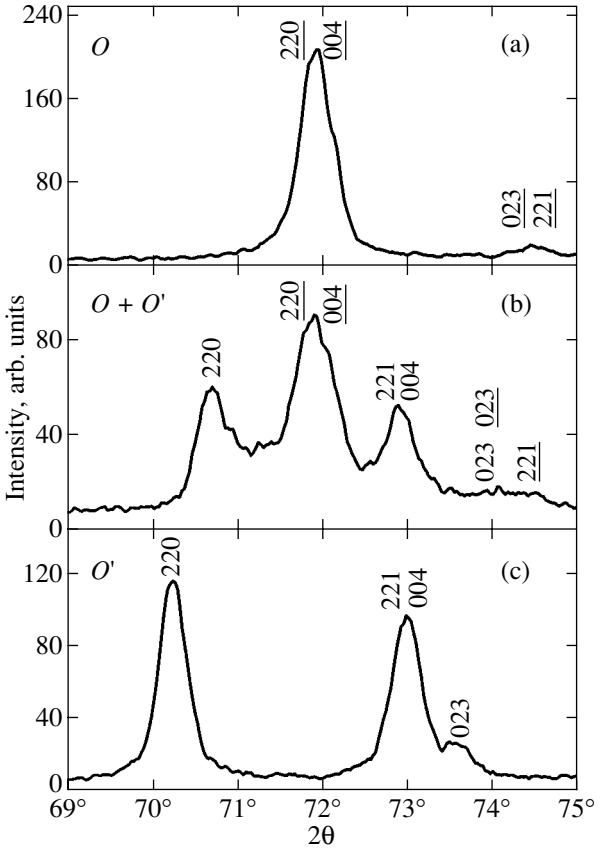


**Fig. 1.** Fragments of X-ray diffraction patterns for compounds with λ = (a) 0.01, (b) 0.05, and (c) 0.07, illustrating the concentration phase transition from the orbital-ordered to the orbital-disordered phase.

removal of cooperative orbital ordering. It is well known [16] that cooperative orbital ordering must be violated upon a dilution of the system with non-Jahn–Teller ions in the case of statistical distribution of different types of ions. Superstructural reflections were not detected in X-ray diffraction analysis. For this reason, we believe that strontium and niobium ions are distributed over the crystal lattice statistically. As the niobium concentration increased, the unit cell volume increased insignificantly. This is due to the fact that $Sr^{2+}$ ion are larger than $La^{3+}$ ion, while the ionic radius of $Nb^{5+}$ ions is slightly smaller than that of $Mn^{3+}$ ions. Niobium ion may, in principle, be in the tetravalent state, but this state is incompatible with the trivalent state of manganese ions. X-ray diffraction analysis of the decay product formed after the reduction of the $La_{1-x}Sr_x(Mn_{1-x/2}Nb_{x/2})O_3$ samples revealed the presence of oxides $La_2O_3$, MnO, and $Nb_2O_5$. Consequently, the chemical formula of the solid solutions has the form $La^{3+}_{1-x}Sr^{2+}_x(Mn^{3+}_{1-x/2}Nb^{5+}_{x/2})O_3$.

Figure 2 shows the results of investigation of elastic properties of some samples in the $LaMnO_{3+\lambda}$ system.

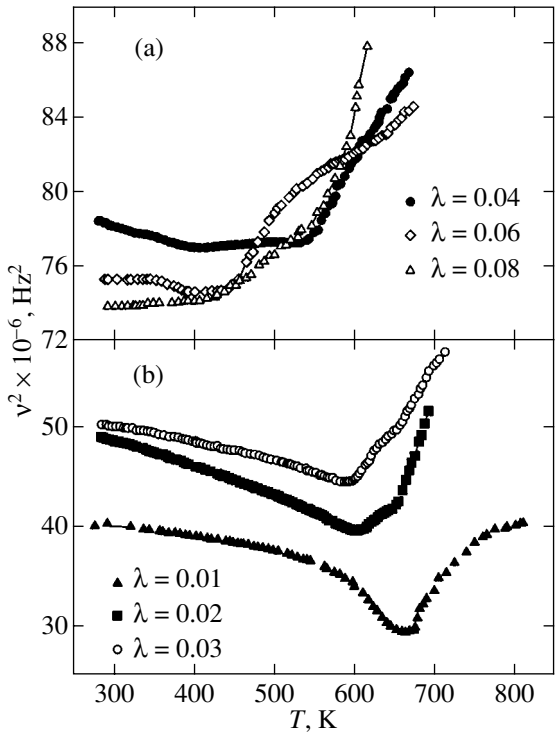


**Fig. 2.** Temperature dependence of the squared resonance frequency (proportional to the Young modulus) for compounds $LaMnO_{3+\lambda}$.

Measurements were made in the temperature range below 800 K. A clearly manifested minimum of the Young modulus was observed for compounds corresponding to the concentration range $0 \le \lambda \le 0.03$. The temperature $T_0$ corresponding to the minimum gradually decreased upon an increase in the oxygen concentration. For example, in the measurements carried out in the heating regime, the value of $T_0$ corresponding to the stoichiometric compound $LaMnO_3$ was 740 K, while $T_0$ = 660 K for $LaMnO_{3.01}$. For measurements made during cooling, the temperature corresponding to the minimum was shifted towards lower temperatures. For example, for stoichiometric $LaMnO_3$, the hysteresis was 10 K. The temperature hysteresis indicates a first-order phase transition. For compounds with $0.04 \le \lambda \le 0.07$, a strongly blurred (on the temperature scale) minimum of the Young modulus or a kink on the temperature dependence was observed, indicating a gradual phase transformation, which is typical of inhomogeneous or two-phase systems. Anomalous behavior of the curve describing the behavior of the squared resonance frequency was also observed in rhombohedrically distorted manganites. In the compound with $\lambda$ = 0.08, the Young modulus remains virtually unchanged in the interval from 270 to 420 K, and then it increases anomalously with temperature, which may indicate instability of the crystal structure.

The minimum of the Young modulus for samples with $\lambda \le 0.03$ is due to orbital disordering. This follows from the fact that temperature $T_0$ in the compound with $\lambda = 0$ coincides with the orbital disordering temperature determined from neutron diffraction measurements [18–20]. The temperature variation of the curve describing the squared resonance frequency in manganites with $0.04 \le \lambda \le 0.07$ is apparently determined by a gradual transition from the orbital-ordered phase to the orbital-disordered one. Such a dependence is possible for a system containing two phases. The concentration of one of these phases gradually decreases at the expense of the increase in the amount of the other phase. The anomalous behavior of elastic properties of the orbital-disordered phase with $\lambda$ = 0.08 can be explained in two different ways. First, the phase of this compound is a phase-inhomogeneous system with competing contributions to lattice dynamics. Second, the dynamics of orbital transitions in a system of Jahn–Teller $Mn^{3+}$ ions changes gradually upon heating; i.e., the rate of transitions between different states increases abruptly with temperature, but the system does not exhibit any "critical" temperature.

Spontaneous magnetization appears in $LaMnO_3$ at the Néel temperature $T_N$ = 143 K. The transition to the magnetically ordered state is abrupt, indicating that this compound is magnetically homogeneous. The spontaneous magnetic moment $M_s = 0.07\mu_B$ per $Mn^{3+}$ ion. This value is typical of weak ferromagnets. The coercive force at 4.2 K is very large (more than 10 kOe), indicating a high magnetic anisotropy associated with orbital ordering and anisotropic nature of exchange interactions in $Mn^{3+}O_6$ octahedra. In the presence of extra oxygen, the Néel temperature decreases up to compounds with $\lambda$ = 0.04. Figure 3 shows the temperature variation of magnetization for the $LaMnO_{3+\lambda}$ system. The dependence obtained during heating after zero field cooling (ZFC) for a sample with $\lambda$ = 0.03 has a peak, while the dependence obtained during heating after field cooling (FC) exhibits a gradual decrease in magnetization up to $T_N$ = 120 K. Such curves are typical of hard magnets. A sharp increase in the critical temperature and spontaneous magnetization was observed for the compound with $\lambda$ = 0.05 (Fig. 4a). The temperature of transition to the paramagnetic state is approximately equal to 160 K. At $T_N \sim 110$ K, the ZFC magnetization exhibits anomalous behavior. Below this temperature, magnetic anisotropy increases jumpwise. Anomalous behavior in the vicinity of $T_N$ = 110 K was observed for all samples in the interval $0.05 \le \lambda \le 0.08$. Spontaneous magnetization attained its peak value for the compound with $\lambda$ = 0.08 (Fig. 4a); in this case, however, the magnetic moment was slightly smaller than the expected value for complete polarization of all magnetic moments of tri- and tetravalent manganese ions; i.e., we can assume that $\mu(Mn^{3+}) = 4\mu_B$ and $\mu(Mn^{4+}) = 3\mu_B$. Further increase in the concentration of tetravalent manga-

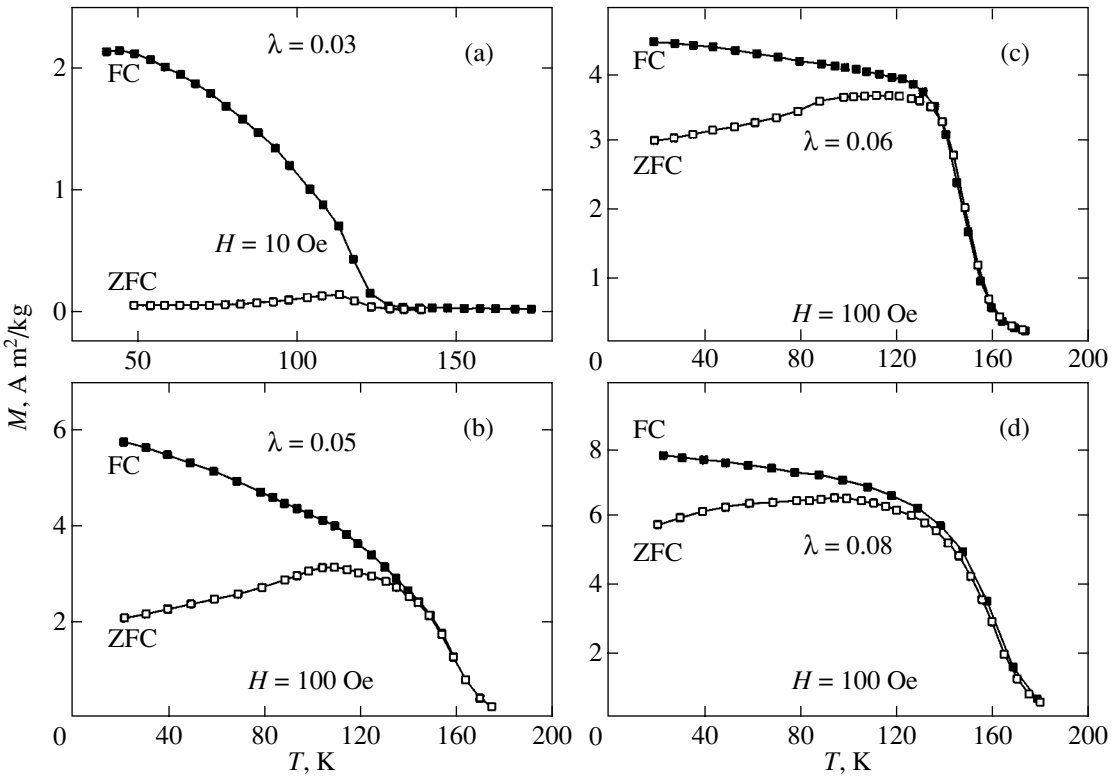


**Fig. 3.** Temperature dependence of magnetization for $LaMnO_{3+\lambda}$ compounds with various compositions.

nese up to 20% ($\lambda = 0.10$) did not lead to a significant change in the Curie temperature $T_C$.

All compounds in the concentration range $0 \le \lambda \le 0.10$ are semiconductors both above and below the magnetic ordering temperature. In the vicinity of $T_C$, we observed a weak anomaly in electrical conductivity and a peak of magnetoresistance defined by the formula $MR = \{[\rho(H = 9\ \text{kOe}) - \rho(H = 0)]/\rho(H = 0)\} \times 100\%$, which amounted to 30% for the compound with $\lambda = 0.06$ in a field $H = 10$ kOe.

Let us consider the magnetic properties of the system $La_{1-x}Sr_x(Mn_{1-x/2}Nb_{x/2})O_3$. It was mentioned above that $LaMnO_3$ at $T = 5$ K is characterized by $T_N = 143$ K and $M_s = 0.07\mu_B$ per structural unit. For the compound with $x = 0.1$, a sharp increase in spontaneous magnetization to $M_s = 1.2\mu_B$ per structural unit was observed (Fig. 4b) in spite of the fact that the temperature of transition to the paramagnetic state decreased to 120 K. Compounds with $0.2 \le x \le 0.4$ possess similar magnetic properties. The temperature of transition to the paramagnetic state amounts to 105–120 K, and spontaneous magnetization at helium temperature is 50–65 A m$^2$/kg. Figure 5 shows the results of measurements of magnetization in a magnetic field of 100 Oe after zero field cooling (ZFC) and after cooling in a field of 100 Oe (FC). It can be seen that the values of magnetization and the critical temperature at which the ZFC and FC curves diverge for $x = 0.5$ have become considerably lower ($T_N = 30$ K). The divergence between the ZFC and FC curves in this case is manifested much more strongly than for the compound with $x = 0.2$, indicating a sharp increase in anisotropy. The magnetization of the sample with $x = 0.5$ is comparatively low and does not attain saturation in fields up to 16 kOe. These facts indicate that the long-range magnetic order is obviously not realized in a sample with $x = 0.5$. It should be noted that a sharp increase in the ZFC magnetization was observed for perovskites with $x = 0.3$ and 0.4 upon heating to 30 K. In all probability, this is due to the presence of a spin-glass component at low temperatures.

An analysis of the temperature dependence of resistance proved that all the compounds mentioned above are characterized by an active type of conduction as in semiconductors. The strongest magnetoresistive effect was observed in perovskites for $0.2 \le x \le 0.4$, in which the magnetic state is the closest to the ferromagnetic state. For a compound with $x = 0.3$, the magnetoresistance in a field of 9 kOe at $T = 80$ K approaches a value of 30% (Fig. 6). Such values of magnetoresistance are usually observed for manganites with a mixed valence of manganese ions.

Figure 7 shows the evolution of the magnetic state in the course of substitution of niobium ions for manganese ions. The basic compound $LaMnO_3$ is a weak ferromagnet [16]. The magnetic properties of the compound with $x = 0.1$ strongly resemble the properties of

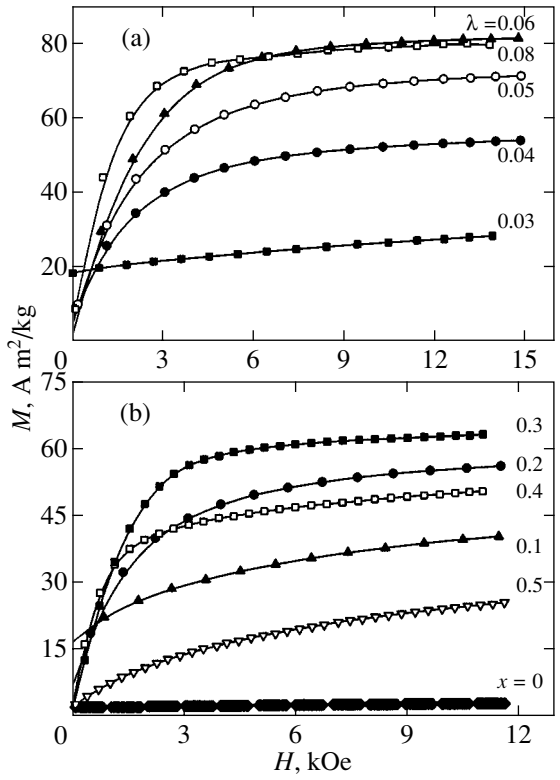


**Fig. 4.** Field dependence of magnetization at $T = 5$ K for compounds (a) $LaMnO_{3+\lambda}$ and (b) $La_{1-x}Sr_x(Mn_{1-x/2}Nb_{x/2})O_3$.

solid solutions of $La_{1-x}Sr_xMnO_3$ in the concentration range $0.05 \le x \le 0.07$. In accordance with the double exchange model, a noncollinear magnetic structure must be realized in $La_{1-x}Sr_xMnO_3$ upon weak doping. However, the sample with niobium ion substitution and with $x = 0.1$ does not contain $Mn^{4+}$ ions; consequently, double exchange in this sample is insignificant. The concentration transition in magnetic crystals from the antiferromagnetic to the ferromagnetic state usually occurs through the state of spin glass or through a two-phase state. The properties of the compound with $x = 0.1$ can be explained using the two-phase model. In manganites with $0.2 \le x \le 0.4$, the long-range antiferromagnetic order is replaced by a long-range ferromagnetic order. The magnetic moment of these compounds is slightly smaller than expected for purely ferromagnetic ordering of magnetic moments; i.e., $\mu(Mn^{3+}) = 4\mu_B$ and $\mu(Mn^{4+}) = 3\mu_B$. For example, the calculated value of the spontaneous magnetic moment of $La_{0.7}Sr_{0.3}(Mn_{0.85}Nb_{0.15})O_3$ in the case of ferromagnetic ordering amounts to $3\mu_B$ per structural unit, while the observed value is slightly smaller ($2.75\mu_B$ per structural unit; see Fig. 4b). Obviously, a part of the manganese ions in the vicinity of niobium ions are in the paramagnetic state. In the compound with $x = 0.5$, the long-range ferromagnetic order is violated due to a high concentration of diamagnetic niobium ions. Ferromagnetic clusters freeze at a temperature below 30 K (see Fig. 5d).

Let us now consider the properties of lanthanum manganite. It should be noted above all that the removal of orbital ordering is a phase transition of the martensite type. In this transition, the shape memory effect and high plasticity of transformation associated with a rearrangement of the ferroelastic domain structure are observed [21]. The coexistence of orbital-ordered *O'* and orbital-disordered *O* orthorhombic phases was detected in stoichiometric manganites $LnMnO_3$ (Ln = La, Pr, Nd) in the temperature interval of phase transformation [14, 22].

In the course of the concentration phase transition from the *O*' to *O* phase, the unit cell parameters become closer, but the two-phase state can still be detected using X-ray diffraction methods (see Fig. 1).

The results of NMR studies [7] and neutron diffraction analysis in a magnetic field [23] indicate the presence of an inhomogeneous magnetic phase state in weakly doped manganites. The existence of two magnetic phases in such compounds is usually attributed to the electron phase separation [24]. However, neutron diffraction and electron microscopic studies of manganites revealed the coexistence of phases with a characteristic size exceeding 1000 Å [25]. The formation of phases with large volumes during electron phase separation is hampered by a strong counteraction of electrostatic forces. In martensite phase transformations of the orbital order–disorder or charged order–disorder type, the two-phase state is a natural consequence of the nature of phase transition and is stabilized by defects and stress fields. Orbital ordering and magnetic properties of manganites are obviously interconnected. The orbital- and charge-ordered state in manganites is antiferromagnetic as a rule, while the orbital-disordered state is ferromagnetic [26]. Such an approach is in accord with the theory of superexchange interactions [26] as well as with the concept of exchange through charge carriers [3, 4]. According to the model of superexchange interactions through oxygen, the exchange interactions $Mn^{3+}$–O–$Mn^{3+}$ and $Mn^{3+}$–O–$Mn^{4+}$ are ferromagnetic in the case of the dynamic Jahn–Teller effect, i.e., in the orbital-disordered phase [16, 26]. We believe that the orbital order–disorder phase transformation in manganites occurs through a two-phase state relative to temperature and concentration of the tetravalent manganese ion. A mixed state containing orbital-ordered and orbital-disordered phases is apparently realized for $0.05 \le \lambda \le 0.08$. This statement is also confirmed by the results of investigation of magnetic properties. The antiferromagnetic phase is orbital-ordered, while the ferromagnetic phase is orbital-disordered. The magnetic phase diagram of the system $LaMnO_{3+\lambda}$ is shown in Fig. 8. A decrease in the Néel temperature from 143 to 120 K was observed upon an increase in the value of $\lambda$ to 0.04. In our opinion, this is associated with the emergence of $Mn^{4+}$ ions. These ions are not of the

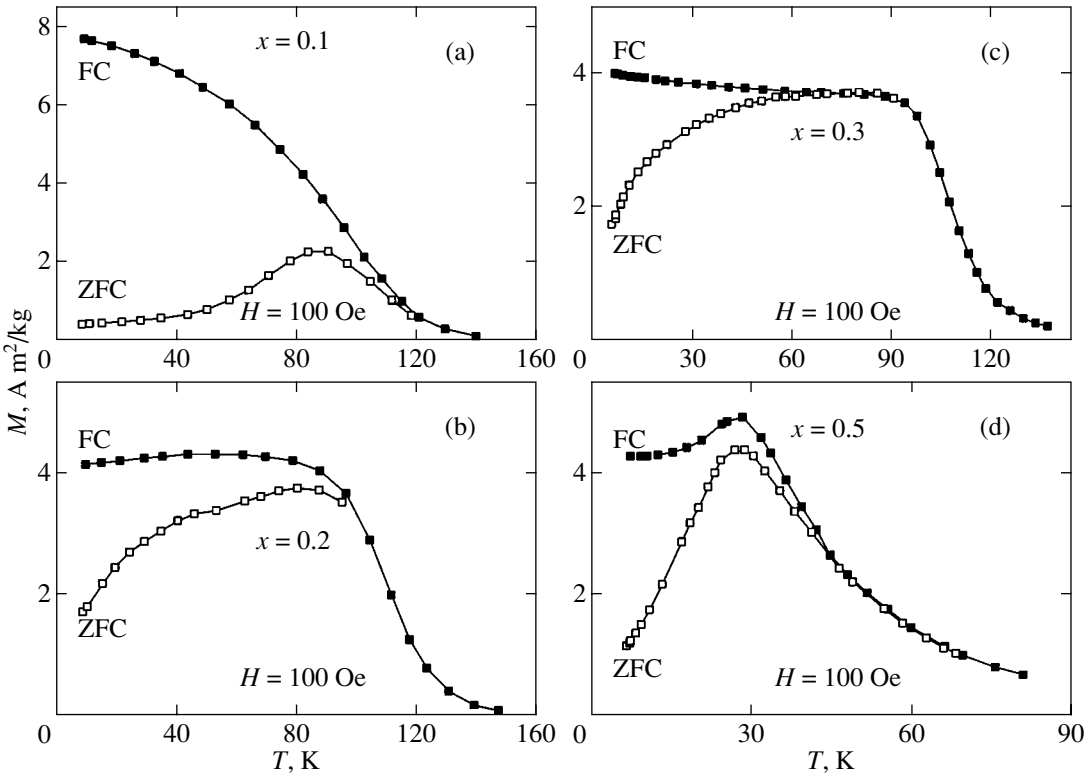


**Fig. 5.** Temperature dependences of magnetization for compounds $La_{1-x}Sr_x(Mn_{1-x/2}Nb_{x/2})O_3$.

Jahn–Teller type and create frustrations of exchange interactions. In the vicinity of $Mn^{4+}$ ions, a tendency to orbital disordering is observed, as a result of which exchange interactions become ferromagnetic. The ferromagnetic nature of the exchange interactions $Mn^{3+}$–O–$Mn^{3+}$ in the orbital-disordered phase follows from the results of investigation of compounds $La_{1-x}Sr_x(Mn_{1-x/2}Nb_{x/2})O_3$ (see Figs. 4b and 5) and is confirmed by the results of analysis of magnetic susceptibility of the high-temperature orbital-disordered phase of the stoichiometric compounds $LaMnO_3$ [27]. As a result of doping of lanthanum manganite, $Mn^{4+}$ ions combine into clusters, and the ferromagnetic phase is formed subsequently (approximately at $\lambda = 0.04$). In the narrow interval $0.04 \le \lambda \le 0.05$, the Curie temperature of the ferromagnetic phase is extremely sensitive to variation of the concentration of $Mn^{4+}$ ions. In the excess oxygen concentration range $0.06 \le \lambda \le 0.10$, the Curie temperature remains virtually unchanged. What is the reason for the anomalies in magnetization near $T_N \sim 110$ K, which were observed in compounds with $0.05 \le \lambda \le 0.08$? We consider here the following two hypotheses. According to the first hypothesis, the anomalous behavior at 110 K may be due to the formation of a noncollinear magnetic structure. However, the results of NMR [7] and neutron diffraction studies in a magnetic field [23] indicate the presence of two phases at low temperatures. One of the phases is magnetically ordered according to the $LaMnO_3$ type, while the other phase is ferromagnetic. Above $T_N$, exchange frustrations of magnetic bonds disappear, which is manifested in a decrease in magnetic anisotropy. For this reason, the second hypothesis, according to which a sample at a temperature below $T_N$ is a mixture of antiferromagnetic and ferromagnetic phases, appears to us as more attractive. The chemical compounds in the two phases are very close, but still differ not only in the magnetic state but also in the crystal structure. The antiferromag-

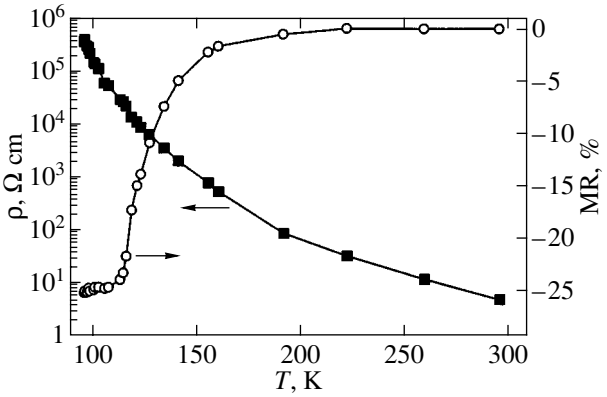


**Fig. 6.** Temperature dependences of electrical conductivity and magnetoresistance for compound $La_{0.7}Sr_{0.3}(Mn_{0.85}Nb_{0.15})O_3$.

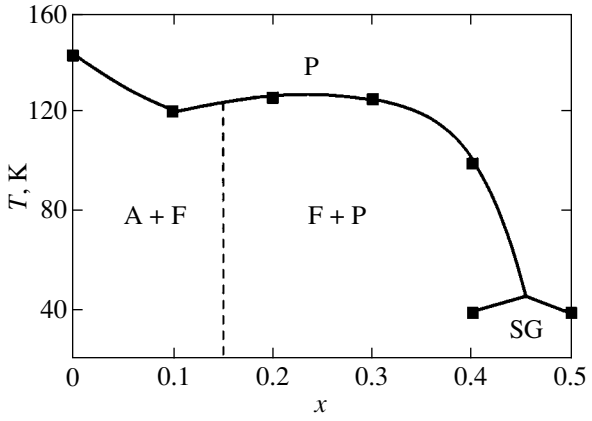


**Fig. 7.** Magnetic phase diagram of the system $La_{1-x}Sr_x(Mn_{1-x/2}Nb_{x/2})O_3$: antiferomagnetically ordered phase (A), ferromagnetic phase (F), paramagnetic phase (P), and spin glass (SG).

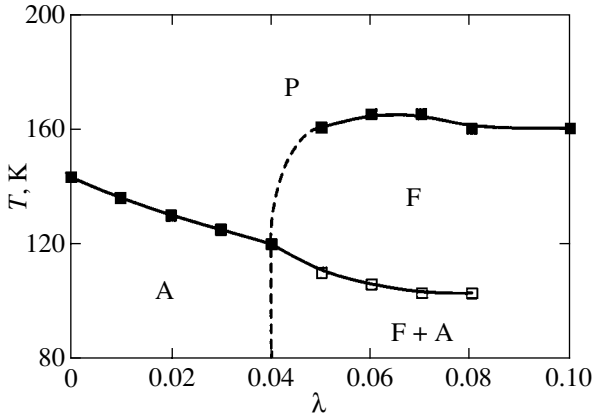


**Fig. 8.** Magnetic phase diagram of the system $LaMnO_{3+\lambda}$: antiferomagnetically ordered phase (A), ferromagnetic phase (F), and paramagnetic phase (P).

netic phase is orbital-ordered according to the $LaMnO_3$ type, while the ferromagnetic phase has a faster orbital dynamics. In all probability, the ferromagnetic dielectric phase in manganites is characterized by a short-range orbital order. This is in accord with the anomalous behavior of the Young modulus in the rhombohedral phase (see Fig. 2).

It is generally accepted that ferromagnetism in dielectric manganites is associated with double exchange between tri- and tetravalent manganese ions [27]. However, the absence of a resistance jump near $T_C$ and the properties of manganites free of $Mn^{4+}$ ions contradict this statement. It has been proved beyond doubt that superexchange interaction through oxygen makes a large contribution to ferromagnetic ordering in manganites. The study of orbital-disordered phase in the stoichiometric $LaMnO_3$ [27] and our results for phases in $La_{1-x}Sr_x(Mn^{3+}_{1-x/2}Nb^{5+}_{x/2})O_3$ (see Figs. 4b and 5) indicate that the exchange interactions $Mn^{3+}$–O–$Mn^{3+}$ may raise the Curie temperature in manganites to above 200 K. The absence of similarity between the hole-doped and electron-doped manganites can be attributed precisely to the ferromagnetic type of the $Mn^{3+}$–O–$Mn^{3+}$ exchange interactions in orbital-disordered manganites. Electron-doped manganites are, as a rule, charge-ordered antiferromagnetic phases, while hole-doped manganites are ferromagnets [24, 28]. Antiferromagnetic $Mn^{4+}$–O–$Mn^{4+}$ superexchange interactions play a significant role in electron-doped manganites. Undoubtedly, the $Mn^{3+}$–O–$Mn^{4+}$ superexchange interactions in orbital-disordered phases are also of the isotropic ferromagnetic type. Doping with Ru and Cr ions in electron-doped manganites is in conformity with this statement [29].

## ACKNOWLEDGMENTS

This study was supported financially by the Belarussian Foundation for Basic Research (project no. F00-111).

## REFERENCES

1. G. H. Jonker, Physica (Amsterdam) **22**, 707 (1956).
2. G. Matsumoto, J. Phys. Soc. Jpn. **29**, 606 (1970).
3. C. Zener, Phys. Rev. **82**, 403 (1951).
4. P. G. de Gennes, Phys. Rev. **118**, 141 (1960).
5. E. Dagotto, T. Hotta, A. Moreo, *et al.*, Phys. Rep. **344**, 1 (2001).
6. E. L. Nagaev, Phys. Rep. **346**, 387 (2001).
7. G. Allodi, R. De Renzi, G. Guidi, *et al.*, Phys. Rev. B **56** (10), 6036 (1997).
8. A. Yakubovskii, K. Kumagai, Y. Furukawa, *et al.*, Phys. Rev. B **62**, 5337 (2000).
9. I. F. Voloshin, A. V. Kalinov, S. E. Savel'ev, *et al.*, Pis'ma Zh. Éksp. Teor. Fiz. **71**, 157 (2000) [JETP Lett. **71**, 106 (2000)].
10. M. Yu. Kagan and K. I. Kugel', Usp. Fiz. Nauk **171**, 577 (2001).
11. K. I. Kugel' and D. I. Khomskiĭ, Usp. Fiz. Nauk **136**, 621 (1982).
12. J. Van den Brink, G. Khaliulin, and D. I. Khomskii, Phys. Rev. Lett. **83**, 5118 (1999).
13. A. Wold and R. J. Arnott, Phys. Chem. Solids **9**, 176 (1959).
14. V. I. Pavlov, A. K. Bogush, and L. V. Balyko, Cryst. Res. Technol. **19**, 237 (1984).
15. J. A. M. van Roosmalen and E. H. P. Cordfunke, J. Solid State Chem. **10**, 183 (1974).
16. J. Töpfer and J. B. Goodenough, J. Solid State Chem. **130**, 117 (1997).
17. I. O. Troyanchuk, Zh. Éksp. Teor. Fiz. **102**, 251 (1992) [Sov. Phys. JETP **75**, 132 (1992)].
18. J. Rodriguez Carvajal, M. Hennion, F. Moussa, *et al.*, Phys. Rev. B **57**, R3189 (1998).

19. C. Ritter, M. R. Ibarra, J. M. De Teresa, and P. A. Algarabel, Phys. Rev. B **56**, 8902 (1997).
20. M. Tovar, G. Alejandro, A. Butera, *et al.*, Phys. Rev. B **60** (14), 10199 (1999).
21. I. O. Troyanchuk, A. I. Akimov, L. A. Bliznjuk, and N. V. Kasper, J. Alloys Compd. **228**, 83 (1995).
22. N. V. Kasper and I. O. Troyanchuk, Phys. Chem. Solids **57** (11), 1601 (1996).
23. E. O. Wollan and W. C. Koehler, Phys. Rev. **100**, 545 (1955).
24. É. L. Nagaev, Usp. Fiz. Nauk **166**, 833 (1996) [Phys. Usp. **39**, 781 (1996)].
25. C. Martin, M. Maignan, M. Hervieu, and B. Raveau, J. Magn. Magn. Mater. **205**, 184 (1999).
26. J. B. Goodenough, A. Wold, R. J. Arnott, and N. Menyuk, Phys. Rev. **124**, 373 (1961).
27. J.-S. Zhou and J. B. Goodenough, Phys. Rev. B **60** (22), R15002 (1999).
28. V. M. Loktev and Yu. G. Pogorelov, Fiz. Nizk. Temp. **26**, 231 (2000) [Low Temp. Phys. **26**, 171 (2000)].
29. C. Martin, A. Maignan, M. Hervieu, *et al.*, Phys. Rev. B **63**, 174402 (2001).

*Translated by N. Wadhwa*

*Journal of Experimental and Theoretical Physics, Vol. 95, No. 2, 2002, pp. 308–315.*
*Translated from Zhurnal Éksperimental'noĭ i Teoreticheskoĭ Fiziki, Vol. 122, No. 2, 2002, pp. 356–365.*


**SOLIDS**
**Structure**

# The Influence of Oxygen Deficiency on the Magnetic and Electric Properties of $La_{0.70}Ba_{0.30}MnO_{3-\gamma}$ ($0 \le \gamma \le 0.30$) Manganite with a Perovskite Structure

**S. V. Trukhanov[a, *], I. O. Troyanchuk[a], N. V. Pushkarev[a], and H. Szymczak[b]**

[a]*Institute of Solid-State and Semiconductor Physics, Belarussian Academy of Sciences, ul. Brovki 17, Minsk, 220072 Belarus*

[b]*Institute of Physics, Polish Academy of Sciences, PL-02-668, Warsaw, Poland*

**e-mail: truhanov@ifttp.bas-net.by*

Received March 2, 2002

**Abstract**—The crystal structure and the magnetic and electric properties of $La_{0.70}Ba_{0.30}MnO_{3-\gamma}$ manganite ($0 \le \gamma \le 0.30$) with a perovskite structure were studied experimentally depending on the concentration of oxygen vacancies. The stoichiometric $La_{0.70}Ba_{0.30}MnO_3$ compound ($\gamma = 0$) had cubic unit cell symmetry, which did not change as oxygen deficiency increased up to $\gamma = 0.30$. A decrease in the content of oxygen in the compound under study caused the occurrence of several sequential magnetic phase transitions in the ground state, from the ferromagnetic state at $\gamma = 0$ through the cluster spin glass state ($\gamma = 0.15$) to the antiferromagnetic state ($\gamma = 0.30$) with the presence of a small ferromagnetic component. The specific electric resistance grew to become activation in character at $\gamma = 0.11$, and the metal–semiconductor transition disappeared as oxygen deficiency increased. The magnetoresistance of anion-deficient compositions included (1) magnetoresistance close to the temperature of the transition to the magnetically ordered state and (2) low-temperature magnetoresistance. The magnetoresistance peak at $T_C$ disappeared as $\gamma$ increased ($\gamma = 0.11$), whereas the low-temperature magnetoresistance component first increased to attain a maximum of about 34% at $\gamma = 0.15$ and then decreased. The results of experimental studies were used to construct a magnetic phase diagram. These results could be interpreted within the framework of superexchange magnetic ordering theory. The suggestion was made that $Mn^{3+}$–O–$Mn^{3+}$ indirect exchange interactions were positive in the orbitally disordered phase only when manganese was in octahedral coordination, whereas these interactions became negative if at least one of the $Mn^{3+}$ ions was five-coordinate or had a smaller coordination number. © *2002 MAIK "Nauka/Interperiodica".*

## 1. INTRODUCTION

Currently, substituted manganites of rare-earth metals with perovskite structures, $Ln_{1-x}D_xMnO_3$, where Ln is a trivalent rare-earth metal ion and D is a divalent alkaline-earth ion [1], attract special attention of researchers in the field of magnetic and magnetoresistance studies. Interest in these compounds stems from the diversity of physical properties that they exhibit. Manganites can combine the properties of metals and dielectric substances, ionic and covalent crystals, and systems with magnetic, orbital, and charge ordering and can also experience phase stratification. The diversity of these properties is determined by close interrelation of the orbital, charge, spin, and lattice degrees of freedom [2].

Manganites with perovskite structures are thermodynamically stable phases from the Raddlesden–Popper family of the general chemical formula $(Ln_{1-x}D_x)_{n+1}Mn_nO_{3n+1}$ ($n \ge 1$), $n = \infty$ [3]. The crystal structure, magnetic, and electric properties of these compounds were fairly completely studied in the early 1950s [4]. Dutch physicists Jonker and Van Santen discovered an unexpected correlation between conductivity and magnetization in $LaMnO_3$ caused by the replacement of lanthanum with $Ca^{2+}$ ions. In the range of calcium concentrations $0.20 \le x \le 0.50$, the compound not only became a strong ferromagnet but also exhibited metallic conduction below the Curie temperature. Strong interest in these compounds, however, arose much later, in the early 1990s, when the so-called giant magnetoresistance effect [5, 6] and, especially, magnetic field-induced metal–semiconductor and charge order–disorder phase transitions [7] were discovered. The giant magnetoresistance effect is in essence a sharp decrease in the resistance of substituted manganites accompanying phase transitions to the ferromagnetic state under an applied magnetic field. The magnetoresistance of manganites is many orders of magnitude larger than that of multilayer films and granulated systems, and this effect is observed at room temperatures and in weak magnetic fields [8]. This circumstance offers much promise for using manganites in practical applications.

Currently, interest in manganites is explained not only by possible technical applications of the giant

magnetoresistance effect but also by the possibility of using these compounds as very good model objects for studying the physics of strongly correlated systems. As mentioned, of particular interest is close correlation between the orbital, charge, spin, and lattice degrees of freedom.

The compound most completely studied to date is $LaMnO_3$. This is an antiferromagnetic semiconductor with an *A*-type magnetic structure [9]. The weak ferromagnetic component is caused by antisymmetric Dzyaloshinski–Moriya exchange. The Néel temperature for this composition is close to 140 K. Note that the magnetic properties of all manganites are determined by manganese ion spins, because the orbital magnetic momenta of these ions are "frozen" in the crystal field of anions. The presence of $Mn^{3+}$ Jahn–Teller ions with the $t_{2g}^3 e_g^1$ ($S = 2$) electronic configuration in stoichiometric $La^{3+}Mn^{3+}O_3^{2-}$ determines *O*'-orthorhombic symmetry of its unit cell. The *d* shell of the $Mn^{3+}$ ion octahedrally environed by oxygens splits into a doublet and a triplet. The triply degenerate $t_{2g}$ level is completely occupied by three electrons, whereas the doubly degenerate $e_g$ level contains only one electron. Such a high-spin configuration is caused by strong Hund exchange coupling, which orients the spins of all electrons in one direction; the $t_{2g}^3$ electrons form the $S = 3/2$ local spin. It is believed that the $e_g^1$ electron is localized on manganese and cannot freely move over the crystal lattice.

The replacement of $La^{3+}$, for instance, by $Ca^{2+}$ ions formally causes the appearance of $Mn^{4+}$ ions with the $t_{2g}^3$ ($S = 3/2$) electronic configuration. At substituent ion concentrations of $x \sim 0.10$, the transition from *O*'-orthorhombic to *O*-orthorhombic unit cell symmetry is observed, which is caused by the removal of static cooperative Jahn–Teller distortions [10]. At $x = 0.20$, spontaneous magnetization and magnetic ordering temperature increase considerably, and the transition to metallic conduction occurs below $T_C$. It is believed that the $e_g$ electrons are then collectivized and can freely move over the crystal lattice.

Zener [11] was the first to suggest the so-called double exchange mechanism to explain the magnetic and electric properties of manganites. This model was developed in more detail in [12]. Double exchange is based on the actual electron transition from the half-filled $e_g$ orbital of $Mn^{3+}$ to the free $e_g$ orbital of $Mn^{4+}$. Such a transition is energetically favorable at a parallel arrangement of local spins *S* of the nearest-neighbor $Mn^{3+}$ and $Mn^{4+}$ ions. Ferromagnetic ordering of local spins increases the probability of $e_g$ electron jumps and facilitates the arising of metallic conduction in the system. It follows that double exchange favors ferromagnetism and the metallic conduction type. Some authors, however, give preference to the superexchange interaction model [13]. This model is based on virtual exchange of electrons between manganese atoms and predicts the anisotropic character of their exchange interactions. Interaction between manganese atoms is determined by several factors such as the Mn–O bond length, the Mn–O–Mn bond angle, and the ratio between the concentrations of manganese ions in different valence states [14]. Note that, according to the superexchange model, the ferromagnetic order state does not necessarily correlate with the behavior of electric conduction. In spite of a wealth of accumulated data on the properties of manganites, the nature of magnetic and electric processes that occur in them remains poorly understood and is widely discussed.

The mean valence of manganese ions can be changed by different methods [15]. An analysis of the literature data shows that, of all the methods for varying the $Mn^{i+}/Mn^{j+}$ ratio ($i, j = 2, 3$, and 4), the influence of oxygen deficiency on the magnetic and electric properties of substituted manganites has been studied least completely.

Note that, of all compounds based on 3*d* transition metals, manganites provide the best possibilities for varying oxygen nonstoichiometry. For instance, the oxygen index value can change in manganites from 2.5 [16] to 3.27 [17]. The degree of nonstoichiometry characteristic of titanates (from 3 to 3.08) and vanadates (from 3 to 3.05) is much smaller. Deviations from oxygen stoichiometry in chromites and ferrites were not observed unless their structures were destroyed. Such a unique behavior of manganites may be a consequence of substantial changes in the ionic radius of manganese, much more substantial than with other 3*d* transition metals, that accompany changes in its oxidation state [18]. This circumstance allows oxygen content variations to be extensively used for varying the $Mn^{i+}/Mn^{j+}$ ratio.

In this work, the object of study was $La_{0.70}Ba_{0.30}MnO_3$. The electric resistance, magnetization, and magnetoresistance effect of anion-deficient $La_{0.67}Ba_{0.33}MnO_z$ were studied in [19]. The specific resistance of the compound gradually increased as the content of oxygen *z* decreased from 2.99 to 2.80, and its behavior acquired a semiconductor character. Simultaneously, the transition temperature to the magnetically ordered state decreased. A high magnetoresistance was observed in a wide temperature range for all samples except that with $z = 2.80$. The magnetic transition temperature was, however, measured in a fairly high (5 kOe) magnetic field, and the structural data were insufficiently complete. In this work, we performed a detailed study of the crystal structure and the magnetic and electric properties of anion-deficient $La_{0.70}Ba_{0.30}MnO_{3-\gamma}$ compositions. At the same time, it should be noted that manganites are fairly sensitive to the degree of substitution [20], and data on the influence of oxygen deficiency on the magnetic and electric

properties of $La_{0.70}Ba_{0.30}MnO_{3-\gamma}$ with $0 \le \gamma \le 0.30$ are therefore of obvious interest.

## 2. EXPERIMENTAL

A ceramic $La_{0.70}Ba_{0.30}MnO_3$ sample was prepared by the usual ceramic technique. The $La_2O_3$ and $Mn_2O_3$ oxides and $BaCO_3$ carbonate (of special purity) were weighed to provide the Ln : Ba : Mn = 0.70 : 0.30 : 1 ratio between the cations and thoroughly mixed. The mixture was ground in an agate mortar with the addition of a small amount of ethanol. Lanthanum oxide was fairly hygroscopic, and $La_2O_3$ was calcined in air at 1000°C for 2 h to remove water and carbon dioxide prior to weighing. The mixture of lanthanum and manganese oxides and barium carbonate obtained in this way was pressed into a pellet 2 cm in diameter and 1.5 cm high. The pellet was annealed in air at 1100°C for 2 h and ground. The synthesis was eventually performed in air at 1550°C for 2 h. The chemical reaction of formation of substituted lanthanum manganite can be written as

$$0.35La_2O_3 + 0.30BaCO_3 + 0.50Mn_2O_3 \longrightarrow La_{0.70}Ba_{0.30}MnO_z + 0.30CO_2\uparrow. \quad (1)$$

The sample was placed on a platinum substrate. The composition with the oxygen content close to stoichiometric was prepared by cooling the sample to room temperature at a rate of 100 K/h. Strongly substituted compositions ($x > 0.30$) obtained as described above are known to contain oxygen in amounts close to stoichiometric [21].

The X-ray diffraction patterns of the sample were obtained on a DRON-3 diffractometer using chromium $K_\alpha$ radiation at room temperature in the range of angles $30° \le 2\theta \le 100°$. Chromium $K_\beta$ radiation was filtered off by a graphite monochromator. Oxygen contents were determined thermogravimetrically. According to our data, the sample synthesized in air had a stoichiometric oxygen content.

The reduced $La_{0.70}Ba_{0.30}MnO_{3-\gamma}$ compositions ($\gamma$ = 0.05, 0.11, 0.15, 0.18, 0.20, and 0.30) were obtained in topotactic reactions. The samples were placed in evacuated ($P \sim 10^{-4}$ Pa) quartz ampules together with a certain amount of tantalum metal, which was used as an oxygen absorber. The ampules were held at 900°C for 10 h and then cooled to room temperature at a rate of 100 K/h. The reduction reaction can be described by the equation

$$La_{0.70}Ba_{0.30}MnO_3 + (2\gamma/5)Ta \longrightarrow La_{0.70}Ba_{0.30}MnO_{3-\gamma} + (\gamma/5)Ta_2O_5. \quad (2)$$

The contents of oxygen in reduced samples were determined from weight loss by weighing them prior to and after reduction. To decrease the relative error of oxygen content measurements, samples 2–3 g by weight were usually placed in a quartz ampule. The error then did not exceed 0.3%. The reduced samples were subjected to reoxidation in air at 900°C for 5 h. The corresponding reaction can be written as

$$La_{0.70}Ba_{0.30}MnO_{3-\gamma} + (\gamma/2)O_2 \longrightarrow La_{0.70}Ba_{0.30}MnO_3. \quad (3)$$

The content of oxygen in reoxidized samples was also determined by weighing. Our studies showed that the accuracy of oxygen index determinations was ±0.01.

Magnetization measurements were performed on an OI-3001 commercial vibrating-coil magnetometer in the temperature range 4–400 K. The Curie temperature was determined as the temperature of a sharp decrease in magnetization in a fairly weak (100 Oe) magnetic field. Electric resistance was measured in the temperature range 77–370 K by the four-point-probe technique using well-sintered $10 \times 2 \times 2$ mm$^3$ samples without visible cracks. Magnetoresistance was calculated by the formula

$$MR[\%] = \{[\rho(H) - \rho(0)]/\rho(0)\} \times 100\%, \quad (4)$$

where $MR$ is the negative isotropic magnetoresistance in percent, $\rho(H)$ is the specific electric resistance in a 9 kOe magnetic field, and $\rho(0)$ is the specific resistance in zero magnetic field. The electric current direction coincided with that of the longer sample edge. The magnetic field was applied parallel to the electric current in the sample.

The activation energy was calculated by the equation

$$E_{ac} = 2k_B[\partial(\ln\rho)/\partial(T^{-1})], \quad (5)$$

where $E_{ac}$ is the activation energy, $k_B$ is the Boltzmann constant, and $\rho$ is the specific electric resistance.

## 3. RESULTS

An ideal perovskite unit cell possesses cubic symmetry, space group $Pm3m$. Compounds with cubic perovskite structures are, however, fairly rare. Usually, the perovskite crystal lattice is distorted (1) because the cation size does not correspond to the size of the pore it occupies and (2) as a result of the Jahn–Teller effect. In case (1), the transition to a free energy minimum is effected by cooperative rotation of oxygen octahedra. Rotations about the [100] axis of the initial cubic lattice produce tetragonal distortions ($a = b \ne c$, $\alpha = \beta = \gamma$), rotations about the [110] axis cause orthorhombic distortions ($a \ne b \ne c$, $\alpha = \beta = \gamma$), and rotations about the [111] axis yield rhombohedral distortions ($a = b = c$, $\alpha = \beta = \gamma \ne 90°$). In case (2), distortions arise because of the removal of degeneracy from the electronic $e_g$ levels of Jahn–Teller $Mn^{3+}$ ions in an octahedral field of oxygen ions [8].

According to the X-ray powder patterns, the synthesized $La_{0.70}Ba_{0.30}MnO_3$ composition had a perovskite structure with cubic unit cell symmetry. Oxide compounds are known to have perovskite structures if the Goldschmidt tolerance factor $t$ [22] is in the range $0.82 < t < 1.02$. The $t$ value is calculated by the equation

$$t = \frac{\langle r(\mathrm{A})\rangle + \langle r(\mathrm{O})\rangle}{\sqrt{2}(\langle r(\mathrm{B})\rangle + \langle r(\mathrm{O})\rangle)}, \quad (6)$$

where $\langle r(\mathrm{A})\rangle$, $\langle r(\mathrm{B})\rangle$, and $\langle r(\mathrm{O})\rangle$ are the mean ionic radii of ions in the A and B $ABO_3$ perovskite sites and of oxygen, respectively.

At lower $t$ values, ilmenite structures are formed, and at higher $t$ values, oxides have calcite or aragonite structures. The $t$ values for the compositions studied in this work are listed in the table. The X-ray powder patterns did not contain features indicative of the presence of some other impurity phases (Fig. 1). The unit cell symmetry type did not change as oxygen deficiency in $La_{0.70}Ba_{0.30}MnO_{3-\gamma}$ increased up to $\gamma = 0.30$. The X-ray reflections were, however, shifted to smaller angles, which corresponded to an increase in the unit cell volume caused by an increase in $\gamma$. The unit cell parameters are listed in the table. The removal of oxygen anions from the perovskite crystal lattice is accompanied by several simultaneous processes: (1) vacancies in anionic sites appear, (2) the coordination number of cations decreases, and (3) the mean oxidation state of manganese ions decreases. The first two processes should cause a decrease in lattice cell parameters, and the last process should favor their increase. The ionic radius of $Mn^{i+}$ is known to be larger than that of $Mn^{j+}$ if $i < j$ and manganese coordination remains unchanged. For instance, the radius of $Mn^{3+}$ ion is 0.645 Å, and that of $Mn^{4+}$ is 0.530 Å in the octahedral coordination [23]. The increase in the unit cell volume can therefore be explained by the transition of manganese ions to a state with a lower degree of oxidation.

The magnetic properties of the samples were studied by measuring the temperature dependence of magnetization after zero field cooling and after cooling in a fairly low (100 Oe) field (field cooling) (Fig. 2) and the field dependence of magnetization at 6 K (Fig. 3). The stoichiometric $La_{0.70}Ba_{0.30}MnO_3$ compound is a ferromagnet with a Curie temperature of 350 K and spontaneous magnetic moment value of about $3.6\mu_B$ per Mn ion. An increase in the concentration of oxygen vacancies causes the Curie temperature to gradually decrease to 210 K at $\gamma = 0.11$. The spontaneous moment also decreases to $2.3\mu_B$ per Mn ion at the same $\gamma$ value, which is much lower than the value about $3.92\mu_B$ for complete ferromagnetic ordering of manganese spins expected on the assumption that $\mu(Mn^{3+}) = 4\mu_B$ and $\mu(Mn^{4+}) = 3\mu_B$. The temperature dependences of the zero-field-cooling and field-cooling magnetizations insignificantly depend on $\gamma$ in the range $0 \le \gamma \le 0.11$. Such a behavior of magnetization shows that long-range ferromagnetic order persists in this composition range.

Goldschmidt tolerance factor ($t$) and unit cell parameters ($a$ and $V$) of $La_{0.70}Ba_{0.30}MnO_{3-\gamma}$ samples ($\gamma = 0.05$, 0.11, 0.15, 0.18, 0.20, and 0.30) calculated on the assumption of cubic symmetry

| | $t$, Å | $a$, Å | $V$, Å$^3$ |
|---|---|---|---|
| $La_{0.70}Ba_{0.30}MnO_3$ | 0.9970 | 3.910 | 59.79 |
| $La_{0.70}Ba_{0.30}MnO_{2.95}$ | 0.9912 | 3.916 | 60.04 |
| $La_{0.70}Ba_{0.30}MnO_{2.89}$ | 0.9842 | 3.923 | 60.38 |
| $La_{0.70}Ba_{0.30}MnO_{2.85}$ | 0.9796 | 3.928 | 60.61 |
| $La_{0.70}Ba_{0.30}MnO_{2.82}$ | 0.9722 | 3.933 | 60.84 |
| $La_{0.70}Ba_{0.30}MnO_{2.80}$ | 0.9673 | 3.935 | 60.93 |
| $La_{0.70}Ba_{0.30}MnO_{2.70}$ | 0.9435 | 3.947 | 61.51 |

Note: The ionic radii were taken from [23]: $r[La^{3+}(12)] = 1.36$ Å, $r[La^{3+}(10)] = 1.27$ Å, $r[Ba^{2+}(12)] = 1.61$ Å, $r[Ba^{2+}(10)] = 1.52$ Å, $r[Mn^{2+}(6)] = 0.90$ Å, $r[Mn^{3+}(6)] = 0.645$ Å, $r[Mn^{3+}(5)] = 0.580$ Å, and $r[Mn^{4+}(6)] = 0.530$ Å.

A sharp change in the magnetic state occurs in $La_{0.70}Ba_{0.30}MnO_{2.85}$; namely, zero-field-cooling magnetization increases to a maximum value at 40 K and then

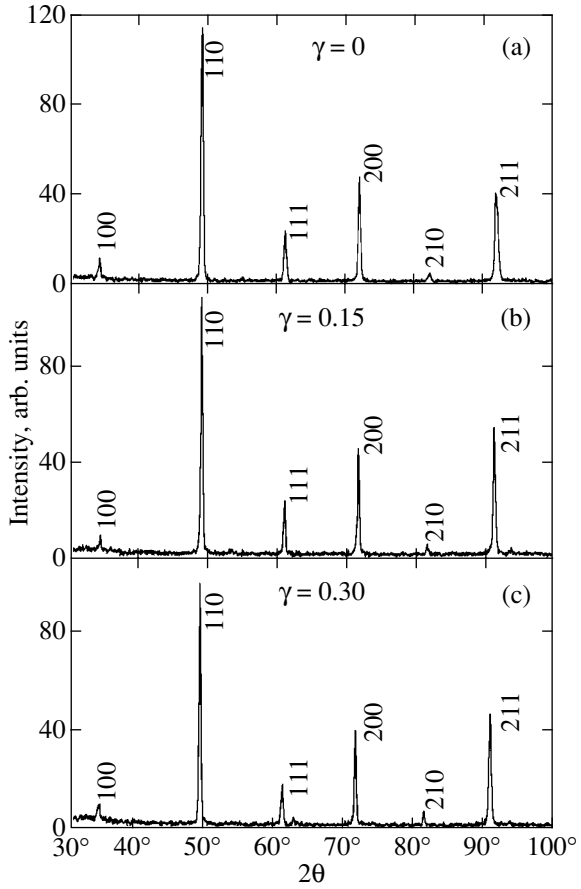


**Fig. 1.** X-ray powder patterns of $La_{0.70}Ba_{0.30}MnO_{3-\gamma}$ with $\gamma$ = (a) 0, (b) 0.15, and (c) 0.30 at room temperature.

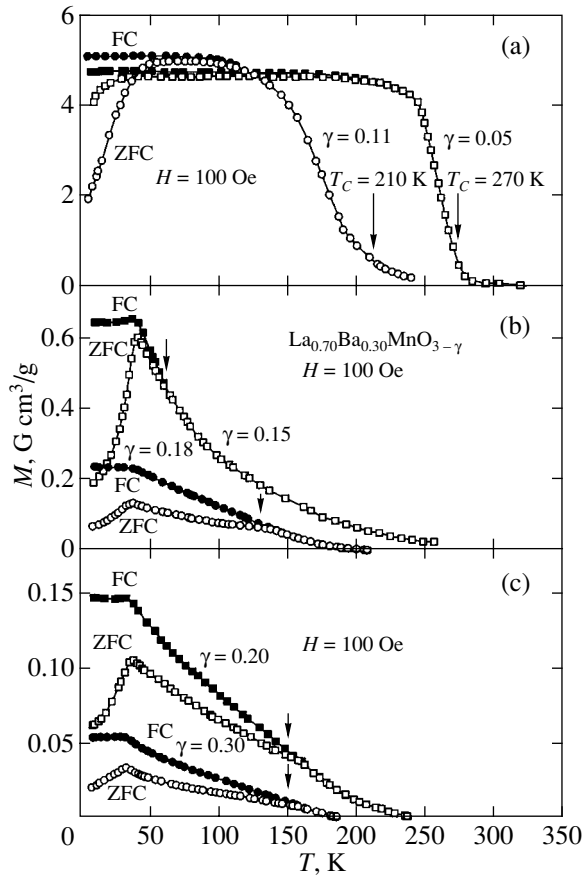


**Fig. 2.** Temperature dependences of magnetization after zero field cooling (ZFC) (open symbols) and after field cooling (FC) in a 100-Oe field (solid symbols) for $La_{0.70}Ba_{0.30}MnO_{3-\gamma}$ samples with various γ. Arrows indicate critical temperatures of magnetic transitions.

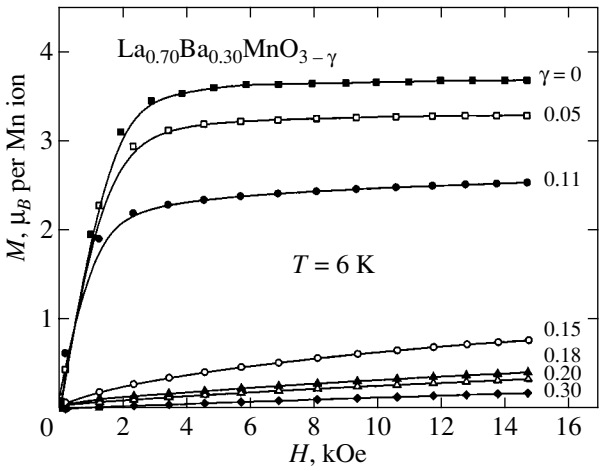


**Fig. 3.** Applied field dependences of magnetization at 6 K for $La_{0.70}Ba_{0.30}MnO_{3-\gamma}$ samples with various γ.

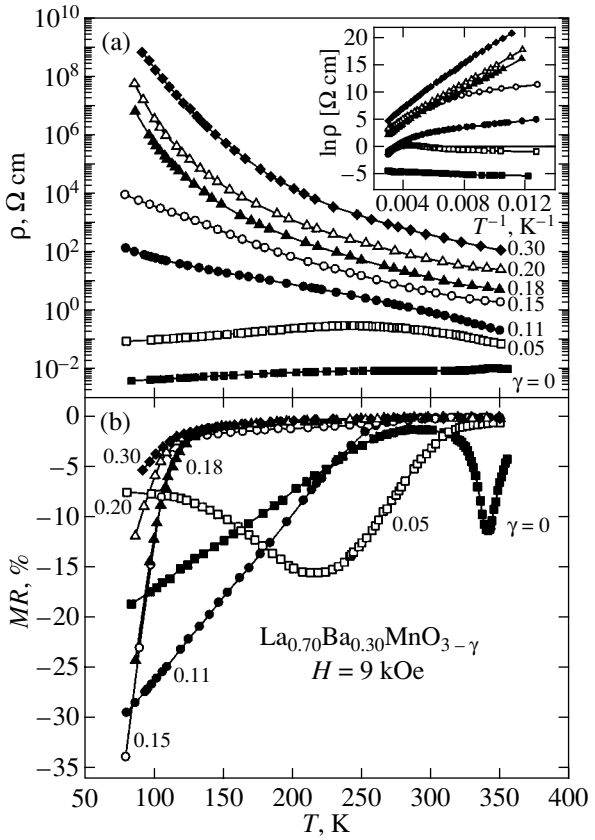


**Fig. 4.** Temperature dependences of (a) specific electric resistance and (b) magnetoresistance measured in a 9-kOe applied field for $La_{0.70}Ba_{0.30}MnO_{3-\gamma}$ samples with various γ. The dependences of the logarithm of specific electric resistance on reciprocal temperature for the same samples are shown in the inset.

smoothly decreases to zero, whereas field-cooling magnetization is constant at low temperatures. The spontaneous moment value for the composition with $\gamma = 0.15$ is close to $0.3\mu_B$ per Mn ion. Note that $La_{0.70}Ba_{0.30}MnO_{2.85}$ only contains $Mn^{3+}$ ions. Such a low spontaneous moment value most likely corresponds to a nonuniform magnetic state which is a combination of antiferromagnetically and ferromagnetically ordered clusters. Competition in interaction between these clusters can lead to the cluster spin glass state [24]. Note also that a temperature of 40 K is typical of cluster spin glass states in manganites [25]. This is the $T_f$ temperature of freezing of cluster magnetic moments.

Similar magnetic properties are characteristic of samples with $0.15 \le \gamma \le 0.30$. The region of transition into the paramagnetic state remains fairly broad. Interestingly, the temperature of the divergence of the zero-field-cooling and field-cooling curves gradually increases as γ grows. For instance, this temperature is 60 K for $\gamma = 0.15$ and 150 K for $\gamma = 0.30$.

The temperature dependences of specific electric resistance and magnetoresistance for reduced $La_{0.70}Ba_{0.30}MnO_{3-\gamma}$ samples are shown in Fig. 4. The samples with $\gamma = 0$ and $\gamma = 0.05$ exhibit the classical electric resistance behavior characteristic of degenerate magnetic semiconductors with the metal–semiconductor transition below $T_C$ and have a magnetoresistance peak, which amounts to 15%. The increase in the mag-

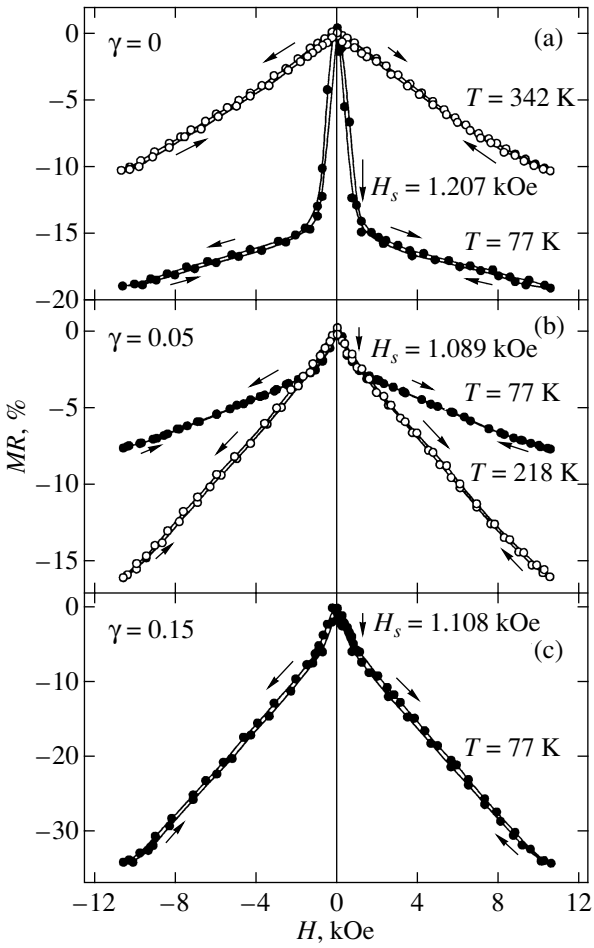


**Fig. 5.** Field dependences of magnetoresistance for $La_{0.70}Ba_{0.30}MnO_{3-\gamma}$ samples with various $\gamma$ at various temperatures. Arrows indicate the direction of measurements.

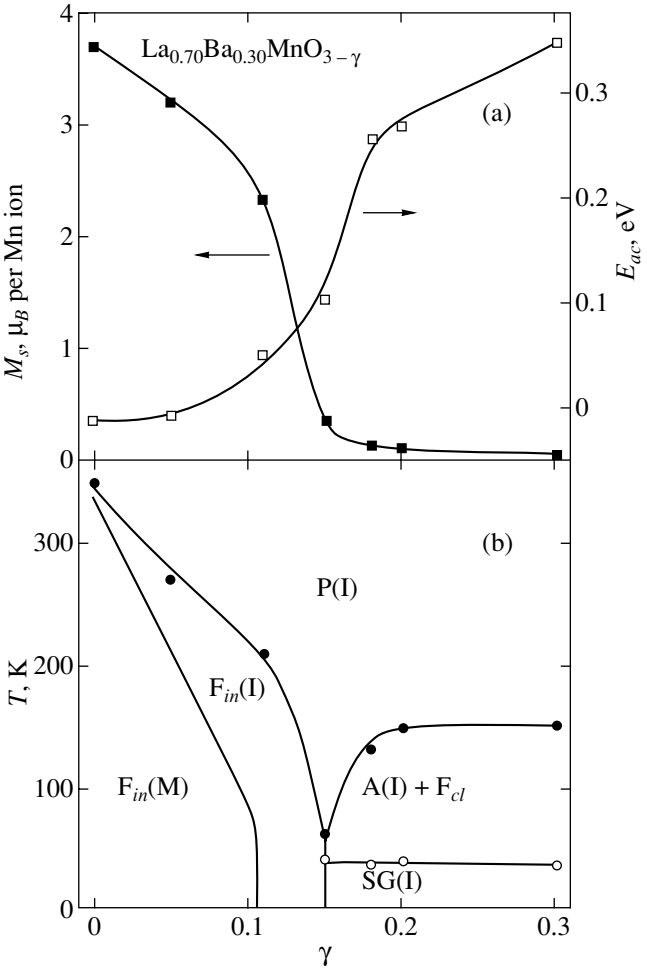


**Fig. 6.** (a) Dependences of spontaneous magnetization measured at 6 K and activation energy determined at 77 K on the concentration of oxygen vacancies and (b) hypothetical magnetic phase diagram for $La_{0.70}Ba_{0.30}MnO_{3-\gamma}$. $F_{in}$(M) denotes nonuniform ferromagnetic metallic state, $F_{in}$(I) is the nonuniform ferromagnetic semiconductive state, SG(I) is the cluster spin glass state with semiconductor-type conduction, A(I) + $F_{cl}$ is the antiferromagnetic state with a small amount of ferromagnetic clusters, and P(I) is the semiconducting paramagnet.

netoresistance of the stoichiometric sample ($\gamma = 0$) as temperature decreases is likely to be caused by intergranule effects, as in other polycrystalline manganites.

The samples with $0.11 \le \gamma \le 0.30$ show the activation character of electric resistance, which continuously grows as temperature decreases. Note that the specific resistance of these samples at low temperatures is satisfactorily described by the equation $\ln\rho \propto T^{-1}$ (also see the inset in Fig. 4). The magnetoresistance of samples with $0.11 \le \gamma \le 0.30$ correlates with the absence of any anomalies of electric resistance close to the transition temperature to the magnetically ordered state. Below this temperature, magnetoresistance begins to continuously increase even to liquid nitrogen temperature and does not show any peak. Increasing $\gamma$ causes low-temperature magnetoresistance to first increase to a maximum of about 34% at $\gamma = 0.15$ and then gradually decrease approximately to 5% at $\gamma = 0.30$.

The dependences of magnetoresistance on applied magnetic field are shown in Fig. 5 for reduced $La_{0.70}Ba_{0.30}MnO_{3-\gamma}$ samples. Measurements were performed at two specially selected temperatures, namely, (1) at the temperature corresponding to the magnetoresistance peak and (2) at liquid nitrogen temperature. The figure shows that the field dependence of magnetoresistance at the peak temperature for the $\gamma = 0$ and 0.15 samples is linear and is characterized by a small hysteresis. The field dependence of magnetoresistance at 77 K is different. The magnetoresistance then rapidly increases at low fields and continues to gradually grow at a very low rate as the field increases. A small hysteresis is also observed for low-temperature magnetoresistance. The saturation field approximately equals 1.1 kOe.

The results of measuring the magnetic and electric properties of reduced $La_{0.70}Ba_{0.30}MnO_{3-\gamma}$ samples allowed us to construct the hypothetical magnetic phase diagram shown in Fig. 6.

Compounds with $\gamma = 0$, 0.05, and 0.11 exhibit a sharp transition to the paramagnetic state and a gradual decrease in the temperature of magnetic ordering and in spontaneous moment as $\gamma$ increases. Conversely, the activation energy increases. These compounds can be treated as nonuniform ferromagnets. The samples with $\gamma = 0.15$, 0.18, 0.20, and 0.30 exhibit properties typical of cluster spin glasses with a 40 K temperature of freezing of cluster magnetic moments. It is most likely that a gradual increase in the temperature corresponding to the beginning of the divergence of the zero-field-cooling and field-cooling curves shows that the Néel temperature of antiferromagnetic interactions, which arise when the compound is reduced, grows as $\gamma$ increases. These compositions are antiferromagnetic matrices with small amounts of the ferromagnetic phase above 40 K. The sharpest change in the magnetic and electric properties is observed for the $La_{0.70}Ba_{0.30}MnO_{2.85}$ compound.

## 4. DISCUSSION

Substituted manganites with perovskite structures are of interest for experimentally studying 180° indirect exchange between manganese cations through oxygen anions, because direct exchange and 90° indirect exchange are absent in these compounds [26].

As mentioned, Zener developed a special theory of indirect exchange interactions through charge carriers (double exchange theory) to explain the magnetic properties of substituted manganites. Interactions of this type are characterized by ferromagnetism and metallic conduction. Many observations, however, cannot be explained by double exchange theory [27].

Goodenough formulated the main principles of the theory of superexchange, which is a special type of indirect exchange interaction. He suggested that ferromagnetism was determined not only by strong double exchange but also by the special features of exchange interactions in systems with $Mn^{3+}$ Jahn–Teller ions. When static Jahn–Teller distortions are removed, the orbital configuration of 3*d* electrons is determined by the positions of manganese ions; that is, the electronic configuration and the core vibrational modes should correlate with each other for $Mn^{3+}$–O–$Mn^{3+}$ interactions to become ferromagnetic. This so-called quasistatic Goodenough hypothesis based on virtual exchange of electrons between manganese ions predicts the anisotropic character of their exchange interactions.

According to [13], $Mn^{3+}$–O–$Mn^{3+}$ superexchange interactions are anisotropic in the orbitally ordered phase [positive in the (001) plane and negative along the [001] direction] and isotropic in the orbitally disordered state (positive along all directions). Orbital ordering is not observed for the $La_{0.70}Ba_{0.30}MnO_3$ stoichiometric composition, and $Mn^{3+}$–O–$Mn^{3+}$ superexchange interactions in this compound are therefore positive. According to the experimental data reported in [28, 29], $Mn^{3+}$–O–$Mn^{3+}$ superexchange interactions change sign from positive to negative as the coordination number of manganese ions decreases. It follows that the antiferromagnetic component of exchange interactions should increase as the concentration of oxygen vacancies grows. For compounds with $0 \le \gamma \le 0.11$, this causes a gradual decrease in the Curie temperature and spontaneous magnetic moment without radical changes in the magnetic state. The $\gamma \le 0.15$ concentration of oxygen vacancies appears to be critical: at this concentration, the volumes of two phases (ferromagnetic and antiferromagnetic) become comparable. The system experiences separation into clusters with different magnetic orders. Competition in interaction between ferromagnetically and antiferromagnetically ordered clusters results in the arising of a state of the type of cluster spin glasses with a 40 K temperature of freezing of cluster magnetic moments. The presence of the temperature of the divergence of the zero-field-cooling and field-cooling magnetization curves can be evidence that the temperature of antiferromagnetic phase ordering is lower than the temperature of ferromagnetic phase ordering. A gradual increase in the divergence temperature most likely shows that the volume of the antiferromagnetic phase continuously increases as the concentration of oxygen vacancies grows up to $\gamma = 0.30$.

The behavior of the electric resistance of reduced polycrystalline $La_{0.70}Ba_{0.30}MnO_{3-\gamma}$ compositions can be understood taking into account two contributions, (1) intragranular contribution and (2) the contribution of intergranular regions (the surface of granules). The diffusion coefficient of oxygen anions on the surface of granules is known to be one order of magnitude higher than that of anions inside granules [30]. Reduction therefore causes the formation of microregions depleted of oxygen on the surface of granules. It is also known that the size of granules decreases as a result of reduction and their number increases [31]. It follows that the intergranular contribution should predominate in reduced samples, which should increase their resistance. The metal–semiconductor transition caused by the intragranular contribution disappears at a certain $\gamma$ value. The higher the concentration of oxygen vacancies, the higher the resistance. The behavior of magnetoresistance substantiates the predominance of the intergranular contribution in strongly reduced samples. The existence of a saturation field is related to a lower energy of exchange interactions on the surface of granules; magnetic moments are then oriented in fairly low fields, which facilitates tunneling of charge carriers between granules. A further increase in magnetoresistance as the field grows is related to a change in the orientation of magnetic moments inside granules. The highest magnetoresistance of nonuniform magnetic systems is observed at low temperatures at which the degree of magnetic ordering increases.

## 5. CONCLUSION

In this work, we performed an experimental study of the properties of $La_{0.70}Ba_{0.30}MnO_{3-\gamma}$ manganites ($0 \le \gamma \le 0.30$) with perovskite structures. The crystal structure parameters and the magnetic and electric properties of polycrystalline $La_{0.70}Ba_{0.30}MnO_{3-\gamma}$ samples ($0 \le \gamma \le 0.30$) were determined depending on the concentration of oxygen vacancies. It was found that long-range ferromagnetic order disappeared and the volume of the antiferromagnetic phase increased as the concentration of oxygen vacancies grew. In all probability, competition between ferromagnetically and antiferromagnetically ordered clusters resulted in the formation of a cluster spin glass-type state. The data obtained in this work allowed us to construct a magnetic phase diagram for $La_{0.70}Ba_{0.30}MnO_{3-\gamma}$ depending on the concentration of oxygen vacancies. The experimental data can be interpreted within the framework of the theory of indirect superexchange interactions through 180°. Superexchange $Mn^{3+}$–O–$Mn^{3+}$ interactions are anisotropic [positive in the (001) plane and negative in the [001] direction] in the orbitally ordered phase and isotropic (positive in all directions) in the orbitally disordered phase. The suggestion was made that indirect exchange $Mn^{3+}$–O–$Mn^{3+}$ interactions were positive in the orbitally disordered phase only if manganese ions had an octahedral environment, whereas exchange interactions became negative if the coordination number of at least one of the $Mn^{3+}$ ions was five or smaller.

## ACKNOWLEDGMENTS

This work was financially supported by the Belarussian Foundation for Basic Research (project no. F02M-069) and the Committee for Science of Poland (KBN grant 5 PO3B 016 20).

## REFERENCES

1. E. Dagotto, T. Hotta, and A. Moreo, Phys. Rep. **344**, 1 (2001).
2. J. M. D. Coey, M. Viret, and S. von Molnar, Adv. Phys. **48**, 167 (1999).
3. V. M. Loktev and Yu. G. Pogorelov, Fiz. Nizk. Temp. **26**, 231 (2000) [Low Temp. Phys. **26**, 171 (2000)].
4. G. H. Jonker and J. H. van Santen, Physica (Utrecht) **16**, 337 (1950).
5. R. von Helmholt, J. Wecker, B. Holzapfel, *et al.*, Phys. Rev. Lett. **71**, 2331 (1993).
6. S. Jin, T. H. Tiefel, M. McCormack, *et al.*, Science **264**, 413 (1994).
7. Y. Tomioka, A. Asamitsu, Y. Moritomo, *et al.*, Phys. Rev. Lett. **74**, 5108 (1995).
8. E. L. Nagaev, Phys. Rep. **346**, 387 (2001).
9. G. Matsumoto, J. Phys. Soc. Jpn. **29**, 606 (1970).
10. J. B. Goodenough, Phys. Rev. **100**, 564 (1955).
11. C. Zener, Phys. Rev. **82**, 403 (1951).
12. P.-G. de Gennes, Phys. Rev. **118**, 141 (1960).
13. J. B. Goodenough, A. Wold, R. J. Arnott, and N. Menyuk, Phys. Rev. **124**, 373 (1961).
14. E. E. Havinga, Philips Res. Rep. **21**, 432 (1966).
15. S. V. Trukhanov, I. O. Troyanchuk, *et al.*, Fiz. Nizk. Temp. **27**, 385 (2001) [Low Temp. Phys. **27**, 283 (2001)].
16. F. Millange, V. Caignaert, B. Domenges, *et al.*, Chem. Mater. **10**, 1974 (1998).
17. I. Maurin, P. Barboux, Y. Lassailly, *et al.*, J. Magn. Magn. Mater. **211**, 139 (2000).
18. B. C. Tofield and W. R. Scott, J. Solid State Chem. **100**, 183 (1974).
19. H. L. Ju, J. Gopalakrishnan, J. L. Peng, *et al.*, Phys. Rev. B **51**, 6143 (1995).
20. S. I. Patil, S. M. Bhagat, Q. Q. Show, *et al.*, Phys. Rev. B **62**, 9548 (2000).
21. P. Schiffer, A. P. Ramirez, W. Bao, and S.-W. Cheong, Phys. Rev. Lett. **75**, 3336 (1995).
22. V. M. Goldschmidt, Geochemische Verteilungsgesetze der Elemente **VII** (1928).
23. R. D. Shannon, Acta Crystallogr. A **32**, 751 (1976).
24. K. Moorjani and J. M. D. Coey, in *Magnetic Glasses, Methods and Phenomena* (Elsevier, Amsterdam, 1984), Vol. 6.
25. I. O. Troyanchuk, S. V. Trukhanov, H. Szymczak, *et al.*, Zh. Éksp. Teor. Fiz. **120**, 183 (2001) [JETP **93**, 161 (2001)].
26. J. B. Goodenough, *Magnetism and the Chemical Bond* (Wiley, New York, 1963).
27. I. O. Troyanchuk, S. V. Trukhanov, H. Szymczak, and K. Bärner, J. Phys.: Condens. Matter **12**, L155 (2000).
28. K. R. Poeppelmeier, M. E. Leonowicz, and J. M. Longo, J. Solid State Chem. **44**, 89 (1982).
29. K. R. Poeppelmeier, M. E. Leonowicz, J. C. Scanlon, *et al.*, J. Solid State Chem. **45**, 71 (1982).
30. K. A. Thomas, P. S. I. P. N. de Silva, L. F. Cohen, *et al.*, J. Appl. Phys. **84**, 3939 (1998).
31. J. M. Gonzalez-Calbet, E. Herrero, N. Rangavittal, *et al.*, J. Solid State Chem. **148**, 158 (1999).

*Translated by V. Sipachev*

*Journal of Experimental and Theoretical Physics, Vol. 95, No. 2, 2002, pp. 316–324.*
*Translated from Zhurnal Éksperimental'noĭ i Teoreticheskoĭ Fiziki, Vol. 122, No. 2, 2002, pp. 366–376.*


**SOLIDS**
**Structure**

# Fluctuation Mechanism of Formation of Discontinuous Tracks by Fast Ions in Solids

**F. F. Komarov* and V. A. Belyĭ**

*Sevchenko Institute of Applied Problems, Belarussian State University, Minsk, 220064, Belarus*
**e-mail: komarov@bsu.by*

Received April 10, 2001

**Abstract**—The effect of one-electron and many-electron charge-exchange processes involving fast heavy ions on the formation of tracks in crystals is considered. The proposed model of fluctuations of charge distributions gives reasonable estimates for the length of defects regions and the distance between defects in discontinuous tracks. The modified model of a thermal peak predicts the track radius. The validity of the model for explaining all the properties of formation of discontinuous and continuous tracks is demonstrated by the example of InP crystals irradiated by 250-MeV xenon ions. © *2002 MAIK "Nauka/Interperiodica".*

## 1. INTRODUCTION

For fast ions with the kinetic energy $E > 1$ MeV/au, the intensity of energy release to the electron subsystem is $10^3$–$10^4$ times greater than that to the nuclear subsystem. The specific energy loss per unit length $(dE/dx)_e$ can be as high as several tens of keV/nm. A high energy release to the electron subsystem of a solid enhances the contribution of electronic excitations to the generation of structural defects and the intense inelastic sputtering of materials, and induces such specific effects as the formation of tracks and amorphous states, local melting, formation of unusual phases (high-pressure phases, nanotubes, fullerenes), generation of shock waves, and the destruction of materials (see, for example, [1, 2]). The most important for applications (filters, sensors, detectors, elements for nanoelectronics [2]) and interesting scientific result of the propagation of high-energy ions in solids is the formation of tracks—macroscopic defects elongated along the ion trajectory.

In many experimental studies (for example, [3–7]) of formation of tracks upon irradiation of materials by high-energy ions, along with continuous tracks, discrete discontinuous tracks were observed whose geometry changed from quasi-continuous to bead-shaped upon penetration of an ion inside a target. These experimental data were interpreted by means of different mechanisms [5, 8, 9]. The authors of [9] assumed that tracks were produced predominantly due to the ionization of the inner shells of atoms of the medium, which is accompanied by the intense formation of low-energy δ electrons. According to [9], the discrete structure of the tracks is explained by the discrete ionization of the inner electron shells. Nevertheless, the authors of paper [9] point out that only a small part of the ion energy can be released due to ionization of the inner shells of atoms and assume that the tracks are mainly produced due to a continuous release of the ion energy to the electron subsystem of a solid. In addition, they assume that tracks are not produced in the parts of the ion trajectory in the target where the inner electron shells are not ionized.

The authors of paper [8] explained the discrete structure of tracks by the discrete formation of an electron flux along the ion path caused by the law of conservation of momentum. In our opinion, the most fruitful concept was proposed by Dartyge and Sigmund [5], who suggested that the average number of defects observed in a track is directly related to fluctuations in the ionization density rather than to its average value.

## 2. MECHANISM OF FORMATION OF DISCONTINUOUS AND CONTINUOUS TRACKS

The authors of papers [5, 8, 9] have not considered the primary processes related to the statistical fluctuations of the charge state of ions moving in a solid due to the electron stripping and capture. In our opinion, however, fluctuations of the ion charge state can cause a significant change in the energy loss released to the electron subsystem at certain parts of the ion trajectory. The role of these processes becomes noticeable when the energy of the moving ion is close to the energy corresponding to the threshold value $(dE/dx)_e^{\text{th}}$ of the mean energy loss required for the track formation.

Therefore, the discontinuous tracks observed in experiments can be caused by statistical fluctuations during charge exchange, when an ion loses one or several electrons, and the value of $(dE/dx)_e$ becomes greater, at a certain part of the ion path, than the value of $(dE/dx)_e^{\text{th}}$ required for the track formation. At the

initial part of the fast ion path, when $(dE/dx)_e > (dE/dx)_e^{th}$, a continuous track is formed. The mean path propagated by the ion until a change in its charge state will determine the length of the defect region in a discontinuous track and the distance between the defects. The diameter of the defect or its geometry is determined by the number of electrons detached per event. We briefly discussed this idea earlier in papers [10, 11].

The process of track formation is most often described by the thermal peak model [12–14]. Although this model qualitatively describes the experimental data, the question remains why the latent heat of melting is usually not considered. Also, the role of phonons in the propagation of energy from a highly excited region and the concept of phonons itself, when the calculated temperature achieves 2000 K and above, remain to be discussed. It seems that the plasma approximation [15, 16] is more adequate.

To consider the problem of formation of continuous and discontinuous tracks in solids caused be electronic excitations, it is necessary first to separate two main processes of the energy dissipation from a strongly excited region: (i) the relaxation of this region accompanied by partial energy transfer to the electron and atomic subsystems and (ii) partial energy transfer from the perturbed atomic region to the surrounding matrix (thermalization of this region).

The first process is substantially determined by the material type (metal, semiconductor, or dielectric), the electron concentration in the conduction band (at the Fermi level), and their mobility; it also depends on the spectrum of electronic excitations [1, 2, 17]. The energy transfer from the electron subsystem to the atomic subsystem also depends on the structural properties of a material (bulk material, thin film, grain size, and the concentration of structural defects in polycrystals) [1–3, 18, 19].

The thermalization and structural properties of a region after its "cooling" depend on the types of material and crystal lattice, the matrix structure, the relation between the volumes of the material in liquid and solid phases, and the presence of allotropic phases [1, 2, 18, 19].

It is especially important to consider accurately energy transfer from the excited region around the ion trajectory in the case of structurally perfect crystals of metals and narrow-gap semiconductors. Indeed, the typical time of cooling of an electron plasma in metals due to the electron heat conduction does not exceed $10^{-14}$ s even for plasma temperature of the order of the Fermi energy $E_F$, when the electron heat conduction is minimal [16]; therefore, the cooling time of a plasma is shorter than the typical time of thermal oscillations (of the order of $10^{-13}$ s). Then, during cooling of the electron plasma, the electrons interact with virtually immobile individual atoms (ions) rather than with collective atomic oscillations (phonons); i.e., the plasma approximation will be more realistic. In the presence of grain boundaries, structural defects, and impurities, the characteristic times of the electron–electron and electron–phonon relaxation can substantially change [2, 18, 19].

Below, we consider the modified thermal peak model describing the formation of continuous and discontinuous tracks, which includes both processes of energy dissipation from the initially excited region discussed above. The model is based on the assumption that the region surrounding the ion trajectory is a two-component plasma consisting of electrons and highly ionized atoms of a target. This approximation is confirmed by the initial stage of the penetration of an ion, which produces a high degree of ionization of target atoms adjacent to the ion trajectory. The modern theory of track formation allows one to take into account only the main factors determining the stages of relaxation and thermalization of the excited region.

## 3. STOPPING AND CHARGE-EXCHANGE PROCESSES

In the case of penetration of high-energy ions, the elastic energy losses play a minor role, and more than 90% of the ion energy is lost in inelastic collisions (i.e., in collisions with target electrons). This stopping is described by the Bethe formula [20]

$$\left(\frac{dE}{dx}\right)_e = \frac{4\pi Z_2 Z_{1,\text{eff}}^2 e^4 N}{mv^2}\ln\frac{2mv^2}{I}, \qquad (1)$$

where $Z_{1,\text{eff}}$ is the average effective charge of ions; $Z_2$ and $N$ are the atomic number and atomic density of a target, respectively; $e$ and $m$ are the electron charge and mass, respectively; $v$ is the ion velocity; and $I$ is the average ionization potential of atoms. The numerical integration of this equation gives the dependence of $(dE/dx)_e$ on the depth $x$ for 250-MeV $Xe^+$ ions (the middle curve in Fig. 1).

According to the experimental study [4] of the track formation in InP irradiated by 250-eV $Xe^+$ ions, the region of formation of a continuous track is characterized by high ion energy losses [$(dE/dx)_e \geq 14$ keV/nm for depths $x \leq 7$ μm], while, in the region without tracks, the ion energy losses are low [$(dE/dx)_e \leq 10$ keV/nm for depths $x \geq 10$ μm]. In the intermediate region 7 μm $\leq x \leq$ 10 μm, discontinuous discrete tracks were observed [4].

One of the processes that can lead to the formation of discontinuous tracks can be fluctuations of the charge state of moving ions, which is accompanied by a decrease or an increase in the ion charge by one or several units (electron capture or stripping, respectively).

To simplify the statistical picture of variations in the charge distributions of ions over the target thickness, which is typical for a large ensemble of moving parti-

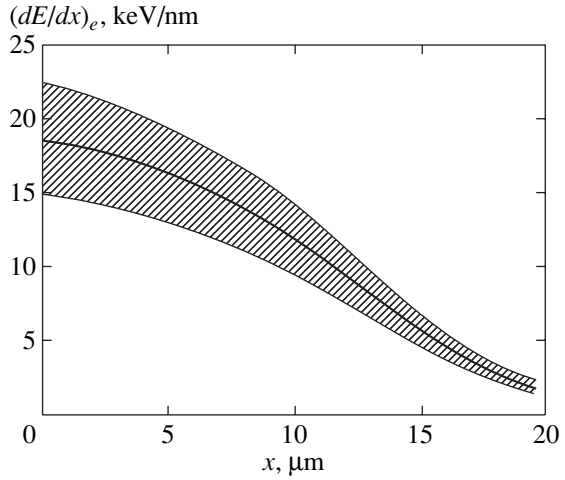


**Fig. 1.** Dependence of the energy loss by 250-MeV xenon ions on the penetration depth (thick line). The dashed region corresponds to the possible fluctuations of the dynamic charge of the ion.

cles, we consider the role of such fluctuations relative to the average effective ion charge in formula (1). Because the effects of track formation and the real picture of the track detected by the method of high-resolution transmission electron microscopy are related to a single actual ion, such an approach seems to be reasonable. The statistical nature of the ion distribution over charges at any depth for the entire flux of particles is manifested in the scatter of the properties (lengths of the continuous and discontinuous parts of the track, their diameters, etc.) of individual tracks relative to the average characteristics.

It is well known (see, for example, [20–22]) that a fast ion moving in a solid loses some electrons, so that its charge can vary from zero to the atomic number $Z_1$ of the ion in the Periodic Table. Due to the loss (capture) of electrons, this charge does not remain constant and fluctuates about its average value. Only in the case of well-channeled ions can their charge state be "frozen" [21, 23–25] because of a low electron density at the central part of a channel along which the ions are moving.

The ion charge-exchange processes were described by several expressions (see, for example, expressions presented in [21, 22]). The ion beam propagated through a solid with a sufficient thickness will have the equilibrium charge distribution

$$F_g \approx (2\pi d^2)\exp\left[-\frac{(g-g_0)^2}{2d^2}\right], \qquad (2)$$

which is close to a Gaussian and is characterized by two parameters: the average charge

$$g_0 = \sum_g gF_g$$

and the distribution half-width

$$d = \sqrt{\sum_g (g-g_0)^2 F_g},$$

where $g$ is the ion charge, which can vary from 1 to $Z_1$.

In a broad region of ion velocities, where $g_0 \approx (0.3–0.8)Z_1$, the value of $d$ is almost independent of $v$. In the general case, $d$ is approximately described by the expression [26]

$$d = d_1\sqrt{g_0[1-(g_0/Z_1)^k]}, \qquad (3)$$

where $d_1 = 0.5$ and $k = 0.6$.

The asymmetry of the experimental distribution (2) and its width, which exceeds the theoretical value predicted by expression (2), are mainly caused by many-electrons losses in one collision.

We will find the average effective ion charge $Z_{1,\,\mathrm{eff}}$ from the semiempirical expression in [26] and determine its fluctuations from the Bohr formula [20]:

$$g_0 = Z_1\left[1+\left(\frac{1}{Z_1^\alpha}\frac{v}{v'}\right)^{-1/k}\right]^{-k},$$
$$\sigma_0 \approx \pi a_0^2 (Z_1^{1/3}+Z_2^{1/3})(v_0/v)^2, \qquad (4)$$

where it is assumed for estimates that $g_0 \approx Z_{1,\,\mathrm{eff}}$ (a more rigorous relation between these quantities is presented in [27]; $\sigma_0$ is the cross section for the electron capture (stripping); $v' = 3.6 \times 10^6$ m/s and $\alpha = 0.48$ are the model parameters; and $v_0 = 2.19 \times 10^6$ m/s and $a_0 \approx 0.053$ nm are the Bohr velocity and radius, respectively. For 250-MeV xenon ions propagating in InP in the region of a discrete track, these expressions give the values $g_0 \approx 25$ and $\sigma_0 \approx 1.8 \times 10^{-17}$ cm$^2$.

Note that our calculations [27–30] of the distributions of ions over their penetration paths, taking into account fluctuations of the charge states, showed that the depths $x$ at which equilibrium charge distributions are established are quite large. Thus, $x \approx 0.8$ μm for 50-MeV $B^+$ ions in silicon and $x = 1$ μm for 59-MeV $Ni^+$ ions in diamond. The depth $x$ decreases with increasing $Z_2$. Therefore, the average charge of 250-MeV $Xe^+$ ions in InP also will strongly differ from $Z_{1,\,\mathrm{eff}}(E)$ at the initial part of their trajectory in the crystal, and hence, the energy loss $(dE/dx)_e$ of the ion per unit length will be substantially lower than that predicted by expression (1). This circumstance can be responsible for the absence of tracks and weak distortions in the near-surface region of the crystal ($x \le 35$ nm) and the presence of discontinuous tracks which we observed [4, 7, 28] at depths from 35 to 100 nm. The continuous tracks were observed at depths from 100 nm to 7 μm. The discontinuous tracks were again observed at depths 7 μm $\le x \le$ 10 μm, when the values of $(dE/dx)_e$ become close or smaller than $(dE/dx)^{\mathrm{th}}$. The thickness

of these regions for 340-MeV ions increases approximately proportionally to the ratio of the initial energies of the ions [28], i.e., $\eta = 340/250 = 1.36$.

According to (1), even small variations in the effective charge can cause fluctuations in the ion energy losses. For example, the loss (capture) of one electron results in oscillations of almost 8% of the value of $(dE/dx)_e$ [$(g_{max}/g_{min})^2 \approx 1.08$, where $g_{max}$ and $g_{min}$ are the ion charge after the charge exchange with the electron loss or capture, respectively], whereas the loss (capture) of three electrons causes oscillations amounting to 30%. The dashed region in Fig. 1 shows possible energy losses when up to two electrons are stripped (captured). Along with the experimental data available, these estimates allow us to propose the following model.

At small distances from the target surface, where the equilibrium distribution of the ion flux over charges was not established yet, the energy loss can be lower than the track-formation threshold. At such depths, simple point defects and their complexes are formed. It is known that the crystal surface is an efficient sink for such defects, which causes a substantial decrease in the final concentration of structural defects. As the penetration depth of the ion flux increases, many-electron charge-exchange processes cause fluctuations of the average charge when $(dE/dx)_e > (dE/dx)^{th}$ (i.e., the energy losses in a certain part of the ion trajectory become greater than the threshold track formation energy losses). The mean free path of an ion in a higher charge state determines the length of a discontinuous track. Let us emphasize again that a number of statements of the statistical theory of propagation of the ion flux in solids are applied to a single ion (i.e., a "statistically averaged" ion). In the region of a continuous track, the values of $(dE/dx)_e$ considerably exceed $(dE/dx)^{th}$. When the energy losses approach the track formation threshold (they can be associated, for example, with melting of a local region), the oscillations of stopping caused by the charge exchange of ions result in frequent crossings of this threshold, thereby producing a discontinuous track. At large depths, such crossings become rare and short in time; i.e., rare and short defect regions are formed. Note here an important role of rare head-on or almost head-on elastic collisions of ions with atoms of the medium, which stimulate charge-exchange processes accompanied by the loss of several electrons. At large depths, elastic collisions of ions with atoms of the medium begin to play a main role. These processes lead to the formation of usual structural defects and amorphous regions.

We verified this model by calculating the mean size of defects in discontinuous tracks. As mentioned above, their length is equal to the mean free path propagated by the ion until the next charge exchange. The probability of this process at the distance $x$ is calculated from the expression

$$p = N\sigma x,$$

where $N$ is the density of target atoms and $\sigma$ is the total charge-exchange cross section. Then, the defect length in a discontinuous track is defined as $\lambda = 1/N\sigma$. This value of $\lambda$, which takes into account only one-electron charge-exchange processes, is two to three times smaller than the size of defects observed in a discontinuous track [4, 7, 28]. According to the data reported in review [22], the relative probability of many-electron charge-exchange processes for fast ions compared to one-electron processes is about 60% for the loss (capture) of two electrons, 40% for three-electron processes, 20% for four-electron processes, etc. Many-electron processes lead to strong fluctuations of energy losses [see expression (1)]. When two- and three-electron losses are taken into account, the calculated length of defects becomes approximately two to three times larger than that calculated considering only one-electron processes. This corresponds qualitatively and quantitatively to the experimental lengths of defect regions [3, 4, 7, 28].

Note that our theory [27, 29, 30], which describes the distribution of ions over their paths taking into account the fluctuations of charge distributions of ions, provided much better agreement between the theoretical and experimental distributions of atoms over their penetration depth in the target compared to conventional calculations neglecting this effect [31]. However, although the theory gave the distribution widths that were 1.5–5 times larger than those reported in [31], these widths were nevertheless always smaller than experimental widths. Our theory [27, 29, 30] takes into account only one-electron charge-exchange processes. It seems that many-electron charge-exchange processes substantially affect the distribution of high-energy ions over their paths in a solid. The consideration of many-electron processes strongly affects the width of the charge distribution of the ion flux as a function of the penetration depth in the target.

## 4. MODEL OF TRACK FORMATION

A particle propagating in a target produces a certain number of hot electrons. If the particle energy is completely imparted to atoms, then 250-MeV xenon ions can melt a cylindrical region of diameter ~25 nm. Nevertheless, some electrons ($\delta$ electrons) acquire a kinetic energy that is sufficient for their departure from the ion trajectory by large distances. Because the total energy of such electrons is large, the track formed in this way will be thin. To take this process into account, one should know the initial distribution of excited ions. Free electrons appear in the track region due to inelastic collisions between an incident particle and target atoms. The incident particle excites a certain fraction of electrons in target atoms that are weakly bound to nuclei. Because the energy $E_e$ of these electrons is

much smaller than the energy $E$ of the incident particle with the mass $M_1$,

$$E_{e,\max} = \frac{4M_1 m}{(M_1+m)^2}E \approx \frac{4m}{M_1}E,$$

we can use the Rutherford formula to describe the energy imparted to one electron [32]:

$$\varepsilon = \varepsilon_{\max}/(\chi r^2 + 1), \quad (5)$$

$$\xi = (4\pi\varepsilon_0 m v^2/Z_1 e^2)^2, \quad (6)$$

$$\varepsilon_{\max} = 2mv^2, \quad (7)$$

where $r$ is the impact parameter of the collision, $v$ is the ion velocity, $\varepsilon_{\max}$ is the maximum energy imparted to one electron, and $\varepsilon_0$ is the dielectric constant.

The maximum distance at which the inelastic collision of an ion accompanied by energy transfer to electrons takes place is determined by the energy gap of a semiconductor:

$$r_{\max} = \sqrt{\frac{1}{\chi}\left(\frac{\varepsilon_{\max}}{\varepsilon_g} - 1\right)}, \quad (8)$$

where $\varepsilon_g$ is the energy gap.

Inelastic collisions can occur at small distances and depend on the distance between colliding atoms and ions. Calculations [21] showed that the incident particle excites in an InP crystal three to five outer-shell electrons, which correspond to all electrons in the outer shell of In and P atoms. This means that excitation of any additional electron from a deeper electron shell requires a much greater energy and, therefore, is unlikely. Thus, we assume below that target atoms lose the same number $k_a$ of electrons. In this case, the energy distribution of excited electrons can be found from the expression

$$n(\varepsilon)d\varepsilon = 2\pi r k_a n\, dr,$$

where $n(\varepsilon)$ is the energy density of the excited electrons per unit length of the ion trajectory. By substituting expression (5), we obtain

$$n(\varepsilon) = \frac{\pi k_a n \varepsilon_{\max}}{\chi(\varepsilon_g + \varepsilon)^2}. \quad (9)$$

The total energy imparted to electrons is equal to the energy lost by a particle per unit length

$$\int_0^{\varepsilon_{\max}} (\varepsilon + \varepsilon_g) n(\varepsilon) d\varepsilon = \left(\frac{dE}{dx}\right)_e,$$

which gives

$$k_a = \frac{\chi (dE/dx)_e}{\pi n \varepsilon_{\max} \ln(\varepsilon_{\max}/\varepsilon_g)}. \quad (10)$$

Expression (10) neglects in the first approximation the contribution of plasmons, i.e., collective plasma excitations in solids, thereby overestimating somewhat the role of one-particle excitations. This can be corrected by subtracting from expression (10) for $(dE/dx)_e$ the contribution of plasmons [21], which is calculated from the expression

$$\left(\frac{dE}{dx}\right)_{pl} = \frac{4\pi Z_1 e^4 N n_0}{m v^2} \ln\frac{v}{v_F},$$

where $n_0$ is the number of valence electrons per atom and $v_F$ is the velocity of Fermi electrons.

For the region of discontinuous tracks in InP, when the energy losses are from 10 to 14 keV/nm, the coefficient $k_a = 3$–$5$. This confirms the above assumption that the target atoms involved in collisions lose all outer-shell electrons.

The excited electrons have a radial velocity component and attempt to leave the excited region around the ion trajectory. An uncompensated positive charge produced near the ion trajectory due to the departure of some electrons from the track region will attract all electrons. Assuming that this charge is uniformly distributed inside a cylindrical region of radius $r_0$, we can write the potential energy of any electron in the established electric field in the form

$$\varphi(g, r) = \frac{ge^2}{4\pi\gamma\varepsilon_0}\begin{cases}(r/r_0)^2 & r < r_0,\\ 2\ln(r/r_0) + 1, & r > r_0,\end{cases} \quad (11)$$

where $ge$ is the linear charge density in this region, $r$ is the distance from the ion trajectory, and $\gamma\varepsilon_0$ is the dielectric constant of the target.

At first, all the electrons, which have a high energy and a noticeable transverse energy component ($E_\perp = m v_\perp^2/2$, where $v_\perp$ is the electron velocity component perpendicular to the ion trajectory), go away much further from the ion trajectory than electrons with lower energy. Therefore, any individual electron will be attracted by an uncompensated charge produced due to the escape of fast electrons from the region near the ion trajectory:

$$g(\varepsilon) = \int_\varepsilon^{\varepsilon_{\max}} n(\varepsilon) d\varepsilon. \quad (12)$$

Each fast electron will move from the ion trajectory until all its kinetic energy is converted to potential energy. By substituting expressions (12) and (9) into (11), we obtain the dependence shown in Fig. 2.

Stopped electrons are attracted by a Coulomb force back to the region of initial excitations. However, the Coulomb attraction is not sufficient for returning some

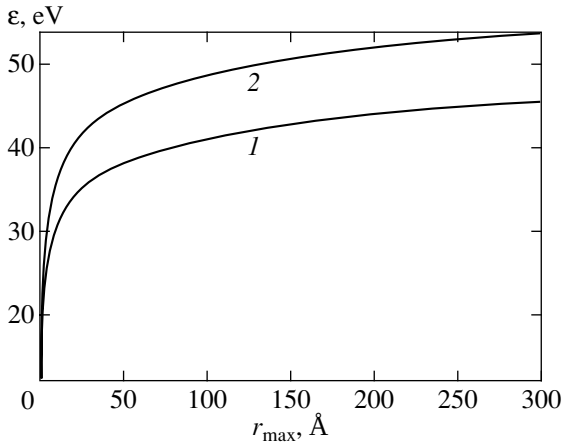


**Fig. 2.** Relation between the initial energy of an electron and its maximum distance from the track center at the initial stage for energy losses 10 (*1*) and 14 keV/nm (*2*).

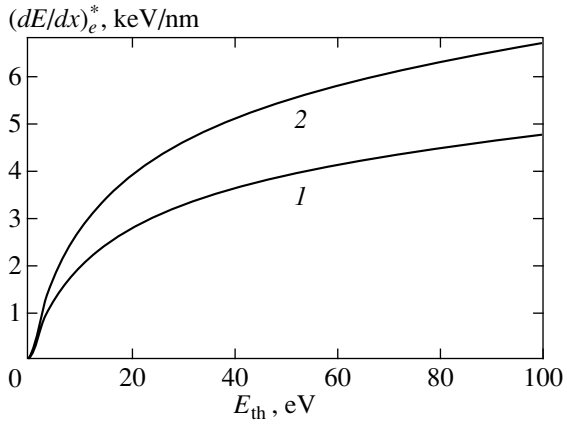


**Fig. 3.** Total energy of electrons remaining in the track region and involved in the track formation as a function of the threshold energy $E_{th}$ for energy losses 10 (*1*) and 14 keV/nm (*2*).

far removed electrons, which are either captured by genetic defects (growth defects) or lose their energy, which was acquired due to the action of a Coulomb force, during the electron–phonon interaction. Thus, to separate electrons that are not involved in the track formation, we can introduce a phenomenological energy $E_{th}$, which depends on the properties of the target material (density and energy gap $Z_2$), but at the same time is not a constant for a given material, being dependent on the value of $(dE/dx)_e$ or on the ion velocity when the values of $(dE/dx)_e$ are the same. When ion velocities are lower (for example, in the case of cluster ions or fullerene ions), the low-energy electronic excitations dominate, and almost all excited electrons remain in the region of localization of a future track.

This energy can be estimated from Fig. 2 as $E_{th} \approx$ 40 eV for $(dE/dx)_e$ = 10 keV/nm and $E_{th} \approx$ 50 eV for $(dE/dx)_e$ = 14 keV/nm.

As mentioned above, the introduction of the threshold electron energy results in the fact that a fraction of energy from the excited region is carried away by fast electrons and is no longer involved in the formation of a defect (track) region. The energy $(dE/dx)_e^*$ remaining within the track can be obtained by integrating expression (10) with the upper limit $E_{th}$ (Fig. 3). It follows from Fig. 3 that only about half the energy imparted to the electronic subsystem from the ion is spent for the track formation, whereas, according to calculations, about 97–98% of excited electrons remain within the track. Note that the estimate of the fraction of energy spent for the track formation is a lower limit because we did not take the angular distribution of δ electrons explicitly into account.

## 5. FORMATION OF THE EQUILIBRIUM ELECTRONIC DISTRIBUTION

When a small fraction (several percent) of hot electrons leave the track, the remaining electrons are involved in random motion with frequent collisions. Because the electronic density is very high (above $10^{23}$ cm$^{-3}$), the characteristic time of these collisions is very small and does not exceed $10^{-14}$ s. Therefore, a system of free electrons can be described at times longer than $10^{-14}$ s by the Maxwell–Boltzmann distribution [the distribution function has a classical form because the electron energy is comparatively high (a few electronvolts)]

$$f(\varepsilon) = f_{00}e^{-\varepsilon/T}, \tag{13}$$

where $T$ is the electron temperature and $f_{00}$ is a normalization constant. The constant $f_{00}$ and temperature $T$ can be determined from the total number $N_{left}$ of excited electrons within the track region and their total energy $E_{left}$:

$$\int_0^{R_{max}} 2\pi r dr \int_{\varphi(r)}^{E_{th}} f(\varepsilon)q(\varepsilon, r)d\varepsilon = f_0 \int_0^{R_{max}} r dr \int_{\varphi(r)}^{E_{th}} (\varepsilon - \varphi(r))^{1/2} e^{-\varepsilon/T} d\varepsilon = N_{left}, \tag{14}$$

$$\int_0^{R_{max}} 2\pi r dr \int_{\varphi(r)}^{E_{th}} \varepsilon f(\varepsilon)q(\varepsilon, r)d\varepsilon = f_0 \int_0^{R_{max}} r dr \int_{\varphi(r)}^{E_{th}} \varepsilon[\varepsilon - \varphi(r)]^{1/2} e^{-\varepsilon/T} d\varepsilon = E_{left}, \tag{15}$$

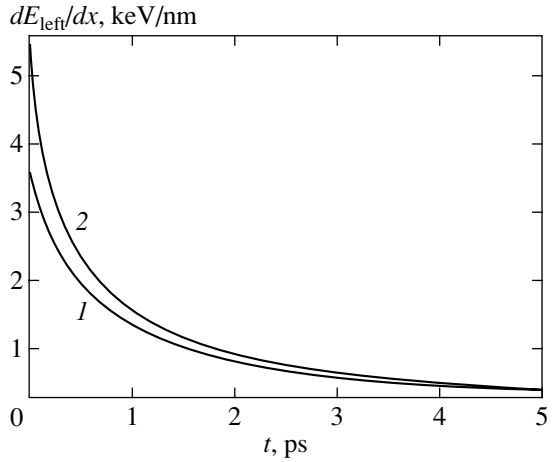


**Fig. 4.** Dependence of the total energy of the electron gas on time for energy losses 10 (*1*) and 14 keV/nm (*2*).

where

$$q(\varepsilon, r) = g_0^*\varepsilon[\varepsilon - \varphi(r)]^{1/2},$$
$$R_{max} = \left(\frac{4\pi\gamma\varepsilon_0 E_{th}}{g_0^* e^2}\right)^{1/2} r_0, \quad (16)$$

where $q(\varepsilon, r)$ is the density of states, $f_0$ is a new normalization constant, and $R_{max}$ is the maximum distance from the ion trajectory at which an electron with energy $E_{th}$ can move away. The most important region for the track formation is located near the ion trajectory; therefore, we can neglect the logarithmic part in the potential energy in Eq. (11):

$$\varphi(r) = \frac{g_0^* e^2}{4\pi\gamma\varepsilon_0}\left(\frac{r}{r_0}\right)^2, \quad (17)$$

$$g_0^*(\varepsilon) = \int_0^{E_{th}} n(\varepsilon)d\varepsilon, \quad (18)$$

where $g_0^*$ is the total number of electrons involved in the further track formation.

The integration of expressions (14)–(18) shows that, upon irradiation of InP by 100-MeV xenon ions, the linear dependence

$$T \approx 2.5E_{left}/N_{left} \quad (19)$$

between the electron temperature and the average electron energy is observed, so that the initial temperature of hot electrons is close to 1.2 eV (14 000 K).

## 6. HEATING AND MELTING OF LOCAL REGIONS

In summing the above discussion, note that the target region adjacent to the fast ion trajectory resembles a two-component plasma. It consists of highly ionized target atoms and hot electrons. Nevertheless, the temperatures of these components are substantially different, resulting in energy transfer from electrons to atoms. The energy transfer rate is described by the expression

$$\frac{dQ}{dt} = \int_0^{R_{max}} 2\pi r dr \int_{\varphi(r)}^{E_{th}} f(\varepsilon)q(\varepsilon, r)\int_0^{\varepsilon} EN v_1(\varepsilon)d\sigma(E), \quad (20)$$

where $N$ is the atomic density of the target, $v_1(\varepsilon) = \sqrt{2\varepsilon/m}$ is the electron velocity, and $d\sigma(E)$ is the differential cross section for electron–atom scattering accompanied by the transfer of energy $E$. According to the Rutherford formula [32], we have

$$d\sigma(E) = \frac{\pi m(k_a e^2)^2}{(4\pi\varepsilon_0)^2 M_2[\varepsilon - \varphi(r)]}\frac{dE}{E^2}, \quad (21)$$

where $M_2$ is the target atom mass, $k_a$ is the average charge of ionized target atoms [see (9)], and $\varepsilon - \varphi(r)$ is the kinetic energy of an electron with the total energy $\varepsilon$.

After substitution of (21) into (20), the rate of energy transfer to atoms from electrons with a temperature lower than 2 eV will take the form

$$\frac{dQ}{dt} = \mu T^2, \quad (22)$$

where the coefficient $\mu \approx 1 \times 10^{-17}$ eV$^{-1}$ s$^{-1}$. Taking into account (19), we obtain the expression for the total energy in the electron subsystem as a function of time

$$E_{left}(t) = \frac{1}{E_{left,0}^{-1} + \lambda t}, \quad (23)$$

where $\lambda = \mu/(2.5N_{left})^2$ and $E_{left,0}^{-1}$ is the electron gas energy at $t = 0$. This dependence normalized to the unit path length ($dE_{left}/dx$)) of 100-eV xenon ions in InP is shown in Fig. 4. One can see from this figure that about 5 keV of energy is transferred from electrons to target atoms during first $10^{-12}$ s. The effect of this process on the target (thermalization of the excited region) can be studied by using the nonstationary heat conduction equation

$$C\rho\frac{\partial T}{\partial t} = \xi\nabla^2 T + \frac{dQ_V}{dt}, \quad (24)$$

where $C$, $\rho$, $\xi$, and $T$ are the specific heat, density, heat conduction, and temperature of the target, respectively, and $dQ_V/dt$ is the energy density imparted to atoms.

The solution of this equation gives the expression for the temperature at different distances from the ion trajectory [3, 13]

$$T(r, t) = \int_0^t \frac{dQ/dt}{4\xi\pi(t-\tau)} \exp\left(-\frac{C\rho r^2}{4\xi(t-\tau)}\right) d\tau. \qquad (25)$$

Figure 5 shows the dependences $T(r, t)$ taking into account that all the energy is spent on heating, but no melting occurs. It would be incorrect in the case of a real crystal, in which melting occurs after heating up to 1350 K. Nevertheless, in our case, the target need not be melted. A track can be formed after an addition of a sufficiently large portion of energy after reaching the melting point. Indeed, this energy addition can cause the displacement of several nearest atoms, so that the final structure in the region around the ion trajectory will differ from the initial one, and the track can be detected with a high-resolution electron microscope.

Nevertheless, the energy required for the displacement of atoms strongly depends on the radius of a heated region. The smaller its radius, the greater the energy required, and one can expect that the temperature required for the activation of this process will be substantially higher than 1350 K. Therefore, the values of $T$ calculated from expression (25) are too small, and no tracks are formed in the energy loss region where $(dE/dx)_e \leq 10$ keV/nm (Fig. 5a). On the contrary, if the energy loss reaches approximately 14 keV/nm (Fig. 5b), the heated region proves to be sufficiently broad, and the threshold energy for the displacement of atoms from the equilibrium position can be substantially lower than in the previous case. A temperature that slightly exceeds the melting temperature will be sufficient for melting a local quasi-cylindrical region and track formation at the stage of its sharp cooling.

The results of calculations (Fig. 5b) show that the track radius can achieve 4–5 nm and more for $(dE/dx)_e = 14$ keV/nm, in good agreement with experimental data [4, 28] (the diameter of tracks produced by 250-keV xenon ions in InP at depths from 100 nm to 10 μm varied from 7 to 15 nm).

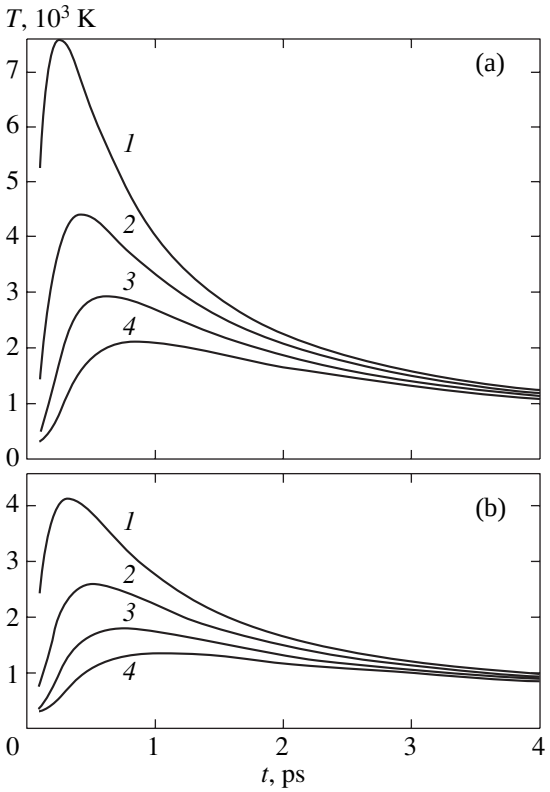


**Fig. 5.** Time dependences of the target temperature for energy losses 10 (a) and 14 keV/nm (b) at distances from the track center equal to 2 (*1*), 3 (*2*), 4 (*3*), and 5 nm (*4*).

## 7. CONCLUSIONS

The model that was discussed above describes the formation of continuous and discontinuous tracks. The consideration of fluctuations of the charge state of ions, including many-electron processes, allowed us to calculate the depths in an InP crystal at which discontinuous tracks are formed, as well as linear sizes of defects. These data are in good agreement with experimental data.

The radii of continuous and discontinuous tracks were determined using the plasma approximation, which assumes that the track region represents a two-component plasma instead of a heated solid, which was usually considered in previous papers. Our calculations showed that, although only a few percent of fast electrons leave the region of a track being formed, nevertheless they carry away almost half the energy released by the ion to the electron subsystem of the target. In this case, the rate of energy transfer from the electron subsystem to the atomic subsystem is substantially higher than that predicted earlier by the thermal peak model [3, 12–14] based on the electron–phonon interaction. For this reason, even half the energy released by the ion is sufficient for producing changes in the crystal lattice, which result in the formation of tracks in semiconductors or metals.

## ACKNOWLEDGMENTS

The authors thank W. Wesch, A. Yu. Didyk, P. Sigmund, Yu. N. Yavlinskiĭ, V. A. Skuratov, L. Chadderton, P. I. Gaĭduk, and A. F. Komarov for useful discussions and comments at the stage of preparation of the article.

## REFERENCES

1. *Proceedings of the 3rd International Symposium on Swift Heavy Ions in Matter, Caen, 1995*, Nucl. Instrum. Methods Phys. Res. B **107** (1996).
2. F. F. Komarov and A. F. Komarov, *Physical Processes under Ionic Implantation of Solids* (Tekhnoprint, Minsk, 2001).

3. S. Furuno, H. Otsu, K. Hojou, and K. Izui, Nucl. Instrum. Methods Phys. Res. B **107**, 223 (1996).
4. O. Herre, W. Wesch, E. Wendler, *et al.*, Phys. Rev. B **58**, 4832 (1998).
5. E. Dartyge and P. Sigmund, Phys. Rev. B **32**, 5429 (1985).
6. F. Studer, M. Hervieu, J.-M. Costantini, and M. Toulemonde, Nucl. Instrum. Methods Phys. Res. B **122**, 449 (1997).
7. P. I. Gaiduk, F. F. Komarov, and W. Wesch, Nucl. Instrum. Methods Phys. Res. B **164/165**, 377 (2000).
8. D. P. Ertchak, V. G. Efimov, and V. F. Stelmakh, J. Appl. Spectrosc. **64**, 433 (1997).
9. T. A. Tombrello, C. R. Wie, M. Itoh, and T. Nakayama, Phys. Lett. A **100A**, 42 (1984).
10. V. A. Belyĭ and F. F. Komarov, Zh. Tekh. Fiz. **68** (9), 42 (1998) [Tech. Phys. **43**, 1048 (1998)].
11. F. F. Komarov and A. F. Komarov, Zh. Éksp. Teor. Fiz. **113**, 489 (1998) [JETP **86**, 270 (1998)].
12. I. M. Lifshits, M. I. Kachanov, and L. V. Tantarov, At. Énerg. **6**, 391 (1959).
13. A. I. Glushtsov, F. F. Komarov, A. P. Novikov, *et al.*, Dokl. Akad. Nauk BSSR **31**, 609 (1987).
14. M. Toulemonde, E. Paumier, and Ch. Dufour, Radiat. Effects Defects Solids **126**, 201 (1993).
15. Yu. V. Martynenko and Yu. N. Yavlinskii, At. Energy **62**, 80 (1987).
16. A. E. Volkov and V. A. Borodin, Nucl. Instrum. Methods Phys. Res. B **107**, 172 (1996).
17. M. Toulemonde, Ch. Dufour, A. Meftah, and E. Paumier, Nucl. Instrum. Methods Phys. Res. B **166/167**, 903 (2000).
18. A. Yu. Didyk, V. K. Semina, A. Khalil, *et al.*, Pis'ma Zh. Tekh. Fiz. **26** (2), 1 (2000) [Tech. Phys. Lett. **26**, 46 (2000)].
19. Yu. Yavlinskii, Nucl. Instrum. Methods Phys. Res. B **146**, 142 (1998).
20. N. Bohr, *The Penetration of Atomic Particles through Matter* (Munksgaard, Copenhagen, 1948; Inostrannaya Literatura, Moscow, 1950).
21. M. A. Kumakhov and F. F. Komarov, *Energy Loss and Ranges of Ions in Solids* (Gordon and Breach, New York, 1981).
22. H. Betz, Rev. Mod. Phys. **44**, 465 (1972).
23. F. Martin, Phys. Rev. Lett. **22**, 329 (1969).
24. C. Moak, Phys. Rev. B **10**, 2681 (1974).
25. Sh. Datz, Radiat. Effects **12**, 163 (1972).
26. I. S. Dmitriev and V. S. Nikolaev, Zh. Éksp. Teor. Fiz. **47**, 615 (1964) [Sov. Phys. JETP **20**, 409 (1964)].
27. A. F. Burenkov, F. F. Komarov, and S. A. Fedotov, Nucl. Instrum. Methods Phys. Res. B **67**, 35 (1992).
28. P. I. Gaĭduk, F. F. Komarov, V. S. Tishkov, *et al.*, Phys. Rev. B **61**, 15785 (2000).
29. A. F. Burenkov, F. F. Komarov, and S. A. Fedotov, Phys. Status Solidi B **169**, 33 (1992).
30. A. F. Burenkov, F. F. Komarov, and S. A. Fedotov, Nucl. Instrum. Methods Phys. Res. B **67**, 30 (1992).
31. J. F. Ziegler, J. P. Biersack, and C. U. Littmark, *The Stopping and Range of Ions in Solids* (Pergamon, New York, 1985).
32. N. Bohr, Philos. Mag. **30**, 681 (1915).

*Translated by M. Sapozhnikov*

*Journal of Experimental and Theoretical Physics, Vol. 95, No. 2, 2002, pp. 325–336.*
*Translated from Zhurnal Éksperimental'noĭ i Teoreticheskoĭ Fiziki, Vol. 122, No. 2, 2002, pp. 377–391.*


**SOLIDS**
**Electronic Properties**

# Electron Relaxation Mechanisms in *n*-Bi–Sb Semiconducting Alloys

**V. D. Kagan, N. A. Red'ko*, N. A. Rodionov, and V. I. Pol'shin**

*Ioffe Physicotechnical Institute, Russian Academy of Sciences,*
*ul. Politekhnicheskaya 26, St. Petersburg, 194021 Russia*
**e-mail: nikolaj.a.redko@pop.ioffe.rssi.ru*

Received December 26, 2001

**Abstract**—The magnetic field dependence of diffusion thermal electromotive force $\alpha_{22}(H)$ ($\nabla T \parallel C_1$) in degenerate *n*-Bi–Sb semiconducting alloys, in which only *L* electrons participate in transfer phenomena, had a maximum at $\mathbf{H} \parallel C_3$. The electron relaxation time was determined from the magnetic field value corresponding to this maximum. The dependences of the electron relaxation time on temperature and the concentration of alloy components and the dopant (on the concentration of electrons) were used to separate electron relaxation time components corresponding to scattering by phonons, ionized impurities, and component concentration fluctuations. The latter ("alloy") mechanism of electron scattering by concentration fluctuations was for the first time considered for Bi–Sb alloys; its contribution was found to be comparable with those of the other scattering mechanisms. The obtained relaxation times were used to calculate theoretical magnetic field dependences of thermal electromotive force and the Nernst–Ettingshausen coefficient. The calculation results were in satisfactory agreement with experiment. © *2002 MAIK "Nauka/Interperiodica".*

## 1. INTRODUCTION

Binary $Bi_{1-x}Sb_x$ alloys form a continuous series of solid solutions with Bi ($m_{Bi} = 209$) and Sb ($m_{Sb} \approx 172$) atoms in $D_{3d}$ crystal lattice sites. The differences of the bismuth and antimony atomic weights and ionic radii ($r_{Bi} \approx 0.62$ Å and $r_{Sb} \approx 0.74$ Å) and of the force constants in the $Bi_{1-x}Sb_x$ alloy crystal lattice results in (1) the formation of local defects, (2) the dependence of the alloy lattice constant on the concentration of antimony [1], and (3) rearrangement of the energy spectrum of charge carriers in alloys depending on the concentration of antimony, from the spectrum corresponding to the semimetallic state ($0 \le x < 0.07$) to that characteristic of the semiconducting state ($0.07 < x < 0.22$) and then again to a semimetallic state spectrum ($0.22 < x \le 1$) [2].

The presence of local defects caused by the difference of the bismuth and antimony atomic parameters and by the existence of a fluctuation potential caused by an irregular arrangement of antimony atoms in alloy crystal lattice sites results in scattering of charge and heat carriers, that is, electrons and phonons. The influence of this scattering in Bi–Sb alloys on phonon thermal conductivity was studied in [3]. Scattering of electrons by the fluctuation potential in Bi–Sb alloys is considered in this work for the first time.

In transverse magnetic fields, a monotonic dependence of thermal electromotive force (EMF), which attains a constant value in classically strong magnetic fields, is observed in semiconductors with isotropic electronic spectra [4]. Electron scattering by acoustic phonons or point defects increases the diffusion thermal EMF in transverse magnetic fields in magnitude, and scattering by ionized impurities decreases it.

A nonmonotonic dependence of thermal EMF in transverse magnetic fields was for the first time observed in Bi–Sb semiconducting alloys with *L* electrons participating in transfer phenomena [5]. Note that the presence of a thermal EMF maximum in a transverse magnetic field was also observed earlier for bismuth samples doped with tellurium, in which *L* electrons participated in transfer phenomena [6]. At the same time, the field dependences of thermal EMF of *n*-Bi–Sb alloys and *n*-Bi contained no maxima.

The presence of a maximum in the field dependence of thermal EMF is explained in [7] by the many-valley character of the semiconductor and strong anisotropy of its electron energy spectrum. According to [7], the electron relaxation time can be determined from the magnetic field value corresponding to the maximum of diffusion thermal EMF. This problem is also considered in this work.

Usually, relaxation time tensor components for charge carriers in bismuth and Bi–Sb alloys are determined using specific resistance and magnetoresistance tensor components [8–13].

Studies of kinetic coefficients in Bi–Sb alloys showed that the mechanism of electron scattering was mixed; at low temperatures ($T < 10$ K), scattering by ionized impurities and point defects predominated [2, 10], and, at $T > 10$ K, the predominant mechanism was scattering by acoustic phonons [10].

**Table 1.** Principal parameters of $n$-$Bi_{1-x}Sb_x$ semiconducting alloy samples ($0.07 \le x \le 0.16$)

| No. | $x$ | φ | $\varepsilon_{gL}$, meV | $n$, $10^{17}$ cm$^{-3}$ | ζ, meV | $m_1/m_0$, $10^{-3}$ | $m_2/m_0$ | $m_3/m_0$, $10^{-3}$ |
|---|---|---|---|---|---|---|---|---|
| 1 | 0.07 | 5.7° | 7.5 | 1.37 | 18.6 | 0.91 | 0.32 | 1.2 |
| 2 | 0.09 | 5.55° | 11 | 1.95 | 19 | 1.43 | 0.48 | 1.74 |
| 3 | 0.12 | 5.3° | 16.4 | 1.57 | 15.5 | 2.42 | 0.72 | 2.58 |
| 4 | 0.13 | 5.14° | 19 | 1.58 | 14.3 | 3.1 | 0.83 | 3.0 |
| 5 | 0.15 | 4.97° | 22 | 1.61 | 13.7 | 3.86 | 0.94 | 3.45 |
| 6 | 0.16 | 4.88° | 23.6 | 1.71 | 13.5 | 4.37 | 1.0 | 3.7 |

Note: Here, $x$, φ, $\varepsilon_{gL}$, $n$, ζ, and $m_i$ are the antimony concentration in the alloy, bandgap width in the semiconducting alloy, the electron concentration in the sample, the chemical potential of electrons in the sample, and the effective masses of electrons in the ellipsoid at the band bottom in the alloy, respectively.

In this work, we analyze the mechanisms of relaxation of $L$ electrons in $Bi_{1-x}Sb_x$ semiconducting alloys ($0.07 \le x \le 0.16$). Its results augment and extend the earlier views on the problem.

## 2. SAMPLES AND PROCEDURES FOR MEASUREMENTS

The temperature dependence of thermal EMF $\alpha_{22}(0)$ ($\nabla T \parallel C_1$) in zero field, thermomagnetic effects $Q_{12,3}(H, T)$ ($\nabla T \parallel C_1$, $\mathbf{H} \parallel C_3$), and magnetic field-induced thermal EMF changes $\Delta\alpha_{22}(H) = \alpha_{22}(H) - \alpha_{22}(0)$ were measured for single crystals of $Bi_{1-x}Sb_x$ ($0.07 \le x \le 0.16$) semiconducting alloys doped with a donor admixture (tellurium). The samples were cut out on a unit for electroerosion from the middle of a single crystalline ingot grown by horizontal zone recrystallization; we used a modified zone melting procedure with a cooled seed [14].

The cut out middle part of the ingot was cleaved along the cleavage (basal) plane, on which an equilateral triangle of cleavage traces along binary axes ($C_2$) was usually discernible. Cleavage traces along binary axes in the form of a triangle in the basal plane and the trigonal axis ($C_3$) normal to the basal plane were used to cut out samples from the ingot by electroerosion in the form of rectangular parallelepipeds with faces normal to the $C_1$, $C_2$, and $C_3$ crystallographic axes. The cut out samples were etched in a $C_2H_5OH$–$HNO_3$ (1 : 1) solution. The dimensions of the samples for measurements were $3 \times 3 \times 30$ mm$^3$; the longest edge was oriented along the $C_1$ bisector axis. The alloy composition was determined by X-ray diffraction, and the nonuniformity of the concentration of electrons was estimated by measuring the Hall coefficient along the sample; its value did not exceed 5%. The conclusion of a low electron concentration nonuniformity was substantiated by the presence of quantum oscillations of thermal EMF at $T \le 4.2$ K. The principal parameters of the samples are listed in Table 1.

The sample under study with heaters at its ends was soldered to the bottom of a vacuum chamber (about 18 mm in diameter) immersed into a constant-temperature liquid (helium, hydrogen, or nitrogen). The heater on the sample at the bottom of the chamber was used to control the mean temperature of the sample, and the heater at the opposite end, to create a temperature gradient ($\nabla T$) along the sample. Temperature was measured at two sample points ($l_T \approx 15$ mm) at a constant heat flux by carbon resistance thermometers at $1.5 < T < 40$ K and by copper–constantan thermocouples at $30 < T < 80$ K. The thermal EMF of the samples was measured in a pair with copper, whose thermal EMF did not exceed 1 μV/K in magnitude in the whole temperature range of our measurements. The experimental thermal EMF values are given below without the corresponding corrections. Thermomagnetic effects were measured in magnetic fields $0 \le H < 18$ kOe at temperatures $1.4 \le T < 40$ K.

## 3. EXPERIMENTAL RESULTS

In $n$-Bi–Sb semiconducting alloys, electron gas in the region of impurity conduction ($T < 40$ K) is degenerate, and the Fermi surface consists of three electron ellipsoids with centers at the $L$ Brillouin zone points situated in the mirror-reflection planes (Fig. 1). One of the smaller ellipsoid axes coincides with the $C_2$ binary axis of the crystal. The ellipsoids are rotated about this axis through small angle φ; the φ values for the alloys studied in this work are listed in Table 1. Because of this rotation, two other ellipsoid axes make angles φ with the $C_1$ and $C_3$ crystallographic axes. The electron ellipsoids in the alloys are equivalent by crystal symmetry and have strongly anisotropic effective masses (Table 1), which are responsible for the nonmonotonic magnetic field dependence of diffusion thermal EMF.

The thermal EMF changes $\Delta\alpha_{22}(H) = \alpha_{22}(H) - \alpha_{22}(0)$ ($\nabla T \parallel C_1$) are shown in Fig. 2 as functions of magnetic field at $\mathbf{H} \parallel C_3$ for $Bi_{1-x}Sb_x$ semiconducting alloys with $x = 0.07$ and $x = 0.13$ at various temperatures. The same dependences at $T = 21$ K and the theoretical dependences discussed below are plotted in Fig. 3.

The temperature dependence of thermal EMF for $Bi_{0.93}Sb_{0.07}$ is shown in Fig. 4. The observed deviations

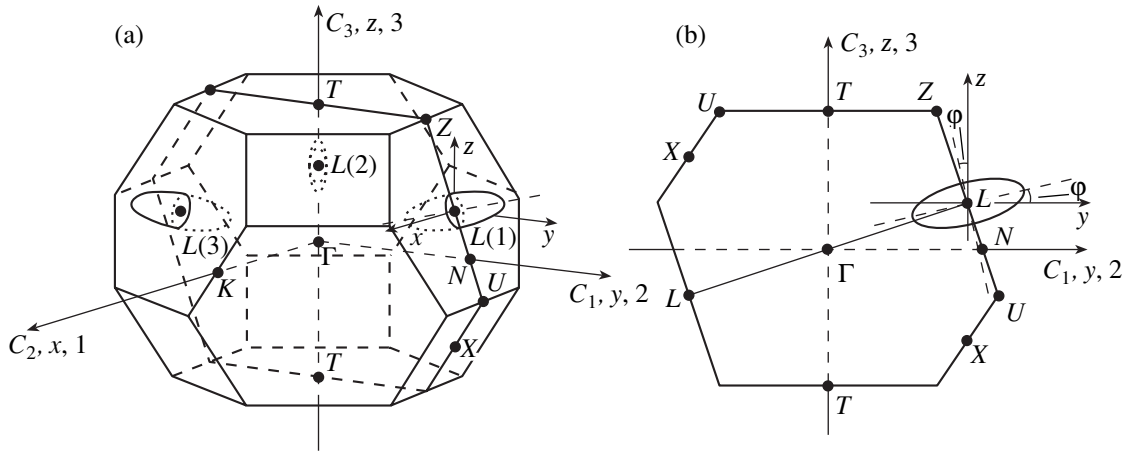


**Fig. 1.** (a) Brillouin zone of *n*-Bi–Sb degenerate semiconducting alloys with three electron ellipsoids whose centers are situated at points *L* in mirror-reflection planes and (b) one of three cross sections of the Brillouin zone by mirror-reflection planes. Ellipsoids in the zone are equivalent and tilted with respect to crystal axes. One of the shorter ellipsoid axes coincides with the $C_2$ binary axis of the crystal, and two other ellipsoid axes make angles φ with the $C_3$ trigonal and $C_1$ bisector axes.

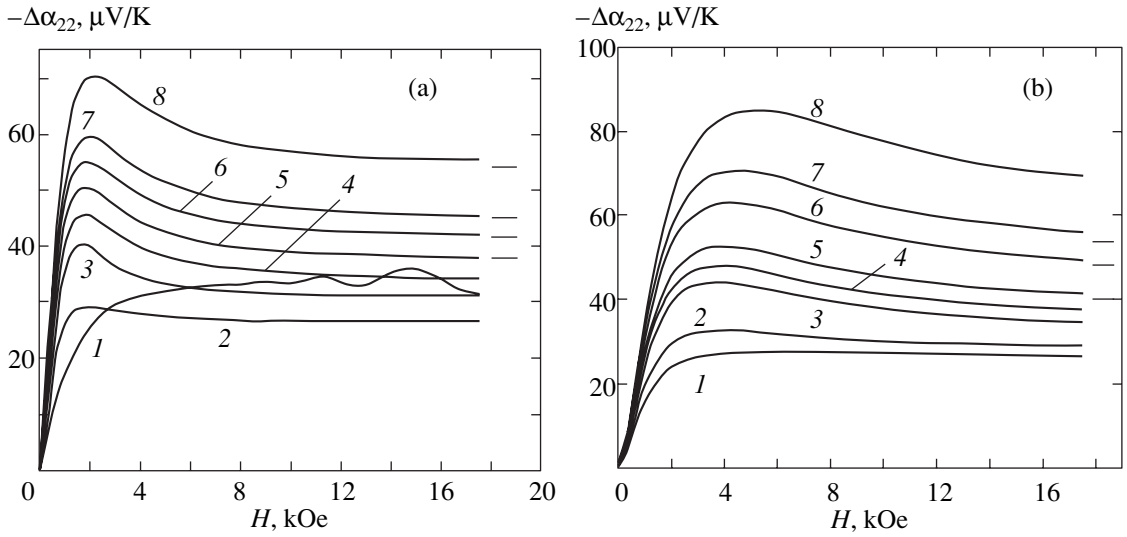


**Fig. 2.** Field dependences of diffusion thermal EMF changes $\Delta\alpha_{22}(H) = \alpha_{22}(H) - \alpha_{22}(0)$ ($\nabla T \parallel C_1$) in transverse magnetic field $\mathbf{H} \parallel C_3$ for (a) *n*-$Bi_{0.93}Sb_{0.07}$ and (b) *n*-$Bi_{0.87}Sb_{0.13}$ semiconducting alloys at various temperatures, (a) at (*1*) 4.8, (*2*) 10.6, (*3*) 12.3, (*4*) 15.4, (*5*) 18.6, (*6*) 21, (*7*) 23.2, and (*8*) 25.1 K and (b) at (*1*) 9.6, (*2*) 12.6, (*3*) 17.2, (*4*) 18.9, (*5*) 21, (*6*) 25.2, (*7*) 28, and (*8*) 35.4 K. Lines given at the ends of curves corresponding to various temperatures correspond to $\Delta\alpha_{\infty}$.

from the linear temperature dependence for $\alpha_{22}(0)$ and $\alpha_{\infty}$ at $T < 18$ K are evidence of the predominance of the phonon thermal EMF component caused by the entrainment of electrons with phonons. The thermal EMF linearly depends on temperature at $T > 18$ K, which is evidence of the predominance of the diffusion thermal EMF component. The deviation of the temperature dependence of diffusion thermal EMF from linearity at $T > 40$ K is related to the transition from the region of impurity conduction at $T < 40$ K to intrinsic conductivity at $T > 40$ K. Such a transition in the semiconducting alloy is caused by a low bandgap width, which results in thermal injection of electrons from the valence band to the conduction band at $\varepsilon_g \approx 2kT$. The injection rate increases as temperature grows. As a consequence, the concentration of electrons in the conduction band and the concentration of holes in the valence band also increase. This results in the experimentally observed thermal EMF decrease in magnitude in the region of intrinsic conductivity [$\alpha = (\alpha_h\sigma_h - \alpha_e\sigma_e)/(\sigma_h + \sigma_e)$, where $\alpha_{e,h}$ and $\sigma_{e,h}$ are the partial thermal EMF and conductivity values, respectively, for electrons and holes]. Note that such a behavior of the temperature dependence of thermal EMF is also characteristic of other alloys. In this work, we study

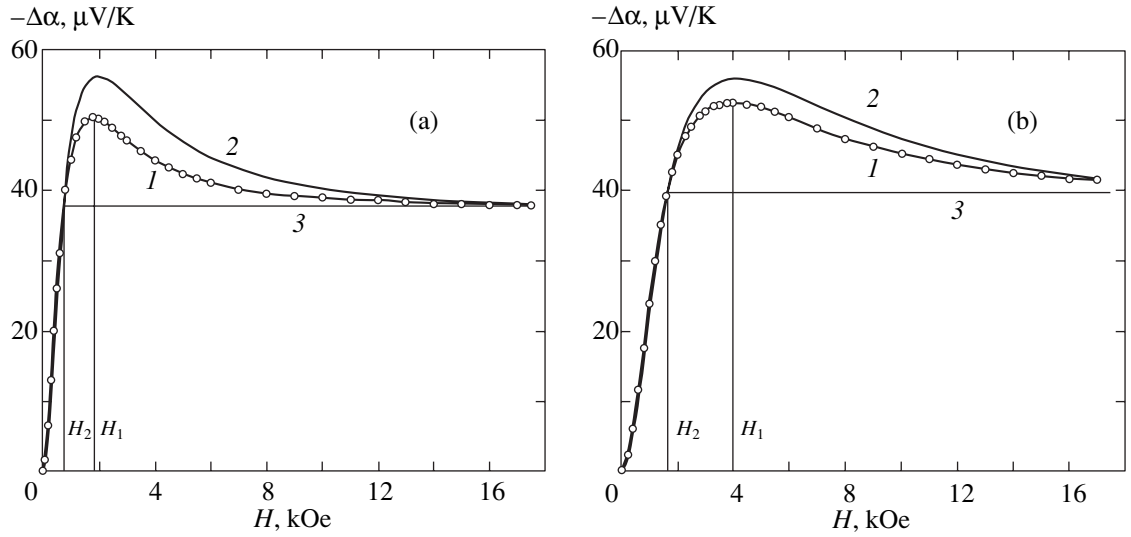


**Fig. 3.** Experimental and calculated field dependences of diffusion thermal EMF changes $\Delta\alpha(H) = \alpha(H) - \alpha(0)$ in transverse magnetic field with electron parameters for (a) $n$-$Bi_{0.93}Sb_{0.07}$ and (b) $n$-$Bi_{0.87}Sb_{0.13}$ alloys: (*1*) experimental $\Delta\alpha_{22}(H)$ ($\nabla T \parallel C_1$, $\mathbf{H} \parallel C_3$) curves at $T = 21$ K, (*2*) $\Delta\alpha(H)$ curves calculated by (7) at $T = 21$ K with $\beta$ = (a) 1.33 and (b) 1.04, and (*3*) straight lines corresponding to the $\Delta\alpha_\infty$ values. $H_1$ and $H_2$ are the magnetic fields found from $\Delta\alpha_{max}$ and $\Delta\alpha_{22}(H_2) = \Delta\alpha_\infty$, respectively.

transfer phenomena in Bi–Sb alloys in the region of impurity conduction at $T < 40$ K.

The $\Delta\alpha_{22}(H)$ dependences for the diffusion ($T >$ 18 K) and phonon ($T < 10$ K) thermal EMFs are shown in Fig. 2 by curves *5–8* and *1*, respectively. The thermal EMF in the temperature range 10–18 K contains diffusion and phonon components; the corresponding $\Delta\alpha_{22}(H)$ dependences are shown by curves *2–4*.

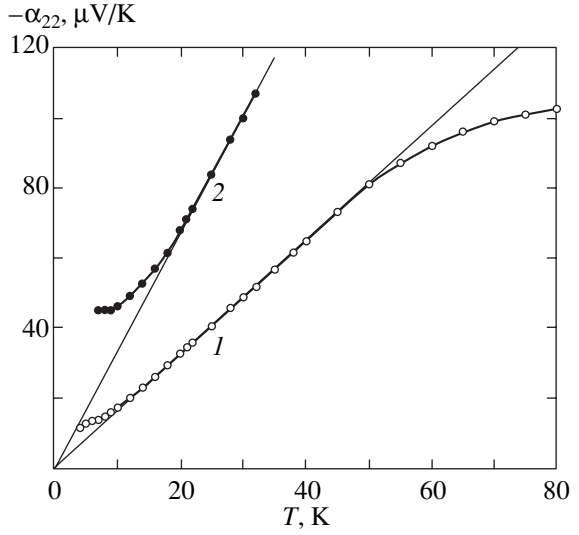


**Fig. 4.** Temperature dependences of thermal EMF of the $n$-$Bi_{0.93}Sb_{0.7}$ semiconducting alloy (*1*) in zero magnetic field, $\alpha_{22}(0)$, at $\nabla T \parallel C_1$ and (*2*) in a classically strong transverse magnetic field, $\alpha_\infty$, at $\mathbf{H} \parallel C_3$. Solid lines pass through the experimental diffusion thermal EMF values at $T > 18$ K; they are extrapolated to $T = 0$ K.

According to curves *2–8* (Fig. 2), the diffusion thermal EMF component $\Delta\alpha_{22}(H)$ is a nonmonotonic magnetic field function, whereas the phonon component monotonically depends on magnetic field up to quantizing magnetic fields (curve *1*). The maximum observed in the magnetic field dependence of the diffusion thermal EMF is caused by strong anisotropy of the electron energy spectrum in alloys and the involvement of electrons of three equivalent ellipsoids in transfer phenomena. We have discussed this problem in more detail in [7].

The diffusion thermal EMF is zero in the absence of temperature smearing of the Fermi surface. It is only nonzero in the first approximation with respect to the ratio between $kT$ and the Fermi energy; that is, it is proportional to the small difference of thermoelectric electron currents above and below the Fermi surface. The differential character of diffusion thermal EMF lays emphasis on the special features of the energy dependence of relaxation time and, if the electron spectrum is strongly nonparabolic, on the energy dependence of the effective mass. For this reason, a maximum can appear under certain conditions in the field dependence of thermal EMF.

Unlike diffusion thermal EMF, phonon thermal EMF is an integral characteristic, in which the special features of anisotropy of the electron and phonon spectra and relaxation processes are averaged. It therefore monotonically depends on magnetic field. In this respect, phonon thermal EMF is similar to such integral kinetic coefficients as resistance and the Hall coefficient, which also monotonically depend on magnetic field. The phonon entrainment thermal EMF in alloys with a degenerate electronic spectrum increases in

magnitude in a magnetic field (Figs. 2, 4). An analysis shows that such behavior of thermal EMF can only be explained by taking into account electronic spectrum anisotropy.

Note that the behavior of the thermal EMF of Bi–Sb alloys in a magnetic field allows conclusions to be drawn as to which of its components, phonon [the absence of a $\Delta\alpha_{22}(H)$ maximum] or diffusion [the presence of a $\Delta\alpha_{22}(H)$ curve maximum], predominates at a given temperature (see Fig. 2).

## 4. A THEORY OF ELECTRON RELAXATION

The magnetic field dependence of diffusion thermal EMF was found by solving the kinetic equation for a strongly anisotropic nonparabolic dispersion law of *L* electrons in Bi–Sb semiconducting alloys within the framework of the Lax model,

$$\varepsilon_{\mathbf{p}} = \sqrt{\left(\frac{\varepsilon_g}{2}\right)^2 + \frac{\varepsilon_g}{2}\left(\frac{p_1^2}{m_1} + \frac{p_2^2}{m_2} + \frac{p_3^2}{m_3}\right)} - \frac{\varepsilon_g}{2}, \quad (1)$$

where $\varepsilon_{\mathbf{p}}$ is the energy of the electron with momentum $\mathbf{p}$, $m_i$ is the effective mass of electrons in the ellipsoid, and $\varepsilon_g$ is the bandgap width. In solving the kinetic equation, we restricted ourselves to the isotropic relaxation time $\tau$ approximation for electron scattering. This gave the following equation for the magnetic field dependence of diffusion thermal EMF at $\mathbf{H} \parallel C_3$ [7]:

$$\alpha(H) = -\frac{\pi^2 k^2 T}{3e\zeta} \times \left\{\frac{3(1+2\zeta/\varepsilon_g)}{2(1+\zeta/\varepsilon_g)} + \beta\frac{\Omega^2\tau^2(\delta-2)-\delta}{(1+\Omega^2\tau^2)(\delta+\Omega^2\tau^2)}\right\}, \quad (2)$$

where $e$ is the absolute value of the charge of the electron; $\zeta$ is the chemical potential of electrons; $\Omega = eH/c\sqrt{M_1M_4}$ is the cyclotron frequency of electrons, the same for all three ellipsoids at $\mathbf{H} \parallel C_3$; $\delta = (M_1 + M_4)^2/4M_1M_4$ is the parameter taking into account anisotropy of the electron energy spectrum; and $M_i = m_i(1 + 2\zeta/\varepsilon_g)$ are the effective masses of electrons at the Fermi level. Because the ellipsoids make angles $\varphi$ with the $C_1$ and $C_3$ crystal axes in Bi–Sb alloys, the effective electron mass along $C_1$ is given by [7]

$$\frac{1}{M_4} = \frac{\cos^2\varphi}{M_2} + \frac{\sin^2\varphi}{M_3}. \quad (3)$$

The $\beta$ parameter in (2) appears because of the differential character of diffusion thermal EMF and is related to the Fermi energy dependences of relaxation time $\tau$ and effective electron mass $M$ as

$$\beta = \frac{d\ln(1/\tau(\zeta))}{d\ln\zeta} + \frac{d\ln M}{d\ln\zeta}. \quad (4)$$

Equation (2) for *n*-type semiconductors can be used to separate out the expressions for diffusion thermal EMF in both zero and transverse classically strong magnetic fields, $\alpha_\infty$ ($\Omega\tau \gg 1$), at $\mathbf{H} \parallel C_3$ and for diffusion thermal EMF changes in an arbitrary transverse magnetic field, $\Delta\alpha(H) = \alpha(H) - \alpha(0)$, and in a classically strong magnetic field, $\Delta\alpha_\infty$ [7]:

$$\alpha(0) = -\frac{\pi^2 k^2 T}{3e\zeta}\left\{\frac{3(1+2\zeta/\varepsilon_g)}{2(1+\zeta/\varepsilon_g)} - \beta\right\}, \quad (5)$$

$$\alpha_\infty = -\frac{\pi^2 k^2 T(1+2\zeta/\varepsilon_g)}{2e\zeta(1+\zeta/\varepsilon_g)}, \quad (6)$$

$$\Delta\alpha(H) = -\frac{\pi^2 k^2 T\beta}{3e\zeta}\left\{1 + \frac{\Omega^2\tau^2(\delta-2)-\delta}{(1+\Omega^2\tau^2)(\delta+\Omega^2\tau^2)}\right\}, \quad (7)$$

$$\Delta\alpha_\infty = -\frac{\pi^2 k^2 T\beta}{3e\zeta}. \quad (8)$$

It follows from (7) that only at $\delta > 2$ does the $\Delta\alpha(H)$ function have a maximum at

$$(\Omega_1\tau)^2_{\max} = \frac{\delta + (\delta-1)\sqrt{2\delta}}{\delta-2}. \quad (9)$$

For the alloys studied in this work, $\delta > 2$; for instance, $\delta = 24.5$ for alloys with $x = 0.07$ and $\delta = 21.6$ for alloys with $x = 0.13$.

We compare theoretical formula (7) with the experimental $\Delta\alpha_{22}(H)$ dependences at $\mathbf{H} \parallel C_3$ to determine the relaxation time of electrons in alloys by two methods. First, $\tau_1$ can be found by (9) from the magnetic field $H_1$ value corresponding to the maximum of the $\Delta\alpha_{22}(H)$ dependence. In the second method, $\tau_2$ is determined from the magnetic field $H_2$ value in $\Delta\alpha_{22}(H_2) = \Delta\alpha_\infty$ by the equation

$$(\Omega_2\tau)^2 = \delta/(\delta-2) \quad (10)$$

obtained from (7). The procedure for determining magnetic fields $H_1$ and $H_2$ using the $\Delta\alpha_{\max}$ and $\Delta\alpha_\infty$ values obtained from the $\Delta\alpha_{22}(H)$ dependences is illustrated by Fig. 3 for the $Bi_{1-x}Sb_x$ alloys with $x = 0.07$ and $x = 0.13$.

Magnetic fields up to 18 kOe used in our experiments only satisfy the condition of classically strong magnetic fields ($\Omega\tau \gg 1$) at low temperatures and do not satisfy this condition at elevated temperatures. For this reason, $\Delta\alpha_\infty$ at elevated temperatures was found by the Rodo-type extrapolation formula

$$\Delta\alpha(H) = AH^2/(BH^2 - 1), \quad \Delta\alpha_\infty = A/B. \quad (11)$$

The positive term (+1) in the Rodo formula is replaced by the negative one (–1) in (11) because (11) is applied in the decreasing region of the $\Delta\alpha_{22}(H)$ field dependence (Fig. 2), to the right of the maximum. The lines

in Fig. 2 separately drawn to the right of the family of $\Delta\alpha_{22}(H)$ curves correspond to $\Delta\alpha_\infty$ values in classically strong magnetic fields at various temperatures.

Electrons are scattered in semiconductors by phonons and impurities. We have

$$1/\tau = 1/\tau_{ph} + 1/\tau_{im}. \quad (12)$$

Impurity scattering of electrons in Bi–Sb semiconducting alloys is the sum of scattering by ionized impurities and "alloy" scattering (see below),

$$1/\tau_{im} = 1/\tau_{ion} + 1/\tau_{alloy}. \quad (13)$$

When electrons are scattered on ionized impurities, the relaxation time can rigorously be calculated only for an isotropic parabolic potential [4],

$$\frac{1}{\tau_{ion}} = \frac{\sqrt{m^3[\varepsilon_{\mathbf{p}}(1+\varepsilon_{\mathbf{p}}/\varepsilon_g)]}(1+2\varepsilon_{\mathbf{p}}/\varepsilon_g)}{m^2\varepsilon_{\mathbf{p}}^2(1+\varepsilon_{\mathbf{p}}/\varepsilon_g)^2}C_1N_{ion}, \quad (14)$$

where $C_1$ is the coefficient determined by the charge of impurity particles and crystal permittivity, and $N_{ion}$ is the concentration of ionized impurities, which equals the concentration of electrons. For an anisotropic electron spectrum, the action of the collision operator on the nonequilibrium current distribution function cannot be represented in the form of the product of this function and the inverse relaxation time. Nevertheless, let us introduce the electron relaxation time for scattering by ionized impurities in form (14), where $m^3$ in the numerator will be replaced by $m_1m_2m_3$, and $m^2$ in the denominator, by $m_1m_3$. The denominator in (14) is the density of electron states with energy $\varepsilon_{\mathbf{p}}$,

$$\rho(\varepsilon_{\mathbf{p}}) = 2\int\frac{d^3p'}{(2\pi\hbar)^3}\delta(\varepsilon_{\mathbf{p}}-\varepsilon_{\mathbf{p}'}) = \frac{1}{\pi^2\hbar^3}\left(1+\frac{2\varepsilon_{\mathbf{p}}}{\varepsilon_g}\right)\sqrt{2m_1m_2m_3\varepsilon_{\mathbf{p}}\left(1+\frac{\varepsilon_{\mathbf{p}}}{\varepsilon_g}\right)}. \quad (15)$$

Equation (15) gives the density of electron states in one ellipsoid. The denominator in (14) is determined by the Coulomb interaction matrix element between an electron and a charged impurity atom.

Consider another electron scattering mechanism in Bi–Sb semiconducting alloys. $Bi_{1-x}Sb_x$ ($0 \le x \le 1$) alloys form a continuous series of solid solutions, in which antimony atoms ($m_{Sb} = 121.76$) replace Bi atoms ($m_{Bi} = 209$). The concentrations of component atoms experience fluctuations in alloys because of a statistical distribution of atoms, which results in the formation of a fluctuating potential, by which electrons are scattered ("alloy" scattering). Note that this scattering mechanism in Bi–Sb alloys has not been considered as thoroughly as was done in [15] for Ge–Si semiconducting solid solutions and in [16] for PbTe-based solid solutions. The authors of [15, 16] were the first to analyze the contribution of alloy scattering to the mobility of electrons in solid solutions. For this scattering mechanism, the relaxation time is given by the formula

$$\frac{1}{\tau_{alloy}^{(1)}} = \int\frac{d^3p'}{(2\pi\hbar)^3}\frac{2\pi}{\hbar}|U_{\mathbf{p}-\mathbf{p}'}|^2 \times x(1-x)(1-\cos\theta)\delta(\varepsilon_{\mathbf{p}}-\varepsilon_{\mathbf{p}'}), \quad (16)$$

where $\theta$ is the angle between the initial $\mathbf{p}$ and final $\mathbf{p}'$ electron momenta. Alloy component concentration fluctuations give the usual $x(1-x)$ dependence, which shows that the alloy scattering is absent in pure substances. The $U(\mathbf{r})$ atomic potential is short-range [15], which allows us to ignore the dependence of the $U_{\mathbf{p}-\mathbf{p}'}$ matrix element on its argument, that is, $\mathbf{p}-\mathbf{p}'$ can be set equal to zero. The term with $\cos\theta$ then also vanishes, and the relaxation time is only determined by the departure terms in the kinetic equation. Eventually, the $1/\tau_{alloy}^{(1)}$ value is proportional to the density of electron states given by (15),

$$\frac{1}{\tau_{alloy}^{(1)}} = \frac{\pi}{\hbar}|U_0|^2x(1-x)\rho(\varepsilon_{\mathbf{p}}) \quad (17)$$

(for the alloys under consideration, $\rho(\zeta) \approx 10^{31}$ erg$^{-1}$ cm$^{-3}$). This relaxation time describes electron transitions caused by alloy scattering within one valley. Alloy scattering can, however, cause electron transitions between equivalent valleys. For such a transition,

$$\frac{1}{\tau_{alloy}^{(2)}} = \int\frac{d^3p'}{(2\pi\hbar)^3}\frac{2\pi}{\hbar}|U_{\mathbf{p}_0+\mathbf{p}-\mathbf{p}'}|^2x(1-x)\delta(\varepsilon_{\mathbf{p}}-\varepsilon_{\mathbf{p}'}), \quad (18)$$

where $\mathbf{p}_0$ is the momentum connecting the centers of valleys in the momentum space and the $\mathbf{p}$ and $\mathbf{p}'$ kinetic electron momenta are counted from the center of the initial valley. The $p_0$ momentum far exceeds $p$ and $p'$. We will therefore only leave momentum $\mathbf{p}_0$ in the argument of the matrix element. Then, $1/\tau_{alloy}^{(2)}$ takes a form similar to $1/\tau_{alloy}^{(1)}$, namely,

$$\frac{1}{\tau_{alloy}^{(2)}} = \frac{\pi}{\hbar}|U_{\mathbf{p}_0}|^2x(1-x)\rho(\varepsilon_{\mathbf{p}}). \quad (19)$$

If the $U(\mathbf{r})$ atomic potential radius was much smaller than the lattice constant, we might set $\mathbf{p}_0$ equal to zero, and the relaxation time for alloy scattering into an equivalent valley would equal the intravalley relaxation time. The atomic potential radius and lattice constant are, however, commensurate, and we cannot ignore $\mathbf{p}_0$ in the argument of $U_{\mathbf{p}_0}$. The modulus of the Fourier component of the potential $U_{\mathbf{p}_0}$ is always smaller than the modulus of the zero Fourier component $U_0$, and the ratio $\xi$ of $1/\tau_{alloy}^{(2)}$ and $1/\tau_{alloy}^{(1)}$ is therefore positive and

smaller than unity. The total electron relaxation time for alloy scattering is

$$\frac{1}{\tau_{\text{alloy}}} = \frac{1}{\tau^{(1)}_{\text{alloy}}} + \frac{N-1}{\tau^{(2)}_{\text{alloy}}}$$
$$= C_2 x(1-x)\left(1+\frac{2\varepsilon_{\mathbf{p}}}{\varepsilon_g}\right)\sqrt{m_1 m_2 m_3 \varepsilon_{\mathbf{p}}\left(1+\frac{\varepsilon_{\mathbf{p}}}{\varepsilon_g}\right)}. \quad (20)$$

Here, the $C_2$ coefficient is determined by the short-range potential value and $N$ is the number of equivalent valleys ($N = 3$ in the problem under consideration). Therefore,

$$\frac{1}{\tau_{\text{alloy}}} = \frac{1+2\xi}{\tau^{(1)}_{\text{alloy}}}. \quad (21)$$

Note that the alloy scattering mechanism is absent in classic many-valley semiconductors such as Ge and Si. Intervalley scattering of electrons in these semiconductors is therefore effected, for instance, by short-wave phonons [17].

Next consider electron–phonon interaction. Let the inverse electron relaxation time for electron–phonon scattering be written in the elastic approximation

$$\frac{1}{\tau_{\text{ph}}} = \frac{2\pi}{\hbar}\int \frac{d^3p'}{(2\pi\hbar)^3}|C_{\mathbf{p}-\mathbf{p}'}|^2 \quad (22)$$
$$\times (2N_{\mathbf{p}-\mathbf{p}'}+1)(1-\cos\vartheta)\delta(\varepsilon_{\mathbf{p}}-\varepsilon_{\mathbf{p}'}),$$

where $C_{\mathbf{q}}$ is the electron–phonon interaction constant ($\mathbf{q} = \mathbf{p} - \mathbf{p}'$), $\vartheta$ is the angle between the $\mathbf{p}$ and $\mathbf{p}'$ momenta, and $N_{\mathbf{q}}$ is the Planck equilibrium distribution function for phonons. At temperatures exceeding the Debye electron temperature, $T > \Theta_e$ (for the electronic ellipsoid in the alloys under consideration, $\Theta_{\min} \approx 1\ \text{K} \le \Theta_e \le \Theta_{\max} \approx 20\ \text{K}$), the number of phonons is large, and the Planck distribution function transforms into the Rayleigh function

$$N_{\mathbf{q}} = kT/\hbar\omega_{\mathbf{q}},$$

where $\omega_{\mathbf{q}}$ is the phonon frequency. In (22), only the term proportional to temperature is retained. The $|C_{\mathbf{q}}|^2$ and $N_{\mathbf{q}}$ values for isotropic deformation interaction between electrons and longitudinal acoustic phonons are proportional to $q$ and $1/q$, respectively; that is, the resulting $|C_{\mathbf{q}}|^2 N_{\mathbf{q}}$ matrix element does not depend on the momentum, as with electron scattering by a point potential. After averaging over momenta $\mathbf{p}'$, the term containing $\cos\vartheta$ vanishes. The remaining expression is proportional to the density of states of electrons with energy $\varepsilon_{\mathbf{p}}$, and its energy dependence coincides with dependence (20) for alloy scattering.

We have four deformation potential components for bismuth and Bi–Sb alloys, and electron–phonon interaction is not isotropic. The energy dependence of the inverse electron relaxation time is, for this reason, difficult to calculate for different acoustic phonon spectrum branches and for an anisotropic electronic spectrum. An important result for the inverse electron relaxation time related to scattering by phonons at $T > \Theta_e$ is, however, its linear temperature dependence.

As we consider a degenerate electron gas, Eqs. (2), (7), (9), and (10) contain $\tau$ values for the energy equal to the Fermi energy. We ignore small corrections related to temperature smearing of the Fermi distribution function.

The electron relaxation time in alloys depends on temperature; the doping tellurium admixture concentration, which coincides with the concentration of electrons; and the concentrations of alloy component atoms. The temperature dependence of the total electron relaxation time is only determined by electron–phonon scattering (22). Scattering by ionized impurities (14) contains a direct dependence on the concentration of impurity particles, but there is also an appreciable indirect dependence. Indeed, electron concentration $n$ depends on the chemical potential,

$$n = \frac{1}{\pi^2\hbar^3}\sqrt{m_1 m_2 m_3\left[2\zeta\left(1+\frac{\zeta}{\varepsilon_g}\right)\right]^3}. \quad (23)$$

All three terms of the total inverse relaxation time indirectly depend on the concentration of electrons. The dependence on the concentrations of alloy components is equally complex. In addition to the direct dependence of alloy scattering (20) on the concentrations of alloy components, there is a noticeable indirect dependence contained in the dependences of the effective masses on the bandgap width, which, in turn, depends on antimony concentration $x$ [2, 5]. It follows that each of the three terms of the total electron relaxation time in a certain way depends on the concentrations of antimony and bismuth in the alloy. The inverse relaxation time for each of the electron scattering mechanisms was separated out in treating theoretical formulas (14) and (20) taking into account both direct and indirect dependences on $n$ and $x$.

## 5. THE DETERMINATION OF ELECTRON RELAXATION TIMES FROM EXPERIMENT

Our goal was to separate out electron relaxation time components corresponding to different scattering mechanisms, which would allow us to determine coefficients $C_i$ in (14) and (20) for the inverse relaxation time related to electron scattering by ionized impurities and by bismuth and antimony concentration fluctuations.

The experimental $\Delta\alpha_{22}(H)$ curves obtained for $Bi_{1-x}Sb_x$ ($0.07 \le x \le 0.16$) semiconducting alloys at various temperatures were used to determine electron relaxation times $\tau_1$ and $\tau_2$ by (9) and (10). The characteristic magnetic field dependences of the diffusion thermal EMF, $\Delta\alpha_{22}(H)$, measured at 21 K and the $H_1$ and $H_2$ magnetic field values determined from $\Delta\alpha_{\max}$

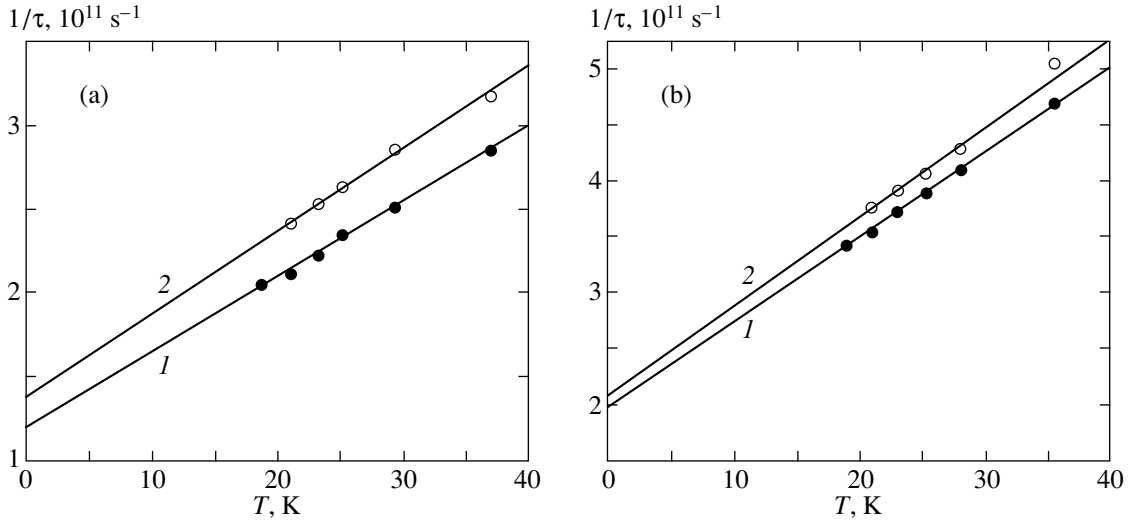


**Fig. 5.** Temperature dependences of inverse electron relaxation times (*1*) $1/\tau_1$ and (*2*) $1/\tau_2$ for (a) *n*-$Bi_{0.93}Sb_{0.07}$ and (b) *n*-$Bi_{0.87}Sb_{0.13}$ semiconducting alloys found from diffusion thermal EMF in a magnetic field by (9) and (10). The dependences are linearly extrapolated to $T = 0$ K.

and $\Delta\alpha_\infty$ are shown in Fig. 3. The electron relaxation times obtained for the alloys studied in this work at different temperatures were used to plot the temperature dependences of $1/\tau_1$ and $1/\tau_2$. These dependences are shown in Fig. 5 for the $x = 0.07$ and 0.13 alloys. They were approximated by linear temperature dependences because of the presence of electron–phonon scattering. The difference of the $1/\tau_1$ and $1/\tau_2$ values can be a consequence of the inadequacy of the model that we use, in which the action of the integral scattering operator on the electron distribution function is replaced by the product of the inverse relaxation time and this distribution function. Strictly mathematically, this cannot be done, and solutions to the integral equation should be found. At the same time, the closeness of the $1/\tau_1$ and $1/\tau_2$ values and their identical temperature behaviors show that the model of isotropic relaxation time gives fairly good results for the alloys under consideration.

The slope of these straight lines equals the inverse relaxation time component related to electron scattering by phonons, $1/\tau_{ph}$, and the *y* intercept ($T = 0$ K) corresponds to electron scattering by impurities, $1/\tau_{im}$. The obtained electron relaxation time components for all Bi–Sb compositions are listed in Table 2.

The $1/\tau_{im}$ value includes electron scattering by ionized impurities (14) and alloy scattering (20). To determine these inverse relaxation time components, $1/\tau_{ion}$ and $1/\tau_{alloy}$, we introduced new variables *y* and *Z*, which included both direct and indirect antimony concentration *x* and electron concentration *n* effects,

$$y = x(1-x)b/a, \tag{24}$$

$$Z = 1/\tau_{im}a, \tag{25}$$

where

$$a = \frac{\sqrt{m_1m_2m_3\zeta(1+\zeta/\varepsilon_g)}(1+2\zeta/\varepsilon_g)n}{m_1m_3\zeta^2(1+\zeta/\varepsilon_g)^2}, \tag{26}$$

$$b = \sqrt{m_1m_2m_3\zeta(1+\zeta/\varepsilon_g)}(1+2\zeta/\varepsilon_g). \tag{27}$$

**Table 2.** Electron relaxation times in *n*-$Bi_{1-x}Sb_x$ semiconducting alloys ($0.07 \le x \le 0.16$)

| No. | $\tau$, $10^{-12}$ s ($T = 21$ K) | $\tau_{ph}$, $10^{-12}$ s ($T = 21$ K) | $\tau_{im}$, $10^{-12}$ s | $\tau_{ion}$, $10^{-11}$ s | $\tau_{alloy}$, $10^{-11}$ s |
|---|---|---|---|---|---|
| 1 | 4.4 | 9.9 | 7.5 | 1.3 | 1.8 |
| 2 | 3.4 | 8 | 5.8 | 1.1 | 1.2 |
| 3 | 3.5 | 7.8 | 5.6 | 1.2 | 1 |
| 4 | 2.7 | 6.2 | 5 | 1.2 | 0.87 |
| 5 | 2.7 | 6.6 | 4.5 | 1.2 | 0.7 |
| 6 | 2.4 | 5.9 | 4.2 | 1.2 | 0.64 |

Note: Here, $\tau$, $\tau_{ph}$, $\tau_{im}$, $\tau_{ion}$, and $\tau_{alloy}$ are the total electron relaxation time and its components corresponding to electron scattering by acoustic phonons, impurity particles, ionized impurity particles, and fluctuations of alloy component concentrations, respectively.

Equations (14) and (20) written in terms of these variables take the form

$$Z = C_2 y + C_1, \tag{28}$$

where coefficients $C_1$ and $C_2$, as in (14) and (20), characterize scattering of electrons by ionized impurities and alloy component concentration fluctuations, respectively.

The inverse electron relaxation times related to scattering by impurity particles, $1/\tau_{im}$, which were obtained for the $Bi_{1-x}Sb_x$ alloys ($0.07 \le x \le 0.16$), were used to calculate the $Z$ and $y$ variables by (24)–(28), plot the $Z(y)$ dependence, and approximate this dependence by a linear function (Fig. 6). Such an approximation was possible because of fairly small $x$ values ($x \le 0.16$). Two straight lines in Fig. 6 correspond to two procedures used to determine relaxation times [$\tau_1$ by (9) and $\tau_2$ by (10)]. The slope of these lines gave the mean $C_2$ value, which characterized alloy scattering, and the $z$ intercept at $y = 0$ gave the mean $C_1$ coefficient value, which characterized electron scattering by ionized impurities in the alloys. The alloys were doped with a $10^{-3}$ at. % Te donor admixture and had an electron concentration of approximately $1.5 \times 10^{17}$ cm$^{-3}$. The mean coefficient values were $C_1 = 1.75 \times 10^{-43}$ g$^2$ cm$^6$ s$^{-4}$ and $C_2 = 1.65 \times 10^{61}$ g$^{-2}$ cm$^{-1}$. These coefficients and the values of $x$, $n$, and the other parameters of the Bi–Sb samples (see Table 1) were used to determine the $\tau_{ion}$ and $\tau_{alloy}$ relaxation times listed in Table 2.

The antimony concentration $x$ dependences of the total electron relaxation time and its components are plotted in Fig. 7 (curves *1* and *2–4*, respectively). These components are the inverse relaxation times corresponding to electron scattering by acoustic phonons at $T = 21$ K (curve *2*), by alloy component concentration fluctuations (curve *3*), and by ionized impurities (curve *4*). The antimony concentration dependence of the inverse relaxation time related to electron scattering by acoustic phonons is well extrapolated by a linear function (curve *2*). The $y$ intercept of the corresponding straight line ($x = 0$) gives the inverse relaxation time $1/\tau_{ph} = 5 \times 10^{10}$ s$^{-1}$, which corresponds to bismuth electrons. The predominant mechanism of electron scattering in pure bismuth is intravalley scattering by acoustic phonons (e.g., see [9, 18, 19]). The relaxation time components for bismuth electrons were determined in [8] as functions of temperature (4.2–15.7 K). The extrapolation of these temperature dependences of the components of the tensor of inverse relaxation times toward higher temperatures gives $1/\tau_{ie}$ ($i = 1, 2, 3$) at $T = 21$ K; their mean value is $1/\tau_e = 1/(\prod_i \tau_{ie})^{1/3} \approx 6 \times 10^{10}$ s$^{-1}$. The $1/\tau_{ph} \approx 5 \times 10^{10}$ s$^{-1}$value obtained for pure bismuth by extrapolating the $\tau_{ph}^{-1}(x)$ dependence to $x = 0$ closely agrees with the value reported in [8]. The linear $\tau_{ph}^{-1}(x)$ dependence in alloys with the concentration

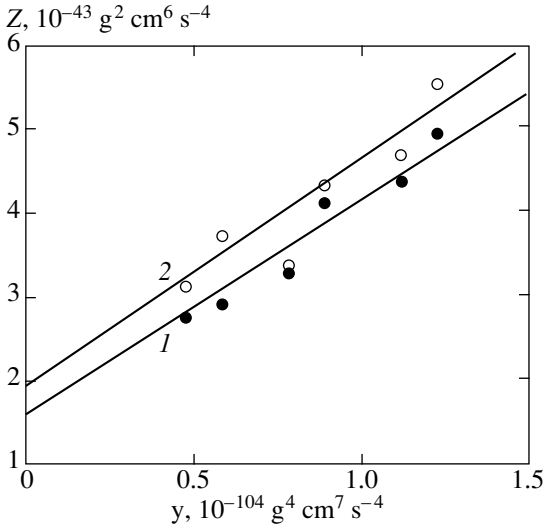


**Fig. 6.** Dependences of $Z$ (25) on $y$ (24) for $n$-$Bi_{1-x}Sb_x$ semiconducting alloys ($0.07 \le x \le 0.16$) and linear extrapolation of the results to $y = 0$. Here, (*1*) $Z \propto 1/\tau_{1im}$ and (*2*) $Z \propto 1/\tau_{2im}$ in accordance with two procedures for determining relaxation times in alloys by (9) and (10).

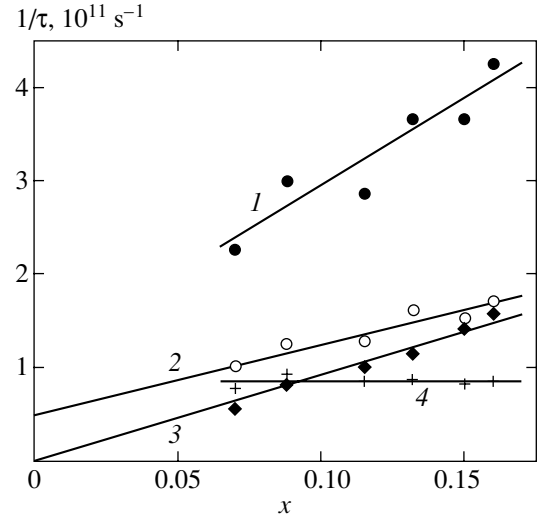


**Fig. 7.** Dependences of inverse electron relaxation time on antimony concentration in $n$-$Bi_{1-x}Sb_x$ alloys ($0.07 \le x \le 0.16$) and linear extrapolation of the results to $x = 0$. (*1*) Total electron inverse relaxation time in alloys $1/\tau$ and its components corresponding to electron scattering (*2*) by acoustic phonons $1/\tau_{ph}$, (*3*) by fluctuations of Bi and Sb concentrations in alloys $1/\tau_{alloy}$, and (*4*) by ionized impurities $1/\tau_{ion}$.

of electrons $n \approx 1.5 \times 10^{17}$ cm$^{-3}$ ($T = 21$ K) is described by the equation

$$1/\tau_{ph}[\text{s}^{-1}] = 7.3 \times 10^{11} x + 5 \times 10^{10}. \tag{29}$$

Equation (29) can be used to find $1/\tau_{ph}$ at temperatures $T > \Theta_e$,

$$1/\tau_{ph}[\text{s}^{-1}] = (3.48 \times 10^{10} x + 2.38 \times 10^{9}) T. \tag{30}$$

The data on the antimony concentration $x$ dependence of the inverse relaxation time component related to alloy electron scattering (straight line *3* in Fig. 7) can be linearly extrapolated at $x \le 0.16$. For the samples under consideration, this dependence is described by the equation

$$1/\tau_{\text{alloy}}[\text{s}^{-1}] = 9.1 \times 10^{11} x. \quad (31)$$

For $Bi_{1-x}Sb_x$ semiconducting alloys, the $1/\tau_{\text{alloy}}$ component of the inverse relaxation time can be found by (20) using the $C_2 = 1.65 \times 10^{61}$ g$^{-2}$ cm$^{-1}$ coefficient and the $x$, $m_i$, $\varepsilon_g$, and $\zeta$ parameter values.

The inverse relaxation time component related to scattering by ionized impurity particles is on average a constant value for the alloys under consideration, $1/\tau_{\text{ion}} = 8.5 \times 10^{10}$ s$^{-1}$ (Fig. 7, straight line *4*). The $1/\tau_{\text{ion}}$ value depends on the degree of alloy doping and can be estimated by (25) and (28), $1/\tau_{\text{ion}} = C_1 a$, using the $C_1 = 1.75 \times 10^{-43}$ g$^2$ cm$^6$ s$^{-4}$ coefficient.

The determination of the components of the inverse electron relaxation time allows the total inverse electron relaxation time to be estimated,

$$1/\tau = 1/\tau_{\text{ph}} + 1/\tau_{\text{alloy}} + 1/\tau_{\text{ion}}.$$

Calculations of the components of the inverse relaxation time corresponding to electron scattering by ionized impurities, Eqs. (25) and (28), and fluctuations of alloy component concentrations, Eq. (20), as functions of Fermi energy (electron concentration) performed for the alloys under consideration allow the following conclusion to be drawn. At low temperatures ($T \le 4.2$ K), electrons present in alloys in an $n < 10^{16}$ cm$^{-3}$ concentration are predominantly scattered by ionized impurities, whereas alloy scattering becomes predominant at $n > 10^{17}$ cm$^{-3}$.

Shubnikov–de Haas quantum oscillations in $Bi_{1-x}Sb_x$ ($0.1 < x < 0.16$) semiconducting alloys were measured in [11, 12, 20] under the conditions of strong uniaxial deformation. This caused the electron energy spectrum to transform from three- to one-valley when the sample was compressed along the $C_1$ bisector axis and to two-valley when the sample was compressed along the $C_2$ binary axis.

Electron scattering by impurities at low temperatures causes broadening of Landau quantum levels in semiconductors. As a result, the amplitude of quantum oscillations in a magnetic field exponentially decreases. Theoretically, such a decrease is described by introducing the Dingle effective temperature $T_D = h/2\pi k\tau_D$, where $\tau_D$ is the characteristic electron relaxation time [21, 22].

The authors of [11, 12, 20] observed a five- to sixfold decrease in the Dingle temperature under strong uniaxial deformation of Bi–Sb semiconducting alloys. They explained this decrease by switching off of intervalley alloy electron scattering, which they believed to essentially predominate over the total impurity intravalley scattering. In these works, the role played by alloy scattering in Bi–Sb alloys was taken into account, but only for intervalley scattering. The neglect of intravalley alloy scattering was, however, groundless because of the universal relation between intravalley and intervalley scattering [Eq. (21)], which is a consequence of the unified nature of alloy scattering phenomena. For this reason, complete overflow of all electrons into one ellipsoid having the lowest energy, that is, complete switching off of intervalley scattering, decreases alloy scattering $1 + 2\xi$ times. In addition, determining the total change in alloy scattering requires taking into account changes in the density of states at the Fermi level: as the total concentration of electrons remains unchanged, redistribution of electrons from three valleys into one changes the chemical potential value. The ratio between the changed and initial chemical potential values is determined precisely by this condition of a constant electron concentration. It is important to know deformation-induced changes in $\varepsilon_g$ and $m_i$. Assuming these values to remain unchanged allows us to determine the changed chemical potential and the changed density of states at the Fermi level. After deformation, the inverse relaxation time corresponding to alloy scattering equals

$$\frac{1}{\tau_{\text{alloy}}^{(3)}} = \frac{3^{1/3}\sqrt{\varepsilon_g^2 + 4 \times 3^{2/3}\zeta(\varepsilon_g + \zeta)}}{\tau_{\text{alloy}}(1 + 2\xi)(\varepsilon_g + 2\zeta)}, \quad (32)$$

where $\zeta$ is the chemical potential of electrons in the alloy prior to deformation. If $\xi$ is small, the $1/\tau_{\text{alloy}}^{(3)}$ value can even be larger than $1/\tau_{\text{alloy}}$. For instance, for alloys with $x = 0.07$ and 0.13, we have $1/\tau_{\text{alloy}}^{(3)} \approx 1/\tau_{\text{alloy}}$ at $\xi = 0.5$ and $1/\tau_{\text{alloy}}^{(3)} \approx 0.75/\tau_{\text{alloy}}$ at $\xi = 1$.

In our view, substantial changes in $T_D$ under uniaxial deformation observed in [11, 12, 20] cannot be explained by switching off of intervalley scattering if we assume that the $\varepsilon_g$ and $m_i$ parameters remain unchanged.

Consider the influence of various scattering mechanisms contained in coefficient $\beta$ on the thermal EMF and the Nernst–Ettingshausen coefficient [7]. The $\beta$ value can be written in the form

$$\beta = \beta_1\frac{\tau}{\tau_{\text{alloy}}} - \beta_2\frac{\tau}{\tau_{\text{ion}}} + \beta_3\frac{\tau}{\tau_{\text{ph}}} + \frac{2\zeta}{\varepsilon_g + 2\zeta}. \quad (33)$$

The last term is determined by the energy dependence of the effective mass for nonparabolic spectrum (4),

$$\frac{d\ln M}{d\ln\zeta} = \frac{2\zeta}{\varepsilon_g + 2\zeta}.$$

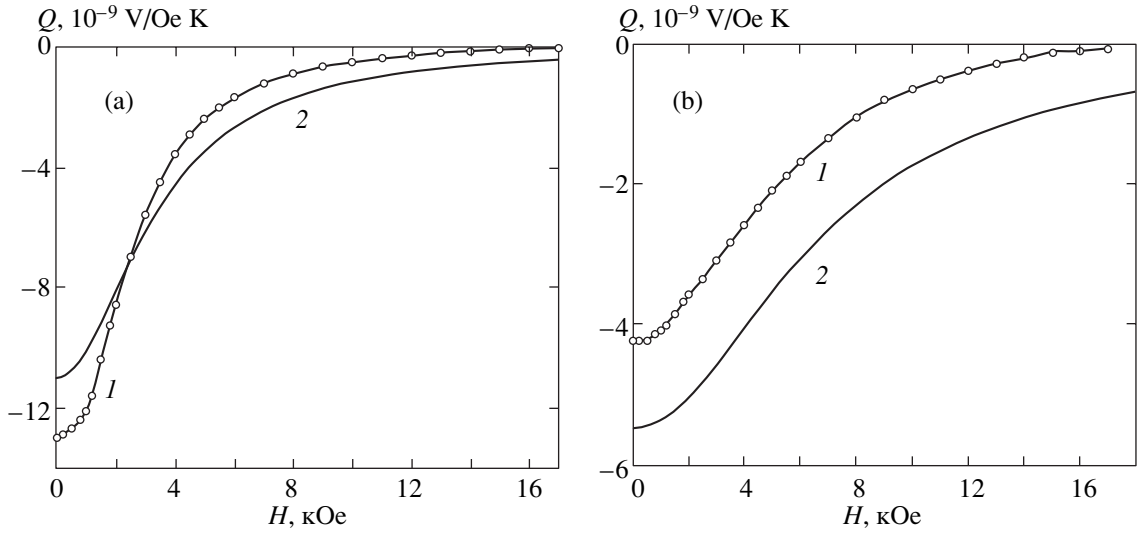


**Fig. 8.** Magnetic field dependences of the Nernst–Ettingshausen coefficient $Q_{12,3}$ ($\nabla T \parallel C_1$, $\mathbf{H} \parallel C_3$) for (a) *n*-$Bi_{0.93}Sb_{0.07}$ and (b) *n*-$Bi_{0.87}Sb_{0.13}$ semiconducting alloys at $T = 21$ K: (*1*) experimental dependences and (*2*) dependences calculated by (36) with $\beta$ = (a) 1.33 and (b) 1.04.

According to (4), we can calculate coefficients $\beta_1$ and $\beta_2$ corresponding to the alloy scattering mechanism and electron scattering by ionized impurities,

$$\beta_1 = \frac{\varepsilon_g^2 + 8\zeta\varepsilon_g + 8\zeta^2}{2(\varepsilon_g + \zeta)(\varepsilon_g + 2\zeta)}, \quad (34)$$

$$\beta_2 = \frac{3\varepsilon_g^2 + 8\zeta\varepsilon_g + 8\zeta^2}{2(\varepsilon_g + \zeta)(\varepsilon_g + 2\zeta)}. \quad (35)$$

The equation for $\beta_2$ is determined by dependence (14) valid for scattering of electrons with an isotropic spectrum by ionized impurities. Adopting the hypothesis that we can use this dependence also for electrons with an anisotropic spectrum can introduce an error into the $\beta_2$ value.

In the model of isotropic interactions between electrons and longitudinal phonons, we have $\beta_3 = \beta_1$. This model is, however, insufficient for treating bismuth and Bi–Sb alloys. In these alloys, the experimental $\beta$ value is always positive, in our view, because of a substantial contribution of the alloy mechanism of electron scattering. The $\alpha_{22}(0)$ value, thermal EMF (5) in the absence of a magnetic field, is expressed through $\beta$. If $\beta_3$ was calculated theoretically, like $\beta_1$ (34) and $\beta_2$ (35), we would be able to use (5) for determining $\alpha(0)$ as a function of temperature.

Calculations of $\alpha(0)$ with $\beta_3$ set equal to $\beta_1$ give poor agreement with experiment. In our view, the reason for this is the inapplicability of the model of isotropic electron–phonon scattering to Bi–Sb alloys, that is, the inequality of $\beta_3$ to $\beta_1$. The $\beta$ coefficient can be found from the experimental diffusion thermal EMF values in zero magnetic field, $\alpha_{22}(0)$, with the use of (5) or from diffusion thermal EMF changes in a classically strong magnetic field, $\Delta\alpha_\infty$, with the use of (8). The $\beta$ value found from the experimental data allowed us to calculate the $\Delta\alpha(H)$ magnetic field dependence by (7). These calculations use the mean electron relaxation time $\tau$ determined by (9) and (10) following the procedure described above. The calculated $\Delta\alpha(H)$ curves for alloys with $x = 0.07$, $\beta = 1.33$ and $x = 0.13$, $\beta = 1.04$ are shown in Figs. 3a and 3b, respectively; these $\beta$ values were found from the experimental data.

The last term in (33), $2\zeta/(\varepsilon_g + 2\zeta) = d\ln M/d\ln\zeta$, amounts to about 60% of the experimental $\beta$ values for the alloys under consideration. It follows that the substantial positive contribution to $\beta$ is not related to electron scattering mechanisms but is determined by the nonparabolic character of the electron energy spectrum.

We measured the Nernst–Ettingshausen coefficient for the alloys studied. This coefficient changes sign at about $T = 10$ K as temperature varies. The Nernst–Ettingshausen coefficient is positive at low and negative at high temperatures [7]. At low temperatures, Nernst–Ettingshausen coefficient $Q$, like thermal EMF, is determined by the entrainment of electrons with phonons. In the absence of phonon entrainment ($T > 10$ K), the equation for $Q$ obtained with the use of the same model as with diffusion thermal EMF has the form [7]

$$Q = -\frac{\pi^2 k^2 T\beta}{6\zeta}\frac{(M_1 + M_4)\tau}{M_1 M_4 c(\delta + \Omega^2\tau^2)}. \quad (36)$$

Equation (36) contains the same $\beta$ coefficient as that present in (2). The relation between diffusion thermal EMF growth in a magnetic field and the negative sign of $Q$, which are determined by the mechanism of electron scattering [7], is substantiated experimentally.

Although the Nernst–Ettingshausen coefficient is differential, which manifests itself by the presence of coefficient $\beta$ in (36), its magnetic field dependence is monotonic, as distinguished from the magnetic field dependence of thermal EMF. The experimental results obtained for alloys with $x = 0.07$ and 0.13 at $T = 21$ K and the results of calculations by (36) with the use of the averaged $\tau$ values found above from the $\Delta\alpha(H)$ dependence are shown in Fig. 8. The calculated $\Delta\alpha(H)$ curves obtained using the averaged electron relaxation time are shown in Fig. 3. The behavior of the calculated $\Delta\alpha(H)$ curves is on the whole similar to that of the experimental curves, but quantitative discrepancies are observed near curve maxima. These deviations of the calculation results from the experimental data on both $\Delta\alpha(H)$ and $Q$ can be explained by drawbacks of the model, which replaces the action of the collision operator on the nonequilibrium electron distribution function by the product of this function and the isotropic relaxation time. We nevertheless believe that the relaxation times determined in this work correctly reproduce the order of magnitude of the collision operator.

## 6. CONCLUSION

Note that nonmonotonic magnetic field dependences of diffusion thermal EMF observed in semiconducting alloys can not only be qualitatively explained but also be used to analyze the electron relaxation mechanisms at various temperatures and concentrations of alloy components and doping admixture atoms (electron concentrations). In *n*-Bi–Sb alloys with a strongly anisotropic electron energy spectrum, an increase in diffusion thermal EMF in a magnetic field and the negative sign of the Nernst–Ettingshausen coefficient observed experimentally at $T > 18$ K and the predominance of the alloy and electron–phonon scattering mechanisms over electron scattering by ionized impurities are in agreement with a similar behavior of diffusion thermal EMF in a magnetic field and the negative sign of Nernst–Ettingshausen coefficients characteristic of degenerate semiconductors with isotropic electronic spectra [4].

The analysis performed in this work showed that alloy electron scattering is comparable in magnitude with the usual mechanism of electron scattering by acoustic phonons and ionized impurities. We think that alloy scattering should necessarily be taken into account in studying kinetic phenomena not only in Bi–Sb alloys but also in other solid solutions.

## REFERENCES

1. H. Berger, B. Christ, and J. Troschke, Cryst. Res. Technol. **17**, 1233 (1982).
2. N. B. Brandt, R. Germann, G. I. Golysheva, *et al.*, Zh. Éksp. Teor. Fiz. **83**, 2152 (1982) [Sov. Phys. JETP **56**, 1247 (1982)]; G. A. Mironova, M. V. Sudakova, and Ya. G. Ponomarev, Fiz. Tverd. Tela (Leningrad) **22**, 3628 (1980) [Sov. Phys. Solid State **22**, 2124 (1980)].
3. V. D. Kagan and N. A. Red'ko, Zh. Éksp. Teor. Fiz. **100**, 1205 (1991) [Sov. Phys. JETP **73**, 664 (1991)]; V. D. Kagan and N. A. Red'ko, Fiz. Tverd. Tela (St. Petersburg) **35**, 1686 (1993) [Phys. Solid State **35**, 849 (1993)]; Fiz. Tverd. Tela (St. Petersburg) **36**, 1978 (1994) [Phys. Solid State **36**, 1081 (1994)].
4. B. M. Askerov, *Kinetic Effects in Semiconductors* (Nauka, Leningrad, 1970).
5. N. A. Red'ko, V. I. Pol'shin, V. V. Kosarev, and G. A. Ivanov, Fiz. Tverd. Tela (Leningrad) **25**, 3138 (1983) [Sov. Phys. Solid State **25**, 1807 (1983)].
6. I. Ya. Korenblit, M. E. Kuznetsov, and S. S. Shalyt, Zh. Éksp. Teor. Fiz. **56**, 8 (1969) [Sov. Phys. JETP **29**, 4 (1969)].
7. V. D. Kagan, N. A. Red'ko, N. A. Rodionov, and V. I. Pol'shin, Fiz. Tverd. Tela (St. Petersburg) **42**, 1376 (2000) [Phys. Solid State **42**, 1414 (2000)].
8. R. Hartman, Phys. Rev. **181**, 1070 (1969).
9. V. N. Kopylov and L. P. Mezhov-Deglin, Zh. Éksp. Teor. Fiz. **65**, 720 (1973) [Sov. Phys. JETP **38**, 357 (1974)].
10. N. A. Rodionov, N. A. Red'ko, and G. A. Ivanov, Fiz. Tverd. Tela (Leningrad) **21**, 2556 (1979) [Sov. Phys. Solid State **21**, 1473 (1979)]; N. A. Red'ko, V. I. Pol'shin, and G. A. Ivanov, Fiz. Tverd. Tela (Leningrad) **26**, 10 (1984) [Sov. Phys. Solid State **26**, 5 (1984)].
11. L. A. Kirakozova, N. Ya. Minina, and A. M. Savin, Pis'ma Zh. Éksp. Teor. Fiz. **52** (1), 693 (1990) [JETP Lett. **52**, 45 (1990)].
12. N. Ya. Minina and L. A. Kirakozova, Zh. Éksp. Teor. Fiz. **101**, 1663 (1992) [Sov. Phys. JETP **74**, 886 (1992)].
13. N. A. Red'ko, Pis'ma Zh. Éksp. Teor. Fiz. **55**, 268 (1992) [JETP Lett. **55**, 266 (1992)].
14. V. I. Bochegov, K. G. Ivanov, and N. A. Rodionov, Prib. Tekh. Éksp., No. 2, 218 (1980).
15. I. S. Shlimak, A. L. Éfros, and I. Ya. Yanchev, Fiz. Tekh. Poluprovodn. (Leningrad) **11**, 257 (1977) [Sov. Phys. Semicond. **11**, 149 (1977)].
16. E. A. Gurieva, B. A. Efimova, and Yu. I. Ravich, Fiz. Tekh. Poluprovodn. (Leningrad) **8**, 1261 (1974) [Sov. Phys. Semicond. **8**, 819 (1974)].
17. V. F. Gantmakher and Y. B. Levinson, *Carrier Scattering in Metals and Semiconductors* (Nauka, Moscow, 1984; North-Hooland, New York, 1987).
18. S. M. Cheremisin, Zh. Éksp. Teor. Fiz. **65**, 1564 (1973) [Sov. Phys. JETP **38**, 779 (1974)].
19. V. S. Vinnik, I. Ya. Korenblit, E. A. Okhrem, and A. G. Samoĭlovich, Zh. Éksp. Teor. Fiz. **80**, 2031 (1981) [Sov. Phys. JETP **53**, 1057 (1981)].
20. E. V. Bogdanov, N. B. Butko, L. A. Kirakozova, *et al.*, Fiz. Nizk. Temp. **18**, 404 (1992) [Sov. J. Low Temp. Phys. **18**, 274 (1992)].
21. N. B. Brandt and S. M. Chudinov, *Experimental Methods for Research of Energy Spectrum of Electrons and Phonons in Metals* (Mosk. Gos. Univ., Moscow, 1983).
22. D. Shoenberg, *Magnetic Oscillations in Metals* (Cambridge Univ. Press, Cambridge, 1984; Mir, Moscow, 1986).

*Translated by V. Sipachev*

*Journal of Experimental and Theoretical Physics, Vol. 95, No. 2, 2002, pp. 337–347.*
*Translated from Zhurnal Éksperimental'noĭ i Teoreticheskoĭ Fiziki, Vol. 122, No. 2, 2002, pp. 392–403.*


**SOLIDS**
**Electronic Properties**

# Critical Scattering of Low-Energy Electrons by a Ferromagnet in the Neighborhood of the Curie Point

**M. A. Vasil'ev*, M. A. Ivanov, M. B. Shevchenko, and A. G. Blashchuk**

*Kurdyumov Institute of Physics of Metals, Ukrainian National Academy of Sciences, Kiev-142, 03680 Ukraine*
**e-mail: vasil@imp.kiev.ua*

Received February 26, 2002

**Abstract**—It is found that the temperature dependence of the intensity of Bragg maxima arising upon diffraction of low-energy electrons elastically reflected from the (100) plane of a nickel crystal exhibits a critical singularity in the neighborhood of the Curie point. A theory is suggested which describes this effect as the scattering of incident electrons from critical fluctuations of magnetic moment. A comparison is made of the experimentally and theoretically obtained temperature dependences of the intensity of magnetic scattering of electrons, for both three- and two-dimensional models of magnetic ordering. For these models, the radius of interatomic spin-exchange interaction is estimated. © *2002 MAIK "Nauka/Interperiodica".*

## 1. INTRODUCTION

It is known that anomalous temperature dependences are observed for the scattering cross sections of X-rays, light, and neutrons in the vicinity of the point of phase transition [1–5]. Such anomalies in the neighborhood of the Curie point $T_C$ exhibit some physical properties of ferromagnets, such as electric, emission, structural, optical, and galvanomagnetic properties [6]. All of these effects turn out to be associated with critical fluctuations of the order parameter, which arise in the vicinity of the point of phase transition. However, in the case of low-energy electrons scattered by magnets, the question of critical scattering remained open. To a considerable degree, this was due to the imperfection of the previously employed experimental procedures. As a result, the scattering of low-energy electron beams in the immediate vicinity of $T_C$ was not studied in detail (see, for example, [7]). Attention to this phenomenon was given only by Mroz *et al.* [8] in studying the temperature dependence of the intensity $I_{hk}(T)$ of scattering of elastically reflected electrons from the nickel surface. They pointed out that an abrupt increase in the spread of experimental data is observed in the neighborhood of $T_C$. For a fairly large deviation from $T_C$, the dependence $I_{hk}(T)$ is described by the Debye–Waller factor. The results of detailed investigation of this phenomenon using an ingenious experimental procedure have led one to conclude that, in the vicinity of $T_C$, the intensity of elastically scattered slow electrons exhibits an anomalous behavior [9]. As was noted in [10], this feature arises most probably as a result of critical fluctuations of magnetic moment. Further investigations of this phenomenon performed by us have revealed that the observed singularity in the behavior of the scattering intensity of low-energy electrons by magnets indeed corresponds to the critical scattering of low-energy electrons by magnets. It is believed that this inference may be quite important, because the effect of critical electron scattering could serve as a basis for developing a new and more perfect method for the investigation of magnetic phase transitions. Such an approach based on detection and registration of electron current would make it possible to determine the critical exponents and other parameters of magnetic phase transitions with a much higher degree of accuracy and reliability than in the cases of X-rays and neutron scattering.

It is the objective of this study, first, to use the temperature dependences of the intensity of Bragg maxima of specular reflection to experimentally investigate the effect of critical scattering of low-energy electrons from the (100) plane of a nickel crystal and, second, to use numerical calculations for comparison of the theoretically and experimentally obtained temperature dependences of scattering intensity.

## 2. EXPERIMENT

The experiments were performed using a DME-EOS high-vacuum electron spectrometer with photometric recording of diffraction reflections. The residual gas pressure in the working chamber did not exceed $10^{-8}$ Pa. We investigated a cylinder-shaped single crystal of nickel 9 mm in diameter and 2.5 mm thick, oriented along the (100) face. Thanks to the etching by $Ar^+$ ions with simultaneous and subsequent high-temperature annealing and to the monitoring of the chemical composition and surface structure of the sample being investigated (both after cleaning and in the course of experiment) by means of Auger electron spectroscopy and slow-electron diffraction, the investigations could be performed on an atomically clean surface.

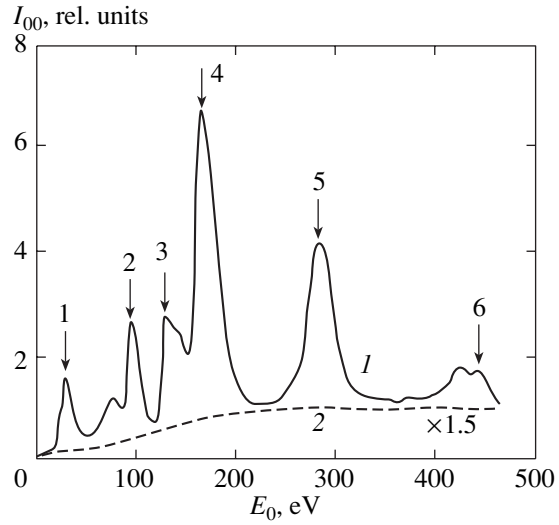


**Fig. 1.** The intensity of specular reflection as a function of the energy of primary electrons for a crystal of nickel in the (100) plane. Curve *1* was obtained at room temperature, and curve *2*, at 1200 K (the values given here are 1.5 times less than the observed values). The arrows indicate Bragg peaks, and the numerals indicate their diffraction order *n*.

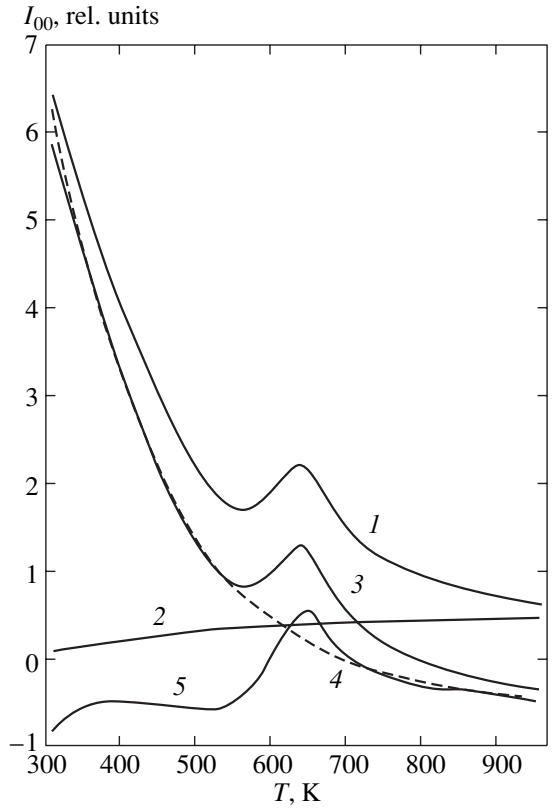


**Fig. 2.** The experimentally obtained temperature dependence of the intensity of a Bragg maximum with the energy $E_0$ = 183 eV and $n$ = 4 (curve *1*) and various results of its treatment (see Section 4). Curve *5* describes the temperature dependence of critical magnetic scattering of electrons obtained as a result of treatment.

The diffraction pattern observed at room temperature for the cleaned (100) surface of nickel exhibited a bodylike symmetry characteristic of the unreconstructed (100) face of an fcc crystal. The atomic structure of the sample surface at temperatures from 300 to 1200 K remained unvaried. The temperature was measured by a Chromel–Alumel thermocouple welded directly to the sample surface. The measurement accuracy was ±2 K. The primary beam current was 20 μA, and the primary electron energy $E_0$ varied in the range from 20 to 600 eV. The accuracy of measuring the energy $E_0$ was approximately 2% of its value. The diffraction pattern was observed using a quasi-spherical four-grid energy analyzer with the grid diameter of 110 mm and a collector screen coated with ZnS luminophor.

In order to eliminate the effect of "parasitic light" from a heated sample, the procedure of modulation of the diffraction pattern was used with subsequent extraction of useful signal [10]. The modulation was performed by applying an ac voltage to the control electrode of a slow-electron gun. A photometer was used to convert the intensity of the selected diffraction reflection to an ac electric signal delivered to the input of a narrow-band selective amplifier tuned to the frequency ω. A synchronous detector improving the signal-to-noise ratio was connected to the amplifier input. The optimal mode of modulation was selected by measuring the current–voltage characteristics from the control electrode and selecting linear portions on them. The dc bias voltage was 3 V, and the ac bias voltage, 6 V; the working frequency ω = 22 Hz. The modulation procedure was also used for self-tuning of the diffraction reflection to the intensity maximum, because its energy position was affected by the thermal expansion of the sample crystal lattice. In the case of investigations using the method of slow-electron diffraction, the principal experimental objective was the photometering of the energy or temperature dependences of the intensity of the selected *hk* reflection. In this case, the temperature dependence of reflection was continuously recorded in the process of cooling off of a sample heated to $T$ = 1200 K. This made possible the elimination of the effect of the magnetic field of the heating spiral on the correctness of the experiment.

The energy dependence of the intensity of specular reflection for nickel oriented along the (100) plane is given in Fig. 1. Curve *1* was obtained at room temperature, and curve *2*, at $T$ = 1200 K. The arrows in Fig. 1 indicate Bragg maxima which have the diffraction order $n$. The energy of these maxima (in eV) is defined by the Wulf–Bragg relation [11],

$$E_{0n} = (37.6/\cos^2\vartheta)(n/d)^2 - V_0/\cos^2\vartheta, \qquad (1)$$

where ϑ is the incidence angle of primary electrons relative to the normal to the surface, which was taken to be 12°. On analyzing Eq. (1) for different diffraction orders, one can determine the interplane distance $d$ and

internal potential $V_0$ of the face being investigated. As a result, it was found that, for nickel in the (100) plane, the best agreement with the experimental data is reached when $d = 1.763$ Å and $V_0 = 16.9$ eV.

We have experimentally recorded the temperature dependence of the intensity of a Bragg maximum with the energy $E_0 = 183$ eV and $n = 4$, and the respective results are given in Fig. 2 (curve *1*). One can see in the figure that this dependence is nonmonotonic in the neighborhood of the Curie point of nickel ($T_C = 631$ K). A similar effect caused by the critical scattering of slow electrons in the vicinity of $T_C$ was observed for Bragg maxima with $n = 2$, 3, and 5. For higher diffraction orders, this feature could not be registered because of the low intensity of the diffracted wave. The choice of the fourth maximum was defined by the maximal intensity of this peak. This made possible the recording of the effect of critical scattering of slow electrons with the least signal-to-noise ratio.

## 3. THEORY

### *3.1. Case of Three-Dimensional Magnetic Ordering*

It is known that low-energy electrons interacting with crystal atoms experience a fairly strong scattering. As a result, the depth of penetration of such electrons into a crystal is relatively small, of the order of several nanometers. Therefore, the physical properties of the crystal surface may have a considerable effect on the diffraction of slow electrons, which must apparently occur in the case of a magnetically ordered surface. Under conditions of ferromagnetic ordering of the surface and adjacent layers, it is of special interest to investigate the processes of slow-electron scattering at temperatures close to $T_C$. This is associated with the fact that critical fluctuations of the magnetic moment arise in the neighborhood of the Curie point. It is natural to assume that such fluctuations will have a significant effect on the pattern of scattering of low-energy electrons by magnets. However, it appears quite difficult to perform a direct investigation, both theoretical and experimental, of critical fluctuations in the crystal surface region. Therefore, for simplicity, we will ignore the effect of the crystal boundary on critical fluctuations and assume that a phase transition both in the surface region and in the bulk of the crystal occurs at one and the same temperature $T = T_C$. In fact, this assumption makes it possible to ignore the relatively minor variation of the value of magnetic moment associated with the presence of a surface. At the same time, one can use this approach to determine critical fluctuations in the entire crystal, including those in the surface region. Note further that, according to the approach suggested by Mills [12], the critical fluctuations in the crystal surface region were in fact ignored. As a result, in treating the critical state of low-energy electrons by the magnet surface alone, Mills has concluded that, in this case, no anomalous feature is present in the behavior of scattering intensity in the vicinity of $T_C$. This conclusion is not at all surprising because Mills [12] did not take into account the critical fluctuations in the surface region, while it was these fluctuations that could cause the critical scattering of slow electrons.

We will demonstrate that, within the suggested approach, a maximum in the temperature range of $T \approx T_C$ is indeed observed in the intensity of scattering of quasi-elastically reflected electrons due to spin-exchange interaction of these electrons with crystal electrons. For simplicity, we will use the kinematic scattering theory; this theory is known to be quite valid for describing diffuse electron scattering. As a result, the following expression may be derived for the magnetic component of intensity of diffuse electron scattering $I(\mathbf{k})$ averaged over spin fluctuations:

$$I(\mathbf{k}) \equiv \langle I(\mathbf{k})\rangle = \sum_{n,n'} J_{n,n'} \langle S_n^+ \big| S_{n'}^- \rangle \times \exp\{i\mathbf{k}(\mathbf{R}_n - \mathbf{R}_{n'})\} \exp\{-\kappa d(n_z + n_z')\}. \quad (2)$$

Here, $\mathbf{k} = \mathbf{k}_1 - \mathbf{k}_0$ is the scattering vector lying on the Ewald sphere, and $\mathbf{k}_0$ and $\mathbf{k}_1$ are the wave vectors of incident and diffracted waves, with $|\mathbf{k}_0| = |\mathbf{k}_1|$ because of the quasi-elastic pattern of scattering; $S_n^\pm$ and $\mathbf{R}_n$ denote the spin operators and the coordinate of the $n$th atom; the angular brackets indicate the quantum-statistical averaging; $\kappa \equiv \kappa(E_0)$ is the coefficient allowing for the layer-by-layer absorption of electrons, where $E_0$ is the incident electron energy; and $d$ is the lattice constant along the axis $z$ directed normally to the surface. In expression (2), the quantities $J_{n,n'}$ describe the exchange interaction between incident electrons and atomic spins. A further line of reasoning does not depend on the concrete values of their parameters. Therefore, we will assume the quantities $J_{n,n'}$ to be preassigned and will not perform the calculation of this coefficient, which is a fairly complicated problem in the general case. (For some particular cases, the relevant calculation is described in [3, 13].)

We will expand the spin correlation function $\langle S_n^+ | S_{n'}^- \rangle$ in terms of wave vectors in reciprocal space,

$$\langle S_n^+ \big| S_{n'}^- \rangle = \frac{1}{N} \sum_{\mathbf{q},\mathbf{q}_1} \exp\{i\mathbf{q}\mathbf{R}_n - i\mathbf{q}\mathbf{R}_{n'}\} \langle S^+(\mathbf{q}) \big| S^-(\mathbf{q}_1)\rangle, \quad (3)$$

where $N$ is the number of atoms in the crystal. In view of the statistical pattern of spin fluctuations, one can demonstrate that, after averaging, only diagonal terms are retained in Eq. (3) for the correlator of spin fluctuations in reciprocal space, i.e.,

$$\langle S^+(\mathbf{q}) \big| S^-(\mathbf{q}_1)\rangle = \chi(\mathbf{q})\Delta(\mathbf{q} - \mathbf{q}_1).$$

We will use the simplest expression given in [14] for describing the behavior of $\chi(\mathbf{q})$ in the fluctuation region in the neighborhood of $T_C$,

$$\chi(\mathbf{q}) \approx \frac{1}{\Gamma^{\pm}|\tau|^{\gamma}} \frac{1}{[1 + q^2 r_c^2/(1-\eta_0/2)]^{1-\eta_0/2}}. \quad (4)$$

Here, the critical radius of fluctuations is $r_c = r_{c0}^{\pm}/|\tau|^{\nu}$; $\tau = (T - T_C)/T_C$; $r_{c0}^{\pm}$ denotes some constants characterizing the radius of interatomic spin-exchange interaction (the values with ± relate to the regions of $T > T_C$ and $T < T_C$, respectively); $\nu$, $\gamma$, and $\eta_0$ are critical exponents: $\nu = 1/2$, $\gamma = 1$, and $\eta_0 = 0$ in the Landau model; $\nu \approx 0.630$, $\gamma \approx 1.241$, and $\eta_0 \approx 0.04$ in the scale-invariant theory for a three-dimensional system with one order parameter (3D Ising model), and $\nu \approx 1$, $\gamma \approx 7/4$, and $\eta_0 \approx 1/4$ for the 2D Ising model [15]; and $\Gamma^{\pm}$ denotes dimensional coefficients independent of temperature. Note that, with this definition of the spin correlator, one can further include the critical fluctuations of the magnetic moment on the crystal surface region.

Then, assuming that the quantity $J_{n,n'}$ is the same for all atoms, with due regard for Eqs. (3) and (4), we will derive the following expression for the intensity of magnetic diffuse scattering of electrons averaged over spin fluctuations:

$$I(\mathbf{k}) = \frac{J}{N}\sum_{n,n'}\sum_{\mathbf{q}} \exp\{i(\mathbf{k}-\mathbf{q})(\mathbf{R}_n - \mathbf{R}_{n'}) - \kappa(n_z + n_z')d\}\chi(\mathbf{q}). \quad (5)$$

Expression (5) may be simplified if the crystal is assumed to be infinite along the direction parallel to the surface ((*xy* plane) and semi-infinite along the direction perpendicular to the surface (*z* axis). In view of this, the summation in the *xy* plane yields

$$\sum_{n_{\|}, n_{\|}'} \exp\{i(\mathbf{k}_{\|} - \mathbf{q}_{\|})(\boldsymbol{\rho}_n - \boldsymbol{\rho}_{n'})\} = N_{\|}^2 \sum_{\boldsymbol{\tau}} \Delta(\mathbf{k}_{\|} - \mathbf{q}_{\|} - \boldsymbol{\tau}), \quad (6)$$

where $\boldsymbol{\rho}_n = (x_n, y_n)$, $\mathbf{k}_{\|}$, $\mathbf{q}_{\|}$, and $\boldsymbol{\tau}$ are components parallel to the surface of the vectors $\mathbf{R}_n$, $\mathbf{k}$, and $\mathbf{q}$ and of the reciprocal lattice vector $\mathbf{g}$, respectively, and $N_{\|}$ ($N_{\|} \longrightarrow \infty$) is the number of atoms along the surface. It is clear that the delta function in Eq. (6) describes the two-dimensional Bragg conditions of diffraction which, in the case of $\boldsymbol{\tau} = 0$ (i.e., under conditions of specular reflection), have the form $\mathbf{q}_{\|} = \mathbf{k}_{\|}$. It is this case that will be treated below. As a result, in view of Eq. (6), we will write the respective scattering intensity in the form

$$I(\mathbf{k}) = J\frac{N_{\|}^2}{N}\sum_{n_z, n_z' = 0}^{\infty}\sum_{q_z} \exp\{i(k_z - q_z)d(n_z - n_z') - \kappa d(n_z + n_z')\}\chi(\mathbf{k}_{\|}, q_z). \quad (7)$$

We will investigate the case when, along with the two-dimensional Bragg conditions described by expression (6), a third Bragg condition is valid which corresponds to the electron diffraction on planes parallel to the surface. In doing so, the condition $k_z d = 2\pi n$ must be valid, where $n$ is the integer characterizing the diffraction order (see Section 2). Then, one can use the spin operator in the form given in Eq. (4) to reduce expression (7) to

$$I(\mathbf{k}) = I(\mathbf{k}_{\|}) = \frac{N_{\|}^2}{N}\frac{J}{d^2}\sum_{q_z}\chi(\mathbf{k}_{\|}, q_z)\frac{1}{\kappa^2 + q_z^2} = \frac{N_{\|}^2}{N}\frac{J}{d^2}\frac{1}{\Gamma^{\pm}|\tau|^{\gamma}} \times \sum_{q_z}\frac{1}{[1 + (k_{\|}^2 + q_z^2)r_c^2/(1-\eta_0/2)]^{1-\eta_0/2}}\frac{1}{\kappa^2 + q_z^2}. \quad (8)$$

Note that it was assumed during summation over $n_z$ and $n_z'$ that $\kappa$ is rather small compared with the size of a reciprocal cell. Indeed, in the case when the incident electron energy is of the order of several hundred electronvolts, it is known (see, for example, [11]) that $\kappa \approx 10^{-1}$ Å$^{-1}$.

It follows from the results of experimental investigations described in Section 2 that, in the case of minor deviations of the scattering vector from the mirror point, the following correlation is observed between the vector $\mathbf{k}_{\|}$ and the geometric shift of a diffusely scattered beam from that point: $\mathbf{k}_{\|} = k_z\mathbf{r}/R$ and $k_z = 2\pi n/d$, where $\mathbf{r}$ is the shift of the diffusely scattered beam on the screen and $R$ is the distance from the sample to the screen. Because the characteristic values of $r$ and $R$ are of the order of $r \sim 10^{-3}$ m and $R \sim 10^{-1}$ m, the correlation $\kappa \gg k_d$ is valid, where $k_d$ is the characteristic value of $k_{\|}$ associated with the photometer aperture.

Note that expression (8), which is valid in the case of three-dimensional magnetic ordering, corresponds to quite definite experimental conditions in which a photometer is used to register electrons with Bragg energy which are formed due to three-dimensional diffraction processes. However, the approach developed by us also makes possible the treatment of the case in which the electrons being recorded satisfy only the two-dimensional Bragg conditions. In the region of energies away from those defined by expression (1), one only has to replace the factor $1/(\kappa^2 + q_z^2)$ in expression (8) for the

scattering intensity by $1/\kappa$. Still, it appears that the use of electron beams with an energy corresponding to a three-dimensional diffraction pattern is preferable from the experimental standpoint. This is due, first, to the higher scattering intensity and, second, to the fact that, in this case, one can use an experimental procedure which makes it possible to keep track of the maximal value of the diffraction spot intensity by varying the energy slightly. As to the drift of the diffraction spot, it may be caused, for example, by the fact that, as the temperature varies, the value of the lattice constant also varies, as well as by some other reasons associated with the special features of the experimental procedure.

We will start to analyze expression (8) from the case of the temperature being rather different from the critical point (weak fluctuations of magnetization) so that the condition $r_c^{-1} > \kappa$ is valid. Then,

$$I(\mathbf{k}_\parallel) = \frac{N_\parallel J}{2\kappa d\Gamma^\pm|\tau|^\gamma}\frac{1}{[1+k_\parallel^2 r_c^2/(1-\eta_0/2)]^{1-\eta_0/2}}. \quad (9)$$

The scattering intensity $I(\mathbf{k}_\parallel)$ increases with decreasing values of the transferred momentum and, in the region where $k_\parallel r_c \ll 1$, approaches the constant value of $I(0) \propto |\tau|^{-\gamma}$; i.e., the intensity at the maximum point decreases away from the critical point by the power law with respect to $|\tau|$ with the exponent equal to the critical exponent $\gamma$. In the region of high values of transferred momentum, when $k_\parallel r_c \gg 1$, the intensity decreases fairly rapidly with increasing $k_\parallel$ ($I(\mathbf{k}_\parallel) \propto 1/(k_\parallel)^{2-\eta_0}$) and, at the same time, by virtue of the well-known condition $\gamma = \nu(2-\eta_0)$ [16], ceases to depend on $|\tau|$.

In the temperature range in the vicinity of the critical point, when fluctuations are rather significant and the condition $r_c^{-1} < \kappa$ is valid, the dependence on $q_z$ in the second propagator may be omitted from Eq. (8), and the expression for the scattering intensity takes the form

$$I(\mathbf{k}_\parallel) = \frac{N_\parallel^2}{N}\frac{J}{d^2\kappa^2}\sum_{q_z}\chi(\mathbf{k}_\parallel, q_z). \quad (10)$$

We substitute the expression for the spin correlator from Eq. (4) into Eq. (10) to derive, in view of the fact that $r_c \gg d$,

$$I(k_\parallel) = \frac{A}{\Gamma^\pm r_c|\tau|^\gamma}\left[1+\frac{(k_\parallel r_c)^2}{(1-\eta_0/2)}\right]^{-(1-\eta_0/2)}. \quad (11)$$

Here, only the temperature-dependent cofactors are given in an explicit form, while the remaining parameters are included in the coefficient $A$,

$$A = \frac{N_\parallel J}{\pi d\kappa^2}\left(1-\frac{\eta_0}{2}\right)^{1/2}\int_0^\infty \frac{dx}{(1+x^2)^{1-\eta_0/2}}.$$

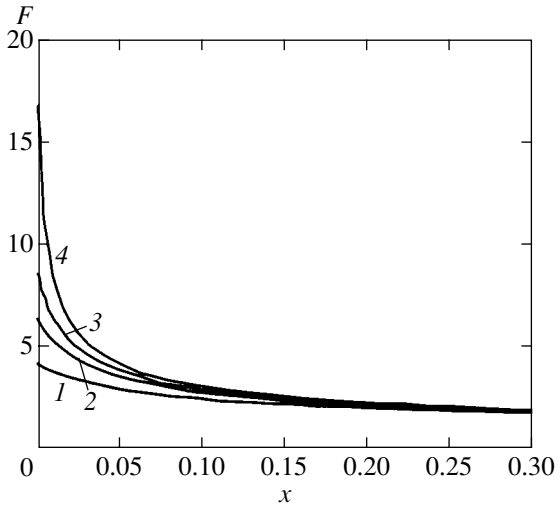


**Fig. 3.** The intensity of critical electron scattering as a function of the transferred wave vector for the 3D Ising model: $F(x) = I(\mathbf{k}_\parallel)\Gamma^\pm r_{c0}^\pm/A$, $x = (k_\parallel r_{x0}^\pm)^2$. Curve *1* corresponds to $|\tau| = 0.1$, *2* to 0.05, *3* to 0.03, and *4* to 0.01.

It follows from expression (11) that the critical electron scattering occurs in the neighborhood of $T_C$. When $k_\parallel r_c \ll 1$, the intensity tends to the limiting value of $I(\mathbf{k}_\parallel) \propto |\tau|^{\nu-\gamma}$ with a lower exponent than away from the critical point where $r_c^{-1} > \kappa$; in the case of $k_\parallel r_c \gg 1$, the scattering intensity is $I(\mathbf{k}_\parallel) \propto k_\parallel^{\eta_0-1}$ and is once again independent of $|\tau|$, with this value turning out to be the same on the right and left of the critical point because of the validity of the relation $\Gamma^+(r_{c0}^+)^{2-\eta_0} = \Gamma^-(r_{c0}^-)^{2-\eta_0}$ (it was a relation of this type that was in fact used in [14]). The behavior of the $I(\mathbf{k}_\parallel)$ curve for different values of $|\tau|$ for the 3D Ising model is shown in Fig. 3. Note further that, if the intensity is treated as a function of $\tau$ for the preassigned value of transferred momentum, $I(\mathbf{k}_\parallel)$ will be maximal at point $\tau = 0$ and will exhibit at this point a kink characteristic of critical scattering. An example of such dependence for different models is given in Fig. 4.

### *3.2. Averaging over the Photometer Aperture*

The experimental approach employed by us involves measuring the overall intensity of scattered electrons penetrating into the photometer aperture. As to the expressions for the scattering intensity given above, they describe the intensity for a preassigned value of the scattering vector $\mathbf{k}_\parallel$ lying on the Ewald sphere, i.e., for some value of the scattering angle. Therefore, in order to obtain the experimentally observed intensity, one must integrate the resulting expressions over all angles $\vartheta_a$ falling within the above-mentioned aperture. Below, we will assume for sim-

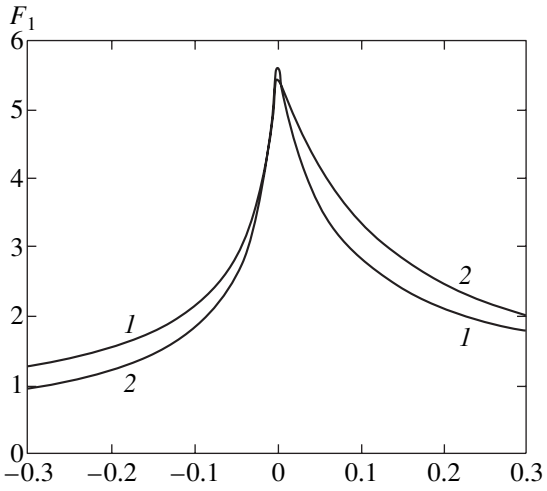


**Fig. 4.** The intensity of critical electron scattering as a function of temperature $F_1(\tau) = I(\mathbf{k}_\parallel)\Gamma^+ r_{c0}^+/A$ for the preassigned value of the transferred wave vector $((k_\parallel r_{c0}^+)^2 = 0.03)$. Curve *1* corresponds to the Landau theory in which $m = \Gamma^-/\Gamma^+ = 2$; curve *2* corresponds to the 3D Ising model, $m \approx 5.1$.

plicity that the aperture is a circle of radius $r_d$ and the center of this circle (in view of the fact that the above-described self-tuning of the photometer occurs) coincides with the maximum of the intensity of observed reflection; i.e., it corresponds to $\mathbf{k}_\parallel = 0$. In the case of minor deviations from the maximum, the angle $\boldsymbol{\vartheta}_a$ is related to the geometric deflection of the ray from the maximum on the photometer screen $\mathbf{r}$ and to the wave vector $\mathbf{k}_\parallel$ by the following relations: $\boldsymbol{\vartheta}_a = \mathbf{r}/R = \mathbf{k}_\parallel/k_z$, where the component $k_z$ of the wave vector of the scattered wave in the case of validity of three-dimensional Bragg conditions is $k_z = 2\pi n/d$.

So, the observed intensity of scattered electrons as a function of the photometer aperture angle $\vartheta_d = r_d/R$ has the form

$$I_i(\vartheta_d) \equiv I_i(k_d) = \int I(\mathbf{k}_\parallel)\, d\boldsymbol{\vartheta}_a = \frac{2\pi}{k_z^2}\int_0^{k_d} I(\mathbf{k}_\parallel) k_\parallel dk_\parallel, \quad (12)$$

where $k_d = \vartheta_d k_z = 2\pi n r_d/Rd$.

In order to find $I_i(k_d)$, we will use the values of $I(\mathbf{k}_\parallel)$ determined in Eqs. (10) and (11). As a result, we derive

$$I_i(k_d) = \frac{A_1}{\Gamma^\pm r_c^3 |\tau|^\gamma} \times \left\{\left[1 + \frac{(r_c k_d)^2}{1-\eta_0/2}\right]^{(1+\eta_0)/2} - 1\right\}, \quad (13)$$

where

$$A_1 = \frac{2\pi}{k_z^2}\frac{1-\eta_0/2}{1+\eta_0}A.$$

Or, in view of the fact that $r_c = r_{c0}^\pm/|\tau|^\nu$ and using the well-known coupling relation for the critical exponents $\gamma = \nu(2-\eta_0)$, we derive

$$I_i(k_d) = \frac{A_1}{\Gamma^\pm (r_{c0}^\pm)^3} \times \left\{\left[|\tau|^{2\nu} + \frac{(r_{c0}^\pm k_d)^2}{1-\eta_0/2}\right]^{(1+\eta_0)/2} - |\tau|^{\nu(1+\eta_0)}\right\}. \quad (14)$$

It follows from Eqs. (13) and (14) that, on approaching the point of phase transition, the intensity $I_i(k_d)$ of electrons registered by the photometer, as well as the quantity $I(\mathbf{k}_\parallel)$, tends to the maximal value equal, in this case, to

$$I_i(k_d) = \frac{A_1 (k_d)^{1+\eta_0}}{\Gamma^\pm (r_{c0}^\pm)^{2-\eta_0}},$$

while the kink at the point $\tau = 0$ is retained. Note that the foregoing value of intensity increases with $k_d$, i.e., with the photometer aperture. However, because usually $\eta_0 \ll 1$, this increase is still less than the increase in the aperture proper proportional to $k_d^2$.

The half-width of the intensity curve may be determined from the condition $r_c k_d \approx 1$. Therefore, the respective characteristic values of $|\tau|$ are of the order of $(r_{c0}^\pm k_d)^{1/\nu}$ and increase with the photometer aperture.

Expression (14) enables one to directly determine the asymptotic behavior of the temperature dependence $I_i(k_d)$ quite far away from $T_C$. We assume that $r_c k_d \ll 1$ to derive

$$I_i(k_d) = \frac{A_1(1+\eta_0)}{\Gamma^\pm r_{c0}^\pm (2-\eta_0)|\tau|^{\nu(1-\eta_0)}}\frac{k_d^2}{}. \quad (15)$$

It follows from Eq. (15) that the temperature dependence of $I_i(k_d)$ is rather weak. For example, in the Landau theory, the intensity away from $T_C$ decreases as $|\tau|^{-1/2}$. In the case of a three-dimensional system with one order parameter, $I_i(k_d)$ decreases as $|\tau|^{-0.605}$. Note further that expression (15) remains valid until condition $r_c > \kappa^{-1}$ is valid and, quite far away from the critical point, when $r_c < \kappa^{-1}$, the intensity $I_i(k_d)$, as $I(\mathbf{k}_\parallel)$ in Eq. (9), turns out to be proportional to $|\tau|^{-\nu(2-\eta_0)}$.

It follows from the expressions derived above that the behavior of the temperature dependence of the intensity of scattered low-energy electrons is primarily defined by the critical exponent $\nu$. Therefore, an accu-

rate measurement of the temperature dependence of scattering may provide a convenient method of determining some of the critical exponents during second-order phase transitions.

Note further that the intensity of magnetic scattering of slow electrons depends on their energy $E_0$ as well. As follows from Eq. (10), the form of this dependence in the neighborhood of $T_C$ will be primarily defined by the factor $J(E_0)/\kappa^2(E_0)$, where $J(E_0)$ is the energy-dependent coefficient of exchange interaction between incident electrons and magnetic excitations of the matrix.

### *3.3. Case of Two-Dimensional Magnetic Ordering*

The case of two-dimensional magnetic ordering is of special interest in studying magnetic structures. The detection and investigation of quasi-two-dimensional magnetic structures was reported, for example, by Alvarado *et al.* [17, 18] and Weller *et al.* [19, 20]. Furthermore, this case is of considerable importance for solving the problem of purely surface magnetism, when only the surface layer atoms possess the magnetic moment.

We will demonstrate below that fluctuations of the order parameter observed in the case of two-dimensional magnetic ordering may also bring about the critical scattering of low-energy electrons. Indeed, we can use the simplest correlation function given in [14] for describing the critical fluctuations (as in the three-dimensional case) to derive the following expression for the intensity $I_2(\mathbf{k}_\parallel)$ of two-dimensional magnetic diffuse scattering, averaged over spin fluctuations and corresponding to specular reflection:

$$I_2(\mathbf{k}_\parallel) = N_\parallel J\chi(\mathbf{k}_\parallel) = N_\parallel J\frac{1}{\Gamma^\pm|\tau|^\gamma}\frac{1}{[1+k_\parallel^2 r_c^2/(1-\eta_0/2)]^{1-\eta_0/2}}. \quad (16)$$

Note that Eq. (16), compared with the previously derived expression, does not contain, in particular, the large factor $(\kappa d)^{-2}$. The emergence of the latter factor is associated with the electron scattering in the bulk of a crystal away from its surface.

As in the previous subsection, we will calculate the scattering intensity integral over the aperture. On integrating Eq. (16) with respect to $\mathbf{k}_\parallel$ within the circular aperture, we immediately derive the expression for the respective integral intensity $I_{i2}(k_d)$ of magnetic diffuse scattering,

$$I_{i2}(k_d) = \frac{A_2}{\Gamma^\pm r_c^2|\tau|^\gamma}\left\{\left(1+\frac{k_d^2 r_c^2}{1-\eta_0/2}\right)^{\eta_0/2}-1\right\}, \quad A_2 = \frac{2\pi}{\eta_0}\frac{N_\parallel J}{k_z^2}. \quad (17)$$

We will calculate the asymptotic behavior of $I_{i2}(k_d)$ at $|\tau| \longrightarrow 0$. We assume in Eq. (17) that $k_d r_c \gg 1$ to derive

$$I_{i2}(k_d) = \frac{A_2}{\Gamma^\pm (r_{c0}^\pm)^{2-\eta_0}} \times\left\{\left(\frac{k_d^2}{1-\eta_0/2}\right)^{\eta_0/2}-(r_{c0}^\pm)^{-\eta_0}|\tau|^{\nu\eta_0}\right\}. \quad (18)$$

In this case, the maximal value of intensity is proportional to $k_d^{\eta_0}$; i.e., it is much less dependent on the photometer aperture width compared with the case of three-dimensional scattering. As to the width of the line of critical scattering at half-height, it may be estimated from the condition $r_c k_d \approx 1$, as for the three-dimensional case. So, the respective values of $|\tau|$ once again turn out to be of the order of $(r_{c0}^\pm k_d)^{1/\nu}$.

On assuming in Eq. (17) that $k_d r_c \ll 1$, one can readily determine the asymptotic behavior of the intensity $I_{i2}(k_d)$ quite far away from $T_C$,

$$I_{i2}(k_d) \approx \frac{A_2\eta_0 k_d^2}{(2-\eta_0)\Gamma^\pm|\tau|^\gamma}. \quad (19)$$

So, $I_{i2}(k_d)$, for example, in the 2D Ising model, is proportional to $|\tau|^{-7/4}$; i.e., it decreases faster than in the three-dimensional case.

In the two-dimensional case, one can see from Eq. (17) that the dependence of the intensity of magnetic scattering of slow electrons on their energy $E_0$ is defined by the factor $J(E_0)/k_z^2$. It is obvious that this quantity will decrease significantly with increasing energy of incident electrons, so that the intensity of magnetic scattering of electrons will decrease with increasing $E_0$ in this case as well.

## 4. NUMERICAL CALCULATIONS AND DISCUSSION OF THE RESULTS

We will compare the experimentally and theoretically obtained integrated temperature dependences of magnetic scattering intensity. For this purpose, we will transform the obtained expressions to a form convenient for numerical calculation. So, in the three-dimensional case of magnetic ordering, expression (14) for the scattering intensity $I_i(k_d) \equiv I_i(k_d, T)$ may be reduced

to the form

$$I_i(k_d, T) = C_1 \begin{cases} m^{(1+\eta_0)/(2-\eta_0)} \left\{ \left[ (-\tau)^{2\nu} + \dfrac{B^2}{(1-\eta_0/2)m^{2/(2-\eta_0)}} \right]^{(1+\eta_0)/2} - (-\tau)^{\nu(1+\eta_0)} \right\}, \\ \tau < 0, \\ [\tau^{2\nu} + B^2/(1-\eta_0/2)]^{(1+\eta_0)/2} - \tau^{\nu(1+\eta_0)}, \quad \tau \geq 0, \end{cases} \tag{20}$$

where

$$B = r_{c0}^{+} k_d = \frac{2\pi n r_d r_{c0}^{+}}{Rd}, \quad m = \frac{\Gamma^{-}}{\Gamma^{+}}.$$

In the case of two-dimensional scattering, expression (18) may be transformed to

$$I_{i2}(k_d, T) = C_2 \begin{cases} m^{\eta_0/(2-\eta_0)} \left\{ \left[ (-\tau)^{2\nu} + \dfrac{B^2}{(1-\eta_0/2)m^{2/(2-\eta_0)}} \right]^{\eta_0/2} - (-\tau)^{\nu\eta_0} \right\}, \\ \tau < 0, \\ \left[ \left( \tau^{2\nu} + \dfrac{B^2}{1-\eta_0/2} \right)^{\eta_0/2} - \tau^{\nu\eta_0} \right], \quad \tau \geq 0. \end{cases} \tag{21}$$

Here, the factors $C_{1,2}$ include all quantities which do not change significantly in the fluctuation region in the neighborhood of the critical point.

Note that the quantity $B$, which is a parameter in expressions (20) and (21), characterizes the correlation radius of spin-exchange interaction of magnet atoms which scatter electrons in the critical manner in the neighborhood of $T_C$. At the same time, the parameter $\alpha$ also entering these expressions describes the asymmetry of these curves relative to the straight line $\tau = 0$. It is clear that the quantities $B$ and $\alpha$ depend on the models of magnetic ordering. Therefore, the determination of these quantities is of great interest from the standpoint of identifying such models. If we regard the parameters $B$ and $\alpha$ to be fitting parameters, their values may be determined using the optimization procedure when comparing the predicted curves and experimental data. For this purpose, we have performed the necessary treatment of both experimentally obtained and predicted curves.

The contribution due to the lattice vibrations was subtracted from the experimental data. In order to correctly perform such subtraction, we used a self-consistent iterative approach which included the temperature dependence of diffuse background. After the iterative subtraction of the background from the intensity curve and the recovery of the Debye–Waller factor, this dependence was calculated in the approximation of two-phonon electron scattering according to [21, 22]. In a zeroth approximation, the background saturation curve *2* in Fig. 1 was used for the background. As a result, after a series of converging iterations, the thermodiffuse background was described by curve *2* in Fig. 2, and curve *3* in this figure was obtained for the intensity of Bragg scattering "cleared" of the background. The approximation curve *4* describing the temperature dependence of intensity due to the Debye–Waller factor must be subtracted from curve *3*. As a result, the contribution to the intensity, which is independent of the lattice vibrations and corresponds to electron–magnon scattering, was described by curve *5* in Fig. 2.

We will now proceed to describe the treatment of the predicted curves describing the temperature dependence of the intensity of magnetic scattering. These curves are defined by expressions (20) and (21), and their qualitative form is given in Fig. 4. The need to significantly adapt these curves when performing a comparison with experimental data is associated with the special features of the experimental procedure employed. The latter procedure consisted essentially in that the temperature dependence of diffraction maximum was recorded continuously in the process of cooling of the sample preheated to 1200 K. As a result, it was not the value of $I_i(k_d, T)$ that was recorded, but the respective quantity averaged over some temperature interval $\Delta T$. Therefore, in comparing the predicted and experimental results, we used the quantity $\tilde{I}_i(T)$ defined as

$$\tilde{I}_i(T) = \frac{1}{\Delta T} \int_{T-\Delta T/2}^{T+\Delta T/2} I_i(k_d, T')dT'. \tag{22}$$

(A similar expression may be written for the quantity $\tilde{I}_{i2}(T)$ in analyzing the electron scattering from a two-dimensional magnet system.)

The following estimate may be used to determine the value of the width of the temperature interval $\Delta T$: $\Delta T = v_0 t_0$, where $v_0$ is the rate of cooling the sample and $t_0$ is the time characterizing the half-width of the photometer spread function. However, under real experimental conditions, the $\Delta T$ broadening was not measured. Therefore, we performed the broadening of predicted curves for some preassigned values of this quantity such as $\Delta T/2$ = 2, 10, and 20 K. The relatively high values of $\Delta T$ selected here are due to restrictions in the employed experimental procedure, in which, on the one hand, it was the temperature on the sample surface that could not be measured with sufficient accuracy and, on the other hand, a certain time was required for statistical accumulation of the signal being recorded.

The experimental curves normalized to respective maximal values and the predicted curves broadened in accordance with Eq. (22) were compared by minimizing the reliability factor selected in the form indicated in [11]. For four models (3D Landau model and 3D and 2D Ising models, as well as the model of Bray and Moor suggested in [23], in which $\nu \approx 1.353$, $\gamma \approx 1.066$, and $\eta_0 \approx 1.212$), the obtained results were analyzed for different values of $\Delta T$ in order to reach the best agreement between the experimental and theoretical data. Given by way of example in Fig. 5 (solid curves) are the theoretically obtained results for the 3D Landau model for three values of $\Delta T$. Also given in the same figures (dotted curves) are the experimentally obtained curves of magnetic scattering (curve *5* in Fig. 2). The numerical minimization of the reliability factor with respect to two fitting parameters $B$ and $m$ was determined by the method of coordinate descent. The values of $B$ and $m$ for the treated models of magnetic ordering and $\Delta T$ intervals which correspond to the best fit are given in the table. Also given in the table is the $r_{c0}^{+}/d$ ratio.

It is the analysis of this very quantity characterizing the ratio between the radius of exchange interaction of magnet atoms and the interatomic distance that may be of interest from the standpoint of determining the type of magnetic ordering which causes the observed critical electron scattering. One can see in the table that the most realistic value of $r_{c0}^{+}/d$ is observed for the 3D and 2D Ising models and for the 3D Landau model. Among these models, the least value of the ratio being treated ($r_{c0}^{+} \gg d \approx 0.56$) is obtained for the 3D Ising model, and the highest value ($r_{c0}^{+}/d \approx 1.36$), for the 2D Ising model. As to the model of Bray and Moor (which was also used in [24, 25]), this model, in spite of the fact that it provides the best fit of the prediction and experimental data, gives the value of $r_{c0}^{+}/d \approx 0.1$; i.e., the radius of exchange interaction (within the layer) turns out to be much less than the interatomic distance, which appears to be rather unrealistic.

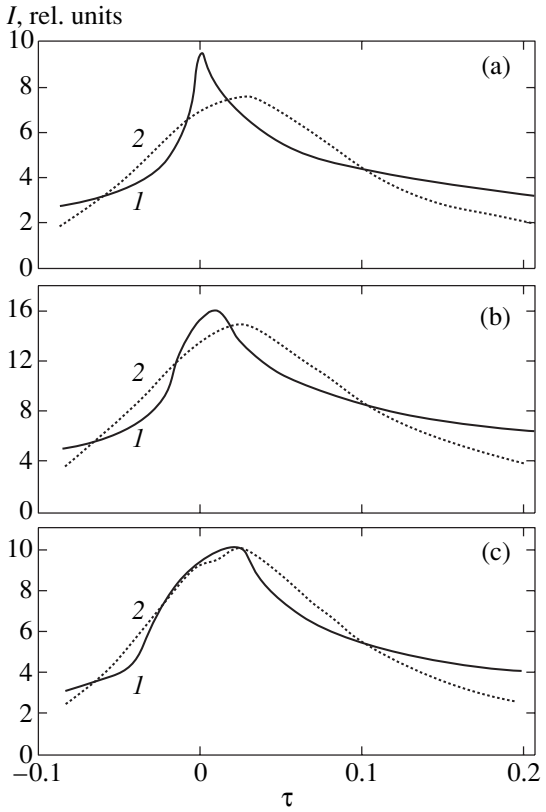


**Fig. 5.** The experimentally obtained (dotted curves) and optimal predicted curves according to expression (22) (solid curves) for the 3D Landau model for three different values of instrumental broadening: $\Delta T/2$ = (a) 2, (b) 10, and (c) 20 K, respectively. The experimental curve is normalized to the maximal value.

It has already been mentioned in Section 3 that the intensity of magnetic scattering of electrons may decrease significantly as their energy $E_0$ increases. This inference is supported by the experimental data

The optimal values of predicted parameters obtained by minimization of the reliability factor for different models of magnetism for three preassigned values of instrumental broadening. The energy of Bragg maximum $E_0$ = 183 eV, diffraction order $n$ = 4

| Models | $\Delta T/2$, K | $B$ | $r_{c0}^{+}/d$ | $m$ |
|---|---|---|---|---|
| 3D Landau model | 2 | 0.278 | 1.101 | 4.17 |
| | 10 | 0.249 | 0.991 | 4.48 |
| | 20 | 0.170 | 0.675 | 5.05 |
| 3D Ising model | 2 | 0.209 | 0.831 | 5.14 |
| | 10 | 0.191 | 0.761 | 5.45 |
| | 20 | 0.142 | 0.564 | 6.16 |
| 2D Ising model | 2 | 0.342 | 1.359 | 7.34 |
| | 10 | 0.337 | 1.341 | 7.86 |
| | 20 | 0.283 | 1.124 | 8.62 |
| Bray and Moor model [23] | 2 | 0.0282 | 0.112 | 3.01 |
| | 10 | 0.0270 | 0.107 | 3.07 |
| | 20 | 0.0232 | 0.092 | 3.36 |

which indicate that, as the energy increases, the critical scattering decreases quite strongly. For energy $E_0 > 400$ eV, the critical scattering is almost completely absent.

## 5. CONCLUSION

In this study, the following has been accomplished.

(i) The effect of critical scattering of low-energy electrons in the neighborhood of $T_C$ has been experimentally confirmed. This effect consists in an abrupt violation of the monotonicity of the temperature dependence of the intensity of specular Bragg maxima from the (100) plane of a nickel crystal in the above-identified temperature region.

(ii) A theory has been suggested which describes the effect of slow-electron scattering from the critical fluctuations of magnetic moment and takes into account the fluctuations in the surface region of a ferromagnet.

(iii) The experimentally obtained and predicted temperature dependences of the scattering intensity have been compared for different models of magnetic ordering using the optimization procedure. For these models, estimates are given of the radius of interatomic spin-exchange interaction.

The critical scattering of low-energy electrons may be of great interest from the standpoint of developing new express methods for the investigation of second-order magnetic phase transitions. Using this phenomenon, one can easily estimate $T_C$ in the vicinity of the crystal surface. Detailed analysis of the critical scattering intensity may further help to determine the pattern of magnetic ordering.

However, in order to unambiguously determine the model of magnetic order, the critical electron scattering must be investigated more thoroughly. For this purpose, it would be interesting to further improve the experimental procedure, in particular, to provide for a photometer tracking of the shift of the diffraction spot maximum both with respect to energy and in space. Such a drift of the diffraction spot is an inevitable side effect observed in experiments and caused, for example, by the shift of scattered electrons under the effect of the magnetic field of the sample. Therefore, its correct inclusion, which could be accomplished with the aid of appropriate scanning methods, would undoubtedly improve the accuracy of the experimental results. This would enable one to use the asymptotic characteristics of scattering intensity obtained above for determining the critical exponents with a higher degree of reliability. Yet another improvement in the experimental procedure employed by us may be the use of the discrete method of recording the temperature dependence of the intensity of diffraction maximum. In this case, one could avoid the temperature spreading of the observed dependence described by expression (22), which would make it possible to determine the critical exponents directly by the half-width and shape of the curves describing the critical electron scattering. Along with the modernization of the experiment, it apparently makes sense to further develop the theoretical approach describing this phenomenon; in particular, it would be interesting to include the dynamic effects of scattering which may be quite significant during diffraction of low-energy electrons.

## REFERENCES

1. L. D. Landau, Zh. Éksp. Teor. Fiz. **7**, 1232 (1937).
2. L. D. Landau and E. M. Lifshitz, *Course of Theoretical Physics*, Vol. 8: *Electrodynamics of Continuous Media* (Nauka, Moscow, 1982; Pergamon, New York, 1984).
3. Yu. A. Izyumov and R. P. Ozerov, *Magnetic Neutron Diffraction* (Nauka, Moscow, 1966; Plenum, New York, 1970).
4. A. W. McReynolds and T. Riste, Phys. Rev. **95**, 116 (1954).
5. H. A. Gersch, C. G. Shull, and M. K. Wilkinson, Phys. Rev. **103**, 525 (1956).
6. S. V. Vonsovskiĭ, *Magnetism* (Nauka, Moscow, 1971; Wiley, New York, 1974).
7. R. E. DeWames and T. Wolfram, Phys. Rev. Lett. **22**, 137 (1969).
8. S. Mroz, A. Mroz, A. Grudniewski, and E. Bak, Phys. Status Solidi B **117**, 683 (1983).
9. M. A. Vasiliev and S. D. Gorodetsky, Vacuum **37**, 723 (1987).
10. M. A. Vasil'ev, S. D. Gorodetskiĭ, and M. B. Shevchenko, Poverkhnost, No. 7, 50 (1991).
11. M. A. Vasil'ev, *Surface Structure and Dynamics of Transition Metals* (Naukova Dumka, Kiev, 1988).
12. D. L. Mills, Phys. Rev. B **3**, 3887 (1971).
13. V. G. Bar'yakhtar, D. A. Yablonskiĭ, and V. I. Krivoruchko, *Green Functions in Theory of Magnetism* (Naukova Dumka, Kiev, 1984).
14. M. A. Krivoglaz, *Diffuse Scattering of X-rays and Neutrons by Fluctuation Irregularities in Nonideal Crystals* (Naukova dumka, Kiev, 1984).
15. A. Z. Patashinskiĭ and V. A. Pokrovskiĭ, *Fluctuation Theory of Phase Transitions* (Nauka, Moscow, 1975; Pergamon, Oxford, 1979).
16. L. D. Landau and E. M. Lifshitz, *Course of Theoretical Physics*, Vol. 5: *Statistical Physics* (Nauka, Moscow, 1982; Pergamon, Oxford, 1980).
17. S. F. Alvarado, M. Campagna, and H. Hopster, Phys. Rev. Lett. **48**, 51 (1982).
18. S. F. Alvarado, H. Hopster, and M. Campagna, Surf. Sci. **117**, 294 (1982).

19. D. Weller, S. F. Alvarado, M. Campagna, *et al.*, J. Less-Common Met. **111**, 277 (1985).

20. D. Weller, S. F. Alvarado, W. Gudat, *et al.*, Phys. Rev. Lett. **54**, 1555 (1985).

21. M. G. Lagally and M. B. Webb, in *The Structure and Chemistry of Solid Surface*, Ed. by G. A. Somorjai (Wiley, New York, 1968), vol. 20, p. 1.

22. R. F. Barnes, M. G. Lagally, and M. B. Webb, Phys. Rev. **171**, 627 (1968).

23. A. J. Bray, M. A. Moor, and M. B. Webb, J. Phys. A **10**, 1927 (1977).

24. S. F. Alvarado, E. Kisrer, and M. Campagna, in *Magnetic Properties of Low Dimension Systems*, Ed. by L. M. Falicov and J. L. Moran-Lopez (Springer-Verlag, Berlin, 1986), Springer Proc. Phys., Vol. 14, p. 52.

25. D. P. Landau, in *Monte Carlo Methods in Statisical Physics*, Ed. by K. Binder (Springer-Verlag, Berlin, 1986), p. 337.

*Translated by H. Bronstein*

*Journal of Experimental and Theoretical Physics, Vol. 95, No. 2, 2002, pp. 348–353.*
*Translated from Zhurnal Éksperimental'noĭ i Teoreticheskoĭ Fiziki, Vol. 122, No. 2, 2002, pp. 404–410.*


**SOLIDS**
**Electronic Properties**

# The Influence of Nonlocality of Quasi-Particle Response to the Nonlinear Meissner Effect in *d*-Wave Superconductors

**M. S. Kalenkov**

*Lebedev Physical Institute, Russian Academy of Sciences, Leninskii pr. 53, Moscow, 119991 Russia*
*e-mail: kalenkov@lpi.ru*

Received March 6, 2002

**Abstract**—A nonlinear correction to the magnetic penetration depth into a $d_{x^2-y^2}$-wave superconductor is found that takes into account nonlocal effects. The calculation is carried out for the self-consistent distribution of the screening supercurrent. An analytical expression for the nonlinear correction is obtained in the limit of the pure superconductor for orientations that do not admit the formation of surface states. It is shown that the presence of unitary impurities makes the nonlinear Meissner effect unobservable in the nonlocal regime for almost all orientations of the crystal either due to the suppression of the nonlocal response of quasi-particles by impurities or due to a considerable contribution of Andreev low-energy surface states to the penetration depth. In the Born scattering limit, there exists a broad interval of orientations and mean free paths in which the nonlocality of the response must be taken into account in the calculation of the nonlinear correction to the penetration depth at rather low temperatures. © *2002 MAIK "Nauka/Interperiodica".*

## 1. INTRODUCTION

The penetration depth of a magnetic field into a superconductor depends on the type of pairing and mutual orientation of the crystal and the magnetic field; this is especially so at low temperatures. The observation of the linear temperature dependence of the magnetic penetration depth at low temperatures shows beyond doubt that the order parameter has node lines on the Fermi surface in $YBa_2Cu_3O_{7-\delta}$ [1, 2]. In addition, in $YBa_2Cu_3O_{7-\delta}$ and some other HTSC compounds, the magnetic penetration depth $\lambda$ exceeds the coherence length $\xi$ by several orders of magnitude ($\lambda/\xi \sim 100$ for $YBa_2Cu_3O_{7-\delta}$). In most cases, this enables one to consider the relationship between the current and the field to be local. It was shown in [3, 4] that, at low temperatures, the local response of quasi-particles in superconductors with $d_{x^2-y^2}$ symmetry of the order parameter leads to a linear (proportional to $|\mathbf{H}|$) correction to the penetration depth with respect to the magnetic field. In the presence of impurities, the dependence of the penetration depth becomes quadratic ([4, 5]). Despite all efforts to discover the nonlinear Meissner effect experimentally in [6–9], no agreement between the theory and experiment was reached in the magnitude of the effect nor in its dependence on temperature and field.

It was first shown in [10] that electrodynamics in its local form is not always applicable to quasi-particles with momenta close to node directions of the order parameter. The effective coherence length of such particles $\xi_{\mathbf{p}_f} \sim \hbar v_f/|\Delta(\mathbf{p}_f)|$ can easily exceed the magnetic penetration depth. The fraction of such particles is usually small relative to the total number of excited particles, and their contribution may be neglected. At temperatures $T < T^* \sim \hbar v_f/\lambda$, all quasi-particles are localized (in the momentum space) near the nodes of the order parameter, and the computation of their response to the magnetic field must take into account nonlocal effects. For the nonlinear correction to the penetration depth, such a computation was carried out in [11], where it was shown that the inclusion of nonlocality of the response yields a quadratic field dependence of the penetration depth. However, the approximation used in [11] results in an oversized estimate (by about an order of magnitude). In this paper, we suggest a method for computing the nonlinear correction to the penetration depth with regard for the nonlocality of quasi-particle response that is free of the drawbacks inherent in the approach used in [11].

The inclusion of impurities changes the effective coherence length of quasi-particles $\xi_{\mathbf{p}_f}$ and makes the response of the superconductor local if the concentration of scatterers is sufficiently high. It is shown that a moderate amount of Born impurities affects the nonlinear correction to the penetration depth hardly at all, while even a small amount of resonance scattering impurities is sufficient to make the superconductor response completely local.

The change of sign of the order parameter depending on the direction on the Fermi surface can result in the formation of low-energy surface states [12–15]. Their contribution to the penetration depth at low temperatures and impurity concentrations becomes signifi-

cant [16–18], which makes the effect of nonlocality on the superconductor response unobservable.

## 2. THE MODEL

The computation of the nonlinear correction to the penetration depth is based on the quasi-classical theory of superconductivity. The matrix Matsubara Green's $2 \times 2$ function satisfies the Eilenberger equation

$$-i\mathbf{v}_f(\mathbf{p}_f)\nabla\hat{g}(\mathbf{p}_f, \omega_n, \mathbf{r}) \tag{1}$$
$$= \left[\left(i\omega_n + \frac{e}{c}\mathbf{v}_f(\mathbf{p}_f)\mathbf{A}(\mathbf{r})\right)\hat{\tau}_3 - \hat{\Delta}(\mathbf{p}_f, \mathbf{r}) - \hat{\sigma}, \hat{g}(\mathbf{p}_f, \omega_n, \mathbf{r})\right],$$

$$\hat{g}^2(\mathbf{p}_f, \omega_n, \mathbf{r}) = -\pi^2\hat{1}, \tag{2}$$

where $\mathbf{p}_f$ is the momentum of quasi-particles on the Fermi surface, $\mathbf{v}(\mathbf{p}_f)$ is the Fermi velocity, $\mathbf{A}(\mathbf{r})$ is the vector potential, $\omega_n = \pi(2n + 1)T$ is the Matsubara frequency, $\hat{\Delta}$ is the matrix of the order parameter, and $\hat{\sigma}$ is the impurity self-energy part. The hat over a symbol denotes the $2 \times 2$ matrix in the particle–hole space. The matrix Green's function and the matrix of the order parameter have the form

$$\hat{g} = \begin{pmatrix} g & f \\ f^+ & -g \end{pmatrix}, \quad \hat{\Delta} = \begin{pmatrix} 0 & \Delta \\ -\Delta^* & 0 \end{pmatrix}. \tag{3}$$

The distribution of the electric current in a superconductor is associated with the diagonal element of the Green's function

$$\mathbf{j}(\mathbf{r}) = 2eTN_f \sum_{\omega_n = -\infty}^{\infty} \langle \mathbf{v}_f g(\mathbf{p}_f, \omega_n, \mathbf{r})\rangle_{S_f}. \tag{4}$$

Here, $N_f$ is the density of states on the Fermi surface of the normal metal per one spin projection. The angle brackets $\langle \ldots \rangle_{S_f}$ denote the normalized averaging over the Fermi surface.

The penetration depth of the magnetic field into a superconductor is determined from the equation

$$\lambda = \frac{\int_0^\infty H(x)dx}{H(0)}, \tag{5}$$

where $H(x)$ is the distribution of the magnetic field in the superconductor found by solving the system of Eqs. (1), (4) and the Maxwell equations. It is assumed that the superconductor occupies the half-space $x > 0$, and the magnetic field is applied along the axis $z$. In what follows, we will assume that the electric current and the vector potential have nonzero components only along the axis $y$.

The nonlinear correction to the penetration depth heavily depends on the relative position of nodes of the order parameter and the direction of the screening current. This is because, at small temperatures, the contribution to the correction is made by low-energy quasi-particles ($\varepsilon \sim T$), i.e., quasi-particles with momenta close to a node of the order parameter. For such particles, the response to the magnetic field becomes nonlocal at temperatures $T \lesssim T^*$ only if the magnetic field varies along the trajectory of the quasi-particle. In this case, the quasi-particle propagates in a variable magnetic field, and the nonlocality of the response becomes necessary.

The further presentation is based on the analytic expansion of the solution to Eq. (1) in powers of the magnetic field. This means that nonanalytic corrections, which appear for certain crystal orientations (see [3, 4, 11], cannot be found with this approach. Let us represent all the involved quantities as series in powers of the external magnetic field

$$\hat{g}(\mathbf{p}_f, \omega_n, x) = \hat{g}^{(0)}(\mathbf{p}_f, \omega_n, x) + \hat{g}^{(1)}(\mathbf{p}_f, \omega_n, x) + \hat{g}^{(2)}(\mathbf{p}_f, \omega_n, x) + \hat{g}^{(3)}(\mathbf{p}_f, \omega_n, x) + \ldots, \tag{6}$$

$$j(x) = j^{(1)}(x) + j^{(3)}(x) + \ldots. \tag{7}$$

Terms with even powers in the expansion of the electric current are zero due to symmetry considerations. Let us explicitly write out the local and linear (with respect to the field) contribution to the current:

$$j^{(1)}(x) = -\frac{c}{4\pi\lambda_0^2}A(x) - \int_0^\infty \tilde{K}^{(1)}(x, x')A(x')dx'. \tag{8}$$

Here, $\lambda_0$ is the penetration depth of the magnetic field at zero temperature in the local approximation, and the kernel $\tilde{K}^{(1)}(x, x')$ contains small temperature corrections, accounts for the influence of nonlocality, and includes the linear response of surface states, which is assumed to be small. Then, the equation of the vector potential takes the form

$$A''(x) - \frac{1}{\lambda_0^2}A(x) = \frac{4\pi}{c}\int_0^\infty \tilde{K}^{(1)}(x, x')A(x')dx' - \frac{4\pi}{c}j^{(3)}(x), \tag{9}$$
$$A'(0) = H(0).$$

Considering the terms involving $K^{(1)}$ and $j^{(3)}$ as small perturbations, we find that the nonlinear correction to the penetration depth has the form

$$\Delta\lambda_{nl} = -\frac{4\pi\lambda_0}{cH(0)}\int_0^\infty \exp(-x/\lambda_0)j^{(3)}(x)dx. \tag{10}$$

In Eq. (10), the current $j^{(3)}(x)$ is determined from the Eilenberger equations with the zero-order approximation of the vector potential

$$A(x) = -\lambda_0 H(0)\exp(-x/\lambda_0).$$

Representing $j^{(3)}(x)$ with the help of (4) in terms of $g^{(3)}(\mathbf{p}_f, \omega_n, x)$, we obtain

$$\Delta\lambda_{nl} = -\frac{8\pi e N_f T\lambda_0}{cH(0)}\sum_{\omega_n}\int_0^\infty \exp(-|x|/\lambda_0) \times \langle v_{f,y}(\mathbf{p}_f) g^{(3)}(\mathbf{p}_f, \omega_n, x)\rangle_{S_f} dx. \quad (11)$$

Equation (11) for the nonlinear correction to the penetration depth is rather general. It is applicable in the case of spatially nonuniform distributions of the order parameter and includes the contributions both of the bulk of the superconductor and of the surface states. In the derivation of this equation, we only assumed that all the involved quantities could be expanded in powers of the magnetic field and the smallness of the parameter $\xi/\lambda$.

For arbitrary orientations of the crystal axes with respect to the plane $yz$, $g^{(3)}(\mathbf{p}_f, \omega_n, x)$ cannot be found analytically because of the spatial nonuniformity of the order parameter (suppression near the superconductor–vacuum boundary). This makes it impossible to find even the Green's function for the zero-order approximation. For this reason, we consider below only the particular case with the spatially uniform order parameter; this case is realized when the order parameters of the incident and reflected directions of the momentum are equal (for example, in the model of the *d*-wave superconductor with the cylindrical Fermi surface and the order parameter $\Delta(\mathbf{p}_f, \mathbf{r}) = \Delta_0(p_{f,x}^2 - p_{f,y}^2)/p_f^2$). In this case, it is easily seen that the Green's function for the zero approximation is independent of the spatial coordinates, which makes it possible to find an explicit analytical expression for $g^{(3)}(\mathbf{p}_f, \omega_n, x)$. We also assume that the scattering of quasi-particles from impurities can be neglected. The influence of impurities and the crystal orientation is qualitatively discussed at the end of the paper.

## 3. PENETRATION DEPTH

To find the Green's function from the magnetic field using perturbation theory, it is convenient to use the following parametrization [19]:

$$\begin{cases} f(\mathbf{p}_f, \omega_n, x) = (-i\pi\,\mathrm{sgn}\, v_{f,x}(\mathbf{p}_f) - g(\mathbf{p}_f, \omega_n, x)) \\ \times \exp\{i\eta(\mathbf{p}_f, \omega_n, x)\}, \\ f^+(\mathbf{p}_f, \omega_n, x) = (-i\pi\,\mathrm{sgn}\, v_{f,x}(\mathbf{p}_f) + g(\mathbf{p}_f, \omega_n, x)) \\ \times \exp\{-i\eta(\mathbf{p}_f, \omega_n, x)\}. \end{cases} \quad (12)$$

The normalization condition (2) is automatically fulfilled. The substitution of (12) into (1) yields an independent equation for $\eta$:

$$-\frac{v_{f,x}(\mathbf{p}_f)}{2}\frac{\partial\eta(\mathbf{p}_f, \omega_n, x)}{\partial x} + i\omega_n + \frac{e}{c}v_{f,y}(\mathbf{p}_f)A(x) - |\Delta(\mathbf{p}_f, x)|\cos(\eta(\mathbf{p}_f, \omega_n, x) - \phi(\mathbf{p}_f, x)) = 0 \quad (13)$$

with the asymptotic condition

$$v_{f,x}(\mathbf{p}_f)\mathrm{Re}\sin(\eta(\mathbf{p}_f, \omega_n, x) - \phi(\mathbf{p}_f, x)) > 0, \quad x \longrightarrow \infty, \quad (14)$$

which ensures a proper behavior of the Green's function in the bulk of the superconductor. The function $\phi(\mathbf{p}_f, x)$ is the phase of the order parameter $\Delta(\mathbf{p}_f, x) = |\Delta(\mathbf{p}_f, x)|\exp\{i\phi(\mathbf{p}_f, x)\}$. The function $g$ satisfies the linear nonhomogeneous equation. Its solution is simple, but cumbersome, and is not presented here. The initial condition is the value of $g$ on the surface $x = 0$. In the case of specular reflection, this initial condition has the form (see [20])

$$g(\mathbf{p}_f, \omega_n, 0) = \pi\cot\left(\frac{\eta(\mathbf{p}_f, \omega_n, 0) - \eta(\mathbf{p}'_f, \omega_n, 0)}{2}\right), \quad (15)$$

where $\mathbf{p}_f$ and $\mathbf{p}'_f$ are the momenta of the incident and reflected quasi-particle, respectively.

For the spatially uniform distribution of the order parameter and the vector potential $A(x) = A(0)\exp(-x/\lambda_0)$, it is easy to find the solution to Eq. (13) up to the third order with respect to the magnetic field:

$$\begin{aligned} \eta(\mathbf{p}_f, \omega_n, x) &= \frac{\pi}{2}\mathrm{sgn}\, v_{f,x}(\mathbf{p}_f) + \phi(\mathbf{p}_f) - i\sinh^{-1}\frac{\omega_n}{|\Delta(\mathbf{p}_f)|} \\ &- \mathrm{sgn}\, v_{f,x}(\mathbf{p}_f)\left[\frac{e v_{f,y}(\mathbf{p}_f)A(x)}{c\Omega_{\mathbf{p}_f}}\right]\frac{\alpha}{1+\alpha} \\ &- \mathrm{sgn}\, v_{f,x}(\mathbf{p}_f)\left[\frac{e v_{f,y}(\mathbf{p}_f)A(x)}{c\Omega_{\mathbf{p}_f}}\right]^2 \\ &\times \frac{i\omega_n}{\Omega_{\mathbf{p}_f}}\frac{\alpha^3}{(1+\alpha)^2(2+\alpha)} \\ &- \mathrm{sgn}\, v_{f,x}(\mathbf{p}_f)\left[\frac{e v_{f,y}(\mathbf{p}_f)A(x)}{c\Omega_{\mathbf{p}_f}}\right]^3 \\ &\times \frac{\alpha^4}{2(1+\alpha)^3(3+\alpha)}\left\{\frac{1}{3} - \frac{\omega^2}{\Omega_{\mathbf{p}_f}^2}\frac{\alpha}{2+\alpha}\right\}. \end{aligned} \quad (16)$$

Here, $\Omega_{\mathbf{p}_f} = \sqrt{\omega_n^2 + |\Delta(\mathbf{p}_f)|^2}$ and $\alpha = 2\Omega_{\mathbf{p}_f}\lambda_0/|v_{f,x}(\mathbf{p}_f)|$. Let us substitute (16) into the expression for the Green's function and separate out the third-order terms with respect to the magnetic field. Then, from (11) some tedious transformations yield the final expression for

the nonlinear correction to the penetration depth with allowance for the influence of nonlocality:

$$\Delta\lambda_{nl} = \frac{8\pi^2 e^4 N_f T\lambda_0^8}{c^4} \times H^2(0)\sum_{\omega_n}\left\langle \frac{v_{f,y}^4}{|v_{f,x}|^3} S(\mathbf{p}_f, \omega_n)\right\rangle_{S_f}, \quad (17)$$

where

$$S(\mathbf{p}_f, \omega_n) = \frac{\Delta^2(\mathbf{p}_f)}{\Omega_{\mathbf{p}_f}^2}\frac{1}{(\alpha+1)^2(\alpha+3)} \times\left[4\omega_n^2\frac{\alpha^2+9\alpha+16}{(\alpha+2)^2} - \Delta^2(\mathbf{p}_f)\frac{\alpha^2+7\alpha+8}{(\alpha+1)^2}\right]. \quad (18)$$

The dimensionless parameter $\alpha$ describes the degree of nonlocality influence. The local limit corresponds to the case $\alpha \gg 1$. The major contribution to the averaging over the Fermi surface in (17) is made by the regions of momenta in the vicinity of the nodes of the order parameter $|\Delta(\mathbf{p}_f)| \lesssim \max(T, T^*)$. For the sake of simplicity, the analysis of the nonlinear correction (17) is carried out for the model of $d_{x^2-y^2}$ superconductor with the cylindrical Fermi surface with the symmetry axis oriented along the magnetic field. The order parameter is chosen in the form $\Delta(\mathbf{p}_f) = \Delta_0\cos 2\varphi$, where $\varphi$ is the angle between the normal to the surface of the superconductor and the direction of the momentum. In this model, the parameter $\lambda_0$ is equal to $\sqrt{c^2/(4\pi e^2 N_f v_f^2)}$.

At temperatures $T \ll T^*$, the sum over Matsubara frequencies in (17) can be replaced by an integral, which is taken analytically:

$$\Delta\lambda = 1.05\times 10^{-2}\frac{\lambda_0^2}{\xi_0}\left(\frac{H(0)}{H^*}\right)^2, \quad T \ll T^*, \quad T^* = \Delta_0\frac{\xi_0}{\lambda_0}, \quad \xi_0 = \frac{v_f}{\pi\Delta_0}, \quad H^* = \frac{c}{e\xi_0\lambda_0}. \quad (19)$$

Comparing the terms of series (16), we see that, at temperatures $T \lesssim T^*$, the parameter of the expansion is $\lambda_0 H(0)/4\xi_0 H^*$. Thus, expression (17) for the nonlinear correction is applicable in the entire Meissner region $H \le H_{c1}$ except for, possibly, a small region in the neighborhood of $H_{c1}$. As the temperature increases, the contribution to the nonlinear correction to the penetration depth is made mainly by the regions of the Fermi surface for which the parameter $\alpha$ is large (this corresponds to the local limit). In this approximation, computations by formula (17) yield the well-known expression for the nonlinear correction to the penetration depth:

$$\Delta\lambda = 3.3\times 10^{-2}\frac{v_f}{T}\frac{\lambda_0}{\xi_0}\left(\frac{H(0)}{H^*}\right)^2, \quad T^* \ll T \ll T_c. \quad (20)$$

The inverse temperature dependence of the penetration depth in this case shows that the response of quasi-particles must be considered nonlocally for low temperatures. This removes the singularity at $T = 0$ in (20). In the range of temperatures $0 < T \ll T_c$, the nonlinear correction to the penetration depth can be written as

$$\Delta\lambda = \beta(T/T^*)\frac{\lambda_0^2}{\xi_0}\left(\frac{H(0)}{H^*}\right)^2, \quad 0 < T \ll T_c. \quad (21)$$

The function $\beta(x)$ is calculated by formula (17), and its plot is shown in the figure. It is seen that $\beta$ is not monotonic due to the nonlocality of the response of quasi-particles at low temperatures. However, the complete penetration depth

$$\lambda(T, H) = \lambda_0 + \Delta\lambda(T) + \beta\left(\frac{T}{T^*}\right)\frac{\lambda_0^2}{\xi_0}\left(\frac{H(0)}{H^*}\right)^2$$

is a monotonic function of temperature for magnetic fields for which formula (17) is true. The nonlinear correction turns out to be about an order of magnitude less than that reported in [11]. This difference can be

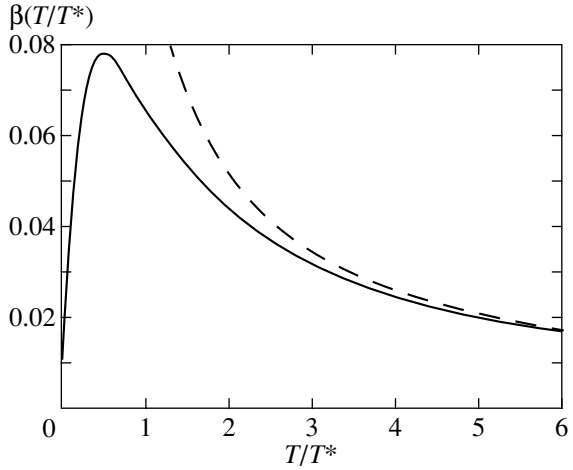


The coefficient in the nonlinear correction to the penetration depth in the $d_{x^2-y^2}$-superconductor model with the cylindrical Fermi surface as a function of temperature. The magnetic field and the symmetry axis of the Fermi surface are assumed to be oriented along the axis $z$. The order parameter is chosen as $\Delta(\mathbf{p}_f) = \Delta_0\cos 2\varphi$, where $\varphi$ is the angle between the normal to the surface and the direction of the momentum. The function $\beta(x)$ is depicted by the solid curve, and the dashed curve corresponds to the coefficient obtained when the nonlocality of the quasi-particle response is neglected (formula (20)).

explained by an approximate calculation of the penetration depth at the background of the spatially uniform distribution of supercurrent in [11], which yields an exaggerated result in this problem.

When deriving the formula for the nonlinear correction to the penetration depth, we neglected the dependence of the order parameter on the magnetic field. It was shown in [4] that this is reasonable in the local approximation; indeed, it yields a correction of order

$$\lambda_0\left(\frac{T}{\Delta_0}\right)^2\left(\frac{H(0)}{H^*}\right)^2.$$

When the temperature decreases below $T^*$, this estimate also remains true when the response of quasi-particles is assumed to be nonlocal and $T$ is replaced by $T^*$. Hence, it follows that, even though the coefficient in (19) is abnormally small, the correction to the penetration depth for type II superconductors with $\lambda_0/\xi_0 \sim 100$, which appears due to the suppression of the order parameter by the magnetic field, is negligibly small at temperatures in the range $0 < T \ll T_c$.

## 4. INFLUENCE OF IMPURITIES AND SURFACE STATES

The nonlinear correction to the penetration depth at low temperatures is sensitive to the presence of impurities in the superconductor since it depends solely on thermally excited quasi-particles. Nonlocal effects may be completely ignored if the diagonal element of the self-energy at zero energy in the bulk of the superconductor satisfies the inequality $|\sigma(0)| \gg v_f/\lambda_0$. In this case, the parameter $2\lambda_0\left|\sqrt{(\omega_n + i\sigma(\omega_n))^2 + |\Delta(\mathbf{p}_f)|^2}\right|/|v_{f,x}(\mathbf{p}_f)|$, which describes the degree of influence of the nonlocality of quasi-particle response, is much greater than unity at all temperatures and arbitrary orientations of the momentum. Then, the local approximation to the calculation of the nonlinear correction to the penetration depth is applicable. In the case of Born impurities, this condition is not very severe due to an exponentially small value of $|\sigma(0)|$ at small concentrations of impurities [21]; more precisely, $|\sigma(0)| \approx a\Delta_0\exp(-bt\Delta_0)$, where the coefficients $a$ and $b$ are of the order of unity. In this case, the nonlocality of response is important when the mean free path satisfies the condition: $l = v_f\tau \gtrsim \xi_0\ln(\lambda_0/\xi_0)$. The presence of strong scatterers (the unitary limit) in the superconductor leads to a much stricter condition for the mean free path. In the unitary limit, $|\sigma(0)| \sim \sqrt{\Gamma_u\Delta_0}$ with a logarithmic accuracy [22], and the nonlocality is important only at very small scattering rates $\Gamma_u \lesssim \Delta_0(\xi_0/\lambda_0)^2$.

The nonlocal response of the superconductor can also be disguised by the presence of surface low-energy Andreev states, which can make a noticeable contribution to the nonlinear correction to the penetration depth [17]. If the crystal orientation admits the existence of such states, then the contribution of surface states to the nonlinear correction to the penetration depth considerably exceeds that from the superconductor bulk when the concentration of unitary impurities is small. As this concentration increases, the contribution of the surface states decreases and the effect of nonlocality becomes negligible. In the Born limit, the comparison of the nonlinear correction due to surface states with the contribution of the superconductor bulk shows that the contribution from the bulk may be neglected at $l \gg (\lambda_0^2\xi_0)^{1/3}$. If $\xi_0\ln(\lambda_0/\xi_0) \ll l \lesssim (\lambda_0^2\xi_0)^{1/3}$, the nonlinear correction must take into account both the contribution of the surface states and the nonlocal effects due to the bulk of the superconductor.

## 5. CONCLUSIONS

It is shown that the spatial dependence of the screening current substantially affects the magnitude of the nonlinear correction to the penetration depth. The previous results obtained in [11] considerably differ from those obtained in this paper, since they are based on a simplified model of the distribution of electric current in a superconductor.

The influence of nonlocality of quasi-particles can manifest itself only in very pure samples in which the penetration depth linearly depends on temperature up to the temperatures $T \lesssim T^*$. It is shown that, in the presence of unitary impurities, the nonlocal effect is important only for orientations that do not admit Andreev low-energy states. In the case of Born scatterers, there exists an interval of mean free paths in which the nonlinear Meissner effect should be considered in combination with the nonlocal response of quasi-particles and the contribution of surface states. The influence of nonlocality can be best observed in an experiment with a magnetic field oriented along the axis $\hat{c}$ of a $d$-wave superconductor when the surface orientation does not allow the formation of Andreev low-energy states (for example, the orientation [100]).

## ACKNOWLEDGMENTS

I am grateful to Yu.S. Barash for useful discussions. This work was supported by the Russian Foundation for Basic Research, project no. 02-02-16643, and by the Jülich Research Center (Landau Scholarship).

## REFERENCES

1. W. N. Hardy, D. A. Bonn, D. C. Morgan, *et al.*, Phys. Rev. Lett. **70**, 3999 (1993).
2. S. Kamal, Ruixing Liang, A. Hosseini, *et al.*, Phys. Rev. B **58**, R8933 (1998).
3. S. K. Yip and J. A. Sauls, Phys. Rev. Lett. **69**, 2264 (1992).

4. D. Xu, S. K. Yip, and J. A. Sauls, Phys. Rev. B **51**, 16233 (1995).
5. T. Dahm and D. J. Scalapino, Phys. Rev. B **60**, 13125 (1999).
6. A. Maeda, Y. Iino, T. Hanaguri, *et al.*, Phys. Rev. Lett. **74**, 1202 (1995).
7. A. Maeda, T. Hanaguri, Y. Iino, *et al.*, J. Phys. Soc. Jpn. **65**, 3638 (1996).
8. A. Carrington, R. W. Giannetta, J. T. Kim, and J. Giapintzakis, Phys. Rev. B **59**, R14173 (1999).
9. C. P. Bidinosti, W. N. Hardy, D. A. Bonn, and Ruixing Liang, Phys. Rev. Lett. **83**, 3277 (1999).
10. I. Kosztin and A. J. Leggett, Phys. Rev. Lett. **79**, 135 (1997).
11. M.-R. Li, P. J. Hirschfeld, and P. Wölfle, Phys. Rev. Lett. **81**, 5640 (1998); Phys. Rev. B **61**, 648 (2000).
12. C.-R. Hu, Phys. Rev. Lett. **72**, 1526 (1994).
13. L. J. Buchholtz, M. Palumbo, D. Rainer, and J. A. Sauls, J. Low Temp. Phys. **101**, 1079 (1995); **101**, 1099 (1995).
14. Yu. S. Barash, A. A. Svidzinsky, and H. Burkhardt, Phys. Rev. B **55**, 15282 (1997).
15. M. Fogelström, D. Rainer, and J. A. Sauls, Phys. Rev. Lett. **79**, 281 (1997).
16. H. Walter, W. Prusseit, R. Semerad, *et al.*, Phys. Rev. Lett. **80**, 3598 (1998).
17. Yu. S. Barash, M. S. Kalenkov, and J. Kurkijärvi, Phys. Rev. B **62**, 6665 (2000).
18. A. Carrington, F. Manzano, R. Prozorov, *et al.*, Phys. Rev. Lett. **86**, 1074 (2001).
19. Yu. S. Barash and A. M. Bobkov, Pis'ma Zh. Éksp. Teor. Fiz. **73**, 470 (2001) [JETP Lett. **73**, 420 (2001)].
20. Yu. S. Barash, M. S. Kalenkov, and J. Kurkijärvi, private communication.
21. L. P. Gor'kov and P. A. Kalugin, Pis'ma Zh. Éksp. Teor. Fiz. **41**, 208 (1985) [JETP Lett. **41**, 253 (1985)].
22. P. J. Hirschfeld and N. Goldenfeld, Phys. Rev. B **48**, 4219 (1993).

*Translated by A. Klimontovich*

*Journal of Experimental and Theoretical Physics, Vol. 95, No. 2, 2002, pp. 354–360.*
*Translated from Zhurnal Éksperimental'noĭ i Teoreticheskoĭ Fiziki, Vol. 122, No. 2, 2002, pp. 411–418.*


**SOLIDS**
**Electronic Properties**

# Shift and Damping of Optical Phonons Caused by Interaction with Electrons

**L. A. Falkovsky**

*Landau Institute for Theoretical Physics, Russian Academy of Sciences, Moscow, 117337 Russia*

*e-mail: falk@itp.ac.ru*

Received March 12, 2002

**Abstract**—Frequency shift and damping of long-wave optical phonons caused by interaction with electrons are calculated. The equations of the dynamic theory of elasticity are considered together with the Maxwell equations and the kinetic equation for determining the deformation field, the electric field, and the distribution function of electrons. Changes in the spectrum of electrons are described using a local potential. Coulomb screening of the longitudinal electric field is taken into account. © *2002 MAIK "Nauka/Interperiodica".*

## 1. INTRODUCTION

In one of the earliest works in which field theory methods were applied to condensed matter, Migdal [1] calculated the renormalization of the electron and phonon spectra in metals caused by electron–phonon interaction. He found that the vertex corrections are small by the adiabatic parameter (the Migdal theorem). He, however, arrived at the conclusion that the renormalization of the phonon spectrum was substantial. Namely, the velocity $s$ of acoustic phonons should change in the order of magnitude, $\tilde{s} = s\sqrt{1-2\lambda}$, where $\lambda$ is the dimensionless electron–phonon interaction constant. This shows that considerable softening of the acoustic mode should be expected as a result of interaction with electrons, and the electron–phonon system becomes unstable when $\lambda \longrightarrow 1/2$. This result contradicts the concept of adiabaticity of the electron–phonon system (e.g., see [2]), according to which light electrons should follow comparatively slow lattice vibrations. Changes in the phonon spectrum should therefore be small by the adiabatic parameter $\sqrt{m/M}$, where $m$ and $M$ are the masses of the electron and the ion, respectively.

At the same time, Akhiezer, Silin, Gurevich, Kontorovich, *et al.* (see review [3]) used the kinetic equation to calculate sound damping in metals. The influence of electron–phonon interaction was indeed shown to be determined by the adiabatic parameter. The change $\delta s$ in the velocity of sound and the damping $\Gamma$ for phonons with wave vector $k$ and frequency $\omega_k = sk$ are described by the equations

$$\frac{\delta s}{s} - i\frac{\Gamma}{\omega_k} = \lambda\begin{cases}\dfrac{s^2}{v_F^2} - i\dfrac{\pi s}{2v_F}, & kv_F > |\omega_k + i\gamma|,\\[2ex] \dfrac{\omega_k}{\omega_k + i\gamma}, & kv_F < |\omega_k + i\gamma|,\end{cases} \quad (1)$$

where $\gamma$ is the electron collision rate, the $\lambda = \zeta_{ik}^2 \nu_0/\rho s^2$ is the constant of coupling with phonons is proportional to the density $\nu_0$ of electron states on the Fermi surface (for the isotropic case, $\nu_0 = m^* p_F/\pi^2$, where $m^*$ is the effective mass of electrons), and $\rho$ is the density of the metal. The deformation potential $\zeta_{ik}$ describes the local deformation-induced change in the spectrum of electrons,

$$\varepsilon(\mathbf{p}, \mathbf{r}, t) = \varepsilon_0(\mathbf{p}) + \zeta_{ik}(\mathbf{p})u_{ik}(\mathbf{r}, t), \quad (2)$$

where $u_{ik}$ is the strain tensor. Equations (1) give correct results for various limiting conditions: for absorption of sound in the hydrodynamic limit ($\omega_k \ll \gamma$ and $k \longrightarrow 0$), for absorption of zero sound ($\omega_k \gg \gamma$ and $k \longrightarrow 0$), and for Landau damping in the ballistic regime ($kv_F \gg |\omega_k + i\gamma|$). It is obvious that the shift of sound velocity and damping in the ballistic regime are small by the adiabatic parameter because $s/v_F \sim \sqrt{m/M}$, which contradicts the result obtained by Migdal.

This contradiction was resolved by Brovman and Kagan [4] (also see work [5] by Geilikman). They showed the shortcomings of the Fröhlich model, which predicted anomalously large phonon renormalization: two large terms compensate each other in perturbation

theory equations second-order in electron–phonon interaction. The remaining contribution was therefore small in conformity with the adiabatic approximation. This compensation could formally be taken into account by subtracting from the phonon self-energy its value at zero frequency: $\Pi(\omega, k) - \Pi(0, k)$.

Large renormalizations were reported by Engelsberg and Schrieffer [6] also for the spectrum of optical phonons. These authors applied the results obtained by Migdal to nondispersion optical phonons. More recently, Ipatova and Subashiev [7] considered the spectrum of optical phonons under collisionless conditions to show that the subtraction suggested in [4] should be performed in this case too. Nevertheless, Alexandrov and Schrieffer recently [8] applied the diagram technique to again obtain huge dispersion of optical phonons, $\omega_k = \omega_0 + \lambda v_F^2 k^2/3\omega_0$, determined by the Fermi velocity, which contradicts the adiabatic approximation. Note that the usual dispersion of optical phonons is of the order of the velocity of sound. Recently, Reizer [9] somewhat improved the situation by considering screening of the long-range electric field that arises in longitudinal optical vibrations.[1] Large dispersion disappeared, but the electron–phonon interaction entered into the result in a nonphysical way. In [6–9], collisions in the phonon and electron systems were not taken into account, and damping of optical phonons caused by both electron–phonon interaction and Coulomb screening was fully ignored.

In this work, we consider the influence of electron–phonon interaction and Coulomb screening on the spectrum of optical phonons. Special attention is given to the accompanying damping of phonons. We use the kinetic equation method earlier applied to acoustic phonons [3] and to problems of surface optical phonons [11].

## 2. THE CONTRIBUTION OF ELECTRON–PHONON INTERACTION TO THE KINETIC EQUATION

Two electron–phonon interaction types are known for optical phonons. First, the Fröhlich interaction, which is determined by polarization caused by relative displacement **u** of ionic sublattices. For simplicity, consider a cubic crystal with two atoms per unit cell, when three optical branches exist. The local change in the electron spectrum can then be written in the form

$$\varepsilon(\mathbf{p}, \mathbf{r}, t) = \varepsilon_0(\mathbf{p}) + \zeta(\mathbf{p})\mathrm{div}\mathbf{u}(\mathbf{r}, t), \quad (3)$$

where $\zeta(\mathbf{p})$ is the scalar function of the electron momentum. Similarly to (2), interaction of this type tends to zero in the long-wave limit. Secondly, there can exist interaction which is directly caused by the optical shift of sublattices and does not vanish in the long-wave limit,

$$\varepsilon(\mathbf{p}, \mathbf{r}, t) = \varepsilon_0(\mathbf{p}, t) + \zeta_i(\mathbf{p})u_i(\mathbf{r}, t), \quad (4)$$

where the coupling $\zeta_i(\mathbf{p})$ is a vector function. These two interaction types are essentially different because only the longitudinal phonon mode interacts with electrons in (3). We will therefore assume that the **k** wave vector of phonons is directed along the symmetry axis (below, axis *z*) for separating the longitudinal and transverse modes. We will first consider polarization interaction (3).

A solution to the kinetic equation for the electronic distribution function will be sought in the form $f_0[\varepsilon(\mathbf{p}, \mathbf{r}, t) + \delta f_p(\mathbf{r}, t)]$, where the $f_0$ equilibrium distribution function depends on the local energy value. Such an equilibrium function reduces the collision integral to zero. The chemical potential value is determined by the condition that the electron charge density should not change in local equilibrium. It is easy to see that this requirement results in redefining the coupling constant with phonons, $\zeta(\mathbf{p}) \longrightarrow \zeta(\mathbf{p}) - \langle\zeta(\mathbf{p})\rangle$, where angle brackets denote averaging over the Fermi surface,

$$\langle\ldots\rangle = \frac{1}{\nu_0}\int(\ldots)\frac{2dS_F}{v(2\pi)^3}.$$

It follows that the mean renormalized coupling constant vanishes,

$$\langle\zeta(\mathbf{p})\rangle = 0. \quad (5)$$

The equation for the Fourier component of the nonequilibrium addition to the distribution function can be written in the form

$$-i(\omega - \mathbf{k}\cdot\mathbf{v})\delta f_p(\mathbf{k}, \omega) + \gamma[\delta f_p(\mathbf{k}, \omega) - \langle\delta f_p(\mathbf{k}, \omega)\rangle] = -\psi_p(\mathbf{k}, \omega)\frac{df_0}{d\varepsilon}, \quad (6)$$

where we use the notation

$$\psi_p(\mathbf{k}, \omega) = \omega\zeta(\mathbf{p})\mathbf{k}\cdot\mathbf{u}(\mathbf{k}, \omega) + e\mathbf{v}\cdot\mathbf{E}(\mathbf{k}, \omega). \quad (7)$$

We use the relaxation time approximation, which is valid for scattering of electrons by defects and for electron–phonon scattering at temperatures above the Debye temperature when this scattering can be considered elastic. Electric field **E** that accompanies optical vibrations is an unknown function and, along with the optical shift, should be determined by simultaneously solving the equations that will be written below. The addition to the distribution function is sought in the form

$$\delta f_p(\mathbf{k}, \omega) = -\chi_p(\mathbf{k}, \omega)\frac{df_0}{d\varepsilon}.$$

Solving (6) yields

$$\chi_p(\mathbf{k}, \omega) = i[\psi_p(\mathbf{k}, \omega) + \gamma\langle\chi_p(\mathbf{k}, \omega)\rangle]/\Delta_p(\mathbf{k}), \quad (8)$$

[1] To my knowledge, the Coulomb screening of optical phonons was originally considered by Gurevich *et al.* [10].

where

$$\langle \chi_p(\mathbf{k}, \omega)\rangle = \frac{i\langle \psi_p(\mathbf{k}, \omega)/\Delta_p(\mathbf{k})\rangle}{1 - i\langle \gamma/\Delta_p(\mathbf{k})\rangle} \quad (9)$$

and

$$\Delta_p(\mathbf{k}) = \omega - \mathbf{k}\cdot\mathbf{v} + i\gamma. \quad (10)$$

This solution to the kinetic equation will be used to determine the electric field and the optical shift.

## 3. THE MAXWELL EQUATION FOR THE ELECTRIC FIELD

The Maxwell equations allow electric field **E** to be expressed via polarization **P**,

$$\mathbf{E}(\mathbf{k}, \omega) = -\frac{4\pi[\mathbf{k}(\mathbf{k}\cdot\mathbf{P}) - \omega^2\mathbf{P}/c^2]}{k^2 - \omega^2/c^2}. \quad (11)$$

Frequency $\omega$ that we are interested in is of the order of the frequency of optical phonons, that is, $10^2$ cm$^{-1}$. The wave vector $k$ of a light-excited phonon equals the wave vector of light in order of magnitude (in Raman scattering, the wave vector is determined by the transferred momentum), which amounts to $10^5$ cm$^{-1}$. This means that the condition $k \gg \omega/c$ is satisfied. We can then ignore the terms with $c^2$ in (11), and the relation between field and polarization takes the simple form

$$\mathbf{E}(\mathbf{k}, \omega) = -4\pi\mathbf{k}(\mathbf{k}\cdot\mathbf{P})/k^2. \quad (12)$$

It is clear from (12) that the electric field is longitudinal and only the longitudinal polarization component $P_z$ is essential.

Contributions to the electric polarization

$$P_z = NZu_z(\mathbf{k}, \omega) + \alpha E(\mathbf{k}, \omega) + \frac{ie}{k}\int \frac{2d^3p}{(2\pi)^3}\delta f_p(\mathbf{k}, \omega) \quad (13)$$

are made, first, by the dipole moment related to the optical shift ($N$ is the number of unit cells in unit volume, and $Z$ is the effective charge of ions) and, next, by polarization $\alpha$ of filled electron shells, and, lastly, there is the $\mathbf{P}_e$ contribution of free carriers determined by the density of their charge $\rho_e = -i\mathbf{k}\cdot\mathbf{P}_e$. Equation (13) and solution (8), (9) to the kinetic equation can be used to recast Maxwell equation (12) as

$$\varepsilon_e(k, \omega)E(\mathbf{k}, \omega) = -4\pi\beta_{fd}(k, \omega)u_z(\mathbf{k}, \omega), \quad (14)$$

where the electronic contribution to permittivity is

$$\varepsilon_e(k, \omega) = \varepsilon_\infty - \frac{4\pi e^2\nu_0\langle v_z/\Delta_p(\mathbf{k})\rangle}{k(1 - i\langle \gamma/\Delta_p(\mathbf{k})\rangle)} \quad (15)$$

and the high-frequency permittivity is $\varepsilon_\infty = 1 + 4\pi\alpha$.

The function

$$\beta_{fd}(k, \omega) = NZ - e\omega\nu_0\frac{\langle \zeta(\mathbf{p})/\Delta_p(\mathbf{k})\rangle}{1 - i\langle \gamma/\Delta_p(\mathbf{k})\rangle} \quad (16)$$

introduced by us is the Coulomb response of longitudinal optical phonons.

## 4. THE EQUATION OF MOTION FOR OPTICAL PHONONS

The equation of motion in the long-wave approximation for interaction (3) can be written in the form

$$(\omega_k^2 - \omega^2)u_j(\mathbf{k}, \omega) = \frac{Z}{M'}E_j(\mathbf{k}, \omega) + \frac{ik_j}{M'N}\int \frac{2d^3p}{(2\pi)^3}\zeta(\mathbf{p})\delta f_p(\mathbf{k}, \omega), \quad (17)$$

where $M'$ is the reduced mass of two atoms in the unit cell. Let the $\omega_k$ phonon frequency, which should be calculated in the absence of electric field $E$ ignoring all nonadiabatic corrections, be known. In the long-wave approximation, this frequency can be written as $\omega_k^2 = \omega_0^2 \pm s^2k^2$, where $s$ is of the order of the usual velocity of sound in metals and the sign corresponds to a maximum or a minimum of the phonon branch. In addition, it should be borne in mind that optical phonons always have damping $\Gamma^{\text{nat}} \approx \omega_k\sqrt{m/M}$ determined by anharmonic processes of decay to two or more phonons. The damping can be added to $\omega_k$ in the form $-i\Gamma^{\text{nat}}/2$.

The first term on the right-hand side of (17) is the force with which the electric field acts on the unit cell dipole moment that arises in optical vibrations. The last term is the driving force of conduction electrons, which appears as a result of deviations from adiabaticity conditions. Importantly, the local-equilibrium distribution function value makes no contribution to this force in conformity with the adiabatic approximation concept. As the problem under consideration is essentially classical, the equation for the driving force can formally be obtained from the Lagrangian of the electron–phonon system taking into account interaction (3). The $k_j$ wave vector then appears as a consequence of the integration by parts.

Using solution (8), (9) to the kinetic equation, we can rewrite equation of motion (17) in the form

$$(\tilde{\omega}^2 - \omega^2)u_z(\mathbf{k}, \omega) = \tilde{Z}E(\mathbf{k}, \omega)/M', \quad (18)$$

where $\tilde{\omega}$ is the renormalized phonon frequency,

$$\tilde{\omega}^2 = \omega_k^2 + \frac{\nu_0\omega k^2}{M'N}\left(\left\langle \frac{\zeta^2(\mathbf{p})}{\Delta_p(\mathbf{k})}\right\rangle + \frac{i\gamma\langle \zeta(\mathbf{p})/\Delta_p(\mathbf{k})\rangle^2}{1 - i\langle \gamma/\Delta_p(\mathbf{k})\rangle}\right) \quad (19)$$

and $\tilde{Z}$ is the renormalized effective charge of ions,

$$\tilde{Z} = Z - \frac{e\nu_0 k}{N} \times \left( \left\langle \frac{\zeta(\mathbf{p}) v_z}{\Delta_p(\mathbf{k})} \right\rangle + i\gamma \frac{\langle v_z/\Delta_p(\mathbf{k}) \rangle \langle \zeta(\mathbf{p})/\Delta_p(\mathbf{k}) \rangle}{1 - i\langle \gamma/\Delta_p(\mathbf{k}) \rangle} \right). \quad (20)$$

Using definition (10) and condition (5), we find

$$\tilde{Z} = \beta_{fd}(k, \omega)/N, \quad (21)$$

which allows the expression for the permittivity of the electron–phonon system to be eventually written as

$$\varepsilon(k, \omega) = \varepsilon_e(k, \omega) + 4\pi N\tilde{Z}^2/M'(\tilde{\omega}^2 - \omega^2). \quad (22)$$

Equation (22) has a clear physical meaning: the electron permittivity is augmented by the contribution of optical shifts determined by the renormalized (because of electron–phonon coupling) effective ionic charge and frequency of optical vibrations.

## 5. THE SHIFT AND DAMPING OF THE LONGITUDINAL OPTICAL MODE

Equation (15) gives known limiting expressions for the permittivity of the metal,

$$\varepsilon_e(k, \omega) - \varepsilon_\infty = \begin{cases} -\varepsilon_\infty \omega_{pe}^2/\omega(\omega + i\gamma), & kv_F < |\omega + i\gamma| \\ \varepsilon_\infty (k_0/k)^2 (1 + i\pi\omega/2kv_F), & kv_F > |\omega + i\gamma|, \end{cases} \quad (23)$$

where $\varepsilon_\infty$ is the high-frequency permittivity. Here, the first formula corresponds to the frequency-dependent Drude conductivity, and the plasma frequency of electrons is given by the integral over the Fermi surface

$$\omega_{pe}^2 = \frac{e^2}{3\pi^2\varepsilon_\infty} \int v\, dS_F.$$

The second formula describes the long-wave limit of Debye screening, and we retain a comparatively small imaginary term in this expression. The screening parameter is $k_0^2 = 4\pi e^2 \nu_0/e_\infty$.

The longitudinal mode frequency $\omega = \omega_{LO}$ is determined by the $\varepsilon(k, \omega) = 0$ condition, that is,

$$\omega^2 = \tilde{\omega}^2 + 4\pi N\tilde{Z}^2/M'\varepsilon_e(k, \omega). \quad (24)$$

The electron permittivity is large at frequencies of the order of the frequency of phonon vibrations and at $k \ll k_0$. The ratio between phonon frequency $\omega$ and the electron plasma frequency in metals contains the same adiabatic parameter, $\omega_0/\omega_{pe} \sim \sqrt{m/M}$, and (24) can be solved iteratively. In a first approximation, we obtain the longitudinal optical mode frequency and damping,

$$\omega_{LO}^2 - i\omega_{LO}\Gamma = \omega_k^2 + \frac{k^2\omega_k\nu_0}{M'N}\left\langle \frac{\zeta^2(\mathbf{p})}{\Delta_p(\mathbf{k})} \right\rangle + \frac{\omega_{pi}^2\varepsilon_\infty}{\varepsilon_e(k, \omega_k)}, \quad (25)$$

where $\omega_{pi}^2 = 4\pi NZ^2/\varepsilon_\infty M'$ is the square of the plasma frequency of ions, $\omega_{pi}^2 \sim \omega_0^2$.

In the absence of free electrons, the density of states $\nu_0 = 0$, and (24) gives the longitudinal mode frequency, $\omega_{LO}^2 = \omega_k^2 + \omega_{pi}^2$. The electric field does not influence the transverse mode, $\omega_{TO}^2 = \omega_k^2$. If two atoms in the cell are identical, we should set $Z = 0$, and the longitudinal mode frequency in the center of the Brillouin zone coincides with the transverse mode frequency; the difference, which we do not consider here, only appears in dispersion.

In the presence of carriers, (25) allows limiting expressions to be obtained for small and large parameter $\kappa = kv_F/|\omega_k + i\gamma|$ values. For small $\kappa$ values, factoring $\Delta_p(k = 0)$ out and using the asymptotic behavior of $\varepsilon_e(k, \omega)$ given by (23), we obtain

$$\omega_{LO}^2 - i\omega_{LO}\Gamma = \omega_k^2 - \omega_k(\omega_k + i\gamma)\left(\frac{\omega_{pi}}{\omega_{pe}}\right)^2 + \frac{\lambda\omega_k}{\omega_k + i\gamma}(sk)^2, \quad \kappa \ll 1, \quad (26)$$

where the dimensionless coupling constant is determined by the equality $\lambda = \langle \zeta^2(\mathbf{p}) \rangle \nu_0/M'Ns^2$. The equation for the density $\nu_0$ of electron states in the isotropic case contains the $ap_Fm^*/m$ factor, which takes into account the size of the Fermi surface and the effective mass ($a$ is the cell parameter).

In the opposite limiting case, the permittivity is determined by the second formula in (23), and the principal (purely imaginary) contribution of electron–phonon coupling is given by the integral over the Fermi surface band on which $v_z = 0$,

$$\nu_0\left\langle \frac{\zeta^2(\mathbf{p})}{\Delta_p(\mathbf{k})} \right\rangle = -i\pi \int \frac{2dS_F}{v(2\pi)^3} \zeta^2(\mathbf{p}) \delta(\mathbf{k} \cdot \mathbf{v}),$$

where $\delta(x)$ is the Dirac function. We can, through introducing some mean velocity $v_F$ on this band, express the integral via the dimensionless $\lambda$ constant by assuming

$$\frac{\nu_0 \langle \zeta^2(\mathbf{p})/\Delta_p(\mathbf{k}) \rangle}{M'N} = -\frac{i\pi s^2 \lambda}{2kv_F}.$$

As a result, we obtain

$$\omega_{LO}^2 - i\omega_{LO}\Gamma = \omega_k^2 - i\frac{\pi\omega_k s^2 k}{2v_F}\left(\lambda + \frac{\omega_{pi}^2}{s^2 k_0^2}\right) + \left(\frac{\omega_{pi}k}{k_0}\right)^2, \quad \kappa \gg 1. \tag{27}$$

Note that $\lambda$ in (26) and (27) vanishes in the isotropic case by virtue of condition (5).

It follows that, in the presence of free electrons, the frequency of longitudinal phonons is substantially, by $\omega_{pi}$, smaller than the corresponding frequency for a dielectric. This is a result of Coulomb screening. This decrease in frequency is accompanied by additional softening, broadening, and dispersion (26), which are small in the adiabatic parameter. The most substantial change is the appearance in limit (27) of positive dispersion independent of the electron–phonon coupling constant. As $\omega_{pi}^2/k_0^2 \approx s^2$, this dispersion has a reasonable value determined by the velocity of sound in order of magnitude. This term is absent at $Z = 0$, but there exists a contribution (not given in this work) of the order of $m/M$ of the same origin as the shift in the first formula in (1).

Another important change is additional damping [the terms in first parentheses in (27)]. Although this damping contains the $s/v_F \sim \sqrt{m/M}$ small adiabatic parameter, it is comparable with natural damping $\Gamma^{\text{nat}}$. Note that the term with $\lambda$ (electron–phonon coupling) is comparable here with the term resulting from Coulomb screening.

## 6. DEFORMATION ELECTRON–PHONON INTERACTION

The question of which one of interactions (3) and (4) is observed in reality should be answered experimentally. Both are possible in principle, but in case (4), transverse modes do not interact with free carriers. Consider the results obtained for deformation interaction (4).

The $\psi_p$ function in kinetic equation (6) changes as

$$\psi_p(\mathbf{k}, \omega) = -i\omega\zeta_i(\mathbf{p})u_i(\mathbf{k}, \omega) + e\mathbf{v}\cdot\mathbf{E}.$$

The right-hand side of the equations of motion [10],

$$(\omega_k^2 - \omega^2)u_i(\mathbf{k}, \omega) = \frac{Z}{M'}E_i - \frac{1}{M'N}\int\frac{2d^3p}{(2\pi)^3}\zeta_i(\mathbf{p})\delta f_p(\mathbf{k}, \omega), \tag{28}$$

and the response function

$$\beta_{fd}(k, \omega) = NZ + \frac{ie\omega\nu_0\langle\zeta_z(\mathbf{p})/\Delta_p(\mathbf{k})\rangle}{k(1 - i\langle\gamma/\Delta_p(\mathbf{k})\rangle)} \tag{29}$$

of the longitudinal optical mode also change [cf. (16)]. For the longitudinal mode, (19) is replaced by

$$\tilde{\omega}^2 = \omega_k^2 + \frac{\nu_0\omega}{M'N}\left(\left\langle\frac{\zeta_z^2(\mathbf{p})}{\Delta_p(\mathbf{k})}\right\rangle + i\gamma\frac{\langle\zeta_z(\mathbf{p})/\Delta_p(\mathbf{k})\rangle^2}{1 - i\langle\gamma/\Delta_p(\mathbf{k})\rangle}\right). \tag{30}$$

The effective renormalized charge $\tilde{Z}$ in (18) now equals

$$\tilde{Z} = Z - \frac{ie\nu_0}{N} \times\left(\left\langle\frac{\zeta_z^2(\mathbf{p})v_z}{\Delta_p(\mathbf{k})}\right\rangle + i\gamma\frac{\langle v_z/\Delta_p(\mathbf{k})\rangle\langle\zeta_z(\mathbf{p})/\Delta_p(\mathbf{k})\rangle}{1 - i\langle\gamma/\Delta_p(\mathbf{k})\rangle}\right). \tag{31}$$

As is easy to see with the help of (10) and condition (5), this equation only differs from $\beta_{fd}/N$ in the sign of the second term in (29).

Substituting (29)–(31) into the equation of motion for the longitudinal mode,

$$\left(\tilde{\omega}^2 - \omega^2 + \frac{4\pi\beta_{fd}(k, \omega)\tilde{Z}}{M'\varepsilon_e(k, \omega)}\right)u_z(\mathbf{k}, \omega) = 0, \tag{32}$$

and reducing the terms in parentheses to a common denominator, we find that large "adiabatic" terms cancel each other because of the vector character of interaction (4). The result for the frequency takes the form

$$\omega_{LO}^2 - i\omega_{LO}\Gamma = \omega_k^2 + \left(\omega_{pi}^2 + \frac{\omega\nu_0}{M'N}\left\langle\frac{\zeta_z^2(\mathbf{p})}{\Delta_p(\mathbf{k})}\right\rangle\right)\frac{\varepsilon_\infty}{\varepsilon_e(k, \omega)}. \tag{33}$$

The electric field does not participate in transverse mode vibrations, and the equation for their frequency and damping is directly obtained from (30),

$$\tilde{\omega}_{TO}^2 - i\omega_{TO}\Gamma = \omega_k^2 + \frac{\nu_0\omega_k}{M'N}\left\langle\frac{\zeta_x^2(\mathbf{p})}{\Delta_p(\mathbf{k})}\right\rangle, \tag{34}$$

where the $x$ axis is perpendicular to the direction $\mathbf{k}$ of phonon propagation.

We will use (33) and (34) to determine mode frequencies and dampings in the limits of small and large $\kappa = kv_F/|\omega_k + i\gamma|$ parameter values.

(1) *For the transverse mode* in the long-wave region,

$$\omega_{TO}^2 - i\omega_{TO}\Gamma = \omega_k^2 + \lambda\omega_0^2\frac{\omega_k}{\omega_k + i\gamma}, \quad \kappa \ll 1, \tag{35}$$

where dimensionless constant $\lambda$ is determined by the relation

$$\frac{\nu_0\langle\zeta_x^2(\mathbf{p})/\Delta_p(\mathbf{k})\rangle}{M'N} = \lambda\omega_0^2.$$

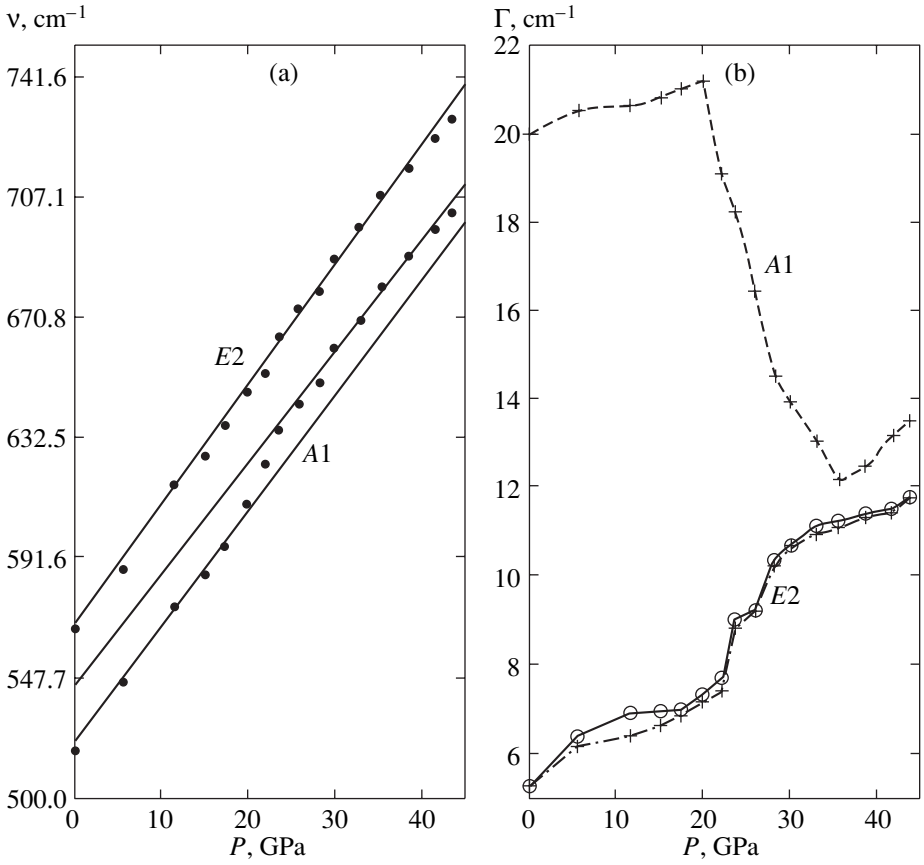


Changes in (a) frequency (quadratic scale) and (b) width for the transverse $E2$ and longitudinal $A1$ phonon modes of GaN under pressure. Straight lines were obtained by linear interpolation; two straight lines for $A1$ correspond to pressures below and above 23 GPa. Sharp changes at 23 GPa are explained by the metal–dielectric transition.

In the short-wave region, we have

$$\omega_{TO}^2 - i\omega_{TO}\Gamma = \omega_k^2 + \lambda\omega_0^2\frac{\omega_k}{kv_F}\left(\frac{\omega_k}{kv_F} - i\frac{\pi}{2}\right), \quad \kappa \gg 1, \tag{36}$$

and $\lambda$ arises in the integration over the Fermi surface band on which $v_z = 0$,

$$\frac{1}{M'N}\int\frac{2dS_F}{v(2\pi)^3}\frac{\zeta_x^2(\mathbf{p})}{\omega - \mathbf{kv} + i\gamma} = \lambda\frac{\omega_0^2}{kv_F}\left(\frac{\omega_k}{kv_F} - i\frac{\pi}{2}\right).$$

(2) *For the longitudinal mode,*

$$\omega_{LO}^2 - i\omega_{LO}\Gamma = \omega_k^2 - (\lambda\omega_0^2 + \omega_{pi}^2)\frac{\omega_k^2}{\omega_{pe}^2} - i\gamma\omega_k\frac{\omega_{pi}^2}{\omega_{pe}^2}, \quad \kappa \ll 1, \tag{37}$$

$$\omega_{LO}^2 - i\omega_{LO}\Gamma = \omega_k^2 - \lambda\omega_K(\omega_k + i\gamma)\frac{\omega_0^2}{(v_F k_0)^2} + \left(1 - i\frac{\pi\omega_k}{2kv_F}\right)\frac{\omega_{pi}^2}{k_0^2}k^2, \quad k \gg 1. \tag{38}$$

The $\lambda$ constant in (38) is given by

$$\frac{1}{M'N}\int\frac{2dS_F}{v(2\pi)^3}\frac{\zeta_z^2(\mathbf{p})}{v_z^2} = \lambda\frac{\omega_0^2}{v_F^2}.$$

Note that all the definitions of the electron–phonon coupling constant $\lambda$ used in this work give dimensionless values of the order of one for a typical metal. The $\lambda$ constant can vary because of changes in the $\nu_0$ density of electronic states.

## 7. DISCUSSION

First, consider the results that do not depend on the electron–phonon interaction model, that is, that do not contain the $\lambda$ constant. These are, first, softening of the longitudinal optical phonon mode by $\omega_{pi}$ compared with its value in the absence of free carriers and an additional decrease in the square of frequency $(\omega_k\omega_{pi}/\omega_{pe})^2$ [see (26) and (37)] in the region of small $\kappa$ values. Secondly, a positive dispersion of the same mode of the type $(\omega_{pi}k/k_0)^2 \approx (sk)^2$ [see (27) and (38)] appears at large $\kappa$ values. Thirdly, we have nonadiabatic damping induced by carriers in the same $\kappa$ region. All

these results arise from Coulomb screening of electric field by free carriers, which accompanies dipole lattice vibrations. They can be obtained by writing permittivity merely as the sum of ionic and electronic contributions and applying limiting equations (23) to it.

In addition, corrections are introduced by electron–phonon coupling, that is, by terms with $\lambda$ and collision frequency $\gamma$, which takes into account the contribution of electron–phonon coupling to conductivity. Clearly, these corrections depend on the character of coupling. They increase longitudinal mode damping for polarization interaction (27). The corresponding term in (38) for deformation interaction contains an additional power of the $\sqrt{m/M}$ adiabatic parameter.

The character of the interaction is essential for transverse modes. Polarization interaction has no effect on these modes, whereas deformation interaction (35) and (36) increases the mode frequency and introduces additional damping, as with acoustic modes (1). The only difference is in the shape of the $\omega_k$ spectrum, which now describes optical phonons.

Note that region (27) is most interesting for elucidating the role played by electron–phonon coupling. In this region, the contribution of electron–phonon coupling to damping competes with screening (terms in parentheses). In Raman experiments, the wave vector of phonons is determined by the $k \sim \omega^{in}/c$ wave vector of the incident laser beam of frequency $\omega^{in}$. We therefore have $\kappa = kv_F/|\omega_0 + i\gamma| \approx 0.3$ if $\omega^{in} \sim 10^4$ K, the frequency of the phonon excited in the center of the Brillouin zone is $\omega_0 \sim 10^2$ K, and the typical Fermi velocity value is $v_F \sim 10^8$ cm/s. Measurements of $\lambda$ therefore require the use of higher incident laser beam frequencies.

There is no experimental data on the influence of free electrons on damping of optical phonons in metals. We will, therefore, use the data on doped GaN obtained in [12]. The metal–dielectric transition occurs in GaN at 23 GPa as a result of electron band shifts. The density of free carriers then substantially decreases, from $5 \times 10^{19}$ cm$^{-3}$ to a value determined by the concentration of defects with shallow levels. The pressure dependence of the frequencies and widths of two phonon (transverse $E2$ and longitudinal $A1$) modes are shown in the figure borrowed from [13]. In addition to a monotonic increase in the frequencies and widths of both modes as pressure grows, the longitudinal mode experiences a sharp increase in frequency and a sharp decrease in width at 23 GPa, whereas no distinct changes occur in transverse mode characteristics at this pressure. These observations are unambiguous evidence that electron–phonon coupling in GaN results from the polarization interaction. The abrupt change in damping allows the frequency of collisions to be estimated by (26); this gives $\gamma = 3.5 \times 10^{14}$ s$^{-1}$. The effective mass is known, $m^* = 0.2m$; this gives mobility $\mu = 25$ cm$^2$/(s V), which corresponds with the experimental conductivity data.

## ACKNOWLEDGMENTS

The author thanks E.Zh. Mishchenko for discussions. This work was financially supported by the Russian Foundation for Basic Research (project no. 01-02-16211) and the Program of the Ministry of Industry, Science, and Technologies of Russian Federation for "Studies of Collective and Quantum Effects in Condensed Media."

## REFERENCES

1. A. B. Migdal, Zh. Éksp. Teor. Fiz. **34**, 1438 (1958) [Sov. Phys. JETP **7**, 996 (1958)].
2. M. Born and K. Huang, *Dynamical Theory of Crystal Lattices* (Clarendon, Oxford, 1954; Inostrannaya Literatura, Moscow, 1958), Chap. 4.
3. V. M. Kontorovich, Usp. Fiz. Nauk **142**, 265 (1984) [Sov. Phys. Usp. **27**, 134 (1984)].
4. E. G. Brovman and Yu. Kagan, Zh. Éksp. Teor. Fiz. **52**, 557 (1967) [Sov. Phys. JETP **25**, 365 (1967)].
5. B. T. Geilikman, J. Low Temp. Phys. **4**, 189 (1971).
6. S. Engelsberg and J. R. Schrieffer, Phys. Rev. **131**, 993 (1963).
7. I. P. Ipatova and A. V. Subashiev, Zh. Éksp. Teor. Fiz. **66**, 722 (1974) [Sov. Phys. JETP **39**, 349 (1974)].
8. A. S. Alexandrov and J. R. Schrieffer, Phys. Rev. B **56**, 13731 (1997).
9. M. Reizer, Phys. Rev. B **61**, 40 (2000).
10. V. L. Gurevich, A. I. Larkin, and Yu. A. Firsov, Fiz. Tverd. Tela (Leningrad) **4**, 185 (1962) [Sov. Phys. Solid State **4**, 131 (1962)].
11. L. A. Falkovsky and E. G. Mishchenko, Phys. Rev. B **51**, 7239 (1995); E. Zh. Mishchenko and L. A. Falkovsky, Zh. Éksp. Teor. Fiz. **107**, 936 (1995) [JETP **80**, 531 (1995)].
12. P. Perlin, W. Knap, J. Camassel, *et al.*, Phys. Status Solidi B **198**, 223 (1996); P. Perlin, C. Jauberthie-Carilon, J. P. Itie, *et al.*, Phys. Rev. B **45**, 83 (1992).
13. L. A. Falkovsky, W. Knap, J. C. Chervin, and P. Wisniewski, Phys. Rev. B **57**, 11349 (1998).

*Translated by V. Sipachev*

*Journal of Experimental and Theoretical Physics, Vol. 95, No. 2, 2002, pp. 361–370.*
*Translated from Zhurnal Éksperimental'noĭ i Teoreticheskoĭ Fiziki, Vol. 122, No. 2, 2002, pp. 419–428.*


**SOLIDS**
**Electronic Properties**

# The Theory of Conductivity of Ternary Composite Films with a Two-Sublattice Structure

**B. Ya. Balagurov**

*Emanuel Institute of Biochemical Physics, Russian Academy of Sciences, Moscow, 119991 Russia*
*e-mail: balagurov@deom.chph.ras.ru*

Received March 20, 2002

**Abstract**—A general method is suggested for solving problems on the conductivity and other effective characteristics of two-dimensional ternary two-sublattice models with inclusions of arbitrary shape. The complex potential outside of the inclusions is expressed in terms of the Weierstrass zeta function and its derivatives. The electric field induced on a separate inclusion is described using the matrix of multipole polarizabilities, for which the symmetry relation is found. The suggested approach enables one to find exact virial expansions for the basic electrophysical characteristics of such systems. © *2002 MAIK "Nauka/Interperiodica".*

## 1. INTRODUCTION

Certain progress has been made in studying the electrophysical properties of binary composites, which is especially significant in the case of two-dimensional systems. A number of analytical results were obtained, such as conductivity [1] and galvanomagnetic [2] and thermoelectric [3] characteristics of randomly inhomogeneous models with the critical composition. As was demonstrated in [4, 5], the results of [2, 3] may be extended to the case of arbitrary concentrations; for this, it is sufficient to know the dimensionless effective conductivity $f$. However, in the case of randomly inhomogeneous systems, the function $f$ in the entire range of variation of arguments is known only for unordered lattices as a result of numerical experiment.

Periodic models are in a more advantageous position: a number of exact results were obtained for their conductivity [6, 7] in the case of dielectric or ideally conducting inclusions. A closed solution of the problem with finite nonzero conductivity of both components was given in [1] for a model with a chessboard structure [6]. The conductivity and other effective characteristics of the more realistic Rayleigh model [8] were treated in sufficient detail in [9]. And, finally, a general method was suggested in [10] for the calculation of various electrophysical characteristics of two-dimensional binary periodic systems with inclusions of arbitrary shape.

The theory of ternary systems with much more varied properties is much less studied. Note the studies [11, 12] dealing with a two-dimensional two-sublattice system which is a generalization of the Rayleigh model—an isotropic matrix with staggered circular inclusions of two types with different radii and different conductivities. In [11], an approximate method was suggested for the calculation of the conductivity of this system. A solution to the problem on conductivity and other effective characteristics of a two-sublattice model (which is valid in the case of arbitrary concentrations) was given in [12]. Note that the methods used in [11, 12] are valid only for systems with circular inclusions.

In this study, I have treated the basic electrophysical characteristics of a two-dimensional ternary two-sublattice model with inclusions of arbitrary (though fairly symmetric—see Section 2) shape. The generalization of the method strength [10] made it possible to derive solutions to problems on the conductivity, thermal emf, Hall coefficient, and second-order partial moments of the electric field strength. The complex potential outside of the inclusions is expressed in terms of the Weierstrass zeta function [13] and its derivatives. The properties of the inclusions are entered in the form of multipole polarizabilities, i.e., of respective coefficients in the "responses" of these inclusions to various external fields. The symmetry relation is determined for the matrix of multipole polarizabilities.

## 2. MULTIPOLE POLARIZABILITIES

Let a medium of conductivity $\sigma_1$ have an inclusion (body) of conductivity $\sigma_2$. If a uniform field of developed in $\mathbf{E}_0$ is applied, the electric potential $\varphi$ in the dipole approximation has the following form (two-dimensional case) at large distances from the body:

$$\varphi(\mathbf{r}) = -\mathbf{E}_0 \cdot \mathbf{r} + 2\frac{\mathbf{p} \cdot \mathbf{r}}{r^2} + \ldots, \quad r \longrightarrow \infty. \qquad (1)$$

Here,

$$\mathbf{p} = \hat{\Lambda}\mathbf{E}_0 \qquad (2)$$

is the dipole moment of the inclusion, and $\hat{\Lambda}$ is the tensor of dipolar polarizability. If field $\mathbf{E}_0$ is directed along

one of the principal axes of the tensor $\hat{\Lambda}$ (we will select this axis to be the coordinate axis $x$), then

$$\varphi^{(x)}(r) = -E_0\left\{x - 2\frac{x\Lambda^{(x)}}{r^2} + \ldots\right\}, \quad r \longrightarrow \infty, \qquad (3)$$

where $\Lambda^{(x)}$ is the respective principal value of the tensor $\hat{\Lambda}$. For simplifying the rather cumbersome problems treated in Sections 3–7, we will restrict ourselves (as in [10]) to the case of fairly symmetric inclusions with a symmetry as that in the case of ellipse or higher.

In what follows, it will be convenient to use the complex potential

$$\Phi(z) = \varphi - iA, \quad z = x + iy. \qquad (4)$$

Here, $\varphi$ is the electric potential, and $A$ is the $z$ component of the vector potential determined according to

$$E = \mathrm{curl}\mathbf{A}, \quad \mathbf{A} = \{0, 0, A\}, \qquad (5)$$

so that

$$E_x = \frac{\partial A}{\partial y}, \quad E_y = -\frac{\partial A}{\partial x}, \qquad (6)$$

where $E_x$ and $E_y$ are the components of the electric field strength $\mathbf{E}$ outside of the inclusion. The derivative of the complex potential is related to $E_x$ and $E_y$ as

$$\Phi'(z) = -E_z + iE_y. \qquad (7)$$

The complex potential corresponding to expression (3) has the form

$$\Phi^{(x)}(z) = -E_0\left\{z - \frac{2\Lambda^{(x)}}{z} + \ldots\right\}, \quad |z| \longrightarrow \infty \qquad (8)$$

with the real constant $\Lambda^{(x)}$.

When the higher-order (multipole) moments are included, the expression for $\Phi(z)$ at high values of $|z|$ takes the form

$$\Phi^{(x)}(z) = z + \sum_{m=0}^{\infty}\frac{\Lambda^{(x)}_{1,2m+1}}{z^{2m+1}}. \qquad (9)$$

In Eq. (9), the common factor is omitted; the quantities $\Lambda^{(x)}_{1,2m+1}$ are real. A comparison of Eq. (9) with (8) reveals that $\Lambda^{(x)}_{11} = -2\Lambda^{(x)}$.

In what follows, we will further require the response of inclusion to a nonuniform external field of the form

$$\mathrm{Re}z^{2n+1} = r^{2n+1}\cos(2n+1)\vartheta,$$

where $\vartheta$ is the polar angle. In this case, we have, similarly to Eq. (9),

$$\Phi^{(x)}(z) = z^{2n+1} + \sum_{m=0}^{\infty}\frac{\Lambda^{(x)}_{2n+1,2m+1}}{z^{2m+1}} \qquad (10)$$

with real constants $\Lambda^{(x)}_{2n+1,2m+1}$, which will be referred to as multipole polarizabilities. Similarly, for an external field of the form

$$\mathrm{Im}z^{2n+1} = r^{2n+1}\sin(2n+1)\vartheta,$$

we have

$$\Phi^{(y)}(z) = -i\left\{z^{2n+1} - \sum_{m=0}^{\infty}\frac{\Lambda^{(y)}_{2n+1,2m+1}}{z^{2m+1}}\right\}. \qquad (11)$$

The constants $\Lambda^{(y)}_{2n+1,2m+1}$ are also taken to be real.

Dykhne's transformation [1] enables one to relate the complex potentials of the initial and so-called reciprocal (differing from the initial one by the substitutions $\sigma_1 \longrightarrow \sigma_2$, $\sigma_2 \longrightarrow \sigma_1$) systems (compare with [10]),

$$\Phi^{(x)}(z) = i\tilde{\Phi}^{(y)}(z). \qquad (12)$$

Here and below, the tilde indicates the quantities pertaining to the reciprocal system. The substitution of Eqs. (10) and (11) into (12) gives the relation [10]

$$\tilde{\Lambda}^{(y)}_{2n+1,2m+1} = -\Lambda^{(x)}_{2n+1,2m+1}. \qquad (13)$$

The following symmetry relation is valid for the multipole polarizabilities $\Lambda^{(v)}_{2n+1,2m+1}$ (see Appendix A):

$$(2m+1)\Lambda^{(v)}_{2n+1,2m+1} = (2n+1)\Lambda^{(v)}_{2m+1,2n+1}, \quad v = x, y. \qquad (14)$$

From considerations of dimensionality, it follows from Eqs. (10) and (11) that

$$\Lambda^{(v)}_{nm} = R^{n+m}\alpha^{(v)}_{nm}, \qquad (15)$$

where $R$ is the characteristic dimension (in the $xy$ plane) of inclusion and $\alpha^{(v)}_{nm}$ denotes dimensionless quantities dependent on the shape of inclusion and on the argument $h = \sigma_2/\sigma_1$.

## 3. ELECTRIC FIELD OUTSIDE OF INCLUSIONS

The model being investigated is a two-dimensional isotropic matrix of conductivity $\sigma_1$ with staggered inclusions of two types. The inclusions of the first type (identical and identically oriented) have the conductivity $\sigma_2$ and form a square lattice with a period of $2a$. The inclusions of the second type (also identical and identically oriented) have the conductivity $\sigma_3$ and form a similar lattice shifted by a half-period on the $x$ and $y$ axes. We will assume that the principal axes of the tensors of polarizability of inclusions of both types coincide with the axes of the lattice and with the $x$ and $y$ coordinate axes. Then, if the average electric field strength $\langle\mathbf{E}\rangle$ is directed along the $x$ or $y$ axis, all quantities $\Lambda_{nm}$ in Eqs. (10) and (11) are real. The problem on finding the

potential outside of inclusions is solved with the aid of an expansion in terms of the formally small parameter $R/a$, where, in this case, $R$ is the maximal "radius" of inclusions.

In a zero approximation, the complex potential corresponding to the uniform external field applied along the $x$ axis has the form

$$\Phi^{(0)}(z) = \beta z \tag{16}$$

with the real constant $\beta$. The response of inclusion of the first type, located at the origin of coordinates, to the field (16) is given, according to Eq. (9), by the expression

$$\begin{aligned}\Phi_{\mathrm{I}}^{(1)}(z) &= \beta\sum_{n=0}^{\infty}\frac{\Lambda_{1,2n+1}}{z^{2n+1}}\\ &= \beta\sum_{n=0}^{\infty}\frac{\Lambda_{1,2n+1}}{(2n)!}\left(\frac{d^{2n}}{dz^{2n}}\frac{1}{z}\right).\end{aligned} \tag{17}$$

Here and below, we omit the superscript $x$ on $\Phi^{(x)}(z)$ and $\Lambda_{nm}^{(x)}$. Similarly, for the response of inclusion of the second type with the center at the point $z = z_0$ to the field according to Eq. (16), we have

$$\begin{aligned}\Phi_{\mathrm{II}}^{(1)}(z) &= \beta\sum_{n=0}^{\infty}\frac{\lambda_{1,2n+1}}{(z-z_0)^{2n+1}}\\ &= \beta\sum_{n=0}^{\infty}\frac{\lambda_{1,2n+1}}{(2n)!}\left(\frac{d^{2n}}{dz^{2n}}\frac{1}{z-z_0}\right),\end{aligned} \tag{18}$$

where $z_0 = (1 + i)a$. Here, the superscript $x$ is also omitted, and $\lambda_{nm}$ denotes the matrix of multipole polarizabilities of inclusions of the second type.

We add up the responses of the type given by Eqs. (17) and (18) from all inclusions to derive the following expression for the first-approximation correction to Eq. (16):

$$\begin{aligned}&\Phi^{(1)}(z)\\ &= \beta\sum_{n=0}^{\infty}\{B_n^{(1)}\zeta^{(2n)}(z) + D_n^{(1)}\zeta^{(2n)}(z-z_0)\},\end{aligned} \tag{19}$$

$$B_n^{(1)} = \frac{1}{(2n)!}\Lambda_{1,2n+1}, \quad D_n^{(1)} = \frac{1}{(2n)!}\lambda_{1,2n+1}. \tag{20}$$

In Eq. (19), $\zeta(z)$ is the Weierstrass zeta function [13], and $\zeta^{(2n)}(z)$ is the derivative of the order $2n$ of $\zeta(z)$. The functions $\zeta(z)$ and $\zeta(z - z_0)$ (the terms with $n = 0$ in Eq. (19)) arise as a result of summation of the dipole potentials induced by the external field. In doing so, as in [9, 10], the respective sums are regularized, which provides for their convergence. The terms with $n \geq 1$ in Eq. (19) correspond to higher-order multipoles.

In the next approximation, the external (with respect to the preferred inclusion of the first type) potential is provided by $\Phi^{(1)}(z)$ from Eq. (19) less the eigenfield $\Phi_{\mathrm{I}}^{(1)}(z)$, i.e., the quantity $\Phi^{(1)}(z) - \Phi_{\mathrm{I}}^{(1)}(z)$. In searching for the response to this field, the following expansions in the neighborhood of the point $z = 0$ [12] are used:

$$\zeta^{(2n)}(z) = \frac{(2n)!}{z^{2n+1}} - \sum_{k=0}^{\infty}\frac{(2n+2k)!}{(2k+1)!}c_{n+k+1}z^{2k+1}, \tag{21}$$

$$\begin{aligned}\zeta^{(2n)}(z-z_0) &= -\zeta(z_0)\delta_{n0}\\ &- \sum_{k=0}^{\infty}\frac{(2n+2k)!}{(2k+1)!}d_{n+k+1}z^{2k+1},\end{aligned} \tag{22}$$

where $\zeta(z_0) = \pi(1 - i)/4a$ and $\delta_{nm}$ is the Kronecker symbol. The coefficients $c_{2n}$ have the following values [13]:

$$\begin{aligned}c_2 &= \frac{g_2}{20}, \quad g_2 = \frac{1}{a^4}\left[K\left(\frac{1}{\sqrt{2}}\right)\right]^4,\\ c_4 &= \frac{1}{3}c_2^2, \quad c_6 = \frac{2}{3\times 13}c_2^3,\\ c_8 &= \frac{5}{3\times 13\times 17}c_2^4, \ldots.\end{aligned} \tag{23}$$

Here, $K(1/\sqrt{2}) = 1.85407\ldots$ is the complete elliptic integral of the first kind $K(k)$ with the modulus $k = 1/\sqrt{2}$. The quantities $d_{2n}$ may be expressed in terms of $c_{2n}$ [12],

$$d_{2n} = [(-4)^n - 1]c_{2n}. \tag{24}$$

The coefficients $c_n$ and $d_n$ with odd subscripts in the case of square lattice being treated are zero [13].

Accordingly, for the inclusion of the second type (with the center at the point $z = z_0$), the external potential is provided by $\Phi^{(1)}(z) - \Phi_{\mathrm{II}}^{(1)}(z)$. Here, in searching for the response, the following expansions in the neighborhood of the point $z = z_0$ [12] are used:

$$\begin{aligned}\zeta^{(2n)}(z) &= \zeta(z_0)\delta_{n0}\\ &- \sum_{k=0}^{\infty}\frac{(2n+2k)!}{(2k+1)!}d_{n+k+1}(z-z_0)^{2k+1},\end{aligned} \tag{25}$$

$$\begin{aligned}\zeta^{(2n)}(z-z_0) &= \frac{(2n)!}{(z-z_0)^{2n+1}}\\ &- \sum_{k=0}^{\infty}\frac{(2n+2k)!}{(2k+1)!}d_{n+k+1}(z-z_0)^{2k+1}\end{aligned} \tag{26}$$

with the same coefficients $c_n$ and $d_n$.

On finding corrections of the second and subsequent orders (compare with [10]), we conclude that the total

potential outside of the inclusions has exactly the same form as in the case of circular inclusions [12],

$$\Phi(z) = \beta\left\{z + \sum_{n=0}^{\infty} B_n \zeta^{(2n)}(z) + \sum_{n=0}^{\infty} D_n \zeta^{(2n)}(z - z_0)\right\}. \quad (27)$$

The coefficients $B_n$ and $D_n$ satisfy the set of equations

$$B_n + \sum_{m=0}^{\infty} (F_{nm} B_m + H_{nm} D_m) = \frac{1}{(2n)!}\Lambda_{1,2n+1}, \quad (28)$$

$$D_n + \sum_{m=0}^{\infty} (K_{nm} B_m + L_{nm} D_m) = \frac{1}{(2n)!}\lambda_{1,2n+1}. \quad (29)$$

Here,

$$F_{nm} = \sum_{k=0}^{\infty} \frac{(2k+2m)!}{(2k+1)!} c_{k+m+1} \frac{\Lambda_{2k+1,2n+1}}{(2n)!}, \quad (30)$$

$$H_{nm} = \sum_{k=0}^{\infty} \frac{(2k+2m)!}{(2k+1)!} d_{k+m+1} \frac{\Lambda_{2k+1,2n+1}}{(2n)!}, \quad (31)$$

$$K_{nm} = \sum_{k=0}^{\infty} \frac{(2k+2m)!}{(2k+1)!} d_{k+m+1} \frac{\lambda_{2k+1,2n+1}}{(2n)!}, \quad (32)$$

$$L_{nm} = \sum_{k=0}^{\infty} \frac{(2k+2m)!}{(2k+1)!} c_{k+m+1} \frac{\lambda_{2k+1,2n+1}}{(2n)!}. \quad (33)$$

If field $\langle \mathbf{E} \rangle$ is directed along the $y$ axis, the complex potential outside of the inclusions has the form (the quantities relating to this case are marked with a bar above the letter),

$$\bar{\Phi}(z) = -i\beta \times\left\{z - \sum_{n=0}^{\infty} \bar{B}_n \zeta^{(2n)}(z) - \sum_{n=0}^{\infty} \bar{D}_n \zeta^{(2n)}(z - z_0)\right\}. \quad (34)$$

The coefficients $\bar{B}_n$ and $\bar{D}_n$ satisfy the set of equations

$$\bar{B}_n - \sum_{m=0}^{\infty} (\bar{F}_{nm} \bar{B}_m + \bar{H}_{nm} \bar{D}_m) = \frac{1}{(2n)!}\bar{\Lambda}_{1,2n+1}, \quad (35)$$

$$\bar{D}_n - \sum_{m=0}^{\infty} (\bar{K}_{nm} \bar{B}_m + \bar{L}_{nm} \bar{D}_m) = \frac{1}{(2n)!}\bar{\lambda}_{1,2n+1}. \quad (36)$$

The expressions for the matrices $\bar{F}_{nm}$, $\bar{H}_{nm}$, $\bar{K}_{nm}$, and $\bar{L}_{nm}$ follow from Eqs. (30)–(33) upon the substitutions $\Lambda_{nm} \longrightarrow \bar{\Lambda}_{nm} \equiv \Lambda^{(y)}_{nm}$, $\lambda_{nm} \longrightarrow \bar{\lambda}_{nm} \equiv \lambda^{(y)}_{nm}$. Formulas (27)–(36) provide the solution to the problem set.

## 4. SOME RELATIONS

We will introduce the "variables" $x_k$ and $y_k$ in accordance with

$$B_n = \frac{1}{(2n)!}\sum_{k=0}^{\infty} \Lambda_{2k+1,2n+1} x_k, \quad D_n = \frac{1}{(2n)!}\sum_{k=0}^{\infty} \lambda_{2k+1,2n+1} y_k. \quad (37)$$

For $x_k$ and $y_k$, we have the following set of equations:

$$x_k + \sum_{l=0}^{\infty} (M_{kl} x_l + P_{kl} y_l) = \delta_{k0}, \quad (38)$$

$$y_k + \sum_{l=0}^{\infty} (Q_{kl} x_l + N_{kl} y_l) = \delta_{k0}, \quad (39)$$

where $\delta_{k0}$ is the Kronecker symbol. The matrices $M_{kl}$, $P_{kl}$, $Q_{kl}$, and $N_{kl}$ satisfy the equations

$$M_{kl} = \sum_{m=0}^{\infty} \frac{(2k+2m)!}{(2k+1)!} c_{k+m+1} \frac{\Lambda_{2l+1,2m+1}}{(2m)!}, \quad (40)$$

$$P_{kl} = \sum_{m=0}^{\infty} \frac{(2k+2m)!}{(2k+1)!} d_{k+m+1} \frac{\lambda_{2l+1,2m+1}}{(2m)!}, \quad (41)$$

$$Q_{kl} = \sum_{m=0}^{\infty} \frac{(2k+2m)!}{(2k+1)!} d_{k+m+1} \frac{\Lambda_{2l+1,2m+1}}{(2m)!}, \quad (42)$$

$$N_{kl} = \sum_{m=0}^{\infty} \frac{(2k+2m)!}{(2k+1)!} c_{k+m+1} \frac{\lambda_{2l+1,2m+1}}{(2m)!}. \quad (43)$$

In view of definitions (37), one can readily make sure that Eqs. (38)–(43) yield the set of equations (28)–(33).

Similarly, we assume that

$$\bar{B}_n = \frac{1}{(2n)!}\sum_{k=0}^{\infty} \bar{\Lambda}_{2k+1,2n+1} \bar{x}_k, \quad \bar{D}_n = \frac{1}{(2n)!}\sum_{k=0}^{\infty} \bar{\lambda}_{2k+1,2n+1} \bar{y}_k, \quad (44)$$

to derive from Eqs. (35) and (36) the set of equations

$$\bar{x}_k - \sum_{l=0}^{\infty} (\bar{M}_{kl} \bar{x}_l + \bar{P}_{kl} \bar{y}_l) = \delta_{k0}, \quad (45)$$

$$\bar{y}_k - \sum_{l=0}^{\infty} (\bar{Q}_{kl} \bar{x}_l + \bar{N}_{kl} \bar{y}_l) = \delta_{k0}. \quad (46)$$

The expressions for the matrices $\bar{\bar{M}}_{kl}$, $\bar{\bar{P}}_{kl}$, $\bar{\bar{Q}}_{kl}$, and $\bar{\bar{N}}_{kl}$ follow from Eqs. (40)–(43) upon the substitutions $\Lambda_{nm} \longrightarrow \bar{\bar{\Lambda}}_{nm}$, $\lambda_{nm} \longrightarrow \bar{\bar{\lambda}}_{nm}$.

The introduction of the quantities $x_k$ and $y_k$ makes it possible to derive a number of useful relations (identities). We will treat a system of the same structure as the initial one but with different conductivities $\kappa_1$, $\kappa_2$, and $\kappa_3$ ($\kappa_i$ may be provided by, for example, thermal conductivity; see below). The quantities related to this system will be marked with a double bar. In this case, an equation similar to Eq. (38) will have the form

$$\bar{\bar{x}}_k + \sum_{l=0}^{\infty}(\bar{\bar{M}}_{kl}\bar{\bar{x}}_l + \bar{\bar{P}}_{kl}\bar{\bar{y}}_l) = \delta_{k0}. \tag{47}$$

We multiply Eq. (38) by $(2k+1)!\,\bar{\bar{B}}_k$ and Eq. (47) by $(2k+1)!\,B_k$, subtract one from the other, and sum over all values of $k$. As a result, in view of definitions (37) and symmetry relation (14), we have

$$\sum_k\sum_l(2k+1)[\bar{\bar{\Lambda}}_{2l+1,2k+1} - \Lambda_{2l+1,2k+1}]x_k\bar{\bar{x}}_l + \sum_k\sum_l(2k+2l)![\bar{\bar{B}}_kD_l - B_k\bar{\bar{D}}_l]d_{k+l+1} = \bar{\bar{B}}_0 - B_0. \tag{48}$$

In a similar manner, we find one more relation

$$\sum_k\sum_l(2k+1)[\bar{\bar{\lambda}}_{2l+1,2k+1} - \lambda_{2l+1,2k+1}]y_k\bar{\bar{y}}_l - \sum_k\sum_l(2k+2l)![\bar{\bar{B}}_kD_l - B_k\bar{\bar{D}}_l]d_{k+l+1} = \bar{\bar{D}}_0 - D_0. \tag{49}$$

Equations (48) and (49) yield the identity

$$\sum_k\sum_l(2k+1)[\bar{\bar{\Lambda}}_{2l+1,2k+1} - \Lambda_{2l+1,2k+1}]x_k\bar{\bar{x}}_l + \sum_k\sum_l(2k+1)[\bar{\bar{\lambda}}_{2l+1,2k+1} - \lambda_{2l+1,2k+1}]y_k\bar{\bar{y}}_l = \bar{\bar{B}}_0 - B_0 + \bar{\bar{D}}_0 - D_0. \tag{50}$$

The summation over $k$ and $l$ in Eqs. (48)–(50) proceeds from zero to $\infty$.

We will now multiply Eq. (38) by $(2k+1)!\,\bar{B}_k$ and Eq. (45) by $(2k+1)!\,B_k$, add up, and then sum over all values of $k$. As a result, we have

$$\sum_k\sum_l(2k+1)[\Lambda_{2l+1,2k+1} + \bar{\Lambda}_{2l+1,2k+1}]x_k\bar{x}_l + \sum_k\sum_l(2k+2l)![\bar{B}_kD_l - B_k\bar{D}_l]d_{k+l+1} = B_0 + \bar{B}_0. \tag{51}$$

In a similar manner, we find

$$\sum_k\sum_l(2k+1)[\lambda_{2l+1,2k+1} + \bar{\lambda}_{2l+1,2k+1}]y_k\bar{y}_l - \sum_k\sum_l(2k+2l)![\bar{B}_kD_l - B_k\bar{D}_l]d_{k+l+1} = D_0 + \bar{D}_0. \tag{52}$$

Equations (51) and (52) yield the identity

$$\sum_k\sum_l(2k+1)[\Lambda_{2l+1,2k+1} + \bar{\Lambda}_{2l+1,2k+1}]x_k\bar{x}_l + \sum_k\sum_l(2k+1)[\lambda_{2l+1,2k+1} + \bar{\lambda}_{2l+1,2k+1}]y_k\bar{y}_l = B_0 + \bar{B}_0 + D_0 + \bar{D}_0. \tag{53}$$

The summation over $k$ and $l$ in Eqs. (51)–(53) likewise proceeds from zero to $\infty$.

## 5. EFFECTIVE CONDUCTIVITY

We use the complex potential $\Phi(z)$ from Eq. (27) to calculate the voltage drop $U_x$ across a unit cell and the total current $I_x$ through the latter in the direction of the $x$ axis to derive, analogously with [12],

$$U_x = -2a\beta\left[1 + (B_0 + D_0)\frac{\pi}{4a^2}\right], \tag{54}$$

$$I_x = -2\sigma_1 a\beta\left[1 - (B_0 + D_0)\frac{\pi}{4a^2}\right]. \tag{55}$$

We find

$$\sigma_{xe} = \sigma_1 f_x, \quad f_x = \frac{1 - (B_0 + D_0)\dfrac{\pi}{4a^2}}{1 + (B_0 + D_0)\dfrac{\pi}{4a^2}}, \tag{56}$$

for the effective conductivity $\sigma_{xe} = I_x/U_x$ in the direction of the $x$ axis (i.e., for the respective principal value $\sigma_{xe}$ of the effective conductivity tensor $\hat{\sigma}_{xe}$).

In the case when field $\langle \mathbf{E} \rangle$ is directed along the $y$ axis, we derive for the effective conductivity $\sigma_{ye}$, similarly to Eq. (56),

$$\sigma_{ye} = \sigma_1 f_y, \quad f_y = \frac{1 - (\bar{B}_0 + \bar{D}_0)\frac{\pi}{4a^2}}{1 + (\bar{B}_0 + \bar{D}_0)\frac{\pi}{4a^2}} \tag{57}$$

with the coefficients $\bar{B}_0$ and $\bar{D}_0$ from Eq. (34).

The system being treated is, generally speaking, anisotropic. For such systems, the reciprocal relation has the form

$$\tilde{f}_x f_y = 1, \tag{58}$$

where tilde indicates a reciprocal system which differs from the initial one by the substitutions $\sigma_i/\sigma_1 \longrightarrow \sigma_1/\sigma_i$, $i = 2, 3$. The substitution of Eqs. (27) and (34) into relation (12) written in the form $\tilde{\Phi}(z) = i\bar{\Phi}(z)$ gives

$$\tilde{B}_n = -\bar{B}_n, \quad \tilde{D}_n = -\bar{D}_n. \tag{59}$$

It follows from Eqs. (56) and (57), in view of equalities (59), that reciprocal relation (58) is valid.

With low concentrations of inclusions, Eqs. (28) and (29) may yield, similarly to [10], the virial expansion for the coefficients $B_0$ and $D_0$ and, thereby, for the effective conductivity $\sigma_{xe}$.

Before turning to the calculation of other electrophysical characteristics of the model being treated, we will find the expressions for the complex potentials in the neighborhood of inclusions of the first ($z = 0$) and second ($z = z_0$) types. In the neighborhood of the point $z = 0$, we substitute expansions (21) and (22) into Eq. (27),

$$\Phi(z) = \beta\Bigg\{z + \sum_n B_n \frac{(2n)!}{z^{2n+1}} - \sum_n \Bigg[\sum_m \frac{(2n+2m)!}{(2n+1)!}(B_m c_{n+m+1} + D_m d_{n+m+1})\Bigg] \times z^{2n+1} - D_0\zeta(z_0)\Bigg\}. \tag{60}$$

Here, the substitution $n \longleftrightarrow m$ is performed in the double sum. We substitute the expressions for $B_m$ and $D_m$ written in terms of $x_l$ and $y_l$ (see Eq. (37)) into the sum over $m$ from Eq. (60). As a result,

$$\Phi(z) = \beta\Bigg\{z + \sum_n B_n \frac{(2n)!}{z^{2n+1}} - \sum_n \Bigg[\sum_l (M_{nl}x_l + P_{nl}y_l)\Bigg] z^{2n+1} - D_0\zeta(z_0)\Bigg\}. \tag{61}$$

We eliminate the sum over $l$ with the aid of Eq. (38) to finally derive

$$\Phi(z) = \beta\sum_{n=0}^{\infty}\Bigg\{B_n\frac{(2n)!}{z^{2n+1}} + x_n z^{2n+1}\Bigg\} - \beta D_0\zeta(z_0). \tag{62}$$

We similarly find from Eq. (34), after the substitution of (21) and (22),

$$\bar{\Phi}(z) = i\beta\sum_{n=0}^{\infty}\Bigg\{\bar{B}_n\frac{(2n)!}{z^{2n+1}} - \bar{x}_n z^{2n+1}\Bigg\} - i\beta\bar{D}_0\zeta(z_0). \tag{63}$$

In the neighborhood of the point $z = z_0$, we use expansions (25) and (26) to derive, respectively,

$$\Phi(z) = \beta\sum_{n=0}^{\infty}\Bigg\{D_n\frac{(2n)!}{(z-z_0)^{2n+1}} + y_n(z-z_0)^{2n+1}\Bigg\} + \beta[z_0 + B_0\zeta(z_0)], \tag{64}$$

$$\bar{\Phi}(z) = i\beta\sum_{n=0}^{\infty}\Bigg\{\bar{D}_n\frac{(2n)!}{(z-z_0)^{2n+1}} - \bar{y}_n(z-z_0)^{2n+1}\Bigg\} - i\beta[z_0 - \bar{B}_0\zeta(z_0)]. \tag{65}$$

## 6. THERMAL ELECTROMOTIVE FORCE

For a structurally anisotropic system, the effective thermoelectric coefficient is preassigned by the tensor $\hat{\alpha}_e$. In the case of a weak thermoelectric coupling, the principal values of the tensor $\hat{\alpha}_e$ are given by the expressions [14]

$$\alpha_{ve} = \frac{1}{\sigma_{ve}}\frac{\langle\alpha\sigma\mathbf{E}^{(v)}\mathbf{G}^{(v)}\rangle}{\langle\mathbf{E}^{(v)}\rangle\langle\mathbf{G}^{(v)}\rangle}, \quad v = x, y. \tag{66}$$

Here, $\langle\ldots\rangle$ is the average over the entire sample volume (area, in the two-dimensional case), $\mathbf{G} = -\nabla T$ is the temperature field "surface," and $T$ is the temperature; the superscript "$v$" in $\mathbf{E}^{(v)}$ and $\mathbf{G}^{(v)}$ indicates that $\langle\mathbf{E}^{(v)}\rangle$ and $\langle\mathbf{G}^{(v)}\rangle$ are directed along the $v$ axis.

For an $N$-component system, from Eq. (66) follows

$$\sigma_{ve} = \sum_{i=1}^{N}\alpha_i\Psi_i^{(v)}, \quad v = x, y, \tag{67}$$

where

$$\Psi_i^{(v)} = \frac{\sigma_i}{\sigma_{ve}}\frac{\langle\mathbf{E}^{(v)}\mathbf{G}^{(v)}\rangle^{(i)}}{\langle\mathbf{E}^{(v)}\rangle\langle\mathbf{G}^{(v)}\rangle}. \tag{68}$$

Here, $\langle\ldots\rangle^{(i)}$ is the volume (surface, in the two-dimensional case) integral of the $i$th component divided by the sample volume (surface).

For the functions $\Psi_i^{(\nu)}$, the "sum rules" similar to the isotropic case are valid [12],

$$\sum_{i=1}^{N} \Psi_i^{(\nu)} = 1, \tag{69}$$

$$\sum_{i=1}^{N} \frac{\kappa_i}{\sigma_i} \Psi_i^{(\nu)} = \frac{\kappa_{ve}}{\sigma_{ve}}; \quad \nu = x, y. \tag{70}$$

Here, $\kappa_i$ is the thermal conductivity of the $i$th component, and $\kappa_{ve}$ denotes the principal values of the effective tensor of thermal conductivity $\hat{\kappa}_e$.

For ternary systems, we use Eq. (69) to find from (67), after elimination of $\Psi_1^{(\nu)}$,

$$\alpha_{ve} = \alpha_1 + (\alpha_2 - \alpha_1)\Psi_2^{(\nu)} + (\alpha_3 - \alpha_1)\Psi_3^{(\nu)}. \tag{71}$$

After a similar procedure, Eq. (70) gives the relation

$$\left(\frac{\kappa_1}{\sigma_1} - \frac{\kappa_2}{\sigma_2}\right)\Psi_2^{(\nu)} + \left(\frac{\kappa_1}{\sigma_1} - \frac{\kappa_3}{\sigma_3}\right)\Psi_3^{(\nu)} = \frac{\kappa_1}{\sigma_1} - \frac{\kappa_{ve}}{\sigma_{ve}}, \tag{72}$$

which makes possible the elimination of $\Psi_3^{(\nu)}$ or $\Psi_2^{(\nu)}$ from Eq. (71).

The problems on thermal conductivity and electrical conductivity in the absence of thermoelectric effects change into one another during the permutation $\kappa \longleftrightarrow \sigma$. Therefore, the results given in Sections 2–5 are extended to the problem on thermal conductivity by means of substitutions $\sigma_i \longrightarrow \kappa_i$, $\sigma_{ve} \longrightarrow \kappa_{ve}$; the quantities related to this system will be marked with a double bar.

In order to calculate the bilinear characteristics of $\langle \mathbf{E}^{(\nu)}\mathbf{G}^{(\nu)}\rangle^{(i)}$ (for $i = 2, 3$), we will use the formula analogous to that derived in [10] (see expression (A.5) in [10]),

$$\int_{S_i} (\mathbf{E}^{(\nu)}\mathbf{G}^{(\nu)})\,d\mathbf{r} = \frac{1}{\frac{\kappa_i}{\kappa_1} - \frac{\sigma_i}{\sigma_1}} \times \int_0^{2\pi} \left(\varphi^{(\nu)}\frac{\partial T^{(\nu)}}{\partial r} - T^{(\nu)}\frac{\partial \varphi^{(\nu)}}{\partial r}\right)\Bigg|_{r=\rho} \rho\, d\vartheta. \tag{73}$$

On the left here is the area integral for inclusion of the first ($i = 2$) or second ($i = 3$) type. On the right is the integral over a circle whose radius $\rho$ exceeds the maximal "radius" of each one of the inclusions.

We calculate the integrals on the right-hand side of Eq. (73) using the potentials given by Eqs. (62) and (64) and the respective "temperature potentials" to find

$$\langle \mathbf{E}^{(x)}\mathbf{G}^{(x)}\rangle^2 = \frac{\pi}{2a^2}\frac{\beta\bar{\bar{\beta}}}{\frac{\kappa_2}{\kappa_1} - \frac{\sigma_2}{\sigma_1}} \times \sum_{n=0}^{\infty}\sum_{m=0}^{\infty} (2n+1)[\Lambda_{2m+1,2n+1} - \bar{\bar{\Lambda}}_{2m+1,2n+1}]x_n\bar{\bar{x}}_m, \tag{74}$$

$$\langle \mathbf{E}^{(x)}\mathbf{G}^{(x)}\rangle^3 = \frac{\pi}{2a^2}\frac{\beta\bar{\bar{\beta}}}{\frac{\kappa_3}{\kappa_1} - \frac{\sigma_3}{\sigma_1}} \times \sum_{n=0}^{\infty}\sum_{m=0}^{\infty} (2n+1)[\lambda_{2m+1,2n+1} - \bar{\bar{\lambda}}_{2m+1,2n+1}]y_n\bar{\bar{y}}_m. \tag{75}$$

The substitution into Eq. (68) of formulas (74) and (75), $\langle E_x^{(x)}\rangle = U_x/2a$ with $U_x$ from (54), and of the similar (with the replacement of $B_0$ and $D_0$ by $\bar{\bar{B}}_0$ and $\bar{\bar{D}}_0$ and $\beta$ by $\bar{\bar{\beta}}$) formula for $\langle G_x^{(x)}\rangle$ gives the sought expressions for the functions $\Psi_2^{(x)}$ and $\Psi_3^{(x)}$. One can readily see that these expressions satisfy relation (72) by virtue of identity (50). The functions $\Psi_2^{(y)}$ and $\Psi_3^{(y)}$ are found analogously.

Directly related to the effective conductivity tensor $\hat{\sigma}_e$ are the partial quadratic characteristics of the electric field strength (see, for example, [10]),

$$\psi_i^{(\alpha)} \equiv \langle (\mathbf{e}^{(\alpha)})^2\rangle^{(i)} = \frac{\partial \sigma_{\alpha e}}{\partial \sigma_i}, \qquad \mathbf{e}^{(\alpha)}(\mathbf{r}) = \frac{\mathbf{E}^{(\alpha)}(\mathbf{r})}{|\langle \mathbf{E}^{(\alpha)}\rangle|}, \tag{76}$$

where $\langle\ldots\rangle^{(i)}$ is as in Eq. (68).

We will use formula (74) in order to calculate $\psi_2^{(x)}$. We assume in Eq. (74) that $\kappa_1 = \sigma_1$, $\kappa_3 = \sigma_3$, and $\bar{\bar{\beta}} = \beta$, and then perform the limiting transition $\kappa_2 \longrightarrow \sigma_2$ to find $\langle \mathbf{E}^2\rangle^{(2)}$. As a result, in view of the equality $\langle E_x^{(x)}\rangle = U_x/(2a)$ (with $U_x$ from Eq. (54)), we find

$$\psi_2^{(x)} = -\sigma_1\frac{\pi}{2a^2}\frac{1}{\Delta^2} \times \sum_{n=0}^{\infty}\sum_{m=0}^{\infty} (2n+1)\frac{\partial \Lambda_{2m+1,2n+1}}{\partial \sigma_2}x_n x_m, \tag{77}$$

$$\Delta = 1 + (B_0 + D_0)\frac{\pi}{4a^2}. \tag{78}$$

We use a similar limiting transition (in view of the fact that $\partial\lambda_{nm}/\partial\sigma_2 \equiv 0$) to find, from identity (50),

$$\sum_{n=0}^{\infty}\sum_{m=0}^{\infty}(2n+1)\frac{\partial\Lambda_{2m+1,2n+1}}{\partial\sigma_2}x_n x_m = \frac{\partial}{\partial\sigma_2}(B_0+D_0), \tag{79}$$

so that

$$\psi_2^{(x)} = -\sigma_1\frac{\pi}{2a^2}\frac{1}{\Delta^2}\frac{\partial}{\partial\sigma_2}(B_0+D_0). \tag{80}$$

One can readily see that the right-hand side of identity (80) is a derivative of $\sigma_{xe}$ from Eq. (56),

$$\psi_2^{(x)} = \frac{\partial\sigma_{xe}}{\partial\sigma_2}. \tag{81}$$

The functions $\psi_3^{(x)}$, as well as $\psi_2^{(y)}$ and $\psi_3^{(y)}$, are found analogously.

## 7. HALL COEFFICIENT

The effective Hall coefficient $R_e$ in a low magnetic field $H$ is expressed in terms of the Hall component $\sigma_{ae}$ of the effective conductivity tensor as follows:

$$R_e = \frac{1}{H}\frac{\sigma_{ae}}{\sigma_{xe}\sigma_{ye}}. \tag{82}$$

For an $N$-component system in a linear (with respect to $H$) approximation, we have [12]

$$\sigma_{ae} = \sum_{i=1}^{N}\sigma_{ai}\varphi_{ai}, \tag{83}$$

$$\varphi_{ai} = \frac{\langle E_x^{(x)}E_y^{(y)} - E_y^{(x)}E_x^{(y)}\rangle^{(i)}}{\langle E_x^{(x)}\rangle\langle E_y^{(y)}\rangle}, \tag{84}$$

where $\langle\ldots\rangle^{(i)}$ is as in Eqs. (68) and (76).

For the functions $\varphi_{ai}$, the "sum rule" is valid [12],

$$\sum_{i=1}^{N}\varphi_{ai} = 1, \tag{85}$$

for both two- and three-dimensional media. Another relation is available in the two-dimensional case [12],

$$\sum_{i=1}^{N}\sigma_i^2\varphi_{ai} = \sigma_{xe}\sigma_{ye}, \tag{86}$$

which relates the quantities $\varphi_{ai}$ to the components of the effective conductivity tensor (at $H = 0$).

For a ternary system, we use Eq. (85) to eliminate $\varphi_{a1}$ and find, from Eq. (83),

$$\sigma_{ae} = \sigma_{a1} + (\sigma_{a2}-\sigma_{a1})\varphi_{a2} + (\sigma_{a3}-\sigma_{a1})\varphi_{a3}. \tag{87}$$

After a similar procedure, Eq. (86) gives the relation

$$(1-h_2^2)\varphi_{a2} + (1-h_3^2)\varphi_{a3} = 1 - f_x f_y, \tag{88}$$

where $h_i = \sigma_i/\sigma_1$. Using equality (88) in the two-dimensional case enables one to restrict oneself to calculating only one of the functions $\varphi_{ai}$, for example, $\varphi_{a2}$. On the other hand, relation (88), as well as (72), may be used to check the accuracy of calculations of the respective effective quantities.

In order to calculate the integrals appearing in the definition of the functions $\varphi_{ai}$, we will use the formula analogous to that derived in [10] (see expression (B.12) in [10]),

$$\int_{S_i}[\mathbf{E}^{(x)}\times\mathbf{E}^{(y)}]_z d\mathbf{r} = \frac{1}{1-h_i^2} \times\int_0^{2\pi}\left\{\varphi^{(x)}\frac{1}{r}\frac{\partial\varphi^{(y)}}{\partial\vartheta} + A^{(x)}\frac{\partial\varphi^{(y)}}{\partial r}\right\}\Bigg|_{r=\rho}\rho\, d\vartheta. \tag{89}$$

On the left here is the surface integral for inclusion of the first ($i = 2$) or second ($i = 3$) type; $[\ldots]_z$ is the $z$ component of the vector product. On the right of Eq. (89) is the integral over a circle of radius $\rho$ within which the inclusion is located.

We substitute into Eq. (89) $\varphi^{(x)} = \mathrm{Re}\,\Phi(z)$, $A^{(x)} = -\mathrm{Im}\,\Phi(z)$, and $\varphi^{(y)} = \mathrm{Re}\,\overline{\Phi}(z)$ with $\Phi(z)$ and $\overline{\Phi}(z)$ from Eqs. (62), (63) and (64), (65), respectively. On calculating the integrals, we derive the following expressions for the functions $\varphi_{a2}$ and $\varphi_{a3}$:

$$\varphi_{a2} = \frac{\pi}{2a^2}\frac{1}{\Delta\bar{\Delta}}\frac{1}{1-h_2^2} \times\sum_{n=0}^{\infty}\sum_{m=0}^{\infty}(2n+1)[\Lambda_{2m+1,2n+1}+\bar{\Lambda}_{2m+1,2n+1}]x_n\bar{x}_m, \tag{90}$$

$$\varphi_{a3} = \frac{\pi}{2a^2}\frac{1}{\Delta\bar{\Delta}}\frac{1}{1-h_3^2} \times\sum_{n=0}^{\infty}\sum_{m=0}^{\infty}(2n+1)[\lambda_{2m+1,2n+1}+\bar{\lambda}_{2m+1,2n+1}]y_n\bar{y}_m, \tag{91}$$

with $\Delta$ from Eq. (78) and

$$\bar{\Delta} = 1 + (\bar{B}_0+\bar{D}_0)\frac{\pi}{4a^2}. \tag{92}$$

Expressions (90) and (91) satisfy relation (88) by virtue of identity (53).

## 8. CONCLUSION

Note that, for circular inclusions, the matrices of multipole polarizabilities are diagonal,

$$\Lambda_{nm} = R^{2n}\frac{1-h_2}{1+h_2}\delta_{nm}, \quad \lambda_{nm} = \rho^{2n}\frac{1-h_3}{1+h_3}\delta_{nm}, \quad (93)$$

where $R$ and $\rho$ are the radii of inclusions. We will introduce new "variables" $\xi_n$ and $\eta_n$ in the following way:

$$\xi_n = \sqrt{2n+1}R^{2n}x_n, \quad \eta_n = \sqrt{2n+1}\rho^{2n}y_n. \quad (94)$$

One can readily make sure that, upon substitution of Eqs. (93) and (94) into the relations and formulas derived in this study, they transform to the respective expressions from [12].

Note further that, at $\lambda_{nm}^{(v)} = 0$ (with $D_n = 0$ and $y_n = 0$), the investigated ternary two-sublattice model transforms into a binary model treated in [10]. A number of formulas derived in this study transform to those derived in [10]. As to the results associated with the "variables" $x_n$, they represent a further development of the method employed in [10].

## *APPENDIX A*

We will treat the surface integral

$$I = \int\limits_{r\le\rho} (\mathbf{E}_n\sigma(\mathbf{r})\mathbf{E}_m)d\mathbf{r} \quad (A.1)$$

for a circle of radius $\rho$, within which some inclusion is located. Here, $\mathbf{E}_n = -\nabla\varphi_n$ and $\mathbf{E}_m = -\nabla\varphi_m$, where $\varphi_n(\mathbf{r}) = \mathrm{Re}\Phi_n(z)$ and $\varphi_m(\mathbf{r}) = \mathrm{Re}\Phi_m(z)$. The complex potentials $\Phi_n(z)$ and $\Phi_m(z)$ exhibit the following asymptotic behavior:

$$\Phi_n(z) = z^n + \sum_{k=1}^{\infty}\frac{\Lambda_{nk}}{z^k}, \quad n \ge 1, \quad (A.2)$$

$$\Phi_m(z) = z^m + \sum_{l=1}^{\infty}\frac{\Lambda_{ml}}{z^l}, \quad m \ge 1. \quad (A.3)$$

On the one hand, integral (A.1) may be written as

$$I = \int\limits_{r\le\rho} (\mathbf{j}_n \cdot \mathbf{E}_m)dr, \quad (A.4)$$

where

$$\mathbf{j}_n = \sigma(\mathbf{r})\mathbf{E}_n \quad (A.5)$$

is the current density. By virtue of the equation $\mathrm{div}\,\mathbf{j}_n = 0$, integral (A.4) may be transformed to

$$\begin{aligned} I &= -\int\limits_{r\le\rho} (\mathbf{j}_n\nabla\varphi_m)d\mathbf{r} = -\int\limits_{r\le\rho}\nabla(\mathbf{j}_n\varphi_m)d\mathbf{r} \\ &= -\sigma_1\int_0^{2\pi}\left[\varphi_n\frac{\partial\varphi_n}{\partial r}\right]\Bigg|_{r=\rho}\rho\,d\vartheta. \end{aligned} \quad (A.6)$$

On the other hand,

$$\begin{aligned} I &= \int\limits_{r\le\rho} (\mathbf{E}_n \cdot \mathbf{j}_m)d\mathbf{r} = \ldots \\ &= -\sigma_1\int_0^{2\pi}\left[\varphi_n\frac{\partial\varphi_m}{\partial r}\right]\Bigg|_{r=\rho}\rho\,d\vartheta. \end{aligned} \quad (A.7)$$

We subtract (A.7) from (A.6) to derive

$$\int_0^{2\pi}\left[\varphi_n\frac{\partial\varphi_m}{\partial r} - \varphi_m\frac{\partial\varphi_n}{\partial r}\right]\Bigg|_{r=\rho}\rho\,d\vartheta = 0. \quad (A.8)$$

Identity (A.8) is valid for arbitrary values of $\rho$ ($\rho > R$, where $R$ is the maximal "radius" of inclusion), including the case of $\rho \longrightarrow \infty$. We use asymptotic expressions (A.2) and (A.3) to derive, from (A.8),

$$m\Lambda_{nm} = n\Lambda_{mn}. \quad (A.9)$$

One can readily make sure that the matrix of multipole polarizabilities for an elliptic inclusion (see [10]) satisfies relation (A.9).

## *APPENDIX B*

We will now treat the integral

$$\int\limits_S (\mathbf{E}_n \cdot \mathbf{G}_m)d\mathbf{r} \quad (B.1)$$

taken over the surface of inclusion $S$. Here, $\mathbf{E}_n$ is as in Eq. (A.1), and $\mathbf{G}_m = -\nabla T_m$, where $T_m(\mathbf{r}) = \mathrm{Re}\,\overline{\overline{\Phi}}_m(z)$ and $\overline{\overline{\Phi}}_m(z)$ exhibits asymptotic behavior similar to that of Eq. (A.3) (with the substitution of $\Lambda_{ml}$ by $\overline{\overline{\Lambda}}_{ml}$). We calculate integral (B.1) using formula (73) to derive

$$\int\limits_S (\mathbf{E}_n \cdot \mathbf{G}_m)d\mathbf{r} = 2\pi\frac{m(\Lambda_{nm} - \overline{\overline{\Lambda}}_{nm})}{\dfrac{\kappa_2}{\kappa_1} - \dfrac{\sigma_2}{\sigma_1}}. \quad (B.2)$$

Symmetry relation (A.9) was used in deriving formula (B.2). We make a transition in Eq. (B.2) to the limit $\kappa_2/\kappa_1 \longrightarrow \sigma_2/\sigma_1$ to find

$$\int\limits_S (\mathbf{E}_n \cdot \mathbf{E}_m)d\mathbf{r} = -2\pi m\frac{\partial\Lambda_{nm}}{\partial h}, \quad h = \frac{\sigma_2}{\sigma_1}. \quad (B.3)$$

In determining the multipole polarizabilities $\Lambda_{nm}$ by numerical methods, relation (B.3) enables one to find the derivatives $\partial\Lambda_{nm}/\partial h$ without performing difficult numerical differentiation.

## REFERENCES


1. A. M. Dykhne, Zh. Éksp. Teor. Fiz. **59**, 110 (1970) [Sov. Phys. JETP **32**, 63 (1971)].
2. A. M. Dykhne, Zh. Éksp. Teor. Fiz. **59**, 641 (1970) [Sov. Phys. JETP **32**, 348 (1971)].
3. B. Ya. Balagurov, Fiz. Tekh. Poluprovodn. (Leningrad) **16**, 259 (1982) [Sov. Phys. Semicond. **16**, 1204 (1982)].
4. B. Ya. Balagurov, Zh. Éksp. Teor. Fiz. **82**, 1333 (1982) [Sov. Phys. JETP **55**, 774 (1982)].
5. B. Ya. Balagurov, Zh. Éksp. Teor. Fiz. **85**, 568 (1983) [Sov. Phys. JETP **58**, 331 (1983)].
6. Yu. P. Emets, *Electrical Properties of Composites with Regular Structure* (Naukova Dumka, Kiev, 1986).
7. B. Ya. Balagurov, Zh. Éksp. Teor. Fiz. **79**, 1561 (1980) [Sov. Phys. JETP **52**, 787 (1980)].
8. Lord Rayleigh, Philos. Mag. **34**, 481 (1892).
9. B. Ya. Balagurov and V. A. Kashin, Zh. Éksp. Teor. Fiz. **117**, 978 (2000) [JETP **90**, 850 (2000)].
10. B. Ya. Balagurov, Zh. Éksp. Teor. Fiz. **120**, 668 (2001) [JETP **93**, 586 (2001)].
11. Yu. P. Emets, Zh. Éksp. Teor. Fiz. **114**, 1121 (1998) [JETP **87**, 612 (1998)].
12. B. Ya. Balagurov, Zh. Éksp. Teor. Fiz. **119**, 142 (2001) [JETP **92**, 123 (2001)].
13. *Handbook of Mathematical Functions*, Ed. by M. Abramowitz and I. A. Stegun (National Bureau of Standards, Washington, 1964; Nauka, Moscow, 1979).
14. B. Ya. Balagurov, Fiz. Tekh. Poluprovodn. (Leningrad) **21**, 1978 (1987) [Sov. Phys. Semicond. **21**, 1198 (1987)].


*Translated by H. Bronstein*